# Correlated Electronic and Vibrational Motion: A Direct Perspective Through Multidimensional Electronic-Vibrational Spectroscopy

James Daniel Gaynor

A dissertation

submitted in partial fulfillment of the

requirements for the degree of

Doctor of Philosophy

University of Washington

2019

Reading Committee:

Munira Khalil, Chair

Anne B. McCoy

Xiaosong Li

Program Authorized to Offer Degree:

Chemistry

University of Washington

## Abstract

Correlated Electronic and Vibrational Motion: A Direct Perspective
Through Multidimensional Electronic-Vibrational Spectroscopy

James Daniel Gaynor

Chair of the Supervisory Committee:
Professor Munira Khalil
Chemistry

Developing a thorough mechanistic understanding of photoexcited charge transfer and proton transfer reactions at the molecular-level requires a deep knowledge of coupled electronic and nuclear motion. Two-Dimensional Electronic-Vibrational (2D EV) spectroscopy and Two-Dimensional Vibrational-Electronic (2D VE) spectroscopy are recently developed techniques that are directly sensitive to molecular vibronic couplings. This dissertation advances 2D EV spectroscopy by implementing new broadband femtosecond light sources in the UV (370 nm – 440 nm) and the mid-IR (1600 $cm^{-1}$-3200 $cm^{-1}$) frequency domains. A theoretical interpretation of 2D EV and 2D VE spectral signals is constructed using a vibronic Hamiltonian to systematically simulate spectra of a single anharmonic vibration with linear (equilibrium displacement) and quadratic (frequency

shifting) vibronic coupling in the first excited electronic state. Selection rules are established from this analysis which demonstrate these techniques' sensitivities to vibronic couplings, non-Condon effects, and electronic-state-dependent vibrational dephasing. This treatment is extended to a system of two coupled anharmonic vibrations with consideration of the orientational response. These simulations show that excited state vibrational (Duschinsky) mixing and non-Condon effects may be directly measured through polarization-dependent 2D EV spectroscopy. Finally, three photochemical reactions are studied using 2D EV spectroscopy: the ligand-to-metal charge transfer (LMCT) of ferricyanide ($[Fe(CN)_6]^{3-}$), the metal-to-ligand charge transfer (MLCT) of the solar cell dye molecule $[Ru(dcbpy)_2(NCS)_2]^{4-}$ (dcbpy = 4,4'-dicarboxy-2,2'-bipyridine) known as $N3^{4-}$, and the excited state intramolecular proton transfer (ESIPT) of 10-hydroxy[*h*]benzoquinoline (HBQ).

Notably, specific MLCT excited states in $N3^{4-}$ are revealed to vibronically couple the intramolecular charge donor and acceptor during the MLCT reaction. Their electronic distributions suggest that excited states with electron density in the charge donating molecular plane aid efficient charge transfer through these vibronically coupled motions. Three-dimensional (3D) EV spectroscopy is then demonstrated for the first time in a time-dependent study of $N3^{4-}$. This 3D EV experiment directly monitors the temporal evolution of vibrational and vibronic coherences involving two MLCT states, high frequency vibrations, and different low frequency vibrations. These coupled motions appear to facilitate the charge transfer and electronic delocalization in photoexcited $N3^{4-}$ through an initial electronically-localized wavepacket and a consequent vibronic coherence participating in non-adiabatic internal conversion lasting for 1 picosecond.

Analysis of the LMCT dynamics in ferricyanide combines 2D EV spectra and 2D VE spectra on the same system for the first time and iteratively fits the spectra using the one mode vibronic Hamiltonian. The LMCT in ferricyanide may be loosely approximated by this one mode picture; however, more subtle structural details become apparent from considering 2D EV and 2D VE spectra simultaneously.

Early results toward a new direction for 2D EV spectroscopy concludes this dissertation: the study of coupled vibronic motions in the case of ESIPT on the benchmark system HBQ. Anisotropic analysis of the transient-IR spectroscopy on HBQ and its deuterated analogue, DBQ, suggest that non-Born-Oppenheimer dynamics play a role in the ESIPT mechanism of HBQ. Polarization-selective 2D EV spectra report a constant electronic excitation dependent anisotropy, indicating that the equilibration of the excited state keto structure does not involve a ~350 fs internal conversion process.

# TABLE OF CONTENTS

List of Figures ..... ix

List of Tables ..... xxxiv

Chapter 1. Prologue ..... 1

1.1 What Motions Are At Play? ..... 1

1.2 Measuring Molecular Dynamics in the Condensed Phase ..... 10

1.2.1 Linear (1D) Absorption Spectra: Electronic and Vibrational ..... 11

1.2.2 Nonlinear Absorption Spectra: Electronic and Vibrational ..... 13

1.3 Surveying the Field: Coherent Femtosecond 2D FT Spectroscopy ..... 15

1.4 Ultrafast Multi-Coordinate Photochemical Phenomena ..... 18

1.4.1 Charge Transfer Reactions in Transition Metal Complexes ..... 18

1.4.2 Excited State Intramolecular Proton Transfer in Small Organic Molecules ..... 20

1.5 Dissertation Outline ..... 20

1.6 References ..... 23

Chapter 2. Signatures of Vibronic Coupling in 2D Electronic-Vibrational and Vibrational-Electronic Spectroscopies ..... 28

2.1 Introduction ..... 28

2.2 Vibronic Material and Interaction Hamiltonians ..... 30

2.3 Third Order Nonlinear 2D EV and 2D VE Spectroscopies ..... 37

2.3.1 Vibronic Signal Pathways in 2D EV Spectroscopy ..... 41

2.3.2 Vibronic Signal Pathways in 2D VE Spectroscopy ..... 52

2.4 2D EV and 2D VE Simulations ..... 59

2.4.1 Case 1: The Undisplaced, Anharmonic Oscillator ..... 62
2.4.2 Case 2: The Undisplaced, Frequency-Shifted, Anharmonic Oscillator ..... 65
2.4.3 Case 3: The Displaced, Anharmonic Oscillator ..... 69
2.4.4 Case 4: The Displaced, Frequency-Shifted, Anharmonic Oscillator ..... 73
2.5 Selection Rules For 2D EV and 2D VE Spectroscopy ..... 77
2.6 Discussion ..... 79
2.7 Conclusion ..... 83
2.8 Appendices ..... 84
2.8.1 Appendix A: 2D EV and 2D VE Energy Gap Correlation Functions ..... 84
2.8.2 Appendix B: Nuclear Coordinate Dependence of $\mathbf{M}_{eg}$ ..... 84
2.8.3 Appendix C: Liouville Pathways for a Third Order Nonlinear Response Tensor ..... 85
2.8.4 Appendix D: Response Functions for 2D Electronic-Vibrational and 2D Vibrational-Electronic Spectroscopies ..... 89
2.8.5 Appendix E: Second Order Energy Corrections using Stationary Perturbation Theory ..... 94
2.9 References ..... 96
Chapter 3. Measuring a Two-Dimensional Electronic-Vibrational Spectrum ..... 101
3.1 Introduction ..... 101
3.2 Overview of the 2D EV Experiment ..... 102
3.3 The 2D EV Spectrometer ..... 104
3.3.1 Generating Phase-Stable UV Pulse Pairs for 2D Spectroscopy ..... 107
3.3.2 Broadband IR (BBIR) Probe Generation and Temporal Compression ..... 115

3.3.3 Mid-IR Pulse Generation from Difference Frequency Mixing of the Output from an Optical Parametric Amplifier (OPA) ..... 118
3.4 Isolating the 2D EV Signal ..... 122
3.5 Demonstrating 2D EV Spectroscopy with a BBIR Probe ..... 125
3.5.1 2D EV in Silicon: Mapping the Spectral Footprint of the 2D EV Spectrometer ..... 125
3.5.2 Demonstrating 2D EV of a Condensed Phase Molecular Ensemble ..... 127
3.6 Conclusion ..... 130
3.7 Appendices ..... 130
3.7.1 Dazzler Alignment Notes ..... 130
3.8 References ..... 133
Chapter 4. Generating Femtosecond Broadband Near-Ultraviolet Pulses for Nonlinear Spectroscopy ..... 136
4.1 Introduction ..... 136
4.2 Theoretical Background: Ultrafast Pulse Propagation in Nonlinear Media (In Brief) 139
4.2.1 Self-Phase Modulation (SPM): Effects from Electric Field Temporal-Dependence ..... 140
4.2.2 Self Focusing: Effects of Electric Field Spatial-Dependence (Beam Mode) ..... 141
4.3 BBUV Pulse Generation ..... 144
4.3.1 Specific Experimental Notes ..... 150
4.4 Conclusion ..... 150
4.5 References ..... 152

Chapter 5. Ligand-to-Metal Charge Transfer of Ferricyanide in Solution: Combining 2D EV and 2D VE Spectroscopies ..... 156

5.1 Introduction ..... 156

5.2 Electronic and Vibrational Linear Absorption Spectra ..... 157

5.3 LMCT Photophysics in Ferricyanide ..... 159

5.4 Comparison and Fitting of 2D EV and 2D VE Spectra ..... 162

5.5 LMCT Dynamics Viewed By 2D EV Spectroscopy ..... 167

5.6 Discussion and Conclusions ..... 173

5.7 References ..... 174

Chapter 6. Polarization-Selective Multimode Two-Dimensional Electronic-Vibrational Spectroscopy ..... 176

6.1 Introduction ..... 176

6.2 Multimode Vibronic Hamiltonian ..... 177

6.3 Polarization-Selective 2D EV Spectroscopy of a Multimode System ..... 182

6.4 Nonlinear Vibronic Response Signal Contributions ..... 186

6.4.1 Peak Positions ..... 189

6.4.2 Peak Amplitudes ..... 193

6.4.3 Peak Line Shapes ..... 195

6.4.4 Duschinsky Mixing ..... 197

6.5 Nonlinear Orientational Response Signal Contributions ..... 201

6.6 Polarization-Selective 2D EV Spectral Simulations ..... 206

6.6.1 Comparing tIR and 2D EV Anisotropies ..... 208

6.6.2 Non-Condon Effects in 2D EV Anisotropy ..... 212
6.7 Discussion ..... 215
6.7.1 Selection Rules in Multimode 2D EV Spectroscopy ..... 215
6.7.2 Duschinsky Mixing and Non-Condon Effects ..... 216
6.8 Conclusions ..... 217
6.9 Appendix ..... 218
6.9.1 Multimode 2D EV Energy Gap Correlation Functions ..... 218
6.9.2 Two Mode Transition Pathways and Orientational Response ..... 219
6.10 References ..... 222

Chapter 7. Mapping Vibronic Couplings in $N3^{4-}$ with Polarization-Selective Two-Dimensional Electronic-Vibrational Spectroscopy ..... 224

7.1 Introduction ..... 224
7.2 Materials and Methods ..... 226
7.2.1 $N3^{4-}$ Sample Preparation ..... 226
7.2.2 Instrumental Details ..... 227
7.2.3 Transient-IR Data Collection and Processing ..... 227
7.2.4 2D EV Data Collection and Processing ..... 228
7.3 Linear Spectra: FTIR and UV-Vis ..... 229
7.4 Identifying Some of the Players: Transient-IR Spectroscopy of Aqueous $N3^{4-}$ ..... 231
7.5 Identifying More of the Players: Polarization-Selective 2D EV Spectra of Aqueous $N3^{4-}$ ..... 233
7.6 Comparison of Experimental and Calculated Transition Dipole Moment Angles ..... 236

7.7 The Nature of the Identified Vibronically Coupled States Facilitating Ultrafast Photoinduced Charge Transfer ..... 239
7.8 Conclusions ..... 240
7.9 Appendices ..... 242
7.9.1 Linear Spectra with Solvent ..... 242
7.9.2 Transient-IR Analysis ..... 242
7.9.3 Computational Methods ..... 244
7.9.4 Transition Dipole Moment Angle Analysis: Comparing Experiment and Calculations ..... 252
7.10 References ..... 255
Chapter 8. Viewing Multidimensional Ultrafast Photochemical Processes: Vibronic Coherence Evolution in $N3^{4-}$ ..... 262
8.1 Introduction ..... 262
8.2 Three-Dimensional Electronic-Vibrational Spectroscopy ..... 264
8.3 Materials and Methods ..... 266
8.3.1 Sample Preparation ..... 266
8.3.2 Experimental Details ..... 266
8.4 The MLCT States and the High Frequency Vibrational Reporter ..... 267
8.5 Time-Dependent Amplitude Oscillations in 2D EV Spectra ..... 268
8.6 Early Time Dynamics: Electronically-Localized Excited State Vibrational Wavepacket ..... 272
8.7 Later Time Dynamics: Vibronic Coherence Aids Nonadiabatic Internal Conversion 274
8.8 Spectral Deconvolution with 3D EV Spectroscopy ..... 277

8.9 Nonsecular Relaxation in the 3D EV Signals: Coherence-to-Population Transfer .... 279

8.10 Discussion ..... 281

8.11 Conclusions ..... 285

8.12 Appendices ..... 287

8.12.1 Instrumental Details ..... 287

8.12.2 Data Acquisition ..... 289

8.12.3 2D EV Data Processing: Instrumental Noise Correction ..... 291

8.12.4 2D EV Data Processing: Isolating Coherent Oscillatory Features in $\tau_2$ -Dependent Data ..... 293

8.12.5 A Closer Look at Transient-IR Spectra of $N3^{4-}$ ..... 296

8.12.6 Characterizing the Initially Excited Vibrational Wavepacket ..... 299

8.12.7 Time-Frequency Methods Used in Later Time Data Analysis ..... 303

8.12.8 Nonadiabatic Internal Conversion Simulations: A Two-Level System ..... 307

8.12.9 Redfield Theory and Non-Secular Contributions to Relaxation Dynamics ..... 308

8.12.10 Negligible Frequency Shifting of MLCT Peaks in $\omega_1$ ..... 309

8.12.11 Calculated Low Frequency Vibrational Modes ..... 310

8.13 References ..... 312

Chapter 9. Electronic-Vibrational Anisotropy in Excited State Intramolecular Proton Transfer 316

9.1 Introduction ..... 316

9.2 Background: Excited State Intramolecular Proton Transfer in HBQ ..... 318

9.3 Isotope Effects in the Electronic and Vibrational Linear Absorption Spectra of HBQ .... ..... 324

9.4 Breaking Down Born-Oppenheimer with Transient-IR Anisotropy ..... 334
9.5 Excitation-Dependent Anisotropy Measured by 2D EV: Internal Conversion or Non-equilibrium Vibronic Relaxation? ..... 340
9.6 Conclusions ..... 342
9.7 References ..... 345
Chapter 10. Epilogue ..... 349
10.1 Concluding This Journey ..... 349
10.2 Future Directions and Uses for 2D EV Spectroscopy ..... 352
10.2.1 Coupled Electron-Proton Transfers in the Condensed Phase ..... 352
10.2.2 Multimode Vibronic Couplings in Multiple Excited Electronic States ..... 353
10.2.3 Connecting IR-Active and Raman-Active Excited State Vibrational Spectroscopies ..... 354
10.2.4 Using 2D EV and 2D VE Spectroscopies in Tandem ..... 356
10.2.5 Quantifying Intramolecular Electronic Localization and Delocalization ..... 357
10.3 References ..... 359

# LIST OF FIGURES

Figure 1.1. Positional Distributions of Liverpool Players and the Football During Liverpool's Game Winning Goal over Manchester United. (a, top) Liverpool players A (red, solid) and B (red, dashed) at their positions at the start of the match [($x_A(0)$,$y_A(0)$) and ($x_B(0)$,$y_B(0)$)] and their field position distributions (contours) for the duration of the match (τ minutes) in which they scored their goal. (a, bottom), the lateral position distributions are shown for player A (green, solid) and B (black, dashed) about their average position ( $\overline{x}_A$ or $\overline{x}_B$ ) with their lateral range ( $\Delta x_A$ or $\Delta x_B$ ). (b, top) Positional distribution of the ball (blue) for the same duration; (b, bottom) the lateral spectrum of the ball's motion. (c) Duration of the match, τ minutes, in which the goal was scored; the goal marks the end of the play (after τ minutes). The play can be broken up into shorter time intervals: an earlier interval τ' and a later time interval τ''. As shown in (c), the first interval begins at the beginning of the play (τ minutes before the goal is scored); the second interval begins after the first interval ends (τ-τ' minutes prior to the goal). ..... 3

Figure 1.2. Understanding Players' Motion with Two-Dimensional (2D) Positional Resolution. (a) Player A's distribution during the full play's duration (τ) is shown as the sum of many localized distributions (varied by line thickness) during various shorter time intervals, τ' or τ'', during the play. (b) Player B's positional distribution is more delocalized, sampling the full range of lateral positions during all shorter time intervals. (c) The 2D lateral positional spectrum representing the movement of the two players during τ. The solid green elongated peak at ( $\overline{x}_A(\tau'), \overline{x}_A(\tau'')$ ) shows that player A moves more slowly between periods τ' and τ'', or that at later times there is "memory" of his position at earlier times. The dashed black symmetric peak at ( $\overline{x}_B(\tau'), \overline{x}_B(\tau'')$ ) shows that player B moves very fast by comparison to the shorter time intervals τ' and τ''; there is no relation between his positional distribution during τ' and τ''. Both of these peaks are referred to as "diagonal" peaks as they describe the lateral motion of the same player during the two intervals. The purple peaks at coordinates ( $\overline{x}_A(\tau'), \overline{x}_B(\tau'')$ and $\overline{x}_B(\tau'), \overline{x}_A(\tau'')$ ) are referred to as "cross" peaks as they

describe the coupled motion between player A and player B during the play. They are the result of the mixing between the two players' motions and are depicted with both dashed and solid line contours. Finally, they are positively elongated reflecting that player A's motion in one direction during τ' drives player B to move in the same direction during τ''. 6

Figure 1.3. Understanding the Football's Motion with Two-Dimensional Positional Resolution. In the same way that the players' motion was resolved into two positional dimensions, the football's positional distribution is plotted during τ' and τ''. This distribution is much broader than the players' distributions for the same duration because the ball moves much faster than the players do during this period, giving rise to the largely symmetric feature. The presence of elongation reflects that ball also moves more slowly during some periods of the overall play leading up to Liverpool's goal. ..... 7

Figure 1.4. A 2D Positional Spectrum Correlating the Motions of the Ball and Liverpool Player A. ..... 9

Figure 1.5. Molecular Spectroscopy Overview. (a) a typical vibronic energy potential scheme of the ground (g) and first excited (e) electronic states with their respective vibrational states labeled by the quanta of vibrational energy: v = 0,1,2 in the ground state and v' = 0',1',2' for the excited state. The molecular coordinate is defined by the abscissa which characterizes the electronic potential energy surfaces and the vibrational level progressions in each electronic state; $Q_0$ and Q are the equilibrium positions of this molecular coordinate in the ground and excited states, respectively. The energy gaps between states are given for the electronic and vibrational transitions depicted. (b) The various frequency dimensions and spectra are depicted for a general molecular system. Linear (1D) spectroscopy, such as UV-vis (electronic) or FTIR (vibrational) absorption, is shown on the top panel. The traditional "pump-probe" or transient-absorption spectrum is shown on the side panel as a differential absorption where only the probed frequencies are spectrally resolved. The two-dimensional (2D) spectrum is shown in the center with contours depicting the 2D peaks of different signs corresponding to those measured in the pump-probe spectrum as a differential signal. The additional frequency resolution obtained in the 2D spectrum is the excitation frequency dependence of the spectrally detected signals from the pump-probe experiment, resulting in a 2D frequency spectrum. As the color scheme between (a) and (b)

suggest, the spectra in (b) represent the linear electronic absorption (top panel), the transient-IR spectrum (side panel) and the 2D Electronic-Vibrational (EV) spectrum (middle, contours). ..... 12
Figure 1.6. Coherent Multidimensional Fourier Transform (FT) Spectroscopy Pulse Sequence. 14
Figure 1.7. Spectral Landscape of Femtosecond 2D FT Spectroscopy. All blocks represent published experiments in the various 2D spectral areas. This plot is not meant to include *all* published experiments; it is just meant to give a sampling of the experimental spectral coverage. Figure is adapted from reference [31]; see this paper for citations of the experiments represented by the blocks. ..... 16
Figure 2.1. 2D EV and 2D VE Spectroscopy Pulse Sequences. Three input pulses ($\mathbf{E}_1$, $\mathbf{E}_2$, and $\mathbf{E}_3$; blue or green) are controllably delayed to sequentially interact with a sample and generate the third order nonlinear polarization containing the 2D signal ($\mathbf{E}_{sig}$, purple). The experimental delay times, $\tau_n$, relate the time delay between pulse envelope maxima, $t_n$. The delays between successive field-matter interactions are specified by $\tau'_n=t'_{n+1}-t'_n$. (a) 2D Electronic-Vibrational: $\mathbf{E}_1$ and $\mathbf{E}_2$ are electronically-resonant (blue) excitation interactions, and $\mathbf{E}_3$ is a vibrationally-resonant (green) probe interaction. (b) 2D Vibrational-Electronic: $\mathbf{E}_1$ and $\mathbf{E}_2$ are vibrationally-resonant (green) excitation interactions and $\mathbf{E}_3$ is an electronically-resonant (blue) probe interaction. A coherence is induced by $\mathbf{E}_1$ at time $t_1$ that exists for a coherence period $\tau_1$, at time $t_2$ the field $\mathbf{E}_2$ interacts with the system and collapses the coherence into population states that relax during the population time $\tau_2$, then $\mathbf{E}_3$ probes the molecular response to the initial perturbation at $t_3$. ..... 38
Figure 2.2. An illustration of the potential energy surfaces represented by $H_{\text{vibronic}}$ with linear and quadratic vibronic coupling. The states $|g,v\rangle$ and $|e,v'\rangle$ are the vibronic states in either the electronic ground, g, or excited, e, manifold with vibrational state v, or v', respectively. This model reflects a system of displaced, frequency shifted, anharmonic oscillators. The blue (green) arrows indicate transitions between electronic (vibrational) states. The frequencies $\omega_{eg}$, $\omega_{g,v}$, and $\omega_{e,v'}$ correspond to the energy separation between the electronic manifolds, the vibrational levels in $|g\rangle$, and the vibrational levels in $|e\rangle$, respectively. ..... 41
Figure 2.3. 2D EV Vibronic Signals Overview. All the accessible Liouville transition pathways (a-c) are given for the case that the excitation fields ($\mathbf{k_1}$ and $\mathbf{k_2}$) span frequencies $\omega_{eg} \pm \omega_{g,1}$

(where $\omega_{eg} = (E_{e,0'} - E_{g,0})/\hbar$ and $\omega_{g,v} = (E_{g,(v+1)} - E_{g,v})/\hbar$), and the probe field ($\mathbf{k_3}$) has bandwidth sufficient to resonantly excite single quantum vibrational transitions only. The 2D EV non-rephasing (NR) and rephasing (R) signal pathways represented by the double-sided Feynman diagrams $DNREV$ and $DREV$ in (a) and (b), respectively, represent the contributing 2D EV signal pathways when $\mathbf{k_2}$ and $\mathbf{k_3}$ are beyond temporal overlap (i.e. $\tau'2 \geq \tau p$where $\tau p$ is the longer pulse FWHM duration) such that field-matter interaction time ordering is unambiguous. Additional pathways in (c) contribute only during the $\mathbf{k_2}$ and $\mathbf{k_3}$ temporal overlap ($|\tau'2| < \tau p$). The diagrams have peak labels (I-V) denoting the signal to which that pathway contributes; the R and NR diagrams for a given peak sum to yield the absorptive 2D EV signal. The diagrams are also specified by transition type: ground state bleach (GSB, positive, solid line), excited state absorption (ESA, negative, dashed line), and excited state stimulated emission (ESE, positive, solid line). The illustrated absorptive 2D EV spectrum shown (d) for a system where $\mathcal{V}_j^{(1)} \neq 0$ and $\mathcal{V}_{j,j}^{(2)} \neq 0$ gives peaks I-V at the coordinates $\omega_1 = \omega_{eg}$ , $\omega_{eg}+\omega_{e,1'}$ and $\omega_3 = \omega_{g,1}$, $\omega_{e,1'}$, and $\omega_{e,2'}$ (where $\omega_{e,v'} = (E_{e,(v+1)'} - E_{e,v'})/\hbar$); thus, the frequency difference of the vibration in $|g\rangle$ and $|e\rangle$, $\Delta_{eg} = \omega_{e,1'} - \omega_{g,1}$, and the anharmonicity in $|e\rangle$, $\Delta_{2',1'} = \omega_{e,1'} - \omega_{e,2'}$, can be read off of the 2D EV spectrum directly. ..... 43

Figure 2.4. 2D VE Vibronic Signals Overview. The relevant Liouville pathways that contribute to the 2D VE signal when the excitation fields ($\mathbf{k_1}$ and $\mathbf{k_2}$) have sufficient bandwidth for resonant single quantum vibrational transitions and the probe field ($\mathbf{k_3}$) spans frequencies $\omega_{eg} \pm \omega_{g,1}$. The non-rephasing (NR) and rephasing (R) signal pathways represented by the double-sided Feynman diagrams $DNRVE$ and $DRVE$ in (a) and (b), respectively, are the only contributing 2D VE signal pathways when $\mathbf{k_2}$ and $\mathbf{k_3}$ are beyond temporal overlap (i.e., $\tau'2 \geq \tau p$ where $\tau p$ is the longer pulse FWHM duration) such that field-matter interaction time ordering is well defined. Additional pathways in (c) contribute only during the $\mathbf{k_2}$ and $\mathbf{k_3}$ temporal overlap ($|\tau'2| < \tau p$). The peak labels (I-V) specify the signal to which that pathway contributes; the R and NR diagrams for a given peak sum to yield the absorptive 2D VE signal. The diagrams are also categorized by signal type: ground state bleach (GSB, positive, solid line) and excited state absorption (ESA, negative, dashed line). The fully absorptive 2D VE spectrum is depicted (d) for a system where $\mathcal{V}_j^{(1)} \neq 0$ and $\mathcal{V}_{j,j}^{(2)} \neq 0$; peaks I-

V share the excitation frequency coordinate $\omega_1=\omega_{g,1}$ and they are distinguished by the probed electronic transition frequencies $\omega_3 = \omega_{eg}$, $\omega_{eg} + \Delta_{eg}$, $\omega_{eg} + \omega_{e,1'}$, $\omega_{eg} + \omega_{e,1'} + \Delta_{eg} - \Delta_{2'1'}$, and $\omega_{eg} - \omega_{g,1}$ where the frequencies are defined $\omega_{eg} = (E_{e,0'} - E_{g,0})/\hbar$, $\omega_{g,v} = (E_{g,(v+1)} - E_{g,v})/\hbar$, $\omega_{e,v'} = (E_{e,(v+1)'} - E_{e,v'})/\hbar$, the frequency difference of the vibration in $|g\rangle$ and $|e\rangle$, $\Delta_{eg} = \omega_{e,1'} - \omega_{g,1}$, and the anharmonicity in $|e\rangle$, $\Delta_{2'1'} = \omega_{e,1'} - \omega_{e,2'}$. ..... 54

Figure 2.5. 2D EV and 2D VE Spectral Simulations, Case 1: The Undisplaced Anharmonic Oscillator. The 2D EV (a-c) and 2D VE (d-f) simulations above reflect a system with 30 $cm^{-1}$ anharmonicity and a 2073 $cm^{-1}$ fundamental vibrational frequency in both electronic states. Contour plots (a) and (d) show that there is no signal present in the absence of vibronic coupling ($\mu_{eg}^{(1)}=0$, $\lambda=1$). Weak or distorted signal from a case 1 system may be observed if non-Condon effects are present (b and e; $\mu_{eg}^{(1)}=0.15$, $\lambda=1$) or if the system displays electronic-state-dependent vibrational dephasing (c and f; $\mu_{eg}^{(1)}=0$, $\lambda=1.5$). The grey plots (top and side panels) are simulated linear spectra (i.e., UV-Vis or FTIR) for the corresponding frequency axis and the black plot (side panels) is an integrated projection onto $\omega_3$ obtained by summing over $\omega_1$. Contours are normalized to the absolute maximum of Figure 2.6(a) for 2D EV and Figure 2.8(f) for 2D VE; the contours span -1 to 1 with 5% intervals, bleach and emission signals (positive) are yellow and absorptions (negative) are blue. The framed 2D regions have been scaled by the factors indicated for emphasis. For relative intensities, see Table 2.1. ..... 63

Figure 2.6. 2D EV and 2D VE Spectral Simulations, Case 2: The Undisplaced, Frequency-Shifted, Anharmonic Oscillator. The 2D EV (a-c) and 2D VE (d-f) simulations above reflect a system with 30 $cm^{-1}$ anharmonicity and a 40 $cm^{-1}$ red-shifted excited state vibration ($\omega_{g,1}$ = 2073 $cm^{-1}$ and $\omega_{e,1'}$ = 2033 $cm^{-1}$). Contour plots (a) and (d) show that signal is observed when only quadratic vibronic coupling is present ($\mu_{eg}^{(1)}=0$, $\lambda=1$). Non-Condon effects are evidenced by small intensity contributions from peaks III-V (b and e; $\mu_{eg}^{(1)}=0.15$, $\lambda=1$), and electronic-state-dependent vibrational dephasing effects are observed in the peak II broadening (c and f; $\mu_{eg}^{(1)}=0$, $\lambda=1.5$). The simulated linear spectra (grey plots, top and side panels) are shown for reference. The $\omega_3$ projections (black plots, side panels) are analogous to the pump-probe (or "1D") equivalent signal, and provide comparison between the 2D and pump-probe signals. Contours are normalized to the absolute maximum of Figure 2.6(a) for

2D EV and Figure 2.8(f) for 2D VE; the contours span -1 to 1 with 5% intervals, bleach and emission signals (positive) are yellow and absorptions (negative) are blue. The framed 2D regions have been scaled by the factors indicated for emphasis. For relative intensities, see Table 2.1. ..... 66

Figure 2.7. 2D EV and 2D VE Spectral Simulations, Case 3: The Displaced Anharmonic Oscillator. The 2D EV (a-c) and 2D VE (d-f) simulations above reflect a system with 30 $cm^{-1}$ anharmonicity, an excited state geometry displacement equal to the ground state equilibrium distance, and a 2073 $cm^{-1}$ fundamental vibrational frequency in both electronic states. Contour plots (a) and (d) show that signal is observed when only linear vibronic coupling is present ($\mu_{eg}^{(1)}=0$, $\lambda=1$). Non-Condon effects are evidenced by small intensity contributions to peaks III-V (b and e; $\mu_{eg}^{(1)}=0.15$, $\lambda=1$), and electronic-state-dependent vibrational dephasing effects are observed in broadened 2D EV peaks II,IV, and V, and broadened 2D VE peaks II and IV (c and f; $\mu_{eg}^{(1)}=0$, $\lambda=1.5$). The simulated linear spectra (grey plots, top and side panels) are shown for reference. The $\omega_3$ projections (black plots, side panels) provide comparison between the 2D and pump-probe signals for the respective techniques. Contours are normalized to the absolute maximum of Figure 2.6(a) for 2D EV and Figure 2.8(f) for 2D VE; the contours span -1 to 1 with 5% intervals, bleach and emission signals (positive) are yellow and absorptions (negative) are blue. The framed 2D regions have been scaled by the factors indicated for emphasis. For relative intensities, see Table 2.1. ..... 70

Figure 2.8. 2D EV and 2D VE Spectral Simulations, Case 4: The Displaced, Frequency-Shifted, Anharmonic Oscillator. The 2D EV (a-c) and 2D VE (d-f) simulations above reflect a system with 30 $cm^{-1}$ anharmonicity, an excited state geometry displacement equal to the ground state equilibrium distance, and a 40 $cm^{-1}$ red-shifted excited state vibrational frequency ($\omega_{g,1}$ = 2073 $cm^{-1}$ and $\omega_{e,1'}$ = 2033 $cm^{-1}$). Contour plots (a) and (d) show that signal is observed when both linear and quadratic vibronic coupling are present ($\mu_{eg}^{(1)}=0$ and $\lambda=1$). Non-Condon effects are evidenced by small intensity contributions to all peaks in varying proportion (b and e; $\mu_{eg}^{(1)}=0.15$, $\lambda=1$), and electronic-state-dependent vibrational dephasing effects are observed in broadened 2D EV peaks II,IV, and V, and broadened 2D VE peaks II and IV (c and f; $\mu_{eg}^{(1)}=0$, $\lambda=1.5$). The simulated linear spectra (grey plots, top

and side panels) are shown for reference. The 2D EV $\omega_3$ projections (black plots, side panels) in this case highlight the convoluted nature of the 1D ("transient-IR") signal by comparison with the 2D EV signal. Contours are normalized to the absolute maximum of Figure 2.6(a) for 2D EV and Figure 2.8(f) for 2D VE; the contours span -1 to 1 with 5% intervals, bleach and emission signals (positive) are yellow and absorptions (negative) are blue. For relative intensities, see Table 2.1. ..... 74
Figure 2.9. Third Order Liouville Pathways depicting the time evolution of the system density matrix. The system eigenstates are given by a, b, c, and d. ..... 86
Figure 3.1. The Two-Dimensional Electronic-Vibrational (2D EV) Pulse Sequence ..... 103
Figure 3.2. The 2D EV Experimental Schematic. The Ti:Sapphire output is split into the broadband mid-IR (BBIR) probe pulse (solid green), an alternate mid-IR probe option (solid green, lower), an 800 nm reference pulse for characterization (dashed red), and the pump pulse (solid blue). The BBIR is generated *via* filamentation of the 800 nm fundamental and its harmonics in gaseous media and compressed with material compensation (2mm Ge) and a deformable mirror compressor (DMC). Tunable, narrower-band mid-IR results from difference frequency generation (DFG) of the collinear near-IR output (magenta and orange) from a double-pass optical parametric amplifier (OPA). The pump pulse is chopped (500 Hz) and shaped in an acousto-optic programmable dispersive filter (AOPDF). The orientation of all beams at off axis parabolic mirror 1 (OAP 1) before focusing to the sample area (S) is shown in lower right, filled spots indicate the beams that generate the 2D EV signal using either mid-IR probe source. The signal (Sig, purple) and reference (Ref, dashed green) are both dispersed in a spectrometer (Spec) and detected in a 2 x 64 HgCdTe-pixel array (MCT) detector. $\lambda/2$, half wave plate; Pol, polarizer; 2:1, down-collimating telescope. Spectral and temporal characterization of the reference fundamental have been achieved using the Frequency Resolved Optical Gating (FROG) and Spectral phase Interferometry for Direct Electric-field Reconstruction (SPIDER) techniques. See paragraphs below for full experimental description. ..... 106
Figure 3.3. Schematic Illustration of the Acousto-Optic Programmable Dispersive Filter Operation for Generating Pulse Pairs. An incident optical pulse ($\mathbf{E_{in}(\omega)}$, blue) with center frequency, $\omega_0$, and a bandwidth containing the frequencies $\omega_a$ and $\omega_b$ is aligned through a

nonlinear medium supporting the acousto-optic interaction (gray outlined box). A tailored waveform in the radio frequency regime is generated and sent to a transducer interfaced with the nonlinear crystal which propagates the acoustic wave (**Ac(ω)**) in the crystal. The index of refraction in the nonlinear medium varies as a function of crystal length (Δz) in the presence of the acoustic wave to tailor the pulse shaping of the incident pulse with arbitrary control of phase and amplitude. ..... 110

Figure 3.4. Interpulse Phase Difference in Pulse Pair Generation using the AOPDF. (a) The effect of incrementing the interpulse phase difference, $\Delta\phi_{AOPDF}$, with the pulse envelope to generate electric field interference. The spectral intensities have been scaled for comparison (b) The effect of using the interpulse phase difference to also introduce phase differences for use in phase cycling. ..... 112

Figure 3.5. Demonstration of a $\tau_1$ Scan Spectral Interferogram. (top) a cosine function with the periodicity of a 400 nm wavelength (continuous wave, in this case) is shown. The blue cosine is $\mathbf{E}_1$ held at time zero and the dashed red cosine is $\mathbf{E}_2$ that is varied by $\tau_1$. (bottom) the incident pulse spectrum (dashed black) and the shaped electric field spectrum of the pulse pair delayed at $\tau_1$ = 0 fs, 50 fs, and 100 fs. ..... 113

Figure 3.6. Pump Phase Stability. The upper left contour shows the interferogram collected during 12 minutes of laboratory time. The spectral amplitude is normalized and the contours are plotted in 10% levels; the projection of the contour is shown in blue in the upper right. The fringe spacing reflects the 200 fs delay held constant during this measurement. The incident pulse spectrum is overlaid (black dashed, upper right) for reference. FT spectral interferometry quantifies $\sigma_{\Delta\phi_{12}}$ for every spectral interferogram collected over time and is plotted as black circles in the bottom left for $\omega_0$= 400 nm. The averaged phase stability, $\bar{\sigma}_{\Delta\phi_{12}}$ is spectrally represented by averaging $\sigma_{\Delta\phi_{12}}$ over the 12 minute collection window for each pixel of the spectrometer and plotted as a function of wavelength in red (bottom, right); spectrum shown in black dashed for reference. The connected axes between different panels are used to connect the axes between plots. ..... 114

Figure 3.7. BBIR Generation and Temporal Compression. (a) the BBIR generation schematic as described in section 3.3.2. (b) The deformable mirror grating compressor (DMC) arranged in a typical 4f geometry where the DM sits in the Fourier plane. ..... 116

Figure 3.8. Mid-IR Pulse Characterization Generated from the OPA/DFG Process. The reference fundamental beam is characterized using SHG FROG technique and used in assessing the mid-IR pulse duration from the sum frequency generation (SFG) FROG technique. (a) The experimentally measured SHG FROG spectrum (contours), the sum over the wavelength axis (top panel) is the auto-correlation and the sum over the delay time axis (right panel) is the upconverted spectrum of the reference beam. The retrieved SHG FROG spectrum using the FROG algorithm is shown on the right indicating very good agreement [256x256 pixel grid used, time-bandwidth product: 0.47614. Contours span 1 (red) to 0.1 at 10% intervals, with 2% intervals from 0.1 to 0 (green). (b) The retrieved spectral and temporal intensities and phases of the reference electric field. (c) the SFG FROG spectrum (contours span 1 to 0.2 in 10% intervals). The cross-correlation FWHM = 123 fs; the deconvolved mid-IR pulse duration is 115 fs. A 2 mm $CaF_2$ window is placed in the beam path to account for additional dispersion during an experiment due to the sample windows. ..... 119

Figure 3.9. The 2D EV spectrum of Si; $\tau_2$=200 fs. The real part of the FT is plotted as $-\Delta T$ with red=positive (green=0, blue=negative) contours plotted from -1 to 1 every 10%; Savitzky-Golay filtering is used to remove the effect of atmospheric water absorption in the BBIR spectra. The top and side panels show pump and probe spectra, respectively. ..... 127

Figure 3.10. The 2D EV spectrum of $K_3[Fe(CN)_6]$ in FA. The spectrum is normalized to the absolute maximum value in the 2D plot and plotted from -1 to 1, contour separation = 10%. ..... 128

Figure 3.11. Spectral Effects of Improper Dazzler Alignment. (left) A spectral hole has been programmed for 0.5 nm width, 1.0 depth and to be centered at 400 nm. The solid black line is the incident spectrum, the blue is the correctly aligned spectrum with the hole burnt, and the red line is an improperly aligned Dazzler crystal module (principally due to incorrect rotational setting). (right) the spectra for hole burning widths of 0.5 nm (dashed) and 1.0 nm (solid, thin). ..... 132

Figure 4.1. General Spectral Coverage of Femtosecond Pulsed Light Sources Demonstrated in Nonlinear Spectroscopic Experiments. The solid outlined boxes represent traditional sources derived from parametric amplification to span from the near-IR to the UV ranges.

The dashed outlined boxes represent more recently developed methods employed in nonlinear spectroscopies based on references given in section 4.1. ..... 138
Figure 4.2. Self-Phase Modulation (SPM) induced Spectral Broadening in the UV Using Nonlinear Media of Differing Thickness. (a) An incident 400 nm pulse (1 μJ, gray spectrum) is focused by a f=100 mm lens into a 1 mm thick $CaF_2$ plate that is placed 0.25 cm after the beam focus; resulting broadened UV spectrum is shown in blue. (b) BBBUV spectra from using the multiplate continuum method with 4 BK7 plates (0.14 mm thick) is shown (blue and purple). The plates are set for optimal SPM in the purple spectrum as evidenced by the spectral intensity modulation. The inter-plate separation can be adjusted to minimize the destructive interference from the accumulated nonlinear phase at various points in the temporal propagation of the broadening UV pulse to obtain a less modulated spectral intensity without sacrificing bandwidth. ..... 144
Figure 4.3. Broadband UV Pulse Generation using the Multiplate Continuum Method Schematic. (top) The beam propagation schematic is laid out; SM (1,2) = concave spherical mirrors, M1 = 800 nm HR-coated mirror, M2 = protected Ag-coated mirror, CM(1,2) = dispersion compensating chirped mirrors, BBO = 0.1 mm BBO type 1 crystal, DM = 400 nm HR dichroic mirror, WP = UV λ/2 waveplate, P(1,2) UV fused silica Brewster's angle prisms, UV(1-3) = low-GDD 355-445 HR-coated mirrors, PM = UV-enhanced Al pick-off mirror, L(1,2) f=100 mm UV AR-coated UV fused silica lenses. (bottom) schematic depiction of the broadening fundamental beam propagation through the multiplate continuum generation; here the self-focusing induced by each plate is exaggerated for demonstration. ..... 145
Figure 4.4. BBUV Spectra From Multiplate Continuum Generation. (left) The BBUV generation showing the effect of number of BK7 plates used on the spectral broadening; the FWHM increases from ~8 nm to ~25 nm. (right) BBUV generation using 5 fused silica plates and the spectral tunability by adjusting the tuning angle of the BBO crystal. The nodes appearing on the tails of the spectra reflect phase-mismatch between the bandwidth of the broadened fundamental and the bandwidth of the upconverted BBUV spectra. Note the differences in wavelength axes of the two plots. ..... 147

Figure 4.5. Temporal Compression of the BBUV Pulse. The uncompressed pulse (left) displays primarily positive linear chirp resulting from BBUV generation and inadequate temporal dispersion compensation; FWHM pulse duration is ~350 fs. The compressed pulse (right) results from the BBUV generation including all of the temporal dispersion compensation shown in Figure 4.3. Higher order dispersion limits this FWHM pulse duration to ~30 fs. ..... 149

Figure 5.1. Linear Absorption Spectra of Ferricyanide in Formamide. (left) Vibrational and electronic absorption spectra shown with formamide solvent subtracted, (right) ferricyanide molecular structure..... 158

Figure 5.2. Transient-IR Absorption Spectra of Ferricyanide in Formamide. The contours are plotted in ΔT/T and shown at 10% intervals; red = positive (bleach) signal and blue = negative (absorption) signal. The schematic on the right depicts the generalized photophysics of Ferricyanide as described by Ojeda *et al.*[4]. The blue LMCT excitation occurs instantaneously, leading to the decay of the excited state in less than 1 ps via back electron transfer. The system then equilibrates from vibrationally hot states in the ground electronic state on the several picosecond timescales..... 161

Figure 5.3. Fitting the 2D EV and 2D VE Spectra of Ferricyanide Iteratively with a Vibronic Hamiltonian. The 2D EV spectra (left) and 2D VE spectra (right) as obtained experimentally (top row) and simulated using the single mode vibronic Hamiltonian described in chapter 2. The experimental spectra are collected at $\tau_2$ = 400 fs. The fitting procedure was optimized with residuals ≤ 0.1. Fits to data were optimized by floating the linear vibronic coupling parameter ($\mathcal{V}_i^{(1)}$) with all other parameters fixed in a nonlinear least squares algorithm for the VE spectrum; then fitting the 2D EV spectra using the quadratic vibronic coupling parameter ($\mathcal{V}_{ii}^{(2)}$) and the excited state vibrational dephasing parameter ($\lambda$) while fixing $\mathcal{V}_i^{(1)}$ to the value obtained from previous the VE spectral fit. The anharmonicities were given initial values to reflect the vibrational level separation observed in the tIR measurements; non-Condon effects were not considered; the homogeneous broadening was assumed. Six iterations yielded convergence. Optimized values are $\mathcal{V}_i^{(1)}$ = 0.99, $\mathcal{V}_{ii}^{(2)}$ = -0.038, $\lambda$ =1.62. ..... 164

Figure 5.4. Time-Dependent Relaxation Dynamics of Ferricyanide in Formamide Measured by 2D EV Spectroscopy of the Cyanide Stretches. Ferricyanide (top row) and formamide-only (bottom row) 2D EV spectra are presented at various points throughout the first 5 ps in $\tau_2$. The contour maps are globally normalized to the ferricyanide spectrum at 500 fs; the red contours are positive (bleach) signals and the blue contours are negative (absorption) signals and are given at 10% intervals. ..... 168

Figure 5.5. Time-Dependent Shifts in 2D EV Peak Maxima in Electronic and Vibrational Dimensions. The $\tau_2$-dependence of the peak maxima in the (left) electronic excitation dimension ($\omega_1$) and the (right) vibrational probe dimension ($\omega_3$) are shown for both the ground state bleach (red) and the excited state absorption (blue) as data points. The lines are not analytical fits but only serve as guides to the eye. ..... 169

Figure 5.6. Center Line Slopes of the Ferricyanide 2D EV Spectra of the CN Stretches. (top row) The ground state bleach features are shown and the (bottom row) excited state absorption features are shown for $\tau_2$ = 300, 400, and 500 fs. ..... 171

Figure 6.1. Polarization-Selective Multimode 2D EV Spectroscopy Overview. (a) The 2D EV experimental pulse sequence includes the first electronically resonant pump pulse, $\mathbf{E_1}$ (wave vector $\mathbf{k_1}$, blue), incident on a sample at time $t_1$ triggers an electronic coherence oscillating at an electronic transition frequency. After a coherence time, $\tau_1$, the second pump pulse, $\mathbf{E_2}$ ($\mathbf{k_2}$, blue) is incident at time $t_2$ which collapses the electronic coherence into populated states that evolve during the pump-probe delay time, $\tau_2$. The vibrationally resonant probe pulse, $\mathbf{E_3}$ ($\mathbf{k_3}$, green), interacts with the sample and emits the third order signal field, $\mathbf{E_{sig}}$ ($\mathbf{k_{sig}}$, purple), from which the changes in the vibrational spectrum due to the electronic perturbation are extracted. The two linear polarization combinations considered here are the "parallel" polarization with all fields parallel in polarization, and the "crossed" polarization in which the probe field is perpendicularly polarized to the pump fields. (b) The dipole orientation within the molecular frame, and its relative orientation within the laboratory frame. Each dipole moment is defined in the main text and illustrated in Figure 6.2. Integrating over Euler angles ($\alpha$, $\beta$, $\gamma$) transforms the molecular frame motion into the laboratory frame. ..... 184

Figure 6.2. Two-Mode Vibronically Coupled Eigenstate Basis and Dipole Moments. (a) The vibronic energy levels for the two coupled, displaced, frequency-shifted anharmonic oscillators system described by $H_{vibronic}$. The ket notation describes the vibronic eigenstates; ground electronic state = g, excited electronic state = e, vibrational quanta of oscillator i in g (e) = m (m'), vibrational quanta of oscillator j in g (e) = n (n'); $\omega_{eg}$ = electronic energy gap; $\omega_i$ ($\omega_j$) = fundamental ground state vibrational transition frequencies; $\omega_i$' ($\omega_j$') = fundamental excited state vibrational transition frequencies; $\Delta_i$ ($\Delta_j$ ) = ground state anharmonicities; $\Delta_{ij}$ = ground state mixed anharmonicity; $\Delta_{eg,i}$ ($\Delta_{eg,j}$) = excited state vibrational frequency shifts; $\Delta_{i'}$ ($\Delta_{j'}$) = excited state anharmonicities; and $\Delta_{i'j'}$ = shifting due to Duschinsky mixing. (b) The transition dipole moments are defined for both electronic and vibrational transitions considered in this treatment. ..... 187

Figure 6.3. Multimode 2D EV Signals Schematic. (a) A schematic illustration of the dipole allowed 2D EV signals appearing for a two-mode vibronically coupled system described by $H_{vibronic}$ and the energy level schematic given in Figure 6.2(c). The absorptive peaks are symmetric and result from equally weighted rephasing (R) and non-rephasing (NR) signals at the same ($\omega_1$, $\omega_3$) coordinates; phase twisted peaks result from unequally weighted R and NR signals; red = positive signal [ground state bleaches (GSB) and excited state stimulated emissions (ESE)], blue = negative signal [excited state absorptions (ESA)]. The peak numbering scheme is described in the main text and Table 6.2. (b) Double-sided Feynman diagrams of rephasing pathways for selected 2D EV peaks. Electronic excitations ($\mathbf{k_1}$ and $\mathbf{k_2}$, blue); vibrational interactions ($\mathbf{k_3}$, green); emitted signal ($\mathbf{k_{sig}}$, purple)..... 189

Figure 6.4. Duschinsky mixing effects in nonlinear vibronic response of single vibrational quantum manifold. (a) Both ground state (bilinear) and excited state (Duschinsky) mixing of vibrational modes resulting in vibronic eigenstate energy splitting within each manifold. 2D EV simulated spectral slices at $\omega_1 = \omega_{eg}$ for positive (b) and negative (c) vibrational mixing parameters. These simulations do not include orientational response; the following simulation parameters were used: $\omega_{eg}^0$ = 25500 cm$^{-1}$; $\omega_i^{\,0}$ =1650 cm$^{-1}$; $\omega_j^{\,0}$ =2150 cm$^{-1}$; $\mathcal{V}_i^{(1)} = \mathcal{V}_j^{(1)} = 0$; $\mathcal{V}_{i,i}^{(2)} = \mathcal{V}_{j,j}^{(2)} = -60$; $|B_{i,j}| = |\mathcal{V}_{i,j}^{(2)}| = 60$. Bilinear and Duschinsky mixing were introduced separately with the other set to zero to clarify effects. ..... 199

Figure 6.5. Polarization-Selective Multimode 2D EV Spectral Simulations. The parallel polarized 2D EV spectrum (left) and the perpendicularly polarized 2D EV spectrum (right). The spectra are globally normalized to the ZZZZ spectrum; the color map spans $\pm 0.2$ in order to view the features from the hot vibrational manifold in the excited state more clearly. The contour lines are at 2% intervals spanning [-0.2:0.2]; dashed = negative, solid = positive. ..... 207

Figure 6.6. Comparison of tIR and 2D EV Anisotropies. (a) Transient-IR anisotropy calculated from summing over the parallel and crossed 2D EV spectra. The 2D EV anisotropies for (a) $\mu^{eg}$ excitation at $\omega_1 = \omega_{eg}$ (25180 cm$^{-1}$), (b) $\mu_i^{eg}$ excitation at $\omega_1 = \omega_{eg} + \omega_{i'}$ (26740 cm$^{-1}$), and (c) $\mu_j^{eg}$ at $\omega_1 = \omega_{eg} + \omega_{j'}$ (27260 cm$^{-1}$). In all plots, the blue solid (dashed) lines are the ZZZZ (ZZYY) signal intensities obtained from simulated 2D EV spectra in Figure 6.5, the red lines are the anisotropies where the spectral regions of tIR and 2D EV signal have been emphasized and the regions where the anisotropy is ill-defined have been suppressed. ..... 209

Figure 6.7. Non-Condon effects viewed through excitation dependent 2D EV anisotropies. All spectra result from 2D EV slices at $\omega_3$ = 1627 cm$^{-1}$ (ground state vibration of mode i). Four different simulations are shown for (a) ZZZZ (b) ZZYY and (c) the anisotropy: gray = [$\theta_i^{eg}$ = 0°, $\theta_j^{eg}$ = 0°, $\mu_{eg}^{(1)}$ = 0]; red = [$\theta_i^{eg}$ = 10°, $\theta_j^{eg}$ = 0°, $\mu_{eg}^{(1)}$ = 0]; blue (dashed) = [$\theta_i^{eg}$ = 0°, $\theta_j^{eg}$ = 10°, $\mu_{eg}^{(1)}$ = 0]; and black = [$\theta_i^{eg}$ = 0°, $\theta_j^{eg}$ = 0°, $\mu_{eg}^{(1)}$ = 0.15]. Note the difference in signal intensity axes in (a) and (b). ..... 213

Figure 7.1. Linear absorption of $N3^{4-}$ and laser pulse spectra. A) Electronic absorption spectrum of $N3^{4-}$ (black, solvent-subtracted) in basic, aqueous solution (pH≈13) with the spectrally broadened UV pump spectrum (shaded blue) used in the tIR and 2D EV experiments overlaid to highlight the excitation region. The time-dependent (TD)-B3LYP/def2-SVP calculated electronic absorption spectrum (red, a Gaussian broadening has been applied with a FWHM = 0.18 eV, intensities are normalized for comparison to the experiment; see Appendices for further details) for the optimized $N3^{4-}$ minimum geometry is reported along with $S_0 \rightarrow S_n$ predicted oscillator strengths (red sticks). The transitions associated with the observed $^1$MLCT states are denoted by *, see discussion. The computed spectrum is within ~0.1 eV accuracy with respect to the experimental spectrum; $N3^{4-}$ structure is inset. B) The

solvent-subtracted FTIR spectra for both vibrational regions probed in the experiments; mid-IR probe spectra used in the experiments are overlaid (green). ..... 230

Figure 7.2. Transient-IR (tIR) spectroscopy of $N3^{4-}$. A) Full tIR spectra of the charge donor region (top) and acceptor region (bottom). B) Time traces reflecting the charge donor (green) and charge acceptor dynamics (purple); raw data shown as circles, fits are solid lines, ± 1 standard deviation shown by shaded region. (C) tIR spectra at $\tau_2$ = -1 ps (black), 2 ps (red), and 100 ps (yellow). The excited state absorption (ESA) peaks of interest for the polarization-dependent 2D EV analysis are highlighted by green dashed arrows: $\omega_3$ = 1271 $cm^{-1}$, bpy ring mode with CH wag ($\nu_{BPY}$); $\omega_3$ = 1328 $cm^{-1}$, COO symmetric stretch ($\nu_{COO}$); and $\omega_3$ = 2050 $cm^{-1}$ and 2070 $cm^{-1}$, asymmetric and symmetric CN stretches, respectively (collectively $\nu_{CN}$). The ground state bleach (GSB) features are: $\omega_3$ = 1375 $cm^{-1}$, COO symmetric stretch; $\omega_3$ = 1405 $cm^{-1}$, 1435 $cm^{-1}$, and 1545 $cm^{-1}$, bpy ring modes; $\omega_3$ = 1596 $cm^{-1}$, COO asymmetric stretch; $\omega_3$ = 2120 $cm^{-1}$, CN symmetric and asymmetric stretches. See text for discussion of tIR spectral shifts. D) Calculated difference IR spectrum between the ground state, $S_0$, and the lowest energy triplet state, $T$. Note: the calculated lowest energy triplet state is referred to as "$T$" and the experimental measurements refer to the lowest energy triplet state as "$^3$MLCT". ..... 232

Figure 7.3. Polarization-selective 2D EV spectra. a) 2D EV spectra collected with pump and probe pulses with parallel ($S_{ZZZZ}$) and crossed ($S_{ZZYY}$) relative polarization; the color maps for spectra with the same $\omega_3$ region are comparable using the corresponding color bar. b) The isotropic 2D EV spectrum ($S_{iso} = S_{ZZZZ} + 2S_{ZZYY}$) with white boxes highlighting signals used in the dipole angle analysis described in the text ($\nu_{CN}$ = 1; $\nu_{COO}$ = 2,3; and $\nu_{BPY}$ = 4). Box 1 corresponds to $^1MLCT_C$, box 2 to $^1MLCT_A$, and boxes 3 and 4 correspond to $^1MLCT_B$; see text for full discussion of these $^1$MLCT states. Excited state absorptions are negative (dashed contours) and ground state bleaches are positive (solid contours) in all spectra; note the difference between color maps for the lower and upper panels. The color gradient changes every 5% of the max absolute value signal (of both $S_{ZZZZ}$ and $S_{ZZYY}$ in A)

within the $\omega_3$ region indicated; the contour lines begin at $\pm 10\%$ for clarity and are plotted at 5% intervals thereafter. ..... 235

Figure 7.4. Visualizing electron density trends for vibronically coupled $^1$MLCT states in $N3^{4-}$. Slices from the isotropic 2D EV spectrum at the $\nu_{BPY}$ and $\nu_{COO}$ vibrational frequencies from Figure 7.3 show the $\omega_1$ dependence of these vibronically coupled modes more clearly. The $^1MLCT_A$ and $^1MLCT_B$ states described in the text are shown for the corresponding $\omega_1$ peaks, and the calculated natural transition orbitals (NTOs) for the $S_0 \rightarrow S_n$ transitions that are associated with these states through the dipole angle analysis are indicated by the dashed gray arrows (top left = $S_0 \rightarrow S_{14}$ and top right = $S_0 \rightarrow S_{17}$ , see all calculated NTOs in S.I.). For the calculated states, the isodensity (0.03) contour plots of the electron NTOs for the analyzed electronic transitions (the corresponding hole NTOs all have a similar spatial distribution localized on the Ru-$(NCS)_2$ region are also reported in the S.I) and dipole moments are shown to emphasize the asymmetric electronic distribution on the charge accepting region. The calculated transition dipole moments $\mu_{S_0}^{S_{14}}$ (or $\mu_{S_0}^{S_{17}}$), $\mu_{COO}$, and $\mu_{BPY}$ are overlaid on the $T$ optimized geometry; the dipole magnitudes are not to scale. Cartesian axes are specified for the NTOs and for the dipole angle plots in the top left; the electron donor plane formed by the Ru-$(NCS)_2$ is in the plane of the page for the dipole angle plots. ..... 239

Figure 7.5. FTIR spectra of $N3^{4-}$ without solvent subtraction. A) Charge acceptor region; the solvent is 300 mM NaOH dissolved in $D_2O$. B) Charge donor region; the solvent is 300 mM NaOH dissolved in $H_2O$. The $N3^{4-}$ solution are the solid lines, the solvents are the dashed lines, and the probe spectra are shown in green. ..... 242

Figure 7.6. Transient-IR of Solvent Only. A) $D_2O$ used for charge acceptor tIR and 2D EV measurements. B) $H_2O$ used for charge donor tIR and 2D EV measurements. The color maps are the same as the tIR contour plot in Figure 7.2(a) for comparison. Note the different time scale plotted for solvent only runs versus the $N3^{4-}$ tIR data shown in the $N3^{4-}$ tIR data. ..... 244

Figure 7.7. B3LYP/def2-SVP IR spectrum for the ground state singlet $S_0$ $Ru(dcbpy)_2(NCS)_2^4$ in water using implicit solvent (full line) and explicit water molecules ($Ru(dcbpy)_2(NCS)_2^{--}$

($H_2O)_8$, dotted lines) in the region from 1000-1550 (upper panel), 1550-2100 (middle panel), and 2100-2450 $cm^{-1}$. The higher energy region is not showed for simplicity. A Gaussian broadening has been applied with a full width half maximum value of 4 $cm^{-1}$. . 247
Figure 7.8. B3LYP/def2-SVP IR spectrum for the lowest lying triplet (T) $Ru(dcbpy)_2(NCS)_2^4$ in water using implicit solvent (full line) and explicit water molecules ($Ru(dcbpy)_2(NCS)_2^{--}(H_2O)_8$, dotted lines) in the region from 1000-1550 (upper panel), 1550-2100 (middle panel), and 2100-2450 $cm^{-1}$. The higher energy region is not showed for simplicity. A Gaussian broadening has been applied with a full width half maximum value of 4 $cm^{-1}$. . 248
Figure 7.9. Ball and stick representation of the $S_0$ optimized geometry for the $Ru(dcbpy)_2(NCS)_2^{4-}$-$(H_2O)_8$ cluster at B3LYP/def2-SVP level. Ruthenium in turquoise, carbon in dark grey, oxygen in red, nitrogen in blue, sulfur in orange, and hydrogen in light gray. ..... 249
Figure 7.10. Overlap of Optimized $S_0$ and T Geometries with Same Cartesian Orientation Enforced. The two optimized geometries ($S_0$ and T) are overlapped to show minimal deviations; these structures were used for dipole angle comparison. ..... 249
Figure 7.11. Displacement vectors of the analyzed normal modes for the lowest lying triplet for the $Ru(dcbpy)_2(NCS)_2^{4-}$ at B3LYP/def2-SVP level. Ruthenium in turquoise, carbon in dark grey, oxygen in red, nitrogen in blue, sulfur in orange, and hydrogen in light gray. ..... 250
Figure 7.12. Natural Transition Orbitals (NTOs) hole-electron pairs relative to the optimized $S_0$ geometry along with the calculated dipole angles overlaid on T optimized geometry. The columns are grouped by the hole NTOs, electron NTOs, and Dipole Angles; and the rows are grouped by the corresponding arriving $S_n$ states for each $S_0 \rightarrow S_n$ transition. $\mu_{S_0}^{S_n}$ dipoles are the blue arrows and $\mu_{vib}$ arrows are green. The Cartesian orientation are the same for all hole and electron NTOs, and the dipole angle figures all have the same Cartesian orientation and have been set with the Ru-$(NCS)_2$ plane to be in the plane (YZ) of the page. ..... 251
Figure 8.1. Multidimensional Electronic-Vibrational (EV) Spectroscopy. In each technique, the pulse sequence (a) induces an electronic excitation (pumps: $\mathbf{k}_1$, $\mathbf{k}_2$) and measures a high frequency vibrational response (probe: $\mathbf{k}_3$) in a sample. Consider a system where one high frequency vibration (H) vibronically couples to two electronic excited states (A, B) and to two low frequency vibrations ($L_1$, $L_2$) in A and/or B. (b) The pump-probe experiment (1D

EV) measures the H vibrational spectrum ($\omega_3$) and kinetics during its relaxation times ($\tau_2$). At a given $\tau_2$ delay, (c) the 2D EV experiment resolves the electronic excitation spectrum ($\omega_1$) for H, defining the excited vibronic eigenstates ($\psi(t)$) by the couplings between H, the ground electronic state and either A or B. Collecting 2D EV spectra over a $\tau_2$ range measures population relaxation and coherent superpositions of eigenstates. The latter manifest as peak amplitude modulations; a FT over $\tau_2$ yields a (d) 3D EV spectrum where coherences (rainbow-colored spheres) separate in $\omega_2$ from population decays (black spheres) according to their beat frequency. The $\omega_2$ frequencies can indicate low frequency vibrations ($L_1$, $L_2$) coupled with vibronic eigenstates. Time-dependent 3D EV features, such as frequency shifts of low frequency modes as generally indicated by $L_1$ moving to $L_1$' in the $\omega_2$ frequency space, report on the temporal evolution and non-equilibrium relaxation of the vibronic eigenstates during photoexcited processes (depicted by the sphere coloration gradient). ..... 265

Figure 8.2. Low frequency amplitude modulations in two-dimensional electronic-vibrational (2D EV) spectra. (a) $\tau_2$-dependent 2D EV spectra show oscillatory amplitude; notably, the $\nu_{COO}$ ($\omega_3$ = 1,328 cm$^{-1}$) excited state vibration characterized by $MLCT_B$ ($\omega_1 \cong$ 25,200 cm$^{-1}$) excitation. Contour lines: solid (dashed) = positive (negative) signal, 5% intervals beginning at ±10%. Residual intensity of the integrated ($\omega_1$, $\omega_3$) 2D peak area for the $\nu_{COO}$ coupled to the (b) $MLCT_A$ ($\omega_1 \cong$ 24,700 cm$^{-1}$) and (e) $MLCT_B$ electronic excited states (gray, circles). Temporal filtering (dashed) isolates early relaxation times ($0 < \tau_2 <$ 600 fs, red) or later relaxation times ($400 < \tau_2 <$ 1,500 fs, blue) to identify transient, low frequency amplitude modulations in either time range. Fourier transformed (FT) spectra of the temporally-filtered [(c) early = red; (d) later = blue] 2D residuals of $MLCT_A$ excitation show principal low frequency components (i.e., $\nu_{Ru-N}$ and/or $\nu_{Ru-bpy}$) responsible for the 2D EV peak amplitude modulation. Corresponding FT spectra for $MLCT_B$ excitation are shown in (f) and (g). In all FT spectra, the gray spectra are the background (no EV signal); the shaded regions represent ± 1 standard deviation from the average data (shown by circles). See sections 8.12.3-8.12.4 for discussion of data processing. Number of ($\omega_1$, $\omega_3$) points: $MLCT_A$ = 45; $MLCT_B$ = 24; Background (signal ≤ 5% max) = 3295..... 270

Figure 8.3. Vibronic eigenstate basis and energy level diagram. The measured eigenstate basis of $N3^{4-}$ is cast in terms of $\left|elec;\nu_{Ru-N},\nu_{Ru-bpy},\nu_{COO}\right\rangle$ where elec = A ($MLCT_A$, purple) or B ($MLCT_B$, blue) and the three following quantum numbers relate the quanta in each of the vibrational modes listed in increasing transition energy. The relative energies are derived from the multidimensional EV measurements: $\Delta E_{elec} \cong 500$ cm$^{-1}$ from $\omega_1$; $\nu_{Ru-N}$ = 340 cm$^{-1}$ and $\nu_{Ru-bpy}$ = 742 cm$^{-1}$ from $\omega_2$; and $\nu_{COO}$ = 1,328 cm$^{-1}$ from $\omega_3$. The eigenstates are numbered in increasing energy for reference throughout the discussion. The $N3^{4-}$ structure (top) schematically depicts the electronic excitation (light blue) and the vibrational motions involved with photoexcited charge transfer. The vibrational mode arrow colors correspond to the respective transitions given in the energy level diagram below. ..... 271

Figure 8.4. Early MLCT relaxation dynamics: electronically-localized excited state vibrational wavepacket. The $\omega_2$ spectral amplitude (black; FWHM = gray arrows) of the $MLCT_B$ excited state vibrational wavepacket arises due to coherence between the $\nu_{COO}$ and one quantum of a Ru-N stretching mode ($\nu_{Ru-N}$ = 340 cm$^{-1}$) within the excited state manifold. The $\tau_d$-dependence of the $\omega_2$ frequencies composing the wavepacket (green) indicate blue-shifting as the wavepacket propagates. Although the analytical form of $\tau_d(\omega_2)$ depends heavily on the polynomial function used to fit $\phi(\omega_2)$, the blue-shifting behavior of the wavepacket is consistent across many functions. See section 8.12.6, Figure 8.14 and Table 8.4 for spectral phase fits. ..... 273

Figure 8.5. Later MLCT relaxation dynamics: nonadiabatic internal conversion through vibronic coherence. (a) Residual intensity (gray) of the integrated ($\omega_1$, $\omega_3$) 2D peak areas for the $\nu_{COO}$ vibration with $MLCT_A$ (top) and $MLCT_B$ (bottom) character; data is offset for plotting. Examples of the temporal filters (purple/blue, dashed) used in short time FT analysis (FWHM = 120 fs, centered at $\tau_{center}$ (top axis)) of the $\tau_2$-dependent residual intensity. The purple window ($\tau_{center}$ = 710 fs) highlights the $\nu_{Ru\text{-}bpy}$ (742 cm$^{-1}$) coherent beating with $\nu_{COO}$ having exclusively $MLCT_A$ character while at a later delay ($\tau_{center}$ = 850 fs) the blue window shows the $\nu_{Ru\text{-}bpy}$ coherence having exclusively $MLCT_B$ character. (b) Short time FT results reveal the oscillatory electronic character of the $\nu_{Ru\text{-}bpy}$ coherence signature between $MLCT_A$ and $MLCT_B$ with 340 ± 40 fs periodicity. (c) Simulation of the coherence block in the

Redfield relaxation tensor for $\rho_{14}$ (purple) and $\rho_{36}$ (blue) during $\tau_2$ with an 800 fs coherence decay time where $\omega_{14} = \omega_{36} = 742$ cm$^{-1}$ and a 50 cm$^{-1}$ nonadiabatic coupling reproduces electronic oscillatory behavior for the vibronic coherence involving $\nu_{Ru\text{-}bpy}$ with $MLCT_A$ and $MLCT_B$ (data offset). See section 8.12.9 for discussion of Redfield relaxation dynamics and section 8.12.8 for simulation details. ..... 275

Figure 8.6. Full 3D EV Spectrum of Aqueous $N3^{4-}$. (a) The complete third order vibronic molecular response is plotted in its three frequency dimensions. (b) Slices at the $\nu_{Ru\text{-}N}$ (red) and $\nu_{Ru\text{-}bpy}$ (blue and purple) of the 3D EV spectrum. The time-dependent 3D frequency correlation between $MLCT_A$, $MLCT_B$, $\nu_{COO}$, $\nu_{Ru\text{-}N}$, and $\nu_{Ru\text{-}bpy}$ are described by the peaks at $\omega_3$ ~1328 cm$^{-1}$. Evidence for the other carboxylate modes is present in the 1350 cm$^{-1}$ < $\omega_3$ < 1400 cm$^{-1}$ range. The coloration depicts the time dependence, as schematically illustrated in Figure 8.1. On this scale, 0 < red < blue < purple in $\tau_2$ according to the timescales discussed in the chapter. Note: the dimensionality of this plot does not allow for representing the nonadiabatic internal conversion between $MLCT_A$ and $MLCT_B$ during the later $\tau_2$ period, which is shown in Figure 8.5. ..... 278

Figure 8.7. Exemplary Nonsecular 3D EV Relaxation Pathways in $N3^{4-}$. (a) A representative Feynman Diagram of the excited state vibrational wavepacket present during early time relaxation dynamics which requires a coherence-to-population transition for detection. (b) Two representative Feynman Diagrams depicting the later time relaxation dynamics resulting in the oscillatory electronic character discussed in the manuscript, which still requires a coherence-to-population pathway for detection. The dashed lines connecting different states in the Feynman Diagrams represent transitions undergone without external perturbation from a laser pulse..... 280

Figure 8.8. Coherence evolution during the relaxation of photoexcited $N3^{4-}$. A schematic representation of the first two picoseconds of photoexcited relaxation progresses from left to right (a-c). Initial MLCT electronic excitation (a) with MLCT states coupling the donor-acceptor vibrations shown ($MLCT_A$ = light gray well; $MLCT_B$ = dark gray well) and the initial wavepacket passing through ultrafast ISC. The ~600 fs propagation of the initial excited state vibrational coherence $\rho_{35}$ (b) involving $\nu_{Ru-N}$ of $MLCT_B$ (red wells); a coherence transfer to $\nu_{Ru-bpy}$ of $MLCT_B$ (blue wells) is merely suggested with sufficient

wavefunction overlap involving the $\nu_{Ru-bpy}$ lowest energy vibration. The ~1 ps propagation of the excited state vibronic coherences $\rho_{36}$ and $\rho_{14}$ involving $\nu_{Ru-bpy}$ (c) depicts the nonadiabatic internal conversion between $MLCT_A$ (purple) and $MLCT_B$ (blue) through the 50 $cm^{-1}$ nonadiabatic coupling strength. ..... 282

Figure 8.9. Instrument Characterization. (a) Broadband UV pump pulse spectrum and mid-IR probe pulse spectrum. (b) The instrument response function is assessed using the non-resonant tIR signal of a 250 μm Si wafer (black). The $N3^{4-}$ molecular response is observed outside of pulse overlap for $\tau_2$ > 200 fs from the transient-IR trace for the $\nu_{COO}$ excited state absorption ($\omega_3$=1328 $cm^{-1}$, red ). The signals are normalized by the absolute value of the greatest magnitude signal and overlaid for comparison. The non-resonant solvent-only tIR signal (blue; circles are data and line is three-point moving average) is scaled and offset such that zero signal is ΔT/T = -1 for comparison; the solvent response diminishes for $\tau_2$ > 200 fs, consistent with the decay of the Si signal and the onset of the $N3^{4-}$ molecular signal. ..... 288

Figure 8.10. Solvent Background and Signal Pump Power Dependence. (a) 2D EV spectra of the solvent ($D_2O$ in 300 mM NaOH) collected in the same sample configuration as the $N3^{4-}$; no significant solvent contributions are present. (b) The magnitude of the $\nu_{COO}$ ESA ($\omega_3$=1328 $cm^{-1}$) plotted at different pump pulse energies shows the data measured are linearly dependent on pump energy. Blue squares are average of five difference spectra with the error bars reflecting +/- 1 standard deviation from the mean; the black line is a linear fit with the fit parameters shown on the right. ..... 289

Figure 8.11. Pre-FT Data Processing of $\tau_2$-dependent 2D EV Data. (top, left) The cubic spline interpolated tIR spectrum collected independently, (top, center) the raw 2D EV spectra with $\tau_1$ = 0 for all $\tau_2$ delays, and (top, right) the 2D EV ($\tau_1$ = 0) data corrected for instrumental noise by normalization to the tIR data set. (bottom) The time traces of the carboxylate GSB and ESA for the data sets show the improvement in signal quality after removing further instrumental noise due to fewer 2D EV scans averaged than in the tIR data set. The blue traces = 2D EV ($\tau_1$=0) data set without normalization, red traces = with normalization, and black traces = interpolated tIR data (see discussion for details). ..... 292

Figure 8.12. Assessing Signal-to-Noise in $\omega_2$ Spectra. (a) Averaged 2D EV spectrum over all $\tau_2$ surfaces; gray shows background signal and red boxes highlight 2D EV regions of interest for vibronic couplings between $\nu_{COO}$ and both $MLCT_A$ and $MLCT_B$. Spectra from FT analysis on $0 \leq \tau_2 \leq 600$ fs data (b, red) and on $400 \leq \tau_2 \leq 1500$ fs data (c, blue) for $MLCT_A$ excitation. Spectra from FT analysis on $0 \leq \tau_2 \leq 600$ fs data (d, red) and on $400 \leq \tau_2 \leq 1500$ fs data (e, blue) for $MLCT_B$ excitation. Gray spectra in (b-e) are from FT analysis of the background signal shown in (a). The circles represent the average $\omega_2$ spectrum and the shaded areas represent ± 1 standard deviation from the mean. Number of ($\omega_1$, $\omega_3$) points: $MLCT_A$ = 45; $MLCT_B$ = 24; Background (signal ≤ 5% max) = 3295. ..... 294

Figure 8.13. Transient-IR Spectroscopy of $N3^{4-}$. (a) tIR time traces of the CN stretch region reports on the Ru-$(NCS)_2$ charge donor dynamics; ground state bleach (GSB) = 2116 $cm^{-1}$ (gray circles), excited state absorption (ESA) = 2070 $cm^{-1}$ (purple circles), time trace fits shown by solid black lines. (b) tIR time traces of the dcbpy ligand stretching region reports on the charge acceptor dynamics; carboxylate symmetric stretch GSB = 1375 $cm^{-1}$ (red circles) and ESA = 1328 $cm^{-1}$ (blue circles), bipyridine stretching mode ESA = 1271 $cm^{-1}$ (green circles). (c) tIR line shapes identify which charge acceptor vibrations are sensitive to excited state relaxation, as shown by the $\tau_2$-dependent full-width-at-half-max for all three peaks; the carboxylate symmetric stretch ESA is most sensitive to excited state charge transfer dynamics in the first few picoseconds of relaxation. ..... 297

Figure 8.14. Characterizing the Initially Excited Vibrational Wavepacket. The blue lines in all figures are the same $\omega_2$ spectra for the $\nu_{Ru\text{-}N}$ wavepacket ($\omega_2$ = 340 $cm^{-1}$) present during $0 \leq \tau_2 \leq 600$ fs. The figures in the left column (a,c,e) plot the spectral phase, $\phi(\omega_2)$, in red; experimental data is shown by the open circles and the solid lines are fits. The figures in the right column (b,d,f) plot the group delay, $\tau_d(\omega_2)$, in red, obtained by numerical differentiation of $\phi(\omega_2)$ as explained in equation 5. The different rows denote a different order of polynomial used to fit $\phi(\omega_2)$ during the analysis. ..... 301

Figure 8.15. Short Time Fourier Transform Analysis of Initial Wavepacket. Analysis performed using the same windowing function used in the later time STFT analysis (double-sided tanh) discussed in more detail in section 8.12.7, but with a window FWHM of 500 fs that has $\tau_{center}$ delays varied through the corresponding earlier delay times $0 \leq \tau_2 \leq 600$ fs. The

thick solid black line is a guide to the eye to highlight the blue-shifting of the $\nu_{Ru\text{-}N}$ center frequency. Measured in this way, the $\omega_2$ vibrational frequencies blue-shift by ~60 $cm^{-1}$ over the interval $250 \leq \tau_{center} \leq 570$ fs, consistent with the blue-shift measured by the spectral phase / group delay analysis in Figure 8.14. ..... 302

Figure 8.16. Temporal Windowing Function Effects on Time-Frequency Analysis. The left column (a, c, e) show the 2D EV residual data (gray) for the signal regions of the $\nu_{COO}$ vibronically coupled with the $MLCT_A$ (red) and $MLCT_B$ (blue); the dashed lines show the temporal windowing functions used in the three time-frequency analyses for comparison. The right column (b, d, f) are the time-frequency analyses results from a short time Fourier transform (details in the section 8.12.7 discussion) for $MLCT_A$ (red) and $MLCT_B$ (blue) at $\omega_3$ = 742 $cm^{-1}$. A double-sided hyperbolic tangent window (a,b), Hanning window (c,d), and a Gaussian window (e,f) are compared. ..... 305

Figure 8.17. Effect of Temporal Filter Width on Time-Frequency Analysis. The time-frequency analyses for varying filter widths (FWHM) are shown for the double-sided tanh window: (a,b) 500 fs, (c,d) 350 fs, (e,f) 200 fs, (g,h) 120 fs. The 2D EV residual time-domain data and temporal filtering is shown in the left column and the short time Fourier transformed data is plotted in the right column. The same coloration as Figure 8.16 is used in this figure. ..... 306

Figure 8.18. Carboxylate $\omega_1$ Peak Positions During $\tau_2$. The ground state bleach (top) and excited state absorption (below, $\nu_{COO}$) peak positions in $\omega_1$ show negligible peak shifting over the range $190 < \tau_2 < 2010$ fs. ..... 309

Figure 8.19. (a) Calculated IR spectrum of the lowest energy triplet of $N3^{4-}$ with implicit solvent; inset shows a zoom-in of dashed gray spectral region. (b) Example normal modes from calculations displaying vibrational character of the $\nu_{Ru\text{-}N}$ and $\nu_{Ru\text{-}bpy}$ modes. Mode 39 (303 $cm^{-1}$) shown for $\nu_{Ru\text{-}N}$ and mode 67 (710 $cm^{-1}$) shown for $\nu_{Ru\text{-}bpy}$. ..... 310

Figure 9.1. Molecular structure of 10-Hydroxybenzo-[*h*]-quinoline (HBQ). ..... 317

Figure 9.2. Schematic photophysical picture of ESIPT in HBQ. The colored arrows represent the excitation of the ground state enol to the excited state enol (blue), the ultrafast proton transfer and consequent relaxation in the excited state (green, curved on $S_1$), the fluorescence of the equilibrated keto form in the excited state (orange, wavy), and the

relaxation of the hot ground state keto form as it reverts back to the enol form (green, curved on $S_0$). The gray dashed and solid lines, as well as the $S_2$ excited state (~1860 $cm^{-1}$ lower than the Franck-Condon excitation point) indicate photophysical dynamics that are debated in the literature. ..... 319
Figure 9.3. Electronic and Vibrational Linear Absorption Spectra of HBQ and DBQ. (top row) The electronic absorption of HBQ (left) and DBQ (right) is shown (gray) and the vibronic progression is fit for the $S_1$ (red) and $S_2$ (blue) absorptions to a displaced, anharmonic vibrational mode model (vibronic fits = dashed, sum = solid). The sum of the fits to both absorptions is shown in dashed black, and the residual (gray – dashed black) are in teal below the absorption spectra. (bottom) The solvent subtracted vibrational spectra of the ground electronic state HBQ (purple, solid) and DBQ (green, solid) are shown the fingerprint region and the OH and OD stretching region in the middle and bottom rows. Due to significant spectral overlap in the OH stretch region, the spectrum without solvent subtraction (purple dashed) and the solvent-only spectrum (gray solid) are also shown. .. 325
Figure 9.4. Line Broadening Comparison Between HBQ and DBQ. The ratio of the bandwidths were obtained from the vibronic progression fitted parameters in Table 1. ..... 329
Figure 9.5. Transient-IR Spectra of HBQ and DBQ in the Fingerprint Region. The difference spectra are normalized to the greatest magnitude signal found at 1446 $cm^{-1}$. ..... 334
Figure 9.6. Gas Phase TDDFT Calculation of HBQ in the $S_1$ Keto (K*) State. The vibrational mode was calculated to be at 1457 $cm^{-1}$ and appears to involve the proton participating in ESIPT as an N-H wagging motion with other hydrocarbon backbone motions. (dark gray = carbon, light gray = hydrogen, blue = nitrogen, red = oxygen) ..... 335
Figure 9.7. Polarization-Selective Transient-IR Spectra for HBQ and DBQ. Spectra are locally normalized for comparison of spectral shapes. ..... 336
Figure 9.8. Transient-IR Anisotropy of HBQ and DBQ. (top) the parallel (dark blue) and perpendicular (light blue) time traces for HBQ (left) and DBQ (right) are shown for the first 50 ps of $\tau_2$ and vibrational frequency of 1450 $cm^{-1}$. (bottom) The tIR anisotropy, r(t), is calculated (black) and fits to the anisotropy (red) are shown for both molecules of the first 2 ps on data collected outside of the instrument response function (IRF, teal). The insets shows the 50 ps anisotropy. ..... 338

Figure 9.9. Polarization-Selective 2D EV Spectra of HBQ at $\tau_2$ = 150 fs. The spectra are globally normalized to show the relative signal amplitudes between the two polarized experiments. Dashed contours are negative and spaced at 10% intervals of the maximum 2D EV signal. ..... 341

Figure 9.10. Electronic Excitation Dependent Anisotropy From Polarization-Selective 2D EV of HBQ. The parallel (perpendicular) traces of $\omega_1$ chosen for the 2D EV peak maximum at $\omega_3$=1446 $cm^{-1}$ is shown in solid (dashed) blue, the anisotropy is shown as red open circles. ..... 342

# LIST OF TABLES

Table 2.1. This table summarizes some of the information conveyed in the series of 2D EV and 2D VE simulations shown in Figure 2.5-8. The table is organized by grouping cases 1-4 for three combinations of the $\mu_{eg}^{(1)}$ and $\lambda$ parameters. The first four rows show cases 1-4 under the Condon approximation and with no electronic-state-dependent vibrational dephasing ($\mu_{eg}^{(1)}$=0, $\lambda$=1); rows 5-8 show the influence of non-Condon effects on all cases ($\mu_{eg}^{(1)}$=0.15, $\lambda$=1); rows 8-12 show the effects of electronic-state-dependent vibrational dephasing for all four cases($\mu_{eg}^{(1)}$=0, $\lambda$=1.5); and the last row (simulation not shown) shows a case 4 system where all simulation parameters are nonzero ($\mu_{eg}^{(1)}$=0.5, $\lambda$=1.5). Each row corresponds to a set of conditions used to simulate 2D EV and 2D VE spectra (excluding the last row); the absolute maximum peak intensities ($I_{max}$) for 2D EV and 2D VE simulations are listed and normalized for comparison. The peak with the greatest magnitude and the figure in which the simulation is shown are given for referencing the simulations shown earlier in the text. ..... 78

Table 2.2. 2D Electronic-Vibrational Transition Pathway Index ..... 92

Table 2.3. 2D Vibrational-Electronic Transition Pathway Index ..... 94

Table 5.1. Center Line Slope Fitting Parameters. The ($\omega_1$, $\omega_3$) coordinates for the peak maxima in the range 24800 cm$^{-1}$ $\leq \omega_1 \leq$ 25200 cm$^{-1}$ for both the ground state bleach and the excited state absorption are obtained and fit to the first order polynomial:

$S_{max}(\omega_3) = m \times (S_{max}(\omega_1)) + b$ . ..... 172

Table 6.1. Dipole angle definitions specifying the relative dipole orientation in the molecular frame. ..... 185

Table 6.2. A Multimode 2D EV peak categorization legend. ..... 191

Table 6.3. Comparison of Calculated Dipole Moments for Different Vibronic Hamiltonian Parameters. ..... 200

Table 6.4. Ratios of Calculated Dipole Moments for Different Vibronic Hamiltonian Parameters. ..... 200

Table 6.5. Non-vanishing tensor elements and the orientational part of the response function for the parallel polarized experiment (IJKL = ZZZZ) and the perpendicularly polarized experiment (IJKL = YYZZ), for the two orthogonal dipole directions in z and y within the fixed molecular frame. The diffusional correlation functions are given by $c_1(\tau) = exp\left[-2D_{or}\tau\right]$ and $c_2(\tau) = exp\left[-6D_{or}\tau\right]$. When orientational diffusion is much slower than the vibronic dynamics, $D_{or} \to 0$ and $c_1(\tau),\ c_2(\tau) \to 1$. ..... 203

Table 6.6. Angular dependence of peaks in 2D EV spectroscopy. Each peak is labelled if it occupies a distinct ($\omega_1$,$\omega_3$) peak position; multiple Liouville transition pathways can contribute to the same peak. ..... 205

Table 6.7. Ground State Bleach Multimode Vibronic Transition Pathways ..... 219

Table 6.8. Excited State Stimulated Emission Multimode Vibronic Transition Pathways ..... 220

Table 6.9. Excited State Absorption Multimode Vibronic Transition Pathways ..... 220

Table 6.10. Orientational Response Functions for Parallel and Crossed Polarization Configurations. ..... 221

Table 7.1. Comparison of Experimental and Calculated Relative Dipole Angles, $\theta_{vib}^{S_n}$ (degrees).[a] ..... 237

Table 7.2. Transient-IR Time Trace Fitting Parameters ..... 243

Table 7.3. Computed TD-B3LYP/def2-SVP transition energies and corresponding oscillator strengths relative to the electronic excitations from the ground state singlet optimized structure for the for the $Ru(dcbpy)_2(NCS)_2^{4-}$. The corresponding arriving state are reported in the first column. ..... 252

Table 7.4. Experimentally Determined $\theta_{vib}^{S_n}$ from 2D EV Anisotropy. ..... 253

Table 7.5. Calculated $\theta_{vib}^{S_n}$ Between $\mu_{S_0}^{S_n}$ and $\mu_{vib}$ for Vibrational Modes in $T$. Pink region is the intersection of the $\mu_{S_0}^{S_n}$ and $\mu_{vib}$, each table element in this region is the corresponding $\theta_{vib}^{S_n}$ given in degrees. [b] $\bar{\nu}_{CN}$ denotes the averaged $\nu_{CN}^{sym}$ and $\nu_{CN}^{asym}$ angles for a given $\mu_{S_0}^{S_n}$. ..... 254

Table 8.1. Pump and Probe Beam Center Frequencies and Bandwidths ..... 288

Table 8.2. Regions of Interest for $\omega_2$ Spectral Analysis. ..... 296

Table 8.3. Transient-IR Fitting Parameters ..... 299

Table 8.4. Spectral Phase ($\varphi(\omega_2)$) Fitting with $n^{th}$-order Polynomials..... 301
Table 9.1. Vibronic Progression Fitting Parameters for Electronic Absorption Spectra of HBQ and DBQ. The gray shaded values of $S_2$ reflect less-certain values given the experimental electronic absorption spectra does not extend beyond 300 nm. Accordingly, very little confidence is placed in the fitted anharmonicity for $S_2$, but the fits to the first two vibronic peaks in $S_2$ are reliable. ..... 327
Table 9.2. Transient-IR Anisotropy Fitting Parameters for HBQ and DBQ. The time-dependent anisotropies for data following the instrument response ($\tau_2$ = 100 fs) were fit to the sum of three exponential decays. The amplitudes and lifetimes are given. ..... 339

# ACKNOWLEDGEMENTS

My own efforts alone would have been insufficient to complete the work presented in this dissertation. This compilation of my graduate work is truly a testament to many great people who have helped me in countless ways during graduate school. For all of you, I am very grateful.

I owe my advisor, Munira Khalil, a most genuine thank-you for her guidance, her support, and her trust in me throughout my graduate work. I am indebted to you for the opportunities you have given me to develop into the scientist that I am today and I thank you for taking the responsibility of teaching me how to be a careful and thorough spectroscopist.

I credit Steve Mayer, my undergraduate physical chemistry professor, with helping me realize that I enjoy physical chemistry and, in particular, playing with lasers. I credit Shannon Mayer, my undergraduate optics professor, with fueling my curiosity for understanding the properties of light and how it interacts with nature. Between you both, I owe you each more thanks than one can give. Your kindness, generosity, friendship, brilliance, wit, and love have given me a personal and intellectual foundation on which the rest of my life will be built. I am endlessly grateful and fortunate to have you two in my life.

Perhaps, the single reason I am in this position today is because the late Professor Daniel 'Doc' Wright introduced me to the idea and meaning of pursuing a Ph.D. – even before I was set on studying chemistry! Though a Shakespearean scholar, his curiosity and passion for knowledge knew no bounds. I am eternally grateful for our innumerable late-night conversations over many cups of coffee, our travels abroad, and the lifetime of lessons I learned from Doc. His influence on my life has been substantial and he is a continued source of inspiration for my work.

Of course, my thanks to our research group – the Khalil Krew – is in order. I thank Trevor for teaching me how to build a nonlinear optical experiment with "good form" and for his light-hearted office banter which helped build an enjoyable group culture. Zach and Madhu were the older students with whom I meaningfully overlapped; I thank them for their guidance in navigating my early years of graduate school. I learned a great deal from Zach and Madhu, including how to recognize when a brief prayer to the laser gods for laser stability may be a good idea. I thank Joel Leger for his thorough work in the lab; I enjoyed our work together immensely. Jason, Rob, and Will joined as I was finishing my third year, and they have all contributed positively to the group in many respects. Jason's "by-the-book" attention to detail, optimism, and

genuine care for others are characteristics from which we all benefit and should thank him for; I feel very confident leaving the 2D EV lab in his hands. Rob's relentless persistence through the pains of bringing the 2D VE lab back to productivity is admirable and the fruits of this labor will be harvested, I am sure; his thoroughness in problem solving makes those around him better scientists. Will's meticulousness and thoroughness in building the new spectro-electrochemical capability in our lab have been impressive and I appreciate his philosophical perspectives that pepper many conversations in the office. Ben has made exciting strides in the group's X-ray work and I think we all owe him for contributing to our understanding of inorganic chemistry; together, Ben and I are "top of the league" and will never walk alone. While Chelsea and I have overlapped the least, I am so thrilled to have worked with her; her excitement and precise thinking has influenced me greatly over the past several months. I owe many thanks to Kim and Diana who keep the department functional so we can do great science every day and also for being great people and friends. I am deeply grateful to all of you for helping me grow as a scientist, a teacher, a friend, and as a person; because of you I am honestly sad to leave the U.W.

Graduate school would not have been as enjoyable without a strong group of friends in Seattle, whose friendships I hope never fade. In particular, Brandon, Lucas, Tori, Mikey, Bre, and Caitlin. Our backpacking adventures, camping weekends, parties, and card nights are among my most enjoyable and memorable times in Seattle. I thank you all for being such great people and awesome friends.

My family has played an important role in my life and my work. Without the unending support, encouragement, and love from my parents, I am sure I would not be here today. I am fortunate to have the best brother one could ask for, Eli; his joy and sense of humor are pervasive in everything he does and they have contributed very much to my quality of life. My sister, Abby, has grown into an amazing person and I am excited for her future. Thank you all for your continued love and support.

Finally, the person to whom I am most grateful is my wife, Katie, who began her journey through graduate school with me. Each day, you motivate me to be a better person in every way. Without your love, encouragement, brilliance, and compassion I would not be the person I am today. I am excited for our next chapter of life in Berkeley, and I look forward to growing with you during our lives together. I love you and I am endlessly thankful for your companionship.

# DEDICATION

I dedicate this work to the only person who would have been more excited than me to see that I have earned a Ph.D.; his presence is missed dearly.

To Doc.

*“Oh Captain, My Captain!”*

"**There are cathedrals which**, apart from their consecrated purpose, inspire solemnity and awe. Even the curious visitor speaks of serious things, with hushed voice, and as each whisper reverberates through the vaulted nave, the returning echo seems to bear a message of mystery. The labor of generations of architects and artisans has been forgotten, the scaffolding erected for their toil has long since been removed, their mistakes have been erased, or have become hidden by the dust of centuries. Seeing only the perfection of the completed whole, we are impressed as by some superhuman agency. But sometimes we enter such an edifice that is still partly under construction; then the sound of hammers, the reek of tobacco, the trivial jests bandied from workman to workman, enable us to realize that *these great structures are but the result of giving to ordinary human effort a direction and purpose*."

(Excerpt from "Thermodynamics and the Free Energy of Chemical Substances" by Gilbert Newton Lewis and Merle Randall, McGraw-Hill, 1st Edition, 1923)

# Chapter 1. PROLOGUE

*"Life is itself a game of football."*

*– Sir Walter Scott, Scottish Novelist, Historian, and Poet*

*"In a football match, everything is complicated by the presence of the other team."*

*– Jean-Paul Sartre, French Philosopher and Novelist*

## 1.1 What Motions Are At Play?

Often times, one can productively describe a chemical reaction based upon the energies of the stable species, such as the reactants and the products, and some knowledge of the energy barriers separating these equilibrium chemical species. A more accurate – and rich – description may be obtained by also understanding the nature of any meta-stable intermediate species between the equilibrated structures. Together, these pieces of information allow us to understand the rate of a chemical reaction. However, extending our description of chemical reactivity beyond measuring kinetics to include how the choreography of different molecular degrees of freedom plays out during a chemical reaction is a far more demanding endeavor. This would be true even for studying a single molecule isolated in vacuum; for example, during a photoinduced intramolecular charge transfer chemical reaction. While the assumption that the motions of the electrons and the nuclei within a molecule can be separable has enabled our intuition and understanding of molecular physics,[1] their motions may not be completely independent from each other in some cases. Indeed, the motion of an excited electron may alter the nuclear structure enough to change the relative movement of the nuclei (i.e., the vibrational modes). Likewise, an excited vibrational mode may alter the potential energy landscape sufficiently that the instantaneous definition of the molecule's electronic state is much more ambiguous. Since the chemistry supporting life, and life itself, does not occur in vacuum but

in the presence of other molecules and compounds of widely varied complexity, a truly complete description of a condensed phase chemical reaction is anything but straight-forward. However, a good place to start is by measuring the interplay between the electronic and vibrational motions in condensed phase molecules with the aim of describing the correlations between these different degrees of freedom. This dissertation has exactly this aim.

What are the relevant motions at play and who are the players – both major and minor? If we cannot characterize all of them simultaneously, which can we – or should we? At this point, an analogy will prove useful to discuss these questions and to introduce a conceptual approach for answering them. Consider the analogy of a football (i.e., soccer) match between two teams – let's say Liverpool F.C. versus Manchester United F.C. – where Liverpool has just scored a goal to win the match. Figure 1.1(a) depicts two Liverpool players, A and B, who were involved in the game-winning goal. Their positions on the field are shown at the start of the game (x(0),y(0)) and their movement on the field for the duration of the play ($\tau$ minutes) leading to the game-winning goal is shown as distributions in their lateral (x coordinates) and vertical (y coordinates) positions. A tractable starting point for analyzing how Liverpool scored their goal would be separating their positional distributions shown in Figure 1.1(a) into the ranges of lateral and vertical positions they occupied and consider just one direction; let's focus on their lateral positions. Shown below the field schematic in Figure 1.1(a) is the distribution of lateral positions – or the lateral position "spectrum" – for both players during $\tau$. Each players' average position is reflected by the x-coordinate of the maximum in their positional spectrum (the "center of the peak") and the range of their positions is reflected by the width of their positional spectrum. This spectrum can only communicate that, on average, the two players occupied different lateral positions during the play and that player B moved further

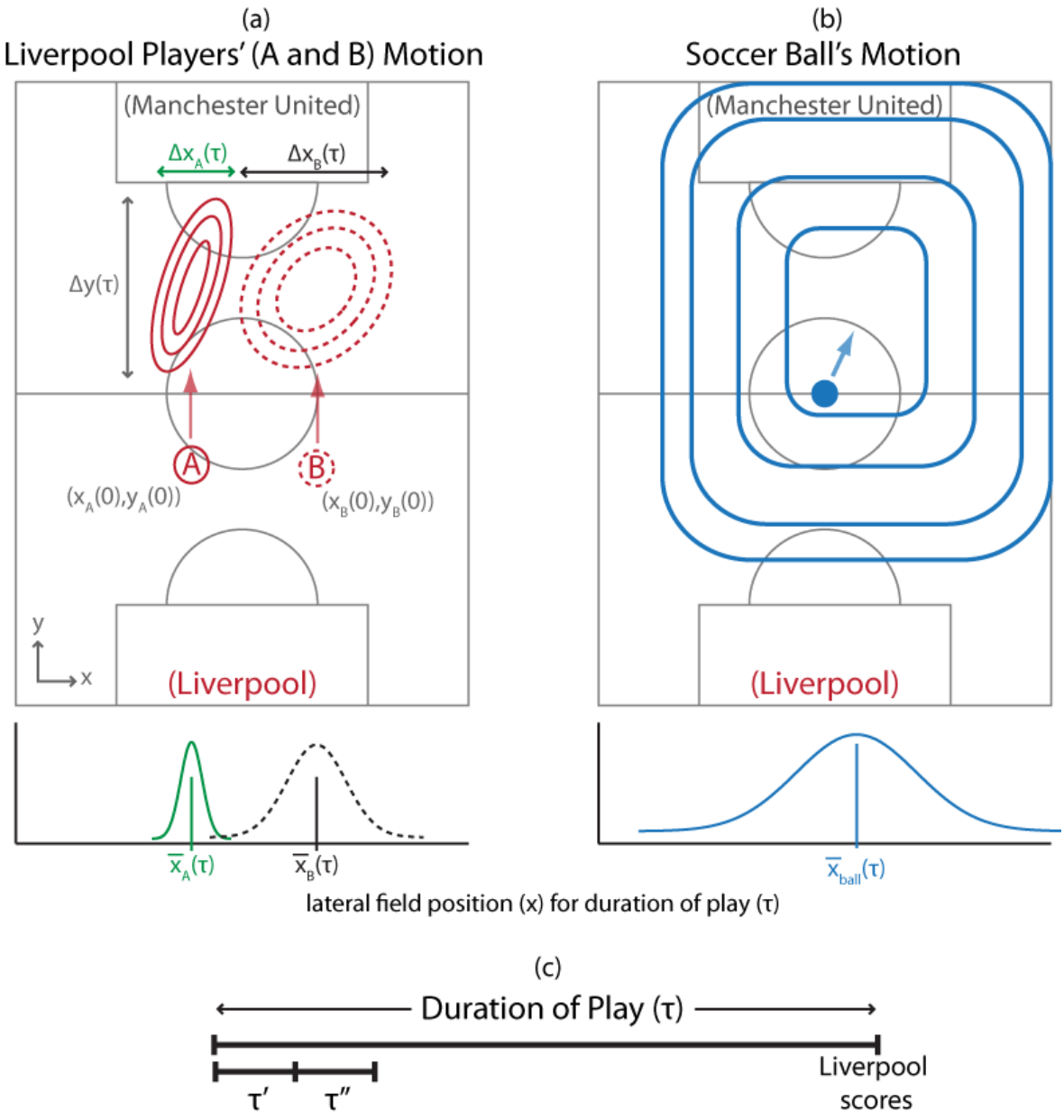


Figure 1.1. Positional Distributions of Liverpool Players and the Football During Liverpool's Game Winning Goal over Manchester United. (a, top) Liverpool players A (red, solid) and B (red, dashed) at their positions at the start of the match [($x_A(0),y_A(0)$) and ($x_B(0),y_B(0)$)] and their field position distributions (contours) for the duration of the match (τ minutes) in which they scored their goal. (a, bottom), the lateral position distributions are shown for player A (green, solid) and B (black, dashed) about their average position ($\overline{x}_A$ or $\overline{x}_B$) with their lateral range ($\Delta x_A$ or $\Delta x_B$). (b, top) Positional distribution of the ball (blue) for the same duration; (b, bottom) the lateral spectrum of the ball's motion. (c) Duration of the match, τ minutes, in which the goal was scored; the goal marks the end of the play (after τ minutes). The play can be broken up into shorter time intervals: an earlier interval τ' and a later time interval τ''. As shown in (c), the first interval begins at the beginning of the play (τ minutes before the goal is scored); the second interval begins after the first interval ends (τ-τ' minutes prior to the goal).

than player A. While this is descriptive, there is important information hidden in that spectrum, such as how *quickly* the players move throughout their lateral ranges during the play and how one player's motion is related to the other player's motion. Arguably, these pieces of information are more important for understanding how the goal was scored.

To extract this information, one could separate the play's duration into finer increments of time. As shown in Figure 1.1(c), the durations $\tau$' and $\tau$'' are two shorter time intervals which begin $\tau$ minutes and $\tau$-$\tau$' minutes prior to the goal being scored, respectively. By comparing the players' lateral position distributions during $\tau$' and $\tau$'', we can extract information related to how quickly they change positions (i.e., their movement) during this time. For example, if player A is moving slowly relative to the chosen intervals, then his position will not have changed much between $\tau$' and $\tau$''. Conversely, if player B is moving very quickly then during each of these intervals he could occupy the full range of lateral positions which he occupies over the course of the whole play. In these scenarios, the two peaks for the two players' lateral positions during $\tau$ would actually describe very different player movement without appearing terribly different from one another. The slow moving player A's distribution would actually be the sum of many smaller positional distributions (Figure 1.2(a)) and the fast moving player B's distribution would be composed of many distributions having the same full width of his lateral position spectrum for all of $\tau$ (Figure 1.2(b)). However, the *one-dimensional* (i.e., only one axis encoding lateral position) spectrum alone is insufficient to obtain this information. Extracting this information requires a *two-dimensional* positional spectrum in which the players' positions during $\tau$'' are shown as a function of their positions during $\tau$'. Such a 2D spectrum directly relates the players' lateral positions during the two intervals and is depicted in Figure 1.2(c). The positions, amplitudes, and line shapes of the 2D peaks appearing for

players A and B will directly convey this information whereas it was hidden in the one-dimensional plot in Figure 1.1(a, bottom). That is, player A's 2D positional spectrum (Figure 1.2(c), green) shows a strong linear correlation in his lateral position between the two intervals through the positively elongated peak along the diagonal line ( $\bar{x}(\tau') = \bar{x}(\tau'')$ ) while player B's 2D positional spectrum (black dashed) shows no correlation in his lateral position between the intervals by the broad, symmetric 2D peak. Only by viewing the players' motion in this way could this information be accessed.

Furthermore, this 2D plot could also determine if player A's motion is coupled to player B's motion. For example, if player A's lateral movement during τ' induces player B to move during τ'' rather than each player moving at random unrelated times during τ, then player B's position during τ'' will have a defined relationship with player A's position during τ'. This correlated motion between the players will manifest in the 2D spectrum as "cross" peaks placed at the intersections of the positions of the different players (i.e., "cross" peaks located at either $(\bar{x}_A(\tau'), \bar{x}_B(\tau''))$ or $(\bar{x}_B(\tau'), \bar{x}_A(\tau''))$ in the 2D spectrum shown in purple in Figure 1.2(c)). Moreover, their motion could be positively or negatively correlated which would appear through the slopes of the cross peaks in the 2D spectrum. These positively or negatively sloped peak shapes would reflect that the players moved in the same direction or in opposite directions, respectively, in a correlated fashion during τ. All of this information is contained in the 1D position spectrum of Figure 1.1(a, bottom), it is just presented differently – more directly – in the 2D positional spectrum of Figure 1.2(c). The integration of the 2D spectrum onto the abscissa would result in the 1D spectrum. Thus, a deeper understanding of how players A and B interacted during this pivotal moment in the game is obtained by measuring the 2D positional spectrum.

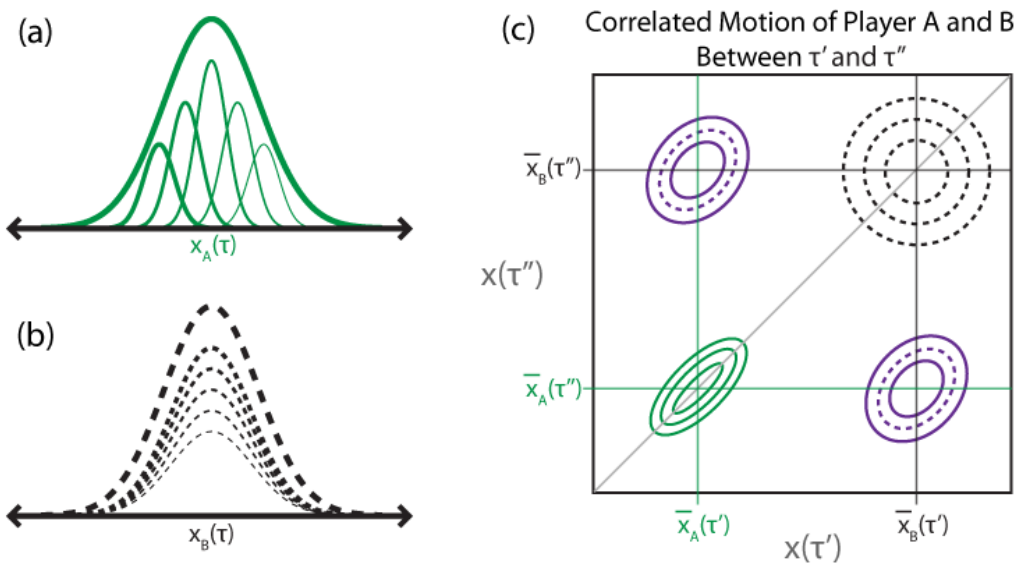


Figure 1.2. Understanding Players' Motion with Two-Dimensional (2D) Positional Resolution. (a) Player A's distribution during the full play's duration (τ) is shown as the sum of many localized distributions (varied by line thickness) during various shorter time intervals, τ' or τ'', during the play. (b) Player B's positional distribution is more delocalized, sampling the full range of lateral positions during all shorter time intervals. (c) The 2D lateral positional spectrum representing the movement of the two players during τ. The solid green elongated peak at ( $\bar{x}_A(\tau'), \bar{x}_A(\tau'')$ ) shows that player A moves more slowly between periods τ' and τ'', or that at later times there is "memory" of his position at earlier times. The dashed black symmetric peak at ( $\bar{x}_B(\tau'), \bar{x}_B(\tau'')$ ) shows that player B moves very fast by comparison to the shorter time intervals τ' and τ''; there is no relation between his positional distribution during τ' and τ''. Both of these peaks are referred to as "diagonal" peaks as they describe the lateral motion of the same player during the two intervals. The purple peaks at coordinates ( $\bar{x}_A(\tau'), \bar{x}_B(\tau'')$ and $\bar{x}_B(\tau'), \bar{x}_A(\tau'')$ ) are referred to as "cross" peaks as they describe the coupled motion between player A and player B during the play. They are the result of the mixing between the two players' motions and are depicted with both dashed and solid line contours. Finally, they are positively elongated reflecting that player A's motion in one direction during τ' drives player B to move in the same direction during τ''.

Of course, one crucial part of Liverpool's goal has been left out so far – the motion of the ball! One could ask: How did the ball move when Liverpool scored? In principle, the ball can move faster than any single player on the field can move. An adult professional footballer can kick a ball ~25-30 m/s whereas the current world-record for the 100 m dash gives a human's top speed of ~10 m/s. Thus, it is safe to assume that the ball can move ~3x faster than the players at any given moment. In this example, the much faster motion of the ball probably results from Liverpool passing the ball around the Manchester United defense to score the goal.

Since the ball can move about a larger area of the field than any single player can cover during a given time period, its positional distribution (lateral and vertical) shown in Figure 1.1(b) is much broader than either of the two players' distributions. The 2D lateral position spectrum (Figure 1.3) of the ball's motion reflects how quickly the ball moved during τ. The 2D peak is largely symmetric, covering the entire lateral area shown in Figure 1.1, which indicates the ball moves very fast during the period in which Liverpool scored. Notably, there is also a clear positive elongation indicating that there are periods during τ in which the ball moves more slowly than others (perhaps, closer to the pace of the players). It may not be terribly surprising to see some elongation in this peak because the players are the ones moving the ball. However, the extent of the elongation is useful for understanding how quickly, and how far, the players pass the ball.

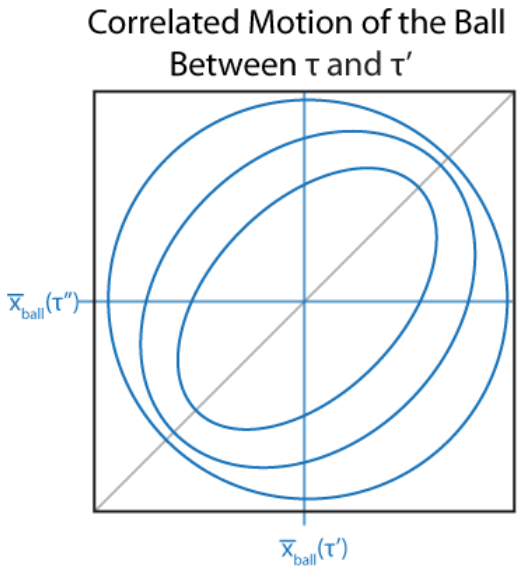


Figure 1.3. Understanding the Football's Motion with Two-Dimensional Positional Resolution. In the same way that the players' motion was resolved into two positional dimensions, the football's positional distribution is plotted during τ' and τ''. This distribution is much broader than the players' distributions for the same duration because the ball moves much faster than the players do during this period, giving rise to the largely symmetric feature. The presence of elongation reflects that ball also moves more slowly during some periods of the overall play leading up to Liverpool's goal.

Now, perhaps the most important question to answer is: How do players A and B move when the ball moves in a specific way? This information is invariably present in all of the plots just described; however, it is not readily accessible to the observer. This is because the two cases described are focused on either the players' motion or the ball's motion. The two axes in the 2D plots shown above are measuring the *same type* of motion at both intervals during $\tau$ to monitor how that particular motion changes. Of course, since each analysis is parametrized by the procession of the match during $\tau$, the motion of the ball is related to the motion of the players who are playing the game, and the players' motion is influenced by the motion of the ball. In football, these two degrees of freedom are inextricably linked (here, I invoke the introductory quote by Sir Walter Scott – indeed, was he correct!).

What motions are at play? Clearly, in this analogy, both the rapid motion of the ball and the correlated motions of the players are present. But, which should we monitor? As discussed above, it is possible and useful to measure these two different motions separately. To begin to understand how the players' motion and the motion of the ball are related, a different kind of experiment is needed. In the same way that the correlated movement of two *different* players was observed through a cross peak in Figure 1.2(c), the relationship between the motion of the ball and the players can also be investigated. The way to directly observe the correlated movement between the ball and the players is through a 2D plot in which one axis describes the motion of the ball and the other axis relates the motion of the players. An example of this 2D spectrum is shown in Figure 1.4. In such a spectrum, all peaks that appear would be cross peaks indicating coupled movement between the ball and the players. The relevant players to be monitored, at least initially, are those for whom cross peak are measured in this "mixed-motion" 2D plot.

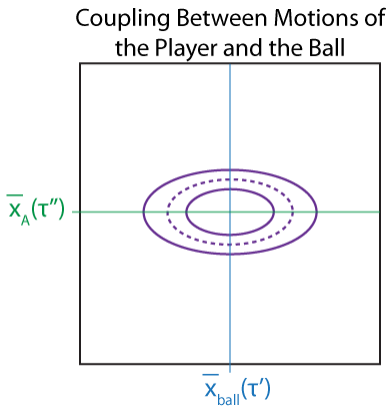


Figure 1.4. A 2D Positional Spectrum Correlating the Motions of the Ball and Liverpool Player A.

And yet, while the observer may now feel all the wiser for revealing a more fundamental relationship explaining how the players move in a correlated fashion with the motion of the ball during the period τ, there are still more complications. As Sartre was keenly aware, one of those complications is the presence of the other team. Specifically, to more completely understand how players A and B move in correlation with the ball during a real football match, the observer must consider other players' motions that may still be affecting the directly measured variables, but which are not as directly accounted for in the analysis. Finally, a most important factor in any football match is the environment: Is the team playing at home, where their loyal fan base can chant, praise, and sing in support of the team's every move? Or, are they playing away, where the fans are constantly heckling every motion and where the referees may provide more extended time than necessary for the away team's detriment?

The above analogy translates into the realm of molecular spectroscopy that is the concern of this dissertation in the following way: the players are the nuclei, specifically they are the relative motions of the nuclei – or the vibrational modes – of the solute (the molecular system of interest); the much faster motion of the soccer ball by comparison to the players represents the electrons, though in the molecular world there would be many soccer balls on the pitch at

one time due to the many electronic states present and participating in molecular dynamics; and the other team, the fans, and the referees all represent the bath composed of other intramolecular coordinates and the solvent environment that is present and actively influencing the dynamics of condensed phase chemical reactions, even though the effects of the environment may be less directly quantifiable. During any condensed phase chemical reaction, these different components all contribute to the reaction's time scale and the mechanism by which it operates. As a chemist, accurately describing a chemical reaction – especially a *photo*chemical reaction occurring in an excited electronic state – requires us to conquer the demanding endeavor of building up a molecular-level understanding of the orchestrated molecular choreography of these different dynamics. We must continue to develop our intuition for how the forces within and between molecules dictate the temporal evolution of a molecular species throughout a chemical reaction. This dissertation contributes toward this end by developing new tools that provide insight into complex, multi-coordinate, photochemical reactions and by applying these tools to interesting reactions.

## 1.2 Measuring Molecular Dynamics in the Condensed Phase

Characterizing photochemical reactions requires sufficient temporal and spectral resolution in an experimental set-up to accurately measure the dynamics of interest. An effective experimental probe of condensed phase molecular dynamics must be sensitive to structural changes of the molecule. Changes in electronic structure can occur on timescales ranging from pure electronic motion on 0.1–1 femtosecond (fs, $10^{-15}$) timescales to the nanosecond (ns, $10^{-9}$ s) and microsecond (μs, $10^{-6}$ s) lifetimes of excited triplet states that characterize phosphorescence. The timescales of vibrational motion range from the single oscillatory period of a high frequency molecular vibration (e.g., an -OH stretch ≈10 fs) to vibrational dephasing

and relaxation occurring on the picosecond (ps, $10^{-12}$ s) timescale. The electro-magnetic spectral regimes relevant to these two degrees of freedom in solution phase small molecules are quite disparate.

As the natural language of molecular spectroscopy is in reference to transitions between different states of a molecule, we typically speak in terms of frequencies of light that match the energy separation between different states. In general, the energy spacing between electronic states is much larger than between different vibrational states. A cartoon representation of these different energy levels is given in Figure 1.5 for the ground (g) and excited (e) electronic potential energy surfaces with vibrational states specified by v = 0, 1, 2, etc. in the ground electronic state and v' = 0',1',2', etc. in the excited state. The energy separating these different levels are represented in frequencies (ω) where the subscripts denote which particular energy spacing a specific frequency references. The electronic transitions, $\omega_{eg}$, typically span the visible and ultraviolet (UV) region (250 – 800 nm, or 40,000 – 12,500 $cm^{-1}$) while the vibrational transitions are roughly 10 times smaller in energy (2,500-10,000 nm, or 4000 – 1000 $cm^{-1}$).

### 1.2.1 *Linear (1D) Absorption Spectra: Electronic and Vibrational*

One-dimensional spectroscopies performed in either the time or the frequency domain are capable of capturing all of the dynamics discussed above. A schematic representation of a generalized 1D spectrum is shown in Figure 1.5(b, top panel). Vibrational frequencies in an ensemble of condensed phase molecules represent the average energy separation between different vibrational levels in a single electronic state. These energies are determined by the chemical structures of the molecular ensemble, which can vary greatly throughout micro-environments in the ensemble.

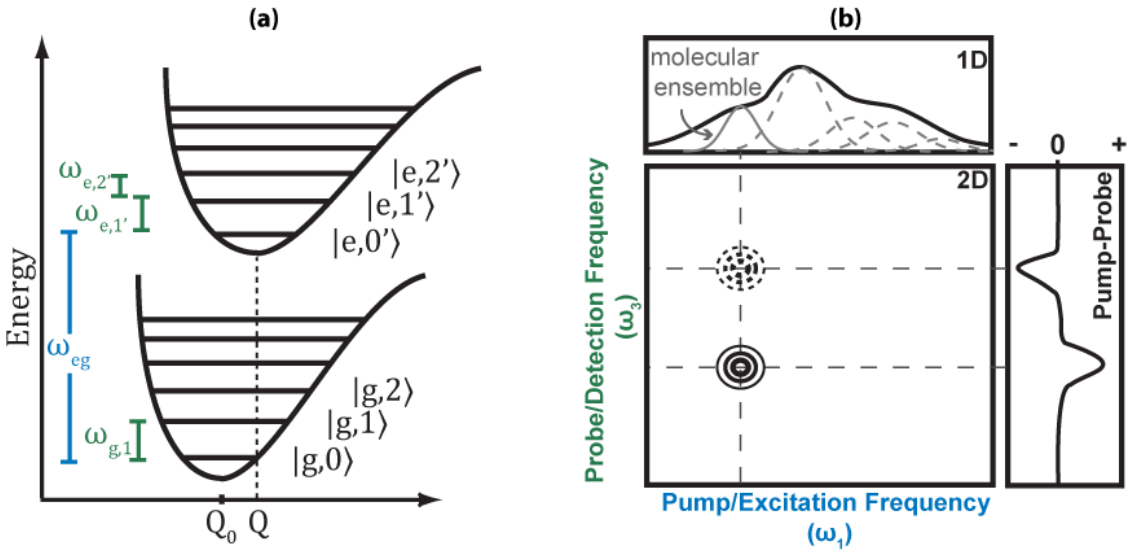


Figure 1.5. Molecular Spectroscopy Overview. (a) a typical vibronic energy potential scheme of the ground (g) and first excited (e) electronic states with their respective vibrational states labeled by the quanta of vibrational energy: v = 0,1,2 in the ground state and v' = 0',1',2' for the excited state. The molecular coordinate is defined by the abscissa which characterizes the electronic potential energy surfaces and the vibrational level progressions in each electronic state; $Q_0$ and Q are the equilibrium positions of this molecular coordinate in the ground and excited states, respectively. The energy gaps between states are given for the electronic and vibrational transitions depicted. (b) The various frequency dimensions and spectra are depicted for a general molecular system. Linear (1D) spectroscopy, such as UV-vis (electronic) or FTIR (vibrational) absorption, is shown on the top panel. The traditional "pump-probe" or transient-absorption spectrum is shown on the side panel as a differential absorption where only the probed frequencies are spectrally resolved. The two-dimensional (2D) spectrum is shown in the center with contours depicting the 2D peaks of different signs corresponding to those measured in the pump-probe spectrum as a differential signal. The additional frequency resolution obtained in the 2D spectrum is the excitation frequency dependence of the spectrally detected signals from the pump-probe experiment, resulting in a 2D frequency spectrum. As the color scheme between (a) and (b) suggest, the spectra in (b) represent the linear electronic absorption (top panel), the transient-IR spectrum (side panel) and the 2D Electronic-Vibrational (EV) spectrum (middle, contours).

The vibrational spectrum is extremely sensitive to localized changes in chemical bond lengths, strengths, and angles reported on through the peak positions and amplitudes. Moreover, the (typically heterogeneous) conformational distribution of a vibration throughout the molecular ensemble will be contained in the line width of the vibrational peak. In the condensed phase, all of these molecular parameters will be influenced by dynamic solvent-induced electric fields and intermolecular interactions. The electronic frequencies of an electronic absorption spectrum reflect the average energy separation between two different

electronic states in the molecular ensemble. The electronic state energies are also sensitive to the ensemble's distribution of chemical structure, the solvent-induced electric fields, and the intermolecular interactions. Due to the much faster dephasing times (10's-100s of fs) and the larger energetic separations of electronic states, the line widths of peaks in an electronic spectrum are much broader than the corresponding vibrational spectrum under the same experimental conditions. Finally, the electronic absorption spectrum represents the sum over all molecular coordinates with allowed vibronic transition probabilities. Therefore, the typically broad and featureless electronic absorption spectrum contains a wealth of microscopic structural information related to the ensemble-averaged electronic and vibrational state energy gaps and the fluctuations in these energy gaps induced by chemical interactions. Unfortunately, 1D spectroscopies necessarily project *all* of this molecular-level detail onto a single axis. Therein lies the ambiguity of a 1D spectrum; one single experimental parameter set is affected by many molecular coordinates which leaves a full microscopic description of the ensemble's behavior hidden from the observer.

### 1.2.2 *Nonlinear Absorption Spectra: Electronic and Vibrational*

The linear absorption spectra discussed above depend on one light-matter interaction; a single absorption event of the molecules in the ensemble understudy describes the measured absorption spectrum. Aided by continued advancement in ultrafast (femtosecond) pulsed laser technologies, coherent nonlinear spectroscopies have been developed that can disentangle some of the hidden information in the linear absorption spectrum by resolving the ensemble molecular response with respect to another frequency dimension, or parameter space. These experiments utilize multiple spatially and temporally overlapped electric fields (light pulses) to generate the detected nonlinear signal.

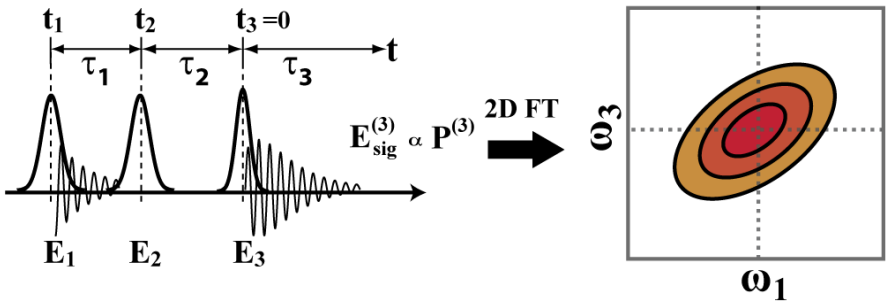


Figure 1.6. Coherent Multidimensional Fourier Transform (FT) Spectroscopy Pulse Sequence.

The multidimensional spectroscopies discussed in this dissertation are third-order nonlinear techniques which employ three light pulses to generate the fourth emitted field that is the signal as shown in Figure 1.6. These experiments are characterized by three experimentally controllable time delays: the coherence time ($\tau_1$), the evolution time ($\tau_2$), and detection time ($\tau_3$) periods which follow three input light pulses. The first pulse ($\mathbf{E}_1$) resonantly induces a transition between two molecular eigenstates (similar to those represented in Figure 1.5(a)) at experimental time $t_1$ which places the molecule in a superposition state generating a coherence oscillating with the frequency of this energy separation as a free induction decay during $\tau_1$. The second pulse ($\mathbf{E}_2$) interacts with the molecular ensemble at time $t_2$ resulting in (i) creation of a population in either the excited state or the ground state, or (ii) creation of another superposition state involving either the same molecular coordinate (a two-quantum superposition) or a new superposition between the initially excited coordinate and another coordinate. These states propagate during the evolution time before the third pulse ($\mathbf{E}_3$) interacts with the ensemble at time $t_3$ which emits the third-order signal of interest, ($\mathbf{E}^{(3)}_{sig}$), that propagates during the detection time. In a multidimensional experiment, the phase and amplitude of the emitted signal field is characterized as a function of the other experimental time delays using heterodyned detection. A 2D Fourier transform (FT) over the coherence and detection periods yields a 2D frequency spectrum where one frequency is the excitation

frequency induced during $\tau_1$ and the other frequency is the detection frequency propagating during $\tau_3$. It has become common to resolve the emitted signal field spectrally using a spectrometer where its amplitude and phase are self-heterodyne detected with the probe field ($\mathbf{E}_3$) due to the geometrical orientation of the input electric fields. The pump-probe spectrum shown in Figure 1.5(b, side panel) is also a third-order technique where the signal is described in the same way but with $\tau_1$=0 for the duration of the experiment. In pump-probe experiments, the operational time delay is the evolution time where the goal is typically to measure excited state lifetimes and kinetics. As depicted in Figure 1.5, the 2D spectrum is related to the pump-probe spectrum by integrating the 2D spectrum over the excitation frequency axis; thus, the additional frequency resolution is lost in pump-probe spectroscopy.

## 1.3 Surveying the Field: Coherent Femtosecond 2D FT Spectroscopy

The third-order pulse sequence in Figure 1.6 is generalized to include sequential resonant interactions between any two molecular states during the experiment. The specific parameter space of a multidimensional experiment is defined by the center frequencies and bandwidths of the femtosecond pulses employed in the experiment.

A fairly representative survey of the spectral coverage currently achievable by spectroscopists using coherent femtosecond 2D FT spectroscopies is shown in Figure 1.7 (this figure is not meant to be comprehensive). The different spectral areas of this plot are accessible based upon the experimentalist's ability (and desire) to tune the center frequencies and bandwidths of their pulses to reach specific regions in this landscape. The colored blocks of this plot reflect different experiments published that cover these spectral regions. Most of the experiments lie along the diagonal ($\omega_1 = \omega_3$) or very close to it; this means these experiments

have characterized couplings and correlations between nominally the same type of motion in the molecular samples understudy.

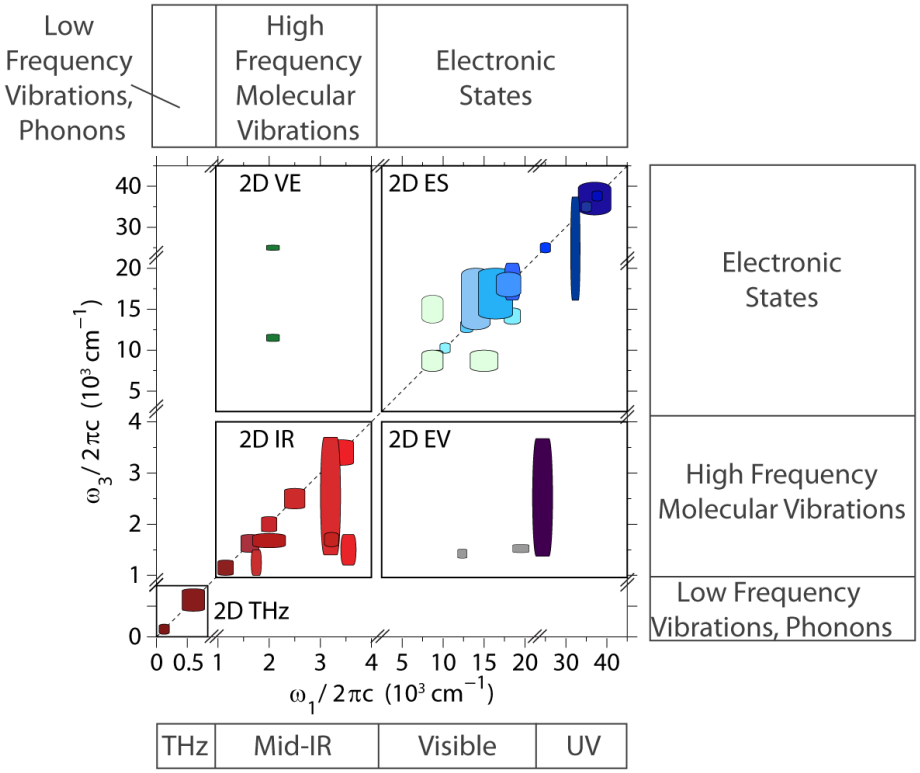


Figure 1.7. Spectral Landscape of Femtosecond 2D FT Spectroscopy. All blocks represent published experiments in the various 2D spectral areas. This plot is not meant to include *all* published experiments; it is just meant to give a sampling of the experimental spectral coverage. Figure is adapted from reference [31]; see this paper for citations of the experiments represented by the blocks.

Using 2D THz spectroscopy correlations between very low frequency vibrations in liquids and lattice distortions in materials have been measured.[2-4] Increasing the center frequencies and bandwidths to cover the mid-IR region of the spectrum, 2D IR spectroscopy has been used to measure correlated motion of high frequency vibrational coordinates to describe vibrational energy transfer, protein and peptide structural dynamics, and proton transfer in liquids.[5-14] The 2D IR spectral quadrant is analogous to the 2D spectrum of the Liverpool players' lateral positions in section 1.1. Increasing the pulse frequencies throughout the visible and UV regions, the couplings between electronic states in molecules, electronic energy transfer in

excited molecular dimers and nanomaterials, and light harvesting in photosynthetic complexes have been measured using 2D electronic spectroscopy (ES).[15-29] These 2D ES experiments are analogous to the 2D spectrum of the soccer ball's lateral positions in section 1.1.

In the off-diagonal quadrants are the 2D Electronic-Vibrational (EV, bottom right) and 2D Vibrational-Electronic (VE, top left) spectroscopies. The information content of these spectra include correlated motions and couplings between very different molecular degrees of freedom: the electronic and the vibrational motions. The 2D VE spectroscopy was first demonstrated by the Khalil group in 2015 and has been used to study how a bridging ligand between two transition metals is involved in metal-to-metal charge transfer of the mixed valence transition metal complex.[30-32] At the beginning of the work described in this dissertation, only one experiment had been published in an off-diagonal quadrant which was the experimental demonstration of 2D EV spectroscopy by the Fleming group in 2014.[33] Since then, more experimental and theoretical 2D EV spectroscopy studies have been published by the Khalil and Fleming groups to understand the information content of these signals,[34-38] to expand the experimentally accessible bandwidth in the 2D EV experiment,[39] and to measure electronic-vibrational dynamics in light harvesting complexes,[40,41] carotenoids,[42] molecular dyes,[43] ligand-to-metal charge transfer (LMCT) dynamics,[39] and metal-to-ligand charge transfer (MLCT) dynamics in a prototypical solar cell dye molecule.[44,45]

Drawing upon the football analogy of section 1.1, the 2D EV spectroscopy is the way to measure the desired cross-peak spectrum shown in Figure 1.4. By flipping the axes of that spectrum, the analogous 2D spectrum to 2D VE spectroscopy would be obtained (although these two experiments are only technically equivalent at $\tau_2 = 0$). Both 2D EV and 2D VE spectroscopies provide complementary insight into how the couplings between electronic and

vibrational degrees of freedom – or vibronic couplings – are utilized by molecules during complex photoexcited chemical reactions.

## 1.4 Ultrafast Multi-Coordinate Photochemical Phenomena

Electron transfer and proton transfer can be considered some of the most fundamental chemical reactions; developing an understanding of how to control these phenomena comprises a very broad and active area of research in chemistry and in many chemistry-related fields.[46,47] These reactions both cause changes in chemical structure (electronic and/or atomic). They are both some of nature's fastest reactions and can occur on femtosecond timescales. In both cases, excited electronic states accessed by light absorption can be exploited to drive these reactions. One type of electron transfer reaction involves the movement of charge density in transition metal complexes due to these molecules containing excited electronic states with charge transfer character. A typical proton transfer reaction involves photoexcitation to an electronically excited state in which the proton migrates intramolecularly to a new equilibrium position in the molecular structure. It turns out that many of these types of reactions proceed through the concerted motions of many molecular coordinates. These two reactions will be discussed in this dissertation.

### 1.4.1 *Charge Transfer Reactions in Transition Metal Complexes*

Charge transfer reactions involve moving electron density from one part of a molecule to another. To an extent, one can consider such a transition to be an internal oxidation-reduction reaction where one part of the molecule is oxidized and the other is reduced. In transition metal complexes, where usually a central transition metal atom has ligands coordinated around it, a class of charge transfers are characterized by an electron moving from an orbital with largely

d-electron character of the transition metal to one that is mainly of ligand character (typically π* orbitals).[48] This type of reaction is known as a metal-to-ligand charge transfer (MLCT) but the opposite reaction, a ligand-to-metal charge transfer (LMCT) reaction, is just as prevalent among solution phase transition metal compounds. Whereas d-d transitions in transitions metal complexes are not spectroscopically allowed, these charge transfer transitions are fully allowed, giving rise to very intense absorptions that are often the reason for observing rich colors in the condensed phase (e.g., dyes). Considering charge transfer as internal redox processes can be useful from the perspective that the synthetic framework for tuning and controlling the motion of electron density within the molecule's structure arises naturally; this is achievable by finding the correct metal-ligand combination to favor a particular motion of the electron density. MLCT transitions are interesting because their photoexcited dynamics are typically characterized by initial electronic delocalization followed by electronic localization to a new part of the molecule, which represents a rich playground for investigating molecular photophysics such as charge and energy transfer. In photovoltaic applications, where the goal is to build a device that uses the absorbed energy from ambient light to separate charge sufficiently for creating useful electrical current, the specific details of charge transfer are paramount for designing molecule photosensitizers that do this intramolecularly. While an incredible amount of literature exists describing the kinetics of MLCT dynamics, there is much to be understood yet in excited state energy and charge transfer research surrounding the mechanistic details and temporal evolution of the molecular states that promote this ultrafast chemical reaction. A prominent molecular photosensitizer is the Ru-centered "N3" molecule [$Ru(NCS)_2(dcbpy)_2$; (dcbpy = dicarboxybipyridine)] which is studied extensively in this dissertation.

### 1.4.2 *Excited State Intramolecular Proton Transfer in Small Organic Molecules*

An important class of chemical reactions resulting in ultrafast proton transfer is known as excited state intramolecular proton transfer (ESIPT). In this reaction, an excited electronic state is utilized to trigger a significant structural isomerization in the molecule. From a fundamental standpoint, this represents one of the fastest isomerization reactions that has been characterized, sometimes proceeding on the same timescale as one high frequency vibrational period (~10-20 fs).[49] This reaction mechanism has been shown to provide a method of protecting against photodamage, as it typically results in extremely large Stokes shifting of the emission arising from the significant structural reorganization during the proton transfer.[50] In more applied fields, engineering the ESIPT mechanism is one avenue toward molecular photo-switching for use in optical data storage.[51] Along with photoinduced *cis-trans* isomerization, the ESIPT reaction is a model for understanding how molecular structural changes can occur efficiently in excited electronic states with desirable outcomes. Despite the vast knowledge of ESIPT kinetics in various systems, many of these reactions lack a clear description of the electronic states promoting such rapid proton transfer and the mechanistic details of the reaction. Investigations into one benchmark ESIPT system, 10-hydroxybenzo-[*h*]-quinoline (HBQ), is presented at the end of this dissertation.

## 1.5 Dissertation Outline

This dissertation is organized as follows: chapter two presents a theoretical treatment of both 2D EV and 2D VE spectroscopies with the goal of laying a foundation for understanding the molecular information present in the spectra measured by these multidimensional experiments. The simplest molecular system is treated in this chapter: a single anharmonic vibrational mode with electronic transitions between the ground state and the first excited state.

A vibronic Hamiltonian is used in which linear and quadratic vibronic couplings are included to characterize excited state displacement and frequency shifting of the vibration. This chapter contributes vibronic selection rules for each of these techniques by systematically varying the parameters of the molecular Hamiltonian and simulating 2D EV and 2D VE spectra using nonlinear response theory. It is demonstrated here that both spectroscopies are directly sensitive to molecular vibronic couplings. Chapters three and four describe the experimental details of the 2D EV spectrometer in the Khalil group. Specifically, chapter three details the implementation of an octave-spanning broadband mid-IR (BBIR) light source as the probe to extend the reach of molecular vibrations simultaneously measureable in a 2D EV experiment. The 2D EV experiment is also demonstrated with UV excitation in this chapter. However, the spectral bandwidth of the pump is still fairly narrow as the second harmonic of the Ti:sapphire laser output. Chapter four details the spectral expansion in the excitation dimension using self-phase modulation in a multiplate continuum generation setup to broaden the fundamental prior to second harmonic generation. The resulting spectra are more than double the bandwidth than shown in chapter three and are tunable across the 375-440 nm region. Chapter five includes the first sets of 2D EV experiments using the spectrometer described in chapter three. These experiments focus on the LMCT dynamics of ferricyanide ($[Fe(CN)_6]^{3-}$) dissolved in formamide. This chapter also includes the first attempt to fully describe the vibronic dynamics of a molecular system studied using both 2D EV and 2D VE spectroscopies. The 2D EV and 2D VE spectra of ferricyanide at one $\tau_2$ delay time are fitted using the vibronic Hamiltonian and the nonlinear response theory built up in chapter two.

Chapter six extends the theoretical framework presented in chapter two in two ways: 1) the orientational response is included in the nonlinear response function to treat polarization-

selective 2D EV experimental spectra, and 2) the vibronic Hamiltonian is extended to treat two anharmonic vibrational modes that experience excited state vibrational mixing (Duschinsky mixing). Chapters seven and eight describe the results of polarization-selective multidimensional EV experiments and TD-DFT calculations on the aqueous, fully deprotonated form of the archetypal solar cell dye molecule, N3. Chapter seven presents a static snapshot of the vibronically coupled MLCT states that facilitate ultrafast charge transfer in this molecule. This effectively maps out some of the major players in this molecules' photochemistry. Chapter eight builds on the conclusions from chapter seven with a $\tau_2$-dependent series of 2D EV spectra on $N3^{4-}$. This allows for the complete third order molecular response to be resolved in a 3D EV spectrum, demonstrating 3D EV spectroscopy for the first time. New mechanistic insights of how the MLCT dynamics occur in the excited states of N3 include answering an outstanding question regarding the existence of an initially excited vibrational coherence and the characterization of a vibronic coherence facilitating non-adiabatic internal conversion for ~1 ps. Altogether, chapters seven and eight showcase the ability of multidimensional EV spectroscopy to follow vibronic coherence evolution in complex multidimensional photochemical processes. Finally, chapter nine embarks on a new line of chemical inquiry for 2D EV studies – that of coupled electron-proton motion. Early results on the ESIPT dynamics of HBQ studied in nonpolar solvent are reported. The polarization-selective transient-IR and 2D EV experimental results contribute to describing what the nature is of the excited state on which ultrafast proton transfer occurs in HBQ.

## 1.6 REFERENCES


(1) Born, M.; Oppenheimer, R. Quantum Theory of Molecules; *Ann. Phys.* **1927**, *389*, 0457-0484.

(2) Savolainen, J.; Ahmed, S.; Hamm, P. Two-dimensional Raman-terahertz spectroscopy of water; *Proc. Natl. Acad. Sci. USA* **2013**, *110*, 20402-20407.

(3) Kuehn, W.; Reimann, K.; Woerner, M.; Elsaesser, T.; Hey, R. Two-Dimensional Terahertz Correlation Spectra of Electronic Excitations in Semiconductor Quantum Wells; *J. Phys. Chem. B* **2011**, *115*, 5448-5455.

(4) Kuehn, W.; Reimann, K.; Woerner, M.; Elsaesser, T.; Hey, R.; Schade, U. Strong Correlation of Electronic and Lattice Excitations in GaAs/AlGaAs Semiconductor Quantum Wells Revealed by Two-Dimensional Terahertz Spectroscopy; *Phys. Rev. Lett.* **2011**, *107*.

(5) Costard, R.; Heisler, I. A.; Elsaesser, T. Structural Dynamics of Hydrated Phospholipid Surfaces Probed by Ultrafast 2D Spectroscopy of Phosphate Vibrations; *J. Phys. Chem. Lett.* **2014**, *5*, 506-511.

(6) Asplund, M. C.; Zanni, M. T.; Hochstrasser, R. M. Two-dimensional infrared spectroscopy of peptides by phase-controlled femtosecond vibrational photon echoes; *Proc. Natl. Acad. Sci. USA* **2000**, *97*, 8219-8224.

(7) Khalil, M.; Demirdoven, N.; Tokmakoff, A. Coherent 2D IR spectroscopy: Molecular structure and dynamics in solution; *J. Phys. Chem. A* **2003**, *107*, 5258-5279.

(8) Zheng, J.; Kwak, K.; Fayer, M. D. Ultrafast 2D IR vibrational echo spectroscopy; *Acc. Chem. Res.* **2007**, *40*, 75-83.

(9) Rubtsov, I. V.; Kumar, K.; Hochstrasser, R. M. Dual-frequency 2D IR photon echo of a hydrogen bond; *Chem. Phys. Lett.* **2005**, *402*, 439-443.

(10) Kurochkin, D. V.; Naraharisetty, S. R. G.; Rubtsov, I. V. A relaxation-assisted 2D IR spectroscopy method; *Proc. Natl. Acad. Sci. USA* **2007**, *104*, 14209-14214.

(11) Mandal, A.; Ramasesha, K.; De Marco, L.; Tokmakoff, A. Collective vibrations of water-solvated hydroxide ions investigated with broadband 2DIR spectroscopy; *J. Chem. Phys.* **2014**, *140*.

(12) Leger, J. D.; Nyby, C. M.; Varner, C.; Tang, J. A.; Rubtsova, N. I.; Yue, Y. K.; Kireev, V. V.; Burtsev, V. D.; Qasim, L. N.; Rubtsov, G. I.; Rubtsov, I. V. Fully automated dual-frequency three-pulse-echo 2DIR spectrometer accessing spectral range from 800 to 4000 wavenumbers; *Rev. Sci. Instrum.* **2014**, *85*.

(13) Roberts, S. T.; Ramasesha, K.; Tokmakoff, A. Structural Rearrangements in Water Viewed Through Two-Dimensional Infrared Spectroscopy; *Acc. Chem. Res.* **2009**, *42*, 1239-1249.

(14) Bakulin, A. A.; Liang, C.; Jansen, T. L.; Wiersma, D. A.; Bakker, H. J.; Pshenichnikov, M. S. Hydrophobic Solvation: A 2D IR Spectroscopic Inquest; *Acc. Chem. Res.* **2009**, *42*, 1229-1238.

(15) Courtney, T. L.; Park, S. D.; Hill, R. J.; Cho, B.; Jonas, D. M. Enhanced interferometric detection in two-dimensional spectroscopy with a Sagnac interferometer; *Opt. Lett.* **2014**, *39*, 513-516.

(16) Brida, D.; Manzoni, C.; Cerullo, G. Phase-locked pulses for two-dimensional spectroscopy by a birefringent delay line; *Opt. Lett.* **2012**, *37*, 3027-3029.

(17) Hybl, J. D.; Albrecht, A. W.; Faeder, S. M. G.; Jonas, D. M. Two-Dimensional Electronic Spectroscopy; *Chem. Phys. Lett.* **1998**, *297*, 307-313.

(18) Jonas, D. M. Two-Dimensional Femtosecond Spectroscopy; *Annu. Rev. Phys. Chem.* **2003**, *54*, 425-463.

(19) Spokoyny, B.; Harel, E. Mapping the Vibronic Structure of a Molecule by Few-Cycle Continuum Two-Dimensional Spectroscopy in a Single Pulse; *J. Phys. Chem. Lett.* **2014**, *5*, 2808-2814.

(20) Spokoyny, B.; Koh, C. J.; Harel, E. Stable and high-power few cycle supercontinuum for 2D ultrabroadband electronic spectroscopy; *Opt. Lett.* **2015**, *40*, 1014-1017.

(21) Tekavec, P. E.; Myers, J. A.; Lewis, K. L. M.; Ogilvie, J. P. Two-dimensional electronic spectroscopy with a continuum probe; *Opt. Lett.* **2009**, *34*, 1390-1392.

(22) Myers, J. A.; Lewis, K. L. M.; Tekavec, P. F.; Ogilvie, J. P. Two-color two-dimensional Fourier transform electronic spectroscopy with a pulse-shaper; *Opt. Express* **2008**, *16*, 17420-17428.

(23) Turner, D. B.; Hassan, Y.; Scholes, G. D. Exciton Superposition States in CdSe Nanocrystals Measured Using Broadband Two-Dimensional Electronic Spectroscopy; *Nano Lett.* **2012**, *12*, 880-886.

(24) Mehlenbacher, R. D.; Mcdonough, T. J.; Grechko, M.; Wu, M. Y.; Arnold, M. S.; Zanni, M. T. Energy transfer pathways in semiconducting carbon nanotubes revealed using two-dimensional white-light spectroscopy; *Nat. Commun.* **2015**, *6*.

(25) Moran, A. M.; Nome, R. A.; Scherer, N. F. Resolving the emission times of solute and solvent four-wave mixing signals by spectral interferometry; *J. Chem. Phys.* **2006**, *125*.

(26) Krebs, N.; Pugliesi, I.; Hauer, J.; Riedle, E. Two-dimensional Fourier transform spectroscopy in the ultraviolet with sub-20 fs pump pulses and 250-720 nm supercontinuum probe; *New. J. Phys.* **2013**, *15*.

(27) Selig, U.; Schleussner, C. F.; Foerster, M.; Langhojer, F.; Nuernberger, P.; Brixner, T. Coherent two-dimensional ultraviolet spectroscopy in fully noncollinear geometry; *Opt. Lett.* **2010**, *35*, 4178-4180.

(28) Tseng, C. H.; Matsika, S.; Weinacht, T. C. Two-Dimensional Ultrafast Fourier Transform Spectroscopy in the Deep Ultraviolet; *Opt. Express* **2009**, *17*, 18788-18793.

(29) West, B. A.; Moran, A. M. Two-Dimensional Electronic Spectroscopy in the Ultraviolet Wavelength Range; *J. Phys. Chem. Lett.* **2012**, *3*, 2575-2581.

(30) Courtney, T. L.; Fox, Z. W.; Estergreen, L.; Khalil, M. Measuring Coherently Coupled Intramolecular Vibrational and Charge-Transfer Dynamics with Two-Dimensional Vibrational Electronic Spectroscopy; *J. Phys. Chem. Lett.* **2015**, *6*, 1286-1292.

(31) Courtney, T. L.; Fox, Z. W.; Slenkamp, K. M.; Khalil, M. Two-Dimensional Vibrational-Electronic Spectroscopy; *J. Chem. Phys.* **2015**, *143*, 154201.

(32) Fox, Z. W. *Two-Dimensional Vibrational-Electronic Spectroscopy: The Design and Development of a Novel Multidimensional Spectroscopic Technique to Directly Measure Coherent coupling Between VIbrational and Electronic Degrees of Freedom* Ph.D. Dissertation, University of Washington, 2018.

(33) Oliver, T. a. A.; Lewis, N. H. C.; Fleming, G. R. Correlating the motion of electrons and nuclei with two-dimensional electronic-vibrational spectroscopy; *Proc. Natl. Acad. Sci. USA* **2014**, *111*, 16628-16628.

(34) Lewis, N. H. C.; Dong, H.; Oliver, T. a. A.; Fleming, G. R. Measuring correlated electronic and vibrational spectral dynamics using line shapes in two-dimensional electronic-vibrational spectroscopy; *J. Chem. Phys.* **2015**, *142*, 174202.

(35) Dong, H.; Lewis, N. H. C.; Oliver, T. a. A.; Fleming, G. R. Determining the static electronic and vibrational energy correlations via two-dimensional electronic-vibrational spectroscopy; *J. Chem. Phys.* **2015**, *142*, 174201.

(36) Lewis, N. H. C.; Dong, H.; Oliver, T. a. A.; Fleming, G. R. A method for the direct measurement of electronic site populations in a molecular aggregate using two-dimensional electronic-vibrational spectroscopy; *J. Chem. Phys.* **2015**, *143*, 124203.

(37) Gaynor, J. D.; Khalil, M. Signatures of vibronic coupling in two-dimensional electronic-vibrational and vibrational-electronic spectroscopies; *J. Chem. Phys.* **2017**, *147*, 094202.

(38) Bhattacharyya, P.; Fleming, G. R. Two-Dimensional Electronic-Vibrational Spectroscopy of Coupled Molecular Complexes: A Near-Analytical Approach; *J. Phys. Chem. Lett.* **2019**, *10*, 2081-2089.

(39) Gaynor, J. D.; Courtney, T. L.; Balasubramanian, M.; Khalil, M. Fourier transform two-dimensional electronic-vibrational spectroscopy using an octave-spanning mid-IR probe; *Opt. Lett.* **2016**, *41*, 2895-2898.

(40) Lewis, N. H. C.; Fleming, G. R. Two-Dimensional Electronic-Vibrational Spectroscopy of Chlorophyll a and b; *J. Phys. Chem. Lett.* **2016**, *7*, 831-837.

(41) Lewis, N. H. C.; Gruenke, N. L.; Oliver, T. a. A.; Ballottari, M.; Bassi, R.; Fleming, G. R. Observation of Electronic Excitation Transfer Through Light Harvesting Complex II Using Two-Dimensional Electronic–Vibrational Spectroscopy; *J. Phys. Chem. Lett.* **2016**, *7*, 4197-4206.

(42) Oliver, T. a. A.; Fleming, G. R. Following Coupled Electronic-Nuclear Motion through Conical Intersections in the Ultrafast Relaxation of beta-Apo-8 '-carotenal; *J. Phys. Chem. B* **2015**, *119*, 11428-11441.

(43) Wu, E. C.; Ge, Q. H.; Arsenault, E. A.; Lewis, N. H. C.; Gruenke, N. L.; Head-Gordon, M. J.; Fleming, G. R. Two-dimensional electronic-vibrational spectroscopic study of conical intersection dynamics: an experimental and electronic structure study; *Phys. Chem. Chem. Phys.* **2019**, *21*, 14153-14163.

(44) Gaynor, J. D.; Petrone, A.; Li, X.; Khalil, M. Mapping Vibronic Couplings in a Solar Cell Dye with Polarization-Selective Two-Dimensional Electronic–Vibrational Spectroscopy; *J. Phys. Chem. Lett.* **2018**, *9*, 6289-6295.

(45) Gaynor, J. D.; Sandwisch, J.; Khalil, M. Vibronic Coherence Evolution in Multidimensional Ultrafast Photochemical Processes; *Nat. Commun.* **2019**, *10*, 5621.

(46) Barbara, P. F.; Meyer, T. J.; Ratner, M. A. Contemporary issues in electron transfer research; *J. Phys. Chem.* **1996**, *100*, 13148-13168.

(47) Hammes-Schiffer, S. Theory of Proton-Coupled Electron Transfer in Energy Conversion Processes; *Acc. Chem. Res.* **2009**, *42*, 1881-1889.

(48) Huheey, J. E.; Keiter, E. A.; Keiter, R. L. *Inorganic Chemistry: Principles of Structure and Reactivity*; Harper Collins: New York, 1993.

(49) Lee, J.; Kim, C. H.; Joo, T. Active Role of Proton in Excited State Intramolecular Proton Transfer Reaction; *J. Phys. Chem. A* **2013**, *117*, 1400-1405.

(50) Lim, S.-J.; Seo, J.; Park, S. Y. Photochromic Switching of Excited-State Intramolecular Proton-Transfer (ESIPT) Fluorescence: A Unique Route to High-Contrast Memory Switching and Nondestructive Readout; *J. Am. Chem. Soc.* **2006**, *128*, 14542-14547.

(51) Chou, P. T.; Solntsev, K. M. Photoinduced Proton Transfer in Chemistry and Biology; *J. Phys. Chem. B* **2015**, *119*, 2089-2089.

# Chapter 2. SIGNATURES OF VIBRONIC COUPLING IN 2D ELECTRONIC-VIBRATIONAL AND VIBRATIONAL-ELECTRONIC SPECTROSCOPIES

*The work presented in this chapter has been published in the following paper:*

*1) Gaynor, J.D.; Khalil, M; "Signatures of Vibronic Coupling in Two-Dimensional Electronic-Vibrational and Vibrational-Electronic Spectroscopies" Journal of Chemical Physics* ***2017****, 147, 094202.*

## 2.1 INTRODUCTION

Vibronic couplings play an important role in energy and charge transfer processes. There is an increasing interest to directly measure and compute these vibronic couplings in complex disordered condensed phase systems and eventually harness them to control chemical and biophysical photo-induced energy conversion processes.[1] Over the last two decades, experimental and theoretical strategies have been developed to obtain microscopic information from analyzing the time-dependent positions, amplitudes and line shapes of the various peaks in 2D IR and 2D electronic spectra. To address the issue of directly measuring vibronic phenomena, 2D Electronic-Vibrational (EV) spectroscopy[2] and 2D Vibrational-Electronic (VE) spectroscopy[3] have been recently developed. These third order nonlinear spectroscopies employ electronically- and vibrationally-resonant excitation and probe fields to directly interrogate inter- and intramolecular vibronic couplings in molecular systems. For example, using 2D VE spectroscopy, mode-dependent vibronic coupling strengths have been determined in a transition metal mixed valence compound and local vibrations have been used to track electronic energy flow among various pigments in a light harvesting complex using 2D EV spectroscopy.[3-5] As detailed in chapters 3-4 of this dissertation, technical developments have extended the range of accessible molecular phenomena by incorporating broadband UV and

octave-spanning mid-IR pulses into the 2D EV experiment.[6] As the 2D EV and 2D VE experimental studies and their interpretation continue to expand and develop,[7-9] it is important to develop an intuitive understanding of how molecular vibronic couplings are encoded in the 2D spectra.

To this end, this chapter details a system Hamiltonian that describes a single anharmonic vibration in the ground electronic state that has linear and quadratic vibronic coupling in the excited electronic state. This Hamiltonian is used in simulating 2D EV and 2D VE spectra of systems that have varying degrees of intramolecular vibronic coupling. This formulation parallels the Herzberg-Teller adiabatic approximation[10] by including a linear dependence of nuclear coordinates on the electronic transition dipole moment. It is shown that the extent of vibronic coupling is reflected in the peak positions, the nuclear dependence of the electronic transition contributes to the peak amplitudes, and electronic-state-dependent vibrational dephasing affects peak line shapes in 2D EV and 2D VE spectra. Selection rules for these 2D spectroscopies are described through systematic simulations of 2D spectra. This chapter does not explicitly include the orientational response which is reserved for a treatment of two vibrational modes detailed in chapter 6.

This chapter is organized as follows: section 2.2 develops the vibronic Hamiltonian and the interaction Hamiltonian; section 2.3 categorizes all contributing 2D EV and 2D VE signals under consideration and characterizes the peak positions, amplitudes, and line shapes for both techniques; section 2.4 discusses simulations for cases of systematically varied degrees of vibronic coupling; section 2.5 summarizes the 2D EV and 2D VE selection rules elucidated through the simulations; and section 2.6 discusses additional signals accessible with different input pulse parameters, polarization-selective signals, and future directions. For reference, the

appendices in section 2.8 include: the definitions of the vibronic energy gap correlation functions (2.8.1, Appendix A), the nuclear coordinate dependence of the electronic transition dipole moment (2.8.2, Appendix B), the Liouville transition pathways for the third order nonlinear response tensor (2.8.3, Appendix C), a complete list of the 2D EV and 2D VE response functions used to simulate the spectra in this chapter (2.8.4, Appendix D), and the derivations of the second order corrections to the excited state energies using stationary perturbation theory (2.8.5, Appendix E).

## 2.2 VIBRONIC MATERIAL AND INTERACTION HAMILTONIANS

A theoretical description of a molecular system under study with nonlinear spectroscopic methods begins with a quantum mechanical material Hamiltonian to describe the molecular system and an interaction Hamiltonian to describe the coupling between the external light fields and the system. The material Hamiltonian is the sum of individual Hamiltonians for the system, the bath and the system-bath interaction. To model the simplest case for 2D EV and 2D VE spectroscopy of systems with vibronic coupling, we use a Hamiltonian, $H_{vibronic}$, that describes a single local vibrational mode and two electronic states: the ground state, $|g\rangle$, and the first excited state, $|e\rangle$. Many treatments of molecular vibronic couplings exist.[11-17] The vibronic system Hamiltonian described by Tonks and Page[16] models equilibrium position displacement, frequency shifting, and vibrational mode mixing (known as Duschinsky rotation[18]) upon electronic excitation. In this formulation, the excited state Hamiltonian includes the effects of excited state equilibrium displacement through a linear vibronic coupling term and the frequency shifting and Duschinsky rotation are included with quadratic vibronic coupling terms.[16,19] More recently, Vallet *et al.* [20] used this model to derive analytical

expressions for simulating doubly-resonant IR-visible sum frequency generation spectra for surface adsorbed molecules with harmonic potentials. We introduce cubic anharmonicity to this vibronic Hamiltonian and use it to describe a single anharmonic vibration in the ground electronic state that has linear and quadratic vibronic coupling in the excited electronic state.

The vibronic Hamiltonian is defined as the sum of the ground and excited state Hamiltonians, $H_{vibronic} = H_g + H_e$. The electronic ground state Hamiltonian, $H_g$, has the form given below:

$$H_g = \frac{P_j^2}{2m_j} + V_g(Q_j) \tag{2.1}$$

$$V_g(Q_j) = \frac{1}{2}\hbar\omega_j^0 Q_j^2 + \frac{1}{6}\hbar\omega_j^0 g_{jjj} Q_j^3. \tag{2.2}$$

In the above equations, $Q_j = \sqrt{\frac{m_j\omega_j^0}{\hbar}} q_j$ is the reduced vibrational coordinate for the $j^{th}$ vibrational coordinate ($q_j$), $m_j$ is the reduced mass, $\omega_j^0$ is the natural oscillator frequency, and $P_j$ is the momentum operator. The vibrational coordinate could be either a local mode or a normal mode, depending on the molecular problem of interest. The ground state potential ($V_g(Q_j)$) for the $j^{th}$ vibration in equation (2.2) is obtained by Taylor expansion of the harmonic potential to include the cubic terms.[21,22] The cubic expansion coefficient, $g_{ijk}$, is dimensionless and related to the third order derivative of $V_g(Q_j)$ evaluated at the equilibrium position. In this particular case $i=j=k$ because only one vibrational mode is being considered. The excited electronic state Hamiltonian, $H_e$, is written as $H_g$ raised in energy by the electronic energy

gap and includes vibronic coupling to first and second order in the vibrational coordinate of the excited state potential, $V_e(Q_j)$,

$$H_e = \frac{P_j^2}{2m_j} + V_e(Q_j) \tag{2.3}$$

$$V_e(Q_j) = V_g(Q_j) + \hbar\omega_{eg}^0 + \hbar\omega_j^0 \mathcal{V}_j^{(1)} Q_j + \frac{1}{2}\hbar\omega_j^0 \mathcal{V}_{j,j}^{(2)} Q_j^2 \tag{2.4}$$

The electronic transition frequency between the lowest vibrational levels of the harmonic ground and excited electronic states is given by $\omega_{eg}^0$. The dimensionless vibronic coupling coefficient $\mathcal{V}_j^{(1)}$ reflects the linear coupling strength of the $j^{th}$ vibration to the electronic transition and results in the equilibrium position displacement of the vibrational mode upon electronic excitation. The dimensionless quadratic vibronic coupling coefficient, $\mathcal{V}_{j,j}^{(2)}$, is responsible for the frequency shifting of the $j^{th}$ vibrational mode in the electronic excited state. When a system with two anharmonic vibrations is considered, both frequency shifting ($\mathcal{V}_{j,j}^{(2)}$) and vibrational mode mixing ($\mathcal{V}_{j,k}^{(2)}$) arise from quadratic vibronic coupling. The linear and quadratic vibronic coupling coefficients are related to the first and second order derivatives of the excited state potential with respect to the vibrational coordinate, respectively.

The material Hamiltonian consists of the vibronic system described above, a bath, and the system-bath interactions. In the context of a solute-solvent molecular system, the "bath" can represent the solvent and all the remaining solute degrees of freedom not described in the system Hamiltonian. The system-bath interaction can lead to shifts in vibronic transition frequencies, electronic and vibrational relaxation dynamics, and reorientational dynamics. For this work, I use the approach of Sung and Silbey [23] to describe the bath and system-bath

Hamiltonians ($H_B$ and $H_{SB}$). Briefly, the bath consists of harmonic oscillators and the system-bath interaction is linear in the bath coordinates, $q_B$. The system-bath interaction is included by diagonalizing $H_{vibronic}$ and coupling the eigenstates to the bath through $H_{SB}$. Here, $H_{SB}$ is diagonal in the system eigenstate basis and it reflects the fluctuations of the vibronic frequencies.[23] The pure dephasing effects of system-bath interactions are considered here and incorporated through energy gap correlation functions. As shown in sections 2.3.1.3, 2.3.2.3, and 2.4, I include electronic dephasing, vibrational dephasing, and electronic-state-dependent vibrational dephasing of the vibronic states and explore how these microscopic effects are observed in 2D EV and VE spectra.

The interaction between an external radiation field ($\mathbf{E}(k,\omega,t)$) and the vibronic system described earlier is encoded in the interaction Hamiltonian, $H_{int}$,

$$\begin{aligned} H_{int} &= -\mathbf{M}\cdot\mathbf{E}(k,\omega,t) \\ &= -\sum_a\sum_b \left|a\right\rangle \mu^{a,b}\cdot\mathbf{E}(k,\omega,t)\left\langle b\right| \end{aligned} \tag{2.5}$$

where the system dipole operator is given by $\mathbf{M}$ and the transition dipole matrix elements are denoted by $\mu^{a,b}$. In the above equation $\left|a\right\rangle$ and $\left|b\right\rangle$ correspond to the vibronic system eigenstates of $H_{vibronic}$ described above, and they are indexed by their electronic state and vibrational state. An eigenstate of the ground electronic manifold $(g)$ with vibrational quanta $(v=0,1,...,n)$ is denoted as $\left|g,v\right\rangle$ and an eigenstate of the excited electronic manifold $(e)$ with vibrational quanta $(v'=0',1',...,n')$ as $\left|e,v'\right\rangle$. In general, the transition moment between the vibronic states $\left|a\right\rangle$ and $\left|b\right\rangle$ is defined as

$$\mu^{a,b} = \langle a(r,Q) | \mathbf{M} | b(r,Q) \rangle \tag{2.6}$$

where the vibronic states depend on both the electronic coordinates, $r$, and the reduced vibrational coordinates, $Q$. The eigenstates are written as Born-Oppenheimer adiabatic eigenstates[24] and expressed as the products of the electronic wave function, $\psi(r,Q)$, and the nuclear wave function, $\chi(Q)$,

$$\begin{aligned} |a(r,Q)\rangle &= |\psi^a(r,Q)\rangle |\chi^a(Q)\rangle \\ |b(r,Q)\rangle &= |\psi^b(r,Q)\rangle |\chi^b(Q)\rangle \end{aligned} \tag{2.7}$$

where superscripts $a$ and $b$ specify wave functions in $|a\rangle$ or $|b\rangle$. The vibronic eigenstates defined in eq. (2.7) fit within the "Born representation" defined by Ballhausen & Hansen.[25] They can be considered eigenfunctions of a dynamical Schrödinger equation in a basis set that spans a complete electronic space for each value of $Q$.

The transition dipole operator can be written as the sum of individual operators for the electronic and vibrational coordinates, $\mathbf{M} = \mathbf{M}_{elec}(r) + \mathbf{M}_{vib}(Q)$.[26-28] By rewriting equation (2.6) using this expression for $\mathbf{M}$ and the Born-Oppenheimer adiabatic wave functions in equation (2.7), the transition dipole moment $\mu^{a,b}$ explicitly includes both electronic and vibrational transitions in the system,[26,28]

$$\begin{aligned} \mu^{a,b} = &\langle \psi^a(r,Q) | \psi^b(r,Q) \rangle \langle \chi^a(Q) | \mathbf{M}_{vib}(Q) | \chi^b(Q) \rangle \\ &+ \langle \chi^a(Q) | \chi^b(Q) \rangle \langle \psi^a(r,Q) | \mathbf{M}_{elec}(r) | \psi^b(r,Q) \rangle . \end{aligned} \tag{2.8}$$

When a vibronic transition between electronic states occurs (i.e., $|g,v\rangle \rightarrow |e,v'\rangle$), the electronic overlap integral in the first term on the right in eq. (2.8) vanishes and $\mu^{a,b}$ reduces to the electronic transition dipole multiplied by the appropriate vibrational overlap integral. The nuclear dependence of the electronic transition dipole moment is included by letting

$\mathbf{M}_{elec}(r) \cong \mathbf{M}_{eg}(Q)$ where $\mathbf{M}_{eg}(Q)$ is the electronic transition dipole operator in terms of Q. The $Q$ dependence is made explicit by Taylor expanding $\mathbf{M}_{eg}(Q)$ over the vibrational coordinate about the equilibrium nuclear configuration, $Q_0$,

$$\mathbf{M}_{eg}(Q) = \mu_{eg}^{(0)} + \sum_j \mu_{eg}^{(1)} Q_j + \frac{1}{2}\sum_{j,k} \mu_{eg}^{(2)} Q_j Q_k + \cdots \tag{2.9}$$

with the expansion coefficients given by $\mu_{eg}^{(0)} = \mathbf{M}_{eg}(Q_0)$, $\mu_{eg}^{(1)} = \left( \frac{\partial \mathbf{M}_{eg}}{\partial Q_j} \right)_{Q_0}$, and $\mu_{eg}^{(2)} = \left( \frac{\partial^2 \mathbf{M}_{eg}}{\partial Q_j \partial Q_k} \right)_{Q_0}$. The Condon approximation breaks down when the linear and higher order terms in $\mathbf{M}_{eg}$ are non-negligible. We include the nuclear dependence of the electronic transition in our approach, allowing for these non-Condon effects to be considered in the vibronic systems of interest. This treatment parallels the Herzberg-Teller adiabatic approximation,[10,25,28-30,31] which includes a linear nuclear coordinate dependence of the electronic transition moment through the first order term in the expansion of the transition dipole moment. The first order terms are referred to as Herzberg-Teller vibronic coupling terms. In this formulation of the transition dipole moment, we include the Herzberg-Teller vibronic coupling phenomenologically through the expansion coefficient $\mu_{eg}^{(1)}$. As will be discussed in section 2.3, peak intensity in 2D EV and 2D VE spectra is proportional to the Franck-Condon factors and also sensitive to contributions from Herzberg-Teller vibronic couplings.

When a vibronic transition occurs in which the electronic state remains unchanged (i.e., $|g,v\rangle \rightarrow |g,n\rangle$ for $n = v \pm 1$, or $|e,v'\rangle \rightarrow |e,n'\rangle$ for $n' = v' \pm 1$), the electronic transition dipole

moment goes to zero and the second term on the right hand side of equation (2.8) vanishes, reducing $\mu^{a,b}$ to the vibrational transition moment. We let $\mathbf{M}_{vib}(Q) \equiv \mathbf{M}_{vn}(Q)$ to specify the vibrational transition $|g,v\rangle \rightarrow |g,n\rangle$, and $\mathbf{M}_{vib}(Q) \equiv \mathbf{M}_{v'n'}(Q)$ to denote $|e,v'\rangle \rightarrow |e,n'\rangle$. The nonlinear dependence of the vibrational transition moment is included through Taylor expansion to account for electrical anharmonicity experienced by the nuclei during vibration in the system. For example, the electrical anharmonicity of a vibration in $|g\rangle$ is given by

$$\mathbf{M}_{vn}(Q) = \mu_{vn}^{(0)} + \sum_j \mu_{vn}^{(1)} Q_j + \frac{1}{2}\sum_{j,k} \mu_{vn}^{(2)} Q_j Q_k + \cdots \tag{2.10}$$

where $\mu_{vn}^{(0)} = \mathbf{M}_{vn}(Q_0)$, $\mu_{vn}^{(1)} = \left(\frac{\partial \mathbf{M}_{vn}}{\partial Q_j}\right)_{Q_0}$, and $\mu_{vn}^{(2)} = \left(\frac{\partial^2 \mathbf{M}_{vn}}{\partial Q_j \partial Q_k}\right)_{Q_0}$. This treatment assumes $\mathbf{M}_{vn}(Q) = \mu_{vn}^{(0)} + \mu_{vn}^{(1)} Q$ where $\mu_{vn}^{(1)} \neq 0$ which gives the selection rule for linear IR spectroscopy, $\Delta v = \pm 1$. The terms $\mu_{vn}^{(m)} \neq 0$ for $m \geq 2$ in equation (2.10) relate the electrical anharmonicity of the vibration in the ground electronic state. Similar considerations applied to $\mathbf{M}_{v'n'}(Q)$ describe the nonlinearity of the vibration in the excited electronic state.

This explicit treatment of the electronic and vibrational transition moments allows the nonlinearity of the respective dipole moments to provide specific insight into the molecular system. The nonlinearity of the electronic transition moment ($\mathbf{M}_{eg}$) is relevant during the dynamic rearrangement of the electronic charge distribution that occurs upon transitioning between electronic states. In comparison, the nonlinearity of the vibrational transition moment ($\mathbf{M}_{vn}$ and $\mathbf{M}_{v'n'}$) represents the nonlinearity of the nuclear motion for an instantaneous and

relatively smaller shift in the electronic charge distribution that characterizes a single electronic state, $|g\rangle$ or $|e\rangle$.

Since the transition moment in equation (2.8) is completely generalized, we can concisely express the specific dipole moments and operators for each of the relevant transitions in 2D EV and 2D VE spectroscopy:

$$\left(\text{for } \psi^a \in |g\rangle,\ \psi^b \in |g\rangle\right) \qquad \mathbf{M}(Q) \to \mathbf{M}_{vn}(Q); \quad \mu^{a,b} \to \mu^{v,n} \tag{2.11}$$

$$\left(\text{for } \psi^a \in |e\rangle,\ \psi^b \in |e\rangle\right) \qquad \mathbf{M}(Q) \to \mathbf{M}_{v'n'}(Q); \quad \mu^{a,b} \to \mu^{v',n'} \tag{2.12}$$

$$\left(\text{for } \psi^a \in |g\rangle,\ \psi^b \in |e\rangle\right) \qquad \mathbf{M}(Q) \to \mathbf{M}_{eg}(Q); \quad \mu^{a,b} \to \mu^{e,g}. \tag{2.13}$$

The notation ($eg$, $vn$, and $v'n'$) in equations (2.11)-(2.13) that specifies the transition dipole operators and matrix elements which reduce from the generalized $\mathbf{M}$ will be followed throughout this discussion.

## 2.3 Third Order Nonlinear 2D EV and 2D VE Spectroscopies

Much of the established formalism for other third order nonlinear techniques (e.g., 2D IR and 2D ES) can be applied to 2D EV and 2D VE spectroscopies. [32-36] Both 2D EV spectroscopy and 2D VE spectroscopy utilize sequential interactions (Figure 2.1(a-b)) of three pulsed electric fields to generate the third order nonlinear polarization, $\mathbf{P}^{(3)}$, and measure the resultant electric field.[2-6,37] In the 2D EV experiment, the first two pulses, $\mathbf{E}_1$ and $\mathbf{E}_2$, are resonant with electronic transitions and the third interaction pulse, $\mathbf{E}_3$, is resonant with vibrational transitions in the ensemble. The ordering of resonant field-matter interaction is reversed in the 2D VE experiment, where $\mathbf{E}_1$ and $\mathbf{E}_2$ resonantly excite vibrational transitions and $\mathbf{E}_3$ resonantly probes electronic transitions. In both of these 2D techniques the correlations between electronic

and nuclear motion are accessed directly by perturbing one degree of freedom with $\mathbf{E}_1$ and $\mathbf{E}_2$ while monitoring the response of the other degree of freedom with $\mathbf{E}_3$.

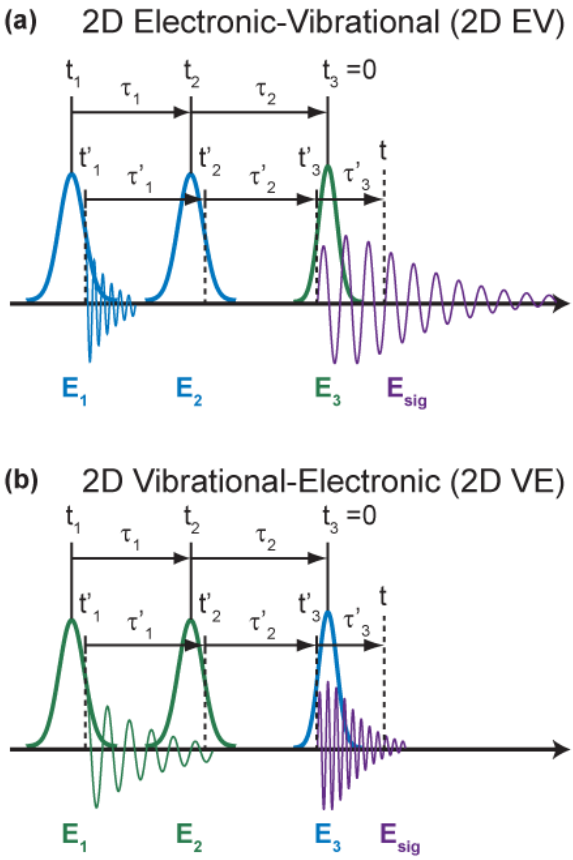


Figure 2.1. 2D EV and 2D VE Spectroscopy Pulse Sequences. Three input pulses ($\mathbf{E}_1$, $\mathbf{E}_2$, and $\mathbf{E}_3$; blue or green) are controllably delayed to sequentially interact with a sample and generate the third order nonlinear polarization containing the 2D signal ($\mathbf{E}_{sig}$, purple). The experimental delay times, $\tau_n$, relate the time delay between pulse envelope maxima, $t_n$. The delays between successive field-matter interactions are specified by $\tau'_n=t'_{n+1}-t'_n$. (a) 2D Electronic-Vibrational: $\mathbf{E}_1$ and $\mathbf{E}_2$ are electronically-resonant (blue) excitation interactions, and $\mathbf{E}_3$ is a vibrationally-resonant (green) probe interaction. (b) 2D Vibrational-Electronic: $\mathbf{E}_1$ and $\mathbf{E}_2$ are vibrationally-resonant (green) excitation interactions and $\mathbf{E}_3$ is an electronically-resonant (blue) probe interaction. A coherence is induced by $\mathbf{E}_1$ at time $t_1$ that exists for a coherence period $\tau_1$, at time $t_2$ the field $\mathbf{E}_2$ interacts with the system and collapses the coherence into population states that relax during the population time $\tau_2$, then $\mathbf{E}_3$ probes the molecular response to the initial perturbation at $t_3$.

All of the microscopic molecular information is contained in the signal field that is emitted in the $\mathbf{k}_{sig}$ direction ($\mathbf{k}_{sig} = \pm\mathbf{k}_1 \mp \mathbf{k}_2 + \mathbf{k}_3$). The signal is generated by $\mathbf{P}^{(3)}$ which is a

convolution of the third order material response function, $\vdots\vdots\mathbf{R}^{(3)}$, and the three incident electric fields as shown below:

$$\begin{aligned}\mathbf{P}^{(3)}(\mathbf{k}_{sig},t,\tau_2,\tau_1)=\int_0^\infty\int_0^\infty\int_0^\infty \vdots\vdots\mathbf{R}^{(3)}(\tau_3',\tau_2',\tau_1'):\mathbf{E}_3(\mathbf{k}_3,t-\tau_3')\mathbf{E}_2(\mathbf{k}_2,t+\tau_2-\tau_3'-\tau_2')\\ \times\mathbf{E}_1(\mathbf{k}_1,t+\tau_2+\tau_1-\tau_3'-\tau_2'-\tau_1')d\tau_1'd\tau_2'd\tau_3'.\end{aligned} \quad (2.14)$$

The nonlinear response function $\vdots\vdots\mathbf{R}^{(3)}$ contains the vibronic signal of interest and is expressed as a four-point correlation function of dipole moment operators with numbered subscripts (1-4) denoting the time-ordering of the field-matter interaction,

$$\vdots\vdots\mathbf{R}^{(3)}(\tau_3',\tau_2',\tau_1')=\left(\frac{i}{\hbar}\right)^3\left\langle\Big[\Big[\Big[\mathbf{M}_4(\tau_3'+\tau_2'+\tau_1'),\mathbf{M}_3(\tau_2'+\tau_1')\Big],\mathbf{M}_2(\tau_1')\Big],\mathbf{M}_1(0)\Big]\rho_0\right\rangle. \quad (2.15)$$

Here, $\rho_0$ is the equilibrium reduced density matrix for the vibronic system eigenstates with its time evolution monitored during three separate time intervals ($\tau_1'$, $\tau_2'$, and $\tau_3'$ as described in Figure 2.1) and the angled brackets $\langle\cdots\rangle$ denote the trace over the system and the bath degrees of freedom. Expanding the commutator in eq. (2.15) yields eight terms grouped into four pairs of complex conjugate field-matter interaction pathways (see Appendix C). $\vdots\vdots\mathbf{R}^{(3)}$ is a fourth-rank tensor that contains the nonlinear vibronic response $R^{abcd}(\tau_3',\tau_2',\tau_1')$ and the orientational response $Y_{IJKL}^{abcd}(\tau_3',\tau_2',\tau_1')$ of the dipoles that interact with the various electric fields in all four conjugate interaction pathways in the system.

$$\vdots\vdots\mathbf{R}^{(3)}(\tau_3',\tau_2',\tau_1')=\sum_{\alpha=1}^{4}\sum_{IJKL}\sum_{a,b,c,d}(Y_\alpha)_{IJKL}^{abcd}(\tau_3',\tau_2',\tau_1')R_\alpha^{abcd}(\tau_3',\tau_2',\tau_1') \quad (2.16)$$

In the above expression, the vibronic eigenstates are given by indices (*a*, *b*, *c*, *d*), where the indices $(IJKL)$ reference a permutation of the electric field polarization over the laboratory coordinates $\{X,Y,Z\}$. This paper solely focuses on the molecular insight contained in the

nonlinear vibronic response function, $R^{abcd}(\tau_3',\tau_2',\tau_1')$, for various transition pathways where the indices (*a, b, c, d*) specify vibronic eigenstates interacting *via* $\mathbf{M}_{vn}$ (eq. (2.11)), $\mathbf{M}_{v'n'}$ (eq.(2.12) ), and $\mathbf{M}_{eg}$ (eq. (2.13)). The response functions for all 2D EV and 2D VE peaks are listed in Appendix D and they are characterized by the combination of involved vibronic eigenstates in Table 2.2 and Table 2.3.

We consider the system composed of two electronic states and one IR-active local vibrational mode, as described by $H_{vibronic}$ in section 2.2 and depicted in Figure 2.2. The parameters in the vibronic Hamiltonian are chosen so that the frequency of the anharmonic vibration is red-shifted in the excited electronic state. Using the transition frequencies shown in Figure 2.2, the vibrational frequency difference between electronic states, ($\Delta_{eg}$) and the mechanical anharmonicity of the excited electronic state ($\Delta_{2',1'}$) can be defined as $\Delta_{eg} = \omega_{e,1'} - \omega_{g,1}$ and $\Delta_{2',1'} = \omega_{e,1'} - \omega_{e,2'}$. These expressions can be evaluated using stationary perturbation theory with second order energy corrections and are given in section 2.8.5. For simplicity, it is assumed in sections 2.3 and 2.4 that the electronically-resonant electric fields have center frequency $\omega_{eg}$ and bandwidth $2\omega_{g,1}$, allowing resonant transitions between states with energy separation corresponding to frequencies within $\omega_{eg} \pm \omega_{g,1}$. The vibrationally-resonant fields are assumed to have sufficient bandwidth to excite one-quantum transitions only. As the input electric fields have a finite pulse duration, it is important to distinguish between the experimentally controlled delay time ($\tau_n$) and the delay between field-matter interactions ($\tau_n'$). The discussion section explores the effects of varying these electric field characteristics on the vibronic transition pathways accessible to the molecular system.

Additionally, we assume the lowest vibrational transition energy in $|g\rangle$ to be larger than $k_B T$ such that only $|g,0\rangle$ is initially populated in the system and all transition pathways originate from this state. Next, I discuss the various rephasing and non-rephasing pathways contributing to the 2D EV and 2D VE signals and their manifestations in the peak positions, amplitudes and lineshapes of the resultant 2D spectra.

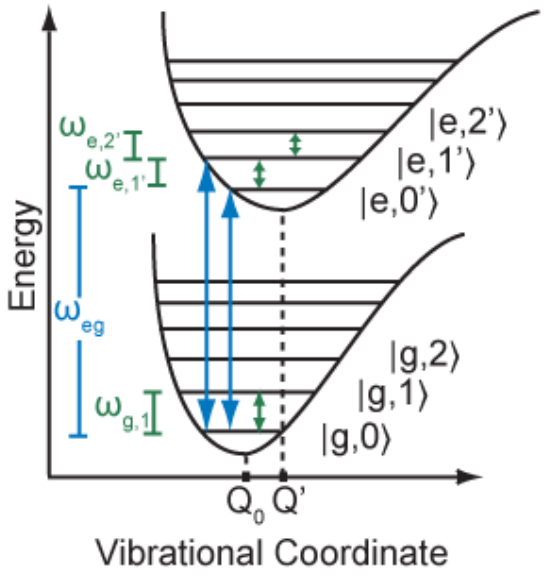


Figure 2.2. An illustration of the potential energy surfaces represented by $H_{\text{vibronic}}$ with linear and quadratic vibronic coupling. The states |g,v⟩ and |e,v'⟩ are the vibronic states in either the electronic ground, g, or excited, e, manifold with vibrational state v, or v', respectively. This model reflects a system of displaced, frequency shifted, anharmonic oscillators. The blue (green) arrows indicate transitions between electronic (vibrational) states. The frequencies $\omega_{eg}$, $\omega_{g,v}$, and $\omega_{e,v'}$ correspond to the energy separation between the electronic manifolds, the vibrational levels in |g⟩, and the vibrational levels in |e⟩, respectively.

### 2.3.1 *Vibronic Signal Pathways in 2D EV Spectroscopy*

Using the material and interaction Hamiltonians described in section 2.2 and Figure 2.2 and the center frequency and bandwidth considerations of the input electric fields described above we can obtain the expression for the material response function and the third-order nonlinear polarization. The 2D EV response tensor, $\vec{\mathbf{R}}^{(3)}$, is obtained from equation (2.15)

when $\mathbf{M_1}$ and $\mathbf{M_2}$ are electronic transition dipole moments and $\mathbf{M_3}$ and $\mathbf{M_4}$ are vibrational transition dipole moments. $\vec{\vec{\mathbf{R}}}^{(3)}(\tau_3', \tau_2', \tau_1')$ includes responses from many possible vibronic transition pathways that the system can access during time intervals $\tau_n'$. The possible vibronic Liouville pathways that can generate a 2D EV signal in the simplified system here while $\tau_2' \geq \tau_p$ are represented in the double-sided Feynman diagrams for the rephasing (R), $\mathbf{k_{sig}} = -\mathbf{k_1} + \mathbf{k_2} + \mathbf{k_3}$, and non-rephasing (NR), $\mathbf{k_{sig}} = +\mathbf{k_1} - \mathbf{k_2} + \mathbf{k_3}$, phase-matched directions (Figure 2.3(a) and (b)). The signals from the R and NR pathways oscillate at conjugate frequencies during the coherence period. Within the center frequency and bandwidth considerations described above, the system can only evolve in a population state of the density matrix during $\tau_2'$ when $\tau_2' \geq \tau_p$ and $\tau_p$ is the longer FWHM pulse duration between the optical and IR electric fields. The evolution of a system in a coherence state of the density matrix during $\tau_2'$ while $\tau_2' \geq \tau_p$ is not phase matched for detection unless the IR probe field bandwidth spans the vibrational frequencies of the fundamental ($\omega_{vib}$) and first overtone ($2\omega_{vib}$) transitions. When $|\tau_2'| < \tau_p$, the time-ordering of the $\mathbf{k_2}$ and $\mathbf{k_3}$ field-matter interactions cannot be rigidly defined, and so the additional transition pathways in Figure 2.3(c) can contribute to the 2D EV spectrum. These pathways will not yield new peaks, but they can contribute intensity to peaks I and III that oscillate at the $\tau_2'$ coherence frequency until the third field-matter interaction occurs. Illustrated in Figure 2.3(d) is a fully absorptive cartoon spectrum for the system with linear and quadratic vibronic coupling. The $m^{th}$ peak consists of signal contributions from the corresponding R ($D_{R,m}^{EV}$) and NR ($D_{NR,m}^{EV}$) double-sided Feynman diagrams. The complete set of vibronic response functions for each of the diagrams is given in

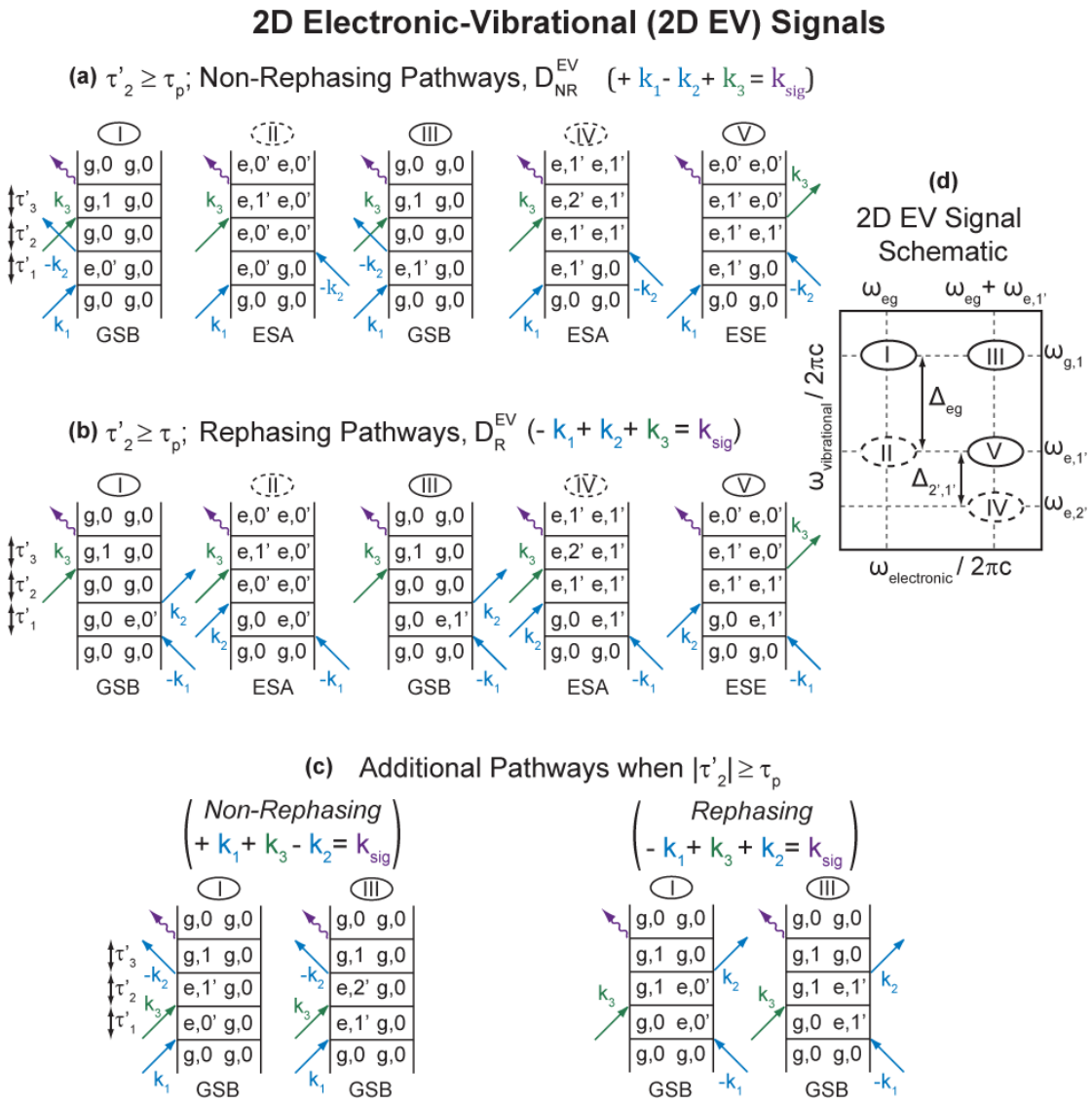


Figure 2.3. 2D EV Vibronic Signals Overview. All the accessible Liouville transition pathways (a-c) are given for the case that the excitation fields ($\mathbf{k_1}$ and $\mathbf{k_2}$) span frequencies $\omega_{eg} \pm \omega_{g,1}$ (where $\omega_{eg} = (E_{e,0'} - E_{g,0})/\hbar$ and $\omega_{g,v} = (E_{g,(v+1)} - E_{g,v})/\hbar$), and the probe field ($\mathbf{k_3}$) has bandwidth sufficient to resonantly excite single quantum vibrational transitions only. The 2D EV non-rephasing (NR) and rephasing (R) signal pathways represented by the double-sided Feynman diagrams $D_{NR}^{EV}$ and $D_R^{EV}$ in (a) and (b), respectively, represent the contributing 2D EV signal pathways when $\mathbf{k_2}$ and $\mathbf{k_3}$ are beyond temporal overlap (i.e. $\tau'_2 \geq \tau_p$where $\tau_p$ is the longer pulse FWHM duration) such that field-matter interaction time ordering is unambiguous. Additional pathways in (c) contribute only during the $\mathbf{k_2}$ and $\mathbf{k_3}$ temporal overlap ($|\tau'_2| < \tau_p$). The diagrams have peak labels (I-V) denoting the signal to which that pathway contributes; the R and NR diagrams for a given peak sum to yield the absorptive 2D EV signal. The diagrams are also specified by transition type: ground state bleach (GSB, positive, solid line), excited state absorption (ESA, negative, dashed line), and excited state stimulated emission (ESE, positive, solid line). The illustrated absorptive 2D EV spectrum shown (d) for a system where $\mathcal{V}_j^{(1)} \neq 0$ and $\mathcal{V}_{j,j}^{(2)} \neq 0$ gives peaks I-V at the coordinates $\omega_1 = \omega_{eg}$, $\omega_{eg} + \omega_{e,1'}$ and $\omega_3 = \omega_{g,1}$, $\omega_{e,1'}$, and $\omega_{e,2'}$ (where $\omega_{e,v'} = (E_{e,(v+1)'} - E_{e,v'})/\hbar$); thus, the frequency difference of the vibration in $|g\rangle$ and $|e\rangle$, $\Delta_{eg} = \omega_{e,1'} - \omega_{g,1}$, and the anharmonicity in $|e\rangle$, $\Delta_{2',1'} = \omega_{e,1'} - \omega_{e,2'}$, can be read off of the 2D EV spectrum directly.

Appendix D. In general, the response function consists of (i) oscillating frequencies which determine the position of the 2D peak in the $\omega_1$ and $\omega_3$ Fourier space, (ii) the product of transition dipole factors which govern the amplitude of the 2D peaks and (iii) a nonlinear dephasing function ( $F^{a,b,c,d}(\tau_3', \tau_2', \tau_1')$ ) which dictates the 2D line shape. Each of these factors is discussed in detail below.

2.3.1.1 2D EV Peak Positions

The 2D EV peak positions identify specific vibrational modes coupled to electronic transitions in the molecular system and they reveal differences between the ground and excited potential energy surfaces. These positions are dictated by the energy separation of the vibronic eigenstates in the molecular ensemble. In the vibronic systems modeled by $H_{vibronic}$, the eigenstate energies are dependent on the vibrational anharmonicity, the equilibrium position displacement in the excited state, and the excited state frequency shift. The peak positions in the $\omega_{electronic}$ dimension indicate the resonance frequencies of the electronic transition $|g,0\rangle \rightarrow |e,v'\rangle$ that are accessed during the electronic coherence time, $\tau_1'$. The positions in the $\omega_{vibrational}$ dimension reveal vibrational modes that are coupled to the electronic transitions. As opposed to degenerate 2D techniques where peaks can exist in the absence of molecular coupling (i.e., on-diagonal peaks), every peak in 2D EV spectroscopy is a cross peak and requires the coupling of electronic and vibrational degrees of freedom to be observed.

Peaks I and II (Figure 2.3(d)) are centered at $\omega_{electronic} = \omega_{eg}$ because the Liouville pathways that contribute to these signals evolve in a coherence between $|g,0\rangle$ and $|e,0'\rangle$ during $\tau_1'$. The Liouville pathways that give rise to peaks I and II differ by the vibronic state population

$|g,0\rangle\langle g,0|$ or the $|e,0'\rangle\langle e,0'|$ in which the system evolves respectively during $\tau_2'$. Therefore, the final probe field interaction is resonant with either $\omega_{g,1}$ or $\omega_{e,1'}$ to yield a ground state bleach (peak I, $(\omega_{eg},\omega_{g,1})$) or an excited state absorption (peak II, $(\omega_{eg},\omega_{e,1'})$) signal, respectively. Peaks III-V have peak centers $\omega_{electronic}=\omega_{eg}+\omega_{e,1'}$ that reflect vibronic transition pathways with electronic coherence between $|g,0\rangle$ and $|e,1'\rangle$ during $\tau_1'$, the vibrationally probed transitions originate from $\tau_2'$ populated states of either $|g,0\rangle\langle g,0|$ or $|e,1'\rangle\langle e,1'|$. When higher lying vibrational states (v'>0) in $|e\rangle$ are accessed, the excited state stimulated emission (ESE) Liouville pathway ( $D_{R,V}^{EV}$ , $D_{NR,V}^{EV}$ ) is possible. Hence, three 2D EV peaks exist for each pathway with electronic coherence between $|g,0\rangle$ and $|e,(v'>0)\rangle$ in $\tau_1'$. In the case where both linear and quadratic vibronic coupling is present, peaks III (GSB), IV (ESA), and V (ESE) may be observed at $(\omega_{eg}+\omega_{e,1'},\omega_{g,1})$, $(\omega_{eg}+\omega_{e,1'},\omega_{e,2'})$, and $(\omega_{eg}+\omega_{e,1'},\omega_{e,1'})$, respectively.

In 2D EV spectroscopy, the ESE is the only transition pathway that can yield positive signal from a vibrational transition in the electronic excited state, which provides an important contrast to the negative ESA signals arising from populated vibronic states in $|e\rangle$. The other source of positive signal is the GSB pathway, which will only result from vibrational transitions in $|g\rangle$. Therefore, the GSB and ESE signals are specific to vibrations in the ground and excited electronic state, respectively. As discusssed later in this chapter, the intensity contributions from these positive signals will be separable in the $\omega_3$ dimension when the anharmonic vibration is frequency-shifted in the excited state. A systematic discussion of how

the anharmonicity, excited state equilibrium displacement, and excited state frequency shifting affects the presence of 2D EV peaks is accompanied by simulated 2D EV spectra in section 2.4.

In all of the 2D EV spectra presented in this dissertation, the observed peaks are peaks I and II. In the case of $[Fe(CN)_6]^{3+}$ studied in chapter 5, apparently only peaks I and II are measured, while further analysis suggests there is more subtlety possibly involving low frequency vibrational modes that modulate the peak positions in both 2D EV and 2D VE spectra. Peaks I and II can also appear for many vibrational modes for multiple electronic states simultaneously in one 2D EV spectrum as for the Ru-centered compound in chapters 7-8. They also may not appear together; in the excited state intramolecular proton transfer complex studied in chapter 9, only peak II is measured as this peak results from the significant structural rearrangement involving proton transfer upon photoexcitation.

#### 2.3.1.2 2D EV Peak Amplitudes

The 2D EV peak amplitudes are determined by the population of molecules in $\left|g,0\right\rangle$ and the relative strength of the four interacting dipoles that generate the third order response, as shown in equations (2.50) and (2.51). Generally, the effects of electrical anharmonicity in the system arise from the nonlinearity of the dipole moments with respect to the vibrational coordinate and have been considered in 2D IR spectroscopy. The explicit treatment of both the electronic and vibrational dipole moments in 2D EV and 2D VE spectroscopies can provide insight into the electrical anharmonicity of the molecule from two perspectives: 1) the nuclear dependence of the electronic redistribution upon changing electronic states, and 2) the nonlinearity of a vibration in an excited electronic state.

The dependence of $\mathbf{M}_{eg}(Q)$ on the vibrational coordinates appears when the coefficients $\mu_{eg}^{(1)}$ and $\mu_{eg}^{(2)}$ are nonzero in the expression for $\mu^{e,g}$ given by

$$\mu^{e,g} = \mu_{eg}^{(0)} \left\langle g,v \middle| e,v' \right\rangle + \mu_{eg}^{(1)} \sum_j \left\langle g,v \middle| Q_j \middle| e,v' \right\rangle + \frac{1}{2} \mu_{eg}^{(2)} \sum_j \left\langle g,v \middle| Q_j Q_j \middle| e,v' \right\rangle + \ldots \tag{2.17}$$

which is obtained by evaluating equation (2.8) for a vibronic transition (i.e., subject to eq. (2.13)). The Condon approximation requires that the electronic transition is independent of the nuclear coordinates, implying $\mu_{eg}^{(m)} = 0$ for $m \geq 1$. In this case, $\mu^{e,g}$ expresses the electronic transition dipole moment for the system at the equilibrium nuclear configuration with the transition strength modulated by the overlap integral of the two involved vibronic states. The zeroth order result implies the reduction of the Born-Oppenheimer adiabatic wave functions to crude adiabatic wave functions because of the constraints imposed by referencing only the equilibrium nuclear configuration;[25,29,30] these constraints are corrected when higher order terms are included. Therefore, to zeroth order the amplitudes of the 2D EV peaks are directly proportional to $\left|\mu^{e,g}\right|^2 = \left|\mu_{eg}^{(0)}\right|^2 \left|\left\langle g,v \middle| e,v' \right\rangle\right|^2$ due to the first two interactions of $\mathbf{M}_{eg}(Q)$ with the density matrix in the nonlinear vibronic response function (eq. (2.15)). This directly demonstrates that all 2D EV peak amplitudes are scaled by the Franck-Condon factors, $\left|\left\langle g,v \middle| e,v' \right\rangle\right|^2$.

For electronic transitions that are dependent on nuclear coordinates, the linear and higher order terms in equation (2.9) may be nonzero and they account for variations in the vibronic transition strength due to the nuclear configuration of the system. This is known as the breakdown of the Condon approximation.[27-29] If the Condon approximation is relaxed, then the

higher order terms that collectively describe the non-Condon effects ( $\mu_{eg}^{(m)} \neq 0$ for $m \geq 1$ ) are included in evaluating $\mu^{e,g}$ and the vibronic transition strength deviates from the zeroth order scaling with the Franck-Condon factor. This demonstrates that the 2D EV peak amplitudes are sensitive to non-Condon effects through intensity contributions from first and higher order terms in $\mu^{e,g}$ . The amplitude ratio that compares 2D EV peaks originating from the vibronic transitions $|g,v\rangle \rightarrow |e,v'\rangle$ and $|g,v\rangle \rightarrow |e,(v+1)'\rangle$ (e.g., peaks I and III in Figure 2.3(d)) should be equal to the ratio of the respective Franck-Condon factors if non-Condon effects are negligible; variations from this amplitude ratio reflect the presence of non-Condon effects.

Effects from the system electrical anharmonicity in the vibration can also be present from the nonlinearity of the vibrational transition dipole moment, in a similar fashion to 2D IR spectroscopy.[33,34,38] The influence of this type of electrical anharmonicity in 2D EV spectroscopy is observed specifically for the vibration in the electronic excited state. A linear dependence of $\mu^{v',n'}$ on the nuclear coordinates yields transition dipoles for the $|e,0'\rangle \rightarrow |e,1'\rangle$ , $\left(\mu^{0',1'}\right)$, and for the $|e,1'\rangle \rightarrow |e,2'\rangle$, $\left(\mu^{1',2'}\right)$, transitions that should scale harmonically as $\mu^{1',2'} = \sqrt{2}\mu^{0',1'}$. Comparison of oppositely-signed peak amplitudes for an electronically excited state vibration (e.g., peaks IV and V in Figure 2.3(d)) will reflect the electrical anharmonicity of the vibrational mode in the excited electronic state specifically.

#### 2.3.1.3 2D EV Line Shapes

The influence of the system-bath dynamics are reflected in the 2D EV line shapes which are described by the nonlinear dephasing function for each vibronic signal pathway. Following the approach of Sung and Silbey,[23] the dephasing functions, $F^{a,b,c,d}(\tau_3', \tau_2', \tau_1')$ , in the nonlinear

vibronic response are composed of line shape functions, $h_{a,b}(t)$ (defined in Appendix C), that describe the time-dependent transition frequency fluctuation between vibronic states $|a\rangle$ and $|b\rangle$ induced by system-bath dynamics. Assuming that the transition frequency fluctuations ( $\delta\omega_{a,b}(t)$ ) about an ensemble average frequency ( $\bar{\omega}_{a,b}$ ) obey Gaussian statistics, the time dependence of a resonant transition frequency is expressed as $\omega_{a,b}(t) = \bar{\omega}_{a,b} + \delta\omega_{a,b}(t)$. The energy gap correlation function $\zeta_{a,b}$ correlates the transition frequency fluctuation $\delta\omega_{a,i}$ with the fluctuation $\delta\omega_{b,i}$ over a time period $t$ where the subscript "*i*" is the initial state of the density matrix. The time scales for these fluctuations are expressed as auto- and cross-correlations, which describe the correlation of a single vibronic transition (a=b) or of two different vibronic transitions (a≠b), respectively. The energy gap correlation function can be expressed in terms of these transition frequency fluctuations by $\zeta_{a,b}(t) = \langle \delta\omega_{a,i}(t)\delta\omega_{b,i}(0) \rangle$.

A simplified notation is used to express the correlation functions in 2D EV and 2D VE spectroscopies. Instead of specifying the correlated eigenstates, the subscripts specify the transition frequency between the correlated eigenstates (i.e., $eg = |g,0\rangle \rightarrow |e,0'\rangle$, $v = |g,0\rangle \rightarrow |g,1\rangle$, and $v' = |e,0'\rangle \rightarrow |e,1'\rangle$ ). The energy gap auto-correlation functions are the fluctuations in the electronic transition frequency ( $\zeta_{eg,eg}$ ), the ground state vibrational frequency ( $\zeta_{v,v}$ ), and the excited state vibrational frequency ( $\zeta_{v',v'}$ ). The cross-correlation functions ( $\zeta_{eg,v}$, $\zeta_{eg,v'}$, $\zeta_{v,v'}$ ) relate the frequency fluctuations in electronic transitions and vibrational transitions. The correlation functions are defined in Appendix A. Both 2D EV and 2D VE spectroscopies access all of the auto-correlation functions. The 2D EV experiment only

accesses the $\zeta_{eg,v'}$ cross correlation, while the 2D VE line shapes include contributions from all three cross correlations. However, as shown below, the line shapes in both techniques can be defined in terms of the same correlation functions and a proportionality constant.

Electronic-state-dependent vibrational dephasing is explored by defining a proportionality constant, $\lambda$, that relates the ratio of the excited electronic state fluctuations to those in the ground electronic state

$$\lambda = \frac{\delta\omega_{e1',e0'}(t)}{\delta\omega_{g1,g0}(t)}. \tag{2.18}$$

This parameter is analogous to the $\alpha_0$ and $\alpha_1$ parameters used by Lewis *et al.*[9] Now the 2D line shapes can be written in terms of only three energy gap correlation functions ($\zeta_{eg,eg}$, $\zeta_{eg,v}$, and $\zeta_{v,v}$) and $\lambda$

$$\zeta_{v',v'} = \lambda^2 \zeta_{v,v} \tag{2.19}$$

$$\zeta_{v,v'} = \lambda \zeta_{v,v} \tag{2.20}$$

$$\zeta_{eg,v'} = \lambda \zeta_{eg,v} \tag{2.21}$$

As shown below, expressing the dephasing functions in terms of auto- and cross-correlation functions demonstrates that 2D EV and 2D VE spectroscopies are sensitive to the coupling between electronic and vibrational degrees of freedom in a molecular ensemble. Additionally, obtaining a proportionality constant relating the nature of the homogeneous vibrational dephasing in the ground and the excited electronic manifolds is a notable advantage of these spectroscopies.

In this work we assume the homogeneous limit where the fluctuations $\delta\omega_{y,i}(t)$ are much faster than the timescale of the experimental measurement and that fluctuations in the

mechanical anharmonicity are negligible. In this limit, the line shape functions become linear with respect to time, $h_{a,b}(t) \approx \Gamma_{a,b} t$, and the dephasing functions ($F^{a,b,c,d}$) reduce to exponentially decaying functions where the $\Gamma_{a,b}$ terms are damping constants, or decay times, that reflect the homogenous dephasing time scales defined as $\Gamma_{a,b} = \int_0^\infty d\tau \zeta_{a,b}(\tau)$. The absorption line shapes are related by the Fourier transform of the dephasing functions, which yield 2D Lorentzian line shapes with spectral widths in $\omega_1$ and $\omega_3$ defined by the $\Gamma_{a,b}$ terms for the $\tau_1'$ and $\tau_3'$ periods, respectively. In future work, we will explore the effects of correlated spectral broadening in these 2D spectroscopies. The 2D EV dephasing functions, $F_{R,I-V}^{a,b,c,d}$ for all five peaks are expressed (R and NR functions have the same form, only R is given) using simplified notation:

$$F_{R,I}^{g0,g1,g0,e0'}(\tau_3',\tau_2',\tau_1') = \Gamma_{v,v}\tau_3' + \Gamma_{eg,eg}\tau_1' \tag{2.22}$$

$$F_{R,II}^{g0,e0',e1',e0'}(\tau_3',\tau_2',\tau_1') = (\lambda^2)\Gamma_{v,v}\tau_3' + \Gamma_{eg,eg}\tau_1' \tag{2.23}$$

$$F_{R,III}^{g0,g1,g0,e1'}(\tau_3',\tau_2',\tau_1') = \Gamma_{v,v}\tau_3' + \left[\Gamma_{eg,eg} + (2\lambda)\Gamma_{eg,v} + (\lambda^2)\Gamma_{v,v}\right]\tau_1' \tag{2.24}$$

$$F_{R,IV}^{g0,e1',e2',e1'}(\tau_3',\tau_2',\tau_1') = (\lambda^2)\Gamma_{v,v}\tau_3' + \left[\Gamma_{eg,eg} + (2\lambda)\Gamma_{eg,v} + (\lambda^2)\Gamma_{v,v}\right]\tau_1' \tag{2.25}$$

$$F_{R,V}^{g0,g1,g0,e1'}(\tau_3',\tau_2',\tau_1') = (\lambda^2)\Gamma_{v,v}\tau_3' + \left[\Gamma_{eg,eg} + (2\lambda)\Gamma_{eg,v} + (\lambda^2)\Gamma_{v,v}\right]\tau_1' \tag{2.26}$$

The sensitivity of 2D EV spectroscopy to electronic-state-dependent vibrational dephasing is demonstrated by the $\lambda^2$ dependence of peaks II, IV, and V during the detection period $\tau_3'$. The comparison of these broadened peaks to peaks I and III in the $\omega_{vibrational}$ dimension will directly reveal electronic-state-dependent vibrational dephasing. There is also a strong, uniform $\lambda$

dependence in the $\omega_{electronic}$ dimension for peaks III, IV, and V; which may reflect deviations from strictly vertical electronic excitation and stronger fluctuations of "hot" vibrations in $|e\rangle$.

The functional form of the 2D EV dephasing functions shown above can provide a direct way to quantify an electronic, vibrational, or vibronic correlation function for a specific sub-ensemble of an electronically excited state vibrational coordinate. Chapter 7 discusses the 2D EV spectrum for a Ru-centered compound in which many vibrational modes are coupled to up to three different metal-to-ligand charge transfer states. Simply treating each of these peaks individually to extract these correlation functions may provide detailed insight into the photochemical dynamics of interest in a given system under study.

### 2.3.2 *Vibronic Signal Pathways in 2D VE Spectroscopy*

Similar to section 2.3.1, I will use the material and interaction Hamiltonians described in section 2.2 and Figure 2.2 and the center frequency and bandwidth considerations of the input electric fields described above to obtain the expression for the material response function and the third-order nonlinear polarization for the 2D VE experiment. In contrast to 2D EV experiments, no vibrational transitions in the excited electronic state are directly observed in 2D VE spectroscopy. Rather, the resonance frequencies of the electronic transitions that are probed with the final probe interaction carry this information. The only vibrationally-resonant field-matter interaction in 2D VE spectroscopy occurs with the first two pulses with frequency $\omega_{g,1}$. The electronic transitions probed with $\mathbf{k}_3$ have energies equal to the sum of the electronic energy gap and some combination of vibrational quanta (see Figure 2.4(d)). As a result, the direct comparison of specific peaks that report on vibrational features in the ground and excited electronic states is not as straightforward as in 2D EV. The reader is directed to recent papers

by Courtney, *et al.*[3,4] and to Dr. Zachary Fox's dissertation[39] for additional discussion of 2D VE transitions.

Considering the same electric field parameters described earlier, the allowed transition pathways in 2D VE only evolve in population states during $\tau_2'$ while $\tau_2' \geq \tau_p$. The 2D VE response tensor is obtained from equation (2.15) when $\mathbf{M_1}$ and $\mathbf{M_2}$ are vibrational transition dipole moments and when $\mathbf{M_3}$ and $\mathbf{M_4}$ correspond to electronic transition dipole moments. The transition pathways available to a molecular system described by $H_{vibronic}$ for the vibronic system in the present discussion are shown as double-sided Feynman diagrams in Figure 2.4(a) and (b), and a fully absorptive 2D VE spectrum is illustrated in Figure 2.4(d). The complete set of vibronic response functions for each of the diagrams in Figure 2.4 is given in Appendix D. In general, the 2D VE response function consists of (i) oscillating frequencies which determine the position of the 2D peak in the $\omega_1$ and $\omega_3$ Fourier space, (ii) product of transition dipole factors which govern the amplitude of the 2D peaks and (iii) nonlinear dephasing function ($F^{a,b,c,d}(\tau_3', \tau_2', \tau_1')$) which dictates the 2D line shape. We will discuss each of these factors in detail below.

#### 2.3.2.1 2D VE Peak Positions

The 2D VE peak positions encode the modulation of the electronic energy gap that is coupled to the nuclear motion of the ground electronic state molecule. The resonance frequencies for the transitions between the vibronic eigenstates modeled by $H_{vibronic}$ govern the positions of the 2D VE peaks. Thus, the 2D VE peak positions are sensitive to the anharmonicity, the excited state equilibrium displacement, and the excited state frequency shift

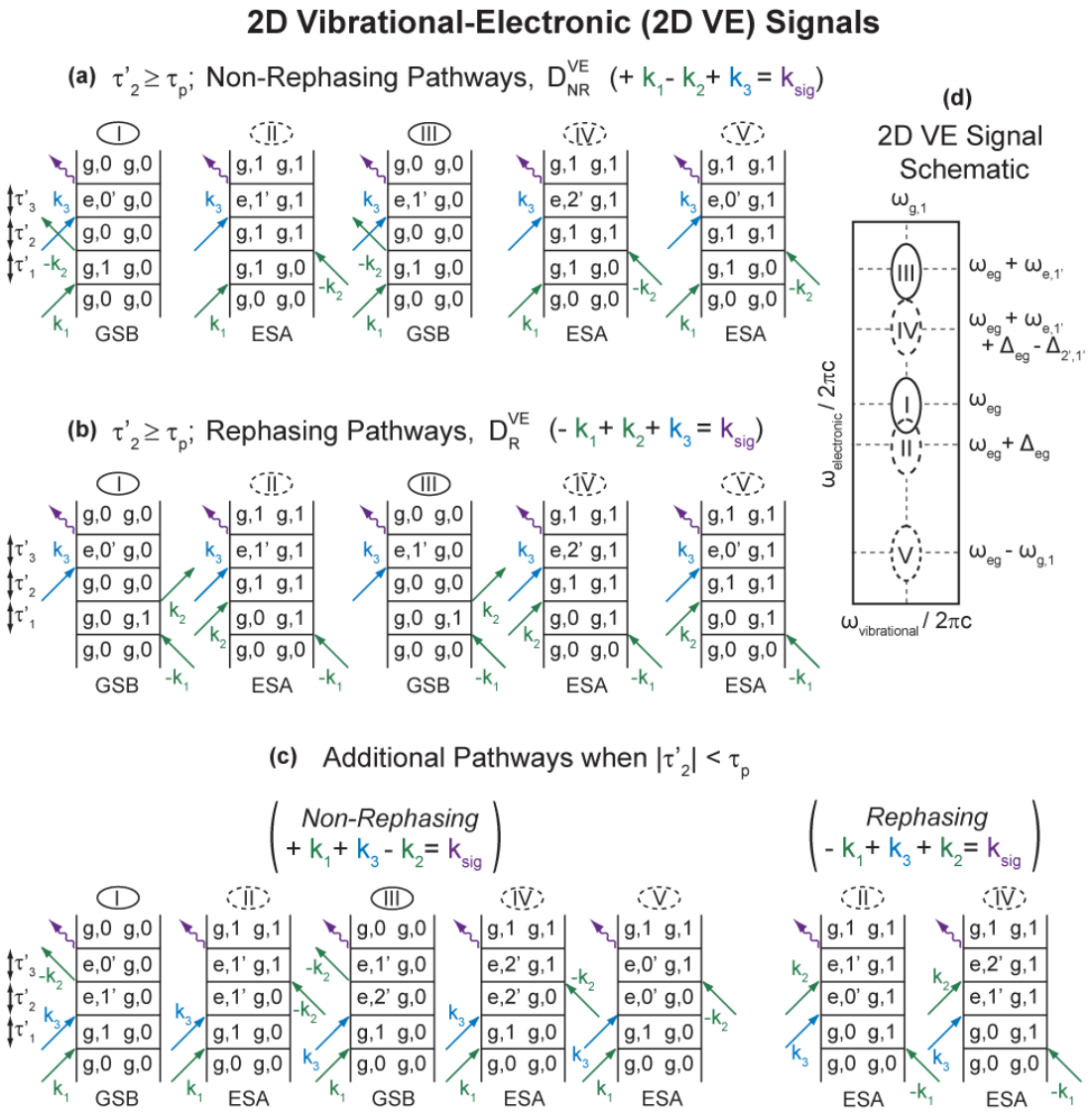


Figure 2.4. 2D VE Vibronic Signals Overview. The relevant Liouville pathways that contribute to the 2D VE signal when the excitation fields ($\mathbf{k_1}$ and $\mathbf{k_2}$) have sufficient bandwidth for resonant single quantum vibrational transitions and the probe field ($\mathbf{k_3}$) spans frequencies $\omega_{eg} \pm \omega_{g,1}$. The non-rephasing (NR) and rephasing (R) signal pathways represented by the double-sided Feynman diagrams $D_{NR}^{VE}$ and $D_R^{VE}$ in (a) and (b), respectively, are the only contributing 2D VE signal pathways when $\mathbf{k_2}$ and $\mathbf{k_3}$ are beyond temporal overlap (i.e., $\tau'_2 \geq \tau_p$ where $\tau_p$ is the longer pulse FWHM duration) such that field-matter interaction time ordering is well defined. Additional pathways in (c) contribute only during the $\mathbf{k_2}$ and $\mathbf{k_3}$ temporal overlap ($|\tau'_2| < \tau_p$). The peak labels (I-V) specify the signal to which that pathway contributes; the R and NR diagrams for a given peak sum to yield the absorptive 2D VE signal. The diagrams are also categorized by signal type: ground state bleach (GSB, positive, solid line) and excited state absorption (ESA, negative, dashed line). The fully absorptive 2D VE spectrum is depicted (d) for a system where $\mathcal{V}_j^{(1)} \neq 0$ and $\mathcal{V}_{j,j}^{(2)} \neq 0$; peaks I-V share the excitation frequency coordinate $\omega_1 = \omega_{g,1}$ and they are distinguished by the probed electronic transition frequencies $\omega_3 = \omega_{eg}$, $\omega_{eg} + \Delta_{eg}$, $\omega_{eg} + \omega_{e,1'}$, $\omega_{eg} + \omega_{e,1'} + \Delta_{eg} - \Delta_{2'1'}$, and $\omega_{eg} - \omega_{g,1}$ where the frequencies are defined $\omega_{eg} = (E_{e,0'} - E_{g,0})/\hbar$, $\omega_{g,v} = (E_{g,(v+1)} - E_{g,v})/\hbar$, $\omega_{e,v'} = (E_{e,(v+1)'} - E_{e,v'})/\hbar$, the frequency difference of the vibration in $|g\rangle$ and $|e\rangle$, $\Delta_{eg} = \omega_{e,1'} - \omega_{g,1}$, and the anharmonicity in $|e\rangle$, $\Delta_{2'1'} = \omega_{e,1'} - \omega_{e,2'}$.

of the vibrational mode. The $\omega_{vibrational}$ peak position indicates the resonant vibrational transition that is initially excited in the ground state molecule during $\tau_1'$, and the peak coordinate along the $\omega_{electronic}$ dimension reflects the energy gap for transitioning into a vibrational state in $|e\rangle$ following the initial vibrational perturbation. Given the considered electric field characteristics, 2D VE transition pathways are resonantly excited with the same excitation frequency $\omega_{g,1}$ resulting in the vertically stacked series of peaks shown in Figure 2.4(d). Resolution of different peaks in the $\omega_{vibrational}$ dimension becomes relevant when more than one vibrational mode is involved in the vibronically coupled system, which could include other high frequency vibrational modes or low frequency structural modes. Since the 2D VE transition pathways never include a vibrationally-resonant field-matter interaction with a vibration in $|e\rangle$, there will not be the same peak separation along $\omega_{vibrational}$ that reflects $\Delta_{eg}$ and $\Delta_{2'1'}$ as occurs in 2D EV spectra. Instead, the peak separation in the $\omega_{electronic}$ dimension is due to the modulation of the electronic energy gap by $\Delta_{eg}$ and $\Delta_{2'1'}$ which are expressed as combinations of vibrational quanta.

A particularly notable feature of 2D VE spectroscopy is the absence of ESE pathways to contribute positive intensity to the spectrum. In general, observed peaks will be broad in the $\omega_3$ dimension due to the electronic transitions that are probed with this technique. The ability to resolve information about the excited electronic state potential energy surface depends on the nature and strength of the system's vibronic coupling and the extent of overlap between these inherently broad signals. Peaks I-IV consist of pairs of bleach and absorption features that have frequency separation on the order of a fraction of one vibrational quantum (i.e., $\Delta_{eg}$

and $\Delta_{2'1'}$). The comparison of the peak separation and the electronic absorption line width dictates the overlap of oppositely-signed 2D VE signals.

The sign of the peaks in the 2D VE spectrum, differ by the populated state over which the system evolves during $\tau_2'$. The positive GSB features arise from electronic transitions into $|e\rangle$ from $|g,0\rangle\langle g,0|$ and the negative ESA features result from electronic transitions originating from $|g,1\rangle\langle g,1|$. Peak I (GSB) is centered at $\omega_{electronic} = \omega_{eg}$ because $\mathbf{k_3}$ induces the transition $|g,0\rangle \rightarrow |e,0'\rangle$, while peak II (ESA) is separated from peak I in $\omega_{electronic}$ by $\Delta_{eg}$ since the $\mathbf{k_3}$ interactions yielding peak II induce the transition $|g,1\rangle \rightarrow |e,1'\rangle$. For the red-shifted anharmonic vibration in $|e\rangle$ discussed here, $\omega_{e,1'} < \omega_{g,1}$ and so $\Delta_{eg}$ is negative resulting in the separation of peaks I and II represented in Figure 2.4(d); if $\omega_{e,1'} = \omega_{g,1}$, then $\Delta_{eg} = 0$ and peaks I and II are centered at the same 2D VE spectral coordinates, ($\omega_{g,1}$,$\omega_{eg}$). Therefore, the difference between the ground and excited electronic state vibrations is contained in the peak separation of peaks I and II, similar to 2D EV. Generally, peaks III (GSB) and IV (ESA) include electronically-resonant field-matter interactions higher in energy by $\sim \hbar\omega_{e,1'}$ than those that contribute to peaks I and II. The probed electronic transitions in peaks III and IV are $|g,0\rangle \rightarrow |e,1'\rangle$ and $|g,1\rangle \rightarrow |e,2'\rangle$, respectively. Peak IV is lower in frequency than peak III in $\omega_{electronic}$ by $\Delta_{eg}$ and the excited state mechanical anharmonicity, $\Delta_{2'1'}$. As a result, the 2D VE spectrum of a red-shifted anharmonic vibrational mode will have greater $\omega_{electronic}$ separation between peaks III and IV than between peaks I and II. Thus, when vibronic states $|e,v'\rangle$ for v'>1 are resonantly accessed via $\mathbf{k_3}$, information about $\Delta_{2'1'}$ is included in the 2D

VE spectral features. Peak V (ESA) is not paired with an oppositely-signed and overlapping peak. The electronically-resonant probe transition that generates peak V utilizes the lower frequency portion of the available bandwidth in $\mathbf{k}_3$ for the transition $|g,1\rangle \rightarrow |e,0'\rangle$; therefore, no lower-lying vibrational state in $|e\rangle$ exists to provide the accompanying positive GSB peak that is observed for peaks I-IV. Peak V is a unique spectral signature in 2D VE as it is inherently less convoluted by other spectral signatures.

As mentioned for 2D EV peak positions in section 2.3.1.1, low frequency vibrational modes can participate in shifting the peak positions in either frequency dimension. Such dynamics have been reported for the 2D VE spectra of $[Fe(CN)_6]^{3+}$ where peaks I and II are modulated with a time-dependent peak position in the electronic domain.[40]

#### 2.3.2.2 2D VE Peak Amplitudes

The 2D VE peak amplitudes depend on the initial ground state population and the strength of the four interacting dipoles of the vibronic system, as shown by the 2D VE response function (see equations (2.52) and (2.53)). The nonlinear nuclear coordinate dependence of the electronic transition dipole as given by eq. (2.17) and the vibrational transition dipoles inherently contribute to the resonant vibronic transitions in 2D VE spectroscopy. However, the effects of the nonlinearity of $\mathbf{M}_{eg}(Q)$ will overwhelm any effects of electrical anharmonicity in $\mathbf{M}_{vn}(Q)$ and $\mathbf{M}_{v'n'}(Q)$ present in 2D VE spectra. Direct observation of the electrical anharmonicity of a vibration in a particular electronic state requires the comparison of features arising from vibrational transitions between a zero and one quantum state and between a one and two quantum state (e.g., $\mu^{0',1'}$ and $\mu^{1'2'}$). Since 2D VE transition pathways include only

one vibrationally-resonant field-matter interaction, no such comparison is easily extracted from the spectra.

An important advantage of 2D VE spectroscopy is that the experiment samples a larger variety of transitions between vibronic states in different electronic manifolds as the electronically-resonant field-matter interaction is the probe interaction. The pathways that contribute the negative ESA features evolve in $|g,1\rangle\langle g,1|$ during $\tau_2'$, which allows the electronic transition to originate from an excited vibrational state in $|g\rangle$ and access higher vibrational states in $|e\rangle$ than is possible in the GSB pathways. This means that an amplitude comparison between GSB and ESA peak pairs includes the magnitudes of the involved dipole moments and the magnitudes of two different vibronic overlap integrals. For example, to zeroth order in $\mathbf{M}_{eg}(Q)$ (eq. (2.9)) the amplitude comparison of peaks I and II considers the difference in magnitudes of Franck-Condon factors for the $|g,0\rangle \rightarrow |e,0'\rangle$ and $|g,1\rangle \rightarrow |e,1'\rangle$ transitions. Similar to 2D EV spectroscopy, the non-Condon effects will manifest themselves as amplitude changes in the 2D VE spectra and will be explored in detail in section 2.4.

#### 2.3.2.3 2D VE Line Shapes

The nonlinear dephasing functions determine the line shapes observed in 2D VE spectra. As described for 2D EV line shapes in the homogenous limit above, the formulation of the 2D VE dephasing functions in terms of auto- and cross-correlation functions demonstrates that 2D VE spectroscopy is sensitive to fluctuations of vibronic frequencies. While the 2D VE dephasing functions are defined by more cross-correlations, the simplification of these expressions using the $\lambda$ parameter (eq. (2.18)) shows that 2D EV and 2D VE can be described by the same three correlation functions. However, the dephasing functions for 2D VE are very

different from those in 2D EV, which is a result of the different sequences of field-matter interactions utilized, and they are expressed for the rephasing contributions to the five peaks as follows:

$$F_{R,I}^{g0,e0',g0,g1}(\tau_3',\tau_2',\tau_1') = \Gamma_{eg,eg}\tau_3' + \Gamma_{v,v}\tau_1' \tag{2.27}$$

$$F_{R,II}^{g0,g1,e1',g1}(\tau_3',\tau_2',\tau_1') = \left[\Gamma_{eg,eg} + 2(\lambda-1)\Gamma_{eg,v} + (\lambda-1)^2\Gamma_{v,v}\right]\tau_3' + \Gamma_{v,v}\tau_1' \tag{2.28}$$

$$F_{R,III}^{g0,e1',g0,g1}(\tau_3',\tau_2',\tau_1') = \left[\Gamma_{eg,eg} + 2(\lambda)\Gamma_{eg,v} + (\lambda)^2\Gamma_{v,v}\right]\tau_3' + \Gamma_{v,v}\tau_1' \tag{2.29}$$

$$F_{R,IV}^{g0,g1,e2',g1}(\tau_3',\tau_2',\tau_1') = \left[\Gamma_{eg,eg} + 2(2\lambda-1)\Gamma_{eg,v} + (2\lambda-1)^2\Gamma_{v,v}\right]\tau_3' + \Gamma_{v,v}\tau_1' \tag{2.30}$$

$$F_{R,V}^{g0,g1,e0',g1}(\tau_3',\tau_2',\tau_1') = \left[\Gamma_{eg,eg} - 2\Gamma_{eg,v} + \Gamma_{v,v}\right]\tau_3' + \Gamma_{v,v}\tau_1' \tag{2.31}$$

The $\lambda$ dependence is limited to only the $\omega_3$ probe dimension in 2D VE spectra given the excitation is vibrationally-resonant. Peaks II, III, and IV have varying extents of quadratic $\lambda$ dependence. Notably, while peak V is the uniquely isolated peak in 2D VE spectra, it carries no information reflecting electronic-state-dependent vibrational dephasing. Peak I is the only peak that does not contain contributions from the cross-correlation; whereas in 2D EV both GSB peaks (I and III) did not include cross-correlation information. Finally, the non-trivial cancellation between oppositely-signed spectral contributions in 2D VE may complicate spectra since GSB and ESA peak pairs (e.g., III and IV) will have different amplitude contributions due to electronic-state-dependent vibrational dephasing.

## 2.4 2D EV AND 2D VE SIMULATIONS

The 2D VE and 2D EV spectra are simulated in this section by calculating the response functions for all the contributing vibronic transition pathways when the electronically-resonant transitions occur within the frequency range $\omega_{electronic} = \omega_{eg} \pm \omega_{g,1}$ and the vibrationally-

resonant transitions occur for single quantum transitions ($\Delta v, \Delta v' = \pm 1$) only. We further assume that all the electric fields are much shorter in time than the dynamics of interest, that $\tau_2' > 0$ such that only the diagrams in Figure 2.3(a,b) and Figure 2.4(a,b) are relevant, and that $\tau_2'$ is sufficiently short to neglect population relaxation during this period. Working in this impulsive limit allows for the signal field to be proportional to the real part of the third-order nonlinear response function (eq.(2.15)) and implies that $\tau_n' = \tau_n$. Lastly, we do not consider the orientational response function ($Y_{IJKL}^{abcd}$) or vibrational electrical anharmonicity here.

The energies of the vibrational eigenstates in both electronic states are obtained by diagonalization of $H_{vibronic}$. In general, $H_{vibronic}$ cannot be block-diagonalized since the linear, quadratic, and cubic perturbations result in the coupling of manifolds with differing numbers of quanta. In principle, the system eigenstates are determined by obtaining the eigenvalues and eigenvectors of $H_{vibronic}$ with infinite size. In practice, this is achieved by choosing a matrix size large enough to obtain numerical convergence of the lowest five vibrational states in both electronic manifolds. For these simulations, $H_{vibronic}$ was expanded to 50 vibrational quanta. The transformation between the local mode basis and the eigenstate basis is defined by $H'_{vibronic} = T^{-1} H_{vibronic} T$ where $H'_{vibronic}$ is in the eigenstate basis and $T$ is the transformation matrix whose columns are the eigenvectors that represent the contributions of the states in the local mode basis to the eigenstates of the vibronic Hamiltonian. The vibrational transition dipole moments are transformed similarly using $T$ to transform an initially harmonic transition dipole moment matrix.

The $H_{vibronic}$ parameters used in the simulation are given in the corresponding figures below. When coefficients are described as nonzero, their values are: $g_{jjj} = 0.25$ yields a 30 cm$^{-1}$ anharmonicity, $\mathcal{V}_j^{(1)} = 1$ reflects an excited state displacement equal to the ground state equilibrium bond length, $\mathcal{V}_{j,j}^{(2)} = -0.038$ translates to a 40 cm$^{-1}$ red-shifted vibrational frequency in $|e\rangle$, Herzberg-Teller couplings (non-Condon effects) are included with $\mu_{eg}^{(1)} = 0.15$, and $\lambda = 1.5$ sets the vibrational dephasing in $|e\rangle$ to be 50% faster than in $|g\rangle$. A zeroth-order vibrational frequency $\omega_j{}^0$ = 2100 cm$^{-1}$ and an unperturbed electronic transition frequency $\omega_{eg}^0$ = 25000 cm$^{-1}$ are used in all cases. The correlation functions contribute spectral broadening of $\Gamma_{eg,eg}$ = 200 cm$^{-1}$, $\Gamma_{eg,v}$ = 10 cm$^{-1}$, and $\Gamma_{v,v}$ = 5 cm$^{-1}$. In each plot, the linear spectrum for the $\omega_1$ ($\omega_3$) axis is plotted in grey on the top (side) panel, and the $\omega_3$ projection plotted in black on the side panel is obtained by integrating over $\omega_1$ for each $\omega_3$. The $\omega_{electronic}$ axes have been subtracted by the $\omega_{eg}$ value calculated by diagonalizing $H_{vibronic}$ to more easily relate peak separation to the vibronic information of interest. To facilitate comparison, the 2D contours in Figure 2.5 -Figure 2.8 are normalized to the signal of greatest magnitude throughout the series of cases for 2D spectra shown. Thus, all 2D EV spectra are normalized to peak II in Figure 2.6(a), and all 2D VE spectra are normalized to peak I in Figure 2.8(f). Similarly, the $\omega_3$ projections in 2D EV simulations are normalized to the greatest magnitude signal of Figure 2.8(b, side panel), and the 2D VE $\omega_3$ projections are normalized to Figure 2.8(f, side panel).

The simulations discussed in the remainder of this section demonstrate that 2D EV and 2D VE signal can be observed when one or more of the following is true for a molecular system: (1) there is linear or quadratic vibronic coupling present, (2) the electronic transition dipole moment has nuclear coordinate dependence, and (3) the system displays electronic-state-dependent vibrational dephasing. These molecular phenomena contribute to the 2D signals through the 2D peak positions, amplitudes, and line shapes. This analysis demonstrates that when condition (1) is fulfilled (i.e., at least $\mathcal{V}_j^{(1)} \neq 0$ or $\mathcal{V}_{j,j}^{(2)} \neq 0$), the 2D EV and 2D VE signals are least ambiguous and greatest in magnitude.

### 2.4.1 *Case 1: The Undisplaced, Anharmonic Oscillator*

The simplest case to consider is the one in which no vibronic coupling is present (Case 1, Figure 2.5(a) and (d)). Here, the potential energy surfaces represented by $H_{vibronic}$ take the form of an undisplaced, anharmonic oscillator where the anharmonicity coefficient is nonzero but the linear and quadratic vibronic coupling coefficients are zero ($g_{jjj} \neq 0,\ \mathcal{V}_j^{(1)} = 0,\ \mathcal{V}_{j,j}^{(2)} = 0$). Additionally, in 5(a) and 5(d) the Condon approximation is valid ($\mu_{eg}^{(1)} = 0$) and the vibrational dephasing rates in $|e\rangle$ are the same as in $|g\rangle$ ($\lambda = 1$). As is clearly seen in Figure 2.5(a) and (d), no 2D signal is observed when there is no vibronic coupling present in the system, $\mu_{eg}^{(1)} = 0$, and $\lambda = 1$. Here, the local vibrational mode has the same frequency in the ground and the excited electronic states and the potential energy surfaces have the same mechanical anharmonicity. Thus, $\omega_{g,1} = \omega_{e,1'}$ and peaks I and II are both centered at the coordinates $(\omega_{eg}, \omega_{g,1})$ in the 2D EV spectrum and $(\omega_{g,1}, \omega_{eg})$ in the 2D VE spectrum. The signal intensities from peaks I and II cancel since the positive signal from the GSB pathways

$\left(D_{R,I}^{EV}, D_{NR,I}^{EV}; D_{R,I}^{VE}, D_{NR,I}^{VE}\right)$ and the negative signal from the ESA pathways $\left(D_{R,II}^{EV}, D_{NR,II}^{EV}; D_{R,II}^{VE}, D_{NR,II}^{VE}\right)$ overlap; complete cancellation occurs because the signal amplitudes are equal in magnitude and the line shapes are the same leaving no signal to be observed.

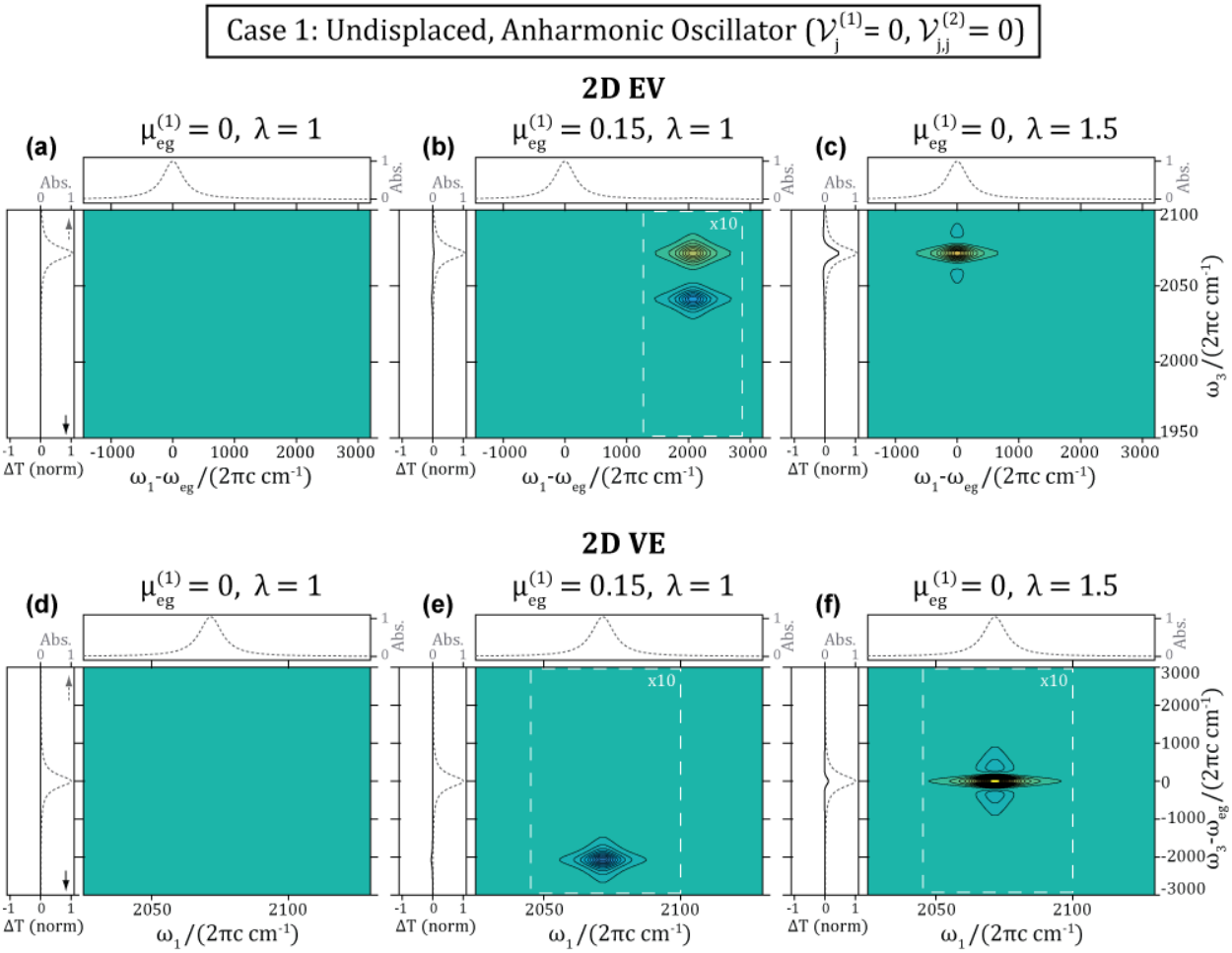


Figure 2.5. 2D EV and 2D VE Spectral Simulations, Case 1: The Undisplaced Anharmonic Oscillator. The 2D EV (a-c) and 2D VE (d-f) simulations above reflect a system with 30 $cm^{-1}$ anharmonicity and a 2073 $cm^{-1}$ fundamental vibrational frequency in both electronic states. Contour plots (a) and (d) show that there is no signal present in the absence of vibronic coupling ($\mu_{eg}^{(1)}=0$, $\lambda=1$). Weak or distorted signal from a case 1 system may be observed if non-Condon effects are present (b and e; $\mu_{eg}^{(1)}=0.15$, $\lambda=1$) or if the system displays electronic-state-dependent vibrational dephasing (c and f; $\mu_{eg}^{(1)}=0$, $\lambda=1.5$). The grey plots (top and side panels) are simulated linear spectra (i.e., UV-Vis or FTIR) for the corresponding frequency axis and the black plot (side panels) is an integrated projection onto $\omega_3$ obtained by summing over $\omega_1$. Contours are normalized to the absolute maximum of Figure 2.6(a) for 2D EV and Figure 2.8(f) for 2D VE; the contours span -1 to 1 with 5% intervals, bleach and emission signals (positive) are yellow and absorptions (negative) are blue. The framed 2D regions have been scaled by the factors indicated for emphasis. For relative intensities, see Table 2.1.

The equivalence of the peaks I and II amplitudes is due to the equivalent magnitudes of the transition dipole moments involved in the $\mathbf{k_3}$ interaction since both peaks utilize the same transition dipole moment during excitation. Therefore, the absence of 2D EV signal in Figure 2.5(a) conveys that $\mu^{g0,g1} = \mu^{e0',e1'}$ in the molecular system, whereas the 2D VE spectrum in 5(d) suggests that $\mu^{g0,e0'} = \mu^{g1,e1'}$. Additionally, the absence of excited state equilibrium displacement $\left(\mathcal{V}_j^{(1)} = 0\right)$ results in negligible Franck-Condon factors for the electronic transitions resonant with $\omega_{electronic} = \omega_{eg} \pm \omega_{e,1'}$ rendering peaks III, IV, and V unobservable in 2D EV and 2D VE. In contrast to other multidimensional spectroscopies such as 2D IR, mechanical anharmonicity in the system is not a sufficient condition to yield 2D EV or 2D VE signal.

2D EV and 2D VE signal may still be observed if $\mu_{eg}^{(1)} \neq 0$, as shown in Figure 2.5(b) and (e). Non-Condon effects manifest themselves in 2D EV and 2D VE spectra through additional peak intensity contributions. This is most easily seen for 2D EV in Figure 2.5(b) and for 2D VE in Figure 2.5(e) where the framed 2D spectral regions have been scaled by a factor of 10 to show the non-Condon intensity contributions, the $\omega_3$ projections (black lines in side panels) relate the magnitude of the non-Condon signal contributions. The 2D EV non-Condon signatures in the absence of vibronic coupling only allow peaks III, IV, and V to appear. Interestingly, the only 2D VE non-Condon signature in this case is peak V because there is no oppositely-signed peak pair to negate the non-Condon intensity contribution. Generally, the non-Condon intensity contributions are a more significant addition for transitions with small Franck-Condon factors (e.g., transitions resonant with $\omega_{electronic} = \omega_{eg} + \omega_{e,1'}$ when $\mathcal{V}_j^{(1)} \approx 0$).

Within the Condon approximation ($\mu_{eg}^{(1)} = 0$), the peak intensities are scaled only by the appropriate Franck-Condon factor for the $|g,v\rangle \rightarrow |e,v'\rangle$ transition. The ratio of peak intensities for signals arising from different electronic transitions should scale with the ratio of the corresponding Franck-Condon factors. The ratio of peak intensities will deviate from the ratio of Franck-Condon factors in the presence of non-Condon effects.

It is also possible to observe 2D EV and 2D VE signal if the line shapes of the positive and negative signals are different, which occurs when the vibrational dephasing rates in the two electronic states are unequal ($\lambda \neq 1$, see Figure 2.5(c) and (f)). The magnitudes of these signals will depend on how different the vibrational dephasing rates are; a faster dephasing rate yields a broadened peak and imperfect cancellation with an accompanying peak of opposite sign. Lacking any quadratic vibronic coupling to separate the oppositely-signed peaks, convoluted peak shapes such as those in Figure 2.5(c) and (f) may be observed.

### 2.4.2 *Case 2: The Undisplaced, Frequency-Shifted, Anharmonic Oscillator*

I next model a case in which vibronic coupling gives rise to 2D EV and 2D VE signal by shifting the frequency of the vibrational mode upon electronic excitation while $\mu_{eg}^{(1)} = 0$ and $\lambda = 1$. This undisplaced, frequency-shifted, anharmonic oscillator (Case 2, Figure 2.6(a) and (d)) potential is modeled by $H_{vibronic}$ with a nonzero anharmonicity coefficient and quadratic vibronic coupling ($g_{jjj} \neq 0$, $\mathcal{V}_j^{(1)} = 0$, $\mathcal{V}_{j,j}^{(2)} \neq 0$). In both techniques, the GSB (peak I) and the ESA (peak II) peaks still have the same magnitude and sign as in Case 1 but the quadratic vibronic coupling separates the two signals along $\omega_3$ because $\omega_{g,1} \neq \omega_{e,1'}$. As in Case 1, peaks III, IV, and V are unobserved since $\mathcal{V}_j^{(1)} = 0$. The two peaks seen in 2D EV for Case 2 (Figure

2.6(a)) originate from the first vibrational transition in two separate electronic manifolds. Thus, the direct comparison of the time-dependent positions, line shapes, and amplitudes of these

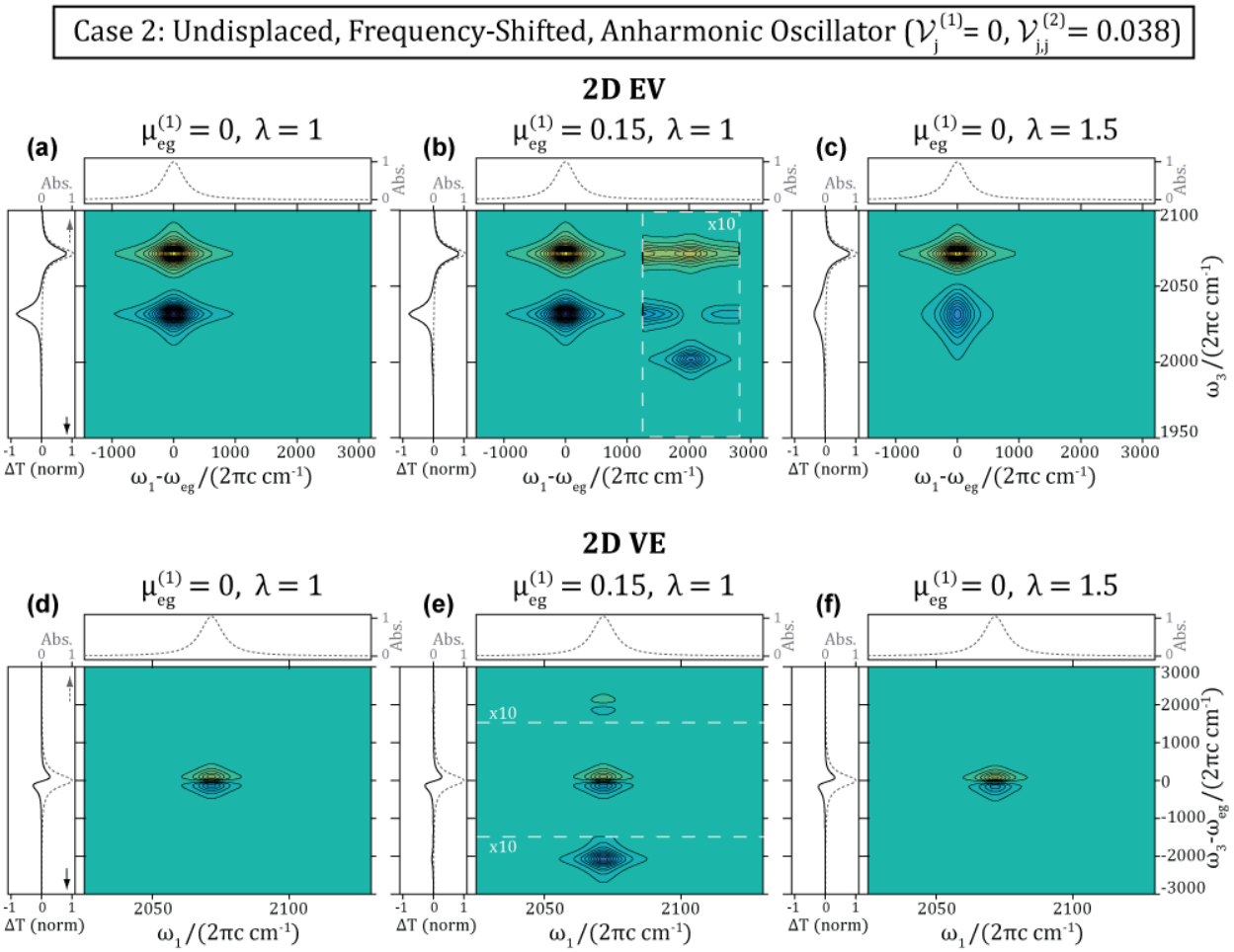


Figure 2.6. 2D EV and 2D VE Spectral Simulations, Case 2: The Undisplaced, Frequency-Shifted, Anharmonic Oscillator. The 2D EV (a-c) and 2D VE (d-f) simulations above reflect a system with 30 cm$^{-1}$ anharmonicity and a 40 cm$^{-1}$ red-shifted excited state vibration ($\omega_{g,1}$ = 2073 cm$^{-1}$ and $\omega_{e,1'}$ = 2033 cm$^{-1}$). Contour plots (a) and (d) show that signal is observed when only quadratic vibronic coupling is present ($\mu_{eg}^{(1)}$=0, $\lambda$=1). Non-Condon effects are evidenced by small intensity contributions from peaks III-V (b and e; $\mu_{eg}^{(1)}$=0.15, $\lambda$=1), and electronic-state-dependent vibrational dephasing effects are observed in the peak II broadening (c and f; $\mu_{eg}^{(1)}$=0, $\lambda$=1.5). The simulated linear spectra (grey plots, top and side panels) are shown for reference. The $\omega_3$ projections (black plots, side panels) are analogous to the pump-probe (or "1D") equivalent signal, and provide comparison between the 2D and pump-probe signals. Contours are normalized to the absolute maximum of Figure 2.6(a) for 2D EV and Figure 2.8(f) for 2D VE; the contours span -1 to 1 with 5% intervals, bleach and emission signals (positive) are yellow and absorptions (negative) are blue. The framed 2D regions have been scaled by the factors indicated for emphasis. For relative intensities, see Table 2.1.

2D EV signals highlights the differences in the potential energy surfaces of the ground and excited electronic state. The comparison of signals for the same vibrational transition in either electronic manifold is a distinct advantage of 2D EV spectroscopy. The 2D VE peaks in this case arise from a difference in electronic energy gaps for the resonant transitions $|g,0\rangle \rightarrow |e,0'\rangle$ and $|g,1\rangle \rightarrow |e,1'\rangle$. In principle, the frequency separation of peaks I and II in the $\omega_3$ dimension for both techniques is represented by $\Delta_{eg} = \omega_{e,1'} - \omega_{g,1}$. However, the resolution of the true $\Delta_{eg}$ from a 2D EV or 2D VE spectrum depends on the relative magnitudes of $\Delta_{eg}$ and the 2D peak linewidths in the $\omega_3$ dimension. Generally, 2D EV spectra provide higher resolution of $\Delta_{eg}$ since the probed vibrations have narrower linewidths than the electronic transitions probed in 2D VE.

Using second-order stationary perturbation theory (see Appendix E) we can show that, $\Delta_{eg}$ directly reports on $\mathcal{V}_{j,j}^{(2)}$ through the relation below:

$$\Delta_{eg} = \frac{\omega_j^{\,0}}{2\pi c}\left( \frac{\mathcal{V}_{j,j}^{(2)}}{2} - \frac{\left(\mathcal{V}_{j,j}^{(2)}\right)^2}{8} \right) \tag{2.32}$$

where *c* is the speed of light. For a more complex system involving two or more coupled vibrational modes that may have different anharmonicities, $\Delta_{eg}$ will include additional terms from the Hamiltonian. This case shows that quadratic vibronic coupling is a sufficient condition for the observation of 2D EV and 2D VE signal.

The intensity contributions from the presence of non-Condon effects allow for peaks III, IV, and V to be weakly observed (Figure 2.6(b) and (e)), in addition to peaks I and II. These non-Condon signal intensities are an order of magnitude less than signals present within the

Condon approximation. Notably, the fact that $\mathcal{V}_{j,j}^{(2)} \neq 0$ allows for 2D VE peaks III and IV to be weakly observed through non-Condon intensity contributions in this case, whereas in case 1 these peaks were still unobservable. Similarly, the positive 2D EV peaks III and V are separated by $\Delta_{eg}$ and they appear as weak shoulder features on the tails of peaks I and II, respectively. Hence, the positive intensity of peak V (an ESE pathway) cancels the tail of the negative intensity of peak II, as shown in Figure 2.6(b). The relative magnitudes of these non-Condon intensity contributions are shown in the $\omega_3$ projections (black lines in side panels, Figure 2.5(b) and (e)), and in the simulated linear electronic absorption spectrum (grey line in top panel, Figure 2.5(b)).

The presence of electronic-state-dependent vibrational dephasing ($\lambda \neq 1$) is now very clearly observed through the difference in line shape between peaks I and II in both 2D EV and 2D VE (Figure 2.6(c) and (f)). The broadened ESA peaks reflect faster vibrational dephasing for a molecule in the excited electronic state when compared to the ground electronic state vibrational dephasing rate. In contrast to the previous case, the quadratic vibronic coupling results in the separation of these peaks with different line shapes which allows for a less ambiguous assessment of the electronic-state-dependent vibrational dephasing. As chapter 5 discusses, the type of peak shape in Figure 2.6(c) is generally measured in the 2D EV spectrum of $[Fe(CN)_6]^{3+}$ dissolved in formamide. However, the 2D VE spectra for $[Fe(CN)_6]^{3+}$ the spectra do not follow Figure 2.6(g) as closely as the EV spectra appear to follow.[40] Chapter 5 uses the 2D EV in tandem with 2D VE spectra of $[Fe(CN)_6]^{3+}$ to explore a more consistent understanding of the vibronic motions at play in its photochemistry. Additionally, the series of 2D and 3D EV spectra presented for a Ru-centered solar cell dye molecule in chapters 7-8 also are principally composed of peaks I and II with $\lambda \neq 1$.

The $\omega_3$ projections in the side panels shown in all of the simulations are the pump-probe analogs to the 2D EV or 2D VE techniques. These can be considered the corresponding "1D" signals for either EV (commonly referred to as "transient-IR absorption") or VE. In case 2, where quadratic vibronic coupling has shifted the excited state vibrational frequency, the transient-IR signal and the 2D EV signal both contain sufficient information to extract $\Delta_{eg}$; the new information obtained in 2D EV comes from analyzing and comparing the time dependent 2D line shapes of peaks I and II. The presence of non-Condon effects may also be detected in the transient-IR signal, albeit very weakly. However, since the transient-IR signal lacks $\omega_1$ resolution the assignment of this intensity contribution to a non-Condon effect is ambiguous because it cannot be correlated with $\omega_{electronic} = \omega_{eg} + \omega_{e,1'}$ excitation, while in 2D EV the correlation is explicit.

### 2.4.3 *Case 3: The Displaced, Anharmonic Oscillator*

In case 3, only linear vibronic coupling is present in the system of anharmonic oscillators ($g_{jjj} \neq 0,\ \mathcal{V}_j^{(1)} \neq 0,\ \mathcal{V}_{j,j}^{(2)} = 0$) and initially it is assumed that $\mu_{eg}^{(1)} = 0$ and $\lambda = 1$ (Figure 2.7(a) and (d)). In this case the vibrational mode oscillates about a different equilibrium position in the excited state due to linear vibronic coupling. The Franck-Condon factors for the vibronic transitions yielding peaks III, IV, and V are non-negligible and so appreciable intensity from these peaks is observed. The 2D EV signal observed (Figure 2.7(a)) is specifically from the pathways which include resonant excitation with $\omega_{electronic} = \omega_{eg} + \omega_{e,1'}$. There are no intensity contributions from vibronic pathways that are excited with a frequency $\omega_{electronic} = \omega_{eg}$ because $\omega_{g,1} = \omega_{e,1'}$, thus peaks I and II cancel. For the same reason, peak III (GSB) and peak V (ESE)

are exactly overlapped in the 2D EV spectrum and only two features are observed overall. However, peaks III and V have the same sign and so their amplitudes add together instead of canceling. The negative ESA signal (peak IV) appears at the frequency of the second

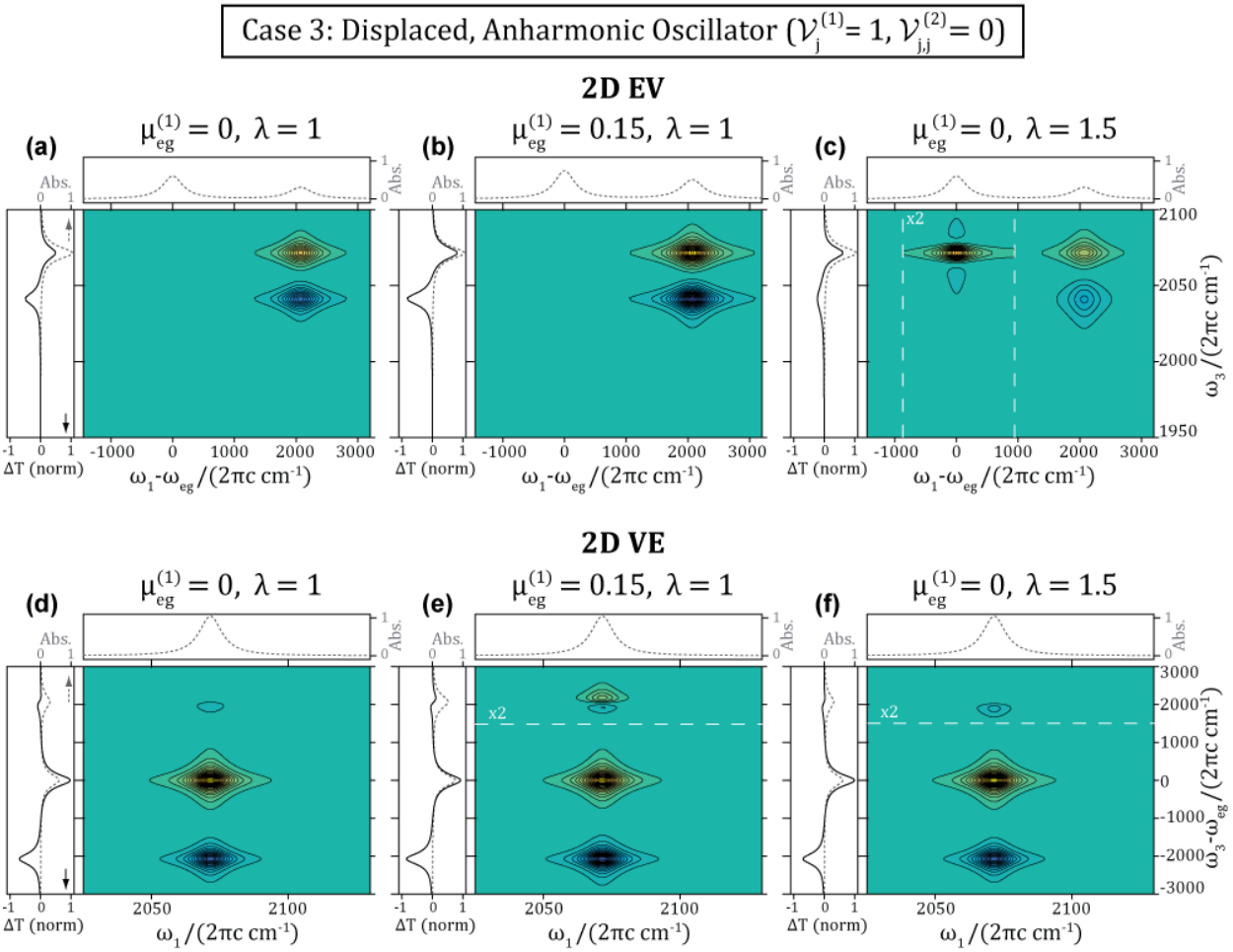


Figure 2.7. 2D EV and 2D VE Spectral Simulations, Case 3: The Displaced Anharmonic Oscillator. The 2D EV (a-c) and 2D VE (d-f) simulations above reflect a system with 30 cm$^{-1}$ anharmonicity, an excited state geometry displacement equal to the ground state equilibrium distance, and a 2073 cm$^{-1}$ fundamental vibrational frequency in both electronic states. Contour plots (a) and (d) show that signal is observed when only linear vibronic coupling is present ($\mu_{eg}^{(1)}$=0, $\lambda$=1). Non-Condon effects are evidenced by small intensity contributions to peaks III-V (b and e; $\mu_{eg}^{(1)}$=0.15, $\lambda$=1), and electronic-state-dependent vibrational dephasing effects are observed in broadened 2D EV peaks II,IV, and V, and broadened 2D VE peaks II and IV (c and f; $\mu_{eg}^{(1)}$=0, $\lambda$=1.5). The simulated linear spectra (grey plots, top and side panels) are shown for reference. The $\omega_3$ projections (black plots, side panels) provide comparison between the 2D and pump-probe signals for the respective techniques. Contours are normalized to the absolute maximum of Figure 2.6(a) for 2D EV and Figure 2.8(f) for 2D VE; the contours span -1 to 1 with 5% intervals, bleach and emission signals (positive) are yellow and absorptions (negative) are blue. The framed 2D regions have been scaled by the factors indicated for emphasis. For relative intensities, see Table 2.1.

vibrational transition in the excited electronic state ( $\omega_{e,2'}$ ) and it is separated in the $\omega_{vibrational}$ dimension by the frequency difference between $\omega_{e,1'}$ and $\omega_{e,2'}$. This frequency difference, $\Delta_{2',1'} = \omega_{e,1'} - \omega_{e,2'}$, reflects the anharmonicity of the excited state potential energy surface and is expressed in terms of the anharmonic coefficient $g_{jjj}$ (as shown in Appendix E): $\Delta_{2',1'} = \left(\omega_j^0 / 2\pi c\right)\left(15 g_{jjj}^2 / 2\right)$. Interestingly, the positive signal for a molecular system modeled in case 3 (Figure 2.7(a)) contains contributions from the equivalent vibrational transition in two different electronic states. Thus, the time-dependent position, line shape, and amplitude of this positive 2D EV feature results from the convolution of the structural dynamics on both potential energy surfaces. In contrast to the 2D EV spectrum, the 2D VE signal observed in case 3 (Figure 2.7(d)) contains contributions from peaks I and II because the amplitudes of these peaks are not equal when $\mathcal{V}_j^{(1)} \neq 0$ . However, since $\mathcal{V}_{j,j}^{(2)} = 0$ there will never be more than one peak observed at $\omega_3 = \omega_{eg}$ in case 3. The positive signal at $\omega_3 = \omega_{eg}$ in Figure 2.7(d) demonstrates that $\left|\langle g,0|e,0'\rangle\right| > \left|\langle g,1|e,1'\rangle\right|$ when $\mathcal{V}_j^{(1)} = 1$, and so the positive GSB signal dominates. Similarly, the overall negative signal at $\omega_3 \cong \omega_{eg} + \omega_{e,1'}$ suggests that the Franck-Condon factor corresponding to peak IV has larger magnitude than the Franck-Condon factor for peak III. More important, however, is the fact that the frequency separation between peaks III and IV is $\omega_{eg} + \omega_{e,1'} + \Delta_{eg} - \Delta_{2',1'}$; thus, peaks III and IV do have frequency separation because of the mechanical anharmonicity of the excited state potential energy surface, $\Delta_{2',1'}$, even though $\Delta_{eg} = 0$ in this case. This combination of magnitude differences in Franck-Condon factors when $\mathcal{V}_j^{(1)} \neq 0$ and the excited state anharmonicity facilitates the

observation of an overall 2D VE signal between peaks III and IV. Overall, case 3 demonstrates that linear vibronic coupling is also a sufficient condition for the observation of 2D EV and 2D VE signal.

The presence of non-Condon effects in case 3 simply enhances the peaks that arise due to linear vibronic coupling in the system. As shown in Figure 2.7(b), the intensity of the 2D EV spectral signatures is greater. The signal magnitude enhancement is also seen by comparing the $\omega_3$ projections in Figure 2.7(a) and (b). While non-Condon intensity contributions to peaks I and II does occur, both of these transition pathways involve the same electronic transition and so the nuclear dependence of this $|g,0\rangle \rightarrow |e,0'\rangle$ excitation is reflected equally in both peaks; thus, peaks I and II still completely cancel. Notably, the 2D VE non-Condon intensity contributions highlight the difference in the nuclear dependence of the different electronic transition dipole moments that contribute to each of the 2D VE peaks. This is demonstrated most clearly by peaks III and IV in Figure 2.7(e). In this case, the non-Condon intensity allows both peaks III and IV to be observed with their separation given by $\Delta_{2',1'}$.

When electronic-state-dependent vibrational dephasing is present in a molecular system modeled by case 3, we see different line shapes in Figure 2.7(c) and (f). In 2D EV, the direct comparison of vibrational dephasing dynamics in the two electronic states is convoluted because peaks III and V are overlapped, as are peaks I and II. However, since peaks III and V are both positive, identifying dephasing dynamics specific to a vibration in one electronic state is ambiguous. Provided that the excited state anharmonicity is large enough to spectrally separate peak IV from peaks III and V, then it is still possible to analyze excited state dephasing information in isolation. The line shapes in 2D VE will be less sensitive to excited-state-

dependent vibrational dephasing due to the inherently large width of the probed electronic transitions and the $\lambda$-dependence of the 2D VE dephasing functions.

It is important to highlight the difference in interpreting the transient-IR signal and the 2D EV signal for this case, in particular. A usual interpretation of transient-IR signals is in the context of excited state frequency shifting of a vibrational mode. However, as is shown in Figure 2.7(a-c, contours), the $\omega_3$ frequency separation of the positive and negative signals is only due to the excited state anharmonicity. There is no quadratic vibronic coupling in case 3 and the mechanical anharmonicities are the same in $|e\rangle$ and $|g\rangle$; therefore, $\Delta_{eg} = 0$. With only the transient-IR signal to conclude about the differences of the molecular system in the ground and excited electronic states, it would be reasonable – but incorrect – to conclude that the measured frequency separation between the positive and negative peaks is the difference in vibrational frequency between the two electronic states. In fact, this frequency separation would be the excited state mechanical anharmonicity.

### 2.4.4 *Case 4: The Displaced, Frequency-Shifted, Anharmonic Oscillator*

The final case considers a system in which all the parameters in $H_{vibronic}$ are nonzero ( $g_{jjj} \neq 0$, $\mathcal{V}_j^{(1)} \neq 0$, $\mathcal{V}_{j,j}^{(2)} \neq 0$ ). Here, the potential energy surfaces take the form of displaced, frequency-shifted, anharmonic oscillators. For 2D EV spectra of molecular systems modeled by case 4 (Figure 2.8(a)), peaks I-V are observable and $\Delta_{eg}$ and $\Delta_{2',1'}$ can be obtained directly from the 2D EV spectrum. The presence of quadratic vibronic coupling uniformly affects the $\omega_{vibrational}$ peak separation of vibrations in $|e\rangle$ (peaks II, IV and V) and vibrations in $|g\rangle$ (peaks I and III). Notably, this results in the separation of the GSB (III) and the ESE (V) signals that

were convolved in case 3. The 2D VE spectrum for case 4 (Figure 2.8(d)) also contains contributions from all vibronic transition pathways, but only four spectral signatures are

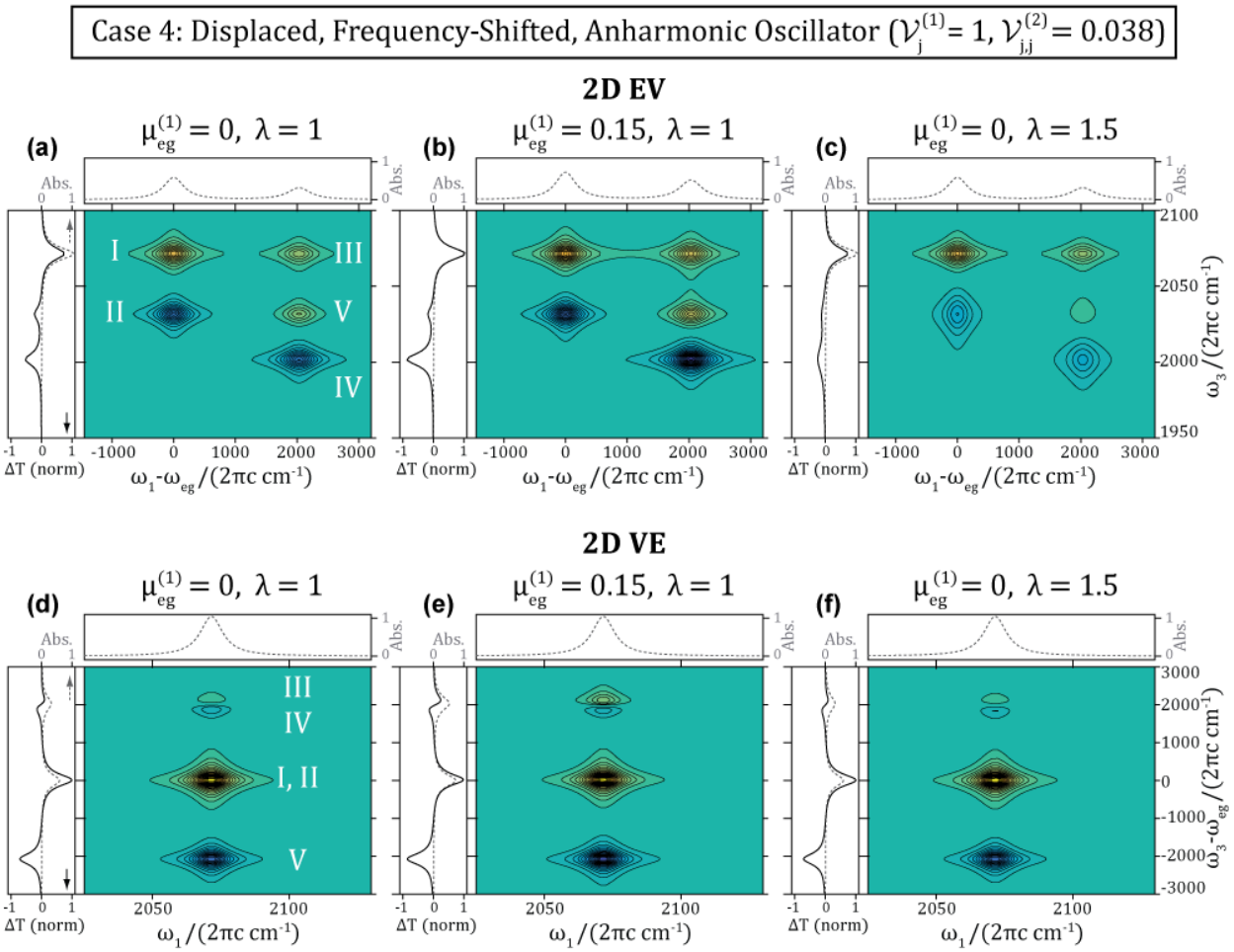


Figure 2.8. 2D EV and 2D VE Spectral Simulations, Case 4: The Displaced, Frequency-Shifted, Anharmonic Oscillator. The 2D EV (a-c) and 2D VE (d-f) simulations above reflect a system with 30 cm$^{-1}$ anharmonicity, an excited state geometry displacement equal to the ground state equilibrium distance, and a 40 cm$^{-1}$ red-shifted excited state vibrational frequency ($\omega_{g,1}$ = 2073 cm$^{-1}$ and $\omega_{e,1'}$ = 2033 cm$^{-1}$). Contour plots (a) and (d) show that signal is observed when both linear and quadratic vibronic coupling are present ($\mu_{eg}^{(1)}$=0 and $\lambda$=1). Non-Condon effects are evidenced by small intensity contributions to all peaks in varying proportion (b and e; $\mu_{eg}^{(1)}$=0.15, $\lambda$=1), and electronic-state-dependent vibrational dephasing effects are observed in broadened 2D EV peaks II,IV, and V, and broadened 2D VE peaks II and IV (c and f; $\mu_{eg}^{(1)}$=0, $\lambda$=1.5). The simulated linear spectra (grey plots, top and side panels) are shown for reference. The 2D EV $\omega_3$ projections (black plots, side panels) in this case highlight the convoluted nature of the 1D ("transient-IR") signal by comparison with the 2D EV signal. Contours are normalized to the absolute maximum of Figure 2.6(a) for 2D EV and Figure 2.8(f) for 2D VE; the contours span -1 to 1 with 5% intervals, bleach and emission signals (positive) are yellow and absorptions (negative) are blue. For relative intensities, see Table 2.1.

observed because the positive signal in peak I eclipses the negative signal from peak II. This occurs for the same reasons described above in case 3 (Figure 2.7(d)).

The non-Condon intensity contributions in case 4 enhance all of the peaks, and the magnitude of the contributions reflect the nuclear dependence of a particular vibronic transition. For vibronic transitions with relatively large Franck-Condon factors, a first order non-Condon ( $\mu_{eg}^{(1)}$ ) contribution will be comparably less noticeable than for transitions with smaller Franck-Condon factors. In 2D EV, the maximum amplitude comparison between peaks I and III will include the Franck-Condon factors and any non-Condon effects. If the Franck-Condon factors for these transitions are obtained using computational methods or measured independently, then a ratio of the measured amplitudes of 2D EV peaks I and III can be used to extract the magnitude of the non-Condon intensity contributions. The non-Condon intensity contributions in 2D VE are most obvious by comparing peaks III and IV, for the same reasons described for case 3 above. However, $\Delta_{eg} \neq 0$ in case 4 so peaks III and IV are further separated and have greater observed amplitude.

In 2D EV, the electronic-state-dependent vibrational dephasing results in the line shapes of the excited state vibrational signatures (II, IV, and V) having broadened features along $\omega_3$ (Figure 2.8(c)). Since all of these features are spectrally resolved, information about vibrational-level-dependent dephasing in the excited electronic state can be extracted by comparing $\tau_2$-dependent line shapes of peaks IV and V in addition to electronic-state-dependent vibrational dephasing information accessible by comparing peaks I and II.

In this case, where peaks I-V contribute appreciable intensity to the 2D EV spectrum, the transient-IR signals will be increasingly complex (Figure 2.8(a-c)). For example, since peaks

II and V are opposite in sign and have the same $\omega_3$ coordinate, the negative transient-IR signal that should be used to extract $\Delta_{eg}$ will be diminished. In this case, the minimum in the transient-IR signal corresponds to the intensity contributions from peak IV at $\omega_3 = \omega_{e,2'}$, which is only realized by resolving the excitation frequency axis in the 2D EV spectrum. The assessment of $\Delta_{eg}$ from transient-IR signal alone should be approached with caution.

It is useful to briefly compare the 2D EV and 2D VE signals in Figure 2.8(a) and (d) for the system described by $H_{vibronic}$ above to the expected 2D EV and 2D VE signals of the displaced harmonic oscillator (DHO) system[46] commonly used to model 2D ES signals. The DHO model is approximated by $H_{vibronic}$ when $g_{jjj} = 0$; quadratic vibronic coupling may be included with $\mathcal{V}_{j,j}^{(2)}$ in the same manner as for the anharmonic oscillator described by $H_{vibronic}$ above. If the oscillators have the same vibrational frequency in both electronic states and they are harmonic then $\Delta_{eg} = 0$ and $\Delta_{2',1'} = 0$. In 2D EV, all peaks would then have the same $\omega_3$ coordinate which would result in their complete cancellation. Therefore, 2D EV signal will not be observed for a DHO system that lacks quadratic vibronic coupling. Of course, signal may be observed if $\lambda \neq 1$ for reasons discussed above. If the DHO system has quadratic vibronic coupling, then $\Delta_{eg} \neq 0$ and 2D EV signal will be observed; however, peaks IV and V will be overlapped (since $\Delta_{2',1'} = 0$) and their amplitudes will incompletely cancel due to the different magnitudes of peaks IV and V. In contrast, 2D VE signal of a DHO system will always be observed because the displacement results in different amplitudes of the oppositely-signed peaks in the 2D VE peak pairs (e.g., peaks I and II).

## 2.5 SELECTION RULES FOR 2D EV AND 2D VE SPECTROSCOPY

The systematic investigation of simulated 2D EV and 2D VE spectra in section 2.4 above suggests that these 2D spectroscopies are subject to these three general selection rules: (1) the presence of vibronic coupling in the system represented by at least one nonzero vibronic coupling coefficient ($\mathcal{V}_j^{(1)} \neq 0$ or $\mathcal{V}_{j,j}^{(2)} \neq 0$), (2) the electronic transition dipole moment is dependent on the nuclear coordinates (i.e., Herzberg-Teller coupling or higher order non-Condon effects are appreciable), and (3) the system displays electronic-state-dependent vibrational dephasing dynamics. These selection rules relate the propensity for molecular systems to display signal when studied with 2D EV or 2D VE spectroscopies through the measured peak positions, amplitudes, and line shapes. A concise summary of the information presented in the simulations above (Figure 2.5-8) is given in Table 2.1 to highlight general trends in 2D EV and 2D VE signals. This information is also useful to compare the sensitivities of 2D EV and 2D VE spectroscopies to different types of vibronic molecular phenomena.

The signals observed in 2D EV spectroscopy are greatest in magnitude when the system only has quadratic vibronic coupling ($\mathcal{V}_{j,j}^{(2)} \neq 0$, case 2). For the cases where linear vibronic coupling is present, the signal is still greater when quadratic vibronic coupling is also present ($\mathcal{V}_j^{(1)} \neq 0$, $\mathcal{V}_{j,j}^{(2)} \neq 0$, case 4). The simulations show that different spectral signatures characterize the different cases but the magnitudes of these signals reflect the sensitivity of the technique to various conditions of molecular vibronic coupling. Thus, while 2D EV spectroscopy is sensitive to both linear and quadratic vibronic coupling, it appears to be more sensitive to quadratic vibronic coupling effects. Herzberg-Teller coupling effects are more noticeable in 2D EV spectra when there is already some degree of excited state displacement

present in the system, which is expected from a system with stronger vibronic coupling. Finally, 2D EV spectroscopy is particularly sensitive to electronic-state-dependent vibrational dephasing dynamics, especially when $\mathcal{V}_{j,j}^{(2)} \neq 0$. Since spectral signatures from vibrations in both electronic states appear in 2D EV, the line shapes that reflect these dephasing dynamics can be analyzed for each electronic state for direct comparison.

Table 2.1. This table summarizes some of the information conveyed in the series of 2D EV and 2D VE simulations shown in Figure 2.5-8. The table is organized by grouping cases 1-4 for three combinations of the $\mu_{eg}^{(1)}$ and λ parameters. The first four rows show cases 1-4 under the Condon approximation and with no electronic-state-dependent vibrational dephasing ($\mu_{eg}^{(1)}$=0, λ=1); rows 5-8 show the influence of non-Condon effects on all cases ($\mu_{eg}^{(1)}$=0.15, λ=1); rows 8-12 show the effects of electronic-state-dependent vibrational dephasing for all four cases($\mu_{eg}^{(1)}$=0, λ=1.5); and the last row (simulation not shown) shows a case 4 system where all simulation parameters are nonzero ($\mu_{eg}^{(1)}$=0.5, λ=1.5). Each row corresponds to a set of conditions used to simulate 2D EV and 2D VE spectra (excluding the last row); the absolute maximum peak intensities ($I_{max}$) for 2D EV and 2D VE simulations are listed and normalized for comparison. The peak with the greatest magnitude and the figure in which the simulation is shown are given for referencing the simulations shown earlier in the text.

| $\mathcal{V}_j^{(1)}$ | $\mathcal{V}_{j,j}^{(2)}$ | $\mu_{eg}^{(1)}$ | $\lambda$ | $I_{max}^{EV}$ | [peak, figure] | $I_{max}^{VE}$ | [peak, figure] |
|---|---|---|---|---|---|---|---|
| 0 | 0 | 0 | 1 | 0 | [ - , 4.5(a)] | 0 | [ - , 4.5(d)] |
| 0 | -0.038 | 0 | 1 | 1.000 | [II , 4.6(a)] | 0.273 | [I/II , 4.6(d)] |
| 1 | 0 | 0 | 1 | 0.535 | [IV , 4.7(a)] | 0.969 | [I , 4.7(d)] |
| 1 | -0.038 | 0 | 1 | 0.581 | [II , 4.8(a)] | 0.986 | [I , 4.8(d)] |
| 0 | 0 | 0.15 | 1 | 0.040 | [II , 4.5(b)] | 0.052 | [V , 4.5(e)] |
| 0 | -0.038 | 0.15 | 1 | 0.999 | [II , 4.6(b)] | 0.274 | [II , 4.6(e)] |
| 1 | 0 | 0.15 | 1 | 0.886 | [IV , 4.7(b)] | 0.918 | [I , 4.7(e)] |
| 1 | -0.038 | 0.15 | 1 | 0.918 | [IV , 4.8(b)] | 0.976 | [I , 4.8(e)] |
| 0 | 0 | 0 | 1.5 | 0.535 | [I , 4.5(c)] | 0.113 | [I , 4.5(f)] |
| 0 | -0.038 | 0 | 1.5 | 0.955 | [I , 4.6(c)] | 0.310 | [I , 4.6(f)] |
| 1 | 0 | 0 | 1.5 | 0.342 | [III/IV,4.7(c)] | 0.985 | [I , 4.7(f)] |
| 1 | -0.038 | 0 | 1.5 | 0.567 | [I , 4.8(c)] | 0.998 | [I , 4.8(f)] |
| 1 | -0.038 | 0.15 | 1.5 | 0.701 | [I , - ] | 1.000 | [I , - ] |

The signals observed in 2D VE spectroscopy appear to be less sensitive to quadratic vibronic coupling and more sensitive to linear vibronic coupling. As seen from Table 2.1, the signals are overwhelmingly larger when $\mathcal{V}_j^{(1)} \neq 0$ (cases 3 and 4) than when $\mathcal{V}_j^{(1)} = 0$ (cases 1 and 2). The broad line widths of the probed electronic transitions result in extensive overlapping features in 2D VE spectra. Therefore, the observed peak is far more dependent on the relative amplitudes between competing spectral features of differing sign and line shape than on peak separation. 2D VE has a unique sensitivity to the nuclear dependence of different vibronic transitions because the 2D VE pathways sample more electronic transition dipole moments within the molecular system than in 2D EV. Thus, Herzberg-Teller coupling effects result in non-trivial amplitude comparisons of oppositely-signed spectrally-congested features.

The propensities for observing 2D EV and 2D VE signals follow for the case in which all simulation parameters are non-zero (Table 2.1, last row), which may be a more realistic case for a molecular system. In 2D EV, the presence of Herzberg-Teller coupling effects increases the observed intensities overall with varying proportion, but the presence of electronic-state-dependent vibrational dephasing disperses the excited state vibrational spectral intensity of the ESA (peak IV) leaving the GSB (peak I) feature with the greatest magnitude. The feature of greatest magnitude does not change in 2D VE because Herzberg-Teller effects and the excited state vibrational dephasing both contribute to enhancing the positive amplitude of peak I, and so this feature still dominates the spectrum.

## 2.6 DISCUSSION

In 2D EV and 2D VE spectroscopies the complexity of the spectral and dynamical signatures can increase depending on the accessible transitions during the field-matter

interactions. As spectrally broadened and temporally compressed ultrafast pulses throughout the UV, visible, and infrared regions are implemented in spectroscopic experiments, a discussion of the newly accessible signals in these spectroscopies is warranted.[41] For simplicity, we assume $\tau_2' \geq \tau_p$ and briefly consider the new 2D signals that arise when the electronically-resonant field reaches higher vibrational levels in $|e\rangle$ with center frequency $\omega_{electronic} = (\omega_{eg} + \omega_{e,1'}) \pm \omega_{g,1}$ and when the vibrationally-resonant field spans an octave of vibrational frequencies to excite two quantum transitions: $\Delta v, \Delta v' = \pm 1, \pm 2$.

If $\omega_{electronic} = (\omega_{eg} + \omega_{e,1'}) \pm \omega_{g,1}$ but $\omega_{vibrational}$ is not octave-spanning ($\Delta v, \Delta v' = \pm 1$), six new 2D EV Liouville pathways and four new 2D VE Liouville pathways are allowed when $\mathbf{k_1}$ and $\mathbf{k_2}$ leave the system in a population state during $\tau_2'$. These new 2D EV signals result in three new peaks (a GSB, an ESA, and an ESE); and these new 2D VE signals yield a GSB and an ESA peak pair at the expense of peak V since it would be outside of the probe bandwidth. If the bandwidth of $\omega_{vibrational}$ is octave-spanning and $\omega_{electronic} = \omega_{eg} \pm \omega_{g,1}$, then the only new 2D EV Liouville pathways that evolve in population states during $\tau_2'$ emit at vibrational overtone frequencies. In contrast, since $\mathbf{k_1}$ and $\mathbf{k_2}$ are vibrationally-resonant in 2D VE, ten new Liouville pathways are accessible to the system that yield a new set of five fully absorptive features at a higher excitation frequency, $\omega_1 = 2\omega_{g,1}$. The dynamics during the $\tau_2'$ delay become complex when $\omega_{vibrational}$ is octave-spanning because the system can evolve in a new set of allowed coherence states during $\tau_2'$ in both experiments. Four 2D EV Liouville pathways arise that evolve in single quantum coherence states (either $|e,0'\rangle\langle e,1'|$ or $|g,0\rangle\langle g,1|$) and

require a vibrational overtone interaction with $\mathbf{k_3}$ to be detected; we note that the conjugates of these pathways emit at overtone frequencies and so would be exceedingly difficult to detect. There are twelve new 2D VE Liouville pathways that evolve as single quantum coherence states ($|g,0\rangle\langle g,1|$+c.c. and $|g,1\rangle\langle g,2|$+c.c.) during $\tau_2'$; in this case the conjugate coherence states still emit at fundamental vibrational frequencies and will equally contribute to the observed $\tau_2'$ dynamics. The signals from these coherence states will contribute additional – and oscillatory – intensity to peaks that already exist from signals that evolve in population states during $\tau_2'$. Similarly, still more signals arise if $\omega_{electronic} = (\omega_{eg} + \omega_{e,1'}) \pm \omega_{g,1}$ *and* $\omega_{vibrational}$ is octave spanning.

A description of the electronic transition dipole moment similar to our approach has been used by Turner and co-workers[42] in three-dimensional electronic spectroscopy (3D ES) to identify Herzberg-Teller signatures through anti-diagonal nodal features in 3D ES spectra. Other nonlinear vibrational spectroscopies also have been used to probe couplings between electronic and vibrational motion in molecules that principally involve Raman-active vibrations, such as 2D fifth-order Raman spectroscopy,[43] femtosecond stimulated Raman spectroscopy,[44] 2D resonance Raman spectroscopy,[45] and 4D coherent Raman spectroscopy.[46,47] The 2D spectroscopies discussed in this chapter contribute the capability for probing IR-active vibrations that are coupled to electronic degrees of freedom. Thus, 2D EV and 2D VE spectroscopies provide an important avenue toward understanding vibronic couplings involving changes in the dipole moment which complement these nonlinear Raman techniques that describe vibronic couplings involving changes in polarizability. Polarization sensitivity has been used in 2D EV experiments to aid with peak assignments in congested

spectra of light harvesting complexes.[5] In principle, a combination of polarization selective 2D EV and 2D VE experiments should yield a rich description of the vibronic coupling present in a system by revealing relative orientations of particular IR-active vibrations with respect to the electronic transition dipole moment. The polarization-dependent effects in a 2D EV spectrum is explored theoretically in chapter 6 and the majority of 2D EV experiments described in the rest of this dissertation utilize polarization selectivity. When polarization-dependence is included, the added layer of orientational response within the molecular framework is revealed. In future experimental studies, I imagine polarization-selective 2D EV and 2D VE spectroscopies will be conducted in tandem to build an intimate intuition for the vibronic couplings and correlations present in condensed phase molecular systems during photochemical reactions.

A wealth of microscopic information is conveyed by the dynamic 2D line shapes in multidimensional spectroscopy. [48-53] Static and dynamic correlations measured in 2D IR and 2D ES experiments reflect the microscopic nature and timescales of fluctuations in molecular vibrational and electronic transition energies. There has been recent work on extracting static and dynamic correlations between vibrational and electronic transition frequencies using 2D EV spectroscopy. [7,9] I anticipate that continued studies of time-evolving 2D EV and 2D VE line shapes will describe molecular phenomena such as non-equilibrium solvation,[54] transient structural heterogeneity, and non-Gaussian frequency distributions[55] on coupled vibronic states.

In this chapter, I have focused my discussion on a single anharmonic vibrational mode coupled to the ground and the first excited electronic states. Most physical systems of interest will include more than one vibration of interest and more than one excited electronic state. It

will be important to extend this work to include a vibronic system with multiple coupled vibrations on multiple electronic states. The framework presented here utilizes adiabatic vibronic eigenstates. Future theoretical work exploring how non-adiabatic effects will manifest themselves in 2D EV and 2D VE spectroscopies will be a welcomed extension of this treatment. In fact, chapter 8 presents the first direct observation of a vibronic coherence facilitating non-adiabatic internal conversion through the use of the third frequency dimension accessible in the third order EV spectroscopy – that is, in the 3D EV spectrum of a photoexcited aqueous Ru-centered compound following metal-to-ligand charge transfer.

## 2.7 Conclusion

A framework for interpreting vibronic coupling signatures of molecular ensembles in 2D EV and 2D VE spectra has been outlined here. The simplest case of a molecular system composed of one anharmonic local vibrational mode and two electronic states has been treated here. A system Hamiltonian is described that uses linear, quadratic, and cubic perturbations to model this simple system of an anharmonic vibration in the ground electronic state that may be displaced and frequency-shifted in the excited electronic state. Notably, this treatment parallels the Herzberg-Teller adiabatic approximation and we show that the nuclear dependence of the electronic transitions can be observed in these 2D spectroscopies. I have described three general selection rules for 2D EV and 2D VE spectroscopies: (1) the presence of molecular vibronic coupling, (2) a nuclear dependence of the electronic transitions, and (3) the system displays electronic-state-dependent vibrational dephasing. These effects manifest themselves in the 2D peak positions, amplitudes, and line shapes. A systematic series of 2D EV and 2D VE spectral simulations generally characterizes the nature and magnitude of signal in systems with varying degrees of vibronic coupling. This chapter emphasizes that a

productive approach to characterizing and understanding complex vibronic couplings present in condensed phase molecules is to combine 2D EV and 2D VE spectroscopies on studies of the same molecular system and analyze both results with the same theoretical framework, as their information is both complementary and supplementary to one another.

## 2.8 APPENDICES

### 2.8.1 *Appendix A: 2D EV and 2D VE Energy Gap Correlation Functions*

The vibronic transition frequency correlation functions relevant for 2D EV and 2D VE spectroscopy are defined as

$$\begin{aligned}
\zeta_{v,v}(t) &= \left\langle \delta\omega_{g1,g0}(t)\delta\omega_{g1,g0}(0)\right\rangle \\
\zeta_{v',v'}(t) &= \left\langle \delta\omega_{e1',e0'}(t)\delta\omega_{e1',e0'}(0)\right\rangle \\
\zeta_{eg,eg}(t) &= \left\langle \delta\omega_{e0',g0}(t)\delta\omega_{e0',g0}(0)\right\rangle \\
\zeta_{eg,v'}(t) &= \left\langle \delta\omega_{e0',g0}(t)\delta\omega_{e1',e0'}(0)\right\rangle \\
\zeta_{eg,v}(t) &= \left\langle \delta\omega_{e1',e0'}(t)\delta\omega_{e0',g0}(0)\right\rangle \\
\zeta_{v,v'}(t) &= \left\langle \delta\omega_{g1,g0}(t)\delta\omega_{e1',e0'}(0)\right\rangle .
\end{aligned} \tag{2.34}$$

Equations (2.19)-(2.21) are obtained by simplifying equation (2.34) using $\lambda$ (eqn. (2.18)).

### 2.8.2 *Appendix B: Nuclear Coordinate Dependence of* $\mathbf{M}_{eg}$

As the Condon approximation is relaxed and the Herzberg-Teller coupling terms are included ($\mu_{eg}^{(1)} \neq 0$) in equation (2.9), the nuclear dependence of the electronic transition contributes additional intensity to the 2D EV or 2D VE spectrum. In this case, $\mathbf{M}_{eg}(Q)$ is expressed for a single vibrational mode $j$,

$$\mathbf{M}_{eg}(Q) = \mu_{eg}^{(0)}\left\langle g,v\middle|e,v'\right\rangle + \mu_{eg}^{(1)}\left\langle g,v\middle|Q_j\middle|e,v'\right\rangle . \tag{2.35}$$

The contributions of the Herzberg-Teller coupling terms to the signal intensity is included phenomenologically through the linear expansion coefficient $\mu_{eg}^{(1)}$, which is a weighting coefficient in a linear combination of vibrational overlap integrals. This may be understood by writing $Q_j$ as a ladder operator that raises (or lowers) the vibrational quantum number in the excited electronic state. With this in mind, the expression in (4.B1) can be rewritten

$$\mathbf{M}_{eg}(Q) = \mu_{eg}^{(0)} \left\langle g,v \middle| e,v' \right\rangle + \mu_{eg}^{(1)} \left\langle g,v \middle| e,(v \pm 1)' \right\rangle . \tag{2.36}$$

Since the vibrational eigenstates in each electronic manifold are obtained through diagonalization of $H_g$ and $H_e$, the values of the vibrational overlap integrals are easily obtained. Thus, the coefficient $\mu_{eg}^{(1)}$ describes the magnitude of the nuclear coordinate dependence of the electronic transition by contributing some character of the $\left|g,v\right\rangle \rightarrow \left|e,(v' \pm 1)\right\rangle$ transition(s) to the $\left|g,v\right\rangle \rightarrow \left|e,v'\right\rangle$ transition.

### 2.8.3 *Appendix C: Liouville Pathways for a Third Order Nonlinear Response Tensor*

The four electric fields involved in a four wave mixing spectroscopy include the three input fields used to generate the third order nonlinear polarization ($\mathbf{k}_1, \mathbf{k}_2, \mathbf{k}_3$) and the radiated signal field ($\mathbf{k}_{sig}$). Each field-matter interaction can be considered as an operation of a transition dipole moment operator on the density matrix, $\rho_0$. The dipole operators (i.e., $\mathbf{M}_1, \mathbf{M}_2, \mathbf{M}_3, \mathbf{M}_4$ in the commutator in equation (2.15)) can operate from the right (bra) or the left (ket) side. This results in 16 different combinations of field-matter interactions, which simplify to eight total combinations by enforcing that only ket-side interactions emit a real observable, $\mathbf{k}_{sig}$. A similar organization of the Liouville pathways below can be found in many

references[23,32,34] the numbering and notation shown here specifically follows Khalil *et al*.[34] The eight Liouville pathways are grouped together into four pairs of complex conjugate pathways. The $i^{th}$ pathway, denoted $R_i$, is differentiated by the order of bra (B) or ket (K) side interactions in the double-sided Feynman diagrams presented below.

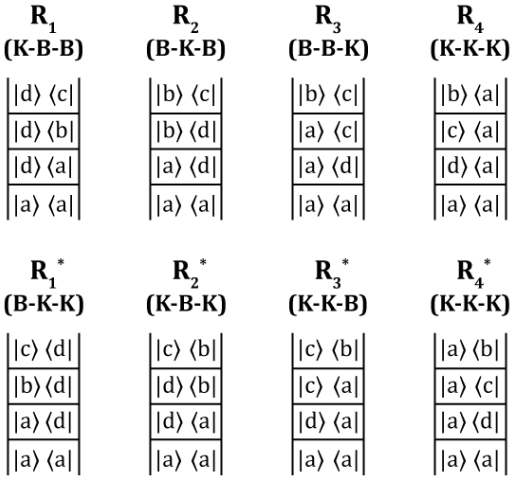


Figure 2.9. Third Order Liouville Pathways depicting the time evolution of the system density matrix. The system eigenstates are given by a, b, c, and d.

A nonlinear response function corresponds to each of these Liouville pathways to describe the time evolution of the density matrix during the time delays $\tau_1'$, $\tau_2'$, and $\tau_3'$ following field-matter interactions at times $t'_1$, $t'_2$, and $t'_3$, respectively. These four response functions are given by

$$R_1^{a,b,c,d}(\tau_3',\tau_2',\tau_1') = P_a \times \left(\left|\mu^{c,d}\right|\left|\mu^{b,c}\right|\left|\mu^{a,b}\right|\left|\mu^{d,a}\right|\right) \times \exp\left[-i\omega_{d,c}^0\tau_3' - i\omega_{d,b}^0\tau_2' - i\omega_{d,a}^0\tau_1'\right] \times F_1^{a,b,c,d}(\tau_3',\tau_2',\tau_1') \tag{2.37}$$

$$R_2^{a,b,c,d}(\tau_3',\tau_2',\tau_1') = P_a \times \left(\left|\mu^{c,b}\right|\left|\mu^{d,c}\right|\left|\mu^{b,a}\right|\left|\mu^{a,d}\right|\right) \times \exp\left[-i\omega_{b,c}^0\tau_3' + i\omega_{d,b}^0\tau_2' + i\omega_{d,a}^0\tau_1'\right] \times F_2^{a,b,c,d}(\tau_3',\tau_2',\tau_1') \tag{2.38}$$

$$R_3^{a,b,c,d}(\tau_3',\tau_2',\tau_1') = P_a \times \left( \left| \mu^{c,b} \right| \left| \mu^{b,a} \right| \left| \mu^{d,c} \right| \left| \mu^{a,d} \right| \right) \times \exp\left[ -i\omega_{b,c}^0 \tau_3' + i\omega_{c,a}^0 \tau_2' + i\omega_{d,a}^0 \tau_1' \right] \times F_3^{a,b,c,d}(\tau_3',\tau_2',\tau_1') \quad (2.39)$$

$$R_4^{a,b,c,d}(\tau_3',\tau_2',\tau_1') = P_a \times \left( \left| \mu^{a,b} \right| \left| \mu^{b,c} \right| \left| \mu^{c,d} \right| \left| \mu^{d,a} \right| \right) \times \exp\left[ -i\omega_{b,a}^0 \tau_3' - i\omega_{c,a}^0 \tau_2' - i\omega_{d,a}^0 \tau_1' \right] \times F_4^{a,b,c,d}(\tau_3',\tau_2',\tau_1') \quad (2.40)$$

and the complex conjugates: $\left[ R_1^{a,b,c,d} \right]^*$, $\left[ R_2^{a,b,c,d} \right]^*$, $\left[ R_3^{a,b,c,d} \right]^*$ and $\left[ R_4^{a,b,c,d} \right]^*$. In equations (2.37)-(2.40), $P_a$ is the probability of the system occupying the initial state of the density matrix, a; the terms $\mu^{x,y}$ are the transition dipole matrix elements obtained by $\langle x | \mathbf{M} | y \rangle$; the frequencies $\omega_{x,y}^0$ correspond to the energy separation between the system eigenstates $|x\rangle$ and $|y\rangle$ that are obtained by diagonalization of a system Hamiltonian; and the terms $F_n^{a,b,c,d}$ are the dephasing functions that contain the dynamical information yielding the line shape of observed signals.

Following the derivation of Sung and Silbey,[23] analytical forms for the dephasing functions are obtained by simplifying the trace over the bath coordinates of the time-evolution of the density matrix. The dephasing functions are exponential functions of linear combinations of the line shape functions, $h_{a,b}(t)$. As discussed in section 2.3.1.3 of this manuscript, the energy gap correlation function that describes the time correlation between fluctuations in transition frequencies is the central component in the line shape functions and it is defined: $h_{a,b}(t) = \int_0^t ds_2 \int_0^{s_2} ds_1 \zeta_{a,b}(s_2 - s_1)$. In this way, the energy gap correlations accessible to a four wave mixing spectroscopy will be included in the nonlinear response tensor through the

dephasing functions. The dephasing functions expressed in terms of the line shape functions are given below.

$$\begin{aligned}-\ln F_1^{a,b,c,d}(\tau_3',\tau_2',\tau_1') &= h_{c,c}(-\tau_3')+h_{b,b}(-\tau_2')+h_{d,d}(\tau_1'+\tau_2'+\tau_3') \\ &+h_{b,c}(-\tau_2'-\tau_3')-h_{b,c}(-\tau_2')-h_{b,c}(-\tau_3') \\ &+h_{c,d}(\tau_1'+\tau_2')-h_{c,d}(\tau_1'+\tau_2'+\tau_3')-h_{c,d}(-\tau_3') \\ &+h_{b,d}(\tau_1')-h_{b,d}(-\tau_3'-\tau_2')-h_{b,d}(\tau_1'+\tau_2')+h_{b,d}(-\tau_3')\end{aligned} \tag{2.41}$$

$$\begin{aligned}-\ln\left[F_2^{a,b,c,d}(\tau_3',\tau_2',\tau_1')\right]^* &= h_{c,c}(\tau_3')+h_{d,d}(\tau_1'+\tau_2')+h_{b,b}(-\tau_2'-\tau_3') \\ &+h_{b,c}(-\tau_2')-h_{b,c}(\tau_3')-h_{b,c}(-\tau_2'-\tau_3') \\ &+h_{c,d}(\tau_1'+\tau_2'+\tau_3')-h_{c,d}(\tau_1'+\tau_2')-h_{c,d}(\tau_3') \\ &+h_{b,d}(\tau_1')-h_{b,d}(\tau_1'+\tau_2'+\tau_3')-h_{b,d}(-\tau_2')+h_{b,d}(\tau_3')\end{aligned} \tag{2.42}$$

$$\begin{aligned}-\ln\left[F_3^{a,b,c,d}(\tau_3',\tau_2',\tau_1')\right]^* &= h_{b,b}(-\tau_3')+h_{c,c}(\tau_2'+\tau_3')+h_{d,d}(\tau_1') \\ &+h_{c,d}(\tau_1'+\tau_2'+\tau_3')-h_{c,d}(\tau_2'+\tau_3')-h_{c,d}(\tau_1') \\ &-h_{b,c}(\tau_2'+\tau_3')-h_{b,c}(-\tau_3')+h_{b,c}(\tau_2') \\ &-h_{b,d}(\tau_1'+\tau_2'+\tau_3')+h_{b,d}(\tau_2'+\tau_3')+h_{b,d}(\tau_2'+\tau_1')-h_{b,d}(\tau_2')\end{aligned} \tag{2.43}$$

$$\begin{aligned}-\ln F_4^{a,b,c,d}(\tau_3',\tau_2',\tau_1') &= h_{b,b}(\tau_3')+h_{c,c}(\tau_2')+h_{d,d}(\tau_1') \\ &+h_{b,c}(\tau_3'+\tau_2')-h_{b,c}(\tau_3')-h_{b,c}(\tau_2') \\ &+h_{c,d}(\tau_2'+\tau_1')-h_{c,d}(\tau_2')-h_{c,d}(\tau_1') \\ &+h_{b,d}(\tau_1'+\tau_2'+\tau_3')-h_{b,d}(\tau_2'+\tau_3')-h_{b,d}(\tau_2'+\tau_1')+h_{b,d}(\tau_2')\end{aligned} \tag{2.44}$$

When the time scales of the transition frequency fluctuations are faster than the experimental measurement and homogenous throughout the molecular ensemble, the line shape functions are simplified ($h_{a,b}(t)\approx\Gamma_{a,b}t$) to be linear in time since the correlation functions reduce to $\zeta_{a,b}(t)\approx\Gamma_{a,b}\delta t$. In this fast modulation limit, the dephasing functions can be written

$$-\ln F_1^{a,b,c,d}(\tau_3',\tau_2',\tau_1')=\left(\Gamma_{c,c}+\Gamma_{d,d}-2\Gamma_{c,d}\right)\tau_3'+\left(\Gamma_{b,b}+\Gamma_{d,d}-2\Gamma_{b,d}\right)\tau_2'+\Gamma_{d,d}\tau_1' \tag{2.45}$$

$$-\ln\left[F_2^{a,b,c,d}(\tau_3',\tau_2',\tau_1')\right]^* = \left(\Gamma_{c,c}+\Gamma_{b,b}-2\Gamma_{b,c}\right)\tau_3' + \left(\Gamma_{b,b}+\Gamma_{d,d}-2\Gamma_{b,d}\right)\tau_2' + \Gamma_{d,d}\tau_1' \quad (2.46)$$

$$-\ln\left[F_3^{a,b,c,d}(\tau_3',\tau_2',\tau_1')\right]^* = \left(\Gamma_{b,b}+\Gamma_{c,c}-2\Gamma_{b,c}\right)\tau_3' + \Gamma_{c,c}\tau_2' + \Gamma_{d,d}\tau_1' \quad (2.47)$$

$$-\ln F_4^{a,b,c,d}(\tau_3',\tau_2',\tau_1') = \Gamma_{b,b}\tau_3' + \Gamma_{c,c}\tau_2' + \Gamma_{d,d}\tau_1' \quad (2.48)$$

The energy gap correlation functions for the 2D vibronic spectroscopies discussed in section 2.3.1.3 are obtained from equations (2.45)-(2.48) and assuming: $\Gamma_{a,b}=\Gamma_{b,a}$, $\Gamma_{a,b}=0$ if $a(b)=|g,0\rangle$, and that the fluctuations in the mechanical anharmonicity of both electronic states are negligible.

### 2.8.4 *Appendix D: Response Functions for 2D Electronic-Vibrational and 2D Vibrational-Electronic Spectroscopies*

The response functions for both spectroscopies are given below. Table 2.2 and Table 2.3 relate the response and dephasing functions for both spectroscopies to the generalized third order response functions given in the above Appendix C. The information is indexed by the peak number and lists the type of response function and dephasing function (from equations (2.45)-(2.48)) for both rephasing (R) and non-rephasing (NR) pathways; the involved vibronic states for 2D EV and 2D VE transitions are also defined. The complete expressions for the 2D vibronic response functions in the homogeneous limit are obtained by using the equations below and the dephasing functions explicitly defined in equations (2.22)-(2.31) in sections 2.3.1 and 2.3.2. One can obtain a particular dephasing function by substituting the correct vibronic state indices specified in Table 2.2 or Table 2.3 into the corresponding dephasing function given in equations (2.45)-(2.48). Then use the relations given in equations (2.49)

below to express the dephasing functions in terms of $\Gamma_{eg,eg}$, $\Gamma_{eg,v}$, $\Gamma_{v,v}$, and $\lambda$, which are directly related to the energy gap correlation functions discussed in the text.

Each of the response functions below has three main components that respectively govern the peak amplitudes, positions, and line shapes. The peak amplitude is governed by the probability of a molecule occupying the initial state of the pathway $\left(P_{|g,0\rangle}\right)$, the Franck-Condon factor for the involved electronic transition $\left(\left|\langle g,v|e,v'\rangle\right|^2\right)$, and the magnitude of the matrix elements of the four interacting transition dipole moments $\left(\mu^{gv,ev'}\right)$ reflecting the transition strengths. The peak position in the 2D spectrum is dictated by the coherent superposition of states induced in the system during $\tau_1'$ and $\tau_3'$, the 2D Fourier transform maps the corresponding frequencies onto the 2D frequency spectrum revealing the resonance frequencies of the electronic transition $\left(e.g.,\ \omega_{eg}+\omega_{e,1'}\right)$ and the vibrational transition $\left(e.g.,\ \omega_{e,1'}\right)$. The line shape of the peak is given by the nonlinear dephasing function $\left(F^{a,b,c,d}(\tau_3',\tau_2',\tau_1')\right)$ which reflects the correlation between the electronic and vibrational degrees of freedom through the nature of the dephasing of the coherences induced in the system. The Roman numeral subscripts in the response functions (equations (2.50)-(2.53)) below refer to the 2D peaks in Figure 2.3(d) and Figure 2.4(d) above.

If we assume that the fluctuations in the mechanical anharmonicity of the two potential energy surfaces are negligible (i.e., $\delta(\Delta_{2',1'})(t)\approx 0$), and that $\Gamma_{a,b}=\Gamma_{b,a}$ and $\Gamma_{a,b}=0$ if $a(b)=|g,0\rangle$, then the dephasing times that compose the homogeneous dephasing functions can be expressed:

$$
\begin{aligned}
\Gamma_{g1,g1} &= \Gamma_{v,v} \\
\Gamma_{e0',e0'} &= \Gamma_{eg,eg} \\
\Gamma_{e1',e1'} &= \Gamma_{eg,eg} + 2\lambda\Gamma_{eg,v} + (\lambda^2)\Gamma_{v,v} \\
\Gamma_{e2',e2'} &= \Gamma_{eg,eg} + 4\lambda\Gamma_{eg,v} + 4(\lambda^2)\Gamma_{v,v} \\
\Gamma_{g1,e0'} &= \Gamma_{eg,v} \\
\Gamma_{g1,e1'} &= \Gamma_{eg,v} + \lambda\Gamma_{v,v} \\
\Gamma_{g1,e2'} &= \Gamma_{eg,v} + 2\lambda\Gamma_{v,v} \\
\Gamma_{e0',e1'} &= \Gamma_{eg,eg} + \lambda\Gamma_{eg,v} \\
\Gamma_{e1',e2'} &= \Gamma_{eg,eg} + 3\lambda\Gamma_{eg,v} + 2(\lambda^2)\Gamma_{v,v}
\end{aligned}
\tag{2.49}
$$

The terms on the right hand side of equations (2.49) are directly related to the energy gap correlation functions through $\Gamma_{a,b} = \int_0^\infty d\tau\zeta_{a,b}(\tau)$ where $\zeta_{a,b}(\tau) = \left\langle \delta\omega_{a,i}(\tau)\delta\omega_{b,i}(0)\right\rangle$. In this way, the dephasing functions are written in terms of the correlation functions defined in equations (2.34).

**2D Electronic-Vibrational Response Functions:**

*Rephasing (R)*

$$
\begin{aligned}
R_{R,I}^{g0,g1,g0,e0'}(\tau_3',\tau_2',\tau_1') = \quad & P_{|g,0\rangle} \times \left|\left\langle g,0\middle|e,0'\right\rangle\right|^2 \left|\mu^{g0,e0'}\right|^2 \left|\mu^{g0,g1}\right|^2 \\
& \times \exp\left[+i\omega_{eg}\tau_1' - i\omega_{g,1}\tau_3'\right] \times F_{R,I}^{g0,g1,g0,e0'}(\tau_3',\tau_2',\tau_1') \\
R_{R,II}^{g0,e0',e1',e0'}(\tau_3',\tau_2',\tau_1') = & -P_{|g,0\rangle} \times \left|\left\langle g,0\middle|e,0'\right\rangle\right|^2 \left|\mu^{g0,e0'}\right|^2 \left|\mu^{e0',e1'}\right|^2 \\
& \times \exp\left[+i\omega_{eg}\tau_1' - i\omega_{e,1'}\tau_3'\right] \times F_{R,II}^{g0,e0',e1',e0'}(\tau_3',\tau_2',\tau_1') \\
R_{R,III}^{g0,g1,g0,e1'}(\tau_3',\tau_2',\tau_1') = \quad & P_{|g,0\rangle} \times \left|\left\langle g,0\middle|e,1'\right\rangle\right|^2 \left|\mu^{g0,e1'}\right|^2 \left|\mu^{g0,g1}\right|^2 \\
& \times \exp\left[+i(\omega_{eg}+\omega_{e,1'})\tau_1' - i\omega_{g,1}\tau_3'\right] \times F_{R,III}^{g0,g1,g0,e1'}(\tau_3',\tau_2',\tau_1') \\
R_{R,IV}^{g0,e1',e2',e1'}(\tau_3',\tau_2',\tau_1') = & -P_{|g,0\rangle} \times \left|\left\langle g,0\middle|e,1'\right\rangle\right|^2 \left|\mu^{g0,e1'}\right|^2 \left|\mu^{e1',e2'}\right|^2 \\
& \times \exp\left[+i(\omega_{eg}+\omega_{e,1'})\tau_1' - i\omega_{e,2'}\tau_3'\right] \times F_{R,IV}^{g0,e1',e2',e1'}(\tau_3',\tau_2',\tau_1') \\
R_{R,V}^{g0,e1',e0',e1'}(\tau_3',\tau_2',\tau_1') = \quad & P_{|g,0\rangle} \times \left|\left\langle g,0\middle|e,1'\right\rangle\right|^2 \left|\mu^{g0,e1'}\right|^2 \left|\mu^{e0',e1'}\right|^2 \\
& \times \exp\left[+i(\omega_{eg}+\omega_{e,1'})\tau_1' - i\omega_{e,1'}\tau_3'\right] \times F_{R,V}^{g0,e1',e0',e1'}(\tau_3',\tau_2',\tau_1')
\end{aligned}
\tag{2.50}
$$

*Non-Rephasing (NR)*

$$
\begin{aligned}
R_{NR,I}^{g0,g1,g0,e0'}(\tau_3',\tau_2',\tau_1') = \quad & P_{|g,0\rangle}\times\left|\langle g,0|e,0'\rangle\right|^2\left|\mu^{g0,e0'}\right|^2\left|\mu^{g0,g1}\right|^2 \\
& \times\exp\left[-i\omega_{eg}\tau_1'-i\omega_{g,1}\tau_3'\right]\times F_{NR,I}^{g0,g1,g0,e0'}(\tau_3',\tau_2',\tau_1') \\
R_{NR,II}^{g0,e0',e1',e0'}(\tau_3',\tau_2',\tau_1') = & -P_{|g,0\rangle}\times\left|\langle g,0|e,0'\rangle\right|^2\left|\mu^{g0,e0'}\right|^2\left|\mu^{e0',e1'}\right|^2 \\
& \times\exp\left[-i\omega_{eg}\tau_1'-i\omega_{e,1'}\tau_3'\right]\times F_{NR,II}^{g0,e0',e1',e0'}(\tau_3',\tau_2',\tau_1') \\
R_{NR,III}^{g0,g1,g0,e1'}(\tau_3',\tau_2',\tau_1') = \quad & P_{|g,0\rangle}\times\left|\langle g,0|e,1'\rangle\right|^2\left|\mu^{g0,e1'}\right|^2\left|\mu^{g0,g1}\right|^2 \\
& \times\exp\left[-i(\omega_{eg}+\omega_{e,1'})\tau_1'-i\omega_{g,1}\tau_3'\right]\times F_{NR,III}^{g0,g1,g0,e1'}(\tau_3',\tau_2',\tau_1') \\
R_{NR,IV}^{g0,e1',e2',e1'}(\tau_3',\tau_2',\tau_1') = & -P_{|g,0\rangle}\times\left|\langle g,0|e,1'\rangle\right|^2\left|\mu^{g0,e1'}\right|^2\left|\mu^{e1',e2'}\right|^2 \\
& \times\exp\left[-i(\omega_{eg}+\omega_{e,1'})\tau_1'-i\omega_{e,2'}\tau_3'\right]\times F_{NR,IV}^{g0,e1',e2',e1'}(\tau_3',\tau_2',\tau_1') \\
R_{NR,V}^{g0,e1',e0',e1'}(\tau_3',\tau_2',\tau_1') = \quad & P_{|g,0\rangle}\times\left|\langle g,0|e,1'\rangle\right|^2\left|\mu^{g0,e1'}\right|^2\left|\mu^{e0',e1'}\right|^2 \\
& \times\exp\left[-i(\omega_{eg}+\omega_{e,1'})\tau_1'-i\omega_{e,1'}\tau_3'\right]\times F_{NR,V}^{g0,e1',e0',e1'}(\tau_3',\tau_2',\tau_1')
\end{aligned}
\tag{2.51}
$$

Table 2.2. 2D Electronic-Vibrational Transition Pathway Index

| Peak | $R_R^{a,b,c,d};F_R^{a,b,c,d}$ | $R_{NR}^{a,b,c,d};F_{NR}^{a,b,c,d}$ | a | b | c | d |
|---|---|---|---|---|---|---|
| I | $R_3;F_3$ | $R_4;F_4$ | $\|g,0\rangle$ | $\|g,1\rangle$ | $\|g,0\rangle$ | $\|e,0'\rangle$ |
| II | $R_1{}^*;F_1$ | $R_2{}^*;F_2$ | $\|g,0\rangle$ | $\|e,0'\rangle$ | $\|e,1'\rangle$ | $\|e,0'\rangle$ |
| III | $R_3;F_3$ | $R_4;F_4$ | $\|g,0\rangle$ | $\|g,1\rangle$ | $\|g,0\rangle$ | $\|e,1'\rangle$ |
| IV | $R_1{}^*;F_1$ | $R_2{}^*;F_2$ | $\|g,0\rangle$ | $\|e,1'\rangle$ | $\|e,2'\rangle$ | $\|e,1'\rangle$ |
| V | $R_2;F_2$ | $R_1;F_1$ | $\|g,0\rangle$ | $\|e,1'\rangle$ | $\|e,0'\rangle$ | $\|e,1'\rangle$ |

**2D Vibrational-Electronic Response Functions:**

*Rephasing (R)*

$$
\begin{aligned}
R_{R,I}^{g0,e0',g0,g1}(\tau_3',\tau_2',\tau_1') = \quad & P_{|g,0\rangle}\times\left|\left\langle g,0\middle|e,0'\right\rangle\right|^2\left|\mu^{g0,g1}\right|^2\left|\mu^{g0,e0'}\right|^2 \\
& \times\exp\left[+i\omega_{g,1}\tau_1' - i\omega_{eg}\tau_3'\right]\times F_{R,I}^{g0,e0',g0,g1}(\tau_3',\tau_2',\tau_1') \\
R_{R,II}^{g0,g1,e1',g1}(\tau_3',\tau_2',\tau_1') = & -P_{|g,0\rangle}\times\left|\left\langle g,1\middle|e,1'\right\rangle\right|^2\left|\mu^{g0,g1}\right|^2\left|\mu^{g1,e1'}\right|^2 \\
& \times\exp\left[+i\omega_{g,1}\tau_1' - i(\omega_{eg}+\Delta_{eg})\tau_3'\right]\times F_{R,II}^{g0,g1,e1',g1}(\tau_3',\tau_2',\tau_1') \\
R_{R,III}^{g0,e1',g0,g1}(\tau_3',\tau_2',\tau_1') = \quad & P_{|g,0\rangle}\times\left|\left\langle g,0\middle|e,1'\right\rangle\right|^2\left|\mu^{g0,g1}\right|^2\left|\mu^{g0,e1'}\right|^2 \\
& \times\exp\left[+i\omega_{g,1}\tau_1' - i(\omega_{eg}+\omega_{e,1'})\tau_3'\right]\times F_{R,III}^{g0,e1',g0,g1}(\tau_3',\tau_2',\tau_1') \\
R_{R,IV}^{g0,g1,e2',g1}(\tau_3',\tau_2',\tau_1') = & -P_{|g,0\rangle}\times\left|\left\langle g,1\middle|e,2'\right\rangle\right|^2\left|\mu^{g0,g1}\right|^2\left|\mu^{g1,e2'}\right|^2 \\
& \times\exp\left[+i\omega_{g,1}\tau_1' - i(\omega_{eg}+\omega_{e,1'}+\Delta_{eg}-\Delta_{2',1'})\tau_3'\right]\times F_{R,IV}^{g0,g1,e2',g1}(\tau_3',\tau_2',\tau_1') \\
R_{R,V}^{g0,g1,e0',g1}(\tau_3',\tau_2',\tau_1') = & -P_{|g,0\rangle}\times\left|\left\langle g,1\middle|e,0'\right\rangle\right|^2\left|\mu^{g0,g1}\right|^2\left|\mu^{g1,e0'}\right|^2 \\
& \times\exp\left[+i\omega_{g,1}\tau_1' - i(\omega_{eg}-\omega_{g,1})\tau_3'\right]\times F_{R,V}^{g0,g1,e0',g1}(\tau_3',\tau_2',\tau_1')
\end{aligned}
$$

(2.52)

*Non-Rephasing (NR)*

$$
\begin{aligned}
R_{NR,I}^{g0,e0',g0,g1}(\tau_3',\tau_2',\tau_1') = \quad & P_{|g,0\rangle}\times\left|\left\langle g,0\middle|e,0'\right\rangle\right|^2\left|\mu^{g0,g1}\right|^2\left|\mu^{g0,e0'}\right|^2 \\
& \times\exp\left[-i\omega_{g,1}\tau_1' - i\omega_{eg}\tau_3'\right]\times F_{NR,I}^{g0,e0',g0,g1}(\tau_3',\tau_2',\tau_1') \\
R_{NR,II}^{g0,g1,e1',g1}(\tau_3',\tau_2',\tau_1') = & -P_{|g,0\rangle}\times\left|\left\langle g,1\middle|e,1'\right\rangle\right|^2\left|\mu^{g0,g1}\right|^2\left|\mu^{g1,e1'}\right|^2 \\
& \times\exp\left[-i\omega_{g,1}\tau_1' - i(\omega_{eg}+\Delta_{eg})\tau_3'\right]\times F_{NR,II}^{g0,g1,e1',g1}(\tau_3',\tau_2',\tau_1') \\
R_{NR,III}^{g0,e1',g0,g1}(\tau_3',\tau_2',\tau_1') = \quad & P_{|g,0\rangle}\times\left|\left\langle g,0\middle|e,1'\right\rangle\right|^2\left|\mu^{g0,g1}\right|^2\left|\mu^{g0,e1'}\right|^2 \\
& \times\exp\left[-i\omega_{g,1}\tau_1' - i(\omega_{eg}+\omega_{e,1'})\tau_3'\right]\times F_{NR,III}^{g0,e1',g0,g1}(\tau_3',\tau_2',\tau_1') \\
R_{NR,IV}^{g0,g1,e2',g1}(\tau_3',\tau_2',\tau_1') = & -P_{|g,0\rangle}\times\left|\left\langle g,1\middle|e,2'\right\rangle\right|^2\left|\mu^{g0,g1}\right|^2\left|\mu^{g1,e2'}\right|^2 \\
& \times\exp\left[-i\omega_{g,1}\tau_1' - i(\omega_{eg}+\omega_{e,1'}+\Delta_{eg}-\Delta_{2',1'})\tau_3'\right]\times F_{NR,IV}^{g0,g1,e2',g1}(\tau_3',\tau_2',\tau_1') \\
R_{NR,V}^{g0,g1,e0',g1}(\tau_3',\tau_2',\tau_1') = & -P_{|g,0\rangle}\times\left|\left\langle g,1\middle|e,0'\right\rangle\right|^2\left|\mu^{g0,g1}\right|^2\left|\mu^{g1,e0'}\right|^2 \\
& \times\exp\left[-i\omega_{g,1}\tau_1' - i(\omega_{eg}-\omega_{g,1})\tau_3'\right]\times F_{NR,V}^{g0,g1,e0',g1}(\tau_3',\tau_2',\tau_1')
\end{aligned}
$$

*(2.53)*

Table 2.3. 2D Vibrational-Electronic Transition Pathway Index

| Peak | $R_R^{a,b,c,d};F_R^{a,b,c,d}$ | $R_{NR}^{a,b,c,d};F_{NR}^{a,b,c,d}$ | a | b | c | d |
|---|---|---|---|---|---|---|
| I | $R_3;F_3$ | $R_4;F_4$ | $\|g,0\rangle$ | $\|e,0'\rangle$ | $\|g,0\rangle$ | $\|g,1\rangle$ |
| II | $R_1^*;F_1$ | $R_2^*;F_2$ | $\|g,0\rangle$ | $\|g,1\rangle$ | $\|e,1'\rangle$ | $\|g,1\rangle$ |
| III | $R_3;F_3$ | $R_4;F_4$ | $\|g,0\rangle$ | $\|e,1'\rangle$ | $\|g,0\rangle$ | $\|g,1\rangle$ |
| IV | $R_1^*;F_1$ | $R_2^*;F_2$ | $\|g,0\rangle$ | $\|g,1\rangle$ | $\|e,2'\rangle$ | $\|g,1\rangle$ |
| V | $R_1^*;F_1$ | $R_2^*;F_2$ | $\|g,0\rangle$ | $\|g,1\rangle$ | $\|e,0'\rangle$ | $\|g,1\rangle$ |

### 2.8.5 *Appendix E: Second Order Energy Corrections using Stationary Perturbation Theory*

Expressions for the $H_{vibronic}$ eigenstate energies $E_{g,v}$ and $E_{e,v'}$ for vibronic states |g,v⟩ and |e,v'⟩, respectively, can be obtained through stationary perturbation theory[21] with energy corrections up to second order

$$\frac{E_{g,v}}{hc}=\frac{\omega_j^{\,0}}{2\pi c}\left[\left(v+\frac{1}{2}\right)-\frac{g_{jjj}^2}{8}\left(30\left(v+\frac{1}{2}\right)^2+\frac{7}{2}\right)\right] \tag{2.54}$$

$$\frac{E_{e,v'}}{hc}=\frac{\omega_{eg}^0}{2\pi c}-\frac{\omega_j^{\,0}}{2\pi c}\left[\left(\frac{\left(\nu_j^{(1)}\right)^2}{2}+\frac{7g_{jjj}^2}{16}\right)-\left(1+\frac{\nu_{j,j}^{(2)}}{2}-\frac{\left(\nu_{j,j}^{(2)}\right)^2}{8}\right)\left(v'+\frac{1}{2}\right)+\frac{15g_{jjj}^2}{4}\left(v'+\frac{1}{2}\right)^2\right] \tag{2.55}$$

where $v$ and $v'$ are the vibrational quantum numbers in |g⟩ and |e⟩, respectively. Using these equations, the vibrational transition frequencies can be calculated in both electronic states. The

frequencies $\omega_{g,v}$ ($\omega_{e,v'}$) correspond to the $v^{th}$ ($v'^{th}$) vibrational transition frequencies in the electronic ground (excited) state and $\omega_{eg}$ is the electronic transition frequency between |g,0⟩ and |e,0'⟩.

$$\omega_{g,v} = \frac{\left(E_{g,v} - E_{g,(v-1)}\right)}{\hbar} \tag{2.56}$$

$$\omega_{e,v'} = \frac{\left(E_{e,v'} - E_{e,(v'-1)}\right)}{\hbar} \tag{2.57}$$

$$\omega_{eg} = \frac{\left(E_{g,0} - E_{e,0'}\right)}{\hbar} \tag{2.58}$$

From the expressions for the transition frequencies, interesting molecular parameters that are directly accessible in these 2D vibronic spectroscopies, such as the frequency difference between the vibration in the ground and excited electronic states, $\Delta_{eg}$, and the excited state mechanical anharmonicity, $\Delta_{2',1'}$, may be expressed in terms of these dimensionless perturbation coefficients

$$\Delta_{eg} = \frac{\omega_j^{\,0}}{2\pi c}\left(\frac{\mathcal{V}_{j,j}^{(2)}}{2} - \frac{\left(\mathcal{V}_{j,j}^{(2)}\right)^2}{8}\right) \tag{2.59}$$

$$\Delta_{2',1'} = \frac{\omega_j^{\,0}}{2\pi c}\left(\frac{15 g_{jjj}^2}{2}\right) \tag{2.60}$$

with $\Delta_{eg}$ and $\Delta_{2',1'}$ given in wavenumbers ($cm^{-1}$). It should be noted that these expressions are valid when the mechanical anharmonicities are the same in both electronic states, which is true in the present discussion.

## 2.9 REFERENCES


(1) Scholes, G. D.; Fleming, G. R.; Chen, L. X.; Aspuru-Guzik, A.; Buchleitner, A.; Coker, D. F.; Engel, G. S.; Van Grondelle, R.; Ishizaki, A.; Jonas, D. M.; Lundeen, J. S.; Mccusker, J. K.; Mukamel, S.; Ogilvie, J. P.; Olaya-Castro, A.*et al.* Using coherence to enhance function in chemical and biophysical systems; *Nature* **2017**, *543*, 647-656.

(2) Oliver, T. a. A.; Lewis, N. H. C.; Fleming, G. R. Correlating the motion of electrons and nuclei with two-dimensional electronic-vibrational spectroscopy; *Proc. Natl. Acad. Sci. U.S.A.* **2014**, *111*, 10061-10066.

(3) Courtney, T. L.; Fox, Z. W.; Estergreen, L.; Khalil, M. Measuring Coherently Coupled Intramolecular Vibrational and Charge-Transfer Dynamics with Two-Dimensional Vibrational–Electronic Spectroscopy; *J. Chem. Phys. Lett.* **2015**, *6*, 1286-1292.

(4) Courtney, T. L.; Fox, Z. W.; Slenkamp, K. M.; Khalil, M. Two-dimensional vibrational-electronic spectroscopy; *J. Chem. Phys.* **2015**, *143*, 154201.

(5) Lewis, N. H. C.; Fleming, G. R. Two-Dimensional Electronic-Vibrational Spectroscopy of Chlorophyll a and b; *J. Phys. Chem. Lett.* **2016**, *7*, 831-837.

(6) Gaynor, J. D.; Courtney, T. L.; Balasubramanian, M.; Khalil, M. Fourier transform two-dimensional electronic-vibrational spectroscopy using an octave-spanning mid-IR probe; *Opt. Lett.* **2016**, *41*, 2895-2898.

(7) Dong, H.; Lewis, N. H. C.; Oliver, T. a. A.; Fleming, G. R. Determining the static electronic and vibrational energy correlations via two-dimensional electronic-vibrational spectroscopy; *J. Chem. Phys.* **2015**, *142*, 174201.

(8) Lewis, N. H. C.; Dong, H.; Oliver, T. a. A.; Fleming, G. R. A method for the direct measurement of electronic site populations in a molecular aggregate using two-dimensional electronic-vibrational spectroscopy; *J. Chem. Phys.* **2015**, *143*, 124203.

(9) Lewis, N. H. C.; Dong, H.; Oliver, T. a. A.; Fleming, G. R. Measuring correlated electronic and vibrational spectral dynamics using line shapes in two-dimensional electronic-vibrational spectroscopy; *J. Chem. Phys.* **2015**, *142*, 174202.

(10) Herzberg, G.; Teller, E. Fluctuation structure of electron transfer in multiatomic molecules.; *Z. Phys. Chem.* **1933**, *21*, 410-446.

(11) Fulton, R. L.; Gouterman, M. Vibronic Coupling. I. Mathematical Treatment for Two Electronic States; *J. Chem. Phys.* **1961**, *35*, 1059-1071.

(12) Koppel, H.; Domcke, W.; Cederbaum, L. S. Theory of Vibronic Coupling in Linear-Molecules; *J. Chem. Phys.* **1981**, *74*, 2945-2968.

(13) Holstein, T. Studies of Polaron Motion .1. The Molecular-Crystal Model; *Ann. Phys.* **1959**, *8*, 325-342.

(14) Capano, G.; Penfold, T. J.; Rothlisberger, U.; Tavernelli, I. A Vibronic Coupling Hamiltonian to Describe the Ultrafast Excited State Dynamics of a Cu(I)-Phenanthroline Complex; *Chimia* **2014**, *68*, 227-230.

(15) Zhao, Z.; Spano, F. C. Vibronic fine structure in the absorption spectrum of oligothiophene thin films; *J. Chem. Phys.* **2005**, *122*, 114701.

(16) Tonks, D. L.; Page, J. B. General theory of vibrational mode mixing and frequency shifts in resonance raman scattering; *Chem. Phys. Lett.* **1981**, *79*, 247-252.

(17) Cho, M. H. Two-dimensional vibrational spectroscopy. VII. Investigation of the vibronic and vibrational couplings by using novel triply resonant two-dimensional vibrational spectroscopies; *J. Chem. Phys.* **2000**, *113*, 7746-7755.

(18) Duschinsky, F. The importance of the electron spectrum in multi atomic molecules. concerning the Franck-Condon principle; *Acta Physicochimica URSS* **1937**, *7*, 551-566.

(19) Lu, H. M.; Page, J. B. General theory of simultaneous mode mixing and non-condon effects in resonance Raman scattering; *Chem. Phys. Lett.* **1986**, *131*, 87-93.

(20) Vallet, J. C.; Boeglin, A. J.; Lavoine, J. P.; Villaeys, A. A. Vibronic mode couplings in adsorbed molecules analyzed by doubly resonant sum-frequency generation; *Phys. Rev. A* **1996**, *53*, 4508-4518.

(21) Cohen-Tannoudji, C.; Diu, B.; Laloe, F. *Quantum Mechanics*; Wiley-Interscience: Paris, 1977.

(22) Herzberg, G. *Molecular Spectra and Molecular Structure I: Spectra of Diatomic Molecules*; 2nd ed.; D. Van Nostrand Company, Inc.: New York, 1950; Vol. I.

(23) Sung, J. Y.; Silbey, R. J. Four wave mixing spectroscopy for a multilevel system; *J. Chem. Phys.* **2001**, *115*, 9266-9287.

(24) Born, M.; Oppenheimer, R. Quantum theory of molecules; *Ann. Phys.* **1927**, *84*, 0457-0484.

(25) Ballhausen, C. J.; Hansen, A. E. Electronic-Spectra; *Annu. Rev. Phys. Chem.* **1972**, *23*, 15-+.

(26) Harris, D. C.; Bertolucci, M. D. *Symmetry and Spectroscopy: An Introduction to Vibrational and Electronic Spectroscopy*; Dover: New York, 1989.

(27) Hollas, J. M. *Modern Spectroscopy*; 2nd ed.; John Wiley & Sons: West Sussex, England, 1992.

(28) Fischer, G. *Vibronic Coupling: The Interaction between Electronic and Nuclear Motions*; Academic Press: London, 1984.

(29) Azumi, T.; Matsuzaki, K. What Does Term Vibronic-Coupling Mean; *Photochem. Photobiol.* **1977**, *25*, 315-326.

(30) Cho, M. H. Correlation between electronic and molecular structure distortions and vibrational properties. I. Adiabatic approximations; *J. Chem. Phys.* **2003**, *118*, 3480-3490.

(31) The Herzberg-Teller adiabatic approximation is obtained by expanding the dynamical electronic wave function in terms of a complete set of static electronic wave functions that reference an equilibrium nuclear configuration. These static electronic wave functions are described within the crude adiabatic approximation and greatly restrict the description of the electronic states. A linear nuclear coordinate dependence of the electronic transition dipole moment is included through the first order term in the expansion in the Herzberg-Teller adiabatic treatment, which relaxes the stringent requires of the crude adiabatic wave functions used in the expansion.

(32) Mukamel, S. *Principles of Nonlinear Optical Spectroscopy*; Oxford University Press: New York, 1995.

(33) Hamm, P.; Zanni, M. T. *Concepts and Methods of 2D Infrared Spectroscopy*; Cambridge University Press: Cambridge, U.K., 2011.

(34) Khalil, M.; Demirdoven, N.; Tokmakoff, A. Coherent 2D IR spectroscopy: Molecular structure and dynamics in solution; *J. Phys. Chem. A* **2003**, *107*, 5258-5279.

(35) Jonas, D. M. Two-dimensional femtosecond spectroscopy; *Annu. Rev. Phys. Chem* **2003**, *54*, 425-463.

(36) Golonzka, O.; Tokmakoff, A. Polarization-selective third-order spectroscopy of coupled vibronic states; *J. Chem. Phys.* **2001**, *115*, 297-309.

(37) Oliver, T. a. A.; Fleming, G. R. Following Coupled Electronic-Nuclear Motion through Conical Intersections in the Ultrafast Relaxation of beta-Apo-8 '-carotenal; *J. Phys. Chem. B* **2015**, *119*, 11428-11441.

(38) Khalil, M.; Tokmakoff, A. Signatures of vibrational interactions in coherent two-dimensional infrared spectroscopy; *Chem. Phys.* **2001**, *266*, 213-230.

(39) Fox, Z. W. *Two-Dimensional Vibrational-Electronic Spectroscopy: The Design and Development of a Novel Multidimensional Spectroscopic Technique to Directly Measure*

*Coherent coupling Between VIbrational and Electronic Degrees of Freedom* Ph.D. Dissertation, University of Washington, 2018.

(40) Courtney, T. L.; Fox, Z. W.; Slenkamp, K. M.; Khalil, M. Two-dimensional vibrational-electronic spectroscopy; *J. Chem. Phys.* **2015**, *143*, 154201/154201-154201/154215.

(41) De A. Camargo, F. V.; Grimmelsmann, L.; Anderson, H. L.; Meech, S. R.; Heisler, I. A. Resolving Vibrational from Electronic Coherences in Two-Dimensional Electronic Spectroscopy: The Role of the Laser Spectrum; *Phys. Rev. Lett.* **2017**, *118*, 033001.

(42) Bizimana, L. A.; Carbery, W. P.; Gellen, T. A.; Turner, D. B. Signatures of Herzberg–Teller coupling in three-dimensional electronic spectroscopy; *J. Chem. Phys.* **2017**, *146*, 084311.

(43) Rector, K. D.; Kwok, A. S.; Ferrante, C.; Tokmakoff, A.; Rella, C. W.; Fayer, M. D. Vibrational anharmonicities and multilevel vibrational dephasing from vibrational echo beats; **1997**, *106*, 10027-10036.

(44) Kukura, P.; Mccamant, D. W.; Mathies, R. A. Femtosecond stimulated Raman spectroscopy; *Ann. Rev. Phys. Chem.* **2007**, *58*, 461-488.

(45) Molesky, B. P.; Giokas, P. G.; Guo, Z.; Moran, A. M. Multidimensional resonance Raman spectroscopy by six-wave mixing in the deep UV; *J. Chem. Phys.* **2014**, *141*, 114202.

(46) Harel, E. Four-dimensional coherent electronic Raman spectroscopy; *J. Chem. Phys.* **2017**, *146*, 154201.

(47) Spencer, A. P.; Hutson, W. O.; Harel, E. Quantum coherence selective 2D Raman-2D electronic spectroscopy; *Nat. Commun.* **2017**, *8*, 14732.

(48) Roberts, S. T.; Loparo, J. J.; Tokmakoff, A. Characterization of spectral diffusion from two-dimensional line shapes; *J. Chem. Phys.* **2006**, *125*, 084502.

(49) Bakker, H. J.; Skinner, J. L. Vibrational Spectroscopy as a Probe of Structure and Dynamics in Liquid Water; *Chem. Rev.* **2009**, *110*, 1498-1517.

(50) Kwak, K.; Rosenfeld, D. E.; Fayer, M. D. Taking apart the two-dimensional infrared vibrational echo spectra: more information and elimination of distortions; *J. Chem. Phys.* **2008**, *128*, 204505.

(51) Šanda, F.; Perlík, V.; Lincoln, C. N.; Hauer, J. Center Line Slope Analysis in Two-Dimensional Electronic Spectroscopy; *J. Phys. Chem. A* **2015**, *119*, 10893-10909.

(52) Zhuang, W.; Hayashi, T.; Mukamel, S. Coherent Multidimensional Vibrational Spectroscopy of Biomolecules: Concepts, Simulations, and Challenges; *Angew. Chem., Int. Ed.* **2009**, *48*, 3750-3781.

(53) Cho, M. Coherent Two-Dimensional Optical Spectroscopy; *Chem. Rev.* **2008**, *108*, 1331-1418.

(54) Kiefer, L. M.; King, J. T.; Kubarych, K. J. Dynamics of Rhenium Photocatalysts Revealed through Ultrafast Multidimensional Spectroscopy; *Acc. Chem. Res.* **2015**, *48*, 1123-1130.

(55) Roy, S.; Pshenichnikov, M. S.; Jansen, T. L. C. Analysis of 2D CS Spectra for Systems with Non-Gaussian Dynamics; *J. Phys. Chem. B* **2011**, *115*, 5431-5440.

# Chapter 3. MEASURING A TWO-DIMENSIONAL ELECTRONIC-VIBRATIONAL SPECTRUM

*The work presented in this chapter has been published in the following papers:*

*1) Gaynor, J.D.; Courtney, T.L.; Balasubramanian, M.; and Khalil, M. "Fourier Transform Two-Dimensional Electronic-Vibrational Spectroscopy using an Octave-Spanning Mid-IR Probe" Optics Letters **2016**, 41, 2895-2898.*

*2) Balasubramanian, M.; Courtney, T.L.; Gaynor, J.D.; and Khalil, M. "Compression of Tunable Broadband Mid-IR Pulses with a Deformable Mirror Pulse Shaper" Journal of the Optical Society of America B **2016**, 33, 2033-2037.*

## 3.1 INTRODUCTION

2D EV spectroscopy has been demonstrated using excitation pulses in the visible region (500 nm – 800 nm) and a mid-IR probe with a 300 $cm^{-1}$ bandwidth generated from difference frequency generation (DFG) of the outputs from an optical parametric amplifier (OPA).[1,2] These experiments have followed structural dynamics on the excited states of laser dyes,[1,2] a model carotenoid complex,[3] and chlorophyll.[4] Extending the excitation to UV frequencies and the detection to a broader range of mid-IR frequencies will enable 2D EV experiments of biological media[5] and proton-coupled electron transfer systems[6,7] to directly explore correlations between UV electronic excitations and a complete set of broad and varied vibrational transitions in a single laser shot. In this Chapter, I detail the development of the coherent FT 2D EV experimental set-up in the Khalil Group which extends the 2D EV spectral window of the electronic excitation ($\omega_1$) to the near-UV (400 nm) range and also extends the mid-IR detection window by incorporating a broadband mid-IR light source (BBIR) that spans an octave (1600 – 3200 $cm^{-1}$).

Generating phase stable pump pulse pairs at UV wavelengths for use in a 2D FT experiment becomes difficult as a given time delay ($\tau_1$) is a larger percentage of an optical cycle at shorter

wavelengths. Experimentalists performing 2D UV spectroscopy have circumvented this problem in the fully noncollinear geometry using diffractive optics[8] and pairwise beam manipulation,[9] and in the partially collinear ("pump-probe") geometry using pulse shapers.[10] The introduction of an AOPDF for the UV using KDP and quartz crystals[11,12] has aided the development of facile 2D UV set-ups employing AOPDF-based pulse shaping[13] that can also use phase cycling schemes to improve signal-to-noise and isolate specific third-order nonlinear signals of interest.[14] I have used this AOPDF-based approach in constructing our 2D EV set-up to produce UV pump pulse pairs with the accurate time delays required for 2D FT experiments.

The feasibility of implementing a BBIR probe[15] is demonstrated here by incorporating it into the 2D EV spectrometer to measure the coherent couplings of electronic transition frequencies in the UV with a large range of mid-IR frequencies. Typical generation of femtosecond mid-IR pulses relies on the DFG of an OPA output to yield tunable mid-IR pulses with ~300 $cm^{-1}$ bandwidths whereas the BBIR source shown here can span more than 1000 $cm^{-1}$.[16] The experiments in this dissertation use both mid-IR light sources which are described in this chapter. This work expands the scope of experimental implementation of BBIR sources to include 2D EV spectroscopy.

## 3.2 Overview of the 2D EV Experiment

2D EV is a third-order nonlinear spectroscopy consisting of three light pulses (see Figure 3.1) with femtosecond durations that are controllably delayed in time with respect to one another and spatially overlapped in a solution phase molecular sample. The three sequential field-matter interactions result in an emitted signal field that reflects the molecular ensemble's response to the three resonant interactions with various transition dipole moments of the

molecules under study. All reported 2D EV experiments to date, including those described in this dissertation, implement the partially collinear beam geometry consisting of two collinear UV or visible pump beams and a non-collinear mid-IR probe beam. The 2D EV spectrometer used in all experiments discussed in this dissertation is schematically outlined in Figure 3.2, consisting of two collinear, UV excitation pulses ($\mathbf{E}_1$ and $\mathbf{E}_2$; Figure 3.1, blue), with wave vectors $\mathbf{k}_1$ and $\mathbf{k}_2$, that are generated with a variable delay time (often called the "coherence" time), $\tau_1$, using an AOPDF-based pulse shaper. These two pulses are resonant with an electronic transition and can create a population in the sample's ground or excited electronic state. After another time delay (often called the "population" time), $\tau_2$, the noncollinear mid-IR probe pulse ($\mathbf{E}_3$, $\mathbf{k}_3$; Figure 3.1, green) impinges on the sample and generates the 2D EV signal according to the four-wave mixing phase matching condition of the four wave vectors involved ($\mathbf{k}_{sig} = \pm \mathbf{k}_1 \mp \mathbf{k}_2 + \mathbf{k}_3$). In the partially collinear geometry, the collinear pumps result in the phase-matched, fully absorptive, third-order signal, $\mathbf{E}_{sig}$, copropagating with the probe pulse ($\tau_3$=0) which acts as an intrinsic local oscillator ($\mathbf{E}_{LO}$) for heterodyne detection. The molecular information of interest is described by the third order macroscopic polarization, $\mathbf{P}^{(3)}$, which is contained within $\mathbf{E}_{sig}$.

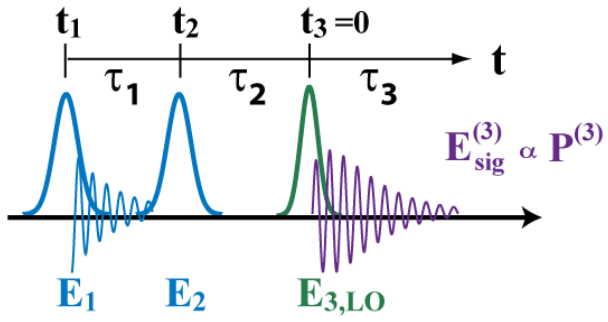


Figure 3.1. The Two-Dimensional Electronic-Vibrational (2D EV) Pulse Sequence

The 2D spectrum is parameterized by a fixed $\tau_2$; the FT over $\tau_1$ yields the excitation frequency, $\omega_1$, while the detection frequency, $\omega_3$, is obtained experimentally using a spectrometer to spectrally disperse the signal frequencies.

## 3.3 THE 2D EV SPECTROMETER

The three pulses derive from the output of a Spectra-Physics Spitfire XP Pro Ti:Sapphire regenerative amplifier (800 nm, 35 fs, ~4.0 W, 1 kHz). A majority (~2.8 mJ) of the amplifier output is separated by the reflection of a 70:30 (R:T) beam splitter and dedicated to the generation and temporal compression of the BBIR probe pulse, which is briefly detailed in section 3.3.2. Roughly 60 μJ of the remaining 1.2 mJ of the amplified fundamental is transmitted through a 95:5 (R:T) beam splitter and used as a reference pulse at various points on the optical table for characterization purposes. The reference fundamental is routed through a gold-coated retroreflector mounted on a computer-controllable delay stage (Newport XMS50, minimum increment = 1 nm (0.001 fs), typical accuracy = ±0.2 μm (±1.3fs)), referred to as "S1", for temporally delaying the reference with respect to other beams on the table. A home-built double-pass OPA is pumped using a ~900 μJ portion of the amplifier output, which is separated by the reflection from an 80:20 (R:T) beam splitter. The OPA generates collinearly propagating signal and idler beams tunable in the near-IR spectral range; a difference frequency generation (DFG) process with the signal and idler beams in a nonlinear crystal is a traditional method for generating tunable mid-IR (1200 – 3000 $cm^{-1}$) with spectral bandwidths of ~200-300 $cm^{-1}$ and is detailed in section 3.3.3. The 2D EV data presented in this dissertation use either the BBIR or the OPA/DFG mid-IR light sources as the probe. The transmission of the 80:20 beam splitter provides the ~240 μJ portion of the amplifier output used to generate UV pump pulse pairs with a central wavelength ($\lambda_c$) of 400 nm and bandwidth (FWHM) of 9-

10 nm. The generation and characterization of the UV pump pulses used in my initial experiments is detailed in section 3.3.1, while technical developments enabling the generation of broadband UV pump pulses with sufficiently high energy and stability for use in 2D EV spectroscopy are the subject of a later chapter.

As in all time-resolved nonlinear spectroscopies, temporal and spatial overlap of all beams are required to perform the 2D EV experiment. The $\tau_1$ delay between the collinear UV pump pulse pairs is controlled by phase and amplitude pulse shaping of the input UV beam to the AOPDF. The BBIR probe is routed through a gold-coated retroreflector mounted on a computer-controlled translation stage (Newport ILS200LM, minimum increment = 10 nm (0.066 fs), typical accuracy = ±1μm (±6.6fs)), referred to as "S2", to precisely adjust the $\tau_2$ delay time. The OPA/DFG mid-IR probe is routed through a gold-coated retroreflector on another computer-controlled translation stage (Newport ILS150PP, minimum increment = 1.0 μm (6.6 fs), typical accuracy = ±1.5μm (± 10 fs)), referred to as "S3", for precise control over $\tau_2$ before being focused at the sample area. For a given experiment, the three input pulses are spatially overlapped using a pinhole (PDT, 100 μm diameter) and temporally overlapped using a nonlinear signal that is maximized when all pulses are exactly overlapped in time. All three beams are arranged in the partially collinear beam geometry at the sample. The pump pulses pass through a half wave plate and polarizer before being focused to the sample with a UV-fused silica plano-convex focal lens (UV AR coated, f=300 mm). This lens is placed on a translation stage for fine adjustments to the spot size of the pump beam at the sample. Adjustments are made to ensure that the pump beam diameter is larger than the probe beam diameter when focused at the sample area. The pump pulses focus through a machined hole in the first of a pair of silver-coated off-axis parabolic mirrors (f=101.5 mm) that focuses all other

beams at the sample. Typically, the focused $1/e^2$ spot sizes on the sample of the UV pump beam are in the range 185-250 μm while the BBIR probe and OPA/DFG mid-IR probe beams are in the range of 160-220 μm.

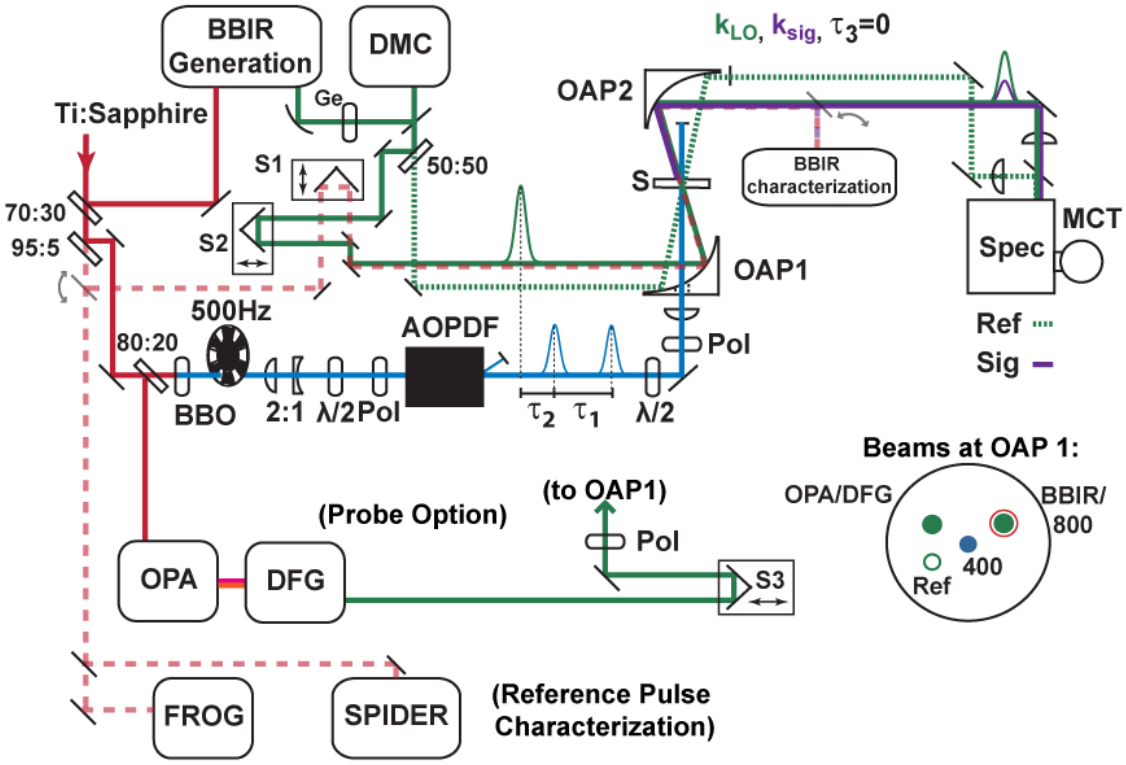


Figure 3.2. The 2D EV Experimental Schematic. The Ti:Sapphire output is split into the broadband mid-IR (BBIR) probe pulse (solid green), an alternate mid-IR probe option (solid green, lower), an 800 nm reference pulse for characterization (dashed red), and the pump pulse (solid blue). The BBIR is generated *via* filamentation of the 800 nm fundamental and its harmonics in gaseous media and compressed with material compensation (2mm Ge) and a deformable mirror compressor (DMC). Tunable, narrower-band mid-IR results from difference frequency generation (DFG) of the collinear near-IR output (magenta and orange) from a double-pass optical parametric amplifier (OPA). The pump pulse is chopped (500 Hz) and shaped in an acousto-optic programmable dispersive filter (AOPDF). The orientation of all beams at off axis parabolic mirror 1 (OAP 1) before focusing to the sample area (S) is shown in lower right, filled spots indicate the beams that generate the 2D EV signal using either mid-IR probe source. The signal (Sig, purple) and reference (Ref, dashed green) are both dispersed in a spectrometer (Spec) and detected in a 2 x 64 HgCdTe-pixel array (MCT) detector. λ/2, half wave plate; Pol, polarizer; 2:1, down-collimating telescope. Spectral and temporal characterization of the reference fundamental have been achieved using the Frequency Resolved Optical Gating (FROG) and Spectral phase Interferometry for Direct Electric-field Reconstruction (SPIDER) techniques. See paragraphs below for full experimental description.

A 50:50 beam splitter in the probe beamline separates a reference pulse that is also aligned through the sample but spatially offset from the pumped volume. The signal (reference) beam is spectrally dispersed in a 0.190 m Czerny-Turner spectrometer (Triax 190, Horiba Jobin Yvon) and focused onto the lower (upper) of two 64-pixel arrays in a liquid $N_2$ cooled HgCdTe array detector (IR-0144, Infrared Systems Development) for single-shot detection. Using the reference pulse, shot-to-shot normalization of the 2D EV signal can be performed before subtracting alternating shots ($pump_{on} - pump_{off}$, *via* mechanically chopping the pump at 500 Hz) to minimize noise due to shot-to-shot laser fluctuations and remove the innate probe background in a pump-probe geometry. The signal is measured as a change in IR transmission ($\Delta T$) of the sample following UV excitation as a function of $\tau_1$ and $\omega_3$ and parametrized by $\tau_2$. The 2D EV signal is isolated from other third-order pump-probe signals through non-zero baseline subtraction and FT processing (see section 3.4). Phase cycling using the AOPDF can improve signal-to-noise and expedite data collection but is not mandatory and decreases the duty cycle (i.e., increases number of pulses required to obtain one spectrum) for the experiment.

### 3.3.1 *Generating Phase-Stable UV Pulse Pairs for 2D Spectroscopy*

UV pulses centered at 400 nm result from the 240 μJ portion of the 800 nm fundamental undergoing second harmonic generation (SHG) in a 0.1 mm-thick β-BBO Type I crystal. The resulting 400 nm pulse is isolated using dichroic mirrors, down-collimated to a ~2 mm beam diameter using a transmissive telescope and polarization-rotated with a half wave plate and linear polarizer before being routed to the AOPDF (Dazzler™, Fastlite). The telescope prior to the AOPDF is used for fine adjustments to the beam collimation to ensure the two pump pulses are maximally overlapped when focused at the sample and spatio-temporal

inhomogeneities are avoided.[17] The AOPDF is an in-line pulse shaper that operates through an acousto-optic interaction in a nonlinear birefringent crystal medium, typically potassium dihydrogen phosphate (KDP), quartz, or tellurium dioxoide ($TeO_2$). The KDP and quartz transparency windows through the UV spectral range (200 – 450 nm) allow for AOPDF pulse shaping using these crystals; AOPDFs using both crystal types are used to collect data presented in this dissertation (KDP-based AOPDF = Crystal Model: KUV50-65.130-240 440-B, SN: 28879, RF generator: DC02KL88/T3; quartz-based AOPDF = Model: TF335-170-1-3-FL2, SN:20061975-002, RF generator: GZ0655).

The operating principle is schematically illustrated in Figure 3.3. An acoustic wave, $\mathbf{Ac}(\omega)$, is generated in the crystal by a custom radio-frequency (RF) waveform that is sent to a transducer coupled to the front of the crystal. $\mathbf{Ac}(\omega)$ is aligned to propagate collinear with an incident optical pulse, $\mathbf{E_{in}}(\omega)$, through the crystal. As $\mathbf{Ac}(\omega)$ propagates, the index of refraction in the crystal is modulated as a function of its local position along the $\mathbf{Ac}(\omega)$ propagation axis, z. Since the optical pulse is aligned collinearly with the acoustic wave, there is a z-dependent acousto-optic interaction which translates into the $\tau_1$ time delay. When the optical field and acoustic wave are optimally overlapped in time and space, an acousto-optic phase matching condition is achieved which diffracts part of the incident field from the crystal's ordinary axis onto the extraordinary axis yielding a newly shaped pulse. Due to the difference in propagation velocity of an acoustic and optical wave, the optical pulse effectively "feels" a temporally static, but z-dependent, index of refraction in the crystal on the time scale of the optical pulse's transmission through the AOPDF. The shaped pulse exits the crystal at a slight angle ($<10^o$) from the incident pulse but with $90^o$ polarization rotation due to the acousto-optic interaction. Since the acoustic wave is entirely dependent on the RF waveform, custom control over this

waveform allows for tailoring the acousto-optic interaction, providing arbitrary amplitude and phase control of shaped pulses. Moreover, the KDP- and quartz-based AOPDFs have different acousto-optic phase-matching conditions which affect the spectral shaping window and the diffraction (or shaping) efficiency of the AOPDF. As manufactured, the KDP-based AOPDF has a spectral shaping window of 250-440 nm and the quartz-based shaper's is 250-400 nm. However, the transducer-crystal interface of the quartz-based AOPDF can support RF waveforms enabling a spectral shaping window of 360-430 nm by changing the RF-generator software parameters, albeit with a lesser shaping efficiency for $\lambda > 400$ nm. Fortunately, this enables the use of the quartz-based AOPDF within most of the broadband UV spectrum detailed in the following chapter.

The RF waveform can also be tailored to generate pulse pairs with well-defined temporal delays, limited only by the phase jitter of the pulse shaper. As I have characterized in Figure 3.6, the phase jitter in our setup is negligible for sub-fs steps in $\tau_1$ which enables us to temporally oversample the UV frequencies during $\tau_1$ of the excitation fields used in these experiments by factors of 10, or greater, if desired. Considering that a UV wavelength cycle is on the order of 1.33 fs, it is clear why the motorized translation stages used for delaying the mid-IR and reference pulses elsewhere in the optical table are incapable of reliably generating UV pulse pairs with interferometric precision. In this way, $\mathbf{k_1}$ and $\mathbf{k_2}$ (125-250 nJ/pulse, 40 fs, S polarized), with a controlled $\tau_1$ delay are generated for use as the excitation pulses in our 2D EV spectrometer.

A prerequisite for conducting a FT 2D experiment is having some method of producing a pair of identical pulses with a precisely controllable interpulse time delay, such as results from an interferometer, to provide the first two light-matter interactions in the 2D pulse sequence.

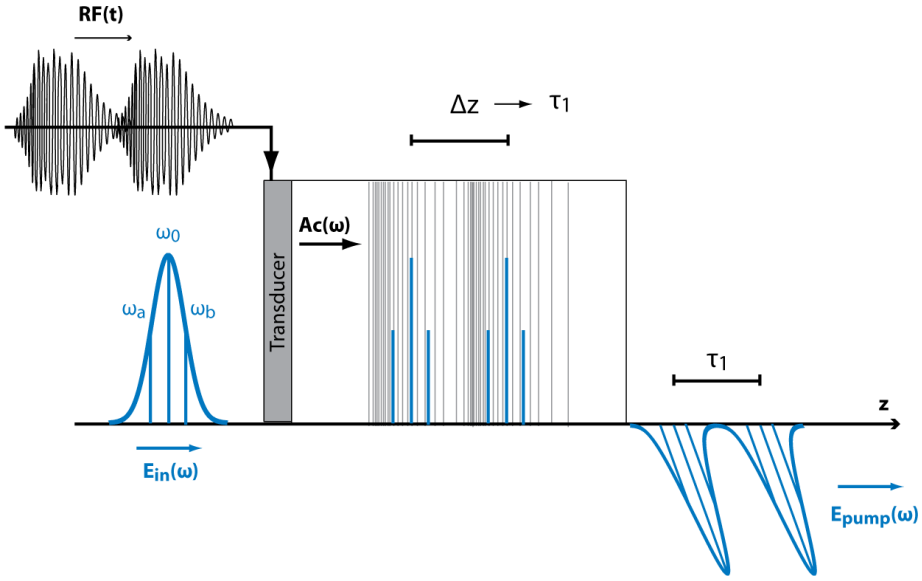


Figure 3.3. Schematic Illustration of the Acousto-Optic Programmable Dispersive Filter Operation for Generating Pulse Pairs. An incident optical pulse (**$E_{in}(\omega)$**, blue) with center frequency, $\omega_0$, and a bandwidth containing the frequencies $\omega_a$ and $\omega_b$ is aligned through a nonlinear medium supporting the acousto-optic interaction (gray outlined box). A tailored waveform in the radio frequency regime is generated and sent to a transducer interfaced with the nonlinear crystal which propagates the acoustic wave (**Ac(ω)**) in the crystal. The index of refraction in the nonlinear medium varies as a function of crystal length (Δz) in the presence of the acoustic wave to tailor the pulse shaping of the incident pulse with arbitrary control of phase and amplitude.

The desired electric field of the two pump pulses, $\mathbf{E}_1(t)$ and $\mathbf{E}_2(t+\tau_1)$, as a function of the $\tau_1$ time delay can be represented as:

$$\mathbf{E}_{pump}(t,\tau_1) = \mathbf{E}_1(t) + \mathbf{E}_2(t+\tau_1) \tag{3.1}$$

$$= A_1(t)e^{-i\omega_0 t} + A_2(t+\tau_1)e^{-i\omega_0(t+\tau_1)} \tag{3.2}$$

where the temporal center of $\mathbf{E}_1(t)$ establishes "time-zero" (t = 0 fs) and is held constant as $\tau_1$ is scanned in time and $\omega_0$ is the angular frequency of the excitation pulse spectrum centroid. The carrier envelope functions for the pulses are given by $A_1(t)$ and $A_2(t+\tau_1)$ which could be defined for Gaussian pulses as $A(t) = e^{-t^2/2\sigma^2}$ where the pulse temporal duration is given by $2\sqrt{2ln(2\sigma)}$. The electric field generated by the AOPDF is expressed as:

$$\mathbf{E}_{AOPDF}(t,\tau_1)=\left[A_1(t)+A_2(t+\tau_1)e^{-i(\Delta\phi_{AOPDF})}\right]e^{-i\omega_{AOPDF}t} \quad (3.3)$$

where $\Delta\phi_{AOPDF}$ and $\omega_{AOPDF}$ are the interpulse phase difference and the angular frequency centroid of the shaped pulse spectral profile, respectively. To correctly generate pulse pairs using the AOPDF, these values must be correctly specified in the AOPDF software to generate the correct RF waveforms for the desired pulse shape. It is important to note that the AOPDF can only directly control the pulse envelope delay and the interpulse phase. The pulse shaper cannot directly delay the entire electric field (e.g., $A_2(t+\tau_1)e^{-i\omega_0(t+\tau_1)}$) but it can control the pulse envelope delay and the interpulse phase to appropriately delay $\mathbf{E}_2$ with respect to $\mathbf{E}_1$ by a given value of $\tau_1$ fs. For a desired $\tau_1$, the $\Delta\phi_{AOPDF}$ value must be equal to the phase defined by[18]

$$\omega_{AOPDF}\tau_1=\Delta\phi_{AOPDF}. \quad (3.4)$$

If this condition is not met, then the pulse envelope $A_2(t+\tau_1)$ is being delayed while the temporal profile of the electric field (i.e., $e^{-i(\omega_{AOPDF}t+\Delta\phi_{AOPDF})}$) remains unshifted, resulting in a carrier-envelope offset rather than the desired temporal field profile reflecting the interference of the two electric fields. The $\Delta\phi_{AOPDF}$ term must also reflect any additional phase offset if phase cycling schemes are used during the experiment. Such a phase offset is simply added to the correct value of $\Delta\phi_{AOPDF}$ for a given $\tau_1$ delay specified by equation (3.4).

The effects of the interpulse phase difference on the resulting time-domain interference of $\mathbf{E}_1$ and $\mathbf{E}_2$ are shown in Figure 3.4. As an example, consider that $\mathbf{E}_1$ and $\mathbf{E}_2$ are replica electric fields delayed by a $\tau_1$ time that is equivalent to an interpulse phase difference of $3\pi$ radians (e.g., 1.5 cycles), then $\mathbf{E}_1$ and $\mathbf{E}_2$ will destructively interfere with each other at the wavelengths which are exactly out of phase. As $\tau_1$ increases to yield an interpulse phase difference equivalent to an integer multiple of $2\pi$ radians, those wavelengths return to constructively

interfering. Clearly, Figure 3.4 (a) shows that the destructive interference is only observed when $\Delta\phi_{AOPDF}$ is properly incremented with $\tau_1$. In those spectra, the pulse spectral centroid is

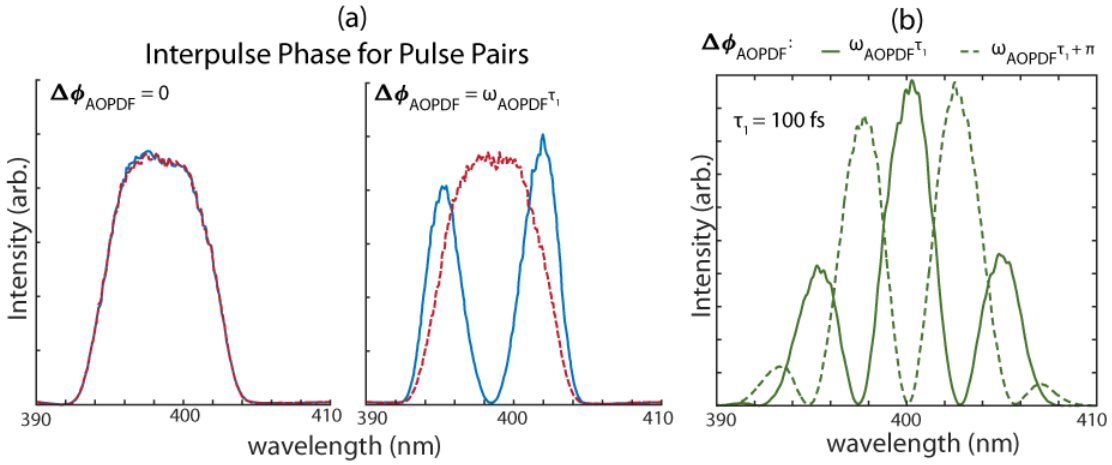


Figure 3.4. Interpulse Phase Difference in Pulse Pair Generation using the AOPDF. (a) The effect of incrementing the interpulse phase difference, $\Delta\phi_{AOPDF}$, with the pulse envelope to generate electric field interference. The spectral intensities have been scaled for comparison (b) The effect of using the interpulse phase difference to also introduce phase differences for use in phase cycling.

398.5 nm, as indicated by the point of complete destructive interference. The effect of an additional phase offset, as would be used in a phase cycling scheme, is shown in Figure 3.4(b), where $\mathbf{E}_1$ and $\mathbf{E}_2$ are delayed by 100 fs and additionally phase shifted by $\pi$ radians. The spectral interferogram indicates this by the fringes being out of phase with respect to one another. It is also important to note that the AOPDF can only produce the desired temporal field of a pulse pair if the spectral centroid of the incident field matches the central frequency parameter input into the AOPDF.[18] That is, $\mathbf{E}_{AOPDF}(t,\tau_1) = \mathbf{E}_{pump}(t,\tau_1)$ from equations (3.1) and (3.3) when $\omega_0 = \omega_{AOPDF}$; in this case, equation (3.4) applies to the shaped electric field correctly. However, if this is not the case, then equation (3.3) must be expressed more accurately as

$$\mathbf{E}_{AOPDF}(t,\tau_1) = \left[A_1(t) + A_2(t+\tau_1)e^{-i(\Delta\phi_{AOPDF})}\right]e^{-i\omega_0 t} \qquad (3.5)$$

while $\Delta\phi_{AOPDF}$ is still evaluated as in equation (3.4), leading to phasing errors in the $\tau_1$ domain data because the delay of the electric field does not match the delay of the electric field envelope: $\omega_0 \neq \omega_{AOPDF}$. These effects can be seen upon Fourier transformation of the $\tau_1$-domain interferences as inaccuracies in the $\omega_1$ frequency axis and through the imaginary part of the FT amplitude containing non-negligible intensity (or conversely, the real part containing significant negative spectral amplitude) as would appear in a traditional interferometer-based 2D experiment. If both $\omega_0$ and $\omega_{AOPDF}$ are known, the true time delay can be determined, and the spectra corrected using the relation

$$\tau_{true} = \frac{\omega_{AOPDF}}{\omega_0}\tau_{AOPDF}. \tag{3.6}$$

An example of the pulse pair being generated correctly and scanned during $\tau_1$ is shown in Figure 3.5 where the spectral interferograms are shown for three delays (0, 50, and 100 fs) for

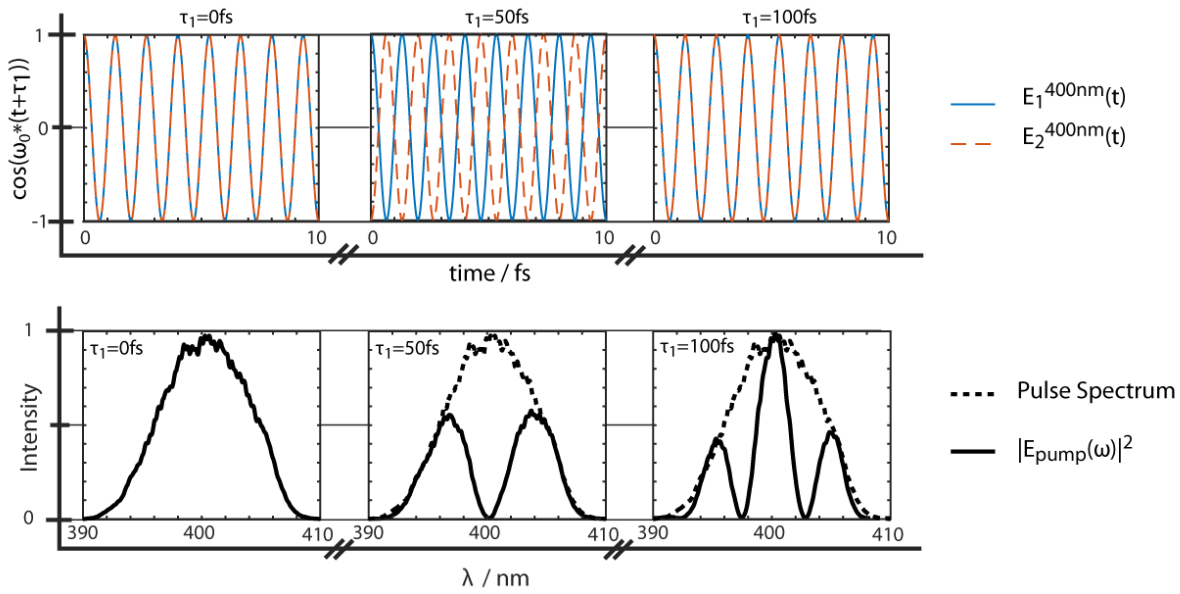


Figure 3.5. Demonstration of a $\tau_1$ Scan Spectral Interferogram. (top) a cosine function with the periodicity of a 400 nm wavelength (continuous wave, in this case) is shown. The blue cosine is $\mathbf{E}_1$ held at time zero and the dashed red cosine is $\mathbf{E}_2$ that is varied by $\tau_1$. (bottom) the incident pulse spectrum (dashed black) and the shaped electric field spectrum of the pulse pair delayed at $\tau_1$ = 0 fs, 50 fs, and 100 fs.

a pulse with a 400 nm centroid. At these delays, the 400 nm wavelength is constructive at 0 and 100 fs but destructive at 50 fs; the periodicity of the 400 nm oscillation is modeled with a cosine function to demonstrate the observed spectral interferogram.

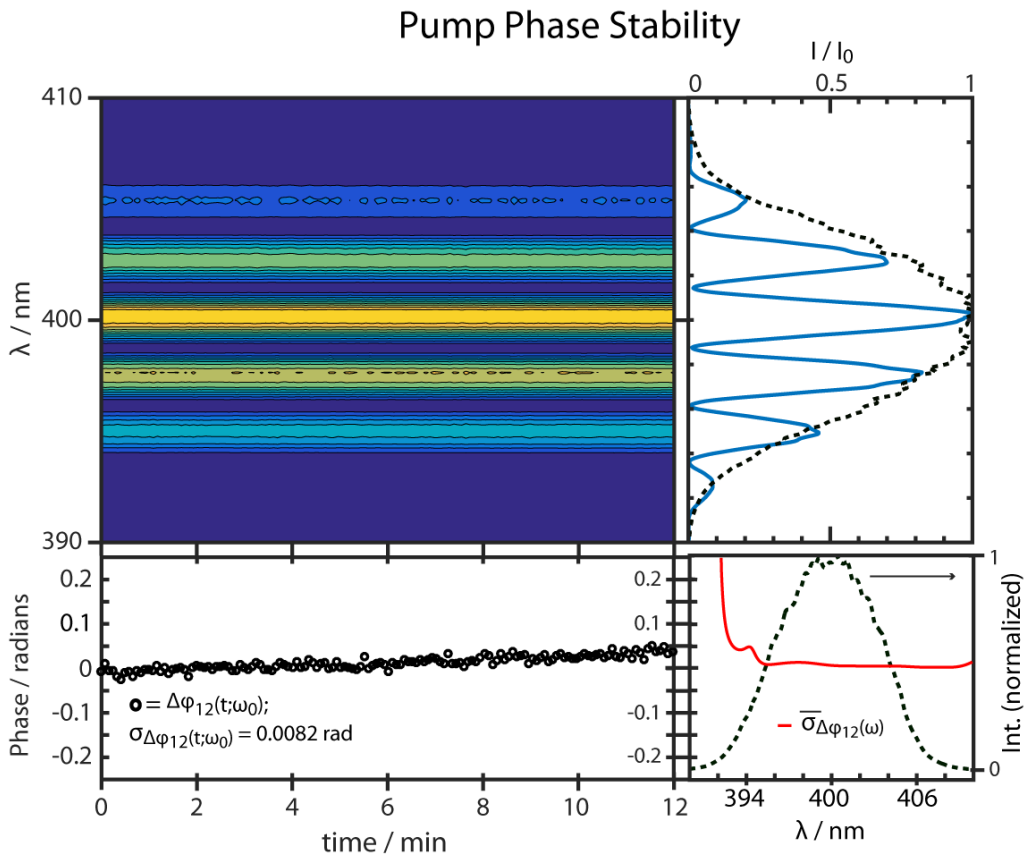


Figure 3.6. Pump Phase Stability. The upper left contour shows the interferogram collected during 12 minutes of laboratory time. The spectral amplitude is normalized and the contours are plotted in 10% levels; the projection of the contour is shown in blue in the upper right. The fringe spacing reflects the 200 fs delay held constant during this measurement. The incident pulse spectrum is overlaid (black dashed, upper right) for reference. FT spectral interferometry quantifies $\sigma_{\Delta\phi_{12}}$ for every spectral interferogram collected over time and is plotted as black circles in the bottom left for $\omega_0$= 400 nm. The averaged phase stability, $\bar{\sigma}_{\Delta\phi_{12}}$ is spectrally represented by averaging $\sigma_{\Delta\phi_{12}}$ over the 12 minute collection window for each pixel of the spectrometer and plotted as a function of wavelength in red (bottom, right); spectrum shown in black dashed for reference. The connected axes between different panels are used to connect the axes between plots.

It is necessary to measure the phase stability of the pump pulse pairs generated in the AOPDF to assess the experimental precision of $\tau_1$. FT spectral interferometry is used to obtain

the experimental interpulse phase difference, $\Delta\phi_{12}$, for a typical 12 minute collection of one 2D EV surface. With $\tau_1$ = 200 fs, a spectral interferogram is obtained every five seconds by collecting 1000 laser shots in an OceanOptics HR2000+ spectrometer (integration time = 1 s). Figure 3.6 shows the interferogram and the extracted $\Delta\phi_{12}$ for the center frequency, respectively. The standard deviation, σ, of $\Delta\phi_{12}$ is measured to quantify the phase stability of the pump pulse pair; $\sigma_{\Delta\phi 12}$ = 0.0082 radians for $\omega_0$, which corresponds to 0.13% of a 400 nm optical cycle and a timing jitter of ±0.0017 fs. The average $\sigma_{\Delta\phi 12}$ for the frequencies within the spectral FWHM of the pump pulses is calculated to be 0.0091 radians. Thus, even for small $\tau_1$ intervals (e.g. $\Delta\tau_1$=0.5 fs), this jitter is negligible.

### 3.3.2 *Broadband IR (BBIR) Probe Generation and Temporal Compression*

The generation of the BBIR probe has been detailed previously[15] and was the subject of Dr. Mark Cheng's dissertation in the Khalil Group;[19] the BBIR temporal compression using a deformable mirror (DM) compressor is discussed in detail elsewhere[20] and was a primary focus of Dr. Madhumitha Balasubramanian's dissertation.[21] The BBIR generation and compression are depicted in Figure 3.7. Briefly, the portion of 2.8 mJ of fundamental undergoes SHG in a BBO (type I) crystal and the resulting 800 nm and 400 nm pulses are matched in polarization, temporally overlapped, and focused into a sealed, 1.2 m stainless steel cell filled with gaseous media, see Figure 3.7(a). Selection of the gas and its pressure produce the BBIR pulse (bandwidth >1000 $cm^{-1}$, 2-8 μm tunable) which is compressed with the combination of a 2 mm Ge plate placed in the beamline for linear dispersion compensation and the DM compressor (see Figure 3.7(b)) with the DM optimized to compress the higher order dispersion and yield the shortest BBIR pulse.[20] The DM consists of a malleable, gold-coated silicon nitride membrane as the reflective surface, behind which are 19 high-voltage actuators (280 V

dynamic range) that deform the surface of the mirror in the horizontal plane; by deforming the mirror's surface, the optical paths of different mid-IR frequencies in the BBIR pulse are varied to achieve temporal compression. The 2D EV spectra shown (Figure 3.9 and Figure 3.10) in this Chapter use air (760 Torr, Figure 3.7(c)) to generate the BBIR pulse (180 nJ, 21 fs); the pulse is characterized by the cross-correlation Frequency Resolved Optical Gating (XFROG) technique[22] using the upconversion signal of BBIR and a small portion of the reference 800 nm pulse in a $LiNbO_3$ crystal (0.1 mm, type I). See Figure 3.7(d) for the temporal intensity and phase of the BBIR as a function of DM optimization. The BBIR characterization signal is collected in an integrated fashion using a photodiode with spectral filters to isolate the sum-frequency signal between the BBIR and the reference 800 nm beams as a function of their temporal delay. To perform the XFROG measurement, the sum-frequency signal is routed to a spectrometer (ThorLabs CCS200) for detection.

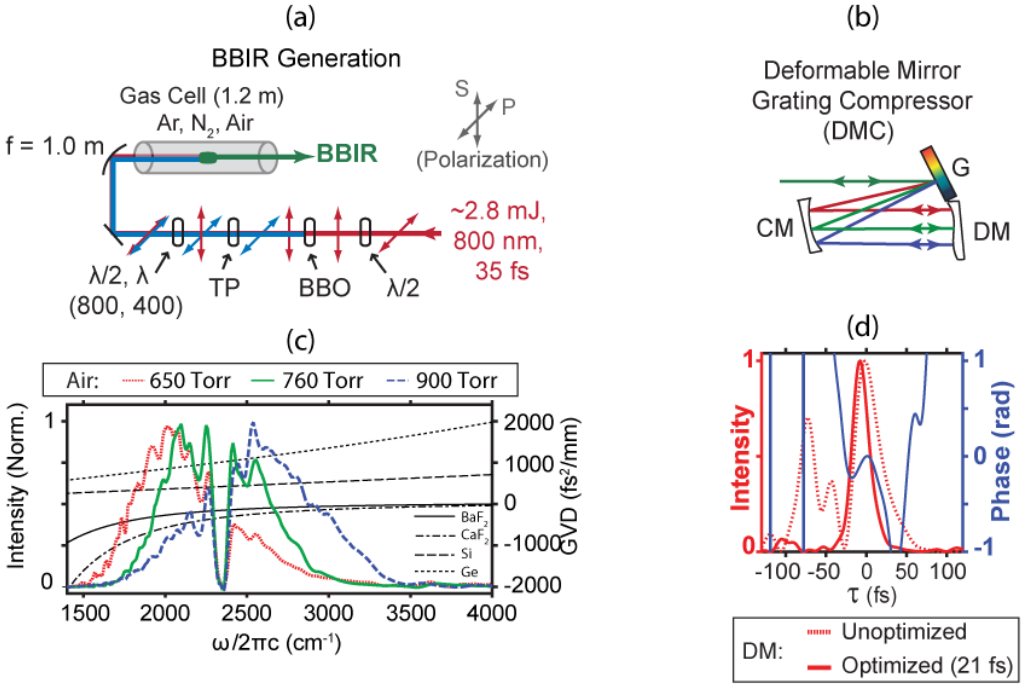


Figure 3.7. BBIR Generation and Temporal Compression. (a) the BBIR generation schematic as described in section 3.3.2. (b) The deformable mirror grating compressor (DMC) arranged in a typical 4f geometry where the DM sits in the Fourier plane.

The temporal intensity and phase of the BBIR field is determined using the FROG algorithm; the spectral and temporal intensities and phases of the reference field are first characterized using the Spectral-phase Interferometry for Direct Electric-field Reconstruction (SPIDER) method, which is then used as an input for the FROG algorithm.

A primary motivation for developing the BBIR probe is to span the entire absorption spectrum of very broad vibrational features of solution phase molecules, such as the OH and NH stretching modes in hydrogen bonded systems where the ground state absorptions can be broader than 500 $cm^{-1}$. Additionally, the FT-limited pulse duration reduces as the spectral content increases which gives the potential to minimize the pulse durations used and measure very fast molecular dynamics with greater temporal resolution. As will be discussed in later chapters, polarization-selective experiments can also be incredibly useful for understanding ultrafast photoexcited molecular dynamics within the molecular frame. These experiments require polarization control using polarizers in the pump and probe beamlines which result in further losses of pulse energy. Given the low BBIR pulse energies generated and the ~50% pulse energy loss through the DMC, additional losses from other optical components are avoided when possible. The BBIR spectra in Figure 3.7 show that our apparatus is tunable, with particular emphasis toward the higher-energy edge of the mid-IR spectrum – towards the OH stretching region (2500-3500 $cm^{-1}$). Experiments targeting the molecular fingerprint region (1200-1600 $cm^{-1}$) are not easily probed in the current configuration of the BBIR pulse generation. For these reasons, the option of using a traditionally generated mid-IR probe source is also used in the experiments presented in this dissertation, as detailed in section 3.3.3.

### 3.3.3 *Mid-IR Pulse Generation from Difference Frequency Mixing of the Output from an Optical Parametric Amplifier (OPA)*

To generate the tunable mid-IR probe, the colinear near-IR output from a home-built, two-pass OPA feeds into a Michelson interferometer which uses a polarizing dichroic beam splitter (SWP-45 RS2000-TP1300; CVI) to separate the OPA signal (1.1-1.5 μm) and idler (1.7-2.1 μm) beams into the two arms of the interferometer and temporally delay the idler pulse with respect to the signal pulse. Each interferometer arm uses a protected gold concave spherical mirror (0.60 m radius of curvature) to retroreflect, spatially overlap back onto the beamsplitter, and focus the beams colinearly into the DFG crystal ($AgGaS_2$, 5 x 5 x 0.5 mm; Newlight Photonics) to generate the mid-IR. Another spherical mirror nearly recollimates the DFG output (leaving the mid-IR slightly diverging) and routes the beam to an AR-coated (2-12 μm) 1 mm Ge window set to Brewster's angle to reflect visible and near-IR beam components while transmitting the mid-IR for use in the experiments and compensating for linear dispersion. A continuous wave HeNe laser is reflectively overlapped spatially with the mid-IR at the Ge filter for alignment throughout the remaining optical setup. The mid-IR probe pulse (~2.5 μJ/pulse when tuned to 5.5-7.8 μm and ~3 μJ/pulse for 3.8-5.3 μm measured after the Ge filter) is delayed by S3 before routing to the pair of Ag-coated off-axis parabolic mirrors (OAP1 and 2, f = 101.5 mm; see Figure 3.2) to focus at the sample area.

The sum frequency generation (SFG) signal between the reference fundamental and the mid-IR in a 100 μm BBO (type I) crystal at the sample area is used for characterization of the OPA/DFG mid-IR pulse (Figure 3.8(c)). First, the reference fundamental must be characterized to deconvolve and extract the mid-IR pulse duration from the SFG FROG measurement; this is achieved using the SHG FROG technique (Figure 3.8(a)). SHG FROG is performed by

splitting the reference beam into two equal intensity portions with one beam routed along a motorized translation stage. The two beams are recombined in a 200 μm thick KDP crystal to produce a delay dependent second harmonic signal as one would do to measure an auto-correlation. Generally, all types of FROG pulse measurement techniques resolve the

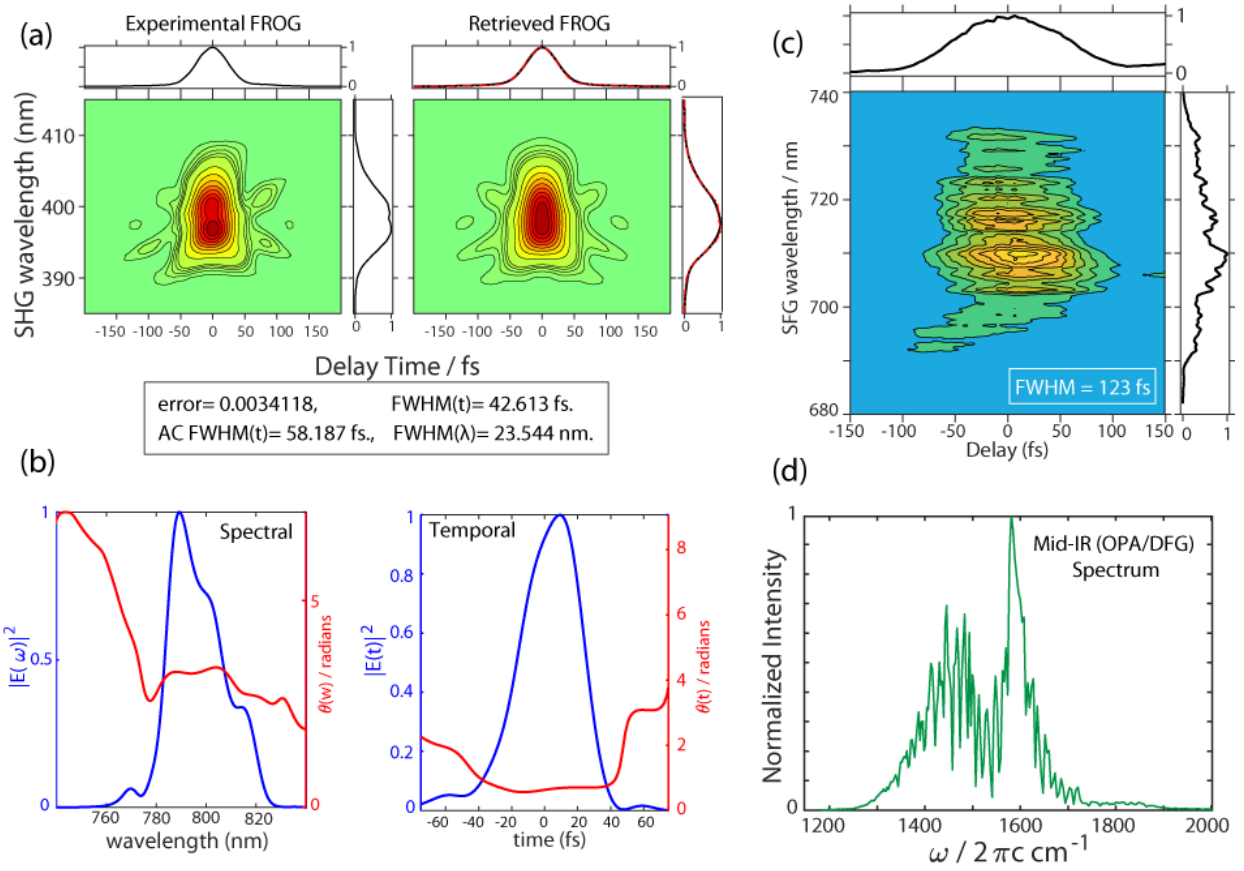


Figure 3.8. Mid-IR Pulse Characterization Generated from the OPA/DFG Process. The reference fundamental beam is characterized using SHG FROG technique and used in assessing the mid-IR pulse duration from the sum frequency generation (SFG) FROG technique. (a) The experimentally measured SHG FROG spectrum (contours), the sum over the wavelength axis (top panel) is the auto-correlation and the sum over the delay time axis (right panel) is the upconverted spectrum of the reference beam. The retrieved SHG FROG spectrum using the FROG algorithm is shown on the right indicating very good agreement [256x256 pixel grid used, time-bandwidth product: 0.47614. Contours span 1 (red) to 0.1 at 10% intervals, with 2% intervals from 0.1 to 0 (green). (b) The retrieved spectral and temporal intensities and phases of the reference electric field. (c) the SFG FROG spectrum (contours span 1 to 0.2 in 10% intervals). The cross-correlation FWHM = 123 fs; the deconvolved mid-IR pulse duration is 115 fs. A 2 mm $CaF_2$ window is placed in the beam path to account for additional dispersion during an experiment due to the sample windows.

time-dependent auto-correlation or cross-correlation signals spectrally using a spectrometer in place of the photodiode.[22-24] The SHG FROG spectrum (Figure 3.8(a), contours) is obtained by collecting a spectrum of the second harmonic signal as a function of time delay between the two portions of the fundamental beam. This describes the auto-correlation in the time-frequency domain, which uniquely allows for the intensity and phase of the electric field to be determined in both the spectral domain and the temporal domain. Visually, the experimentally measured SHG FROG and retrieved SHG FROG spectra (Figure 3.8) show very good agreement; a minimum FROG error of 0.0034 indicates very accurate retrieval of the electric field's intensity and phase profiles while quick algorithm convergence (within a few seconds) confirms that a high-quality (low noise) experimental trace was measured.[22] The extracted 43 fs reference pulse duration (0.476 time-bandwidth product) is reasonable and confirms that our amplifier is producing 35-40 fs pulses as expected; the measured durations are expected to be slightly longer than the ejected pulses from the amplifier as these FROG characterizations are collected at the far end of the optics table after the beams have travelled ~36 feet, interacting with optical components along the way which introduce temporal dispersion.

The SFG FROG spectrum is shown in Figure 3.8(c) for the mid-IR pulse spectrum tuned to the 1200-1700 $cm^{-1}$ region shown in Figure 3.8(d). This spectrum is representative of the OPA/DFG-generated mid-IR probe pulses used during the experiments presented in this dissertation, although some experiments emphasize the 1200-1500 $cm^{-1}$ edge by comparison to this spectrum. Clear spectral distortion due to atmospheric water vapor is present with the $H_2O$ Q-branch resulting in the high-intensity peak at ~1600 $cm^{-1}$. While the mid-IR beam path is enclosed and dried air (~2% relative humidity) is pumped into these boxes, atmospheric water absorption is still present. The FWHM of the SFG cross-correlation is measured to be

123 fs. Deconvolving the cross-correlation with the reference field duration yields a mid-IR probe pulse duration of 115 fs. The SFG signal spectrum (Figure 3.8(c), side panel) results from the sum of one photon of the reference and the mid-IR probe. Considering the FWHM bandwidth of the retrieved reference field (783.5 nm – 806.4 nm), the full-width at 20% of the SFG signal (733 nm – 691 nm) confirms that nearly the entire spectral bandwidth (>2% maximum intensity) of the mid-IR probe is accounted for in this measurement. That is, the SFG signal from the mixing of the low energy side of the reference spectrum and the mid-IR probe at 8065 nm (1240 $cm^{-1}$) yields 733 nm as detected; likewise, the SFG signal of the blue edge of the reference and the mid-IR probe at 5855 nm (1708 $cm^{-1}$) yields 691 nm. While the SFG FROG signal (contours) is principally vertical, there is clearly some higher order dispersion present, likely from the nonlinear dispersion profile of $CaF_2$ in the 5-8μm region, resulting in a positively chirped pulse.

For polarization dependent measurements, the probe transmits through a ZnSe holographic wire grid polarizer (ThorLabs WP25H-Z) set to 45° relative to the input (P) polarized mid-IR pulse immediately prior to OAP1, providing a probe beam incident on the sample which has electric field components in the vertical (S) and horizontal (P) linearly polarized directions. A second ZnSe holographic wire grid polarizer (referred to as the "analyzer") is placed immediately after the sample cell (before OAP2) to select either the P or S polarization component of the signal for detection. The first polarizer is set by finding the maximum and minimum transmission of the incident mid-IR, and then setting it to exactly halfway for the 45° relative polarization during experiments. To set the analyzer, the first polarizer is set at maximum transmission (P) and the analyzer is rotated to maximize (selecting P) and minimize (selecting S) the transmitted intensity. For both polarization experiments, ~325 nJ/pulse of

mid-IR for each polarization is incident on the sample and the analyzer is set to select either P or S polarized signal for the ZZYY or ZZZZ experiments, respectively.

## 3.4 ISOLATING THE 2D EV SIGNAL

As chapter 2 discusses, the 2D EV signal arises from the time dependent third order macroscopic polarization, $\mathbf{P}^{(3)}$, which can be calculated using standard perturbation theory as a convolution of the third order vibronic response function, $\vec{\vec{\mathbf{R}}}^{(3)}$, with the three incident electric fields of the laser pulses. The electric field at the sample representing a sequence of three laser pulses used in a 2D EV experiment can be described by the sum $E(t) = \sum_{i=1}^{3} E_i(t)$ and each pulse field described as

$$E_i(t) = A_i(t - t_i)\exp[-i(\omega_i^0(t - t_i) + \phi_i - \mathbf{k}_i)\cdot\mathbf{r}] \tag{3.7}$$

where $A_i(t)$ is the pulse envelope of the *i*th pulse that is temporally centered at $t_i$, has carrier frequency $\omega_i^0$, an absolute phase $\phi_i$ relative to a common reference and a wavevector $\mathbf{k}_i$ with its projection onto a laboratory frame directional unit vector $\mathbf{r}$. Many different transition pathways contribute to the molecular response, resulting in the third order polarization taking on a complicated form. However, $\mathbf{P}^{(3)}$ can be expressed as the sum of all third order polarizations for each individual pathway

$$\mathbf{P}^{(3)}(t) = \sum_s \mathbf{P}_s^{(3)}(t)\exp[-i\omega_s t + \mathbf{k}_s\cdot\mathbf{r}] \tag{3.8}$$

where the four-wave mixing condition for generating the signal is $\omega_s = \pm\omega_1 \mp \omega_2 + \omega_3$ and the phase-matching condition defining the third-order signals detected is $\mathbf{k}_s = \pm\mathbf{k}_1 \mp \mathbf{k}_2 + \mathbf{k}_3$. Therefore, the frequency and wavevector of the emitted signal field is $\omega_{sig} = \omega_s$ and $\mathbf{k}_{sig} = \mathbf{k}_s$. Notably, the wavevectors' projections into the laboratory frame relate their geometric

orientation with respect to one another and their linear combination has the consequence of determining the direction in which the emitted field radiates. For the same reason, the magnitudes of these wavevectors will also contribute to the spatial direction of the emitted signal which is proportional to the carrier frequencies of the fields. As the magnitudes and directions of the wavevectors differ from one another, the emitted signal field is affected accordingly. In 2D EV spectroscopy, where the magnitudes of the pump and probe fields differ by roughly an order of magnitude, the spatial separation of the emitted signal into a background-free direction becomes very challenging. To circumvent this, the partially collinear ("pump-probe") beam geometry can be used in which $\mathbf{k}_1 = \mathbf{k}_2 \neq \mathbf{k}_3$ resulting in the signal field emitting collinear with the probe field. This is different from the traditional "boxcar" geometry used in fully noncollinear 2D spectroscopies that typically employ laser pulses of nearly degenerate carrier frequencies which facilitates the detection of a spatially isolated signal field. In the partially collinear geometry, the collinear and coincident probe field serves as an intrinsic local oscillator for self-heterodyned detection of the emitted signal.

The partially collinear beam geometry has the disadvantage of the desired 2D EV signal co-propagating with the transient absorption signals that are the result of two light-matter interactions with the same pump pulse as well as a static background from the probe beam. Thus, the total amplitude of the emitted third-order field is expressed

$$\left|\tilde{\mathbf{E}}^{(3)}_{total}(\tau_1,\tau_2,\omega_3;\Delta\phi_{12})\right|^2 = \left|\left(\tilde{\mathbf{E}}^{(3)}_{sig}(\tau_1,\tau_2,\omega_3)+1\right)\mathbf{E}_3(\omega_3)\right|^2 \tag{3.9}$$

where $\mathbf{E}_3(\omega_3)$ is the probe (local oscillator) field and the emitted signal field is expanded as

$$\tilde{\mathbf{E}}^{(3)}_{sig}(\tau_1,\tau_2,\omega_3) = \tilde{\mathbf{E}}^{(3)}_{2D}(\tau_1,\tau_2,\omega_3) + \tilde{\mathbf{E}}^{(3)}_{PP1}(\tau_1=0,\tau_2,\omega_3) + \tilde{\mathbf{E}}^{(3)}_{PP2}(\tau_1+\tau_2,\omega_3). \tag{3.10}$$

The $\tilde{\mathbf{E}}^{(3)}_{PP1}$ and $\tilde{\mathbf{E}}^{(3)}_{PP2}$ terms in equation (3.10) are the background transient-IR signals resulting from $\mathbf{k}_1$ and $\mathbf{k}_2$, respectively, and the 2D EV signal field of interest is $\tilde{\mathbf{E}}^{(3)}_{2D}$. The total amplitude is measured using a square law detector represented by rewriting equation (3.9) as

$$\begin{aligned}&\left|\tilde{\mathbf{E}}^{(3)}_{total}(\tau_1,\tau_2,\omega_3;\Delta\phi_{12})\right|^2 = \\ &\left|\tilde{\mathbf{E}}^{(3)}_{2D}(\tau_1,\tau_2,\omega_3)\mathbf{E}_3(\omega_3)\right|^2+\left|\left(\tilde{\mathbf{E}}^{(3)}_{PP1}(\tau_1=0,\tau_2,\omega_3)+\tilde{\mathbf{E}}^{(3)}_{PP2}(\tau_1+\tau_2,\omega_3)+1\right)\mathbf{E}_3(\omega_3)\right|^2 \\ &+2\,\mathrm{Re}\left[e^{i\Delta\phi_{12}}\tilde{\mathbf{E}}^{(3)}_{2D}(\tau_1,\tau_2,\omega_3)\left(\tilde{\mathbf{E}}^{(3)}_{PP1}(\tau_1=0,\tau_2,\omega_3)+\tilde{\mathbf{E}}^{(3)}_{PP2}(\tau_1+\tau_2,\omega_3)+1\right)^*\right]\left|\mathbf{E}_3(\omega_3)\right|^2\end{aligned} \tag{3.11}$$

where multiplication of each signal field with the probe (local oscillator) field is given in the $\omega_3$ frequency domain obtained by Fourier transformation over the time-domain ($\tau_3$) interference of $\mathbf{E}^{(3)}_{sig}(\tau_1,\tau_2,\tau_3)$ with $\mathbf{E}_3(\tau_3)$ convoluted with the three laser fields and represented as $\tilde{\mathbf{E}}^{(3)}_{sig}(\tau_1,\tau_2,\omega_3)\mathbf{E}_3(\omega_3)$. Importantly, these third order signals differ in their dependence on $\tau_1$ and $\Delta\phi_{12}$, the interpulse phase difference between $\mathbf{k}_1$ and $\mathbf{k}_2$ (i.e., $\Delta\phi_{12}=\phi_1-\phi_2$). The background signals can be removed by modulating this phase difference because $\tilde{\mathbf{E}}^{(3)}_{2D}$ acquires an overall prefactor, $e^{i\Delta\phi_{12}}$, while the others are unaffected. This is where phase cycling schemes can be applied to systematically change $\Delta\phi_{12}$ as a parameter during experimental data collection; repeating the 2D measurement *n* different times with *n* different values of $\Delta\phi_{12}$ that are evenly spaced around the unit circle will modulate the collected signal by this phase factor.[25] Summing over the total collected experimental signals then yields

$$\begin{aligned}&\frac{1}{n}\sum_{j=0}^{n-1}e^{-i(2\pi j/n)}\left|\tilde{\mathbf{E}}^{(3)}_{total}(\tau_1,\tau_2,\omega_3;\Delta\phi_{12}=2\pi j/n)\right|^2 \\ &=2\mathbf{E}^{(3)}_{2D}(\tau_1,\tau_2,\omega_3)\,\mathrm{Re}\left[\mathbf{E}^{(3)}_{PP1}(\tau_1=0,\tau_2,\omega_3)+\mathbf{E}^{(3)}_{PP2}(\tau_1+\tau_2,\omega_3)+1\right]\left|\mathbf{E}_3(\omega_3)\right|^2 \\ &\simeq 2\mathbf{E}^{(3)}_{2D}(\tau_1,\tau_2,\omega_3)\left|\mathbf{E}_3(\omega_3)\right|^2.\end{aligned} \tag{3.12}$$

The experiments described in this dissertation utilize mechanical chopping, where each alternating pump pulse pair is blocked by a chopper operating at half of the laser repetition rate, which removes the probe background signals in the same way as described for phase cycling. It should be noted that the mechanical chopping approach requires two spectra to obtain a difference spectrum: one with the sample "pumped" and one with the sample "un-pumped". The subtraction of these two spectra yield the desired signal for a given $\tau_1$ and $\tau_2$. This is equivalent to a 2x1 (n=2) phase cycling scheme[25] where $\Delta\phi_{12} = [0, \pi]$. Using the chopping method, the $\mathbf{E}^{(3)}_{PP1}(\tau_1 = 0, \tau_2, \omega_3)$ signal results in a $\tau_1$-independent signal offset and is removed by subtraction prior to FT over $\tau_1$. The $\mathbf{E}^{(3)}_{PP2}(\tau_1 + \tau_2, \omega_3)$ signal varies only with the $\mathbf{E}_2$ pulse envelope resulting in a much more slowly decaying $\tau_1$-dependent signal that is easily separated by Fourier transformation.

While the cross-terms between the 2D EV and transient-IR signal terms are not completely removed, they scale quadratically with the third order field and contribute negligible intensity by comparison to the desired 2D signal that scales linearly in the third order field. As implied by equation (3.12), a division of a reference field is necessary to finally isolate the desired 2D EV signal.

## 3.5 Demonstrating 2D EV Spectroscopy with a BBIR Probe

### 3.5.1 *2D EV in Silicon: Mapping the Spectral Footprint of the 2D EV Spectrometer*

To demonstrate the capability of the 2D EV experiment with the BBIR probe, a 2D EV spectrum of a 0.25 mm thick Si wafer is collected at $\tau_2$=200 fs; two 2D EV surfaces (1000 shots per $\tau_1$) are averaged (Figure 3.9, contour). When Si is excited with light of equal or greater energy than its bandgap (1.12 eV, 1107.2 nm) a change in carrier density results from

the excitation of valence band electrons to the conduction band. The long-lived (nanoseconds) electron-hole pairs result in a pump-probe delay-dependent reduction of IR transmission. This effect is often used to characterize the duration of ultrafast mid- to far-IR pulses by fitting the decay width as it corresponds to the convolution of the pump and probe pulse durations [26].

Similarly, I have characterized our 2D EV experiment by detecting the change in BBIR transmission due to pumping Si with AOPDF-generated near-UV pulse pairs (400 nm, FWHM=10 nm). A FT over $\tau_1$ (0-100 fs, $\Delta\tau_1$=0.5 fs) resolves the near-UV pump frequencies coupled to the BBIR probe frequencies. The contour plot in Figure 3.9 shows the real part of the FT of the 2D EV signal. The resultant 2D EV peak extends to all $\omega_1$ and $\omega_3$ positions with appreciable pump and probe spectral amplitude (Figure 3.9, top and side panels). The full BBIR spectral axis for the data shown in Figure 3.9 is stitched together from spectra collected using nine different grating positions and bandpass filters (2.5-5.1 μm or 4.5-8.5 μm) at the spectrometer entrance to eliminate higher diffraction orders from the grating. The 2D EV signal of Si is expected since Si has a bandgap well below the pump frequencies and a broadly uniform transmission curve in the mid-IR. In effect, this is simply a map of our 2D EV instrument response that shows the full range of excitation and detection frequencies usable in this 2D EV experiment.

Notably, significant signal-to-noise in the 2D EV spectrum is obtained even on the wings, as demonstrated by magnifying by factors of 4 (1650-1750 $cm^{-1}$ and 2700-3000 $cm^{-1}$) and 22 (1500-1750 $cm^{-1}$ and 3000-3300 $cm^{-1}$) on either side of $\omega_3$ in the 2D spectrum. More than an octave of mid-IR frequencies are clearly able to be associated with the pump in this 2D EV set-up. Thus, the 2D EV experiment in Si represents the wide range of mid-IR frequencies capable of being directly correlated to photo-induced molecular dynamics arising from the

pumps in this set-up. The incorporation of the BBIR probe in our 2D EV experiment will allow molecular dynamics that display very broad spectral features (e.g. –OH stretches) or involve many well-separated spectral signatures (e.g. –C=O and –NH stretches) to be simultaneously correlated, in a single experiment, with ground and excited electronic state dynamics.

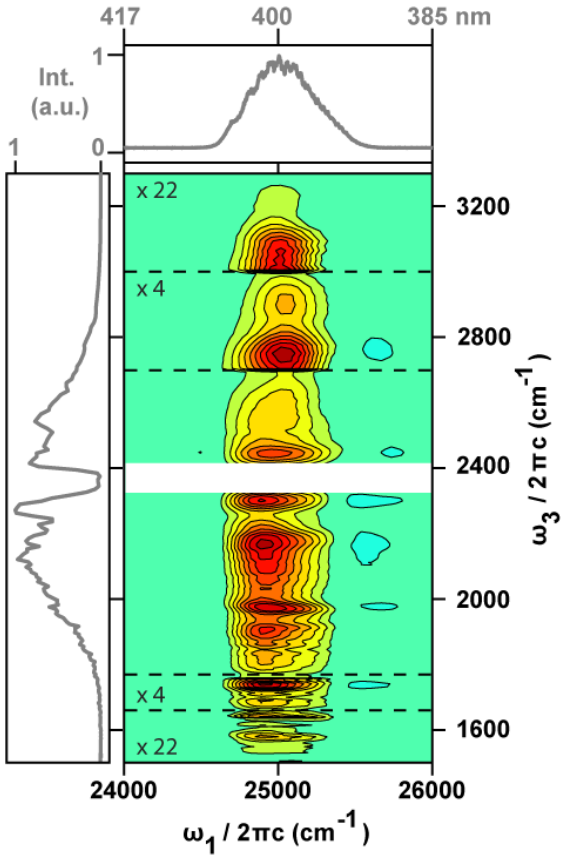


Figure 3.9. The 2D EV spectrum of Si; $\tau_2$=200 fs. The real part of the FT is plotted as –ΔT with red=positive (green=0, blue=negative) contours plotted from -1 to 1 every 10%; Savitzky-Golay filtering is used to remove the effect of atmospheric water absorption in the BBIR spectra. The top and side panels show pump and probe spectra, respectively.

### 3.5.2 *Demonstrating 2D EV of a Condensed Phase Molecular Ensemble*

To demonstrate the viability of our 2D EV set-up for probing condensed-phase molecular systems, a 2D EV spectrum of potassium hexacyanoferrate (III) ($K_3[Fe(CN)_6]$) dissolved in formamide (FA) was measured. The 2D EV spectrum of $K_3[Fe(CN)_6]$ in FA shown in Figure

3.10 is obtained by averaging three 2D EV surfaces; 3000 laser shots are collected for each $\tau_1$ (scanned over 0-100 fs, $\Delta\tau_1$=0.5 fs). The chemicals were used as received from Sigma Aldrich. The sample was held in a 0.14 mm path length enclosed by 1 mm $CaF_2$ windows (ISP Optics) in a brass flow cell to refresh the irradiated sample volume at a 1 kHz rate. Solvent-subtracted linear spectra gave absorbances of 0.42 OD at 25000 $cm^{-1}$ and 0.30 OD in the $\nu_{CN}$ stretching region (2109 $cm^{-1}$) as measured with a JASCO V-630 spectrometer and a JASCO FT/IR 4100 spectrometer.

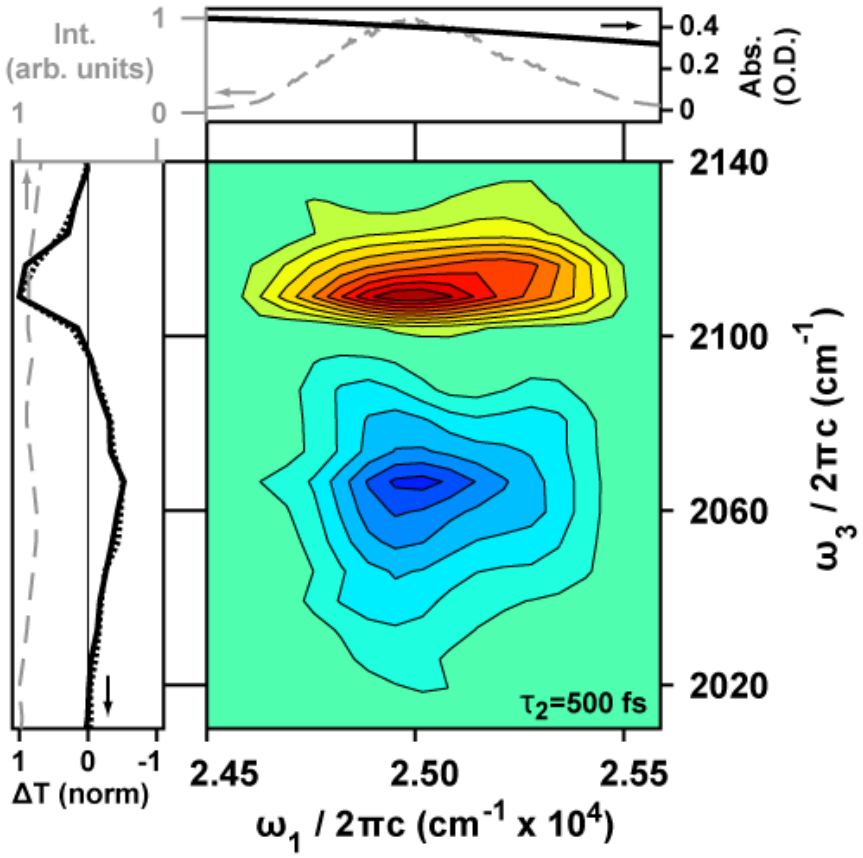


Figure 3.10. The 2D EV spectrum of $K_3[Fe(CN)_6]$ in FA. The spectrum is normalized to the absolute maximum value in the 2D plot and plotted from -1 to 1, contour separation = 10%.

In this iron complex, the goal is to correlate the ligand-to-metal charge transfer (LMCT), $\nu_{LMCT,\ max}$ = 23585 $cm^{-1}$, with the cyanide (CN) stretching vibrations ($\nu_{CN}$). Previous work by

Zhang *et. al.* studied $K_3[Fe(CN)_6]$ in two different solvents using polarization-selective transient-IR spectroscopy to monitor CN vibrations that reflect electron hole delocalization of the photoexcited LMCT state [27]. They identified the population of a secondary LMCT excited state *via* the appearance of two distinct IR-active $\nu_{CN}$ modes and attributed the vibrational dynamics to localization of the LMCT state on a single CN ligand. However, isolating the relevant solute and solvent degrees of freedom for this hole solvation process requires further investigation.

The 2D EV spectrum in Figure 3.10 contains two peaks. The ground state bleach (GSB) is the narrow, positive (red contours) signal at $\omega_3 = 2109$ cm$^{-1}$ that results from a population of the ground electronic state following two light-matter interactions with the near-UV pump pulses and an absorption of the BBIR probe pulse by the $\nu_{CN}$ modes in the sample. The broad excited state absorption (ESA) is the negative (blue contours) signal shifted lower in energy at $\omega_3 = 2067$ cm$^{-1}$ that results from the weakening of the CN bond in the electronic excited-state. The dashed gray lines in the top and side panels show the pump and probe spectra, respectively. The solid black lines in the top and side panels show the electronic absorption spectrum and the transient-IR spectrum, respectively. The dotted black line is the integrated projection onto the probe axis obtained by summing horizontally across the 2D EV spectrum.

As expected, the integrated projection of the 2D EV spectrum onto $\omega_3$ matches the transient-IR spectrum. This confirms that the measured 2D EV spectrum accurately reflects the physical characteristics of the molecular response in accord with the projection slice theorem. The transient-IR spectrum is qualitatively similar to results in.[27] In the spectra reported here, the GSB and ESA peaks are blue shifted by ~10 cm$^{-1}$ as compared to Ref. [27] due to the FA solvent. The third-order signal is found to be linearly dependent on pump power,

which ensures that no higher order signals are contributing to the observed signal. A more in-depth discussion of the amplitudes features in the 2D EV spectra of $K_3[Fe(CN)_6]$ in FA at various $\tau_2$ delays will be presented in a later chapter.

## 3.6 CONCLUSION

In conclusion, this chapter has detailed the development of the 2D EV spectrometer in the Khalil group which uses AOPDF-shaped near-UV pump pulses and mid-IR sources including a temporally compressed, octave-spanning BBIR probe pulse. This work extends the reach of the 2D EV technique along both the pump and probe dimensions. It is expected that BBIR probing in 2D EV experiments will prove useful for studying coupled electronic and vibrational dynamics in the high frequency and, perhaps, finger print region of the vibrational spectrum in the electronic excited state. Further developments of the spectrometer will be discussed in a later chapter that includes implementing broader and tunable UV sources into the pump dimension to explore the relevant electronic and vibrational coordinates driving electron and proton transfer in solution.

## 3.7 APPENDICES

### 3.7.1 *Dazzler Alignment Notes*

Section 3.3.1 describes the operating principle of the AOPDF. Since the acoustic wave is generated in the crystal in a fixed manner using the transducer electronics to translate the RF waveform into a compression wave, it is up to the user to ensure that the optical pulse and the acoustic wave propagation vectors are maximally overlapped. This is achieved by optimizing the vertical and horizontal placement of the Dazzler crystal in the plane perpendicular to the beam propagation using the two-axis micrometer on which the Dazzler is mounted, and by

adjusting the rotation of the Dazzler crystal module. The input beam must be < 3 mm in diameter entering the Dazzler; the UV Poynting vector must be well aligned on the table with the Dazzler removed from the beamline using a dedicated iris (labelled “Dazz in”) to properly optimize the acousto-optic interaction when the Dazzler is placed in the beamline. The alignment is set using both a spectral measurement and a shaped pulse energy measurement. After the UV Poynting beam is well aligned with the Dazzler removed, the Dazzler is raised vertically into the beam path. The user should set the center wavelength and bandwidth to represent the input pulse spectrum; if beginning without prior knowledge of dispersion parameters, the self-compression “self-c” mode should be selected which sets the dispersion to exactly counteract the dispersion of the AOPDF crystal. With an RF waveform loaded in the Dazzler software so that the Dazzler is pulse shaping, the vertical and horizontal movement using the two-axis micrometer is set by optimizing the shaped pulse energy measured further downstream. The shaped pulse will be spatially offset ($<10^{o}$) and clearly viewable after ~1 m of distance after the Dazzler; this shaped beam is isolated and detected spectrally or using a power meter. Once the the vertical and horizontal positions are set, the beam should be viewed spectrally. A comparison of the input beam and the shaped beam spectrum should be used to assess how well the shaping parameters are set in the Dazzler software to shape the incident electric field. Fine adjustment of the vertical and horizontal translation may provide slightly better agreement between the input and shaped pulse spectra without suffering much loss in shaped pulse energy.

If the self-compression settings require dispersion (typically greatest magnitude in $\phi_2$) such that the RF waveform completely fills the crystal shaping window as viewed in the Dazzler

software, then pre-compression of the input pulse (e.g., using a prism compressor) is required to optimally shape the incident field.

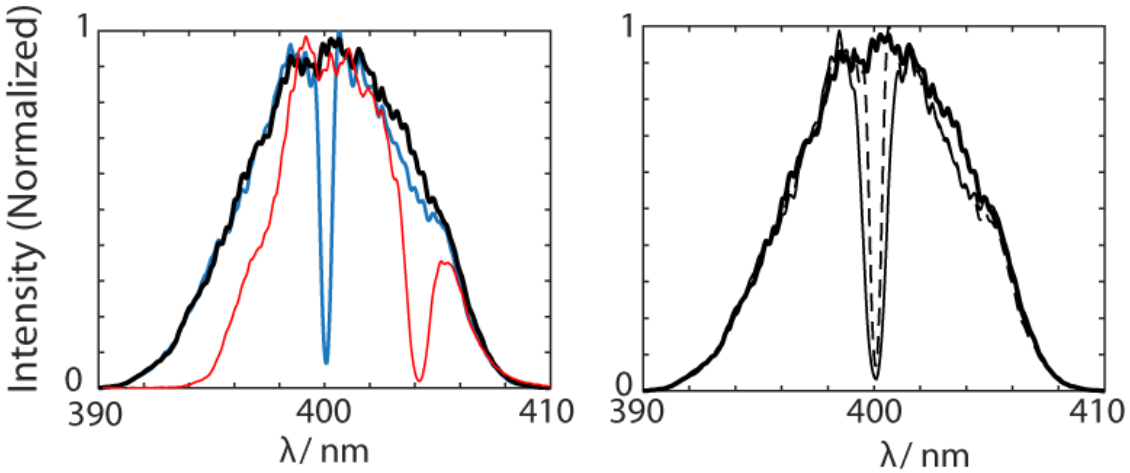


Figure 3.11. Spectral Effects of Improper Dazzler Alignment. (left) A spectral hole has been programmed for 0.5 nm width, 1.0 depth and to be centered at 400 nm. The solid black line is the incident spectrum, the blue is the correctly aligned spectrum with the hole burnt, and the red line is an improperly aligned Dazzler crystal module (principally due to incorrect rotational setting). (right) the spectra for hole burning widths of 0.5 nm (dashed) and 1.0 nm (solid, thin).

Typically, negative dispersion must be added to the incident pulse that is equal to, or greater than, the change in the value of the $\phi_2$ parameter in the Dazzler software necessary for the RF waveform to be contained within the shaping window. Less than optimal shaping will also be clear if the shaped pulse spectrum is not replicating the input pulse spectrum measured in the spectrometer. The final step in alignment is to set the rotation of the Dazzler crystal to optimize the acousto-optic interaction. First, a spectral hole should be burnt in the shaped spectrum using the software settings (typically hole depth = 1.0 and 0.5-1 nm hole width is used) at the spectral centroid, then the rotation of the crystal module is set such that the shaped spectrum has the spectral hole at the intended wavelength set in the Dazzler software software. Repeating this for wavelengths other than the centroid helps to ensure that the rotation is properly set. The effect of improper alignment through the Dazzler is shown in Figure 3.11.

## 3.8 REFERENCES


(1) Lewis, N. H. C.; Dong, H.; Oliver, T. a. A.; Fleming, G. R. Measuring correlated electronic and vibrational spectral dynamics using line shapes in two-dimensional electronic-vibrational spectroscopy; *J. Chem. Phys.* **2015**, *142*, 174202.

(2) Oliver, T. a. A.; Lewis, N. H. C.; Fleming, G. R. Correlating the motion of electrons and nuclei with two-dimensional electronic-vibrational spectroscopy; *Proc. Natl. Acad. Sci. U.S.A.* **2014**, *111*, 10061-10066.

(3) Oliver, T. a. A.; Fleming, G. R. Following Coupled Electronic-Nuclear Motion through Conical Intersections in the Ultrafast Relaxation of beta-Apo-8 '-carotenal; *J. Phys. Chem. B* **2015**, *119*, 11428-11441.

(4) Lewis, N. H. C.; Fleming, G. R. Two-Dimensional Electronic-Vibrational Spectroscopy of Chlorophyll a and b; *J. Phys. Chem. Lett.* **2016**, *7*, 831-837.

(5) West, B. A.; Womick, J. M.; Moran, A. M. Interplay between Vibrational Energy Transfer and Excited State Deactivation in DNA Components; *J. Phys. Chem. A* **2013**, *117*, 5865-5874.

(6) Luber, S.; Adamczyk, K.; Nibbering, E. T. J.; Batista, V. S. Photoinduced Proton Coupled Electron Transfer in 2-(2'-Hydroxyphenyl)-Benzothiazole; *J. Phys. Chem. A* **2013**, *117*, 5269-5279.

(7) Goyal, P.; Schwerdtfeger, C. A.; Soudackov, A. V.; Hammes-Schiffer, S. Nonadiabatic Dynamics of Photoinduced Proton-Coupled Electron Transfer in a Solvated Phenol-Amine Complex; *J. Phys. Chem. B* **2015**, *119*, 2758-2768.

(8) West, B. A.; Moran, A. M. Two-Dimensional Electronic Spectroscopy in the Ultraviolet Wavelength Range; *J. Phys. Chem. Lett.* **2012**, *3*, 2575-2581.

(9) Selig, U.; Schleussner, C. F.; Foerster, M.; Langhojer, F.; Nuernberger, P.; Brixner, T. Coherent two-dimensional ultraviolet spectroscopy in fully noncollinear geometry; *Opt. Lett.* **2010**, *35*, 4178-4180.

(10) Tseng, C. H.; Matsika, S.; Weinacht, T. C. Two-Dimensional Ultrafast Fourier Transform Spectroscopy in the Deep Ultraviolet; *Opt. Express* **2009**, *17*, 18788-18793.

(11) Coudreau, S.; Kaplan, D.; Tournois, P. Ultraviolet acousto-optic programmable dispersive filter laser pulse shaping in KDP; *Opt. Lett.* **2006**, *31*, 1899-1901.

(12) Weber, S.; Barthelemy, M.; Chatel, B. Direct shaping of tunable UV ultra-short pulses; *Appl. Phys. B* **2010**, *98*, 323-326.

(13) Krebs, N.; Pugliesi, I.; Hauer, J.; Riedle, E. Two-dimensional Fourier transform spectroscopy in the ultraviolet with sub-20 fs pump pulses and 250–720 nm supercontinuum probe; *New J. Phys.* **2013**, *15*, 085016.

(14) Myers, J. A.; Lewis, K. L. M.; Tekavec, P. F.; Ogilvie, J. P. Two-color two-dimensional Fourier transform electronic spectroscopy with a pulse-shaper; *Opt. Express* **2008**, *16*, 17420-17428.

(15) Cheng, M.; Reynolds, A.; Widgren, H.; Khalil, M. Generation of tunable octave-spanning mid-infrared pulses by filamentation in gas media; *Opt. Lett.* **2012**, *37*, 1787-1789.

(16) Cerullo, G.; De Silvestri, S. Ultrafast optical parametric amplifiers; *Rev. Sci. Instrum.* **2003**, *74*, 1-18.

(17) Krebs, N.; Probst, R. A.; Riedle, E. Sub-20 fs pulses shaped directly in the UV by an acousto-optic programmable dispersive filter; *Opt. Express* **2010**, *18*, 6164-6171.

(18) Krebs, N. *New Insights for Femtosecond Spectroscopy: From transient absorption to 2-dimensional spectroscopy in the UV spectral domain* Ph.D. Dissertation, Ludwig Maximilian University, 2013.

(19) Cheng, M. *Application and Development of 2D IR spectroscopy for the Study of Complex Biological Systems* Ph.D. Dissertation, University of Washington, 2013.

(20) Balasubramanian, M.; Courtney, T. L.; Gaynor, J. D.; Khalil, M. Compression of Tunable Broadband Mid-IR Pulses with a Deformable Mirror Pulse Shaper; *J. Opt. Soc. Am. B* **2016**, *33*, 2033-2037.

(21) Balasubramanian, M. *Studying Ultrafast Vibrational Dynamics of Intramolecular Hydrogen Bonds using Broadband Infrared Pump-Probe Spectroscopy* Ph.D. Dissertation, University of Washington, 2018.

(22) Trebino, R. *Frequency-Resolved Optical Gating: The Measurement of Ultrashort Laser Pulses*; Kluwer Academic Publishers: Boston, MA. USA, 2000.

(23) Kane, D. J.; Trebino, R. Single-Shot Measurement of the Intensity and Phase of an Arbitrary Ultrashort Pulse by Using Frequency-Resolved Optical Gating; *Opt. Lett.* **1993**, *18*, 823-825.

(24) Kane, D. J.; Trebino, R. Characterization of Arbitrary Femtosecond Pulses Using Frequency-Resolved Optical Gating; *IEEE J. Quantum Elect.* **1993**, *29*, 571-579.

(25) Tan, H. S. Theory and phase-cycling scheme selection principles of collinear phase coherent multi-dimensional optical spectroscopy; *J. Chem. Phys.* **2008**, *129*.

(26) Zheng, L.; Meyerhofer, D. D. Cross-Correlation Technique for Single-Shot Measurements of Weak Light-Pulses; *Opt. Lett.* **1995**, *20*, 407-409.

(27) Zhang, W. K.; Ji, M. B.; Sun, Z.; Gaffney, K. J. Dynamics of Solvent-Mediated Electron Localization in Electronically Excited Hexacyanoferrate(III); *J. Am. Chem. Soc.* **2012**, *134*, 2581-2588.

# Chapter 4. GENERATING FEMTOSECOND BROADBAND NEAR-ULTRAVIOLET PULSES FOR NONLINEAR SPECTROSCOPY

*The work presented in this chapter has been published in the following papers:*

*1) Gaynor, J.D.; Leger, J.D.; Khalil, M. "Generating Broadened UV Pulses for Ultrafast Nonlinear Experiments" Frontiers in Optics + Laser Science Conference Proceedings* ***2018****, DOI:10.1364/FIO.2018.JTu2A.8.*

*2) Gaynor, J.D.; Petrone, A.; Li, X.; Khalil, M. "Mapping Vibronic Couplings in a Solar Cell Dye with Polarization-Selective Two-Dimensional Electronic-Vibrational Spectroscopy" Journal of Physical Chemistry Letters* ***2018****, 9, 21, 6289-6295.*

*3) Khalil, M., Gaynor, J.D., Leger, J.D.; Sandwisch, J.W. "Efficient Generation of Stable sub-20 fs 400 nm Pulses for High Order Nonlinear Spectroscopy" U.S. Provisional Patent Application* ***2019****, 62/897,032; (filed on 6 Sept. 2019).*

## 4.1 INTRODUCTION

A natural requirement for the progress of ultrafast molecular spectroscopy is the ability to generate spectrally broadband light sources in regions where molecular transitions of interest reside. Often, an extension of the spectroscopic toolbox is a primary catalyst for new and exciting scientific enquiry. In practice, the contemporary optical table for performing coherent multidimensional spectroscopies will have on it many more optical components than detectors, filters, lenses, mirrors, and gratings; likely including much more sophisticated components making use of specific types of nonlinear processes with ever tighter performance thresholds. An important parameter is the pulse energy cost of using an optical component. While femtosecond pulse shaping technologies have made more complicated experiments feasible, especially in the UV spectral ranges studied in this dissertation, they are accompanied with a typical pulse energy cost on the order of 50-90% of the incident pulse energy. Thus, sufficiently

high energy pulses are required for multidimensional spectroscopic applications using pulse shapers, such as the 2D EV experiments described in this dissertation.

Recently, more advanced broadband pulse generation methods have been demonstrated,[1] such as filamentation in gaseous media,[2] gas-filled hollow core fibers,[2-7] self-phase modulation (SPM) in bulk media[8-10] and in thin-media,[7,11-14] and achromatic frequency doubling;[15] many of which have since been implemented successfully in nonlinear molecular spectroscopies.[16-27] The plot in Figure 4.1 displays a generalized parameter space of typical femtosecond pulsed light sources demonstrated in nonlinear molecular spectroscopies in terms of the spectral bandwidth and pulse energies available for spectroscopic use. The optical parametric amplification (OPA) methods are reliable and proven for generating stable, tunable, and fairly broadband femtosecond pulsed light sources that have been used in nonlinear spectroscopies;[28-33] these sources are shown as solid outlined boxes. However, this figure shows that these OPA methods generally result in an order of magnitude loss in pulse energy moving from the near-IR region (1-2 μm) to the UV region (0.2-0.4 μm). The more recent pulse generation methods including filamentation, hollow core fiber compressors, and self-phase modulation discussed above can provide higher pulse energies in various spectral regimes throughout the near-IR and visible but they have been limited in spectroscopic application in the UV range. In many cases, 0.1-1 μJ pulse energies are important in nonlinear spectroscopies when used for the initial excitation of the sample whereas the probe interaction can comfortably be in the ≤100 nJ regime. These more recent broadband pulse generation techniques have been applied in nonlinear molecular spectroscopies throughout the UV region with UV pump pulse energies less than 0.1 μJ,[34,35] with a few exceptions.[36,37] While some nonlinear multidimensional experiments can successfully operate in the UV within this low pulse energy regime, these are

usually energetically degenerate techniques meaning they interact with electronic transition dipole moments in each light-matter interaction. This is important because the magnitude of the molecular extinction coefficients for the transitions in the pump and probe interactions are very similar which provides a nonlinear signal magnitude that can be sufficiently resolved. The 2D EV and 2D VE experiments differ greatly from the nearly degenerate multidimensional spectroscopies in this respect. The relevant extinction coefficients in these experiments can vary by several orders of magnitude so a greater fraction of excited state molecules may be necessary to achieve sufficient signal to noise. Thus, greater excitation pulse energy is needed.

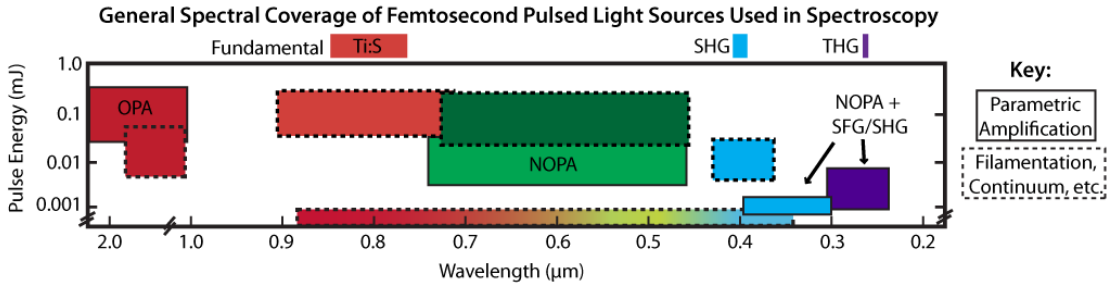


Figure 4.1. General Spectral Coverage of Femtosecond Pulsed Light Sources Demonstrated in Nonlinear Spectroscopic Experiments. The solid outlined boxes represent traditional sources derived from parametric amplification to span from the near-IR to the UV ranges. The dashed outlined boxes represent more recently developed methods employed in nonlinear spectroscopies based on references given in section 4.1.

Additionally, having a broad spectral bandwidth in the excitation domain for 2D spectroscopies is important because the intrinsic advantage to a 2D spectroscopy over its pump-probe analogue is the spectral resolution of the excitation axis. Here, the goal is to correlate as many molecular dynamics as possible among many different excited states and many different detected states through correlations revealed in 2D peaks defined by different excitation ($\omega_1$) and detection ($\omega_3$) frequencies. Altogether, a spectrally broadened UV excitation pulse is needed which has $\geq$ 10 μJ / pulse energies prior to pulse shaping to be used in our 2D EV spectrometer due to the 10-15% conversion efficiency of the UV pulse shaper in

the 380-440 nm region. This region in Figure 4.1 is empty except for the dashed box centered at 400 nm which is the subject of this chapter. The multiplate continuum generation method[9,10,32] has been driven largely by the need for broadband, single-cycle driving pulses for higher harmonic generation in the high energy physics community; it is adapted here for the needs of our tIR and 2D EV spectrometer. Much of the established spectroscopic toolbox employed in studies described in this dissertation was detailed in chapter 3. In this chapter, the development and implementation of a broadband near-UV (BBUV, 380-440 nm) light source for use in tIR and 2D EV experiments is detailed. The focus of this chapter is on the light source's generation, while a complete discussion of the temporal compression will be discussed in future work.

## 4.2 Theoretical Background: Ultrafast Pulse Propagation in Nonlinear Media (In Brief)

The index of refraction, $\eta$, in a transparent nonlinear medium can be expressed as

$$\eta = \eta_0 + \eta_2 I(t) \tag{4.1}$$

where the linear index of refraction, $\eta_0$, is the real part of the material dielectric constant which accurately describes the electric field propagation in the low intensity limit and scales the propagation velocity of an optical wavevector through the material by the relation $\mathbf{k}(\omega) = \eta_0(\omega)\left(\frac{\omega}{c}\right)$ with the angular velocity of the electric field, $\omega$, and the speed of light in vacuum, *c*. The speed of a light wave travelling through a transparent medium is then defined by $v = c/\eta$ where $\eta > 1$ because the propagating electric field in the dielectric material is slowed by its interaction with the dielectric environment resulting from the electronic structure

of the material. The nonlinear index of refraction, $\eta_2$, is an expansion coefficient of $\eta$ about a time-dependent electric field propagating through the material truncated to second order; the coefficient is of second order because $I(t) = \langle \mathbf{E} \cdot \mathbf{E} \rangle \propto |\mathbf{E}|^2$.[38] This nonlinear coefficient contributes non-negligibly when the material's electronic structure can be polarized by strong enough electric fields transmitting through a dielectric material (a distortion which occurs on 0.1-1 fs timescales). In the case of a tens of femtoseconds duration optical field (i.e., with high peak power) propagating through a dielectric medium with high nonlinearity, the temporal- and spatial-dependence of the electric field will have significant consequences for the pulse propagation through the medium.

### 4.2.1 *Self-Phase Modulation (SPM): Effects from Electric Field Temporal-Dependence*

For the electric fields relevant to the experiments in this discussion, the slowly varying envelope approximation is valid since the pulse durations generally represent several cycles of the UV fields of interest. Thus, $I(t)$ describes the pulse envelope ( $A(t)$ ) rather than the UV carrier frequencies. As the pulse traverses the nonlinear medium, the electric field induces a change in $\eta$ through $\eta_2$ that is proportional to the instantaneous pulse intensity. This results in a nonlinear phase shift of the electric field propagating through a material of length, L, which can be defined as

$$\Delta\phi_{NL}(t) = -\frac{\omega}{c}\eta_2 I(t) L = -\frac{2\pi}{\lambda}\eta_2 I(t) L \tag{4.2}$$

and results from the optical Kerr effect.[32,33] The temporal phase of the electric field is used to great effect in continuum generation through imparting SPM in the electric field to produce spectrally broader bandwidths of the propagating electric fields.[39] The effect on the pulse envelope's temporal duration due to nonlinear time-dependent phase is given by

$$A'(t) = e^{i\Delta\phi_{NL}(t)} A(t). \tag{4.3}$$

The relation to the resulting pulse spectrum, $\tilde{A}'(\omega)$, is directly dependent on the instantaneous frequency, $\omega_{inst}$, of the electric field which is simply the temporal derivative of the electric field's phase given by

$$\omega_{inst} = \omega_0 + \frac{d\Delta\phi_{NL}(t)}{dt}. \tag{4.4}$$

For materials with $\eta_2 > 0$, the temporal variation in $\omega_{inst}$ (commonly known as "chirp") of the pulse is positive since the rising and falling edges in the temporal intensity cause the spectrally broadened pulse frequencies to increase with time. Equation (4.4) demonstrates that the new frequency components in $\tilde{A}'(\omega)$ are directly dependent on the temporal derivative of $\Delta\phi_{NL}(t)$. In the pure SPM limit (no dispersion or losses), the spectral shape becomes symmetrically broadened about $\omega_0$ with a periodically modulated intensity profile due to the interference between the spectral components generated from the rising edge and the falling edge of the temporal pulse intensity. In principle, nearly destructive interference between these two periods of phase modulation should occur; in practice, the incident electric field's temporal profile and dispersion, and the temporal distortions and dispersion accumulated during the SPM process can wash-out this modulation (see Figures 6.1-6.3 in *Ultrafast Optics* (Weiner, 2009) and discussion therein).[32]

### 4.2.2 *Self Focusing: Effects of Electric Field Spatial-Dependence (Beam Mode)*

The spatial-dependence of the incident electric field is also important when considering that the $\eta_2$ is a material property that will vary spatially in the plane perpendicular to the pulse propagation. For $\eta_2 > 0$, a larger phase shift is experienced on the beam propagation axis (z)

than at its wings resulting in the focusing of the beam as a function of its propagation along z. The spatial mode of the electric field can induce an index modulation along the propagation distance described in terms of a two-dimensional (x and y which define the plane perpendicular to beam propagation) Gaussian intensity distribution with a uniform phase front as

$$\eta \simeq \eta_0 \left( 1 - \frac{2\eta_2 I_0 r^2}{\eta_0 w^2} \right) \tag{4.5}$$

where $w$ is the $1/e^2$ beam radius, $I_0$ is the on-axis intensity, and r is the radial distance in (x,y) away from the z axis describing the beam mode. Using the thin lens and paraxial approximations[38] for the case of a thin dielectric medium, the z-dependent phase accumulated as a result of self-focusing describes the phase shift spatially imprinted onto the beam as a function of the $1/e^2$ beam radius at a given z position through the medium,

$$\Delta\phi_{NL}(z,r,t) = \frac{(2\pi/\lambda)\eta_2 I_0(t) L}{1+(z/z_R)^2} \mathrm{e}^{-2r^2/w^2(z)} \equiv \Delta\phi_{NL}(z,t) e^{-2r^2/w^2(z)} \tag{4.6}$$

where $z_R$ is the Rayleigh range, and z = 0 is assumed to be at the beam waist.

Comparison of equations (4.2) and (4.6) demonstrate that the spectral bandwidth and the spatial beam mode will be coupled to one another through the accumulated nonlinear phase, $\Delta\phi_{NL}(t)$. The dielectric medium thickness, L, is also a major parameter in these equations. In thick media, the beam can actually come to a focus resulting in spatially and temporally localized ultrahigh amplitude fields generating unwanted filamentation (unstable white light generation), beam breakup, dielectric breakdown, and other parasitic nonlinear effects.[38] The distinction between “thin” and “thick” depend heavily on the dielectric material and the spatial and temporal properties of the electric field. In the application and implementation of the BBUV light source discussed below, multiple “thin” plates are used in sequence to spectrally

broaden a portion of the 800 nm fundamental beam prior to SHG. These plates are "thin" because the self-focal distance is placed outside of the dielectric medium (i.e., after the pulse has exited the medium) due to the pulse's time-dependent intensity profile and the glass plates used as the dielectric broadening media which avoids unwanted nonlinear processes and emphasize SPM. The spectral profile and spatial (beam mode) uniformity of the resulting BBUV pulse are parameters considered for optimization.

A comparison of SPM broadened UV spectra is shown in Figure 4.2 using a thick nonlinear medium (1 mm $CaF_2$) and multiple thin media (the multiplate continuum scheme described in section 4.3). While the thicker medium can still effectively broaden incident electric fields, the pulse energies required in this broadening geometry were limited to ~1 μJ before undesirable beam break up and multiple filamentation dominated the beam propagation. Although more effort to loosen the beam focal conditions for using SPM in thick media could improve the spectral broadening and beam quality, the multiple thin plate medium shows much greater pulse broadening and control over the spectral intensity profile. The multiple thin plates method can emphasize SPM as the main broadening mechanism to greater effect for the reasons described above. The strong intensity modulation of the purple spectrum in Figure 4.2(b) demonstrates strong SPM broadening, as expected for a pulse with normal dispersion affecting the temporal profile at each plate transmission.[32] Since the accumulated nonlinear phase is directly responsible for the SPM broadening, the temporal intensity dependence of $\Delta\phi_{NL}(t)$ can be exploited by adjusting the thin plate positions with respect to the focal position of the broadening beam induced by the self-focusing from the previous thin plate. In this way, the strong spectral intensity modulations can be washed out by adjusting the last few plates to obtain a smoother spectral intensity profile that may be desired in nonlinear spectroscopic use.

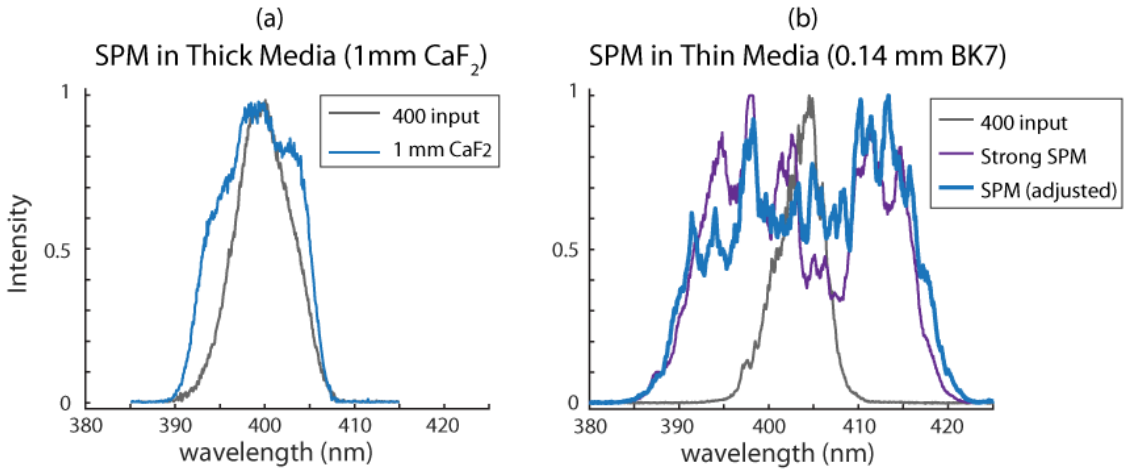


Figure 4.2. Self-Phase Modulation (SPM) induced Spectral Broadening in the UV Using Nonlinear Media of Differing Thickness. (a) An incident 400 nm pulse (1 μJ, gray spectrum) is focused by a f=100 mm lens into a 1 mm thick $CaF_2$ plate that is placed 0.25 cm after the beam focus; resulting broadened UV spectrum is shown in blue. (b) BBBUV spectra from using the multiplate continuum method with 4 BK7 plates (0.14 mm thick) is shown (blue and purple). The plates are set for optimal SPM in the purple spectrum as evidenced by the spectral intensity modulation. The inter-plate separation can be adjusted to minimize the destructive interference from the accumulated nonlinear phase at various points in the temporal propagation of the broadening UV pulse to obtain a less modulated spectral intensity without sacrificing bandwidth.

## 4.3 BBUV Pulse Generation

A similar multi-plate continuum method reported by He *et al.*[11] and Lu *et al.*,[14] which has also been successfully used to pump broadband OPA setups[13] was adapted to the 2D EV spectrometer for use in our nonlinear spectroscopies. A similar method was demonstrated for the UV spectral range beginning with an intense second harmonic that was broadened using the multi-plate method[12] rather than broadening the fundamental as discussed in this chapter. This multi-plate method works by minimizing the interaction length of the pulse in the dielectric broadening medium which suppresses parasitic and destructive nonlinear processes (e.g., multiphoton absorption, multiple filamentation, pulse break up) while enhancing self-phase modulation to achieve spectral broadening, as detailed in section 4.2.

The BBUV is generated by focusing a 250 μJ (10 mm beam diameter) portion of the fundamental using a f = 1 m concave mirror (Newport, HR 600-1000 nm) into a series of thin

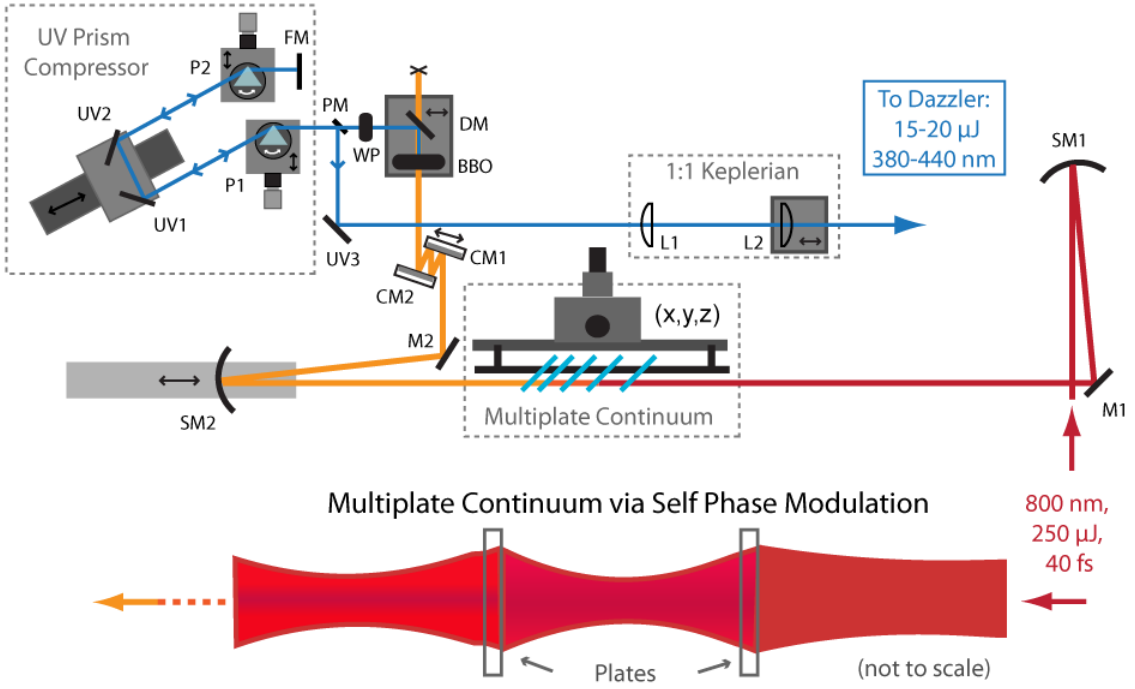


Figure 4.3. Broadband UV Pulse Generation using the Multiplate Continuum Method Schematic. (top) The beam propagation schematic is laid out; SM (1,2) = concave spherical mirrors, M1 = 800 nm HR-coated mirror, M2 = protected Ag-coated mirror, CM(1,2) = dispersion compensating chirped mirrors, BBO = 0.1 mm BBO type 1 crystal, DM = 400 nm HR dichroic mirror, WP = UV λ/2 waveplate, P(1,2) UV fused silica Brewster's angle prisms, UV(1-3) = low-GDD 355-445 HR-coated mirrors, PM = UV-enhanced Al pick-off mirror, L(1,2) f=100 mm UV AR-coated UV fused silica lenses. (bottom) schematic depiction of the broadening fundamental beam propagation through the multiplate continuum generation; here the self-focusing induced by each plate is exaggerated for demonstration.

glass plates of either BK7 (140 μm thick, VWR International microcover glass, 22 x 30 mm) or fused silica (100 μm thick, Valley Design corp., 25 x 25 mm) set at ~Brewster's angle to minimize reflective losses. We generally follow the multiplate design and simulations by Lu *et al.*[14] We place the first plate slightly away from the focus of the beam to avoid pulse break up given our tighter focusing condition and greater incident pulse energy. Placement of the first plate before and after the natural focus of the incident fundamental beam have been used and the plate positions are empirically determined by optimizing the spectral broadening for each added plate while maintaining a spatially homogeneous beam profile. As section 4.2 describes, this is indicative of maximizing the temporal phase accumulated as the beam

propagates through each plate. The high peak power at the focus of the fundamental (~28 TW/cm$^2$) is well above the critical power for self-focusing in fused silica (2 MW),[14,38,40] each transmission through a plate where this is satisfied will induce a self-focusing. The 0.1 mm plate thicknesses are thinner than the self-focal distance in fused silica which has been measured for similar pulse fluences to occur within 0.5 mm of a "thick" fused silica plate at the incident beam waist.[14] Spatio-temporal evolution simulations show that the passage through the first plate results in a ~1.5π phase shift that is sufficient to bring the pulse to a focus within 1 cm of exiting the plate.[40] Such a phase shift is also observed spectrally in our generation scheme by viewing a destructive interference in the spectral center as is expected from the description of $\Delta\phi_{NL}(t)$ given above.[32] As the pulse exits the plate, a change in $\eta$ for atmospheric gaseous media governs the focusing and defocusing of the beam. The approximate point at which the beam begins to defocus is where the next plate is placed to maintain a critical beam fluence high enough to continue inducing spectral broadening through the accumulated nonlinear phase in the SPM process; the exact placement is again optimized by maximizing spectral broadening while maintaining uniformity in the transverse beam profile of the BBUV pulse. In practice, our first and second plates are placed ~2.5-3 cm apart, which is consistent with other multiplate continua set ups.[11,14] Notably, the electric field envelope will become positively chirped at each plate transmission and so the focused beam intensity in consequent plate transmissions will reach a threshold where negligible improvement in spectral broadening is achieved and only unwanted pulse energy losses and distorted beam profiles result. In routine practice, the number of plates used to generate a BBUV spectrum is determined by finding this threshold; typically 2-5 plates are used, depending on the plate material. A notable advantage of this approach is the transmission efficiency of the input fundamental to the output spectrally

broadened pulse – typically 90-95% transmission efficiencies are achieved for spectrally broadening the incident fundamental.

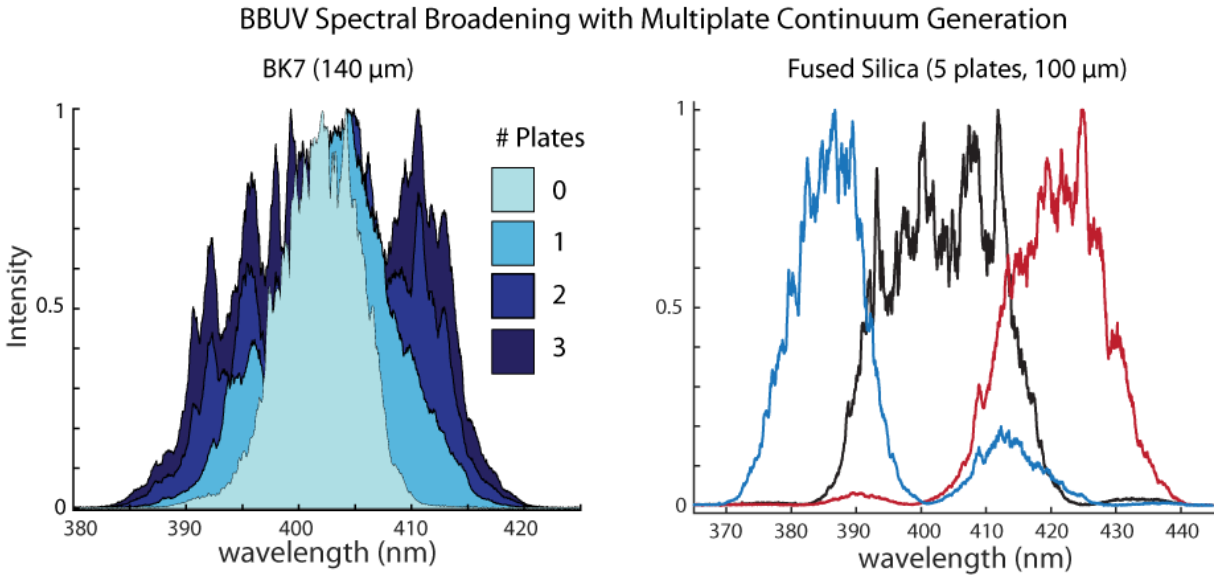


Figure 4.4. BBUV Spectra From Multiplate Continuum Generation. (left) The BBUV generation showing the effect of number of BK7 plates used on the spectral broadening; the FWHM increases from ~8 nm to ~25 nm. (right) BBUV generation using 5 fused silica plates and the spectral tunability by adjusting the tuning angle of the BBO crystal. The nodes appearing on the tails of the spectra reflect phase-mismatch between the bandwidth of the broadened fundamental and the bandwidth of the upconverted BBUV spectra. Note the differences in wavelength axes of the two plots.

The resulting broadened fundamental is recollimated by a concave Ag-coated mirror (Newport, f = 0.4 m, Low-GDD, HR 600-1100 nm, 10BV80EAG.1) which down-collimates the beam to a ~2.5 mm diameter of the $1/e^2$ beam radius. The beam is then routed through a pair of chirped mirrors (Newport, 10Q20UF.42, 700-890 nm, -45 $fs^2$/bounce) using a variable number of bounces (typically either two or four) for dispersion compensation and optimizing BBUV pulse intensity. The broadened fundamental beam is then upconverted in a 100 µm thick BBO (type I, Newlight Photonics) to generate the BBUV pulse which is spectrally isolated from the fundamental using a dichroic HR-coated mirror for the UV. The BBUV beam passes through a waveplate to become P (horizontally) polarized before going through a UV prism compressor (Newport Brewster's angle cut prism pair, 10SB10 UV fused silica, 185-

2100 nm) in a folded geometry. Except for the folding mirror (LayerTech, UV HR-coated, 0° AOI) and the pickoff mirror (ThorLabs, UV enhanced Al, PFSQ05-03-F01), all mirrors used for the rest of the BBUV beam line are low-GDD, UV HR-coated (355-445 nm, ThorLabs UM10-45U) to reduce dispersion. An additional Keplerian telescope (ThorLabs UV fused silica plano-convex lenses, LA4380-UV AR coated, f = 100 mm) prior to passing through the Dazzler is used for controlling shaping efficiency and the shaped beam profile at the sample area.[41] The prism compressor is used to pre-compress the BBUV pulse with a negative chirp (46 cm prism separation) due to the bandwidth of the incident pulse and the accumulated positive chirp resulting from transmission through a ~50 mm quartz crystal. With a negatively chirped incoming pulse to the Dazzler set to shape 30-35 nm bandwidth with a spectral centroid of 390-410 nm (depending on BBUV generation conditions), the second order dispersion can be set to a lesser magnitude value than the self-compression dispersion settings so the RF waveform is not truncated at the edges of the pulse shaping window determined by the crystal length without compromising the performance of the Dazzler.

With the generation scheme described above, BBUV pulse energies of 15-20 μJ prior to pulse shaping in the Dazzler have been readily achievable and are limited largely by the conversion efficiency of the SHG in the BBO. The UV spectral coverage available is also limited by the phase-matching bandwidth in the BBO but can be tuned to cover the range 370-440 nm (see Figure 4.4) by adjusting the BBO tuning angle providing a spectral FWHM ranging from 15-22 nm, more than doubling the 8-9 nm FWHM bandwidth of the SHG of the unbroadened fundamental. Transient-Grating FROG (TG FROG) measurements[42] using the reference fundamental beam characterize the BBUV compressed duration to be ~ 30 fs for use in nonlinear experiments, although the BBUV pulse duration has been measured to be as short

as 15 fs, which is comparable to the 10-12 fs FT limit depending on the BBUV spectral bandwidth.

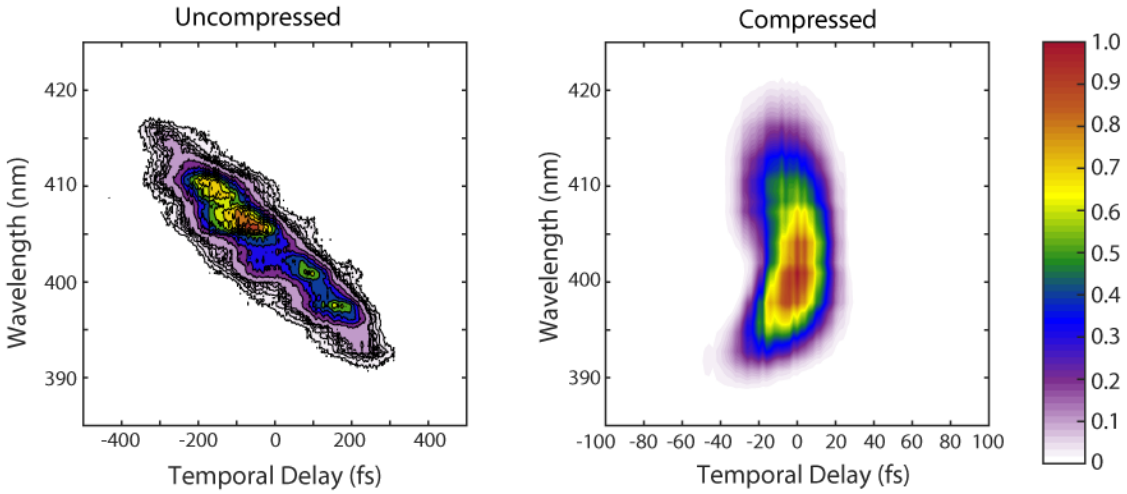


Figure 4.5. Temporal Compression of the BBUV Pulse. The uncompressed pulse (left) displays primarily positive linear chirp resulting from BBUV generation and inadequate temporal dispersion compensation; FWHM pulse duration is ~350 fs. The compressed pulse (right) results from the BBUV generation including all of the temporal dispersion compensation shown in Figure 4.3. Higher order dispersion limits this FWHM pulse duration to ~30 fs.

The RMS fluctuations of the BBUV pulse intensity for 12-16 hour periods are measured to be 1%, compared to a similar stability for ~8 hours using BK7 plates. This is likely due to the order of magnitude difference of the thermal expansion coefficients in these materials. As any single experimental data collection period is typically no longer than 8 hours, both materials provide sufficient stability for use in experiments. During data collection, the shaped pulse energy is measured between data runs to ensure that a consistent pump pulse energy is maintained throughout the experiment. The plates are mounted on a two-axis micrometer so vertical and horizontal adjustments in the perpendicular plane to beam propagation are available to refresh the beam spot on the plates to avoid photodamage during long laser runs. The vertical adjustment is typically used to refresh the beam's spot on the plates because it does not change the relative positioning of the plates to the focusing fundamental while the

horizontal adjustment does change this. We have found empirically that the BBUV spectral shape and pulse energy is less sensitive to fine adjustments in the horizontal position of the plates in the focusing beam path but that the shot-to-shot stability can be optimized with fine horizontal adjustments while monitoring the BBUV pulse train using a detector and an oscilloscope.

### 4.3.1 *Specific Experimental Notes*

#### 4.3.1.1 BBUV Generation for $N3^{4-}$ Experiments

The first iteration of the BBUV generation set-up was used in the $N3^{4-}$ experiments discussed in chapters 7-8. The full details of these experiments can be found in the supporting information of *Gaynor, et al.*[43] The BBUV pulses in those experiments used 2-3 BK7 plates with the fundamental focused in a transmissive geometry using AR-coated lenses of the same focal lengths described above. The dispersion control in these experiments did not include low-GDD mirrors or chirped mirrors and relied entirely on the prism compressor. The temporal profile of the pump pulse (similar to the TG FROG measurement in Figure 4.5(left)) limited the instrument response function to subsiding by $\tau_2$ delays of 180-200 fs.

#### 4.3.1.2 BBUV Generation for HBQ Experiments

The BBUV pulses generated in the tIR and 2D EV experiments on HBQ and DBQ in chapter 9 used the configuration exactly as described in section 4.3.

## 4.4 CONCLUSION

In this chapter, a full description of how the BBUV pulse is generated for use in the nonlinear multidimensional experiments presented in this dissertation. The multiplate continuum generation method is found to broaden the UV pulses *via* SPM with significantly

increased bandwidth than using thicker bulk media to induce SPM. This is principally due to the fact that the thin nonlinear media induce self-focusing to occur outside of the nonlinear medium which minimizes the undesirable nonlinear processes which contribute to pulse break up. The accumulated nonlinear phase, $\Delta\phi_{NL}(t)$, can be optimized by setting the plates to maximize spectral broadening and maintain uniform transverse beam mode of the generated BBUV pulse.

## 4.5 REFERENCES


(1) Dubietis, A.; Couairon, A.; Genty, G. Supercontinuum generation: introduction; *J. Opt. Soc. Am. B* **2019**, *36*, SG1-SG3.

(2) Gallmann, L.; Pfeifer, T.; Nagel, P. M.; Abel, M. J.; Neumark, D. M.; Leone, S. R. Comparison of the filamentation and the hollow-core fiber characteristics for pulse compression into the few-cycle regime; *Appl. Phys. B* **2007**, *86*, 561-566.

(3) Chang, H. T.; Zurch, M.; Kraus, P. M.; Borja, L. J.; Neumark, D. M.; Leone, S. R. Simultaneous generation of sub-5-femtosecond 400 nm and 800 nm pulses for attosecond extreme ultraviolet pump-probe spectroscopy; *Opt. Lett.* **2016**, *41*, 5365-5368.

(4) Duhr, O.; Nibbering, E. T. J.; Korn, G.; Tempea, G.; Krausz, F. Generation of intense 8-fs pulses at 400 nm; *Opt. Lett.* **1999**, *24*, 34-36.

(5) Nibbering, E. T. J.; Duhr, O.; Korn, G. Generation of intense tunable 20-fs pulses near 400 nm by use of a gas-filled hollow waveguide; *Opt. Lett.* **1997**, *22*, 1335-1337.

(6) Belli, F.; Abdolvand, A.; Travers, J. C.; Russell, P. S. J. Highly efficient deep UV generation by four-wave mixing in gas-filled hollow-core photonic crystal fiber; *Opt. Lett.* **2019**, *44*, 5509-5512.

(7) Hwang, S. I.; Park, S. B.; Mun, J.; Cho, W.; Nam, C. H.; Kim, K. T. Generation of a single-cycle pulse using a two-stage compressor and its temporal characterization using a tunnelling ionization method; *Sci. Reports* **2019**, *9*, 1613.

(8) Bradler, M.; Baum, P.; Riedle, E. Femtosecond continuum generation in bulk laser host materials with sub-μJ pump pulses; *Appl. Phys. B* **2009**, *97*, 561-574.

(9) Johnson, P. J. M.; Prokhorenko, V. I.; Miller, R. J. D. Stable UV to IR supercontinuum generation in calcium fluoride with conserved circular polarization states; *Opt. Express* **2009**, *17*, 21488-21496.

(10) Chen, X. W.; Leng, Y. X.; Liu, J.; Zhu, Y.; Li, R. X.; Xu, Z. Z. Pulse self-compression in normally dispersive bulk media; *Opt. Commun.* **2006**, *259*, 331-335.

(11) He, P.; Liu, Y.; Zhao, K.; Teng, H.; He, X.; Huang, P.; Huang, H.; Zhong, S.; Jiang, Y.; Fang, S.; Hou, X.; Wei, Z. High-efficiency supercontinuum generation in solid thin plates at 0.1TW level; *Opt. Lett.* **2017**, *42*, 474-477.

(12) Liu, Y.-Y.; Zhao, K.; He, P.; Huang, H.-D.; Teng, H.; Wei, Z.-Y. High-Efficiency Generation of 0.12 mJ, 8.6 Fs Pulses at 400nm Based on Spectral Broadening in Solid Thin Plates; *Chin. Phys. Lett.* **2017**, *34*, 074204.

(13) Rezvani, S. A.; Hong, Z.; Pang, X.; Wu, S.; Zhang, Q.; Lu, P. Ultrabroadband tunable OPA design using a spectrally broadened pump source; *Opt. Lett.* **2017**, *42*, 3367-3370.

(14) Lu, C.-H.; Tsou, Y.-J.; Chen, H.-Y.; Chen, B.-H.; Cheng, Y.-C.; Yang, S.-D.; Chen, M.-C.; Hsu, C.-C.; Kung, A. H. Generation of intense supercontinuum in condensed media; *Optica* **2014**, *1*, 400-406.

(15) Baum, P.; Lochbrunner, S.; Riedle, E. Tunable sub-10-fs ultraviolet pulses generated by achromatic frequency doubling; *Opt. Lett.* **2004**, *29*, 1686-1688.

(16) Krebs, N.; Pugliesi, I.; Riedle, E. Pulse Compression of Ultrashort UV Pulses by Self-Phase Modulation in Bulk Material; *Appl. Sci.* **2013**, *3*, 153-167.

(17) Son, M.; Mosquera-Vázquez, S.; Schlau-Cohen, G. S. Ultrabroadband 2D electronic spectroscopy with high-speed, shot-to-shot detection; *Opt. Express* **2017**, *25*, 18950-18962.

(18) Spokoyny, B.; Koh, C. J.; Harel, E. Stable and high-power few cycle supercontinuum for 2D ultrabroadband electronic spectroscopy; *Opt. Lett.* **2015**, *40*, 1014-1017.

(19) De Marco, L.; Ramasesha, K.; Tokmakoff, A. Experimental Evidence of Fermi Resonances in Isotopically Dilute Water from Ultrafast Broadband IR Spectroscopy; *J. Phys. Chem. B* **2013**, *117*, 15319-15327.

(20) Calabrese, C.; Stingel, A. M.; Shen, L.; Petersen, P. B. Ultrafast continuum mid-infrared spectroscopy: probing the entire vibrational spectrum in a single laser shot with femtosecond time resolution; *Opt. Lett.* **2012**, *37*, 2265-2267.

(21) Liu, J.; Kida, Y.; Teramoto, T.; Kobayashi, T. Generation of stable sub-10 fs pulses at 400 nm in a hollow fiber for UV pump-probe experiment; *Opt. Express* **2010**, *18*, 4664-4672.

(22) Gueye, M.; Nillon, J.; Cregut, O.; Leonard, J. Broadband UV-Vis vibrational coherence spectrometer based on a hollow fiber compressor; *Rev. Sci. Instrum.* **2016**, *87*.

(23) Ma, X.; Dostál, J.; Brixner, T. Broadband 7-fs diffractive-optic-based 2D electronic spectroscopy using hollow-core fiber compression; *Opt. Express* **2016**, *24*, 20781-20791.

(24) Al Haddad, A.; Chauvet, A.; Ojeda, J.; Arrell, C.; Van Mourik, F.; Auböck, G.; Chergui, M. Set-up for broadband Fourier-transform multidimensional electronic spectroscopy; *Opt. Lett.* **2015**, *40*, 312-315.

(25) Aubock, G.; Consani, C.; Monni, R.; Cannizzo, A.; Van Mourik, F.; Chergui, M. Femtosecond pump/supercontinuum-probe setup with 20 kHz repetition rate; *Rev. Sci. Instrum.* **2012**, *83*.

(26) Prokhorenko, V. I.; Picchiotti, A.; Maneshi, S.; Dwayne Miller, R. J. In *19th International Conference on Ultrafast Phenomena*; Optical Society of America: Okinawa, 2014, p 09.Wed.A.04.

(27) West, B. A.; Molesky, B. P.; Montoni, N. P.; Moran, A. M. Nonlinear optical signatures of ultraviolet light-induced ring opening in alpha-terpinene; *New. J. Phys.* **2013**, *15*.

(28) Cerullo, G.; De Silvestri, S. Ultrafast optical parametric amplifiers; *Rev. Sci. Instrum.* **2003**, *74*, 1-18.

(29) Johnson, P. J. M.; Halpin, A.; Morizumi, T.; Brown, L. S.; Prokhorenko, V. I.; Ernst, O. P.; Miller, R. J. D. The photocycle and ultrafast vibrational dynamics of bacteriorhodopsin in lipid nanodiscs; *Phys. Chem. Chem. Phys.* **2014**, *16*, 21310-21320.

(30) Selig, U.; Schleussner, C. F.; Foerster, M.; Langhojer, F.; Nuernberger, P.; Brixner, T. Coherent two-dimensional ultraviolet spectroscopy in fully noncollinear geometry; *Opt. Lett.* **2010**, *35*, 4178-4180.

(31) Beutler, M.; Ghotbi, M.; Noack, F.; Brida, D.; Manzoni, C.; Cerullo, G. Generation of high-energy sub-20 fs pulses tunable in the 250-310 nm region by frequency doubling of a high-power noncollinear optical parametric amplifier; *Opt. Lett.* **2009**, *34*, 710-712.

(32) Weiner, A. M. *Ultrafast Optics*; Wiley: Hoboken, New Jersey, 2009.

(33) Diels, J.-C.; Rudolph, W. *Ultrashort Laser Pulse Phenomena*; Academic Press: London, 2006.

(34) Krebs, N.; Pugliesi, I.; Hauer, J.; Riedle, E. Two-dimensional Fourier transform spectroscopy in the ultraviolet with sub-20 fs pump pulses and 250-720 nm supercontinuum probe; *New. J. Phys.* **2013**, *15*.

(35) Tseng, C. H.; Matsika, S.; Weinacht, T. C. Two-Dimensional Ultrafast Fourier Transform Spectroscopy in the Deep Ultraviolet; *Opt. Express* **2009**, *17*, 18788-18793.

(36) Borrego-Varillas, R.; Oriana, A.; Ganzer, L.; Trifonov, A.; Buchvarov, I.; Manzoni, C.; Cerullo, G. Two-dimensional electronic spectroscopy in the ultraviolet by a birefringent delay line; *Opt. Express* **2016**, *24*, 28491-28499.

(37) West, B. A.; Womick, J. M.; Moran, A. M. Probing Ultrafast Dynamics in Adenine With Mid-UV Four-Wave Mixing Spectroscopies; *J. Phys. Chem. A* **2011**, *115*, 8630-8637.

(38) Sutherland, R. L. *Handbook of Nonlinear Optics*; Marcel Dekker: New York, 2003.

(39) Alfano, R. R. *The Supercontinuum Laser Source*; Springer: New York, 2006.

(40) Cheng, Y.-C.; Lu, C.-H.; Lin, Y.-Y.; Kung, A. H. Supercontinuum generation in a multi-plate medium; *Opt. Express* **2016**, *24*, 7224-7231.

(41) Krebs, N.; Probst, R. A.; Riedle, E. Sub-20 fs pulses shaped directly in the UV by an acousto-optic programmable dispersive filter; *Opt. Express* **2010**, *18*, 6164-6171.

(42) Trebino, R. *Frequency-Resolved Optical Gating: The Measurement of Ultrashort Laser Pulses*; Kluwer Academic Publishers: Boston, MA. USA, 2000.

(43) Gaynor, J. D.; Petrone, A.; Li, X.; Khalil, M. Mapping Vibronic Couplings in a Solar Cell Dye with Polarization-Selective Two-Dimensional Electronic–Vibrational Spectroscopy; *J. Phys. Chem. Lett.* **2018**, *9*, 6289-6295.

# Chapter 5. LIGAND-TO-METAL CHARGE TRANSFER OF FERRICYANIDE IN SOLUTION: COMBINING 2D EV AND 2D VE SPECTROSCOPIES

## 5.1 INTRODUCTION

Iron hexacyanides are archetypal models for investigating intramolecular charge transfer processes in solution, and while they have been extensively studied their complex photochemical dynamics remain an area of active research.[1-3] The ligand-to-metal charge transfer (LMCT) dynamics of ferricyanide ($[Fe(CN)_6]^{3-}$) are yet to be fully determined. Pronounced solvation effects in both ground and excited electronic states have been reported.[1,4-6] Different explanations for excited state CN stretching vibrational dynamics have included symmetry reduction due to weak Jahn-Teller effects[7] and electron/hole localization arguments.[6] The photo-aquation (formation of $[Fe(CN)_5OH_2]^{2-}$) of the excited state complex has been reported,[4,8] and hot vibrational relaxation in the ground state following non-radiative internal conversion has been suggested to account for changes in the excited state vibrational structure.[4] In all of these explanations, an in-depth understanding of how the electronic and vibrational degrees of freedom are coupled would aid our understanding of the solvated ferricyanide photophysics.

The direct sensitivity of 2D Electronic-Vibrational (EV) and 2D Vibrational-Electronic (VE) spectroscopies to vibronic couplings[9] of condensed phase molecules makes these two techniques promising avenues for developing a better understanding of the vibronic phenomena present in solvated ferricyanide. An added advantage to using these techniques together on one sample is that they may provide a self-consistency check for the interpretation of the vibronic couplings present in a sample by using the same vibronic Hamiltonian to

iteratively fit the spectra measured by each technique; this is an intrinsic advantage because both techniques are directly sensitive to the same molecular parameters. This can provide a convenient framework to test different physical descriptions of a molecular ensemble through the use of different Hamiltonians which may ultimately lead to a more accurate understanding of molecular properties. The solvated ferricyanide complex has been studied using both 2D EV and 2D VE spectroscopies separately.[10,11] In this chapter, these two different measurements are considered in tandem for the first time, comparing the signals at the same delay time ($\tau_2$ = 400 fs). The spectra are analyzed using a vibronic Hamiltonian that describes one anharmonic vibrational mode which has equilibrium displacement (linear vibronic coupling) and frequency-shifting (quadratic vibronic coupling) in the excited electronic state;[9] this theoretical framework is fully described in chapter 2. A closer look at the time-dependent 2D EV spectra suggest reasons for why the simplified theoretical picture of one anharmonic mode in one excited electronic state may not be the most accurate; this provides an initial explanation for the inconsistencies viewed through fitting the 2D EV and 2D VE spectra by comparison to other literature on the ferricyanide photophysics.

## 5.2 Electronic and Vibrational Linear Absorption Spectra

The linear absorption is shown in Figure 5.1 for the CN stretching vibrational region (2100 < ω < 2150 $cm^{-1}$) and the electronic absorption region (22000 < ω < 28000 $cm^{-1}$). The ground state vibrational spectrum of the octahedral hexacyanides is characterized by only one IR-active vibrational mode: the triply-degenerate $T_{1u}$ CN-stretching motion. This can be seen from the narrow peak present at ω = 2109 $cm^{-1}$. The CN stretches present in the IR spectra are well known reporters of metal-ligand bonding interactions in solution.[12] Studies comparing ferricyanide and ferrocyanide IR spectra show that the CN stretches of the reduced aqueous

complex red-shifts by 75-80 $cm^{-1}$, has a three-fold increase in oscillator strength, and roughly doubles the spectral bandwidth.[1] The effective charge of the central iron is directly related to the CN stretching vibrational features; the greater effective charge of the iron center in ferricyanide results in decreased Fe-CN π back-bonding and increased Fe-CN σ-bonding character. The narrower line width of the ferricyanide is due to weaker solvent interactions.

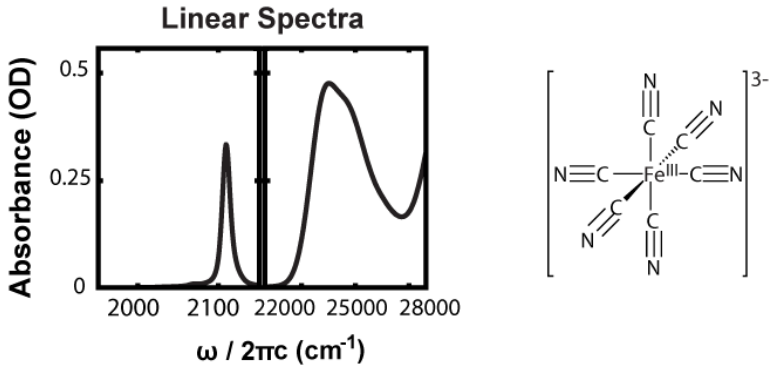


Figure 5.1. Linear Absorption Spectra of Ferricyanide in Formamide. (left) Vibrational and electronic absorption spectra shown with formamide solvent subtracted, (right) ferricyanide molecular structure.

The electronic absorption spectrum of ferricyanide is characterized by four prominent bands at ~23810 $cm^{-1}$, ~31250 $cm^{-1}$, ~33110 $cm^{-1}$, and ~38460 $cm^{-1}$; the lowest energy region is shown in Figure 5.1. Ferricyanide is a low spin $d^5$ octahedral complex due to strong ligand field interactions from the CN ligands; one hold in a 3d-$t_{2g}$ orbital of the ferricyanide electronic structure results in a doublet ground state. The assignments of these electronic bands have been given as resulting from d-d and metal-ligand charge transfer transitions.[8,13,14] While the ground electronic state symmetry is generally assumed to be octahedral, others have pointed out that the uneven populations of the $t_{2g}$ orbitals in the low spin $d^5$ system should result in weak Jahn-Teller distortion.[7] This argument includes the $T_{2g} \otimes (e_g + t_{2g})$ vibronic interaction for the $^2T_{2g}$ doublet ground state with degenerate vibrations leading to a lowered symmetry and two possible configurations of either $D_{4h}$ or $D_{3\infty}$ symmetry; the $D_{3\infty}$ geometry yields the larger

stabilization energy for ferricyanide.[7,15,16] Engel *et al.*[7] discusses that the single CN stretching band observed in the IR spectrum is also consistent with the $D_{3\infty}$ geometry and is adopted in their analysis.

## 5.3 LMCT PHOTOPHYSICS IN FERRICYANIDE

The photoexcited relaxation processes surrounding the LMCT of solvated ferricyanide have been the subject of much debate in the last decade.[2,4,6,7] A paper published by Zhang *et al.*[6] used polarization-selective transient-IR (tIR) spectroscopy to monitor the CN ligand dynamics of ferricyanide in dimethyl-sulfoxide and acetonitrile solvents following LMCT excitation at 400 nm. From a careful anisotropy analysis, these authors show that the initially generated LMCT excited state has one CN stretching vibration with no anisotropy, suggesting that the initially excited state preserves the octahedral symmetry of the ground state. The single ESA band was reported to decay on a 5 ps timescale which occurred concomitantly with the rise of two new ESA features; this observation was reported as strong evidence for the reduction of the octahedral molecular symmetry of the excited state. As the authors acknowledge, this symmetry reduction could result from either excited state electron localization or relaxation from the LMCT excited state to a quartet, $^4T_1$, ligand field excited state. The latter would lead to a Jahn-Teller distortion from the single electron in the $e_g$ level. Comparing quantum chemical calculations of ferricyanide with $[Ru(CN)_6]^{3-}$, the argument was made that the similar behaviors of these two complexes supports the conclusion that electron localization drives the appearance of the two new CN stretching bands because the much larger ligand field splitting of $[Ru(CN)_6]^{3-}$ precludes the involvement of ligand field excited states. A kinetic scheme was proposed consisting of initial electronic delocalization over all six CN ligands followed by localization to one ligand driven by solute-solvent reorganization on a 5

ps timescale. The two CN bands resulting from the reported localization then decay with a ~28 ps timescale.

More recently, the combination of ultrafast photoelectron spectroscopy and tIR spectroscopy with two different LMCT excitations was used to study ferricyanide in water and ethylene glycol.[4] These authors raised doubts about the symmetry breaking arguments used by Zhang *et al.*[6] in describing the electron/hole delocalization/localization dynamics. Using the time-resolved photoelectron spectroscopy to resolve the time-dependent oxidation state of the iron, Ojeda *et al.*[4] reported convincing evidence that the initially excited LMCT state decays via back electron transfer (BET) within 1 ps, and that the appearance of two ESA features in the CN stretching region correspond to the vibrationally hot, ground electronic state ferricyanide, which relax on the picosecond timescales characteristic of vibrations. This explanation is a strong departure from the localization/delocalization arguments made by Zhang *et al.*[6]

The tIR spectra we collected on ferricyanide in formamide solution are presented in Figure 5.2. The same general features are present in our tIR spectra as discussed above; however, the time scales appear to be shorter than those reported by Zhang *et al.* and Ojeda *et al.* The broad initial absorption spanning most of the ESA region is present at early times and has largely decayed within 1 ps, consistent with the BET rate reported by Ojeda et al.[4] Following this broad absorption decay, the same spectral profile of two ESA features are observed to decay on the several picosecond timescale and the ~20 $cm^{-1}$ separation of the hot vibrational states is observed in our measurements. Generally, a solvent dependence could explain differences in vibrational cooling timescales; however, Ojeda *et al.* point out that the vibrational relaxation timescales following BET occur on essentially the same timescales in both water and ethylene

glycol despite these two solvents having very different densities of states in this vibrational region. The most significant solvent-dependent timescales reported by Ojeda *et al.* are the electronic relaxation timescales during BET.[4] Importantly, their tIR studies show the presence of a shoulder feature on the low-energy side of the GSB which they assign to low frequency modes that are anharmonically coupled to the high frequency CN stretching motions.[4,17,18]

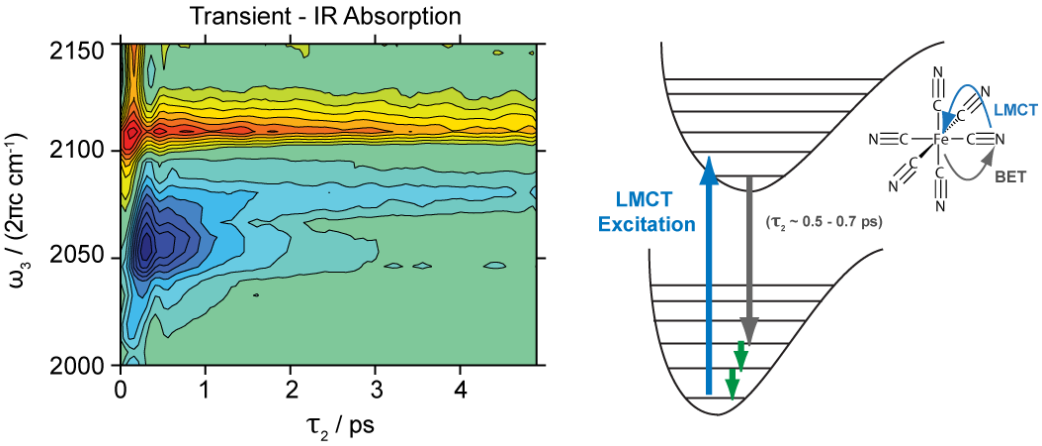


Figure 5.2. Transient-IR Absorption Spectra of Ferricyanide in Formamide. The contours are plotted in ΔT/T and shown at 10% intervals; red = positive (bleach) signal and blue = negative (absorption) signal. The schematic on the right depicts the generalized photophysics of Ferricyanide as described by Ojeda *et al.*[4]. The blue LMCT excitation occurs instantaneously, leading to the decay of the excited state in less than 1 ps via back electron transfer. The system then equilibrates from vibrationally hot states in the ground electronic state on the several picosecond timescales.

The tIR data presented in Figure 5.2 more closely follows the explanation of Ojeda *et al.*[4] and so the photophysical schematic in this figure presents the general photophysics assumed in this treatment. There are obvious spectral distortions at very early delay times present that span most of the vibrational domain which currently have unclear origins; although, a likely explanation is due to solvent interaction persisting for ~200 fs as seen in the $\tau_2$-dependent 2D EV spectra below. The above discussion of ferricyanide has highlighted that the excited state LMCT dynamics occur within the first picosecond before BET has depopulated the excited LMCT states and that the LMCT is sensitive to solvent and may involve low frequency metal-

ligand vibrational motions that anharmonically couple to the CN stretches. Along with this, there remains the ambiguity of exactly how the excited LMCT states and the BET dynamics should be described. In the following, 2D EV and 2D VE spectra collected prior to BET completion ($\tau_2$ = 400 fs) are compared. With the goal of more accurately characterizing the excited state ferricyanide system, the simple vibronic model Hamiltonian and accompanying nonlinear response framework described in chapter 2 is applied to fitting the 2D EV and 2D VE spectra iteratively; this represents a test to determine how well the characteristics of this simplified model could be applied to the ferricyanide system.

## 5.4 Comparison and Fitting of 2D EV and 2D VE Spectra

Initial 2D EV studies on ferricyanide have been reported for one delay time as a means for demonstrating the 2D EV experiment in the condensed phase.[10] Here, a more full discussion about the 2D EV spectral signals of ferricyanide is presented. Courtney *et al.*[11] demonstrated the 2D VE experiment on ferricyanide, which showed the couplings between the high frequency CN stretching motions and the LMCT transitions excited at ~400 nm. Although the electronically resonant electric field is on the higher-energy side of the apparent LMCT band, the 2D EV experimental spectra show no sign of the expected stimulated emission for a higher vibronic level being excited (e.g., $\omega_1 = \omega_{eg} + \omega_{e1'}$) and the 2D VE spectra show a predominantly positive GSB feature assigned as peak I using the labelling of chapter 2 (note: Courtney *et al.* use different peak numbering from those used in this dissertation). Thus, peaks I and II describe the contributions in the 2D EV and 2D VE spectra employing $\omega_{electronic} \cong \omega_{eg}$ electronic transitions excited with 400 nm light.

As chapter 2 describes, the 2D EV and 2D VE techniques mutually sample the same molecular parameter space, but each technique complements the other through having greater sensitivity to one subset of parameters to which the other is less sensitive. The ferricyanide complex is currently the only molecule to have been studied using both techniques. The 2D VE ferricyanide spectra reported by Courtney *et al.*[11] show a single prominent peak reflecting a GSB for the CN stretching motion which is coupled with the LMCT transition. This is characteristic of 2D VE peaks which have broadly overlapping, oppositely signed features in the electronic probe domain;[9,11] the observation of a single peak reflects the relative strengths of the two different Franck-Condon factors in the nonlinear vibronic responses of the ESA and the GSB transitions. In this way, the observation of 2D VE signal becomes a sensitive reporter on linear vibronic coupling (equilibrium displacement). The 2D EV spectra of ferricyanide reported by Gaynor *et al.*[10] show separated GSB and ESA features along the vibrationally-resonant domain; this peak separation due to quadratic vibronic coupling (frequency shifting) upon electronic excitation is characteristic of 2D EV spectroscopy which exploits spectral resolution of structural changes by using a vibrational probe. To compare these two experiments of ferricyanide, a $\tau_2$-dependent 2D EV data set was collected under identical conditions to the spectrum described in chapter 3, and the 2D VE data set reported by Courtney *et al.*[11] was used. The delay time of $\tau_2$ = 400 fs was chosen as it is furthest removed from formamide solvent background signal while still being predominantly in the LMCT excited state according to the timescales observed in the tIR experiments in Figure 5.2 and those reported by Ojeda *et al.*[4] The experimental 2D spectra and the optimized 2D fits using the vibronic Hamiltonian described in chapter 2 are shown in Figure 5.3.

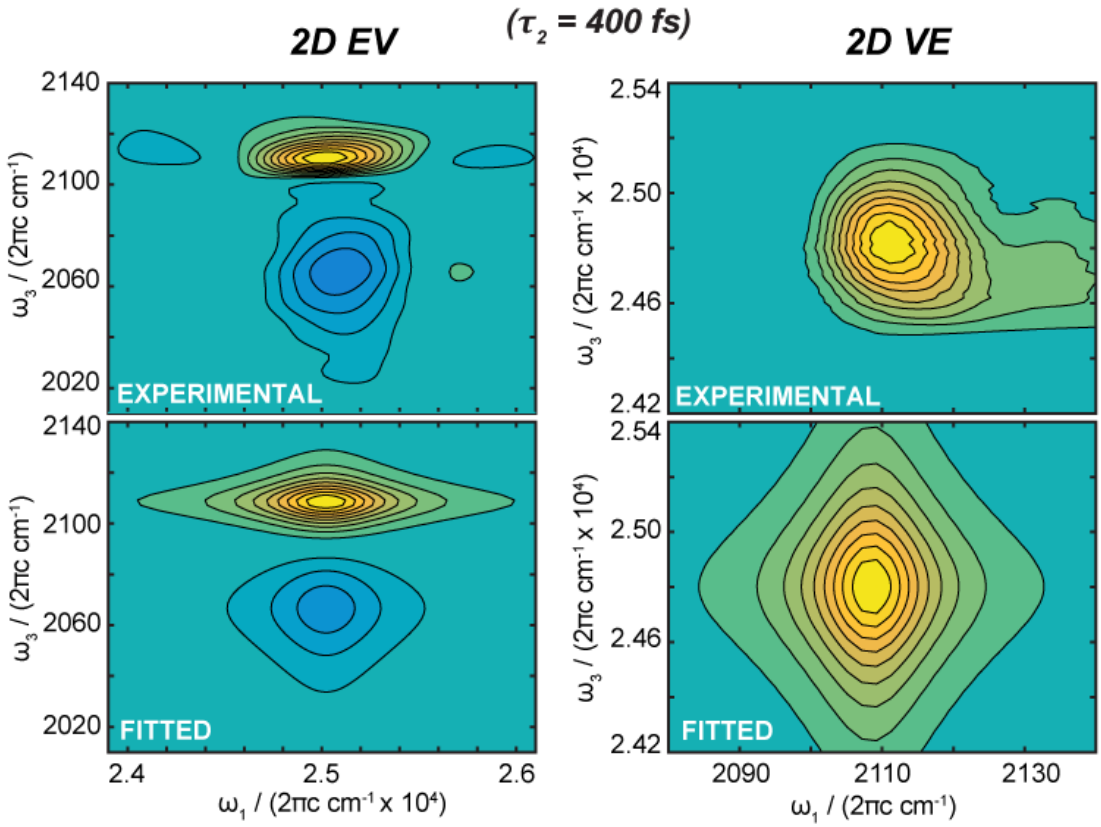


Figure 5.3. Fitting the 2D EV and 2D VE Spectra of Ferricyanide Iteratively with a Vibronic Hamiltonian. The 2D EV spectra (left) and 2D VE spectra (right) as obtained experimentally (top row) and simulated using the single mode vibronic Hamiltonian described in chapter 2. The experimental spectra are collected at $\tau_2$ = 400 fs. The fitting procedure was optimized with residuals ≤ 0.1. Fits to data were optimized by floating the linear vibronic coupling parameter ($\mathcal{V}_i^{(1)}$) with all other parameters fixed in a nonlinear least squares algorithm for the VE spectrum; then fitting the 2D EV spectra using the quadratic vibronic coupling parameter ($\mathcal{V}_{ii}^{(2)}$) and the excited state vibrational dephasing parameter ($\lambda$) while fixing $\mathcal{V}_i^{(1)}$ to the value obtained from previous the VE spectral fit. The anharmonicities were given initial values to reflect the vibrational level separation observed in the tIR measurements; non-Condon effects were not considered; the homogeneous broadening was assumed. Six iterations yielded convergence. Optimized values are $\mathcal{V}_i^{(1)}$ = 0.99, $\mathcal{V}_{ii}^{(2)}$ = -0.038, $\lambda$ =1.62.

The extracted Hamiltonian parameters from fitting the 2D spectra include an excited state frequency shift of $\Delta_{eg}$ = – 40.3 cm$^{-1}$ and excited state anharmonicity of $\Delta_{2'1'}$ = 26 cm$^{-1}$. Since there is no spectral distinction between the ground state anharmonicity and the excited state anharmonicity in either 2D EV or 2D VE spectroscopy, the ground state anharmonicity must be measured separately (e.g., in a 2D IR experiment) to know if the anharmonicity changes in

the excited state.[9] The extracted 26 $cm^{-1}$ excited state anharmonicity compares closely to the ~28 $cm^{-1}$ anharmonicity obtained by comparing the hot vibrational peak separations of the tIR ESA signals at $\tau_2$ = 4 ps; this is a case in which the tIR spectra actually contain the ground state vibrational anharmonicities due relaxation from a displaced excited state. The extracted $\gamma_i^{(1)}$ parameter suggests displacement of the CN stretching coordinate, $Q_{CN}$ (~0.99*$Q_{CN}$), which is consistent with the experimentally observed second and third overtone transitions present in the ground electronic state at later $\tau_2$ times. The excited state vibrational dephasing parameter ($\lambda$) suggests the excited state CN vibrational energy gap fluctuates substantially faster due to the coupling with LMCT and BET processes; specifically, $\lambda$ = 1.62 reflects 62% faster fluctuations. Altogether, this analysis builds up the photophysical picture that the LMCT excited state has strong vibronic coupling through both linear displacement and frequency shifting of the CN stretching coordinates. This is also reasonable when considering the nature of the LMCT transition in light of the vibrational ground state features discussed for the IR spectra. The LMCT transition promotes the reduction of the iron center, decreasing its effective charge (3+→2+) which increases the metal-CN π-backbonding resulting in the red-shift. Reducing the iron also yields a species that is more susceptible to solvent interactions from reduced C σ-donation to the iron center, suggested by a generally broader line width of ferrocyanide,[1] which is consistent with the extracted $\lambda$.

This gives the impression that the simplified single anharmonic vibrational mode on one electronically excited state may be a somewhat decent description of the LMCT excited states in ferricyanide, but there are some notable discrepancies of this simple model. The first, and foremost, is that the electronic excitation profiles of the GSB and ESA peaks in the 2D EV experiment do not have the same central frequency. In general, this could arise from multiple

electronic states being present in the excited manifold (such as in Jahn-Teller systems) or another vibrational mode that is coupled strongly with the electronic transition (such as low frequency vibrations). These cases will both be discussed below in considering $\tau_2$-dependent 2D EV spectral characteristics. Another major limitation of the simplified model is the assumed homogeneously broadened linewidths which represent very different spectral broadening mechanisms than appear to be present in the data. In particular, the resulting Lorentzian linewidths have extended tails by comparison to the Gaussian line shapes resulting from inhomogeneous spectral broadening. This aspect would also obscure low intensity contributions on the wings of the main features which could arise from low frequency mode couplings. Finally, there does appear to be some 2D correlated line shapes present in both the 2D EV and the 2D VE spectra, which implies inhomogeneous broadening mechanisms contribute to the spectral dynamics.

The systematic fitting of the 2D EV and 2D VE spectra of ferricyanide discussed above has demonstrated the benefits of having both spectra to use in tandem during analysis. Fairly consistent results with many other experimental characterizations of ferricyanide are obtained in this approach. The goals of this exercise were two-fold: 1) to see how accurately a very simple vibronic model Hamiltonian could be applied to an excited state charge transfer system of great interest, and 2) to demonstrate the benefits of using 2D EV and 2D VE spectroscopies together to arrive at a more complete vibronic description of a molecular excited state. Regarding the former, this simplified model performed moderately well but with some notable constraints which were not surprising given previous work on LMCT dynamics of ferricyanide.[4,7] Including the more subtle details such as multiple electronic states or low frequency vibrational modes suggested by these studies will require more complex models.

The limits of the simplified single anharmonic vibration model will be discussed in terms of the $\tau_2$-dependent 2D EV spectral analysis below and the $\tau_2$-dependent 2D VE spectra published by Courtney *et al.*[11]

## 5.5 LMCT Dynamics Viewed By 2D EV Spectroscopy

The 2D EV spectra of ferricyanide and the formamide-only spectra are shown for various time points throughout the first 5 ps of the LMCT and its relaxation pathways. The solvent contribution is very strong through the first 100 fs and remains present until 300 fs in $\tau_2$. The broad ESA shown in blue is centered at $\omega_3$ = 2067 cm$^{-1}$ which is between the CN stretching frequencies expected for ferrocyanide (2034 cm$^{-1}$) and ferricyanide (2109 cm$^{-1}$) dissolved in formamide,[11] but it is broad enough to cover effectively this entire range while in the LMCT excited state. The reported ~0.5-0.7 ps BET rate is observed through the blue-shifting, narrowing, and reduction in amplitude of the ESA after $\tau_2$ = 500 fs. By 5 ps after LMCT excitation, the hot vibrations in the ground electronic state are clearly viewed through the first overtone. The ground state bleach is present at the fundamental CN stretch transition frequency 2109 cm$^{-1}$ and remains there for the duration of the LMCT dynamics.

As mentioned in the previous section, upon a closer look at the electronic frequencies of the ESA and GSB peaks after the solvent signal has subsided, the $\omega_1$ peak maxima are different for the GSB and the ESA. The electronic center frequencies during $\tau_2$ are shown in Figure 5.5. During the first 500 fs while in the excited LMCT states, the ESA and GSB features are separated by ~100 cm$^{-1}$ in $\omega_1$. There also appears to be a different time-dependent behavior between the $\omega_1$ maxima of the ESA and the GSB peaks in the 2D EV spectra. The $\omega_1$ maxima of the GSB appear to monotonically decay during $\tau_2$ whereas the $\omega_1$ maxima of the ESA appear

to oscillate for the 2D spectra collected at $\tau_2$ = 300, 400, and 500 fs, changing by ~40 $cm^{-1}$ at each point. It is noted that the $\omega_1$ spectral resolution is 32.5 $cm^{-1}$ so the oscillations result from a change in one pixel. At longer times, after BET has occurred, the $\omega_1$ splitting between the GSB and the ESA increases to ~170 $cm^{-1}$.

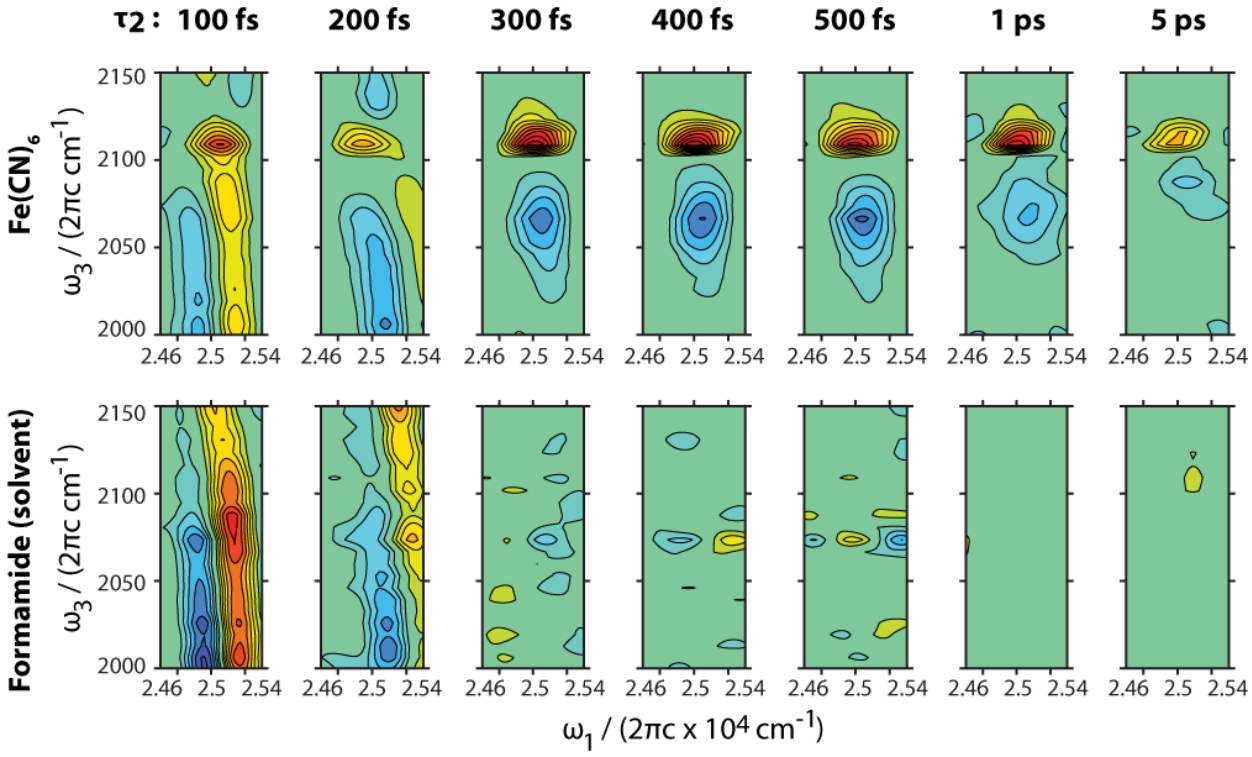


Figure 5.4. Time-Dependent Relaxation Dynamics of Ferricyanide in Formamide Measured by 2D EV Spectroscopy of the Cyanide Stretches. Ferricyanide (top row) and formamide-only (bottom row) 2D EV spectra are presented at various points throughout the first 5 ps in $\tau_2$. The contour maps are globally normalized to the ferricyanide spectrum at 500 fs; the red contours are positive (bleach) signals and the blue contours are negative (absorption) signals and are given at 10% intervals.

While the physical meaning for the $\omega_1$-splitting after BET occurs is unclear, considering the duration of $\tau_2$ while LMCT is occurring is particularly interesting through a comparison of the 2D VE experiments published by Courtney *et al.*[11] In the 2D VE studies on ferricyanide in formamide, the primary GSB feature was observed as shown in Figure 5.3, but an additional ESA was also measured to be 59 $cm^{-1}$ red-shifted in the vibrational excitation domain, $\omega_1$.

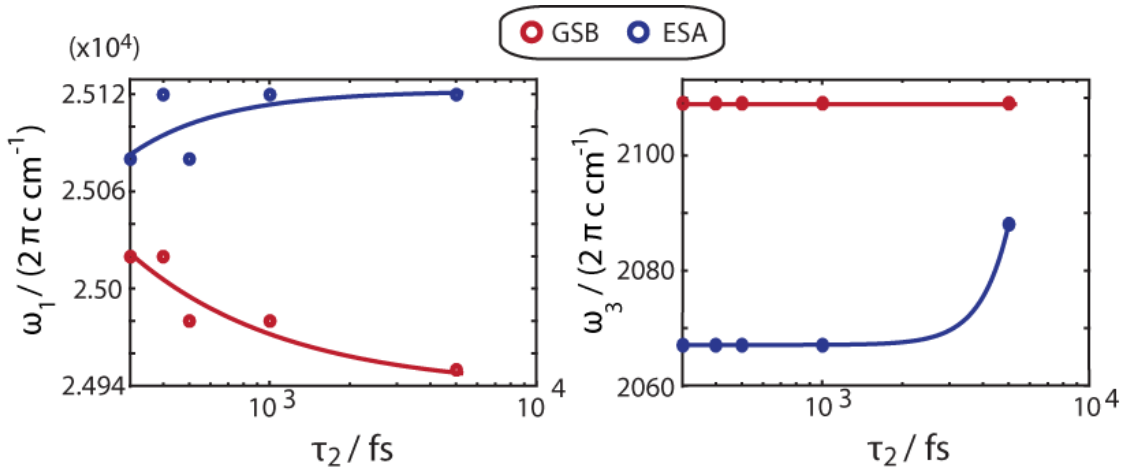


Figure 5.5. Time-Dependent Shifts in 2D EV Peak Maxima in Electronic and Vibrational Dimensions. The $\tau_2$-dependence of the peak maxima in the (left) electronic excitation dimension ($\omega_1$) and the (right) vibrational probe dimension ($\omega_3$) are shown for both the ground state bleach (red) and the excited state absorption (blue) as data points. The lines are not analytical fits but only serve as guides to the eye.

The authors make an important conclusion from this measurement about the displacement of the excited state and the mechanical coupling of a ~59 cm$^{-1}$ vibration referred to as $\nu_{CN-low}$: while the overlap between the $|g;0\rangle$ and $|e;0'\rangle$ is greater than between the $|g;1\rangle$ and $|e;1'\rangle$ states, the excitation of the $\nu_{CN-low}$ mode affects the displacement to favor the overlap between $|g;(1-low)\rangle$ and either $|e;(1-low)'\rangle$ or $|e;1'\rangle$.[11] These observations provide potentially crucial context for interpreting the apparent trends in the $\omega_1$ peak positions shifting by a comparable frequency difference (~40 cm$^{-1}$) in the 2D EV data. Since this $\nu_{CN-low}$ mode is observed in the 2D VE experiment as an ESA, it must originate from the $|g;(1-low)\rangle$ state as the authors explain. Such a state is never involved in a 2D EV transition pathway unless $|g;(1-low)\rangle - |g;0\rangle \propto k_bT$; which is not possible because the observed 59 cm$^{-1}$ $\omega_1$-separation of the 2D VE features results in a vibrational energy difference ~10x larger than $k_bT$. However, if the transition observed in the 2D VE experiment was between $|g;(1-low)\rangle$ and $|e;(1-low)'\rangle$

, instead of $|e;1'\rangle$, it would suggest that this $\nu_{CN-low}$ vibrational motion is relevant in the excited state; then the 2D EV experiment could measure dynamics that involve this ~59 $cm^{-1}$ vibration. Since the $\tau_2$-dependent $\omega_1$ frequency shifting in the 2D EV experiment are of comparable magnitude to the 59 $cm^{-1}$ low frequency mode measured with 2D VE spectroscopy, it is possible that the identified low frequency mode is also coupled to the excited state CN stretching motions.

The 2D VE experiments on ferricyanide also reported a time-dependent shift in the electronic peak maxima for the main GSB feature and attributed this to a $\tau_2$-coherence between $|g;0\rangle$ and other low frequency motions in the ground electronic state. Although 2D VE spectra at only four time delays were reported, the electronic peak maxima measured at $\tau_2$ = 100, 200, 300, and 400 fs suggests that roughly one cycle of the low frequency mode oscillates during this 300 fs interval in $\tau_2$. Assuming the $\tau_2$ time points had properly sampled this low frequency oscillation, this low frequency mode would have ~100-110 $cm^{-1}$ frequency. It is particularly interesting to note that the $\omega_1$ separation between the GSB and the ESA features measured in the 2D EV experiment (Figure 5.5) is comparable to this additionally reported low frequency mode in the 2D VE experiment. There could be a more subtle connection between the two experiments regarding this ~100 $cm^{-1}$ motion because the two experiments induce excitations in opposite molecular degrees of freedom from each other. Thus, the nature of a $\tau_2$ coherence should be very different for the two spectroscopies unless the coherence propagates through the 2D EV ground state bleach transition pathway.

The consideration of this ~100 $cm^{-1}$ motion may be more relevant in the context of a Jahn-Teller distortion for 2D EV spectroscopy. Undoubtedly, the $\tau_2$ coherence identified by Courtney *et al.*[11] highlights the presence of a ground state vibrational mode that is coupled

with the LMCT transition. However, the 2D EV experiments discussed here do not seem to measure a similar 100 $cm^{-1}$ oscillation during $\tau_2$ given the experimental data set presented in Figure 5.4. Instead, the 2D EV measurements show similar splitting of two electronic bands which is reminiscent of a Jahn-Teller effect in which a vibrational mode lifts the degeneracy of two (nearly) degenerate electronic states. In general, vibronic couplings play major roles during Jahn-Teller dynamics.[19] In these systems, the correlations between the electronic motion and the vibrational motions, especially those active in the Jahn-Teller dynamics, should be strong. As such, it may be reasonable to expect a correlated 2D line shape to reflect the fact that these two degrees of freedom are very strongly dependent on one another. The center line slopes of the GSB and ESA peaks are shown in Figure 5.6 for the 2D EV spectra at $\tau_2$ = 300,

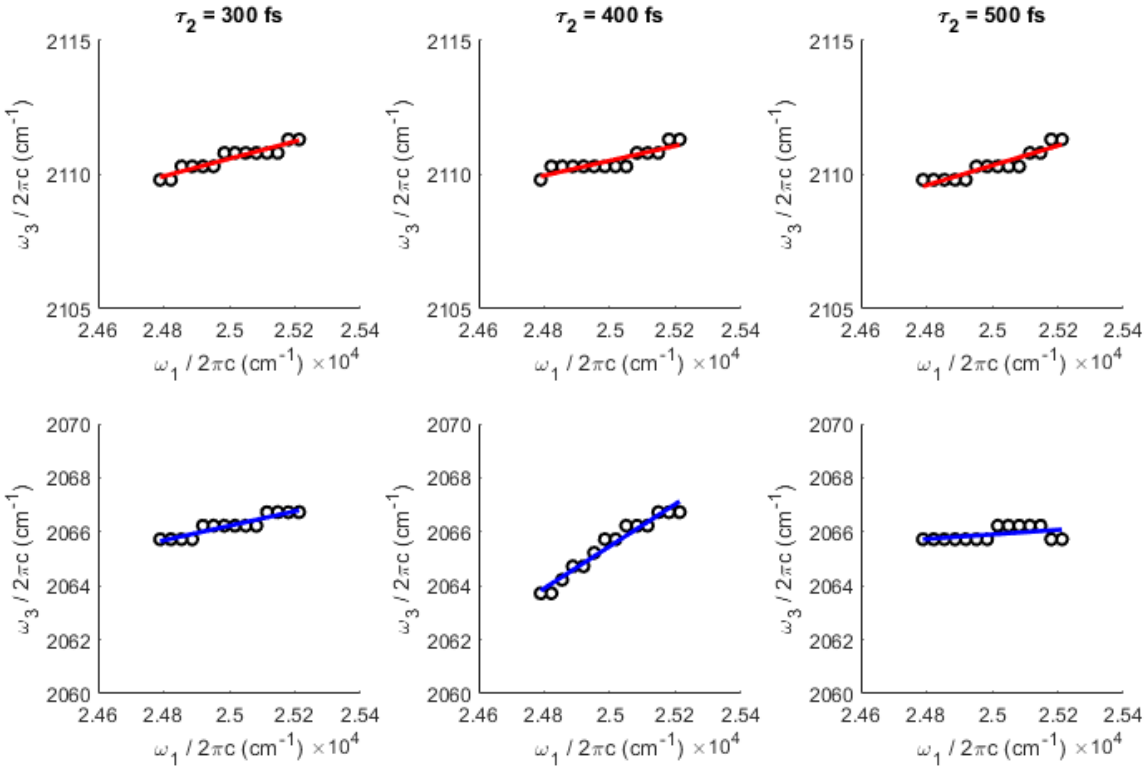


Figure 5.6. Center Line Slopes of the Ferricyanide 2D EV Spectra of the CN Stretches. (top row) The ground state bleach features are shown and the (bottom row) excited state absorption features are shown for $\tau_2$ = 300, 400, and 500 fs.

400, 500 fs and the fitting parameters are given in Table 5.1. Notably, the excited state center line slopes appear to oscillate while the ground state center lines maintain a constant slope during the LMCT process. Although the three 2D EV spectra have only sparsely sampled the LMCT dynamics, the change in the slope for the ESA as a function of these three $\tau_2$ delays seems like it may have undergone roughly a half cycle in 150-200 fs. If this is accurate, it would imply that the electronic-vibrational correlation is oscillating on a ~300-400 fs time scale; this is a very tentative observation. That the GSB appears to maintain some electronic-vibrational correlation is also interesting. Another perspective on these center line slopes could be that they result from the passage through the conical intersection connecting the excited LMCT states and the hot vibrational ground states during the BET process. While a complete treatment of 2D EV line shapes through conical intersections has not been fully worked out, some initial experiments and theory suggest this type of center line slope may indicate such a dynamic.[20-22] Finally, the possibility that excited state solute-solvent reorganization during LMCT and BET is driving the observed 2D line shape changes cannot be discounted.[23]

Table 5.1. Center Line Slope Fitting Parameters. The ($\omega_1$, $\omega_3$) coordinates for the peak maxima in the range 24800 $cm^{-1} \leq \omega_1 \leq$ 25200 $cm^{-1}$ for both the ground state bleach and the excited state absorption are obtained and fit to the first order polynomial: $S_{max}(\omega_3) = m \times (S_{max}(\omega_1)) + b$.

| **Ground State Bleach ($\omega_3$ = 2105-2115 $cm^{-1}$)** | | | |
|---|---|---|---|
| | 300 fs | 400 fs | 500 fs |
| m (cm) | *0.0032* | *0.0028* | *0.0037* |
| b ($cm^{-1}$) | *2029.5* | *2041.2* | *2018.2* |
| $R^2$ | *0.89* | *0.78* | *0.87* |

| **Excited State Absorption ($\omega_3$ = 2060-2070 $cm^{-1}$)** | | | |
|---|---|---|---|
| | 300 fs | 400 fs | 500 fs |
| m (cm) | *0.0027* | *0.0078* | *0.0008* |
| b ($cm^{-1}$) | *1998.6* | *1870.3* | *2044.8* |
| $R^2$ | *0.88* | *0.95* | *0.21* |

## 5.6 Discussion and Conclusions

The ability to test out different vibronic coupling model Hamiltonians through a joint analysis of 2D EV and 2D VE spectroscopies on the same sample can be particularly advantageous. While the LMCT dynamics of ferricyanide may be decently modeled through a simple vibronic Hamiltonian, a more in-depth Hamiltonian including at least one low frequency vibration and perhaps more than one electronic excited state will be needed to more completely model these dynamics. The advantage of using both 2D EV and 2D VE spectroscopies to identify vibronic coherences and the presence of low frequency vibrational motions in either the ground or excited electronic states is also emphasized in this chapter through the consideration of time-dependent spectral features from both techniques. The time-dependent peak maxima and line shape analysis may prove useful for identifying multiple electronic excited states that have well-defined vibronic couplings in (pseudo) Jahn-Teller systems. Although further work is needed to solidify the relationships between center line slopes, passages through conical intersections, and non-adiabatic electronic dynamics in 2D EV and 2D VE spectra, there is clearly evidence in the ferricyanide 2D EV spectra to suggest that excited state vibronic couplings play active roles in the ligand-to-metal charge transfer, and likely the back electron transfer, in this solvated complex. Improvements to the work presented in this chapter could confirm and more rigorously quantify the experimental trends described through the time-dependent frequency shifts and center line slope analysis. Repeating these measurements with finer time resolution in $\tau_2$, finer $\omega_3$ resolution, and perhaps with polarization-selectivity to view any $\omega_1$- dependent anisotropy should be productive and illuminating.

## 5.7 REFERENCES


(1) Ross, M.; Andersen, A.; Fox, Z. W.; Zhang, Y.; Hong, K.; Lee, J. H.; Cordones, A.; March, A. M.; Doumy, G.; Southworth, S. H.; Marcus, M. A.; Schoenlein, R. W.; Mukamel, S.; Govind, N.; Khalil, M. Comprehensive Experimental and Computational Spectroscopic Study of Hexacyanoferrate Complexes in Water: From Infrared to X-ray Wavelengths; *J. Phys. Chem. B* **2018**, *122*, 5075-5086.

(2) Chergui, M. Ultrafast photophysics and photochemistry of iron hexacyanides in solution: Infrared to X-ray spectroscopic studies; *Coord. Chem. Rev.* **2018**, *372*, 52-65.

(3) Chergui, M. Ultrafast Photophysics of Transition Metal Complexes; *Acc. Chem. Res.* **2015**, *48*, 801-808.

(4) Ojeda, J.; Arrell, C. A.; Longetti, L.; Chergui, M.; Helbing, J. Charge-transfer and impulsive electronic-to-vibrational energy conversion in ferricyanide: ultrafast photoelectron and transient infrared studies; *Phys. Chem. Chem. Phys.* **2017**.

(5) Sando, G. M.; Zhong, Q.; Owrutsky, J. C. Vibrational and rotational dynamics of cyanoferrates in solution; *J. Chem. Phys.* **2004**, *121*, 2158-2168.

(6) Zhang, W. K.; Ji, M. B.; Sun, Z.; Gaffney, K. J. Dynamics of Solvent-Mediated Electron Localization in Electronically Excited Hexacyanoferrate(III); *J. Am. Chem. Soc.* **2012**, *134*, 2581-2588.

(7) Engel, N.; Bokarev, S. I.; Moguilevski, A.; Raheem, A. A.; Al-Obaidi, R.; Mohle, T.; Grell, G.; Siefermann, K. R.; Abel, B.; Aziz, S. G.; Kuhn, O.; Borgwardt, M.; Kiyan, I. Y.; Aziz, E. F. Light-induced relaxation dynamics of the ferricyanide ion revisited by ultrafast XUV photoelectron spectroscopy; *Phys. Chem. Chem. Phys.* **2017**, *19*, 14248-14255.

(8) Alexander, J. J.; Gray, H. B. Electronic Structures of Hexacyanometalate Complexes; *J. Am. Chem. Soc.* **1968**, *90*, 4260-+.

(9) Gaynor, J. D.; Khalil, M. Signatures of vibronic coupling in two-dimensional electronic-vibrational and vibrational-electronic spectroscopies; *J. Chem. Phys.* **2017**, *147*, 094202.

(10) Gaynor, J. D.; Courtney, T. L.; Balasubramanian, M.; Khalil, M. Fourier transform two-dimensional electronic-vibrational spectroscopy using an octave-spanning mid-IR probe; *Opt. Lett.* **2016**, *41*, 2895-2898.

(11) Courtney, T. L.; Fox, Z. W.; Slenkamp, K. M.; Khalil, M. Two-dimensional vibrational-electronic spectroscopy; *J. Chem. Phys.* **2015**, *143*, 154201/154201-154201/154215.

(12) Jones, L. H. Nature of Bonding in Metal Cyanide Complexes as Related to Intensity and Frequency of Infrared Absorption Spectra; *Inorg. Chem.* **1963**, *2*, 777-&.

(13) Naiman, C. S. Interpretation of Absorption Spectra of $K_3Fe(CN)_6$; *J. Chem. Phys.* **1961**, *35*, 323-&.

(14) Gray, H. B.; Beach, N. A. Electronic Structures of Octahedral Metal Complexes .1. Metal Hexacarbonyls and Hexacyanides; *J. Am. Chem. Soc.* **1963**, *85*, 2922-&.

(15) Atanasov, M.; Comba, P. On the ground state $T_g$ x $e_{(g)}$ ($T_g$ = $^2T_{(2g)}$, $^3T_{(1g)}$) Jahn-Teller-coupling in hexacyano complexes of 3d-transition metals; *J. Mol. Struct.* **2007**, *838*, 157-163.

(16) Atanasov, M.; Comba, P.; Daul, C. A.; Hauser, A. DFT-based studies on the Jahn-Teller effect in 3d hexacyanometalates with orbitally degenerate ground states; *J. Phys. Chem. A* **2007**, *111*, 9145-9163.

(17) Hamm, P.; Ohline, S. M.; Zinth, W. Vibrational cooling after ultrafast photoisomerization of azobenzene measured by femtosecond infrared spectroscopy; *J. Chem. Phys.* **1997**, *106*, 519-529.

(18) Botan, V.; Hamm, P. Temperature dependence of the IR driven cis-trans isomerization of nitrous acid (HONO); *J. Chem. Phys.* **2008**, *129*.

(19) Bersuker, I. B. Modern Aspects of the Jahn−Teller Effect Theory and Applications To Molecular Problems; *Chem. Rev.* **2001**, *101*, 1067-1114.

(20) Oliver, T. a. A.; Fleming, G. R. Following Coupled Electronic-Nuclear Motion through Conical Intersections in the Ultrafast Relaxation of beta-Apo-8 '-carotenal; *J. Phys. Chem. B* **2015**, *119*, 11428-11441.

(21) Lewis, N. H. C. *Two-Dimensional Electronic-Vibrational Spectroscopy* Ph.D. Dissertation, 2016.

(22) Wu, E. C.; Ge, Q.; Arsenault, E. A.; Lewis, N. H. C.; Gruenke, N. L.; Head-Gordon, M. J.; Fleming, G. R. Two-dimensional electronic-vibrational spectroscopic study of conical intersection dynamics: an experimental and electronic structure study; *Faraday Discuss* **2018**.

(23) Lewis, N. H. C.; Dong, H.; Oliver, T. a. A.; Fleming, G. R. Measuring correlated electronic and vibrational spectral dynamics using line shapes in two-dimensional electronic-vibrational spectroscopy; *J. Chem. Phys.* **2015**, *142*, 174202.

# Chapter 6. POLARIZATION-SELECTIVE MULTIMODE TWO-DIMENSIONAL ELECTRONIC-VIBRATIONAL SPECTROSCOPY

*The work presented in this chapter is being prepared for publication:*

*1) Gaynor, J.D.; Khalil, M. "Polarization-Selective Multimode Femtosecond Coherent Mixed-Frequency Spectroscopy: Two-Dimensional Electronic-Vibrational" (in preparation)*

## 6.1 INTRODUCTION

As studies of excited state dynamics of molecules start to probe more than one vibrational coordinate, it is important to broaden the theoretical framework for 2D EV and 2D VE spectroscopies to include more than one vibrational mode. Surely, much more complicated spectra will result when many different modes are relevant during excited state dynamics. An experimental approach that can be used to great simplify spectral interpretation is a polarization-dependent experiment in which the linear polarization of the incident electric fields are judiciously chosen to obtain molecular-frame information. To map these types of experiments onto the molecular frame, the orientational response of the 2D EV signals must be discussed. This chapter extends the treatment of one displaced, frequency-shifted anharmonic oscillator that is vibronically coupled in the excited electronic state to now include two vibrational modes. Whereas only the nonlinear vibronic response was explicitly treated in chapter 2, here the nonlinear orientational response and the nonlinear vibronic response for the multimode system are treated explicitly. The spectral manifestations of Duschinsky mixing and non-Condon effects are specifically discussed and the molecular-level descriptions of these phenomena are investigated in-detail.

## 6.2 MULTIMODE VIBRONIC HAMILTONIAN

Our previously described vibronic material Hamiltonian and interaction Hamiltonian for a molecular system consisting of a single vibrational mode and two electronic states[1] (i.e., the ground state, $|g\rangle$, and the first excited state, $|e\rangle$) are extended here to describe the same system but now with two vibrational modes of interest: $q_i$ and $q_j$. The vibronic Hamiltonian, $H_{vibronic}$, is defined as the sum of the ground and excited state Hamiltonians, $H_{vibronic} = H_g + H_e$. The ground electronic state Hamiltonian, $H_g$, takes the form of the sum of two bilinearly coupled anharmonic oscillators:

$$H_g(Q_i,Q_j) = \frac{P_i^2}{2m_i} + \frac{P_j^2}{2m_j} + V_g(Q_i,Q_j) \tag{6.1}$$

$$V_g(Q_i,Q_j) = \frac{\hbar\omega_i^o}{2}Q_i^2 + \frac{\hbar\omega_j^o}{2}Q_j^2 + B_{ij}Q_iQ_j + \frac{1}{6}\left(\hbar\omega_i^o g_{iii}Q_i^3 + \hbar\omega_j^o g_{jjj}Q_j^3\right). \tag{6.2}$$

Equations (6.1) and (6.2) express the k[th] reduced vibrational coordinate $Q_k = \sqrt{\frac{m_k\omega_k^o}{\hbar}}q_k$ for the k[th] molecular vibrational coordinate ($q_k$) where $m_k$ is the reduced mass and $\omega_k^o$ is the natural oscillator frequency, and $P_k$ is the momentum operator. Throughout this discussion $k \in i,j$ as only two vibrational coordinates are explicitly considered, though this Hamiltonian may be expanded to include more than two vibrations. The ground state potential, $V_g(Q_i,Q_j)$, is represented as two cubic anharmonic oscillators that are coupled through a bilinear interaction. The cubic anharmonicity coefficients, $g_{iii}$ and $g_{jjj}$, are dimensionless and related to the third order derivative of $V_g(Q_i,Q_j)$ with respect to each vibrational coordinate evaluated

at its equilibrium position. The dimensionless bilinear coupling coefficient, $B_{ij}$, reflects the extent of vibrational mode mixing in the ground electronic state and is related to the second order mixed partial derivative of $V_g(Q_i,Q_j)$ with respect to both vibrational coordinates. The excited electronic state Hamiltonian, $H_e$, is expressed as $H_g$ elevated in energy by the electronic energy gap between $|g\rangle$ and $|e\rangle$, and it includes linear and quadratic vibronic coupling with respect to both $Q_i$ and $Q_j$ in the electronically excited potential, $V_e(Q_i,Q_j)$:

$$H_e = \frac{P_i^2}{2m_i} + \frac{P_j^2}{2m_j} + V_e(Q_i,Q_j) \tag{6.3}$$

$$\begin{aligned} V_e(Q_i,Q_j) = {} & V_g(Q_i,Q_j) + \hbar\omega_{eg}^o \\ & + \hbar\omega_i^o \mathcal{V}_i^{(1)} Q_i + \hbar\omega_j^o \mathcal{V}_j^{(1)} Q_j \\ & + \frac{\hbar\omega_i^o}{2} \mathcal{V}_{i,i}^{(2)} Q_i^2 + \frac{\hbar\omega_j^o}{2} \mathcal{V}_{j,j}^{(2)} Q_j^2 + \mathcal{V}_{i,j}^{(2)} Q_i Q_j . \end{aligned} \tag{6.4}$$

The electronic energy gap between the lowest vibrational levels of the harmonic ground and excited electronic states is given by $\hbar\omega_{eg}^o$. The linear vibronic coupling parameters, $\mathcal{V}_i^{(1)}$ and $\mathcal{V}_j^{(1)}$, are dimensionless and they reflect the linear coupling strength of the respective vibration to the electronic transition which results in excited state equilibrium displacement of each vibrational coordinate. The dimensionless quadratic vibronic coupling coefficients, $\mathcal{V}_{i,i}^{(2)}$ and $\mathcal{V}_{j,j}^{(2)}$, relate the quadratic perturbation of $V_e(Q_i,Q_j)$ with respect to each vibrational coordinate which results in a frequency shift of the respective vibration in the electronic excited state. An additional quadratic perturbation to $V_e(Q_i,Q_j)$ that is linear in $Q_i$ and $Q_j$ is represented by the dimensionless quadratic vibronic coupling coefficient, $\mathcal{V}_{i,j}^{(2)}$, and results in

vibrational mode mixing due to the electronic excitation. Thus, $\mathcal{V}_{i,j}^{(2)}$ reflects the extent of Duschinsky mixing present in a multimode vibronically coupled molecular system. The linear and quadratic vibronic coupling coefficients are proportional to the first and second order derivatives of $V_e(Q_i,Q_j)$ with respect to the appropriate vibrational coordinates, respectively.

The complete material Hamiltonian includes $H_{vibronic}$ and Hamiltonians describing the bath ($H_B$) and the system-bath interactions ($H_{SB}$). Considering a molecular system in solution, the "bath" may include the solvent and all other intramolecular solute degrees of freedom excluded from $H_{vibronic}$. $H_{SB}$ describes the interaction between the bath and the multimode vibronic system; this interaction can result in energy shifting of vibronic eigenstates and it may influence molecular relaxation dynamics. As in our treatment of one vibration,[1] we follow the method of Sung and Silbey[2] to describe the complete material Hamiltonian. We assume the bath to be harmonic and that the system-bath interaction is linear in the bath coordinates and diagonal in the vibronic system eigenstate basis. In this way, $H_{SB}$ reflects the vibronic frequency fluctuations induced by the system-bath interaction.[2] As in the one mode treatment, we use analytical energy gap correlation functions to incorporate the pure dephasing effects of the system-bath interactions including: electronic dephasing, vibrational dephasing, and electronic-state-dependent vibrational dephasing.

The light-matter interaction between the vibronic system described above and the laser pulses is included through an interaction Hamiltonian, $H_{int}$,

$$H_{int} = -\mathbf{M}\cdot\mathbf{E}(k,\omega,t) \tag{6.5}$$

where the system dipole operator, $\mathbf{M}$, is defined as $\mathbf{M}=\sum_a\sum_b \left|a(r,Q)\right\rangle \mu^{a,b} \left\langle b(r,Q)\right|$ with the vibronic system eigenstates represented by $\left|a(r,Q)\right\rangle$ and $\left|b(r,Q)\right\rangle$, and the transition dipole matrix elements for transitions between these eigenstates is given by $\mu^{a,b}$. The vibronic eigenstates are written as Born-Oppenheimer adiabatic eigenstates[3] which depend on both electronic coordinates, $r$, and the reduced vibrational coordinates for all system vibrations, $Q$. As in the one mode case,[1] the vibronic eigenstates used in the two mode system also may be considered eigenfunctions of a dynamical Schrödinger equation in a basis spanning a complete electronic space for each vibrational coordinate, as described by the "Born Representation" defined by Ballhausen and Hansen.[4] We denote an eigenstate of the ground electronic state ($g$) with vibrational quanta in $Q_i$ ($\nu_i = 0,1,...,m$) and vibrational quanta in $Q_j$ ($\nu_j = 0,1,...,n$) as $\left|g;\nu_i,\nu_j\right\rangle$. Likewise, an eigenstate of the excited electronic manifold ($e$) with vibrational quanta in $Q_i$ ($\nu_i' = 0',1',...,m'$) and vibrational quanta in $Q_j$ ($\nu_j' = 0',1',...,n'$) is denoted $\left|e;\nu_i',\nu_j'\right\rangle$.

Separating the transition dipole moment into the sum of operators for the electronic and vibrational coordinates, the transition dipole moment explicitly accounts for both the electronic and vibrational transitions in the multimode vibronic system of interest (i.e., $\mathbf{M}=\mathbf{M}_{elec}(r)+\mathbf{M}_{vib}(Q)$).[5-7] The nuclear dependence of the electronic transition dipole moment is made more explicit by letting $\mathbf{M}_{elec}(r)\cong\mathbf{M}_{eg}(Q)$ and Taylor expanding $\mathbf{M}_{eg}(Q)$ over a specific vibrational coordinate about its equilibrium nuclear configuration, $Q_0$,[7]

$$\mathbf{M}_{eg}(Q)=\mu_{eg}^{(0)}+\sum_{k\in i,j}\mu_{eg}^{(1)}Q_k+... \qquad (6.6)$$

The expansion coefficients in equation (6.6) are expressed as $\mu_{eg}^{(0)} = \mathbf{M}_{eg}(Q_0)$ and $\mu_{eg}^{(1)} = \left( \frac{\partial \mathbf{M}_{eg}}{\partial Q_k} \right)_{Q_0}$. The Franck-Condon limit is obtained when linear ( $\mu_{eg}^{(1)}$ ) and higher order terms in equation (6.6) are negligible. We explore the breakdown of the Condon approximation and how non-Condon effects manifest in polarization-selective 2D EV spectra of multimode vibronically coupled systems by treating the nuclear dependence of the electronic transition dipole moment explicitly up to the first order. The first order terms in $\mathbf{M}_{eg}(Q)$ are referred to as Herzberg-Teller vibronic coupling terms as this formulation parallels the Herzberg-Teller adiabatic approximation.[4,7-9] As in the single mode vibronically coupled system, non-Condon effects may result in "intensity borrowing" from other vibrational levels within the same vibrational mode. An interesting consequence of defining a vibronic system with two coupled vibrational modes is that non-Condon effects may also contribute intensity from vibronic eigenstates in which the electronic transition drives a change in the vibrational quanta of the other vibrational mode (equation (6.9)). Thus, the 2D EV peak intensities are proportional to the Franck-Condon factors for a corresponding vibronic transition, as well as potentially complicated intensity contributions from Herzberg-Teller vibronic couplings that will be system-dependent. Transitions in which the electronic state remains unchanged are also considered explicitly by writing the vibrational transition dipole moment as $\mathbf{M}_{vib}(Q) \equiv \mathbf{M}_{\nu_i \nu_j, mn}(Q)$ to specify the $\left| g;\nu_i,\nu_j \right\rangle \rightarrow \left| g;m,n \right\rangle$ vibrational transition where $m \in \{\nu_i, \nu_i \pm 1\}$ and $n \in \{\nu_j, \nu_j \pm 1\}$. Similarly, the vibrational transitions of the excited electronic states are denoted $\mathbf{M}_{vib}(Q) \equiv \mathbf{M}_{\nu_i' \nu_j', m'n'}(Q)$ for the $\left| e;\nu_i',\nu_j' \right\rangle \rightarrow \left| e;m',n' \right\rangle$ transitions where $m' \in \{\nu_i', \nu_i' \pm 1\}$ and $n \in \{\nu_j', \nu_j' \pm 1\}$. The electrical anharmonicity experienced by the

nuclei during a vibrational oscillation in a given electronic state is accounted for by Taylor expanding the vibrational transition dipole moment as performed in for the single vibrational mode case.[1]

## 6.3 Polarization-Selective 2D EV Spectroscopy of a Multimode System

In the single mode case treated in chapter 2, a simplified interpretation of the desired third order material response, $\vec{\mathbf{R}}^{(3)}$, was obtained by assuming the relatively slower reorientational dynamics of a condensed phase molecule and the comparably faster vibronic motions are separable based upon their timescales. In this limit, each possible quantum evolution pathway through the system vibronic eigenstates driven by sequential field-matter interactions can be written as the product of the nonlinear vibronic response and the nonlinear orientational response. On this basis, the orientational response was neglected and only the vibronic response was treated in chapter 2. The vibronic response and the orientational response are explicitly treated in this chapter. Each possible pathway can still be represented by a Liouville pathway; there are eight distinct Liouville pathway types which group into four pairs of complex conjugate field-matter interaction pathways for a third order response function.[2,10] Therefore, by summing over all $\alpha$ possible third order transition pathways, $\vec{\mathbf{R}}^{(3)}$ may be expressed:

$$\vec{\mathbf{R}}^{(3)}(\tau_3,\tau_2,\tau_1) = \sum_{\alpha=1}^{4} \sum_{IJKL} \sum_{a,b,c,d} (Y_\alpha)_{IJKL}^{abcd}(\tau_3,\tau_2,\tau_1) \times R_\alpha^{abcd}(\tau_3,\tau_2,\tau_1). \tag{6.7}$$

The nonlinear orientational response, $Y_{IJKL}^{abcd}(\tau_3,\tau_2,\tau_1)$, is a tensorial quantity which accounts for the sequential projections of the four linearly polarized electric fields in the fixed laboratory

frame onto the fixed molecular frame as each successive field-matter interaction with a transition dipole occurs during a specific vibronic transition pathway. The indices (a,b,c,d) denote the vibronic eigenstates involved in the vibronic transition pathways accessed through sequential transitions via $\mathbf{M}_{eg}$, $\mathbf{M}_{v_i v_j,mn}$, and $\mathbf{M}_{v_i' v_j',m'n'}$. The time dependence of $Y_{IJKL}^{abcd}(\tau_3,\tau_2,\tau_1)$ includes molecular orientational diffusion between field-matter interactions. The indices $\{I,J,K,L\}\in\{X,Y,Z\}$ are a permutation of the electric field polarization over the laboratory frame coordinates (X,Y,Z). From the initially isotropic orientational distribution of molecules in the ensemble, each linearly polarized electric field selects a subset of molecules from the evolving orientational distribution. Given a combination of three incident pulses with fixed linear polarization, the directional components of the orientational response for a specific transition pathway depend upon the fixed molecular frame directionality of the molecular transition dipoles connecting the vibronic eigenstates. Thus, the orientational response for a particular vibronic transition pathway is calculated by defining the orientation of the four time-ordered transition dipole operators within the fixed molecular frame and then performing an orientational average to transform the motion of the molecular frame into the laboratory frame. The transformation of the orientational motion of the molecular frame into the laboratory frame is achieved by expressing $Y_{IJKL}^{abcd}(\tau_3,\tau_2,\tau_1)$ as a four-point joint probability function where the conditional probability relating an initial orientation of the molecule to its orientation sometime later is evaluated for each field-matter interaction. The solutions to various orientational diffusion equations and the accompanying conditional probability functions are well known.[11,12] We assume the molecular system of interest behaves as a symmetric diffuser in isotropic media; the analytical expressions for $Y_{IJKL}^{abcd}(\tau_3,\tau_2,\tau_1)$ and the calculation of the orientational response are detailed in the Appendix. A more complete treatment of orientational

response in third order nonlinear spectroscopy is beyond the scope of this work, but may found in references[2,11,13-15] . The aim of the current discussion is to understand what structural insights can be obtained for a multimode vibronically coupled system as defined by $H_{vibronic}$ through polarization-selective 2D EV spectra.

The polarization-selective 2D EV pulse sequence is shown in Figure 6.1(a) and an illustration of the molecular transition dipoles of $H_{vibronic}$ considered here are given in Figure 6.1(b) which can be selectively probed.

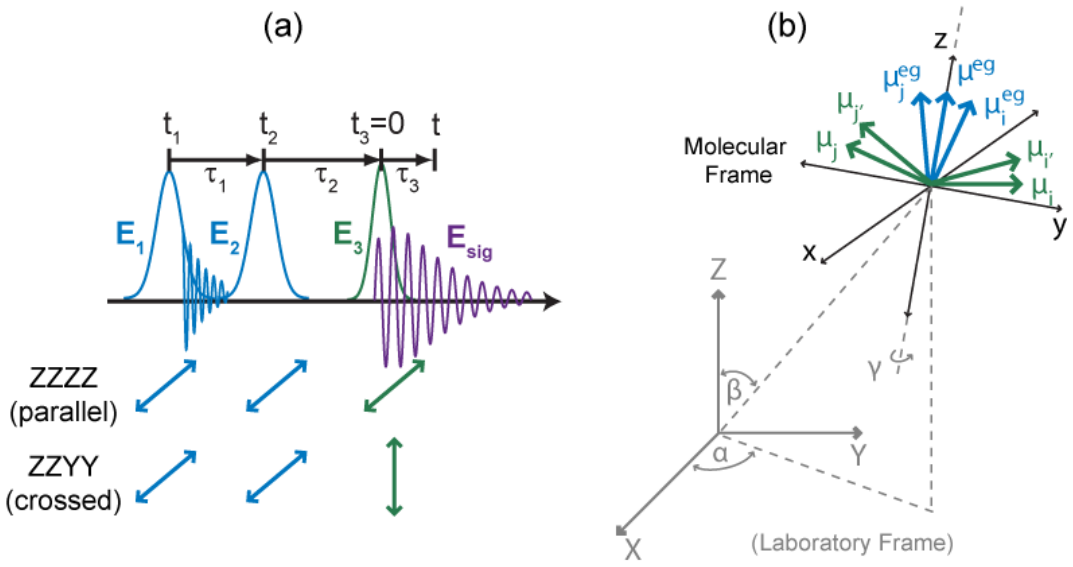


Figure 6.1. Polarization-Selective Multimode 2D EV Spectroscopy Overview. (a) The 2D EV experimental pulse sequence includes the first electronically resonant pump pulse, $\mathbf{E_1}$ (wave vector $\mathbf{k_1}$, blue), incident on a sample at time $t_1$ triggers an electronic coherence oscillating at an electronic transition frequency. After a coherence time, $\tau_1$, the second pump pulse, $\mathbf{E_2}$ ($\mathbf{k_2}$, blue) is incident at time $t_2$ which collapses the electronic coherence into populated states that evolve during the pump-probe delay time, $\tau_2$. The vibrationally resonant probe pulse, $\mathbf{E_3}$ ($\mathbf{k_3}$, green), interacts with the sample and emits the third order signal field, $\mathbf{E_{sig}}$ ($\mathbf{k_{sig}}$, purple), from which the changes in the vibrational spectrum due to the electronic perturbation are extracted. The two linear polarization combinations considered here are the "parallel" polarization with all fields parallel in polarization, and the "crossed" polarization in which the probe field is perpendicularly polarized to the pump fields. (b) The dipole orientation within the molecular frame, and its relative orientation within the laboratory frame. Each dipole moment is defined in the main text and illustrated in Figure 6.2. Integrating over Euler angles (α, β, γ) transforms the molecular frame motion into the laboratory frame.

The orientation of the dipoles are fixed within the molecular frame and defined by their relative orientation. The laboratory frame coordinates (X,Y,Z) are shown in gray with the Euler angles ($\alpha,\beta,\gamma$) that describe the relative orientation of the molecular frame and the laboratory frame. Most generally, the relevant dipoles which fully describe a system with two coupled vibrational modes in the ground and first excited electronic states include: the fundamental electronic dipole, $\mu^{eg}$, for the $|g;00\rangle \rightarrow |e;0'0'\rangle$ transition; the electronic dipole for transitions into "hot" vibrational states, $\mu_i^{eg}$ and $\mu_j^{eg}$ for the respective transitions $|g;00\rangle \rightarrow |e;1'0'\rangle$ and $|g;00\rangle \rightarrow |e;0'1'\rangle$ ; the vibrational dipoles $\mu_i$ and $\mu_j$ for the ground state transitions $|g;00\rangle \rightarrow |g;10\rangle$ and $|g;00\rangle \rightarrow |g;01\rangle$; and the vibrational dipoles $\mu_{i'}$ and $\mu_{j'}$ for the excited state transitions $|e;0'0'\rangle \rightarrow |e;1'0'\rangle$ and $|e;0'0'\rangle \rightarrow |e;0'1'\rangle$. It is assumed that the mechanical anharmonicity does not alter the directionality of the vibrational transition dipole moments significantly (e.g., that $\mu_{i'}$ also describes the $|e;1'0'\rangle \rightarrow |e;2'0'\rangle$ transition dipole, etc.).

Table 6.1. Dipole angle definitions specifying the relative dipole orientation in the molecular frame.

| Angle | Dipoles |
|---|---|
| $\theta_i^{eg}$ | $\mu^{eg} \angle \mu_i^{eg}$ |
| $\theta_j^{eg}$ | $\mu^{eg} \angle \mu_j^{eg}$ |
| $\theta_i$ | $\mu^{eg} \angle \mu_i$ |
| $\theta_j$ | $\mu^{eg} \angle \mu_j$ |
| $\theta_{i'}$ | $\mu^{eg} \angle \mu_{i'}$ |
| $\theta_{j'}$ | $\mu^{eg} \angle \mu_{j'}$ |

Under this description, the effects of vibronic couplings and non-Condon effects are explicitly included as a non-zero angle between $\mu^{eg}$ and either $\mu_i^{eg}$ or $\mu_j^{eg}$ is allowed, and the changes

of a vibrational transition dipole moment due to electronic excitation is included when $\mu_i \neq \mu_{i'}$ or $\mu_j \neq \mu_{j'}$. The angles which define the relative orientation of the dipoles in the molecular frame are arbitrary but fixed and they are listed in Table 6.1.

The nonlinear vibronic response, $R^{abcd}(\tau_3,\tau_2,\tau_1)$, is a scalar quantity which accounts for the vibronic dynamics within the molecular frame of the multilevel vibronic molecular system defined by $H_{vibronic}$. In general, $R^{abcd}(\tau_3,\tau_2,\tau_1)$ for a particular 2D EV transition pathway is composed of (i) exponential functions with oscillating frequencies corresponding to the coherences and population dynamics during the three experimentally controlled intervals, those during $\tau_1$ and $\tau_3$ resulting in the $\omega_1$ and $\omega_3$ peak positions in the 2D EV spectrum, (ii) the product of all four transition dipole moments accessed by the field-matter interactions which contribute to the 2D EV peak amplitude, and (iii) the vibronic dephasing function which governs the 2D EV peak line shape. An in-depth discussion of the vibronic response for a single IR-active vibrational mode vibronically coupled to two electronic states is found in reference[1] and detailed in chapter 2; this chapter extends that treatment to include two coupled IR-active vibrational modes. The signal contributions from the nonlinear vibronic response and the nonlinear orientational response are each discussed in more depth in the following sections.

## 6.4 Nonlinear Vibronic Response Signal Contributions

The eigenstate representation of a system with two coupled IR-active vibrations and two vibronically coupled electronic states as described by $H_{vibronic}$ is given in Figure 6.2(a). The vibronic eigenstates are shown as solid black lines with the respective ket notations to the left in gray (e.g., $|e;0'0'\rangle$). For reference, the harmonic states in both $|g\rangle$ and $|e\rangle$ are shown as

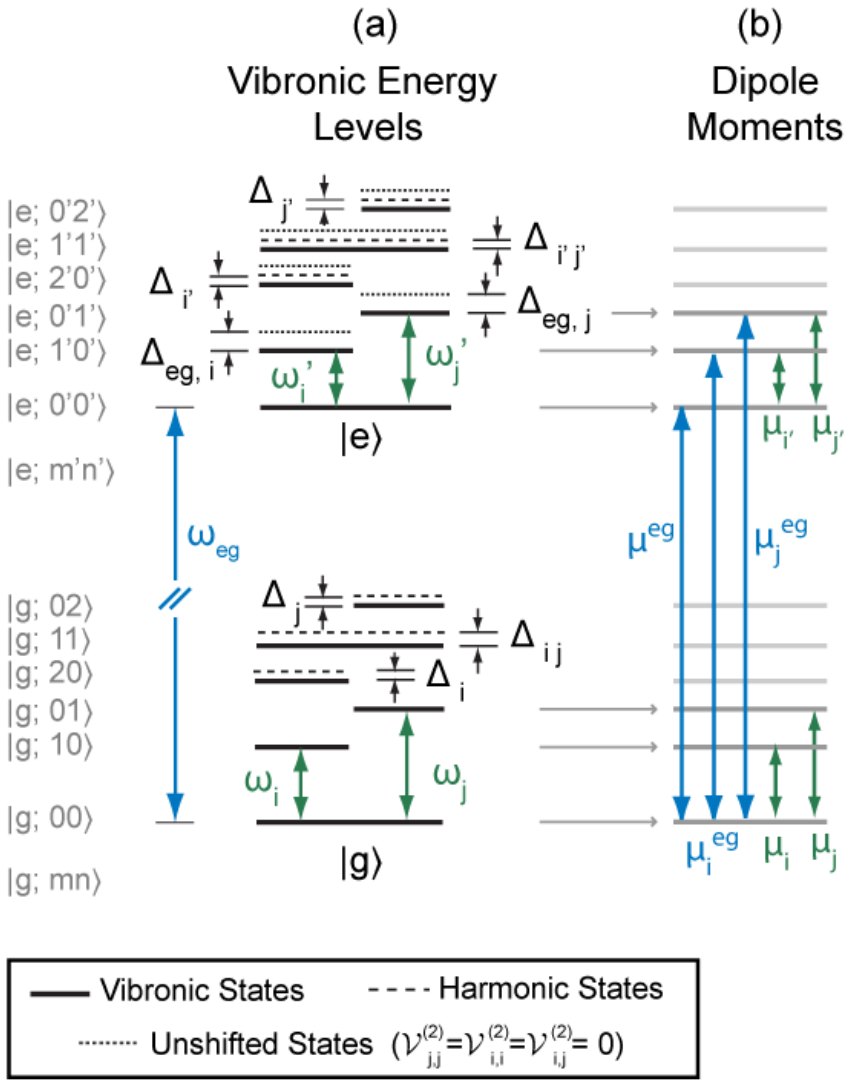


Figure 6.2. Two-Mode Vibronically Coupled Eigenstate Basis and Dipole Moments. (a) The vibronic energy levels for the two coupled, displaced, frequency-shifted anharmonic oscillators system described by $H_{vibronic}$. The ket notation describes the vibronic eigenstates; ground electronic state = g, excited electronic state = e, vibrational quanta of oscillator i in g (e) = m (m'), vibrational quanta of oscillator j in g (e) = n (n'); $\omega_{eg}$ = electronic energy gap; $\omega_i$ ($\omega_j$) = fundamental ground state vibrational transition frequencies; $\omega_i'$ ($\omega_j'$) = fundamental excited state vibrational transition frequencies; $\Delta_i$ ($\Delta_j$) = ground state anharmonicities; $\Delta_{ij}$ = ground state mixed anharmonicity; $\Delta_{eg,i}$ ($\Delta_{eg,j}$) = excited state vibrational frequency shifts; $\Delta_{i'}$ ($\Delta_{j'}$) = excited state anharmonicities; and $\Delta_{i'j'}$ = shifting due to Duschinsky mixing. (b) The transition dipole moments are defined for both electronic and vibrational transitions considered in this treatment.

dashed lines to represent the effect of anharmonicity ($g_{iii}, g_{jjj} \neq 0$). Considering the ground electronic manifold first, the fundamental vibrational transition frequency of $Q_i$ (i.e.,

$|g;00\rangle \rightarrow |g;10\rangle$) is referred to as $\omega_i$; similarly, $\omega_j$ for vibrational coordinate $Q_j$. The shifting of the overtones for $\omega_i$ and $\omega_j$ (i.e., $|g;20\rangle$ and $|g;02\rangle$) due to the anharmonicity of these vibrational coordinates are given by $\Delta_i$ and $\Delta_j$, respectively. The common two-quantum eigenstate to both $Q_i$ and $Q_j$ is $|g;11\rangle$ and it is shifted by $\Delta_{ij}$ due to the mixed anharmonicity arising through the ground state bilinear coupling term, $B_{ij}$. This ground electronic state manifold consisting of two coupled anharmonic oscillators is identical to the well-established eigenstate basis typically used to interpret 2D IR spectra.[15]

In the excited electronic manifold, the two coupled anharmonic oscillators are depicted with quadratic vibronic coupling resulting in the excited state frequency shifting of $Q_i$ and $Q_j$. The unshifted states are shown as dotted black lines in Figure 6.2(a) to reflect the quadratic vibronic coupling effect on the vibronic eigenstates. The first vibrational transition frequency in $|e\rangle$ for $Q_i$ ($Q_j$) is denoted $\omega_i'$($\omega_j'$) where $\omega_i' = \omega_i + \Delta_{eg,i}$ ( $\omega_j' = \omega_j + \Delta_{eg,j}$) and the frequency shift $\Delta_{eg,i}$ ($\Delta_{eg,j}$) is proportional to the quadratic vibronic coupling coefficient $\mathcal{V}_{i,i}^{(2)}$ ($\mathcal{V}_{j,j}^{(2)}$) in $H_{vibronic}$. Like the ground state, the excited state anharmonicities are represented by $\Delta_{i'}$ and $\Delta_{j'}$. For simplicity, this treatment assumes $\Delta_i = \Delta_{i'}$ and $\Delta_j = \Delta_{j'}$ as the only cubic perturbations to $V_e(Q_i, Q_j)$ are included through $V_g(Q_i, Q_j)$. However, the Duschinsky mixing of $Q_i$ and $Q_j$ is included through $\mathcal{V}_{i,j}^{(2)}$ and results in the shared two-quantum state $|e;1'1'\rangle$ shifting in energy by $\Delta_{i'j'}$. Here we have assumed that the two anharmonic oscillators are both linearly displaced and have red-shifted frequencies in the excited electronic state. We also

assume that electronic excitation results in Duschinsky mixing of $Q_i$ and $Q_j$ due to stronger coupling in the excited state such that $\Delta_{ij} < \Delta_{ij'}$.

### 6.4.1 *Peak Positions*

A cartoon schematic of an absorptive 2D EV spectrum for the system described above is shown in Figure 6.3(a). The peaks depicted are those which would arise from electronically resonant electric fields ($\mathbf{E}_1$ and $\mathbf{E}_2$) with center frequency $\omega_{eg}$ and bandwidth $2\omega_j$ to allow resonant transitions into higher lying vibrational states of both $Q_i$ and $Q_j$ (where $\omega_i < \omega_j$).

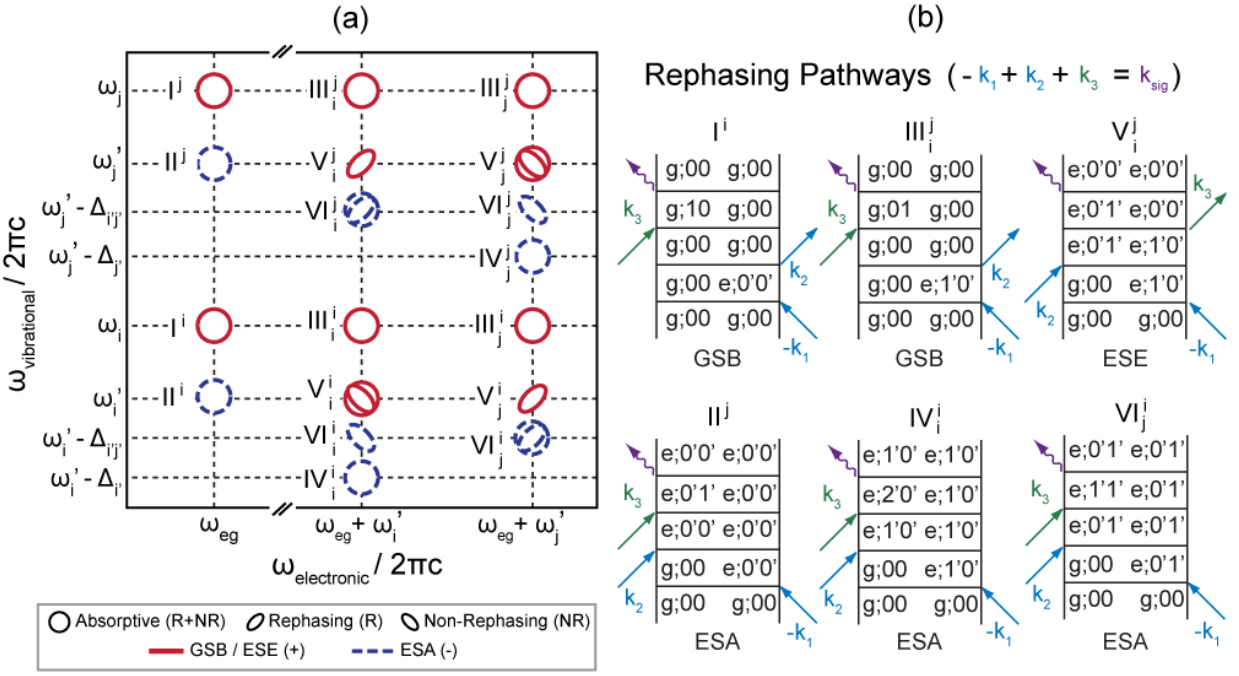


Figure 6.3. Multimode 2D EV Signals Schematic. (a) A schematic illustration of the dipole allowed 2D EV signals appearing for a two-mode vibronically coupled system described by $H_{vibronic}$ and the energy level schematic given in Figure 6.2(c). The absorptive peaks are symmetric and result from equally weighted rephasing (R) and non-rephasing (NR) signals at the same ($\omega_1$, $\omega_3$) coordinates; phase twisted peaks result from unequally weighted R and NR signals; red = positive signal [ground state bleaches (GSB) and excited state stimulated emissions (ESE)], blue = negative signal [excited state absorptions (ESA)]. The peak numbering scheme is described in the main text and Table 6.2. (b) Double-sided Feynman diagrams of rephasing pathways for selected 2D EV peaks. Electronic excitations ($\mathbf{k_1}$ and $\mathbf{k_2}$, blue); vibrational interactions ($\mathbf{k_3}$, green); emitted signal ($\mathbf{k_{sig}}$, purple).

The vibrationally resonant field ($\mathbf{E}_3$) is assumed to have sufficient bandwidth to excite one-quantum transitions only and a spectrum containing the vibrational transition frequencies of interest. The fully absorptive spectrum results from the sum of the rephasing (R, $\mathbf{k}_{sig} = -\mathbf{k}_1 + \mathbf{k}_2 + \mathbf{k}_3$) and non-rephasing (NR, $\mathbf{k}_{sig} = +\mathbf{k}_1 - \mathbf{k}_2 + \mathbf{k}_3$) signal pathways, which differ by the phase of the oscillation propagating during the $\tau_1$ coherence period. When a R and NR signal pathway with the same $(\omega_1, \omega_3)$ coordinates are equally weighted, their sum results in a symmetric peak without any phase twist, as shown in Figure 6.3(a) (e.g., peak $I'$).

By comparison to the one mode case where five distinct peaks with equal R and NR pathways contribute to the spectrum,[1] many more peaks result from expanding $H_{vibronic}$ to include two vibrational modes. An additional set of peaks "$I-V$" arises from transitions exclusively involving the second vibrational mode that are analogous to the single mode case. New contributions to the 2D EV spectrum also arise from transition pathways which involve vibrational transitions in both vibrational coordinates, some of which have unequal numbers of R and NR pathways that are dipole allowed. Peaks with phase twist (i.e., unmatched R or NR pathways resulting in elongated peak shapes) are generated by vibronic transition pathways in which a coherent superposition during the typical "pump-probe delay" time ($\tau_2$) exists. Thus, these peaks should oscillate in amplitude at the frequency difference between the excited state vibrations, $\omega_j' - \omega_i'$ resulting in a dynamic 2D EV line shape during $\tau_2$.

The appearance of more features arising in the two-mode 2D EV spectrum requires a more specific peak labelling scheme than was sufficient in our previous treatment of the single vibrational mode.[1] In general, there are six categories of 2D EV transition pathways that are designated by a Roman numeral as described in Table 6.2.

Table 6.2. A Multimode 2D EV peak categorization legend.
GSB = Ground State Bleach; ESA = Excited State Absorption; ESE = Excited State Stimulated Emission.
† Peak IV is further distinguished by an ESA which does not access the shared excited state $|e;1'1'\rangle$.
†† Peak VI is further distinguished by an ESA which accesses the shared excited state $|e;1'1'\rangle$.

| **Peak Number** | **Signal Type** | $\omega_{\text{electronic}}$ |
|---|---|---|
| I | GSB | $\omega_{eg}$ |
| II | ESA | $\omega_{eg}$ |
| III | GSB | $> \omega_{eg}$ |
| IV | ESA | $> \omega_{eg}$ † |
| V | ESE | $> \omega_{eg}$ |
| VI | ESA | $> \omega_{eg}$ †† |

In addition to categorizing the type of transition pathway with a Roman numeral, further specification of the eigenstates involved in the transition pathway is required to uniquely identify 2D EV signals appearing at particular ($\omega_1, \omega_3$) coordinates in the 2D EV spectrum. To this end, we employ the following scheme: a subscript of "i" or "j" indicates which vibrational coordinate has a different quantum number between the two states in the coherent superposition during $\tau_1$; likewise, a superscript indicates the oscillator with a different quantum number during $\tau_3$. If both vibrational coordinates do not change in quantum number during either period (e.g., $|g;00\rangle \rightarrow |e;0'0'\rangle$), then the corresponding subscript or superscript is omitted. Rephasing double-sided Feynman diagrams for each type of pathway are given in Figure 6.2(b) as an example. We note that in all bra-ket notation and Feynman diagrams used, the vibrational quanta are given from left to right in the order of increasing fundamental

transition frequency. Since we have assumed $\omega_i < \omega_j$, the first vibrational quantum number (m) is given for oscillator "i" followed by the quantum number (n) for oscillator "j".

The peak labelling scheme used here is consistent with the single mode case presented previously,[1] it has merely been expanded. For example, the ground state bleach (GSB) peak $I$ from reference[1] still has the same Roman numeral but is now further specified with a superscript, such as $I^j$. The other analogous GSB peaks in the two-mode case are peaks $III_i^i$ and $III_j^j$, but the new GSB peaks in a multimode 2D EV spectrum contain different subscripts and superscripts ($III_i^j$ and $III_j^i$) because the two coupled oscillators share a common ground state, $|g;00\rangle$, allowing different vibrational coordinates to participate in the same vibronic transition pathway. The different features arising from vibrational transitions in the excited electronic state have also expanded in the two-mode case. While peaks $II^i$ and $II^j$ are essentially no different than in the single mode system, the two mode system permits more features to appear when the electronic excitation populates higher lying vibrational states (e.g., $\omega_{electronic} = \omega_{eg} + \omega_i'$). The excited state vibrational frequency shift ($\Delta_{eg,i}$ and $\Delta_{eg,j}$) can still be directly read off of the 2D EV spectrum as the difference between peaks $I$ and $II$ of either vibrational mode. Equally-weighted R and NR contributions still yield symmetric features for peaks $IV_i^i$ and $V_i^i$ (similarly, $IV_j^j$ and $V_j^j$). However, a shared common ground vibrational state in the electronic excited state, $|e;0'0'\rangle$, allows for additional excited state stimulated emission (ESE) pathways to contribute R and NR signals at different ($\omega_1, \omega_3$) coordinates – i.e., rephasing peaks $V_j^i$ and $V_i^j$ with unique 2D EV coordinates and additional non-rephasing signals to peaks $V_i^i$ and $V_j^j$. The excited state anharmonicity (referred to as $\Delta_{2'1'}$ in reference[1],

but now specified as $\Delta_{i'}$ or $\Delta_{j'}$) of either vibrational coordinate is directly accessible by the difference in $\omega_3$ positions of peaks $IV_i^i$ and $V_i^i$ or $IV_j^j$ and $V_j^j$. An entirely new set of excited state absorption (ESA) peaks appear in the two-mode case indicated by Roman numeral $VI$ because an additional shared vibrational state in the excited electronic state exists for the two coupled anharmonic oscillators: $\left|e;1'1'\right\rangle$. A notable feature of peaks $VI_j^i$ and $VI_i^j$ is they are composed of two transition pathways which *do not* propagate in a coherent superposition during $\tau_2$ which should facilitate a reliable measurement of the population dynamics of $\left|e;1'1'\right\rangle$. This particular state is interesting for two reasons: 1) it is a vibronic eigenstate which is likely to facilitate excited state vibrational energy transfer because it is common to both vibrational coordinates, and 2) its $\omega_3$ position directly reports on $\Delta_{i'j'}$ which is proportional to the strength of Duschinsky mixing and the $\mathcal{V}_{i,j}^{(2)}$ term in $H_{vibronic}$.

### 6.4.2 *Peak Amplitudes*

The amplitudes of the 2D EV peaks are dependent on the ground state population of molecules, (i.e., in $\left|g;00\right\rangle\left\langle g;00\right|$) and the strength of the four transition dipole moments that are accessed by the field-matter interactions during a vibronic transition pathway. It is assumed that $\omega_i, \omega_j >> \kappa_B T$ where $\kappa_B$ is Boltzmann's constant, so all molecules in the ensemble of interest begin in $\left|g;00\right\rangle\left\langle g;00\right|$. The explicit treatment of both the electronic transition dipole moment and the vibrational transition dipole moment in the interaction Hamiltonian allow for considering the nuclear dependence of the electronic transition and the electrical anharmonicity

of a vibration in an excited electronic state. The electronic transition dipole elements are expressed,

$$\mu^{e,g} = \mu_{eg}^{(0)} \left\langle g;\nu_i\nu_j \middle| e;\nu_i'\nu_j' \right\rangle + \mu_{eg}^{(1)} \sum_{k\in i,j} \left\langle g;\nu_i\nu_j \middle| Q_k \middle| e;\nu_i'\nu_j' \right\rangle + \cdots \tag{6.8}$$

To zeroth order, $\mathbf{M}_{eg}(Q)$ is independent of the nuclear degrees of freedom when only $\mu_{eg}^{(0)} \neq 0$ in equation (6.6). In this limit, the Franck-Condon approximation is valid and the electronic transition dipole moment strength is modulated by the square of the overlap integral of the two vibronic eigenstates involved in the transition. Thus, the peak amplitudes are proportional to $\left|\mu^{e,g}\right|^2 = \left|\mu_{eg}^{(0)}\right|^2 \left|\left\langle g;\nu_i\nu_j \middle| e;\nu_i'\nu_j' \right\rangle\right|^2$ from the electronic excitation. When the electronic transitions are dependent on the nuclear coordinates, then $\mu_{eg}^{(1)} \neq 0$ in equation (6.8) and the relative amplitudes of the 2D EV peaks will vary from the amplitudes expected from the Franck-Condon factors. This represents the breakdown of the Condon approximation, in which case non-Condon effects can contribute intensity to 2D EV peaks. An important distinction between systems in which one versus two coupled vibrational modes are considered arises in the form of the first order non-Condon effect. By treating the vibrational coordinate as a ladder operator, the following expression for the first order contribution to $\mu^{e,g}$ becomes

$$\begin{aligned} \mu_{eg}^{(1)} \sum_{k\in i,j} \left\langle g;\nu_i\nu_j \middle| Q_k \middle| e;\nu_i'\nu_j' \right\rangle = \mu_{eg}^{(1)} \Big[ & \left\langle g;\nu_i\nu_j \middle| e;(\nu_i \pm 1)'\nu_j' \right\rangle \\ & + \left\langle g;\nu_i\nu_j \middle| e;\nu_i'(\nu_j \pm 1)' \right\rangle \Big]. \end{aligned} \tag{6.9}$$

Equation (6.9) reflects the fact that the presence of first order non-Condon effects can result in amplitude "borrowing" from other vibrational levels of the same vibrational coordinate *and* additional amplitude from the overlap integrals involving the other vibrational coordinate. Thus, the displacement of anharmonic oscillator "i" may contribute intensity to a 2D EV peak

that primarily involves anharmonic oscillator "j", and vice versa. Although it is not explicit in equations (6.8) and (6.9), it seems reasonable that the amplitude borrowing between oscillators should depend on how strongly coupled the two anharmonic oscillators are, which may be possible through a more robust definition of the expansion coefficient, $\mu_{eg}^{(1)}$. The 2D EV peak amplitudes are also affected by the electrical anharmonicity of a vibrational coordinate in either electronic state, which arises from the nonlinearity of the vibrational transition dipole moment. The vibrational transition dipole moments are assumed to scale harmonically before being transformed into the vibronic eigenstate basis using the same transformation matrix used to obtain the diagonalized vibronic eigenstates.[1,15] Generally, we assume that the effects of $\mathbf{M}_{eg}$ are more significant than those of $\mathbf{M}_{v_i v_j;mn}$ and $\mathbf{M}_{v_i 'v_j';m'n'}$. As in the single mode case, the comparison of oppositely signed peak amplitudes of the excited electronic state features will reflect the electrical anharmonicity of $|e\rangle$.

### 6.4.3 *Peak Line Shapes*

The 2D EV line shapes are influenced by the system-bath dynamics which are described by a nonlinear dephasing function for each vibronic signal pathway, $F^{a,b,c,d}(\tau_3,\tau_2,\tau_1)$. As in the single mode case, the homogeneous dephasing limit is assumed where the energy gap fluctuations of transitions between vibronic eigenstates are faster than the timescale of our measurement and that the fluctuations in mechanical anharmonicity of both electronic states are negligible. Therefore, the energy gap correlation function and the homogeneous dephasing functions are defined similarly to chapter 2 but extended and adapted for the two-mode case.

Instead of specifying the eigenstates a and b in $\zeta_{a,b}(t)$ and $\Gamma_{a,b}$, we simplify the notation in a similar fashion to reference[1] by specifying the transition frequency between the correlated eigenstates: $eg = |g;00\rangle \rightarrow |e;0'0'\rangle$, $i = |g;00\rangle \rightarrow |g;10\rangle$, $j = |g;00\rangle \rightarrow |g;01\rangle$, $i' = |e;0'0'\rangle \rightarrow |e;1'0'\rangle$, and $j' = |e;0'0'\rangle \rightarrow |e;0'1'\rangle$. The same energy gap auto-correlation functions as in the single vibrational mode case are present for two coupled vibrations: the electronic transition frequency fluctuations ($\zeta_{eg,eg}$), the ground electronic state vibrational frequency fluctuations for both oscillators ($\zeta_{i,i}$, $\zeta_{j,j}$), and the excited electronic state frequency fluctuations for both oscillators ($\zeta_{i',i'}$, $\zeta_{j',j'}$). The energy gap cross correlation functions relate frequency fluctuations between different degrees of freedom, which can either be between electronic and vibrational transitions or between transitions in different vibrational modes. The latter is new to the multimode vibronically coupled system and defined as

$$\zeta_{i',j'} = \left\langle \delta\omega_{i'}(t)\delta\omega_{j'}(0) \right\rangle. \tag{6.10}$$

A complete list and definitions of the energy gap correlations is given in the Appendix. We further simplify the dephasing functions by defining a proportionality constant for each vibrational mode which relates the ratio of the electronically excited state fluctuations to those in the ground electronic state

$$\lambda_k = \frac{\delta\omega_{k'}(t)}{\delta\omega_k(t)},\ (k \in i,j). \tag{6.11}$$

In this way, the electronic-state-dependent vibrational dephasing is explicitly included in the 2D EV line shapes and inherently measured by the line widths of the various peaks in a 2D EV spectrum. The nonlinear dephasing functions for the dipole allowed transitions all reduce to the same form as those for the single vibrational mode case discussed previously.[1]

It is interesting to note that a correlated (or anti-correlated) line shape may be present in the multimode 2D EV spectrum even within the homogeneous limit due to unequal contributions of R and NR pathways at particular ($\omega_1, \omega_3$) coordinates. For example, consider peak $VI_i^j$ in Figure 6.2(a) which has a positively correlated line shape in a 2D EV spectrum when $\tau_2$ is such that the $\left|e;0'1'\right\rangle\left\langle e;1'0'\right|$ coherence is constructively interfering. As discussed above, these contributions will necessarily oscillate at the difference frequency between $\omega_i'$ and $\omega_j'$ during $\tau_2$ resulting in a dynamic center line slope across the bandwidth of this peak. The appearance of this dynamic is inherently linked to the Duschinsky mixing because the oppositely signed ESE, peak $V_i^j$, will have the same oscillatory behavior and can cancel out part of the dynamic signal in peak $VI_i^j$ if $\Delta_{i'j'}$ does not sufficiently separate these two peaks in $\omega_3$.

### 6.4.4 *Duschinsky Mixing*

The discussion of peak positions in the multimode 2D EV experiment above highlighted the fact that peaks $VI_j^i$ and $VI_i^j$ may be particularly interesting because they are potentially strong reporters on the excited state vibrational mixing, also known as Duschinsky mixing.[16] In the language more common to 2D IR spectroscopy, direct measurement of these peaks would provide the excited state "mixed anharmonicity" from the peak splitting $\Delta_{i'j'}$ which is directly dependent on the strength of the $\mathcal{V}_{i,j}^{(2)}$ vibronic Hamiltonian parameter. The language from 2D IR is applicable here because this Duschinsky mixing term has the same form as the bilinear coupling term, $B_{i,j}$, of two coupled anharmonic oscillators in the ground electronic

state;[15] $\mathcal{V}_{i,j}^{(2)}$ is simply the excited electronic state equivalent of $B_{i,j}$. However, peaks $I$ and $II$ for both modes will also be sensitive to Duschinsky mixing of these vibrations because this changes the character of the vibration. Such a mode mixing will result in the splitting of the eigenstate energies as expected in a simple two state system.[17] Thus, Duschinsky mixing effects can be present in both the one-quantum vibrational manifold or the two-quantum vibrational manifold of the excited electronic state.

A comparison of the effects from ground state vibrational mixing ($B_{i,j} \neq 0$) and Duschinsky mixing ($\mathcal{V}_{i,j}^{(2)} \neq 0$) is provided in Figure 6.4; the splitting due to state mixing is given for both electronic states in (a) and simulated 2D EV spectral slices at $\omega_1 = \omega_{eg}$ for various $H_{vibronic}$ parameters (b) show the trends in peak splitting for the single quantum manifold. In these simulations, both vibrational modes are red-shifted in the excited state by 30 cm$^{-1}$ when $B_{i,j} = \mathcal{V}_{i,j}^{(2)} = 0$. However, the positions of peaks $I^i$ and $I^j$ move to lower and higher frequencies, respectively, as the magnitude of $B_{i,j}$ increases (shown by the dashed lines in Figure 6.4); likewise, excited state peaks $II^i$ and $II^j$ respond in the same way as the magnitude of $\mathcal{V}_{i,j}^{(2)}$ increases (solid lines, Figure 6.4). In other words, the ground and excited state vibrations split from their $\Delta_{eg,i}$ and $\Delta_{eg,j}$ values as a result of additional perturbation from either the bilinear or Duschinsky mixing changes the curvature of the potential energy surfaces; the Duschinsky mixing ($\left|\mathcal{V}_{i,j}^{(2)}\right| = 60$) results in an 8 cm$^{-1}$ shift of peaks $II^i$ and $II^j$ from their unmixed equivalents (same peaks in gray) and the bilinear mixing in 2-3 cm$^{-1}$ shifts. It is noted that the $B_{i,j}$ perturbations very slightly affect the ESA peaks in these simulations because $V_e(Q_i, Q_j)$ is expressed to first order as $V_g(Q_i, Q_j) + \hbar\omega_{eg}^0$ with excited state vibronic

perturbations resulting in the $\mathcal{V}_{i,i}^{(2)}$ / $\mathcal{V}_{j,j}^{(2)}$ terms including some character of the $B_{i,j}$ perturbation in the excited state vibrational frequencies.

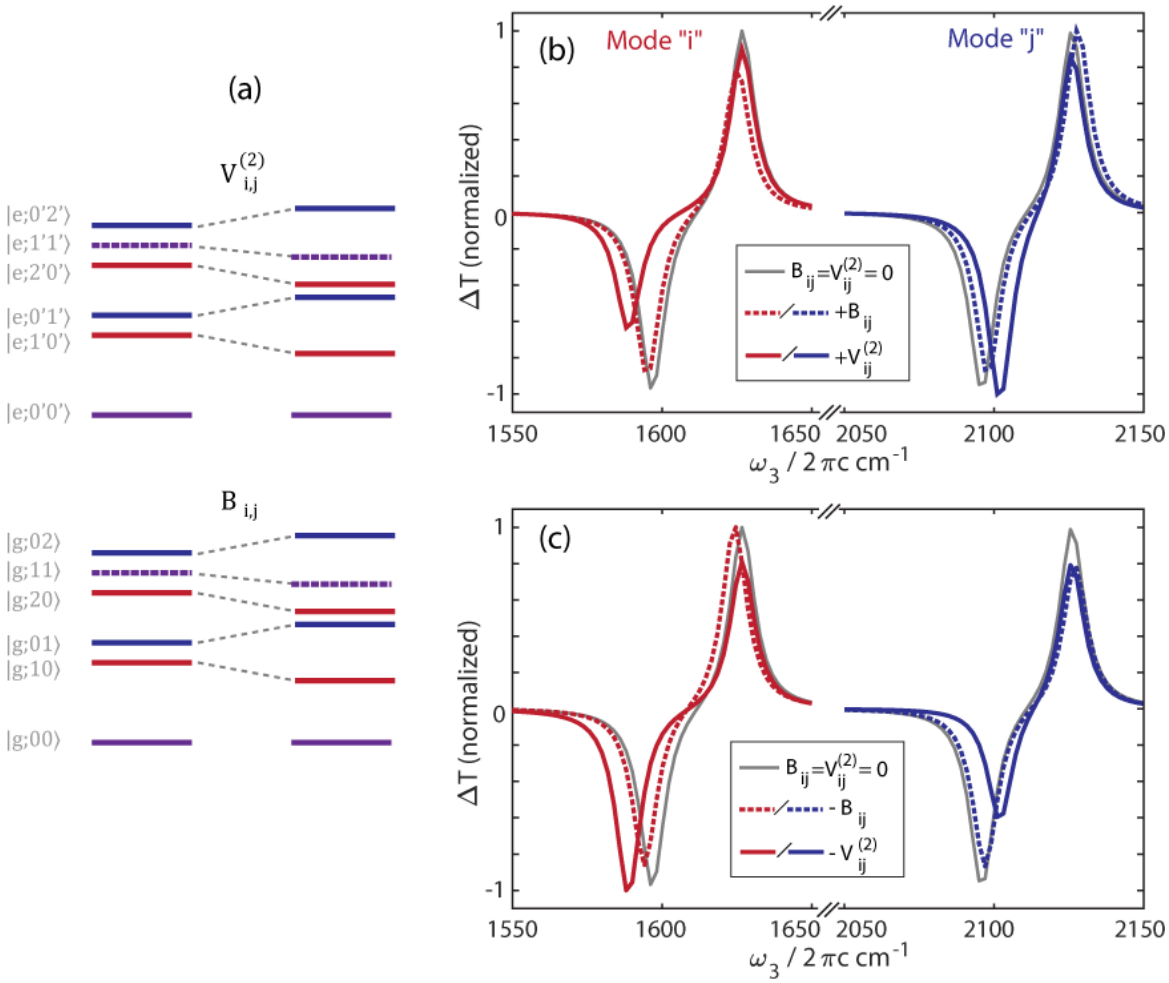


Figure 6.4. Duschinsky mixing effects in nonlinear vibronic response of single vibrational quantum manifold. (a) Both ground state (bilinear) and excited state (Duschinsky) mixing of vibrational modes resulting in vibronic eigenstate energy splitting within each manifold. 2D EV simulated spectral slices at $\omega_1 = \omega_{eg}$ for positive (b) and negative (c) vibrational mixing parameters. These simulations do not include orientational response; the following simulation parameters were used: $\omega_{eg}^0$ = 25500 cm$^{-1}$; $\omega_i^0$ =1650 cm$^{-1}$; $\omega_j^0$ =2150 cm$^{-1}$; $\mathcal{V}_i^{(1)} = \mathcal{V}_j^{(1)} = 0$; $\mathcal{V}_{i,i}^{(2)} = \mathcal{V}_{j,j}^{(2)} = -60$; $|B_{i,j}| = |\mathcal{V}_{i,j}^{(2)}| = 60$. Bilinear and Duschinsky mixing were introduced separately with the other set to zero to clarify effects.

While the shifts in peak positions respond to the magnitude of either ground state or excited state vibrational mixing, Figure 6.4 indicates that the peak amplitude ratios $I^i/I^j$ and $II^i/II^j$

can be used to discern the sign of $B_{i,j}$ and $\mathcal{V}_{i,j}^{(2)}$ respectively for the case that $\omega_i < \omega_j$ as discussed here (the ratios may need to be inverted if $\omega_i > \omega_j$). The change in the amplitudes of the peaks will be influenced by the fact that the vibrational mixing is resulting in shifting vibrational frequencies that change $\Delta_{eg}$ for each mode and affect the signal overlap of the GSB and ESA. Thus, some change in signal intensity will be due to more or less signal cancellation. However, the effect of a mechanical coupling between these two vibrational modes in either electronic state will result in a change in the vibrational dipole moment due to mixing the vibrational wave functions, as shown in Table 6.3 and Table 6.4 below.

Table 6.3. Comparison of Calculated Dipole Moments for Different Vibronic Hamiltonian Parameters.

| μ | $\mathcal{V}_{ii/jj}^{(2)} \neq 0$ (only) | $+\mathcal{V}_{i,j}^{(2)}$ | $-\mathcal{V}_{i,j}^{(2)}$ | $+B_{i,j}$ | $-B_{i,j}$ |
|---|---|---|---|---|---|
| $\|g;00\rangle \rightarrow \|e;0'0'\rangle$ | 0.9979 | 0.9978 | 0.9978 | 0.9980 | 0.9978 |
| $\|g;00\rangle \rightarrow \|g;10\rangle$ | 1.0051 | 1.0051 | 1.0051 | 0.9352 | 1.0728 |
| $\|e;0'0'\rangle \rightarrow \|e;1'0'\rangle$ | 0.9953 | 0.8586 | 1.1235 | 0.9953 | 0.9953 |
| $\|g;00\rangle \rightarrow \|g;01\rangle$ | 1.0041 | 1.0041 | 1.0041 | 1.0542 | 0.9495 |
| $\|e;0'0'\rangle \rightarrow \|e;0'1'\rangle$ | 0.9964 | 1.0887 | 0.8879 | 0.9964 | 0.9964 |

Table 6.4. Ratios of Calculated Dipole Moments for Different Vibronic Hamiltonian Parameters.

| Ratio | $\mathcal{V}_{ii/jj}^{(2)} \neq 0$ (only) | $+\mathcal{V}_{i,j}^{(2)}$ | $-\mathcal{V}_{i,j}^{(2)}$ | $+B_{i,j}$ | $-B_{i,j}$ |
|---|---|---|---|---|---|
| $\mu_i / \mu_j$ | 1.0010 | 1.0010 | 1.0010 | 0.8871 | 1.1299 |
| $\mu_{i'} / \mu_{j'}$ | 0.9989 | 0.7887 | 1.2653 | 0.9989 | 0.9989 |

Importantly, these differences in peak amplitudes among peaks with the same excitation frequency will not show any relative amplitude difference due to non-Condon effects – rather,

they will all be affected by the same amplitude scalar from $\mathbf{M}_{eg}$; this isolates this particular effect to $\mathbf{M}_{v_i v_j, mn}$ and $\mathbf{M}_{v_i' v_j', m'n'}$.

## 6.5 Nonlinear Orientational Response Signal Contributions

The separation of nonlinear vibronic response and the nonlinear orientational response implies that the transition dipole moments can be written as vectoral quantities, possessing both direction and magnitude. Up to this point, the transition dipole moments, $\mu^{a,b}$, have referred to the magnitudes of the transition dipole matrix elements which have only been included as scalars of 2D EV signal amplitudes. However, the complete transition dipole moment, $\boldsymbol{\mu}^{a,b}$, is expressed as the product of a unit vector $\hat{\mu}^{a,b}$ and its magnitude

$$\boldsymbol{\mu}^{a,b} = \hat{\mu}^{a,b}\mu^{a,b}. \tag{6.12}$$

As the molecular insight contained within the nonlinear vibronic response function, $R_\alpha^{a,b,c,d}(\tau_3,\tau_2,\tau_1)$, was discussed in-depth for the multimode system above, this section will focus only on the orientational response, $\sum_{\alpha=1}^{4}\sum_{IJKL}\sum_{a,b,c,d}(Y_\alpha)_{IJKL}^{abcd}(\tau_3,\tau_2,\tau_1)$, contributions to $\ddot{\mathbf{R}}^{(3)}$. The evaluation of the sum over the orientational response indices (I,J,K,L) can be simplified by considering symmetry relationships for isotropic media to yield the four non-vanishing tensor components: $Y_{ZZZZ}$, $Y_{ZZYY}$, $Y_{ZYZY}$, and $Y_{ZYYZ}$, three of which form the independent basis for the all parallel response: $Y_{ZZZZ} = Y_{ZZYY} + Y_{ZYZY} + Y_{ZYYZ}$.[18] Similarly, the response orthogonal to the Z direction in the laboratory frame ($Y_{YYYY} = Y_{YYZZ} + Y_{YZYZ} + Y_{YZZY}$) yields a total of eight non-vanishing tensor components which could potentially contribute to a single vibronic transition pathway.

Assuming an initially isotropic distribution of molecules, each incident electric field projects out an orientational subset of molecules from the evolving orientational distribution. This orientational response is then calculated by first expressing each of the four time-ordered transition dipole moments in the fixed molecular frame ( $i, j, k, l \in x, y, z$ ) where x,y,z are unit vectors of the fixed molecular frame. After projecting each of the transition moments onto the molecular frame, an orientational average transforms the molecular frame motion into the laboratory frame. The sum $\sum_{\alpha=1}^{4}$ differentiates the four vibronic transition pathways (paired with their complex conjugate) according to the interaction sequence of the incident fields:

$$(Y_1)_{IJKL}^{a,b,c,d}(\tau_3,\tau_2,\tau_1) = \sum_{ijkl} \tilde{Y}_{IJKL}^{ijkl}(\tau_3,\tau_2,\tau_1) \left[\hat{\mu}^{c,d}\cdot\hat{i}\right]\left[\hat{\mu}^{b,c}\cdot\hat{j}\right]\left[\hat{\mu}^{a,b}\cdot\hat{k}\right]\left[\hat{\mu}^{d,a}\cdot\hat{l}\right] \qquad (6.13)$$

$$(Y_2)_{IJKL}^{a,b,c,d}(\tau_3,\tau_2,\tau_1) = \sum_{ijkl} \tilde{Y}_{IJKL}^{ijkl}(\tau_3,\tau_2,\tau_1) \left[\hat{\mu}^{c,b}\cdot\hat{i}\right]\left[\hat{\mu}^{d,c}\cdot\hat{j}\right]\left[\hat{\mu}^{b,a}\cdot\hat{k}\right]\left[\hat{\mu}^{a,d}\cdot\hat{l}\right] \qquad (6.14)$$

$$(Y_3)_{IJKL}^{a,b,c,d}(\tau_3,\tau_2,\tau_1) = \sum_{ijkl} \tilde{Y}_{IJKL}^{ijkl}(\tau_3,\tau_2,\tau_1) \left[\hat{\mu}^{c,b}\cdot\hat{i}\right]\left[\hat{\mu}^{b,a}\cdot\hat{j}\right]\left[\hat{\mu}^{d,c}\cdot\hat{k}\right]\left[\hat{\mu}^{a,d}\cdot\hat{l}\right] \qquad (6.15)$$

$$(Y_4)_{IJKL}^{a,b,c,d}(\tau_3,\tau_2,\tau_1) = \sum_{ijkl} \tilde{Y}_{IJKL}^{ijkl}(\tau_3,\tau_2,\tau_1) \left[\hat{\mu}^{a,b}\cdot\hat{i}\right]\left[\hat{\mu}^{b,c}\cdot\hat{j}\right]\left[\hat{\mu}^{c,d}\cdot\hat{k}\right]\left[\hat{\mu}^{d,a}\cdot\hat{l}\right] \qquad (6.16)$$

Each of the four projections of the transition dipole moments onto the molecular frame indices reduces the expression in terms of directional cosines defined by the dipole moments illustrated in Figure 6.1(b) and the angles given in Table 6.1. The indices (a,b,c,d) represent the four vibronic eigenstates accessed during a particular vibronic transition pathway; the transition dipole moments are specified in this way (e.g., $\hat{\mu}^{a,b}$ is for the transition between $|a\rangle$ and $|b\rangle$). The cosine and sine functions are evaluated for the correct angles between the involved transition dipole and the molecular frame coordinates for each non-vanishing tensor component given above. The transformation of the orientational diffusion within the molecular frame into the laboratory frame is achieved through the $\tilde{Y}_{IJKL}^{ijkl}(\tau_3,\tau_2,\tau_1)$ scalar factors which are

defined by a four-point joint probability function of conditional probability distributions for an ensemble of symmetric diffusers.[2,11,13,19] The conditional probability distributions are expressed in terms of Wigner rotation matrices with time-dependent expansion coefficients that can be simplified to only depend on a rotational quantum number and the orientational diffusion coefficient, $D_{or}$, of a symmetric diffuser.[19,20] The orientational part of the response function, $\tilde{Y}^{ijkl}_{IJKL}(\tau_3,\tau_2,\tau_1)$, for a specific transition pathway with projections onto the molecular frame coordinates (i,j,k,l), is determined by selecting a specific set of laboratory frame polarization directions of the incident electric fields, ($I,J,K,L \in X,Y,Z$) where X, Y, and Z are laboratory frame unit vectors; see Table 6.5 for these values of the non-vanishing tensor elements.

Table 6.5. Non-vanishing tensor elements and the orientational part of the response function for the parallel polarized experiment (IJKL = ZZZZ) and the perpendicularly polarized experiment (IJKL = YYZZ), for the two orthogonal dipole directions in z and y within the fixed molecular frame. The diffusional correlation functions are given by $c_1(\tau) = exp\left[-2D_{or}\tau\right]$ and $c_2(\tau) = exp\left[-6D_{or}\tau\right]$. When orientational diffusion is much slower than the vibronic dynamics, $D_{or} \to 0$ and $c_1(\tau),\ c_2(\tau) \to 1$.

| $Y_{ZZZZ}$ (parallel) | | $Y_{YYZZ}$ (perpendicular) | |
|---|---|---|---|
| Tensor Element | Orientational Part | Tensor Element | Orientational Part |
| $\tilde{Y}^{zzzz}_{ZZZZ}$ | $\frac{1}{9}c_1(\tau_1)c_1(\tau_3)\left(1+\frac{4}{5}c_2(\tau_2)\right)$ | $\tilde{Y}^{zzzz}_{YYZZ}$ | $\frac{1}{9}c_1(\tau_1)c_1(\tau_3)\left(1-\frac{2}{5}c_2(\tau_2)\right)$ |
| $\tilde{Y}^{yyyy}_{ZZZZ}$ | 0 | $\tilde{Y}^{yyyy}_{YYZZ}$ | $\frac{1}{9}c_1(\tau_1)c_1(\tau_3)\left(1-\frac{2}{5}c_2(\tau_2)\right)$ |
| $\tilde{Y}^{yyzz}_{ZZZZ} = \tilde{Y}^{zzyy}_{ZZZZ}$ | $\frac{1}{9}c_1(\tau_1)c_1(\tau_3)\left(1-\frac{2}{5}c_2(\tau_2)\right)$ | $\tilde{Y}^{yyzz}_{YYZZ} = \tilde{Y}^{zzyy}_{YYZZ}$ | $\frac{1}{9}c_1(\tau_1)c_1(\tau_3)\left(1+\frac{1}{5}c_2(\tau_2)\right)$ |
| $\tilde{Y}^{zyzy}_{ZZZZ} = \tilde{Y}^{yzyz}_{ZZZZ}$ | $\frac{1}{15}c_1(\tau_1)c_1(\tau_3)c_2(\tau_2)$ | $\tilde{Y}^{yzyz}_{YYZZ} = \tilde{Y}^{zyzy}_{YYZZ}$ | $-\frac{1}{30}c_1(\tau_1)c_1(\tau_3)c_2(\tau_2)$ |
| $\tilde{Y}^{zyyz}_{ZZZZ} = \tilde{Y}^{yzzy}_{ZZZZ}$ | $\frac{1}{15}c_1(\tau_1)c_1(\tau_3)c_2(\tau_2)$ | $\tilde{Y}^{yzzy}_{YYZZ} = \tilde{Y}^{zyyz}_{YYZZ}$ | $-\frac{1}{30}c_1(\tau_1)c_1(\tau_3)c_2(\tau_2)$ |

Note that the non-vanishing tensor elements in Table 6.5 are only given for the polarization geometry in which $\mathbf{k}_1$ and $\mathbf{k}_2$ have the same linear polarization; a complete set of non-vanishing tensor elements for experiments in which these fields have independently controllable polarizations can be found elsewhere.[19,21] Typically, the orientational diffusion is much longer than the timescales of the vibronic dynamics of interest, so the orientational parts of the response function simplify even further. These values can be used directly in equations (6.13) -(6.16) along with the directional cosines to obtain the orientational response for each vibronic transition pathway in a multimode 2D EV experiment.

Using these expressions, the polarization-selective 2D EV signals for specific peaks in the 2D EV spectrum may be calculated. The expressions for the parallel and perpendicularly polarized orientational response can be used to derive the typical expressions for a depolarization ratio and the anisotropy parameter may be obtained. As an example, the orientational responses for the fully absorptive (R+NR) peak $II^j$ are calculated below where $a=|g;00\rangle$, $b=|e;0'0'\rangle$, $c=|e;0'1'\rangle$ and $d=|e;0'0'\rangle$ and $\alpha=1$ specifies the Liouville transition pathway followed by this vibronic transition (see chapter 2).

$$\begin{aligned}(Y_1)^{a,b,c,d}_{ZZZZ} &= \left[\tilde{Y}^{zzzz}_{ZZZZ}(\cos^2(\theta_{j'}))+\tilde{Y}^{yyzz}_{ZZZZ}(\sin^2(\theta_{j'}))\right]_R \\ &\quad +\left[\tilde{Y}^{zzzz}_{ZZZZ}(\cos^2(\theta_{j'}))+\tilde{Y}^{yyzz}_{ZZZZ}(\sin^2(\theta_{j'}))\right]_{NR} \\ &= \frac{2}{15}\left(2\cos^2(\theta_{j'})+1\right)\end{aligned} \tag{6.17}$$

$$\begin{aligned}(Y_1)^{a,b,c,d}_{YYZZ} &= \left[\tilde{Y}^{zzzz}_{YYZZ}(\cos^2(\theta_{j'}))+\tilde{Y}^{yyzz}_{YYZZ}(\sin^2(\theta_{j'}))\right]_R \\ &\quad +\left[\tilde{Y}^{zzzz}_{YYZZ}(\cos^2(\theta_{j'}))+\tilde{Y}^{yyzz}_{YYZZ}(\sin^2(\theta_{j'}))\right]_{NR} \\ &= \frac{2}{15}\left(1+\sin^2(\theta_{j'})\right)\end{aligned} \tag{6.18}$$

For a pump-probe experiment and a 2D experiment in a pump-probe geometry, the depolarization ratio obtained for peak $II^j$ from equations (6.17) and (6.18) is

$$\frac{(Y_1)_{YYZZ}}{(Y_1)_{ZZZZ}} = \frac{2-\cos^2(\theta_{j'})}{1+2\cos^2(\theta_{j'})} \tag{6.19}$$

and the anisotropy is obtained from the ratio of the anisotropic response ($Y_{ZZZZ} - Y_{YYZZ}$) and the isotropic response ($Y_{ZZZZ} + 2Y_{YYZZ}$):[13]

$$r = \frac{Y_{ZZZZ} - Y_{YYZZ}}{Y_{ZZZZ} + 2Y_{YYZZ}} = \frac{1}{5}\left(3\cos^2(\theta_{j'}) - 1\right) \tag{6.20}$$

These equations yield the familiar range of anisotropies of r = 0.4 for transition dipole moments that are parallel and r = -0.2 for orthogonal dipoles.[13,22,23]

Table 6.6. Angular dependence of peaks in 2D EV spectroscopy. Each peak is labelled if it occupies a distinct ($\omega_1$,$\omega_3$) peak position; multiple Liouville transition pathways can contribute to the same peak.

| Peak Label | Signal Type | Angular Dependence | Peak Label | Signal type | Angular Dependence |
|---|---|---|---|---|---|
| $I^i$ | GSB | $\theta_i$ | $II^i$ | ESA | $\theta_{i'}$ |
| $I^j$ | GSB | $\theta_j$ | $II^j$ | ESA | $\theta_{j'}$ |
| $III_i^i$ | GSB | $\theta_i, \theta_i^{eg}$ | $IV_i^i$ | ESA | $\theta_{i'}, \theta_i^{eg}$ |
| $III_i^j$ | GSB | $\theta_j, \theta_i^{eg}$ | $IV_j^j$ | ESA | $\theta_{j'}, \theta_j^{eg}$ |
| $III_j^i$ | GSB | $\theta_i, \theta_j^{eg}$ | $VI_i^j$ | ESA | $\theta_{j'}, \theta_i^{eg}$ |
| $III_j^j$ | GSB | $\theta_j, \theta_j^{eg}$ | $VI_j^i$ | ESA | $\theta_{i'}, \theta_j^{eg}$ |
| $V_i^i$ | ESE | $\theta_{i'}, \theta_i^{eg}, \theta_{j'}, \theta_j^{eg}$ | $VI_i^i$ | ESA | $\theta_{i'}, \theta_{j'}, \theta_j^{eg}, \theta_i^{eg}$ |
| $V_j^j$ | ESE | $\theta_{j'}, \theta_j^{eg}, \theta_{i'}, \theta_i^{eg}$ | $VI_j^j$ | ESA | $\theta_{j'}, \theta_{i'}, \theta_i^{eg}, \theta_j^{eg}$ |
| $V_j^i$ | ESE | $\theta_{i'}, \theta_{j'}, \theta_i^{eg}, \theta_j^{eg}$ | | | |
| $V_i^j$ | ESE | $\theta_{i'}, \theta_{j'}, \theta_i^{eg}, \theta_j^{eg}$ | | | |

Notably, from the anisotropy, one can extract the angle between two different dipole moments directly. However, it is important that the peak amplitudes are not convoluted with different transitions but rather spectrally isolated in order to accurately extract the dipole moment angle from the anisotropy. This is satisfied for the orientational response of peak $II^j$ because it has

angular dependence of only one angle ($\theta_{j'}$) between the transition dipole moments $\mu^{eg}$ and $\mu_{j'}$. The angular dependence of all dipole-allowed 2D EV peaks is given in Table 6.6.

## 6.6 Polarization-Selective 2D EV Spectral Simulations

The nonlinear vibronic response and the nonlinear orientational response can be used as defined in the above sections to simulate the parallel and perpendicularly polarized 2D EV spectra. The same vibronic Hamiltonian parameters still affect the vibronic couplings, non-Condon effects, and Duschinsky mixing; the dipole moment angles are now additional input parameters integrated through the nonlinear orientational responses that allow for simulating orientationally specific 2D EV signals.

In the 2D EV simulations below, the following parameters were used unless otherwise noted: $\omega_i^0$ = 1650 cm$^{-1}$, $\omega_j^0$ = 2150 cm$^{-1}$, $\omega_{eg}^0$ = 26500 cm$^{-1}$, $B_{i,j}$ = 0 cm$^{-1}$, $g_{iii}$ = 0.255 and $g_{jjj}$ = 0.228 which yield 25 cm$^{-1}$ ground state anharmonicities, excited state displacements from linear vibronic couplings $\mathcal{V}_i^{(1)}$ = 0.68 and $\mathcal{V}_j^{(1)}$ = 0.88, quadratic vibronic coupling from $\mathcal{V}_{i,i}^{(2)}$ = -0.006, $\mathcal{V}_{j,j}^{(2)}$ = -0.070, $\mathcal{V}_{i,j}^{(2)}$ = -0.080 resulting in $\Delta_{eg,i}$ = 62 cm$^{-1}$, $\Delta_{eg,j}$ = 37 cm$^{-1}$, $\Delta_{i'}$ = 24 cm$^{-1}$, $\Delta_{j'}$ = 21 cm$^{-1}$, and $\Delta_{i'j'}$ = 12 cm$^{-1}$; non-Condon effects are excluded ($\mu_{eg}^{(1)} = 0$) unless otherwise noted. The dipole angles used were the following unless otherwise specified: $\theta_i$ = 35°, $\theta_j$ = 65°, $\theta_{i'}$ = 45°, $\theta_{j'}$ = 55°, $\theta_i^{eg} = \theta_j^{eg}$ = 0°. The resulting system being simulated can be described as a system of two displaced, frequency-shifted, anharmonic oscillators that are uncoupled in the ground state but become coupled upon electronic excitation through Duschinsky mixing; the angles between the electronic and vibrational transition dipole moments also reflect that delocalization occurs upon excitation as the vibrational dipole moments become more isotropic

(i.e., $\theta_{i'}, \theta_{j'}$ approach the magic angle, 54.7°). The parallel (ZZZZ) and perpendicular (ZZYY) simulated spectra are shown in Figure 6.5.

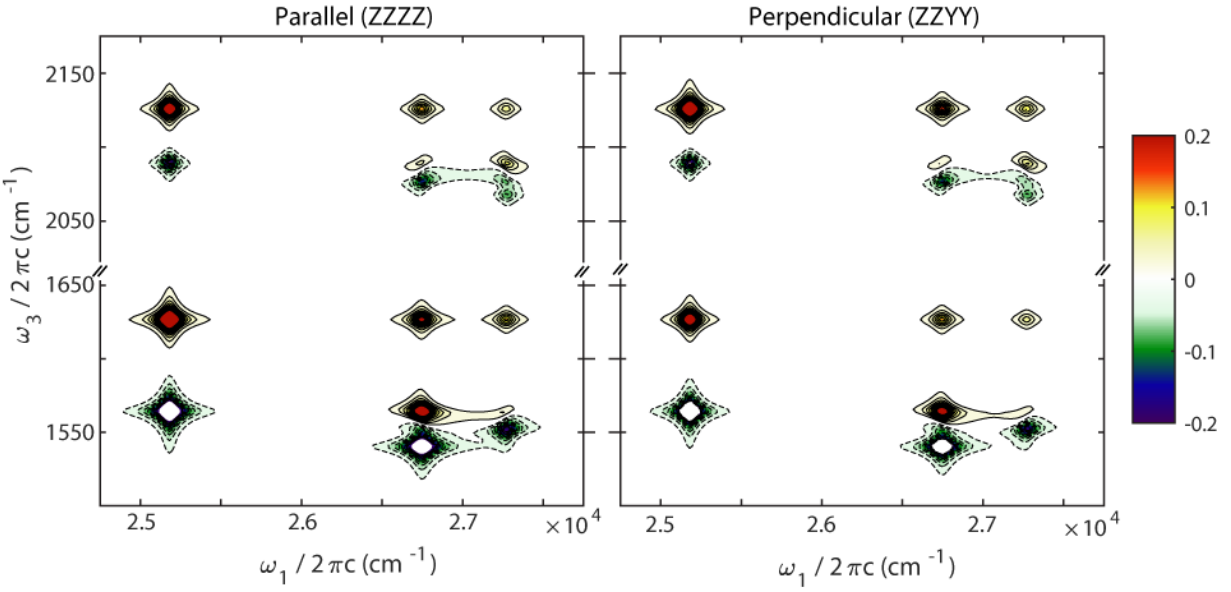


Figure 6.5. Polarization-Selective Multimode 2D EV Spectral Simulations. The parallel polarized 2D EV spectrum (left) and the perpendicularly polarized 2D EV spectrum (right). The spectra are globally normalized to the ZZZZ spectrum; the color map spans $\pm$0.2 in order to view the features from the hot vibrational manifold in the excited state more clearly. The contour lines are at 2% intervals spanning [-0.2:0.2]; dashed = negative, solid = positive.

While the simulated 2D EV contour plots are not the most obvious way of viewing differences in intensities, the general aspects of the simulated system described above can still be discerned qualitatively. The vibrations in the ground electronic state should display stronger polarization-dependence because $\theta_i$ and $\theta_j$ are closer to parallel (0°) and perpendicular (90°), respectively, than their corresponding excited state dipole angles. Hence, the ground state features for the $q_i$ coordinate should give stronger responses for the parallel polarized spectrum and vice versa for the $q_j$ coordinate in the perpendicular polarized spectrum. This is observed by comparing peaks *I* and *III* between the vibrational coordinates; the ZZZZ spectrum shows stronger peaks *I* and *III* at $\omega_3 = \omega_i = 1627$ cm$^{-1}$ than for peaks *I* and *III* at

$\omega_3 = \omega_j = 2127$ cm$^{-1}$ whereas the opposite is true for the ZZYY spectrum. Consistent with this, the excited state absorptions show closer amplitudes between the two differently polarized experimental spectra because the vibrations become more isotropically oriented upon electronic excitation. These angles were chosen in this simulation to demonstrate moderate shifts in dipole angles and a delocalized electronic excited state. However, the maximum polarization-selectivity (i.e., maximum contrast between parallel and crossed polarized signals) for a peak with a single angle dependence would occur if the vibrational dipole moment was either completely parallel or completely orthogonal with respect to the electronic transition dipole moment. As the angular dependence includes more than one angle, the polarization-selectivity of the 2D EV signal becomes more complicated.

### 6.6.1 *Comparing tIR and 2D EV Anisotropies*

Considering the peak intensities and anisotropies along particular slices in the polarization-selective 2D EV spectra yields a more direct comparison of the polarization-dependent responses. Figure 6.6 shows anisotropies as a function of vibrational probe frequency, $\omega_3$, calculated using equation (6.20) which become ill-defined as spectral intensity tends toward zero leading to asymptotic behavior.[24] As the tIR spectrum is obtained by integrating over the excitation frequency dimension, $\omega_1$, the tIR anisotropy has been calculated accordingly. The 2D EV anisotropies have been calculated using spectral slices at $\omega_1 = \omega_{eg}$ (25180 cm$^{-1}$), $\omega_{eg} + \omega_{i'}$ (26740 cm$^{-1}$), and $\omega_{eg} + \omega_{j'}$ (27260 cm$^{-1}$) to show the various signals that are convolved in the tIR anisotropy.

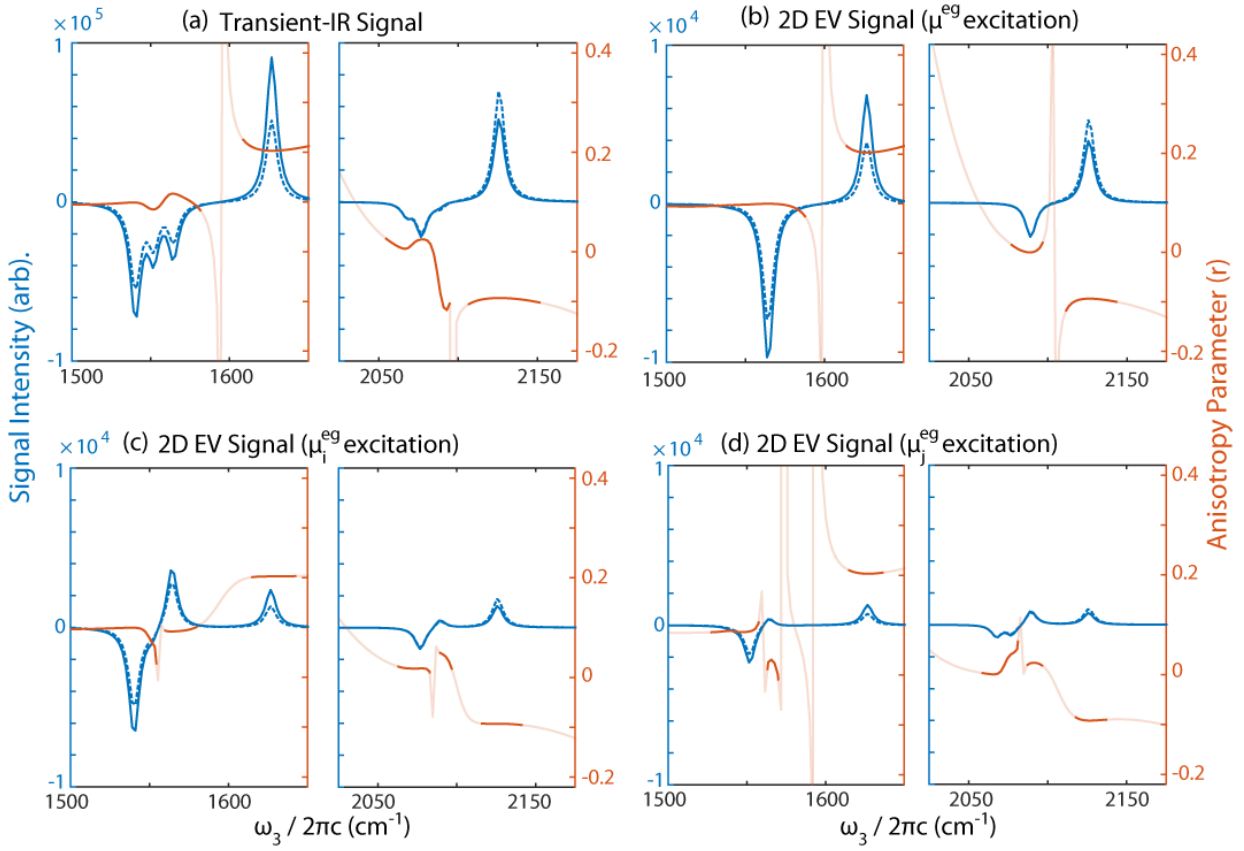


Figure 6.6. Comparison of tIR and 2D EV Anisotropies. (a) Transient-IR anisotropy calculated from summing over the parallel and crossed 2D EV spectra. The 2D EV anisotropies for (a) $\mu^{eg}$ excitation at $\omega_1 = \omega_{eg}$ (25180 cm$^{-1}$), (b) $\mu_i^{eg}$ excitation at $\omega_1 = \omega_{eg} + \omega_{i'}$ (26740 cm$^{-1}$), and (c) $\mu_j^{eg}$ at $\omega_1 = \omega_{eg} + \omega_{j'}$ (27260 cm$^{-1}$). In all plots, the blue solid (dashed) lines are the ZZZZ (ZZYY) signal intensities obtained from simulated 2D EV spectra in Figure 6.5, the red lines are the anisotropies where the spectral regions of tIR and 2D EV signal have been emphasized and the regions where the anisotropy is ill-defined have been suppressed.

Generally, the differences between the tIR signal amplitudes and the $\omega_1$-dependent 2D EV signal amplitudes shows that an inaccurate assessment of the excited state molecular structure would be obtained from the tIR signal alone. In fact, the strongest ESA feature peaks at $\omega_3$ = 1564 cm$^{-1}$ as shown by $\mu^{eg}$ excitation (Figure 6.6b), but the positively signed ESE signal arising from $\mu_i^{eg}$ excitation destructively interferes with the ESA signal to minimize its intensity overall in the tIR spectrum. From the tIR spectrum alone, the ESA peak maximum at

1541 $cm^{-1}$ suggests that the excited state vibrational frequency shift is 24 $cm^{-1}$ larger because the frequency separation of the tIR bleach and absorption maxima is actually equal to $\Delta_{eg,i} + \Delta_{i'}$. Moreover, the ~10 $cm^{-1}$ vibrational bandwidths defined in this simulation allows for the peaks to be somewhat distinguished in the simulated tIR spectrum but in practice, smaller $\Delta_{eg,i}$ and/or $\Delta_{i'}$ values and even slightly broader vibrational line widths would wash out this vibrational spectral resolution. This effect is clear in ESA peaks for the tIR spectrum of mode j (2050 $cm^{-1} < \omega_3 <$ 2100 $cm^{-1}$) in Figure 6.6(a).

In addition to the spectral intensities, the anisotropy values are of interest to understand orientational information of the relevant transitions within the molecular frame. The ground state bleach anisotropies for both vibrational modes ($\omega_i$ = 1627 $cm^{-1}$, $\omega_j$ = 2125 $cm^{-1}$) have the correct anisotropy values, $r(\omega_i) \cong 0.2$ and $r(\omega_j) \cong$ -0.08, as expected for $\theta_i$ = 35° and $\theta_j$ = 65°, respectively. This is due to the fact that the only convolved spectral features are the same type of transition (GSB) and the simulations have assumed that there is no orientational dependence of the electronic transition dipole moment arising from exciting hot vibrations (i.e., $\theta_i^{eg} = \theta_j^{eg} = 0$). The $\omega_1$-dependent anisotropy analysis below shows that the tIR and 2D EV anisotropies would not be the same for the GSB peaks if the direction of the electronic transition dipole moment carries nuclear coordinate dependence.

For the same reasons that the tIR intensity profile of the ESA features resulted from different types of transitions significantly overlapping, the ESA anisotropies will also be very poorly represented in the tIR anisotropy. Since the electronic transition dipole moments do not include any nuclear coordinate dependence in the simulations shown in Figure 6.5 and Figure 6.6, the only angles which contribute to the anisotropy values of the various peaks should be

$\theta_{i'}$ = 45° and $\theta_{j'}$ = 55° yielding r = 0.11 and r = 0.00, respectively. These values are recovered directly in the 2D EV slices (Figure 6.6(b-d)), but not as clearly in the tIR anisotropy (Figure 6.6(a)). Notably, there are overlapping ESA and ESE peaks for each vibrational coordinate with angular dependence on both $\theta_{i'}$ and $\theta_{j'}$. In these cases, the anisotropy should tend toward a value roughly in between the anisotropies for these two dipole angles separately.

By separating out the $\omega_1$-dependent pathways in the 2D EV experiment, the separation of spectral contributions arising from differently overlapped peaks in the $\omega_3$ domain can be achieved. For example, consider the anisotropy resulting from $\mu_i^{eg}$ excitation (Figure 6.6(c)). The ESA feature has contributions from peaks $IV_i^i$ (main peak at 1541 cm$^{-1}$) and $VI_i^i$ (shoulder peak at ~1551 cm$^{-1}$) while the rise of the ESE from peak $V_i^i$ is clearly separated (positive peak at 1564 cm$^{-1}$). Since peaks $IV_i^i$ and $V_i^i$ contain the strong $\theta_{i'}$ angular dependence, the prominent ESA and ESE features have anisotropies of ~0.1 (note that the $\theta_{j'}$ angular dependence arises in $V_i^i$ through one NR pathway which has both $\theta_{i'}$ and $\theta_{j'}$ dependence which is a very small contribution overall to the total anisotropy). However, the ESA shoulder peak from $VI_i^i$ drops the anisotropy to 0.06 before the zero-intensity crossing results in the asymptote between the ESA and ESE regions. This anisotropy results from the fact that peak $VI_i^i$ is composed of only one NR transition pathway that depends on both $\theta_{i'}$ and $\theta_{j'}$ because this transition pathway proceeds in the coherence superposition $|e;1'0'\rangle\langle e;0'1'|$ during $\tau_2$. Thus, the dependence on both vibrational coordinates brings the anisotropy of $VI_i^i$ to 0 < r < 0.1 which can be resolved in the 2D EV anisotropy.

### 6.6.2 *Non-Condon Effects in 2D EV Anisotropy*

Performing the 2D EV experiments in a polarization-selective manner allows for the advantage of viewing electronic-excitation-dependent orientational effects through the $\omega_1$-dependent anisotropy. Figure 6.7 compares the peak intensities for the parallel and perpendicular polarization configurations as well as the anisotropy for slices in the 2D EV spectra taken at the ground state vibrational frequency $\omega_3 = \omega_i$ = 1627 cm$^{-1}$. The three peaks arise from electronic excitation of the dipole moments: $\mu^{eg}$ (25180 cm$^{-1}$), $\mu_i^{eg}$ (26740 cm$^{-1}$), and $\mu_j^{eg}$ (27260 cm$^{-1}$). The appearance of non-Condon effects are observed in the spectral intensities and the anisotropies through both a scalar dependence (when $\mu_{eg}^{(1)} \neq 0$) and an orientational dependence (when $\theta_i^{eg} \neq 0$ or $\theta_j^{eg} \neq 0$). These two types of signal contributions can be separated using polarization-selective 2D EV measurements and analysis of the anisotropy. Importantly, the electronic transition dipole moments are vectoral quantities and so any nuclear dependence of the electronic transition dipole moment can appear as both a scalar contribution to peak intensity typically considered in the Franck-Condon picture and as an orientational contribution represented in this treatment by the electronic transition into hot vibrational states in $|e\rangle$ having a different direction than the $\mu^{eg}$ excitation (i.e., $\theta_i^{eg} \neq 0$ or $\theta_j^{eg} \neq 0$).

The same simulation parameters as used in the Figure 6.5 and Figure 6.6 were used to simulate the 2D EV spectral slices shown in Figure 6.7 except for the parameters related to the non-Condon effects (see Figure 6.7 caption). The simulations without any non-Condon effects are shown in gray and the scalar contributions from non-Condon effects are shown in black. Comparing the black and the gray spectra for both ZZZZ and ZZYY shows that when linear

and higher order expansion terms of $\mathbf{M}_{eg}(Q_i, Q_j)$ are non-zero, the peak amplitudes increase more for peaks resulting from $\mu_i^{eg}$ or $\mu_j^{eg}$ excitation than for $\mu^{eg}$ excitation.

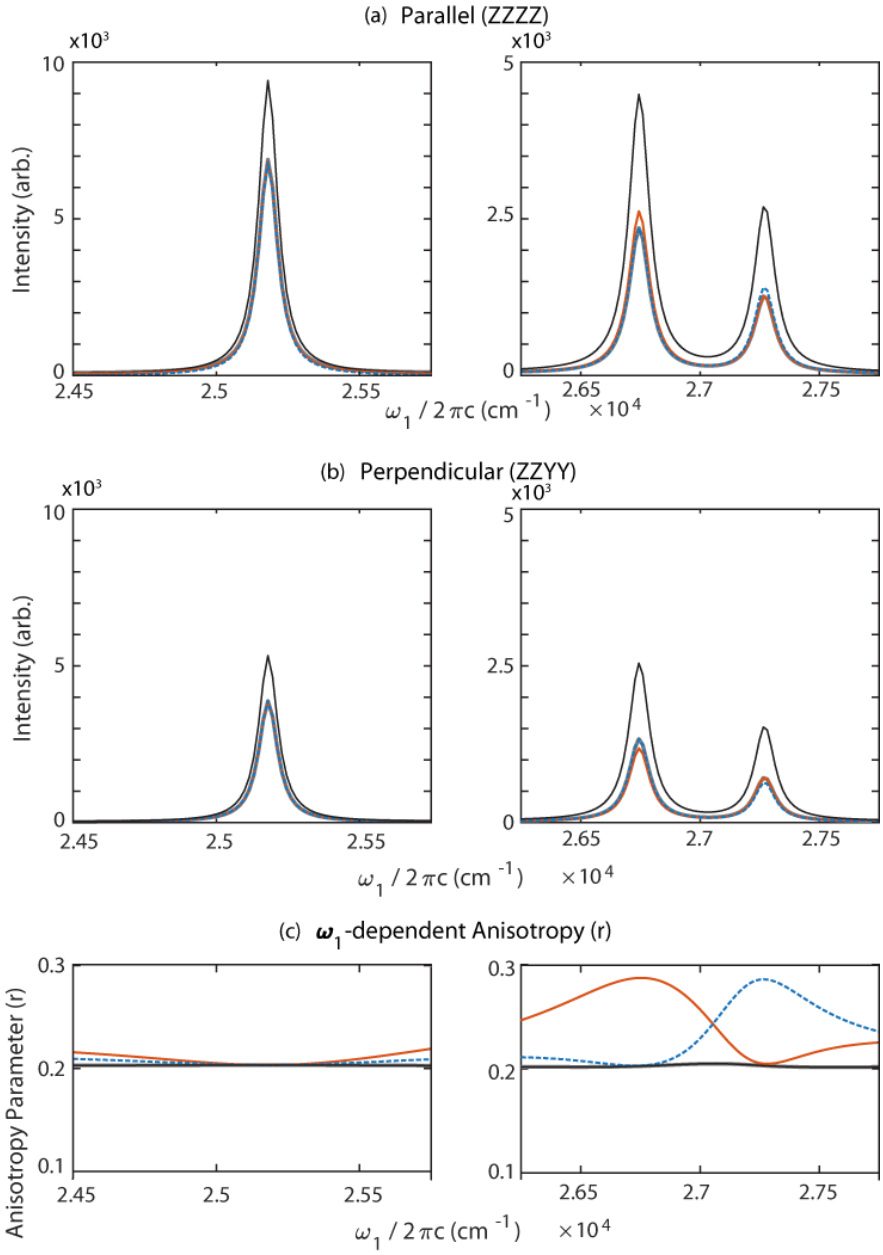


Figure 6.7. Non-Condon effects viewed through excitation dependent 2D EV anisotropies. All spectra result from 2D EV slices at $\omega_3 = 1627$ cm$^{-1}$ (ground state vibration of mode i). Four different simulations are shown for (a) ZZZZ (b) ZZYY and (c) the anisotropy: gray = [$\theta_i^{eg} = 0^o$, $\theta_j^{eg} = 0^o$, $\mu_{eg}^{(1)} = 0$]; red = [$\theta_i^{eg} = 10^o$, $\theta_j^{eg} = 0^o$, $\mu_{eg}^{(1)} = 0$]; blue (dashed) = [$\theta_i^{eg} = 0^o$, $\theta_j^{eg} = 10^o$, $\mu_{eg}^{(1)} = 0$]; and black = [$\theta_i^{eg} = 0^o$, $\theta_j^{eg} = 0^o$, $\mu_{eg}^{(1)} = 0.15$]. Note the difference in signal intensity axes in (a) and (b).

This intensity borrowing is consistent with the breakdown of the Condon approximation and affects both ZZZZ and ZZYY spectra equally, as is seen through a constant anisotropy value (~0.2) for both black and gray spectra in Figure 6.7(c). This effect is the same as described for the one mode case in chapter 2.[1]

The orientational effects from any nuclear dependence of the electronic transition dipole moment may be observed clearly in the excitation-dependent 2D EV anisotropy. These effects are observed through comparison of the red ($\theta_i^{eg} \neq 0$) and dashed blue ($\theta_j^{eg} \neq 0$) polarization-dependent spectra and they are emphasized in the anisotropy. In both parallel and perpendicular polarized spectra for peak $I^i$, no difference in intensity is observed when orientational non-Condon effects are introduced because the electronic excitation dipole moment is $\mu^{eg}$ which connects the common vibrational ground state in each electronic state. There is a difference observed for peaks $III_i^i$ and $III_j^i$ because they have electronic excitation dipole moments which can be affected by the dependence of either coordinate i ($III_i^i$) or coordinate j ($III_j^i$) during the electronic transition. When $\theta_i^{eg} \neq 0$ ($\theta_j^{eg} \neq 0$), the amplitude of peak $III_i^i$ ($III_j^i$) is greater than in the absence of orientational non-Condon effects for the parallel polarized 2D EV signal and lesser in amplitude for the perpendicularly polarized signal. This can be rationalized by considering the depicted dipole moments in Figure 6.1(b); the projection of the vibrational transition dipole moment onto the electronic transition dipole moment is greater when the electronic transition experiences orientational non-Condon effects. Thus, the parallel polarized signal will be stronger than the perpendicularly polarized signal. The anisotropies show a very clear shift from 0.2 to 0.3 due to the presence of orientational

non-Condon effects in Figure 6.7(c). These simulations demonstrate the polarization-sensitivity of orientational non-Condon effects in 2D EV spectroscopy.

## 6.7 DISCUSSION

In general, the above analysis shows that 2D EV spectroscopy can be very useful for isolating the presence of Duschinsky mixing and non-Condon effects in condensed phase molecular ensembles. These topics are discussed more broadly in the following paragraphs.

### 6.7.1 *Selection Rules in Multimode 2D EV Spectroscopy*

The vibronic selection (or propensity) rules for 2D EV and 2D Vibrational-Electronic spectroscopies were established through the theoretical treatment of one displaced, frequency-shifted anharmonic oscillator in chapter 2.[1] These rules were constructed based upon systematic simulations of the 2D spectra in which the effects of simulation parameters on the peak positions, amplitudes, and line shapes were analyzed. These same rules still govern the multimode, polarization-selective 2D EV signals as well. However, the presence of two anharmonic modes that are coupled in the excited state through Duschinsky mixing also has the potential to reveal 2D EV signal in the absence of any other type of vibronic coupling. This is justified because the $\mathcal{V}_{i,j}^{(2)}$ term clearly has the ability to affect both the position and the amplitude of 2D EV peaks as discussed above. This effect manifests as a splitting between the excited state vibrational signatures (e.g., peaks $II^i$ and $II^j$) , which would be sufficient to separate even an overlapping GSB and ESA peak if the quadratic perturbation parameter was equal to zero ( $\mathcal{V}_{i,i}^{(2)}, \mathcal{V}_{j,j}^{(2)} = 0$ ) . Moreover, since the Duschinsky mixing effect can be considered to arise from the vibrational transition dipole moments, a difference in amplitude between peaks $I$ and $II$ for either vibrational coordinate could also contribute to an observed 2D EV

signal even with a fairly small frequency shift. It is still noted that the Duschinsky mixing effects would still likely contribute signals of much weaker magnitude than would be observed if the pure quadratic vibronic coupling ($\mathcal{V}_{i,i}^{(2)}, \mathcal{V}_{j,j}^{(2)}$) was non-zero. Thus, Duschinsky mixing is also a sufficient condition to contribute 2D EV signal.

### 6.7.2 *Duschinsky Mixing and Non-Condon Effects*

Considering all of the factors governing the amplitudes of multimode 2D EV signals, one sees that both scalar and directional contributions are included as a result of the transition dipole moments being vectoral quantities. As discussed in the above sections, the presence of Duschinsky mixing contributes additional amplitude through the vibrational transition dipole moments as well as energetically splits vibronic eigenstates resulting in new peaks being measured (through contributions to $\Delta_{eg,i}$, $\Delta_{eg,j}$, or $\Delta_{i'j'}$). This effect can be largely considered a molecular structural modification of the nuclei in the excited electronic state because their motion is not completely separable from the motion of the electrons. While this effect has largely considered through the scalar contributions as shown in Figure 6.4, it is not unreasonable to expect that a Duschinsky mixing of vibrational modes should also affect the direction of the vibrational transition dipole moment since the character of the two excited state vibrational modes is being mixed.

The non-Condon effects are very different because they concern the nature of the electronic transition, rather than explicitly the vibrational motion. As shown above, the nuclear dependence of the electronic transition dipole moment can be broken down into both a scalar contribution that is independent of dipole orientation and an orientational contribution. The scalar contributions arise from the magnitude of the electronic transition dipole matrix element when the expansion of the electronic transition dipole moment about the relevant nuclear

coordinate includes non-zero linear and higher order terms. These types of contributions would be most easily discernible through a peak amplitude ratio of two peaks in a vibronic progression of the relevant nuclear coordinate. However, some a priori information regarding what the true displacement of the electronic potentials is would likely be necessary to confirm that a measured peak amplitude ratio reflects a non-Condon effect; otherwise one could not distinguish a non-Condon effect from a linear vibronic coupling. The orientational response may provide a more direct way to view a non-Condon effect through the excitation dependent anisotropy; the most clear measurement would still require a polarization-selective experiment that can excite at least two peaks in a vibronic progression so the comparison between the two peaks' anisotropies can be made.

While the scalar and directional aspects of the signal contributions from Duschinsky mixing and non-Condon effects in multimode 2D EV spectra are quite clearly decoupled from one another in this analysis, the more likely scenario will have these effects more strongly coupled in real molecular systems and many of these effects could also be time-dependent.

## 6.8 CONCLUSIONS

The vibronic contributions to polarization-selective multimode 2D EV spectra have been investigated in this chapter in detail. While many more interesting molecular phenomena can occur when more than one vibrational mode is relevant during excited state dynamics, the resulting spectral signatures can also become much more complicated. This analysis has decoupled the nonlinear vibronic response from the nonlinear orientational response and treated each part of the molecular response separately. The separate contributions from Duschinsky mixing and non-Condon effects within either, or both, of the nonlinear vibronic and orientational responses as discussed here provides a simplified guideline for which some

polarization-selective 2D EV experimental spectra may be interpreted. While these contributions have only been considered in this chapter for 2D EV spectroscopy, they are all directly translatable to an interpretation of 2D Vibrational-Electronic spectroscopy, as was done in Chapter 2 for the single vibrational mode. In fact, applying a more subtle interpretation of the orientational and scalar contributions of non-Condon effects in the 2D VE spectroscopy of charge transfers in mixed valence complexes is beginning to prove fruitful.[25] This chapter provides a theoretical framework for understanding how the more subtle details of Duschinsky mixing and non-Condon effects may appear in polarization-selective multimode 2D EV spectroscopy.

## 6.9 APPENDIX

### 6.9.1 *Multimode 2D EV Energy Gap Correlation Functions*

The vibronic transition frequency correlation functions that are accessed for 2D EV spectroscopy of a system with two coupled anharmonic vibrations (i and j) are defined as:

$$\begin{aligned}
\zeta_{i,i}(t) &= \left\langle \delta\omega_{g10,g00}(t)\delta\omega_{g10,g00}(0)\right\rangle \\
\zeta_{j,j}(t) &= \left\langle \delta\omega_{g01,g00}(t)\delta\omega_{g01,g00}(0)\right\rangle \\
\zeta_{eg,eg}(t) &= \left\langle \delta\omega_{e0'0',g00}(t)\delta\omega_{e0'0',g00}(0)\right\rangle \\
\zeta_{eg,i}(t) &= \left\langle \delta\omega_{e0'0',g00}(t)\delta\omega_{e1'0',e0'0'}(0)\right\rangle \\
\zeta_{i',i'}(t) &= \left\langle \delta\omega_{e1'0',e0'0'}(t)\delta\omega_{e1'0',e0'0'}(0)\right\rangle \\
\zeta_{eg,j}(t) &= \left\langle \delta\omega_{e0'0',g00}(t)\delta\omega_{e0'1',e0'0'}(0)\right\rangle \\
\zeta_{j',j'}(t) &= \left\langle \delta\omega_{e0'1',e0'0'}(t)\delta\omega_{e0'1',e0'0'}(0)\right\rangle \\
\zeta_{i',j'}(t) &= \left\langle \delta\omega_{e1'0',e0'0'}(t)\delta\omega_{e0'1',e0'0'}(0)\right\rangle
\end{aligned} \tag{6.21}$$

where the energy gap of the two states that is fluctuating is specified by the two states given in the subscripts. The two mode dephasing functions are obtained in the same way as described for the one mode system discussed in Chapter 2.

### 6.9.2 *Two Mode Transition Pathways and Orientational Response*

The vibronic transition pathways for the multimode 2D EV spectroscopy are organized by the four vibronic eigenstates involved in the Liouville pathway $(a,b,c,d)$, the general type of third order Liouville pathway as defined in the Chapter 2 appendix ( $R_n$, $n \in 1-4$ ) for rephasing (R) and non-rephasing (NR), the non-vanishing tensor components $\{zzzz, zzyy, zyzy, zyyz, yyyy, yyzz, yzyz, yzzy\}$, and the dipole angles for the light-matter interactions composing the pathway ( $\theta_m$, $m \in 1-4$ ). Generalized expressions for the orientational response of each pathway are given which can be used in conjunction with the defined angles for each pathway to obtain the specific orientational response of each transition pathway.

Table 6.7. Ground State Bleach Multimode Vibronic Transition Pathways

| Peak | Pathway Type | | Tensor components | Vibronic States | | | | Angles | | | |
|---|---|---|---|---|---|---|---|---|---|---|---|
| | R | NR | | $\|a\rangle$ | $\|b\rangle$ | $\|c\rangle$ | $\|d\rangle$ | $\theta_1$ | $\theta_2$ | $\theta_3$ | $\theta_4$ |
| $I^i$ | $R_3$ | $R_4$ | zzzz, yyzz | $\|g;00\rangle$ | $\|g;10\rangle$ | $\|g;00\rangle$ | $\|e;0'0'\rangle$ | $\theta_i$ | - | - | - |
| $I^j$ | $R_3$ | $R_4$ | zzzz, yyzz | $\|g;00\rangle$ | $\|g;01\rangle$ | $\|g;00\rangle$ | $\|e;0'0'\rangle$ | $\theta_j$ | - | - | - |
| $III_i^i$ | $R_3$ | $R_4$ | (all 8) | $\|g;00\rangle$ | $\|g;10\rangle$ | $\|g;00\rangle$ | $\|e;1'0'\rangle$ | $\theta_i$ | $\theta_i^{eg}$ | - | - |
| $III_i^j$ | $R_3$ | $R_4$ | (all 8) | $\|g;00\rangle$ | $\|g;01\rangle$ | $\|g;00\rangle$ | $\|e;1'0'\rangle$ | $\theta_j$ | $\theta_i^{eg}$ | - | - |
| $III_j^i$ | $R_3$ | $R_4$ | (all 8) | $\|g;00\rangle$ | $\|g;10\rangle$ | $\|g;00\rangle$ | $\|e;0'1'\rangle$ | $\theta_i$ | $\theta_j^{eg}$ | - | - |
| $III_j^j$ | $R_3$ | $R_4$ | (all 8) | $\|g;00\rangle$ | $\|g;01\rangle$ | $\|g;00\rangle$ | $\|e;0'1'\rangle$ | $\theta_j$ | $\theta_j^{eg}$ | - | - |

Table 6.8. Excited State Stimulated Emission Multimode Vibronic Transition Pathways

| Peak | Pathway Type | | Tensor components | Vibronic States | | | | Angles | | | |
|---|---|---|---|---|---|---|---|---|---|---|---|
| | R | NR | | $\|a\rangle$ | $\|b\rangle$ | $\|c\rangle$ | $\|d\rangle$ | $\theta_1$ | $\theta_2$ | $\theta_3$ | $\theta_4$ |
| $V_i^i$ | $R_2$ | $R_1$ | (all 8) | $\|g;00\rangle$ | $\|e;1'0'\rangle$ | $\|e;0'0'\rangle$ | $\|e;1'0'\rangle$ | $\theta_{i'}$ | $\theta_i^{eg}$ | - | - |
| $V_i^i$ | - | $R_1$ | (all 8) | $\|g;00\rangle$ | $\|e;0'1'\rangle$ | $\|e;0'0'\rangle$ | $\|e;1'0'\rangle$ | $\theta_{i'}$ | $\theta_{j'}$ | $\theta_j^{eg}$ | $\theta_i^{eg}$ |
| $V_j^j$ | $R_2$ | $R_1$ | (all 8) | $\|g;00\rangle$ | $\|e;0'1'\rangle$ | $\|e;0'0'\rangle$ | $\|e;0'1'\rangle$ | $\theta_{j'}$ | $\theta_j^{eg}$ | - | - |
| $V_j^j$ | - | $R_1$ | (all 8) | $\|g;00\rangle$ | $\|e;1'0'\rangle$ | $\|e;0'0'\rangle$ | $\|e;0'1'\rangle$ | $\theta_{j'}$ | $\theta_{i'}$ | $\theta_i^{eg}$ | $\theta_j^{eg}$ |
| $V_j^i$ | $R_2$ | - | (all 8) | $\|g;00\rangle$ | $\|e;1'0'\rangle$ | $\|e;0'0'\rangle$ | $\|e;0'1'\rangle$ | $\theta_{i'}$ | $\theta_{j'}$ | $\theta_i^{eg}$ | $\theta_j^{eg}$ |
| $V_i^j$ | $R_2$ | - | (all 8) | $\|g;00\rangle$ | $\|e;0'1'\rangle$ | $\|e;0'0'\rangle$ | $\|e;1'0'\rangle$ | $\theta_{j'}$ | $\theta_{i'}$ | $\theta_j^{eg}$ | $\theta_i^{eg}$ |

Table 6.9. Excited State Absorption Multimode Vibronic Transition Pathways

| Peak | Pathway Type | | Tensor components | Vibronic States | | | | Angles | | | |
|---|---|---|---|---|---|---|---|---|---|---|---|
| | R | NR | | $\|a\rangle$ | $\|b\rangle$ | $\|c\rangle$ | $\|d\rangle$ | $\theta_1$ | $\theta_2$ | $\theta_3$ | $\theta_4$ |
| $II^i$ | $R_1^*$ | $R_2^*$ | zzzz, yyzz | $\|g;00\rangle$ | $\|e;0'0'\rangle$ | $\|e;1'0'\rangle$ | $\|e;0'0'\rangle$ | $\theta_{i'}$ | - | - | - |
| $II^j$ | $R_1^*$ | $R_2^*$ | zzzz, yyzz | $\|g;00\rangle$ | $\|e;0'0'\rangle$ | $\|e;0'1'\rangle$ | $\|e;0'0'\rangle$ | $\theta_{j'}$ | - | - | - |
| $IV_i^i$ | $R_1^*$ | $R_2^*$ | (all 8) | $\|g;00\rangle$ | $\|e;1'0'\rangle$ | $\|e;2'0'\rangle$ | $\|e;1'0'\rangle$ | $\theta_{i'}$ | $\theta_i^{eg}$ | - | - |
| $IV_j^j$ | $R_1^*$ | $R_2^*$ | (all 8) | $\|g;00\rangle$ | $\|e;0'1'\rangle$ | $\|e;0'2'\rangle$ | $\|e;0'1'\rangle$ | $\theta_{j'}$ | $\theta_j^{eg}$ | - | - |
| $VI_i^i$ | - | $R_2^*$ | (all 8) | $\|g;00\rangle$ | $\|e;0'1'\rangle$ | $\|e;1'1'\rangle$ | $\|e;1'0'\rangle$ | $\theta_{i'}$ | $\theta_{j'}$ | $\theta_j^{eg}$ | $\theta_i^{eg}$ |
| $VI_j^j$ | - | $R_2^*$ | (all 8) | $\|g;00\rangle$ | $\|e;1'0'\rangle$ | $\|e;1'1'\rangle$ | $\|e;0'1'\rangle$ | $\theta_{j'}$ | $\theta_{i'}$ | $\theta_i^{eg}$ | $\theta_j^{eg}$ |
| $VI_j^i$ | $R_1^*$ | $R_2^*$ | (all 8) | $\|g;00\rangle$ | $\|e;0'1'\rangle$ | $\|e;1'1'\rangle$ | $\|e;0'1'\rangle$ | $\theta_{i'}$ | $\theta_j^{eg}$ | - | - |
| $VI_j^i$ | $R_1^*$ | - | (all 8) | $\|g;00\rangle$ | $\|e;1'0'\rangle$ | $\|e;1'1'\rangle$ | $\|e;0'1'\rangle$ | $\theta_{i'}$ | $\theta_{j'}$ | $\theta_i^{eg}$ | $\theta_j^{eg}$ |
| $VI_i^j$ | $R_1^*$ | $R_2^*$ | (all 8) | $\|g;00\rangle$ | $\|e;1'0'\rangle$ | $\|e;1'1'\rangle$ | $\|e;1'0'\rangle$ | $\theta_{j'}$ | $\theta_i^{eg}$ | - | - |
| $VI_i^j$ | $R_1^*$ | - | (all 8) | $\|g;00\rangle$ | $\|e;0'1'\rangle$ | $\|e;1'1'\rangle$ | $\|e;1'0'\rangle$ | $\theta_{j'}$ | $\theta_{i'}$ | $\theta_j^{eg}$ | $\theta_i^{eg}$ |

The generalized orientational response functions for parallel ($Y_{ZZZZ}$) and crossed ($Y_{YYZZ}$) polarized experimental geometries are given below; they are differentiated by the angular dependence and the non-vanishing tensor components contributing to the signal.

Table 6.10. Orientational Response Functions for Parallel and Crossed Polarization Configurations.

| *Angular Dependence (# of angles)* | *Number of Tensor Comps.* | $Y_{ZZZZ}$ | $Y_{YYZZ}$ |
|---|---|---|---|
| 1 | zzzz, yyzz | $\frac{1}{15}\left[2\cos^2(\theta_1)+1\right]$ | $\frac{1}{15}\left[1+\sin^2(\theta_1)\right]$ |
| 2 | (all 8) | $\frac{1}{15}[\cos^2(\theta_1)\left(\cos^2(\theta_2)+1\right)+\cos^2(\theta_2)+\sin(2\theta_1)\sin(2\theta_2)]$ | $\frac{1}{30}\left[3-\cos\left(2(\theta_1-\theta_2)\right)\right]$ |
| 4 | (all 8) | $\frac{1}{60}[12\left(\cos(\theta_1)\cos(\theta_2)\cos(\theta_3)\cos(\theta_4)\right)+\cos(\theta_1+\theta_2-\theta_3-\theta_4)+\cos(\theta_1-\theta_2+\theta_3-\theta_4)+\cos(\theta_1-\theta_2-\theta_3+\theta_4)-3\left(\cos(\theta_1+\theta_2+\theta_3+\theta_4)\right)]$ | $\frac{1}{20}[\cos(\theta_1-\theta_2+\theta_3-\theta_4)+\cos(\theta_1-\theta_2-\theta_3+\theta_4)]-\frac{1}{30}[\cos(\theta_1+\theta_2-\theta_3-\theta_4)]$ |

## 6.10 REFERENCES


(1) Gaynor, J. D.; Khalil, M. Signatures of vibronic coupling in two-dimensional electronic-vibrational and vibrational-electronic spectroscopies; *J. Chem. Phys.* **2017**, *147*, 094202.

(2) Sung, J. Y.; Silbey, R. J. Four wave mixing spectroscopy for a multilevel system; *J. Chem. Phys.* **2001**, *115*, 9266-9287.

(3) Born, M.; Oppenheimer, R. Quantum Theory of Molecules; *Ann. Phys.* **1927**, *389*, 0457-0484.

(4) Ballhausen, C. J.; Hansen, A. E. Electronic-Spectra; *Annu. Rev. Phys. Chem.* **1972**, *23*, 15.

(5) Harris, D. C.; Bertolucci, M. D. *Symmetry and Spectroscopy: An Introduction to Vibrational and Electronic Spectroscopy*; Dover: New York, 1989.

(6) Hollas, J. M. *Modern Spectroscopy*; 2nd ed.; John Wiley & Sons: West Sussex, England, 1992.

(7) Fischer, G. *Vibronic Coupling: The Interaction between Electronic and Nuclear Motions*; Academic Press: London, 1984.

(8) Herzberg, G.; Teller, E. Fluctuation structure of electron transfer in multiatomic molecules.; *Z. Phys. Chem.* **1933**, *21*, 410-446.

(9) Azumi, T.; Matsuzaki, K. What Does Term Vibronic-Coupling Mean; *Photochem. Photobiol.* **1977**, *25*, 315-326.

(10) Mukamel, S. *Principles of Nonlinear Optical Spectroscopy*; Oxford University Press: New York, 1995.

(11) Berne, B. J.; Pecora, R. *Dynamic Light Scattering*; Dover: New York, 2000.

(12) Favro, L. D. Theory of the Rotational Brownian Motion of a Free Rigid Body; *Phys. Rev.* **1960**, *119*, 53-62.

(13) Golonzka, O.; Tokmakoff, A. Polarization-selective third-order spectroscopy of coupled vibronic states; *J. Chem. Phys.* **2001**, *115*, 297-309.

(14) Tokmakoff, A. Orientational correlation functions and polarization selectivity for nonlinear spectroscopy of isotropic media .1. Third order; *J. Chem. Phys.* **1996**, *105*, 1-12.

(15) Khalil, M.; Demirdoven, N.; Tokmakoff, A. Coherent 2D IR spectroscopy: Molecular structure and dynamics in solution; *J. Phys. Chem. A* **2003**, *107*, 5258-5279.

(16) Duschinsky, F. The importance of the electron spectrum in multi atomic molecules. concerning the Franck-Condon principle; *Acta Physicochim Urs* **1937**, *7*, 551-566.

(17) Cohen-Tannoudji, C.; Diu, B.; Laloe, F. *Quantum Mechanics*; Wiley-Interscience: Paris, 1977.

(18) Butcher, P. N.; Cotter, D. *The Elements of Nonlinear Optics*; Cambridge University Press: Cambridge, 1990.

(19) Khalil, M. *A Tale of Coupled Vibrations in Solution Told by Coherent Two-Dimensional Infrared Spectroscopy* Ph.D. Dissertation, MIT, 2004.

(20) Rose, M. E. *Elementary Theory of Angular Momentum*; Dover: New York, 1957.

(21) Hamm, P.; Zanni, M. T. *Concepts and Methods of 2D Infrared Spectroscopy*; Cambridge University Press: Cambridge, U.K., 2011.

(22) Wynne, K.; Hochstrasser, R. M. Anisotropy as an Ultrafast Probe of Electronic Coherence in Degenerate Systems Exhibiting Raman-Scattering, Fluorescence, Transient Absorption and Chemical-Reactions; *J. Raman Spectrosc.* **1995**, *26*, 561-569.

(23) Ferro, A. A.; Jonas, D. M. Pump-probe polarization anisotropy study of doubly degenerate electronic reorientation in silicon naphthalocyanine; *J. Chem. Phys.* **2001**, *115*, 6281-6284.

(24) Lakowicz, J. R. *Principles of Fluorescence Spectroscopy*; Springer: New York, NY, 2006.

(25) Fox, Z. W. *Two-Dimensional Vibrational-Electronic Spectroscopy: The Design and Development of a Novel Multidimensional Spectroscopic Technique to Directly Measure Coherent coupling Between VIbrational and Electronic Degrees of Freedom* Ph.D. Dissertation, University of Washington, 2018.

# Chapter 7. MAPPING VIBRONIC COUPLINGS IN $N3^{4-}$ WITH POLARIZATION-SELECTIVE TWO-DIMENSIONAL ELECTRONIC-VIBRATIONAL SPECTROSCOPY

*The work presented in this chapter has been published in the following paper:*

*1) Gaynor, J.D.; Petrone, A.; Li, X.; Khalil, M. "Mapping Vibronic Couplings in a Solar Cell Dye with Polarization-Selective Two-Dimensional Electronic-Vibrational Spectroscopy" Journal of Physical Chemistry Letters **2018**, 9, 6289-6295.*

## 7.1 INTRODUCTION

The metal-to-ligand charge transfer (MLCT) excited states of transition metal complexes are widely used for light-harvesting and photocatalysis.[1-4] Understanding the ensuing ultrafast relaxation dynamics of the initially excited singlet MLCT state to a triplet MLCT state *via* intersystem crossing (ISC) or to other singlet excited and ground MLCT states via internal conversion is crucial for developing better photo-sensitizers. Considerable research efforts are being directed at understanding the role of coupled vibrations, solvent dynamics, spin-orbit coupling and the available excited density-of-states in determining the ultrafast photochemistry of transition metal complexes.[5-15] The ability of 2D EV spectroscopy to provide a correlation map between electronic and vibrational degrees of freedom in excited states,[16,17] and its direct sensitivity to measuring vibronic couplings,[18] makes it an ideal technique to study photoexcited energy and charge transfer dynamics in transition metal complexes.

A famous molecular photo-sensitizer system is the Ru-centered compound known as "N3" $[Ru(dcbpy)_2(NCS)_2]$, [dcbpy = (4,4'-dicarboxy-2,2'-bipyridine)], which is particularly good at transferring electron density *via* excited MLCT states that are excited by UV-Visible radiation. N3 belongs to a broader class of transition metal compounds undergoing rapid and complex charge transfer (CT) dynamics which can be dictated by structural rearrangement and solvent

environment.[6,19] The rich photoexcited dynamics reported for N3 in solution[20-26] and on semiconductor substrates[3,27-34] suggest that many states in the excited $^1$MLCT manifold participate in various CT and relaxation pathways available to N3. Evidence for nonergodic electron transfer and the involvement of nonthermalized vibronic states within the excited $^1$MLCT manifold have also been reported for N3.[27,35,36] How might vibronic couplings dictate ultrafast photoexcited CT dynamics in this system? Invoking the analogy of Chapter 1, who are the main players in N3's photophysical dynamics, and how do they play their game of ultrafast photoexcited charge transfer?

In this chapter, polarization-selective 2D EV spectroscopy is used to directly correlate specific $^1$MLCT states with vibrations in the $^3$MLCT manifold following photo-excitation of the aqueous, fully-deprotonated form of the famous photo-sensitizer, $N3^{4-}$. As detailed in chapter 2, the 2D EV spectrum measures IR-active vibrational changes due to electronic excitation as a frequency-frequency correlation plot of the electronic excitation frequencies ($\omega_1$) and vibrational detection frequencies ($\omega_3$).[16,17,37,38] While the one-dimensional analog, transient-IR (tIR) spectroscopy, lacks the excitation spectral resolution afforded by 2D EV, it provides a necessary starting point for this investigation by identifying structural differences between the ground state and the excited $^3$MLCT states probed. In the following, we discover experimental evidence for vibronic couplings in $N3^{4-}$ between several excited $^1$MLCT states and vibrational modes observed in the lowest energy $^3$MLCT state for $\tau_2$ = 2 ps. This is effectively a static snapshot of the vibronic couplings present in the $^3$MLCT manifold during non-equilibrium relaxation. As Figure 7.3 reveals, there are many players! Distinct $\omega_1$-dependent features of $^3$MLCT vibrational modes in the polarization-selective 2D EV spectra are associated with different initially-excited $^1$MLCT states based on the agreement of

measured and *ab initio* calculated angles between the electronic and vibrational transition dipole moments probed during the experiment. The electron density reorganization upon exciting the associated $^1$MLCT states lends insight into the microscopic nature of the vibronic couplings used by photoexcited $N3^{4-}$ to transfer energy. A more fundamental point made by these spectra is the fact that the vibronic states in the singlet and triplet manifolds of $N3^{4-}$ must be very strongly mixed, which likely facilitates its <100 fs ISC dynamics.

## 7.2 MATERIALS AND METHODS

### 7.2.1 *$N3^{4-}$ Sample Preparation*

The N3 dye (*cis*-Bis(isothiocyanato)bis(2,2'-bipyridyl-4,4'-dicarboxylato)ruthenium(II)) was purchased from Sigma Aldrich (703206 Alrdich) and used without further purification. A 40 mM sample was prepared in aqueous 300 mM NaOH (pH~13) solvent to fully deprotonate N3 and form $N3^{4-}$. Samples for experiments probing the $\omega_3$=2000-2200 cm$^{-1}$ region were prepared using deionized $H_2O$ as solvent, while those probing the $\omega_3$=1250-1620 cm$^{-1}$ were prepared in $D_2O$. A sample flow cell (Harrick) with a 25 μm path length (25 μm Teflon spacer (Lebow) sandwiched between 1 mm and 2 mm $CaF_2$ windows) driven by a peristaltic pump was used to refresh the volume of molecules illuminated by every laser shot (>1 kHz). Additionally, the sample cell was raster scanned in the orthogonal plane to beam propagation to refresh the illuminated region of the sample cell window which avoided sample build up inside the confined sample flowing volume during long laser runs. The sample was enclosed in a septum-capped vial with needle-connections to the flow cell tubing to minimize solvent evaporation during experiments; the samples with $D_2O$ solvent were sealed carefully and stored in separate dried chamber. The $N3^{4-}$ purity was confirmed by UV-Vis and FTIR spectral

measurements during several experiments with the same samples. UV-Vis and FTIR spectra taken before and after each experimental run confirmed there was no photodegradation during the tIR and 2D EV experiments.

### 7.2.2 *Instrumental Details*

The instrumental configuration used for the experiments presented in this chapter can be found in chapters 3 and 4. These tIR and 2D EV experiments used the broadband UV source generated using the multi-plate method. Two plates (BK7, VWR International micro cover glass, 22 x 30 x 0.14 mm set at Brewster's angle) were used in all data collection in this chapter. The pump spectrum and intensity were checked before and after each experimental run (~8 hours for tIR, ~3 hours for 2D EV) to monitor its stability; the spectral shape was very robust over several days of experiments and the intensity was not observed to fluctuate more than expected laser drift over long periods. The broadband UV pump spectrum used in this experiment is shown in Figure 7.1(a) (FWHM = 19 nm or 1210 $cm^{-1}$, ~125 nJ/pulse, $1/e^2$ beam diameter at sample = 250 μm). After several experimental runs, the plates were translated vertically to refresh the regions incident with the beam and avoid damage. The OPA/DFG generated mid-IR probe source (~325 nJ/pulse, $1/e^2$ beam diameter at sample = 200 μm) with polarizers set as described in chapter 3. The pump power dependence of the signal is shown in the following chapter; all signals measured are linearly dependent with pump pulse power.

### 7.2.3 *Transient-IR Data Collection and Processing*

The tIR data in the charge donor region (2000-2150 $cm^{-1}$) was collected by averaging 15 scans over the pump-probe delay ($\tau_2$) range [-1,100] ps with 1500 laser shots averaged at each time point and the spectrometer grating centered at 4.8 μm (~6.5 $cm^{-1}$ spectral resolution in

this region). The frequency axis in this region was calibrated using the CN stretching frequencies of an aqueous solution of $Fe^{II}(CN)_6$ and $Fe^{III}(CN)_6$ (100mM each), and the CN stretch of the $N3^{4-}$. The tIR data in the charge acceptor region (1250 – 1620 $cm^{-1}$) was collected in the same way using three grating positions (6.5, 7.0, and 7.5 μm; 2-4 $cm^{-1}$ spectral resolution in this region) to span the probed IR region. The spectra were stitched together and averaged to obtain the full spectrum in post-processing. The IR frequency axis in this region was calibrated using the absorption peaks of a polystyrene film. In all experiments, the data were divided by a well averaged spectrum (5000 laser shots) of the $N3^{4-}$ sample with the pump blocked to obtain ΔT/T. All tIR data presented in this chapter were collected with pump and probe polarizations parallel to one another ($S_{ZZZZ}$).

### 7.2.4 *2D EV Data Collection and Processing*

The 2D EV data is obtained by collecting a pump-probe spectrum at a fixed pump-probe delay ($\tau_2$ = 2 ps) and as a function of the delay between the two pump pulses ($\tau_1$). Six $\tau_1$ scans with 1500 laser shots averaged for each difference spectrum at every $\tau_1$ were collected; a well averaged sample spectrum with the pump blocked is used to obtain ΔT/T as described for the tIR data above. For each scan, the 2D EV signal is isolated from the constant ($\tau_1$-independent) pump-probe signal by subtracting the constant offset at long $\tau_1$ delays for each pixel in the spectrally detected data, while the slowly varying, $\tau_1$-dependent pump-probe signal is removed during Fourier transform processing. The $\tau_1$ delay was scanned over [0,80] fs in 0.33 fs steps for the charge donor region and scanned over [0,150] fs in 1.25 fs steps for the charge acceptor region to expedite data acquisition. The time-domain ($\tau_1$) data is zero-padded out to 2048

points, and a hyperbolic tangent apodization function is applied to smoothly transition the data to zero at long $\tau_1$ delays before Fourier transform processing. Each scan is Fourier transformed to obtain one 2D EV surface, and then all six surfaces are averaged to obtain the 2D EV spectra shown in Figure 7.3.

## 7.3 LINEAR SPECTRA: FTIR AND UV-VIS

Calculations of N3 and related compounds discuss the complexity of CT in dense excited $^1$MLCT and $^3$MLCT manifolds.[11,15,39-41] The two lower energy electronic absorption bands in $N3^{4-}$ at $\lambda$ = 500 nm (20000 $cm^{-1}$) and 372 nm (26880 $cm^{-1}$) arise from $^1$MLCT excitations in which electron density with mixed Ru-$(NCS)_2$ character is transferred to the $\pi^*$ orbital of the dcbpy ligand and the highest energy band at $\lambda$ < 330 nm (30303 $cm^{-1}$) is due to $\pi \rightarrow \pi^*$ dcbpy intraligand transitions.[39] The $N3^{4-}$ electronic absorption bands are blue-shifted with respect to the neutral N3 due to a higher energy LUMO for the deprotonated complex leading to higher energy $\pi$-$\pi^*$ transitions.[42,43] Many ground-to-n$^{th}$ excited state ($S_0 \rightarrow S_n$) transitions into $^1$MLCT states underlie these absorption bands (e.g., see the $N3^{4-}$ absorption spectrum, Figure 7.1(a)). Our experiments excite the low-energy edge of the $N3^{4-}$ electronic absorption band centered at 26880 $cm^{-1}$ to populate as many $^1$MLCT states as possible using the broadband UV pump pulse. Vibrational modes reporting on both the Ru-$(NCS)_2$ charge donor segment and the dcbpy charge acceptor segment on the $N3^{4-}$ molecule are then probed with a mid-IR pulse to correlate as many $^1$MLCT states as possible with the excited state CT processes. The spectrally overlapped symmetric and asymmetric CN stretches of the NCS ligands compose the FTIR peak at ~2120 $cm^{-1}$ (Figure 7.1(b)) and report on the $N3^{4-}$ charge donor region.

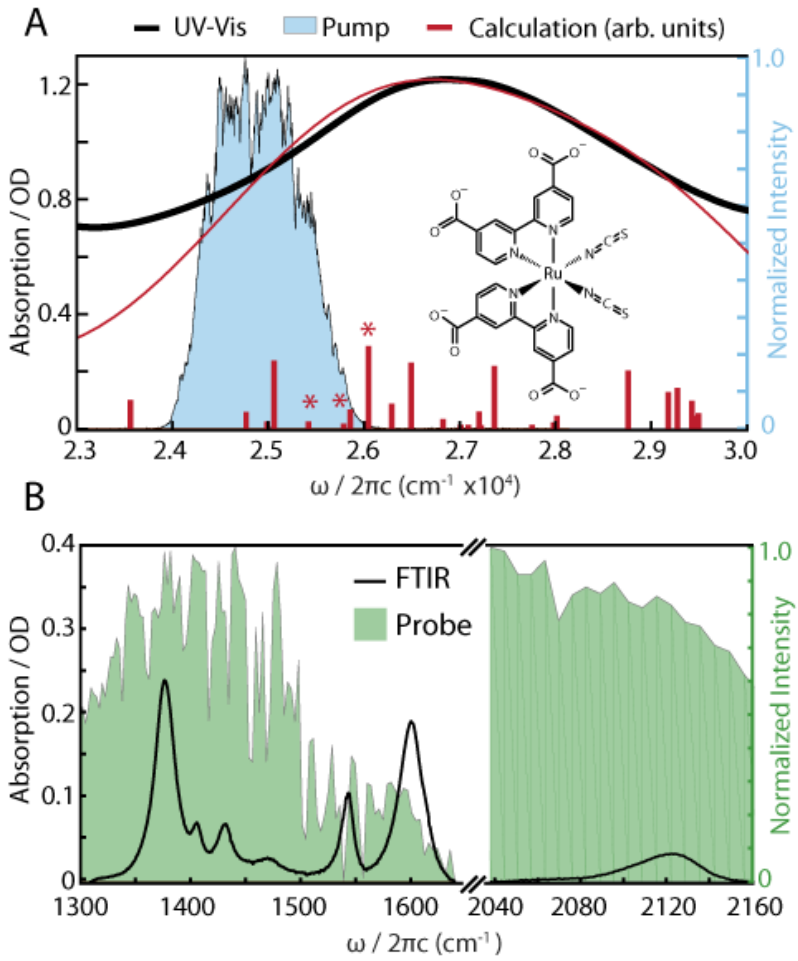


Figure 7.1. Linear absorption of $N3^{4-}$ and laser pulse spectra. A) Electronic absorption spectrum of $N3^{4-}$ (black, solvent-subtracted) in basic, aqueous solution (pH≈13) with the spectrally broadened UV pump spectrum (shaded blue) used in the tIR and 2D EV experiments overlaid to highlight the excitation region. The time-dependent (TD)-B3LYP/def2-SVP calculated electronic absorption spectrum (red, a Gaussian broadening has been applied with a FWHM = 0.18 eV, intensities are normalized for comparison to the experiment; see Appendices for further details) for the optimized $N3^{4-}$ minimum geometry is reported along with $S_0 \rightarrow S_n$ predicted oscillator strengths (red sticks). The transitions associated with the observed $^1$MLCT states are denoted by *, see discussion. The computed spectrum is within ~0.1 eV accuracy with respect to the experimental spectrum; $N3^{4-}$ structure is inset. B) The solvent-subtracted FTIR spectra for both vibrational regions probed in the experiments; mid-IR probe spectra used in the experiments are overlaid (green).

Several dcbpy vibrational modes report on the charge acceptor region, such as bipyridyl (bpy) ring modes (1400-1550 $cm^{-1}$) and the carboxylate (COO) symmetric and asymmetric stretches at 1375 $cm^{-1}$ and 1596 $cm^{-1}$, respectively.[22] Density functional theory (DFT) calculations and time-dependent DFT (TDDFT) computed electronic excited state structures using the Gaussian

electronic structure program[44] confirm our spectral assignments. We note that this computational analysis, described in detail in sections 7.9.3 and 7.9.4, is helpful for interpreting the experimental data, although neither explicit dynamical effects involving non-adiabatic processes, nor matrix elements between vibronic wavefunctions are included here.

## 7.4 IDENTIFYING SOME OF THE PLAYERS: TRANSIENT-IR SPECTROSCOPY OF AQUEOUS $N3^{4-}$

The tIR spectra shown in Figure 7.2 reflect the CT from the Ru-$(NCS)_2$ to the dcbpy ligands as expected. In the lowest energy $^3$MLCT, the CN stretches shift to lower frequency by 50-70 $cm^{-1}$ to form the excited state absorption (ESA) features collectively labelled $\nu_{CN}$, which is consistent with bond weakening due to the removal of electron density from the charge donor region. The arrival of electron density to the dcbpy ligands is reflected as the bpy ring modes all shift to higher frequencies by ~45 $cm^{-1}$ while the COO stretches lower in frequency by ~50 $cm^{-1}$ due to the increased aromaticity of the dcbpy ligands. The anharmonic coupling of the $^3$MLCT symmetric and asymmetric CN stretches is stronger than in the ground state which splits these ESA features, yet they are still not spectrally isolated in the vibrational domain, $\omega_3$. While the COO asymmetric stretch (1596 $cm^{-1}$) and a dcbpy ring mode (1545 $cm^{-1}$) features overlap in the $^3$MLCT, the COO symmetric stretch red-shifts into a spectrally isolated region (ESA, 1328 $cm^{-1}$) and is labelled $\nu_{COO}$. The calculations show that $\nu_{COO}$ consists of one dcbpy-localized COO symmetric stretching modes out of four similar modes involving the four different carboxylates; the other three carboxylate modes are closely spaced and overlapped with the four ground state symmetric stretching carboxylate modes spanning 1365-1385 $cm^{-1}$. An additional, spectrally isolated bpy ring mode (ESA, 1271 $cm^{-1}$) localized to one dcbpy

ligand blue-shifts into the probe window and is labelled $\nu_{BPY}$ (see Figure 7.10). The $\nu_{COO}$ and $\nu_{BPY}$ modes are spectrally isolated, direct reporters on the $N3^{4-}$ charge accepting region and will be the focus of the polarization-selective 2D EV analysis below.

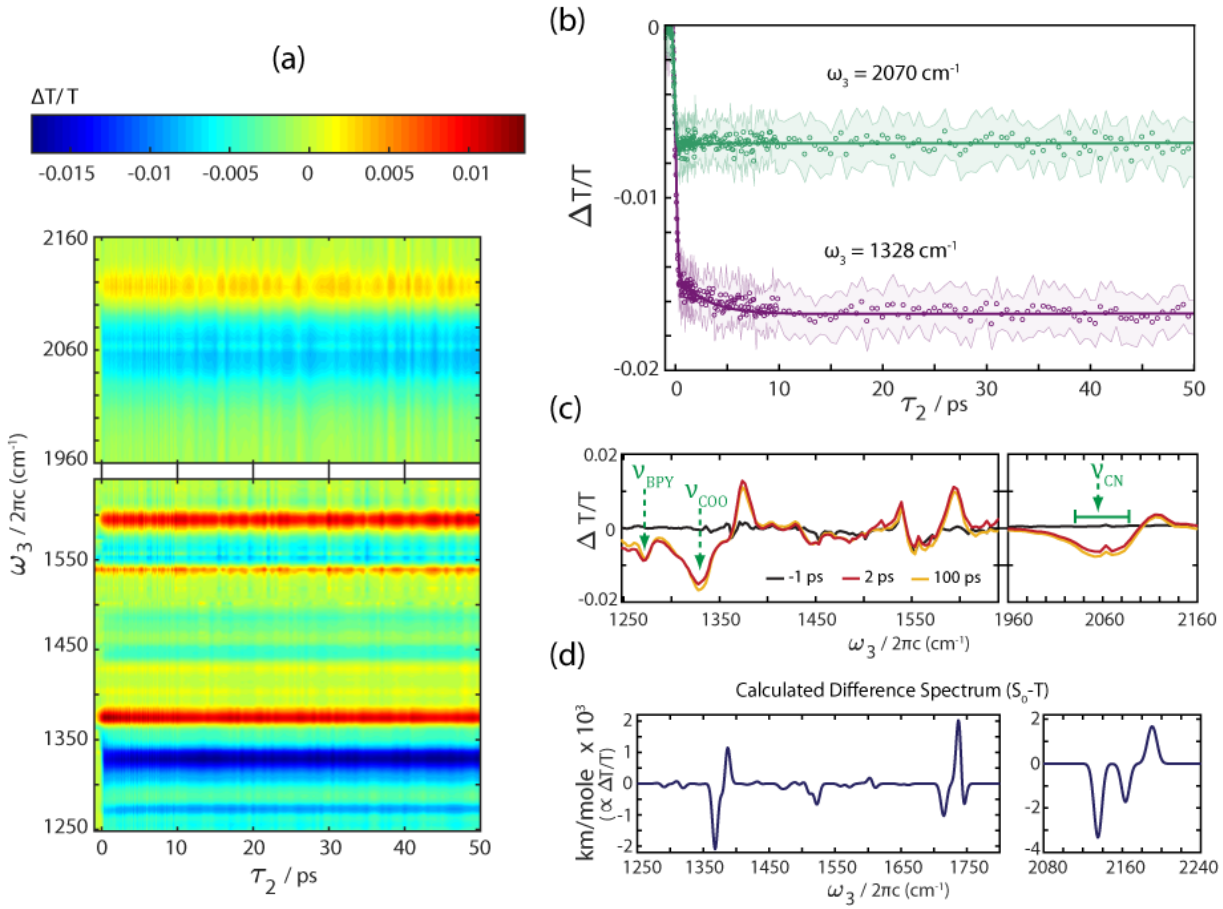


Figure 7.2. Transient-IR (tIR) spectroscopy of $N3^{4-}$. A) Full tIR spectra of the charge donor region (top) and acceptor region (bottom). B) Time traces reflecting the charge donor (green) and charge acceptor dynamics (purple); raw data shown as circles, fits are solid lines, ± 1 standard deviation shown by shaded region. (C) tIR spectra at $\tau_2$ = -1 ps (black), 2 ps (red), and 100 ps (yellow). The excited state absorption (ESA) peaks of interest for the polarization-dependent 2D EV analysis are highlighted by green dashed arrows: $\omega_3$ = 1271 $cm^{-1}$, bpy ring mode with CH wag ($\nu_{BPY}$); $\omega_3$ = 1328 $cm^{-1}$, COO symmetric stretch ($\nu_{COO}$); and $\omega_3$ = 2050 $cm^{-1}$ and 2070 $cm^{-1}$, asymmetric and symmetric CN stretches, respectively (collectively $\nu_{CN}$). The ground state bleach (GSB) features are: $\omega_3$ = 1375 $cm^{-1}$, COO symmetric stretch; $\omega_3$ = 1405 $cm^{-1}$, 1435 $cm^{-1}$, and 1545 $cm^{-1}$, bpy ring modes; $\omega_3$ = 1596 $cm^{-1}$, COO asymmetric stretch; $\omega_3$ = 2120 $cm^{-1}$, CN symmetric and asymmetric stretches. See text for discussion of tIR spectral shifts. D) Calculated difference IR spectrum between the ground state, $S_0$, and the lowest energy triplet state, $T$. Note: the calculated lowest energy triplet state is referred to as "$T$" and the experimental measurements refer to the lowest energy triplet state as "$^3$MLCT".

The tIR dynamics of $N3^{4-}$ reported here are consistent with reports of sub-100 fs ISC and formation of the vibrationally excited $^3$MLCT manifold which relaxes over picoseconds.[3] The picosecond (ps) relaxation dynamics are debated in the literature.[3,45] Typically, three decay components are reported in the 1-2 ps, 7-10 ps, and >50 ps ranges for the N3-$TiO_2$ system. Interligand electron transfer has been reported to have a 20 ps time scale in solvated N3.[28] The tIR spectra (Figure 7.2) at 2 ps and 100 ps delays demonstrate that most molecules probed are at, or near, the $^3$MLCT minimum by 2 ps (see section 7.9.2 for fitted tIR time traces). The calculated difference spectrum ($S_0 - T$, Figure 7.2(b)) provides strong qualitative agreement with the measured tIR spectra and supports our vibrational assignments in $S_0$ and $^3$MLCT. We note that explicit treatment of hydrogen bonded water molecules solvating the carboxylates can partially account for the discrepancy between calculation and measurement (Figure 7.7-Figure 7.8).

## 7.5 Identifying More of the Players: Polarization-Selective 2D EV Spectra of Aqueous $N3^{4-}$

The tIR data highlight the difference in $N3^{4-}$ IR-active vibrations between $S_0$ and the $^3$MLCT state, but the information regarding which $S_0 \rightarrow S_n$ excitation is correlated with the observed changes in the vibrational structure is unresolved. The 2D EV experiment directly accesses this information. The vibrational modes assigned in the tIR experiment will also be observed in the $\omega_3$ dimension of 2D EV spectra along with information in the $\omega_1$ dimension regarding to which $S_0 \rightarrow S_n$ excitation these vibrations are correlated. Additional insight is obtained by collecting the polarization-selective 2D EV response.[37,38] By measuring the 2D EV signal with the polarization of the pump and probe pulses parallel ($S_{ZZZZ}$) and

perpendicular ($S_{ZZYY}$) to one another, the anisotropy parameter (r) can be measured. For a spectrally isolated signal, r is related directly to the angle $\theta$ between the transition dipole moments for the pumped and probed transitions through $r = \frac{1}{5}(3\cos^2(\theta) - 1)$.[46] We measure the relative angle ($\theta_{vib}^{S_n}$) between the initially excited $S_0 \rightarrow S_n$ electronic transition dipole moments ($\mu_{S_0}^{S_n}$) and vibrational transition dipole moments ($\mu_{vib}$) of spectrally isolated dcbpy vibrations in the $^3$MLCT using polarization-selective 2D EV spectroscopy. These measurements provide a static snapshot of the vibronic couplings present in $N3^{4-}$ at a $\tau_2$ delay time of 2 ps, which is before rotational reorientation is expected to affect the anisotropy measurement in N3 and similar Ru compounds,[28,47] and after the vibrationally excited $^3$MLCT has substantially relaxed.[3,45] Agreement between calculated and measured $\theta_{vib}^{S_n}$ allows for associating 2D EV peaks with different $\omega_1$ frequencies to different $S_0 \rightarrow S_n$ excitations.

Figure 7.3 shows polarization-selective 2D EV spectra. Clear $\omega_1$-dependent ESA signals for $\nu_{COO}$ are measured and two peaks are observed in the $S_{ZZZZ}$ ($\omega_1$=24480 cm$^{-1}$, 25110 cm$^{-1}$), $S_{ZZYY}$ ($\omega_1$=24600 cm$^{-1}$, 25010 cm$^{-1}$), and $S_{iso}$ ($\omega_1$=24550 cm$^{-1}$, 25060 cm$^{-1}$) spectra. The $\omega_1$ profile of the $\nu_{BPY}$ ESA is polarization-dependent with distinct features in the $S_{ZZZZ}$ ($\omega_1$=24410 cm$^{-1}$, 25110 cm$^{-1}$), $S_{ZZYY}$ ($\omega_1$=24940 cm$^{-1}$), and $S_{iso}$ ($\omega_1$=25000 cm$^{-1}$) spectra, where the dominant $\omega_1$ peak is at ~25000 cm$^{-1}$ with a weaker shoulder toward the lower $\omega_1$-frequency peak observed predominantly in $S_{ZZZZ}$. It is noted that the 50 cm$^{-1}$ $\omega_1$ resolution and a slightly narrowed pump spectrum between the different experiments accounts for the small variation in $S_{ZZZZ}$ and $S_{ZZYY}$ peak positions.

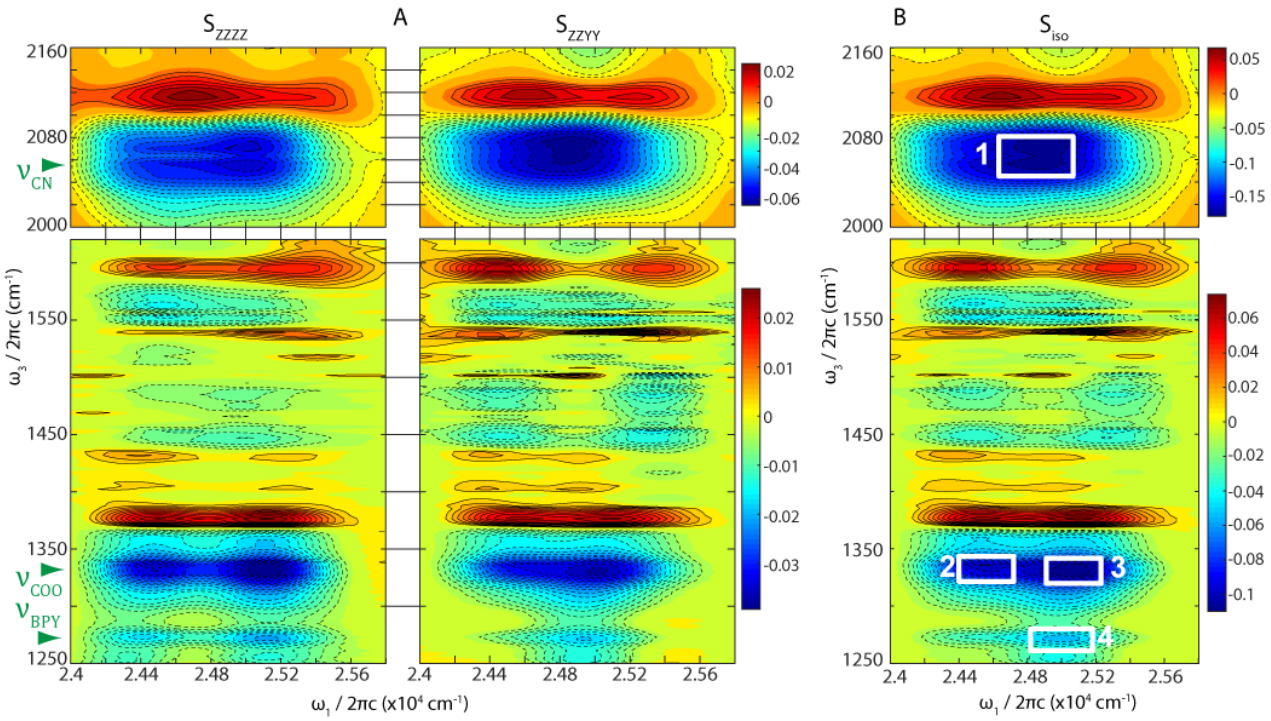


Figure 7.3. Polarization-selective 2D EV spectra. a) 2D EV spectra collected with pump and probe pulses with parallel ($S_{ZZZZ}$) and crossed ($S_{ZZYY}$) relative polarization; the color maps for spectra with the same $\omega_3$ region are comparable using the corresponding color bar. b) The isotropic 2D EV spectrum ($S_{iso} = S_{ZZZZ} + 2S_{ZZYY}$) with white boxes highlighting signals used in the dipole angle analysis described in the text ($\nu_{CN}$ = 1; $\nu_{COO}$ = 2,3; and $\nu_{BPY}$ = 4). Box 1 corresponds to $^1$MLCT$_C$, box 2 to $^1$MLCT$_A$, and boxes 3 and 4 correspond to $^1$MLCT$_B$; see text for full discussion of these $^1$MLCT states. Excited state absorptions are negative (dashed contours) and ground state bleaches are positive (solid contours) in all spectra; note the difference between color maps for the lower and upper panels. The color gradient changes every 5% of the max absolute value signal (of both $S_{ZZZZ}$ and $S_{ZZYY}$ in A) within the $\omega_3$ region indicated; the contour lines begin at $\pm$ 10% for clarity and are plotted at 5% intervals thereafter.

The $\omega_1$ line shapes for the $\nu_{COO}$ and $\nu_{BPY}$ features suggest that the charge acceptor region of the N3$^{4-}$ is coupled to at least two excited $^1$MLCT states; I will refer to these two states as "$^1$MLCT$_A$" (excited in the range $\omega_1 \cong$ 24400-24700 cm$^{-1}$) and "$^1$MLCT$_B$" (excited in the range $\omega_1 \cong$ 25000-25300 cm$^{-1}$) in the following discussion. The experimental spectra show that $\nu_{COO}$ ($\nu_{BPY}$) is strongly (weakly) coupled to $^1$MLCT$_A$ and that $\nu_{COO}$ and $\nu_{BPY}$ are both strongly coupled to $^1$MLCT$_B$. The $S_{iso}$ excitation frequency of the $\nu_{CN}$ ESA is centered at $\omega_1$ = 24870

$cm^{-1}$ and reflects another $^1$MLCT state vibronically coupled with the $N3^{4-}$ charge donor region, which will be referred to as "$^1MLCT_C$". The broad, mildly polarization-dependent electronic excitation observed for $\nu_{CN}$ is consistent with CT from the NCS ligands being delocalized over many excited $^1$MLCT states, likely including $^1MLCT_A$ and $^1MLCT_B$. By contrast, the excitation profile of $\nu_{BPY}$ and $\nu_{COO}$ suggests there are at least two distinct $^1$MLCT states, or two well-defined trajectories through the excited state manifolds participating in ISC. The correlation between three distinct $\omega_1$ bands and the vibrational signatures measured in the $^3$MLCT state at $\tau_2$ = 2 ps indicates that at least three $^1$MLCT states are directly coupled to the lowest energy $^3$MLCT state through different $N3^{4-}$ vibrations. In contrast to vibronic coupling information obtained from resonance Raman excitation profile analyses where the vibrations coupled to the $S_0 \rightarrow S_n$ excitation are enhanced, the 2D EV spectra in Figure 7.3 highlight vibronic couplings between $^3$MLCT state vibrations and initially excited $^1$MLCT states.

## 7.6 Comparison of Experimental and Calculated Transition Dipole Moment Angles

Comparison between experimental and calculated values of $\theta_{vib}^{S_n}$ are used to associate $S_n$ states likely involved in the $S_0 \rightarrow S_n$ transitions with the features corresponding to $^1MLCT_A$, $^1MLCT_B$, and $^1MLCT_C$ in the 2D EV spectra (see Table 7.1 below and comparison details in section 7.9.4). The calculated vectors for the $S_0 \rightarrow S_n$ electronic transition dipole moments and the derivative of the calculated lowest energy triplet ($T$) electric dipole moment with respect to the assigned normal modes are used to obtain the calculated dipole angles discussed here. The angles measured for the $\nu_{COO}$ and $\nu_{BPY}$ modes will be relatively unconvoluted because they

are spectrally separated in both the electronic and vibrational frequency dimensions which should provide accurate experimental measurement of $\theta_{vib}^{S_n}$. The difference between the highest and lowest excitation energies for the associated $S_0 \rightarrow S_n$ transitions should be ~450-650 $cm^{-1}$ as observed in the $\omega_1$ peak separation for excitations into $^1MLCT_A$ and $^1MLCT_B$. The corresponding transition energies for $S_n$ states associated with the coupled $^1MLCT$ states should also scale as $^1MLCT_A < {}^1MLCT_C < {}^1MLCT_B$ to be consistent with trends in $\omega_1$ peak maxima observed in the polarization-dependent 2D EV spectra. Direct agreement with calculated $\theta_{CN}^{S_n}$ is not expected due to spectral convolution of the symmetric and asymmetric CN stretches composing $\nu_{CN}$.

Table 7.1. Comparison of Experimental and Calculated Relative Dipole Angles, $\theta_{vib}^{S_n}$ (degrees).[a]

[a] Calculated angles refer to the angles formed between the vibrational transition dipole moment vectors (calculated as the derivative of the electric dipole moment for the optimized $T$ geometry with respect to atomic displacements of the normal modes) and the electronic transition dipole moments relative to the optimized $S_0$ geometry for the $S_0 \rightarrow S_n$ electronic transition to compare with the excited state absorption 2D EV signals $\nu_{COO}$ and $\nu_{BPY}$.

| | | $\nu_{BPY}$ | $\nu_{COO}$ | | $S_n - S_0$ |
|---|---|---|---|---|---|
| *Exp.* | $\theta_{vib}^{elec}$ | 53.3 ±6.8 | 53.1 ±3.8 | 53.1 ±3.7 | - |
| *Calculated* | $S_0 \rightarrow S_8$ | 53.5 | 53.7 | | 24770 $cm^{-1}$ |
| | $S_0 \rightarrow S_{14}$ | 53.5 | 53.7 | | 25420 $cm^{-1}$ |
| | $S_0 \rightarrow S_{15}$ | 53.5 | 53.7 | | 25790 $cm^{-1}$ |
| | $S_0 \rightarrow S_{17}$ | 53.5 | 53.7 | | 26050 $cm^{-1}$ |

The computed and experimental agreement of 53° (Table 7.1) is strong for the angles between $\mu_{COO}$ and $\mu_{S_0}^{S_n}$ for the $S_0 \rightarrow \{S_8, S_{14}, S_{15}, S_{17}\}$ electronic transitions (see Table 7.4 and

Table 7.5 for all experimental and calculated angles). The frequency differences $\left|S_8 - S_{14}\right|$ = 650 cm$^{-1}$, and $\left|S_{14} - S_{17}\right|$ = 630 cm$^{-1}$ suggest that $^1$MLCT$_A$ and $^1$MLCT$_B$ could reasonably be associated with either $S_8$ and $S_{14}$, or $S_{14}$ and $S_{17}$. However, since the $S_0 \rightarrow S_n$ excitation frequencies imply that the singlet state energies scale as $S_{14} < S_{15} < S_{17}$, the experimentally observed trend (i.e., $^1$MLCT$_A$ < $^1$MLCT$_C$ < $^1$MLCT$_B$ ) is maintained when $^1$MLCT$_A$, $^1$MLCT$_B$, and $^1$MLCT$_C$ are associated with $S_{14}$, $S_{17}$, and $S_{15}$, respectively. While this analysis describes general characteristics of the coupled $^1$MLCT states, it does not provide definitive $^1$MLCT state assignments. The explicit consideration of solvation, vibronic matrix elements, non-adiabatic dynamics, and spin-orbit coupling dynamics are required computationally to make definitive assignments of the coupled $^1$MLCT states observed in the experiment.[9-11,14,15,40,41] However, the agreement between measured and calculated $\theta_{vib}^{S_n}$ strengthens the experimental evidence for at least three different excited $^1$MLCT states being coupled to the $^3$MLCT manifold through these vibrational modes. Notably, the $\nu_{COO}$ and $\nu_{BPY}$ modes are vibronically coupled to two different initially-excited $^1$MLCT states, while the $\nu_{CN}$ is coupled to an additional $^1$MLCT state. There is no requirement for $\nu_{COO}$ or $\nu_{BPY}$ to be coupled to the same $^1$MLCT states as $\nu_{CN}$, but such couplings would be consistent with the <100 fs electron transfer dynamics reported in N3.[30] The weaker bpy modes ($\omega_3$ = 1400-1500 cm$^{-1}$) also provide qualitative support for vibronic coupling signatures from three $^1$MLCT states measured in our experiments.

## 7.7 The Nature of the Identified Vibronically Coupled States Facilitating Ultrafast Photoinduced Charge Transfer

An effective electronic absorption spectrum of the sub-ensemble with this vibronic coupling is formed from 2D EV slices at the $\nu_{COO}$ and $\nu_{BPY}$ vibrational frequencies (Figure 7.4).

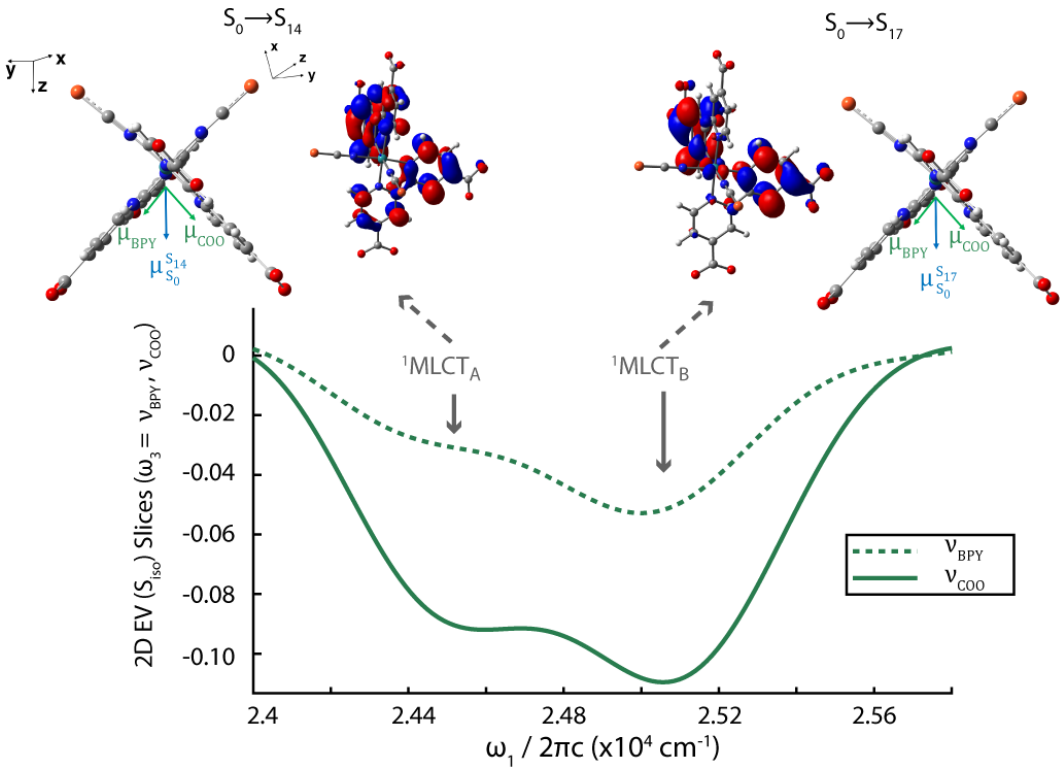


Figure 7.4. Visualizing electron density trends for vibronically coupled $^1$MLCT states in $N3^{4-}$. Slices from the isotropic 2D EV spectrum at the $\nu_{BPY}$ and $\nu_{COO}$ vibrational frequencies from Figure 7.3 show the $\omega_1$ dependence of these vibronically coupled modes more clearly. The $^1MLCT_A$ and $^1MLCT_B$ states described in the text are shown for the corresponding $\omega_1$ peaks, and the calculated natural transition orbitals (NTOs) for the $S_0 \rightarrow S_n$ transitions that are associated with these states through the dipole angle analysis are indicated by the dashed gray arrows (top left = $S_0 \rightarrow S_{14}$ and top right = $S_0 \rightarrow S_{17}$, see all calculated NTOs in S.I.). For the calculated states, the isodensity (0.03) contour plots of the electron NTOs for the analyzed electronic transitions (the corresponding hole NTOs all have a similar spatial distribution localized on the Ru-$(NCS)_2$ region are also reported in the S.I) and dipole moments are shown to emphasize the asymmetric electronic distribution on the charge accepting region. The calculated transition dipole moments $\mu_{S_0}^{S_{14}}$ (or $\mu_{S_0}^{S_{17}}$), $\mu_{COO}$, and $\mu_{BPY}$ are overlaid on the $T$ optimized geometry; the dipole magnitudes are not to scale. Cartesian axes are specified for the NTOs and for the dipole angle plots in the top left; the electron donor plane formed by the Ru-$(NCS)_2$ is in the plane of the page for the dipole angle plots.

The electron-hole natural transition orbital (NTO) pairs[48] associated with the excitation into $S_n$ states reflect the electron density reorganization upon exciting states that likely participate in CT through vibrational modes localized to the charge accepting dcbpy ligand (see Figure 7.12 for all NTO pairs). Thus, the calculations help develop insight into the CT process by informing experimentally observed trends. In particular, the electronic transition dipole moments of the associated states all lie in the electron donating plane formed by the Ru-$(NCS)_2$, and the majority of electron density following excitation resides on dcbpy rings directly opposing NCS ligands – effectively in this plane, as well. One emerging picture from this analysis includes the excited $^1$MLCT states with significant electron density in this electron donating plane participating strongly in CT through these vibronically coupled degrees of freedom.

## 7.8 CONCLUSIONS

An understanding of the ultrafast excited state dynamics and relaxation time scales in N3 and other transition metal complexes has resulted from theoretical investigations and extensive time-resolved experiments from the UV to the mid-infrared spectral ranges.[2-5,27,28,49,50] While transient X-ray methods have begun developing a molecular level description of these processes in N3 using atomically specific signals,[24,25] further development is needed to fully describe ultrafast intramolecular CT in terms of the interplay between valence electron density rearrangement and molecular structural shifts. The polarization-selective 2D EV study presented here directly contributes toward this end by measuring correlations between $^3$MLCT vibrational modes localized to the charge donor and acceptor regions of $N3^{4-}$ with several initially-excited $^1$MLCT states. I emphasize that these experimental spectra provide direct evidence that the vibrational modes localized to the charge donor and charge acceptor regions

of $N3^{4-}$ play a role in coupling the $^{1}$MLCT and $^{3}$MLCT manifolds. The dipole angle analysis shows that the $^{1}$MLCT states with electron density in the plane of the charge donors will strongly participate in ultrafast CT dynamics due to vibronic coupling with the $^{3}$MLCT vibrational modes. Our results suggest that the observed vibronically coupled degrees of freedom likely facilitate the well-known ultrafast ISC of N3.

The 2D EV spectra presented in this chapter describe a static snapshot, which successfully identifies some of the major players in the photoexcited charge transfer behavior of $N3^{4-}$. To monitor *how* the identified vibronically coupled states actively participate in the charge transfer, a $\tau_2$-dependent series of 2D EV spectra is needed; this is the subject of the following chapter. As demonstrated here, polarization-selective 2D EV spectroscopy can be used to map intramolecular CT within the molecular frame and provide physically intuitive molecular insight.

Relating the information presented in this chapter back to the analogy of chapter 1: the 2D spectra in Figure 7.3 are analogous to looking at a 2D spectrum of the correlated motion between the Liverpool players and the football where $\tau$' and $\tau$'' are only at the very beginning and at the very end, respectively, of the play in which Liverpool scored their goal. Surely, this spectrum would show which players move with the ball in a meaningful way, but it would not be clear *how* the players moved during that play and *why* their motion was meaningful for ultimately defeating Manchester United. To answer these more pressing questions, many 2D spectra are needed. The first spectrum will be where $\tau$' and $\tau$'' begin as effectively the same interval at the very beginning of the play, the next 2D spectrum will be collected such that the end of $\tau$' is the beginning of $\tau$'', and so forth. With a collection of 2D spectra spanning the entire range of the match play during Liverpool's goal, an in-depth analysis of how the goal

happened will become possible. In essence, having now identified some major players during the play, the following chapter can build on this chapter to give a detailed account of Liverpool's goal from the perspective of the correlated motion between a major player (which turns out to be the $\nu_{COO}$ mode) and the ball (which are both the $MLCT_A$ and $MLCT_B$ excited electronic states).

## 7.9 APPENDICES

### 7.9.1 *Linear Spectra with Solvent*

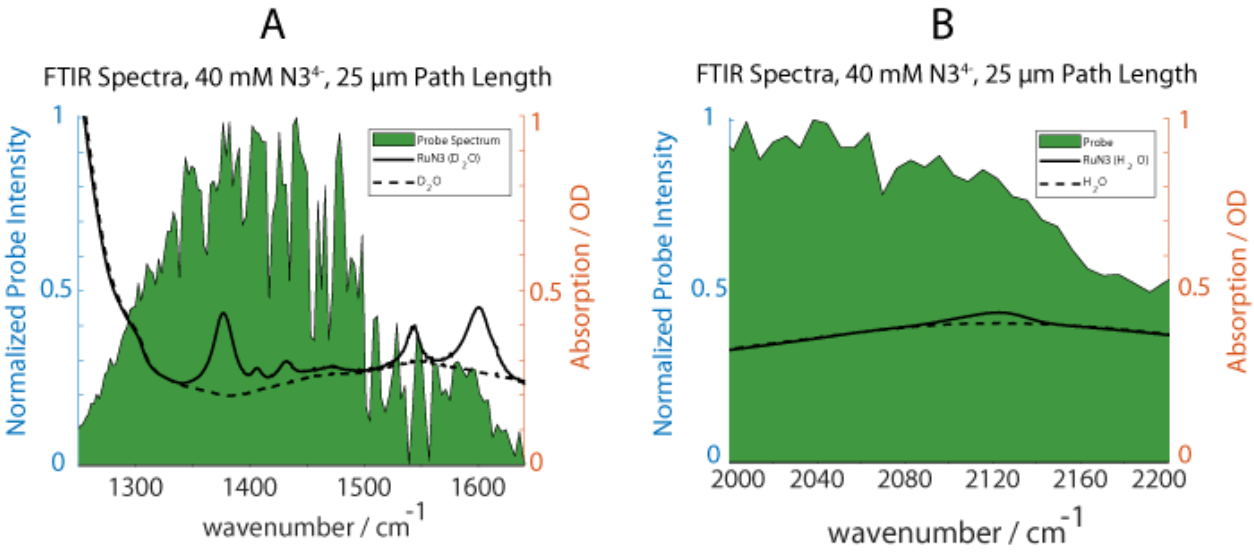


Figure 7.5. FTIR spectra of $N3^{4-}$ without solvent subtraction. A) Charge acceptor region; the solvent is 300 mM NaOH dissolved in $D_2O$. B) Charge donor region; the solvent is 300 mM NaOH dissolved in $H_2O$. The $N3^{4-}$ solution are the solid lines, the solvents are the dashed lines, and the probe spectra are shown in green.

### 7.9.2 *Transient-IR Analysis*

The two time traces for the tIR data discussed in Figure 7.2 were fit to a Gaussian function convoluted with the sum of two exponentials to check that our data is consistent with reported N3 relaxation time scales, which has the form:

$$f(t) = A_1 \exp\left[\left(\frac{B}{4\sqrt{ln(2)}\cdot\tau_{short}}\right)^2 - \frac{t-t_0}{\tau_{short}}\right]\times\frac{1}{2}\left(erf\left[\frac{t-t_0}{B}\cdot 2\sqrt{ln(2)} - \frac{B}{4\sqrt{ln(2)}\cdot\tau_{short}}\right]+1\right)\cdots$$
$$+A_2 \exp\left[\left(\frac{B}{4\sqrt{ln(2)}\cdot\tau_{long}}\right)^2 - \frac{t-t_0}{\tau_{long}}\right]\times\frac{1}{2}\left(erf\left[\frac{t-t_0}{B}\cdot 2\sqrt{ln(2)} - \frac{B}{4\sqrt{ln(2)}\cdot\tau_{long}}\right]+1\right). \quad (7.1)$$

where $A_1$ and $A_2$ are amplitude factors for the two convolutions, B is the temporal FWHM of the Gaussian instrument response function, $t_0$ is time zero, $\tau_{short}$ is the ~ picosecond time constant of one exponential decay and $\tau_{long}$ is the ~ nanosecond time constant of the second exponential decay. An additional constant offset (C) was also considered in fitting, but did not significantly change the fitting results. Table 7.2 gives the parameters obtained for the optimized fits of these two time traces. The 95% confidence interval is given for each fitting parameter, all time values are in units of picoseconds.

Table 7.2. Transient-IR Time Trace Fitting Parameters

| $\omega_3 / cm^{-1}$ | $A_1$ | $\tau_{short}$ | $A_2$ | $\tau_{long}$ | $B$ | $t$ | $C$ | adjusted $R^2$ |
|---|---|---|---|---|---|---|---|---|
| 2070 | -0.0004 ±0.00061 | 0.999 ±1.52 | -0.0068 ±0.00017 | 1.6E4 ±23.7E4 | 0.358 ±0.054 | -0.078 ±0.017 | -8.2E-5±1.4E-4 | 0.9725 |
| 1328 | 0.0024 ±0.0003 | 2.7 ±0.76 | -0.016 ±0.0002 | 1.6E4 ±6.8E4 | 0.45 ±0.039 | 0.037 ±0.010 | - | 0.9936 |

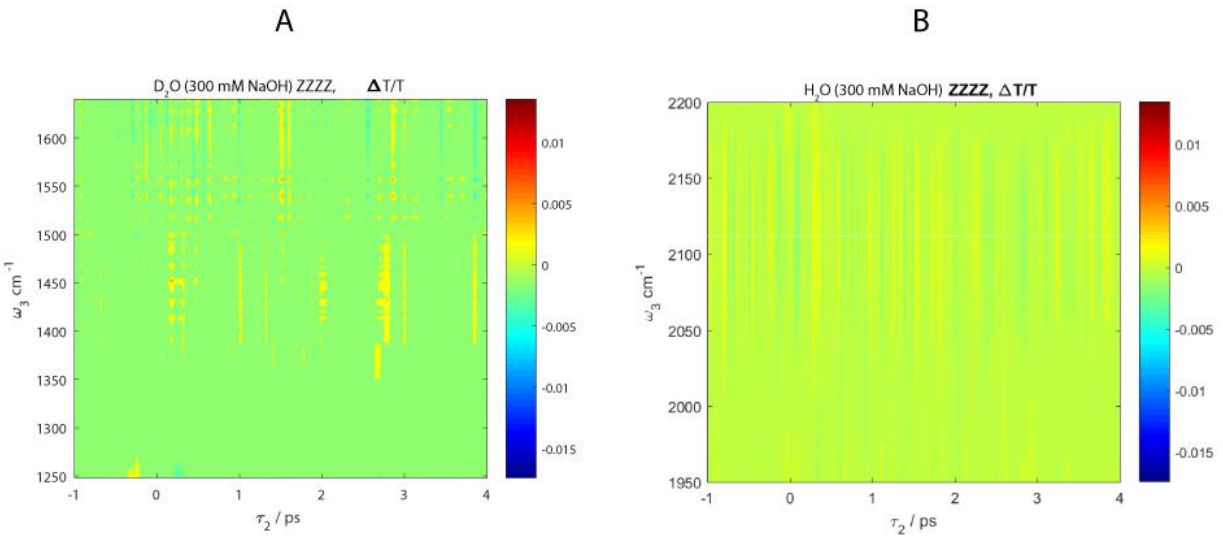


Figure 7.6. Transient-IR of Solvent Only. A) $D_2O$ used for charge acceptor tIR and 2D EV measurements. B) $H_2O$ used for charge donor tIR and 2D EV measurements. The color maps are the same as the tIR contour plot in Figure 7.2(a) for comparison. Note the different time scale plotted for solvent only runs versus the $N3^{4-}$ tIR data shown in the $N3^{4-}$ tIR data.

### 7.9.3 *Computational Methods*

Computational studies were performed using the *Gaussian* electronic structure package.[44] The electronic structures were obtained by solving the Kohn-Sham equation using the hybrid Becke, 3-parameter, Lee-Yang-Parr (B3LYP) density functional [51-53] with the def2-SVP [54] basis set and associated electronic core potential (ECP) for Ru.[55] Aqueous implicit solvent effects were taken into account by the Conductor-like Polarizable Continuum Model (C-PCM). [56-58]

The cis-$Ru(dcbpy)_2(NCS)_2^{4-}$ (termed $N3^{4-}$) was optimized in both low-spin singlet ground state ($S_0$) and the lowest lying metal-to-ligand charge transfer triplet state (T). Geometries were considered optimized when both the forces (maximum and RMS force, 0.000450 and 0.000300 Hartree/bohr, respectively) and displacement (maximum and RMS displacement, 0.0018 and 0.0012 bohr, respectively) values were below the threshold criteria. Vibrational frequencies

were calculated to both verify that structures were at minima on their corresponding potential energy surfaces and to compute the subsequent infrared (IR) spectrum.

The electronic structures of excited states (transition energies, oscillator strengths, and ground to exited state transition electric dipole moments) were calculated using the time depend density functional theory (TDDFT) within the linear response framework.[59-61] Density functional theory (DFT) and its time-dependent version have shown to be effective for theoretical characterization of many Ru complexes in different environments[22,62-68] and the vibrational dynamics of transient species.[69-77] The role of range separated hybrid functional has also been shown to be not mandatory for the accurate description of the electronic excitations in the pumping region for similar Ru compounds. [22] In addition, the level of theory employed has been proven to be accurate for the structural characterization of both the $S_0$ and T states in water solution along with their related X-ray transitions.[67]

The ground ($S_0$) to the corresponding n-th singlet excited states ($S_n$) electronic transition dipole moments $\mu_{S_0}^{S_n}$ for the excited states overlapping with the pump spectral line shape were computed referring to the optimized $S_0$ geometry. The vector representing the electric dipole moment derivative with respect to the corresponding normal modes $\mu_{vib}$ in the T state were also calculated referring to the optimized T geometry. The angles between these vectors were analyzed and compared to the experimental ones, making sure that both the orientation of the two different reference geometries ($S_0$ and T) employed the same coordinate frame and maximizing their overlap in the space, given the limited geometric changes between these two minima.

Effects including explicit solvation on the vibrational structure of the Ru complex were also investigated by optimizing and computing the vibrational spectrum for both $S_0$ and T

$Ru(dcbpy)_2(NCS)_2^{4-}$ by explicitly solvating each carboxylate group with two water molecules (a total of eight water molecules) still in the presence also of implicit solvent. This systems is referred as $Ru(dcbpy)_2(NCS)_2^{4-}$-$(H_2O)_8$.

Natural transition orbitals[78] (NTO, plotting only the most dominant hole/electron pair for each corresponding excitations) were calculated to provide a simpler orbital interpretation of the electronic excitations. This technique is particular useful for metal-to-ligand charge transfer excitations.[78] This analysis was performed on the optimized $S_0$ geometry. Molecular orbital visualization was carried out using GaussView 5.0b (Gaussian, Inc.).

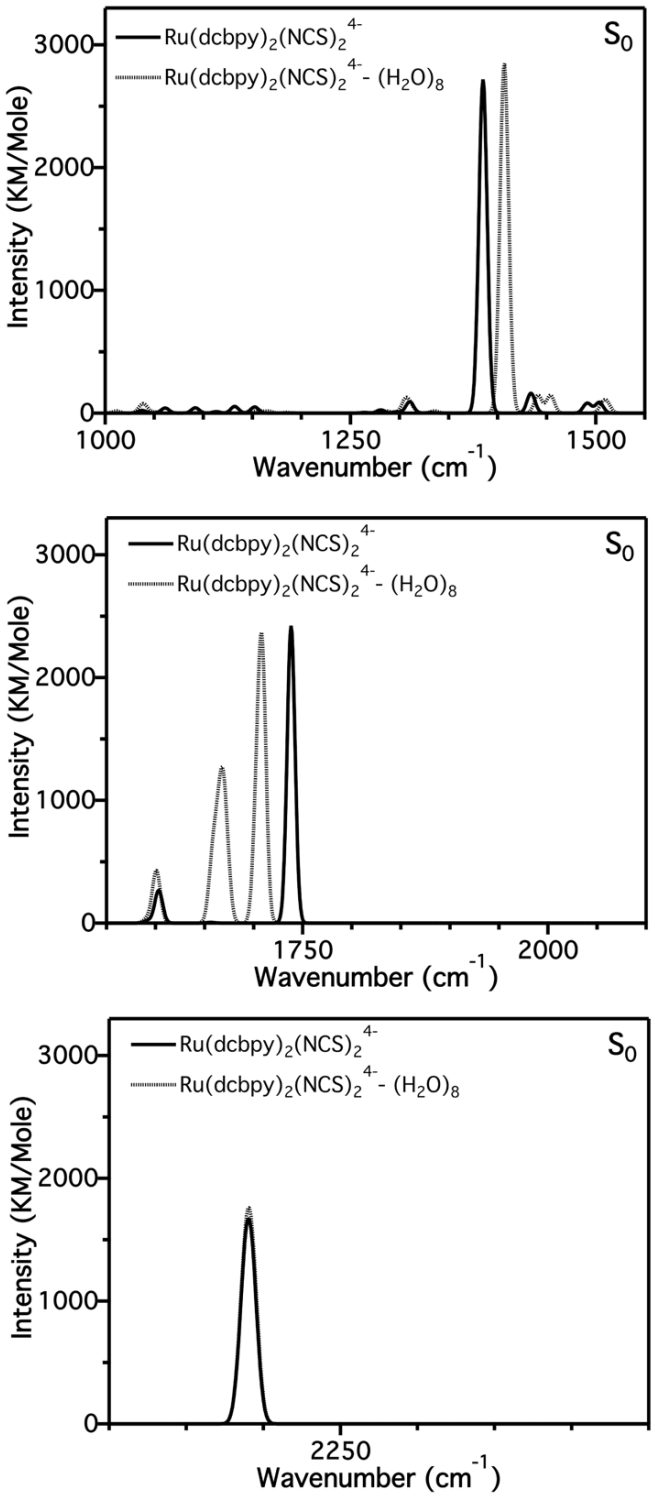


Figure 7.7. B3LYP/def2-SVP IR spectrum for the ground state singlet $S_0$ $Ru(dcbpy)_2(NCS)_2^4$ in water using implicit solvent (full line) and explicit water molecules ($Ru(dcbpy)_2(NCS)_2^-(H_2O)_8$, dotted lines) in the region from 1000-1550 (upper panel), 1550-2100 (middle panel), and 2100-2450 $cm^{-1}$. The higher energy region is not showed for simplicity. A Gaussian broadening has been applied with a full width half maximum value of 4 $cm^{-1}$.

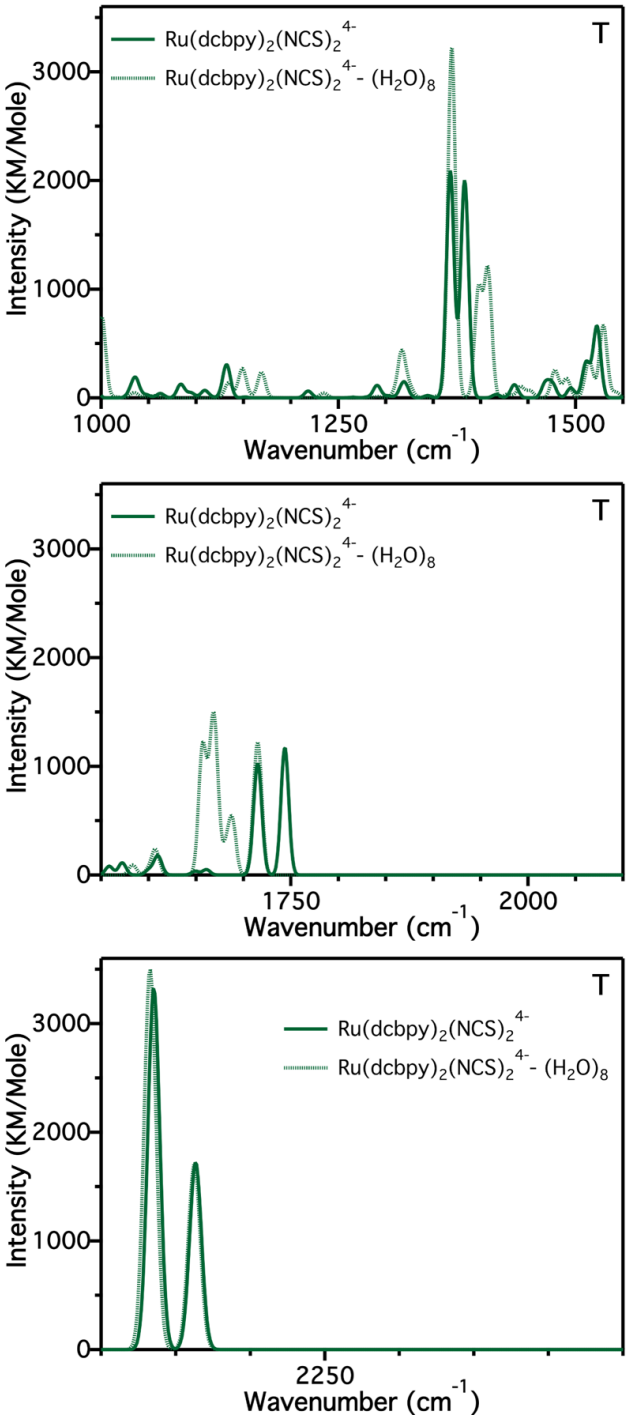


Figure 7.8. B3LYP/def2-SVP IR spectrum for the lowest lying triplet (T) $Ru(dcbpy)_2(NCS)_2^4$ in water using implicit solvent (full line) and explicit water molecules ($Ru(dcbpy)_2(NCS)_2^{-}(H_2O)_8$, dotted lines) in the region from 1000-1550 (upper panel), 1550-2100 (middle panel), and 2100-2450 $cm^{-1}$. The higher energy region is not showed for simplicity. A Gaussian broadening has been applied with a full width half maximum value of 4 $cm^{-1}$.

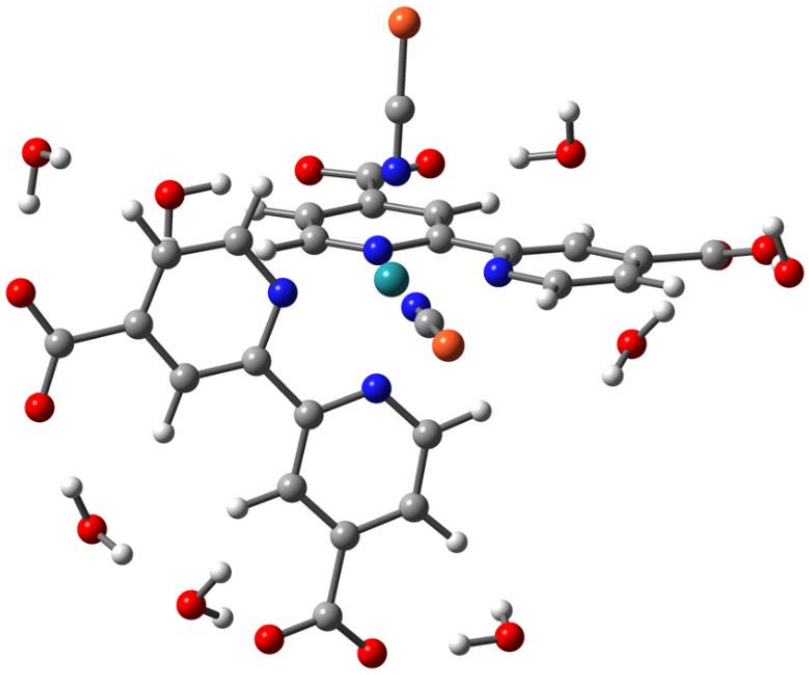

Figure 7.9. Ball and stick representation of the $S_0$ optimized geometry for the $Ru(dcbpy)_2(NCS)_2^{4-}$-$(H_2O)_8$ cluster at B3LYP/def2-SVP level. Ruthenium in turquoise, carbon in dark grey, oxygen in red, nitrogen in blue, sulfur in orange, and hydrogen in light gray.

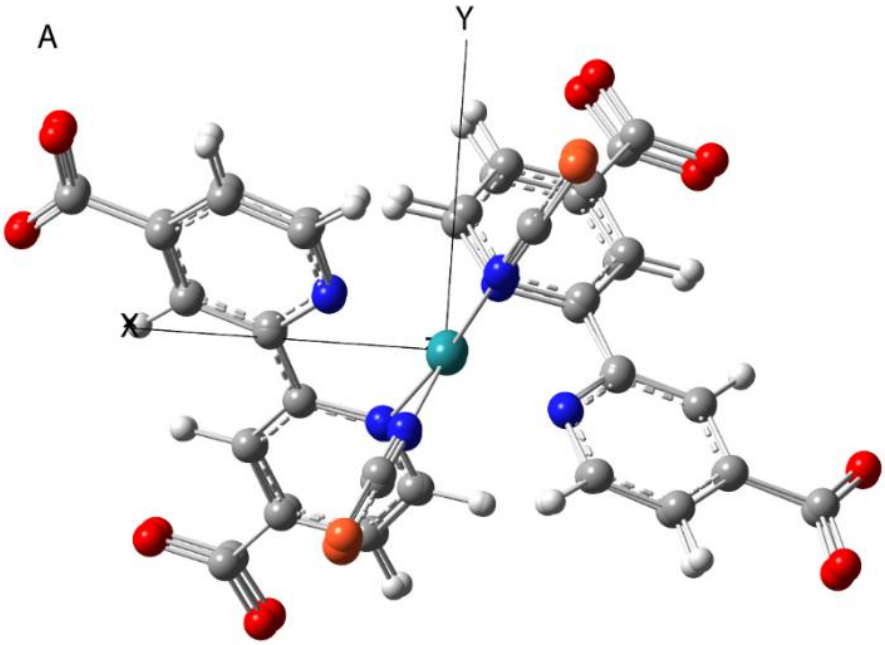


Figure 7.10. Overlap of Optimized $S_0$ and T Geometries with Same Cartesian Orientation Enforced. The two optimized geometries ($S_0$ and T) are overlapped to show minimal deviations; these structures were used for dipole angle comparison.

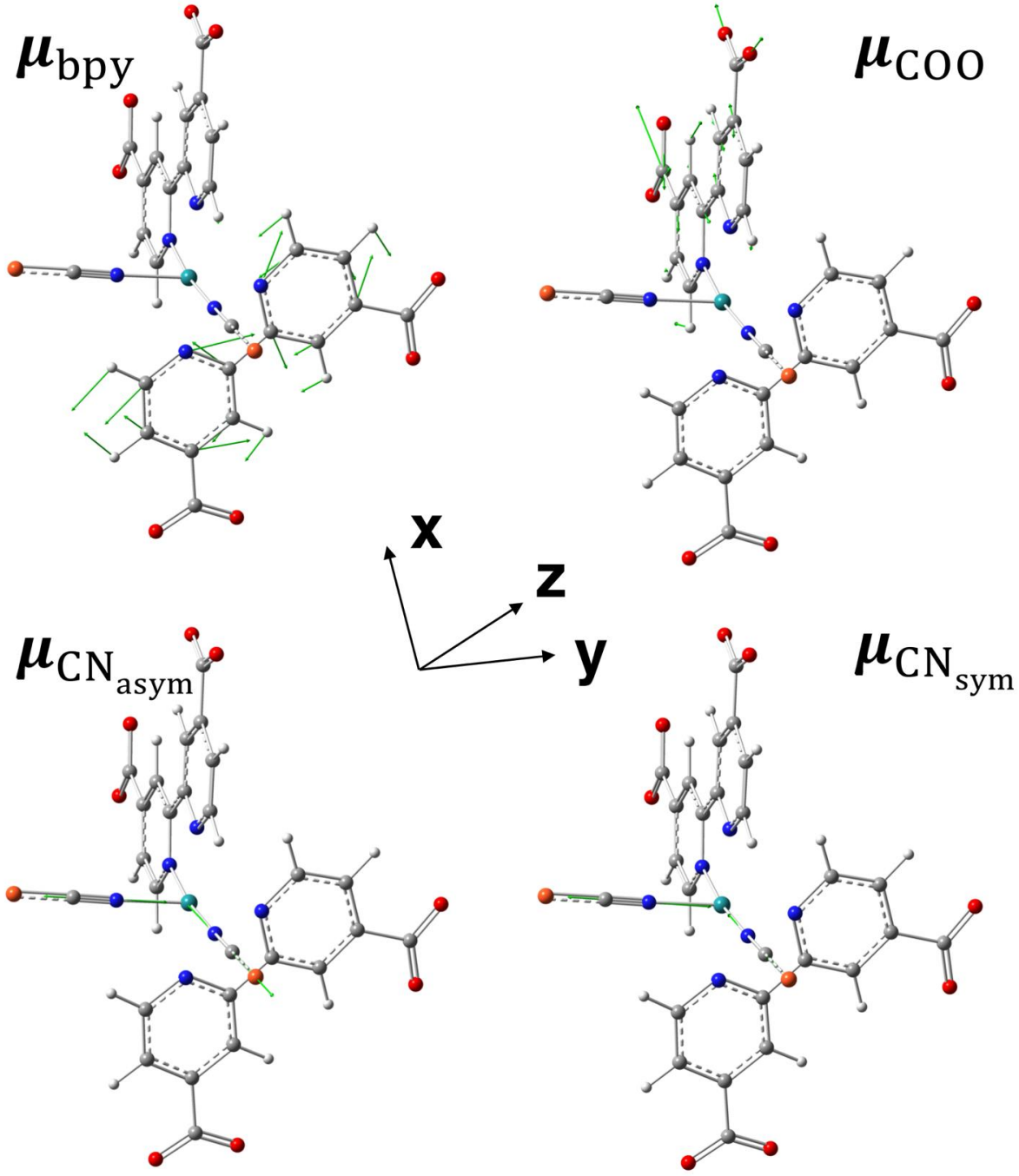


Figure 7.11. Displacement vectors of the analyzed normal modes for the lowest lying triplet for the $Ru(dcbpy)_2(NCS)_2^{4-}$ at B3LYP/def2-SVP level. Ruthenium in turquoise, carbon in dark grey, oxygen in red, nitrogen in blue, sulfur in orange, and hydrogen in light gray.

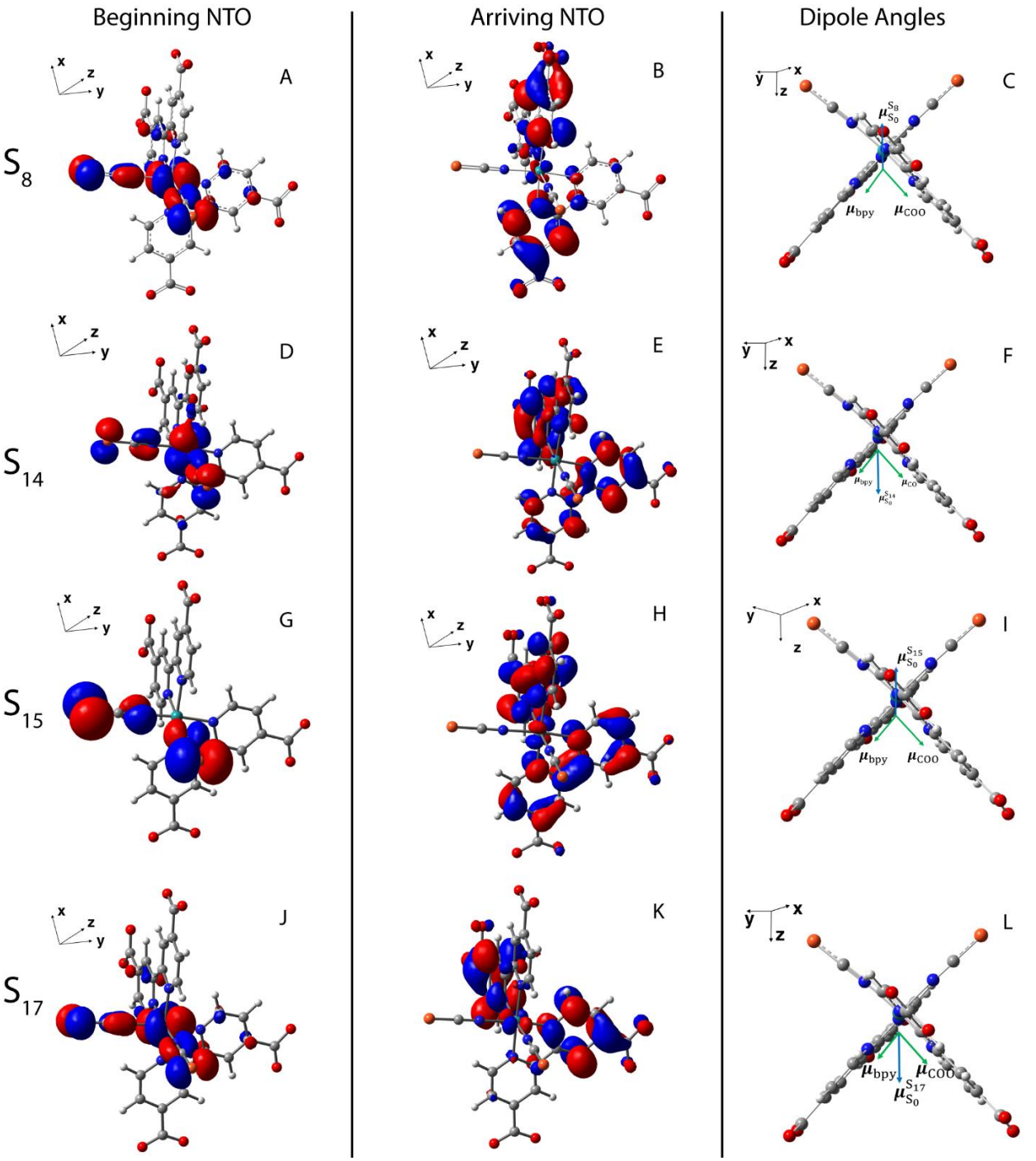


Figure 7.12. Natural Transition Orbitals (NTOs) hole-electron pairs relative to the optimized $S_0$ geometry along with the calculated dipole angles overlaid on T optimized geometry. The columns are grouped by the hole NTOs, electron NTOs, and Dipole Angles; and the rows are grouped by the corresponding arriving $S_n$ states for each $S_0 \rightarrow S_n$ transition. $\mu_{S_0}^{S_n}$ dipoles are the blue arrows and $\mu_{vib}$ arrows are green. The Cartesian orientation are the same for all hole and electron NTOs, and the dipole angle figures all have the same Cartesian orientation and have been set with the Ru-$(NCS)_2$ plane to be in the plane (YZ) of the page.

Table 7.3. Computed TD-B3LYP/def2-SVP transition energies and corresponding oscillator strengths relative to the electronic excitations from the ground state singlet optimized structure for the for the $Ru(dcbpy)_2(NCS)_2^{4-}$. The corresponding arriving state are reported in the first column.

| Arriving State | Energy ($cm^{-1}$) | Oscillator Strength (a.u.) |
|---|---|---|
| S8 | $2.477 * 10^4$ | 0.012 |
| S9 | $2.499 * 10^4$ | 0.003 |
| S10 | $2.499 * 10^4$ | 0.000 |
| S11 | $2.502 * 10^4$ | 0.002 |
| S12 | $2.502 * 10^4$ | 0.000 |
| S13 | $2.506 * 10^4$ | 0.056 |
| S14 | $2.542 * 10^4$ | 0.003 |
| S15 | $2.579 * 10^4$ | 0.002 |
| S16 | $2.585 * 10^4$ | 0.014 |
| S17 | $2.605 * 10^4$ | 0.069 |
| S18 | $2.629 * 10^4$ | 0.019 |

### 7.9.4 *Transition Dipole Moment Angle Analysis: Comparing Experiment and Calculations*

The polarization selective signals were used to determine the relative angles between the electronic and vibrational transition dipole moments of the transitions contributing to the measured signals in the electron donor and acceptor regions. For a given peak at ($\omega_1, \omega_3$), the 2D area of the greatest ~10% (within spectral axes resolution) of the isotropic signal was used to obtain an averaged anisotropy parameter, $\bar{r}$, and a relative dipole angle, $\theta_{vib}^{S_n}$, between the involved dipole moments using the anisotropy relations discussed in the main text. For example, $\bar{r}$ for the 2D EV ESA of the $\nu_{COO}$ mode coupled to the higher energy singlet state centered at (25060 $cm^{-1}$, 1330 $cm^{-1}$) was determined by averaging $r$ over the 2D spectral area ([24830,25210] $cm^{-1}$, [1328,1336] $cm^{-1}$). Then this $\bar{r}$ value yielded a $\theta_{COO}^{S_n}$ of 53.1° between

the initially excited $S_0 \rightarrow S_n$ electronic transition dipole moment and the $\nu_{COO}$ vibrational dipole moment of the system measured at $\tau_2$ = 2 ps, the standard deviation of $\theta_{COO}^{S_n}$ over the integrated 2D region is reported. Table 7.4 contains all of the experimentally measured information relevant for calculating the $\theta_{vib}^{S_n}$; the frequencies are in $cm^{-1}$ units and angles are in degrees.

Table 7.4. Experimentally Determined $\theta_{vib}^{S_n}$ from 2D EV Anisotropy.
(frequencies in $cm^{-1}$, angles in degrees)
[a]Maximum peak intensity for corresponding isotropic 2D EV peak.

| $\omega_3$ | $\omega_3$ integration | $\omega_1$ | $\omega_1$ integration | $\lvert I_{max} \rvert$ [a] | $\bar{r}$ | $\theta_{vib}^{S_n}$ (exp) |
|---|---|---|---|---|---|---|
| 1271 | [1268,1275] | 25000 | [24870,25110] | 0.0534 | 0.0142 | 53.3±6.8 |
| 1330 | [1328,1336] | 24550 | [24420,24720] | 0.0996 | 0.0160 | 53.1±3.8 |
| 1330 | [1328,1336] | 25060 | [24830,25210] | 0.1099 | 0.0160 | 53.1±3.7 |
| 2051 | [2045,2063] | 24870 | [24630,25120] | 0.1763 | -0.0306 | 57.9±3.5 |
| 2070 | [2063,2083] | 24870 | [24630,25120] | 0.1784 | -0.0583 | 60.9±3.4 |

The angles between the calculated $S_0 \rightarrow S_n$ electronic transition dipole moments and the vibrational transition dipole moments in the lowest energy $^3$MLCT ($T$) were compared to the experimental $\theta_{vib}^{S_n}$ to understand the experimentally measured transition dipole moments involved during the tIR and 2D EV experiments. The satisfactory agreement between the calculated and measured electronic absorption spectrum (accurate to within ~0.1 eV) justified limiting our consideration of $S_n$ states which have $S_0 \rightarrow S_n$ transition energies reasonably within, or close to, the experimentally used UV pump spectrum; these states are given in Table 7.3. The calculated transition dipoles and angles were obtained as detailed in *Computational Methods* below. It was important to ensure that the Cartesian reference frame for both

optimized $S_0$ and $T$ geometries were the same, and that the optimized geometries deviated minimally (overlapped maximally) from each other to extract physically meaningful $\theta_{vib}^{S_n}$ reflective of the angles measured experimentally. Since the measured anisotropy, $\bar{r}$, corresponds to four projection angles ($\theta_{vib}^{S_n}, -\theta_{vib}^{S_n}, \pi+\theta_{vib}^{S_n}, \pi-\theta_{vib}^{S_n}$) in the molecular frame, it should be understood that the measured angles reported in Table 7.4 are technically one of four possible angles observable.[79] To compare calculated angles consistently with the experimental result, each calculated electronic transition dipole moment was assumed to also have a solution pointing in the opposite direction and rotated by π radians; thus, 180° was subtracted from all calculated angles larger than 90° for comparison. This treatment presents all possible projections angles for a measured anisotropy to be compared directly between experiment and calculation. Table 7.5 presents all of the information relevant from the calculated dipole angles as described above.

Table 7.5. Calculated $\theta_{vib}^{S_n}$ Between $\mu_{S_0}^{S_n}$ and $\mu_{vib}$ for Vibrational Modes in $T$. Pink region is the intersection of the $\mu_{S_0}^{S_n}$ and $\mu_{vib}$, each table element in this region is the corresponding $\theta_{vib}^{S_n}$ given in degrees. [b] $\bar{\nu}_{CN}$ denotes the averaged $\nu_{CN}^{sym}$ and $\nu_{CN}^{asym}$ angles for a given $\mu_{S_0}^{S_n}$.

| | | | $\theta_{vib}^{S_n}(calculated)$ (°) | | | | |
|---|---|---|---|---|---|---|---|
| | $n$ | $(S_n - S_0)/cm^{-1}$ | $\nu_{BPY}$ | $\nu_{COO}$ | $\nu_{CN}^{sym}$ | $\nu_{CN}^{asym}$ | $\bar{\nu}_{CN}$ [b] |
| $S_n$ | 7 | 2.356 * $10^4$ | 65.1 | 54.9 | 87.0 | 5.9 | 46.5 |
| | 8 | 2.477 * $10^4$ | 53.5 | 53.7 | 3.0 | 88.6 | 45.8 |
| | 9 | 2.499 * $10^4$ | 85.9 | 74.7 | 87.4 | 20.7 | 54.0 |
| | 10 | 2.499 * $10^4$ | 56.2 | 65.6 | 24.6 | 66.3 | 45.4 |
| | 11 | 2.502 * $10^4$ | 84.2 | 73.0 | 87.3 | 18.6 | 52.9 |
| | 12 | 2.502 * $10^4$ | 55.9 | 50.5 | 17.0 | 75.3 | 46.2 |
| | 13 | 2.506 * $10^4$ | 88.1 | 77.0 | 87.5 | 23.5 | 55.5 |
| | 14 | 2.542 * $10^4$ | 53.5 | 53.7 | 3.0 | 88.6 | 45.8 |
| | 15 | 2.579 * $10^4$ | 53.5 | 53.7 | 3.0 | 88.6 | 45.8 |
| | 16 | 2.585 * $10^4$ | 80.3 | 88.5 | 87.9 | 37.8 | 62.9 |
| | 17 | 2.605 * $10^4$ | 53.5 | 53.7 | 3.0 | 88.6 | 45.8 |
| | 18 | 2.629 * $10^4$ | 75.7 | 64.8 | 87.1 | 8.0 | 47.6 |

## 7.10 REFERENCES


(1) Grätzel, M. Solar Energy Conversion by Dye-Sensitized Photovoltaic Cells; *Inorg. Chem.* **2005**, *44*, 6841-6851.

(2) Ardo, S.; Meyer, G. J. Photodriven heterogeneous charge transfer with transition-metal compounds anchored to $TiO_2$ semiconductor surfaces; *Chem. Soc. Rev.* **2009**, *38*, 115-164.

(3) Anderson, N. A.; Lian, T. Q. Ultrafast electron transfer at the molecule-semiconductor nanoparticle interface; *Annu. Rev. Phys. Chem.* **2005**, *56*, 491-519.

(4) Hagfeldt, A.; Boschloo, G.; Sun, L.; Kloo, L.; Pettersson, H. Dye-Sensitized Solar Cells; *Chem. Rev.* **2010**, *110*, 6595-6663.

(5) Chergui, M. Ultrafast Photophysics of Transition Metal Complexes; *Acc. Chem. Res.* **2015**, *48*, 801-808.

(6) Mccusker, J. K.; Vlcek, A. Ultrafast Excited-State Processes in Inorganic Systems; *Acc. Chem. Res.* **2015**, *48*, 1207-1208.

(7) Kiefer, L. M.; Kubarych, K. J. Two-dimensional infrared spectroscopy of coordination complexes: From solvent dynamics to photocatalysis; *Coord. Chem. Rev.* **2018**, *372*, 153-178.

(8) Delor, M.; Sazanovich, I. V.; Towrie, M.; Weinstein, J. A. Probing and Exploiting the Interplay between Nuclear and Electronic Motion in Charge Transfer Processes; *Acc. Chem. Res.* **2015**, *48*, 1131-1139.

(9) Nogueira, J. J.; Gonzalez, L. Computational Photophysics in the Presence of an Environment; *Annu. Rev. Phys. Chem.* **2018**, *69*, 473-497.

(10) Rondi, A.; Rodriguez, Y.; Feurer, T.; Cannizzo, A. Solvation-Driven Charge Transfer and Localization in Metal Complexes; *Acc. Chem. Res.* **2015**, *48*, 1432-1440.

(11) Ronca, E.; De Angelis, F.; Fantacci, S. Time-Dependent Density Functional Theory Modeling of Spin–Orbit Coupling in Ruthenium and Osmium Solar Cell Sensitizers; *J. Phys. Chem. C* **2014**, *118*, 17067-17078.

(12) Zhang, W.; Gaffney, K. J. Mechanistic Studies of Photoinduced Spin Crossover and Electron Transfer in Inorganic Complexes; *Acc. Chem. Res.* **2015**, *48*, 1140-1148.

(13) Hong, K.; Cho, H.; Schoenlein, R. W.; Kim, T. K.; Huse, N. Element-Specific Characterization of Transient Electronic Structure of Solvated Fe(II) Complexes with Time-Resolved Soft X-ray Absorption Spectroscopy; *Acc. Chem. Res.* **2015**, *48*, 2957-2966.

(14) Atkins, A. J.; González, L. Trajectory Surface-Hopping Dynamics Including Intersystem Crossing in $[Ru(bpy)_3]^{2+}$; *J. Phys. Chem. Lett.* **2017**, *8*, 3840-3845.

(15) Mai, S.; Plasser, F.; Dorn, J.; Fumanal, M.; Daniel, C.; González, L. Quantitative wave function analysis for excited states of transition metal complexes; *Coord. Chem. Rev.* **2018**, *361*, 74-97.

(16) Oliver, T. a. A.; Lewis, N. H. C.; Fleming, G. R. Correlating the motion of electrons and nuclei with two-dimensional electronic-vibrational spectroscopy; *Proc. Natl. Acad. Sci. U.S.A.* **2014**, *111*, 10061-10066.

(17) Gaynor, J. D.; Courtney, T. L.; Balasubramanian, M.; Khalil, M. Fourier transform two-dimensional electronic-vibrational spectroscopy using an octave-spanning mid-IR probe; *Opt. Lett.* **2016**, *41*, 2895-2898.

(18) Gaynor, J. D.; Khalil, M. Signatures of vibronic coupling in two-dimensional electronic-vibrational and vibrational-electronic spectroscopies; *J. Chem. Phys.* **2017**, *147*, 094202.

(19) Damrauer, N. H.; Cerullo, G.; Yeh, A.; Boussie, T. R.; Shank, C. V.; Mccusker, J. K. Femtosecond dynamics of excited-state evolution in $[Ru(bpy)(3)]^{(2+)}$; *Science* **1997**, *275*, 54-57.

(20) Waterland, M. R.; Kelley, D. F. Photophysics and Relaxation Dynamics of $Ru(4,4'Dicarboxy\text{-}2,2'\text{-}bipyridine)_2\text{-}cis\text{-}(NCS)_2$ in Solution; *J. Phys. Chem. A* **2001**, *105*, 4019-4028.

(21) Asbury, J. B.; Ellingson, R. J.; Ghosh, H. N.; Ferrere, S.; Nozik, A. J.; Lian, T. Femtosecond IR Study of Excited-State Relaxation and Electron-Injection Dynamics of $Ru(dcbpy)_2(NCS)_2$ in Solution and on Nanocrystalline $TiO_2$ and $Al_2O_3$ Thin Films; *J. Phys. Chem. B* **1999**, *103*, 3110-3119.

(22) Horvath, R.; Fraser, M. G.; Clark, C. A.; Sun, X.-Z.; George, M. W.; Gordon, K. C. Nature of Excited States of Ruthenium-Based Solar Cell Dyes in Solution: A Comprehensive Spectroscopic Study; *Inorg. Chem.* **2015**, *54*, 11697-11708.

(23) Shoute, L. C. T.; Loppnow, G. R. Excited-state metal-to-ligand charge transfer dynamics of a ruthenium(II) dye in solution and adsorbed on $TiO_2$ nanoparticles from resonance Raman spectroscopy; *J. Am. Chem. Soc.* **2003**, *125*, 15636-15646.

(24) Van Kuiken, B. E.; Huse, N.; Cho, H.; Strader, M. L.; Lynch, M. S.; Schoenlein, R. W.; Khalil, M. Probing the Electronic Structure of a Photoexcited Solar Cell Dye with Transient X-ray Absorption Spectroscopy; *J. Phys. Chem. Lett.* **2012**, *3*, 1695-1700.

(25) Zhang, X.; Smolentsev, G.; Guo, J.; Attenkofer, K.; Kurtz, C.; Jennings, G.; Lockard, J. V.; Stickrath, A. B.; Chen, L. X. Visualizing Interfacial Charge Transfer in Ru-Dye-

Sensitized $TiO_2$ Nanoparticles Using X-ray Transient Absorption Spectroscopy; *J. Phys. Chem. Lett.* **2011**, *2*, 628-632.

(26) Bram, O.; Messina, F.; El-Zohry, A. M.; Cannizzo, A.; Chergui, M. Polychromatic femtosecond fluorescence studies of metal-polypyridine complexes in solution; *Chem. Phys.* **2012**, *393*, 51-57.

(27) Kallioinen, J.; Benko, G.; Sundstrom, V.; Korppi-Tommola, J. E. I.; Yartsev, A. P. Electron transfer from the singlet and triplet excited states of $Ru(dcbpy)_2(NCS)_2$ into nanocrystalline $TiO_2$ thin films; *J. Phys. Chem. B* **2002**, *106*, 4396-4404.

(28) Pullerits, T.; Sundstrom, V. In *Energy Harvesting Materials*; Andrews, D. L., Ed.; World Scientific: Hackensack, NJ, 2005, p 164-186.

(29) Asbury, J. B.; Anderson, N. A.; Hao, E. C.; Ai, X.; Lian, T. Q. Parameters affecting electron injection dynamics from ruthenium dyes to titanium dioxide nanocrystalline thin film; *J. Phys. Chem. B* **2003**, *107*, 7376-7386.

(30) Asbury, J. B.; Hao, E.; Wang, Y. Q.; Ghosh, H. N.; Lian, T. Q. Ultrafast electron transfer dynamics from molecular adsorbates to semiconductor nanocrystalline thin films; *J. Phys. Chem. B* **2001**, *105*, 4545-4557.

(31) Tachibana, Y.; Moser, J. E.; Grätzel, M.; Klug, D. R.; Durrant, J. R. Subpicosecond Interfacial Charge Separation in Dye-Sensitized Nanocrystalline Titanium Dioxide Films; *J. Phys. Chem.* **1996**, *100*, 20056-20062.

(32) Durrant, J. R.; Tachibana, Y.; Mercer, I.; Moser, J. E.; Gratzel, M.; Klug, D. R. The excitation wavelength and solvent dependance of the kinetics of electron injection in $Ru(dcbpy)_2(NCS)_2$ sensitized nanocrystalline $TiO_2$ films; *Z. Phys. Chem.* **1999**, *212*, 93-98.

(33) Hannappel, T.; Burfeindt, B.; Storck, W.; Willig, F. Measurement of ultrafast photoinduced electron transfer from chemically anchored Ru-dye molecules into empty electronic states in a colloidal anatase $TiO_2$ film; *J. Phys. Chem. B* **1997**, *101*, 6799-6802.

(34) Rich, C. C.; Mattson, M. A.; Krummel, A. T. Direct Measurement of the Absolute Orientation of N3 Dye at Gold and Titanium Dioxide Surfaces with Heterodyne-Detected Vibrational SFG Spectroscopy; *J. Phys. Chem. C* **2016**, *120*, 6601-6611.

(35) Lenzmann, F.; Krueger, J.; Burnside, S.; Brooks, K.; Gratzel, M.; Gal, D.; Ruhle, S.; Cahen, D. Surface photovoltage spectroscopy of dye-sensitized solar cells with $TiO_2$, $Nb_2O_5$, and $SrTiO_3$ nanocrystalline photoanodes: Indication for electron injection from higher excited dye states; *J. Phys. Chem. B* **2001**, *105*, 6347-6352.

(36) Moser, J. E.; Wolf, M.; Lenzmann, F.; Gratzel, M. Photoinduced charge injection from vibronically hot excited molecules of a dye sensitizer into acceptor states of wide-bandgap oxide semiconductors; *Z. Phys. Chem.* **1999**, *212*, 85-92.

(37) Oliver, T. a. A.; Fleming, G. R. Following Coupled Electronic-Nuclear Motion through Conical Intersections in the Ultrafast Relaxation of beta-Apo-8 '-carotenal; *J. Phys. Chem. B* **2015**, *119*, 11428-11441.

(38) Lewis, N. H. C.; Fleming, G. R. Two-Dimensional Electronic-Vibrational Spectroscopy of Chlorophyll a and b; *J. Phys. Chem. Lett.* **2016**, *7*, 831-837.

(39) Fantacci, S.; De Angelis, F.; Selloni, A. Absorption Spectrum and Solvatochromism of the [Ru(4,4‘-COOH-2,2‘-bpy)$_2$(NCS)$_2$] Molecular Dye by Time Dependent Density Functional Theory; *J. Am. Chem. Soc.* **2003**, *125*, 4381-4387.

(40) Jager, M.; Freitag, L.; Gonzalez, L. Using computational chemistry to design Ru photosensitizers with directional charge transfer; *Coord. Chem. Rev.* **2015**, *304*, 146-165.

(41) Vlcek, A.; Zalis, S. Modeling of charge-transfer transitions and excited states in d(6) transition metal complexes by DFT techniques; *Coord. Chem. Rev.* **2007**, *251*, 258-287.

(42) Shklover, V.; Nazeeruddin, M. K.; Zakeeruddin, S. M.; Barbe, C.; Kay, A.; Haibach, T.; Steurer, W.; Hermann, R.; Nissen, H. U.; Gratzel, M. Structure of nanocrystalline $TiO_2$ powders and precursor to their highly efficient photosensitizer; *Chem. Mater.* **1997**, *9*, 430-439.

(43) Nazeeruddin, M. K.; Zakeeruddin, S. M.; Humphry-Baker, R.; Jirousek, M.; Liska, P.; Vlachopoulos, N.; Shklover, V.; Fischer, C. H.; Gratzel, M. Acid-base equilibria of (2,2 '-bipyridyl-4,4 '-dicarboxylic acid)ruthenium(II) complexes and the effect of protonation on charge-transfer sensitization of nanocrystalline titania; *Inorg. Chem.* **1999**, *38*, 6298-6305.

(44) Frisch, M. J.; Trucks, G. W.; Schlegel, H. B.; Scuseria, G. E.; Robb, M. A.; Cheeseman, J. R.; Scalmani, G.; Barone, V.; Petersson, G. A.; Nakatsuji, H.; Li, X.; Caricato, M.; Marenich, A. V.; Bloino, J.; Janesko, B. G.*et al. Gaussian 16 Rev. A.03*; Gaussian Inc.: Wallingford, CT, 2016.

(45) Pellnor, M.; Myllyperkiö, P.; Korppi-Tommola, J.; Yartsev, A.; Sundström, V. Photoinduced interfacial electron injection in RuN3–$TiO_2$ thin films: Resolving picosecond timescale injection from the triplet state of the protonated and deprotonated dyes; *Chem. Phys. Lett.* **2008**, *462*, 205-208.

(46) Lakowicz, J. R. *Principles of Fluorescence Spectroscopy*; Springer: New York, NY, 2006.

(47) Henseler, A.; Vauthey, E. Picosecond transient grating study of the rotational diffusion of a ruthenium complex in solution; *Chem. Phys. Lett.* **1994**, *228*, 66-72.

(48) Martin, R. L. Natural transition orbitals; *J. Chem. Phys.* **2003**, *118*, 4775-4777.

(49) Ross, M.; Andersen, A.; Fox, Z. W.; Zhang, Y.; Hong, K.; Lee, J. H.; Cordones, A.; March, A. M.; Doumy, G.; Southworth, S. H.; Marcus, M. A.; Schoenlein, R. W.; Mukamel, S.; Govind, N.; Khalil, M. Comprehensive Experimental and Computational Spectroscopic Study of Hexacyanoferrate Complexes in Water: From Infrared to X-ray Wavelengths; *J. Phys. Chem. B* **2018**, *122*, 5075-5086.

(50) Chergui, M. Ultrafast photophysics and photochemistry of iron hexacyanides in solution: Infrared to X-ray spectroscopic studies; *Coord. Chem. Rev.* **2018**, *372*, 52-65.

(51) Becke, A. D. Density-functional thermochemistry. III. The role of exact exchange; *J. Chem. Phys.* **1993**, *98*, 5648-5652.

(52) Lee, C.; Yang, W.; Parr, R. G. Development of the Colle-Salvetti correlation-energy formula into a functional of the electron density; *Phys. Rev. B* **1988**, *37*, 785.

(53) Miehlich, B.; Savin, A.; Stoll, H.; Preuss, H. Results obtained with the correlation energy density functionals of Becke and Lee, Yang and Parr; *Chem. Phys. Lett.* **1989**, *157*, 200-206.

(54) Weigend, F.; Ahlrichs, R. Balanced basis sets of split valence, triple zeta valence and quadruple zeta valence quality for H to Rn: Design and assessment of accuracy; *Phys. Chem. Chem. Phys.* **2005**, *7*, 3297-3305.

(55) Andrae, D.; Häußermann, U.; Dolg, M.; Stoll, H.; Preuß, H. Energy-adjustedab initio pseudopotentials for the second and third row transition elements; *Theor. Chim. Acta* **1990**, *77*, 123-141.

(56) Cossi, M.; Rega, N.; Scalmani, G.; Barone, V. Energies, structures, and electronic properties of molecules in solution with the C-PCM solvation model; *J. Comput. Chem.* **2003**, *24*, 669-681.

(57) Barone, V.; Cossi, M. Quantum Calculation of Molecular Energies and Energy Gradients in Solution by a Conductor Solvent Model; *J. Phys. Chem. A* **1998**, *102*, 1995-2001.

(58) Miertuš, S.; Scrocco, E.; Tomasi, J. Electrostatic interaction of a solute with a continuum. A direct utilizaion of AB initio molecular potentials for the prevision of solvent effects; *Chem. Phys.* **1981**, *55*, 117-129.

(59) Dreuw, A.; Head-Gordon, M. Single-reference ab initio methods for the calculation of excited states of large molecules; **2005**, *105*, 4009-4037.

(60) Casida, M. E. In *Recent Advances in Density Functional Methods:(Part I)*; Chong, D. P., Ed.; World Scientific: Singapore, 1995; Vol. 1, p 155-193.

(61) Stratmann, R. E.; Scuseria, G. E.; Frisch, M. J. An efficient implementation of time-dependent density-functional theory for the calculation of excitation energies of large molecules; **1998**, *109*, 8218-8224.

(62) Vlček, A.; Záliš, S. Modeling of charge-transfer transitions and excited states in d6 transition metal complexes by DFT techniques; *Coord. Chem. Rev.* **2007**, *251*, 258-287.

(63) Jäger, M.; Freitag, L.; González, L. Using computational chemistry to design Ru photosensitizers with directional charge transfer; *Coord. Chem. Rev.* **2015**, *304-305*, 146-165.

(64) Monat, J. E.; Rodriguez, J. H.; Mccusker, J. K. Ground- and Excited-State Electronic Structures of the Solar Cell Sensitizer Bis(4,4‘-dicarboxylato-2,2‘-bipyridine)bis(isothiocyanato)ruthenium(II); **2002**, *106*, 7399-7406.

(65) De Angelis, F.; Fantacci, S.; Selloni, A.; Nazeeruddin, M. K.; Grätzel, M. First-Principles Modeling of the Adsorption Geometry and Electronic Structure of Ru(II) Dyes on Extended TiO2 Substrates for Dye-Sensitized Solar Cell Applications; *J. Phys. Chem. C* **2010**, *114*, 6054-6061.

(66) De Angelis, F.; Fantacci, S.; Mosconi, E.; Nazeeruddin, M. K.; Grätzel, M. Absorption Spectra and Excited State Energy Levels of the N719 Dye on $TiO_2$ in Dye-Sensitized Solar Cell Models; *J. Phys. Chem. C* **2011**, *115*, 8825-8831.

(67) Van Kuiken, B. E.; Huse, N.; Cho, H.; Strader, M. L.; Lynch, M. S.; Schoenlein, R. W.; Khalil, M. Probing the Electronic Structure of a Photoexcited Solar Cell Dye with Transient X-ray Absorption Spectroscopy; *J. Phys. Chem. Lett.* **2012**, *3*, 1695-1700.

(68) Koposov, A. Y.; Cardolaccia, T.; Albert, V.; Badaeva, E.; Kilina, S.; Meyer, T. J.; Tretiak, S.; Sykora, M. Formation of Assemblies Comprising Ru–Polypyridine Complexes and CdSe Nanocrystals Studied by ATR-FTIR Spectroscopy and DFT Modeling; *Langmuir* **2011**, *27*, 8377-8383.

(69) Chong, E. Q.; Lingerfelt, D. B.; Petrone, A.; Li, X. S. Classical or Quantum? A Computational Study of Small Ion Diffusion in II-VI Semiconductor Quantum Dots; *J. Phys. Chem. C* **2016**, *120*, 19434-19441.

(70) Wong, M. W. Vibrational frequency prediction using density functional theory; *Chem. Phys. Lett.* **1996**, *256*, 391-399.

(71) Barone, V.; Bloino, J.; Biczysko, M. Validation of the DFT/N07D computational model on the magnetic, vibrational and electronic properties of vinyl radical; *Phys. Chem. Chem. Phys.* **2010**, *12*, 1092-1101.

(72) Petrone, A.; Lingerfelt, D. B.; Williams-Young, D. B.; Li, X. S. Ab lnitio Transient Vibrational Spectral Analysis; *J. Phys. Chem. Lett.* **2016**, *7*, 4501-4508.

(73) Donati, G.; Lingerfelt, D. B.; Petrone, A.; Rega, N.; Li, X. S. "Watching" Polaron Pair Formation from First-Principles Electron - Nuclear Dynamics; *J. Phys. Chem. A* **2016**, *120*, 7255-7261.

(74) Lingerfelt, D. B.; Williams-Young, D. B.; Petrone, A.; Li, X. S. Direct ab Initio (Meta-)Surface-Hopping Dynamics; *J. Chem. Theory. Comput.* **2016**, *12*, 935-945.

(75) Petrone, A.; Williams-Young, D. B.; Lingerfelt, D. B.; Li, X. S. Ab Initio Excited-State Transient Raman Analysis; *J. Phys. Chem. A* **2017**, *121*, 3958-3965.

(76) Stein, J. L.; Steimle, M. I.; Terban, M. W.; Petrone, A.; Billinge, S. J. L.; Li, X. S.; Cossairt, B. M. Cation Exchange Induced Transformation of InP Magic-Sized Clusters; *Chem. Mater.* **2017**, *29*, 7984-7992.

(77) Gary, D. C.; Petrone, A.; Li, X.; Cossairt, B. M. Investigating the role of amine in InP nanocrystal synthesis: destabilizing cluster intermediates by Z-type ligand displacement; *Chem. Comm.* **2017**, *53*, 161-164.

(78) Martin, R. L. Natural transition orbitals; **2003**, *118*, 4775-4777.

(79) Golonzka, O.; Tokmakoff, A. Polarization-selective third-order spectroscopy of coupled vibronic states; *J. Chem. Phys.* **2001**, *115*, 297-309.

# Chapter 8. VIEWING MULTIDIMENSIONAL ULTRAFAST PHOTOCHEMICAL PROCESSES: VIBRONIC COHERENCE EVOLUTION IN $N3^{4-}$

*The work presented in this chapter has been published in the following paper:*

*1) Gaynor, J.D.; Sandwisch, J.W., Khalil, M. "Vibronic Coherence Evolution in Multidimensional Ultrafast Photochemical Processes" Nature Communications* ***2019*** *10, 1, 5621.*

## 8.1 INTRODUCTION

The complex choreography of electronic, vibrational, and vibronic couplings used by photoexcited molecules to transfer energy efficiently is remarkable, but an unambiguous description of the temporally evolving vibronic states governing these processes has proven experimentally elusive. Photoexcited charge and energy transfer are essential steps in many natural and artificial light harvesting processes[1-4] which often rely on transition metal complexes with characteristically dense manifolds of charge transfer excited states.[5-11] The orchestrated molecular motion of charge and energy transfer can involve structural rearrangement, spin-vibronic interactions, and a dynamic solvent environment. These aspects make transition metal systems fundamentally interesting and challenging to understand. A wealth of experimental and computational studies on Ru-centered complexes have measured their photoexcited dynamics following singlet metal-to-ligand charge transfer (MLCT) excitation such as ultrafast intersystem crossing (ISC). These past studies have established that the excited triplet MLCT states can provide sufficiently long-lived charge separation to yield a useful chemical potential for energy harvesting applications.[12-18] Yet, an essential open question remains: What intramolecular coordinates define the trajectory of a photoexcited complex's evolution into these desirable long-lived charge separated states? To answer this

question, a continually advancing spectroscopic toolbox is required to move beyond measuring kinetics of photoexcited states towards building detailed molecular-level descriptions of important charge and energy transfer mechanisms utilized by transition metal complexes.[19-23] Exciting progress in experimental techniques is making investigations related to the following questions tractable: How do specific molecular coordinates control photoexcited energy transfer dynamics? What role do vibronic couplings and coherences play during photoexcited energy transfer and relaxation?

In this chapter, the complete capability of multidimensional (2D and 3D) EV spectroscopy is showcased by directly following vibronic coherence evolution in the photoexcited aqueous $N3^{4-}$ molecule while it undergoes ultrafast ISC and nonadiabatic internal conversion (IC). This chapter of my dissertation describes the first demonstration of 3D EV spectroscopy.[24] Building on the polarization-selective 2D EV investigations in chapter 7, the dynamics of the identified vibronically coupled states are now monitored throughout the first 2 ps of their photochemical reactivity. An in-depth characterization of an excited state vibrational wavepacket is discussed in photoexcited $N3^{4-}$ as it propagates during the initial 600 femtoseconds (fs), answering an outstanding question about the wavepacket's existence within the N3 triplet manifold.[12] Consequent energy transfer from the initial vibrational wavepacket to a second coherence is observed, which propagates further for ~1 picosecond (ps). Interestingly, the electronic character of the evolving secondary coherence oscillates between two different MLCT states with 340 ± 40 fs periodicity. Our measurement identifies this as a vibronic coherence promoting nonadiabatic IC. We simulate the experimental result and extract the 50 $cm^{-1}$ nonadiabatic coupling driving IC during the excited state triplet relaxation. This study provides

an unambiguous view of a photoexcited vibronic mechanism driving long-lived charge separation in the famous solar cell dye-sensitizing molecule.

## 8.2 THREE-DIMENSIONAL ELECTRONIC-VIBRATIONAL SPECTROSCOPY

The dimensions of multidimensional Electronic-Vibrational spectroscopy are schematically laid out in Figure 8.1. As a third-order nonlinear technique, there are inherently *three* dimensions of the desired third order molecular response function, $\vec{\vec{\mathbf{R}}}^{(3)}$ discussed in chapter 2, which can be resolved. The EV pulse sequence in Figure 8.1(a) is identical to the pulse sequence showed in chapter 2 with the additional details of a population decay superposed with a coherent oscillation shown in gray to propagate during $\tau_2$. This dynamical information depicted during $\tau_2$ represent what we call the third dimension of EV spectroscopy (which will, ironically, be referred to as "$\omega_2$"). Typically, this third dimension only parametrizes a single 2D EV spectrum (i.e., a 2D EV spectrum is viewed at a single point in $\tau_2$). The 1D (Figure 8.1(b)) and 2D (Figure 8.1(c)) spectra have already been discussed in-depth in previous chapters. Presented here is 3D EV spectroscopy (Figure 8.1d), where vibronic couplings between three disparate molecular coordinates are resolved: electronic excitations ($\omega_1$: 24,100-25,500 $cm^{-1}$), low frequency vibrations ($0 < \omega_2 <$ 0-833 $cm^{-1}$), and high frequency vibrations ($\omega_3$: 1,250-1,500 $cm^{-1}$). A real-time microscopic view of photochemical reactivity may be obtained by following the temporal evolution of the vibronic states measured in the 3D EV spectrum. As depicted in Figure 8.1d, vibrational coherences (red/yellow spheres, $L_1/L_1$') can be directly identified by an electronically-localized 3D EV feature and its time-dependent behavior ($L_1$ (red) $\rightarrow L_1$' (yellow)) characterized through its $\omega_2$-dependent spectral phase. Population and coherence transfer (blue and purple spheres, $L_2$) between vibronic states

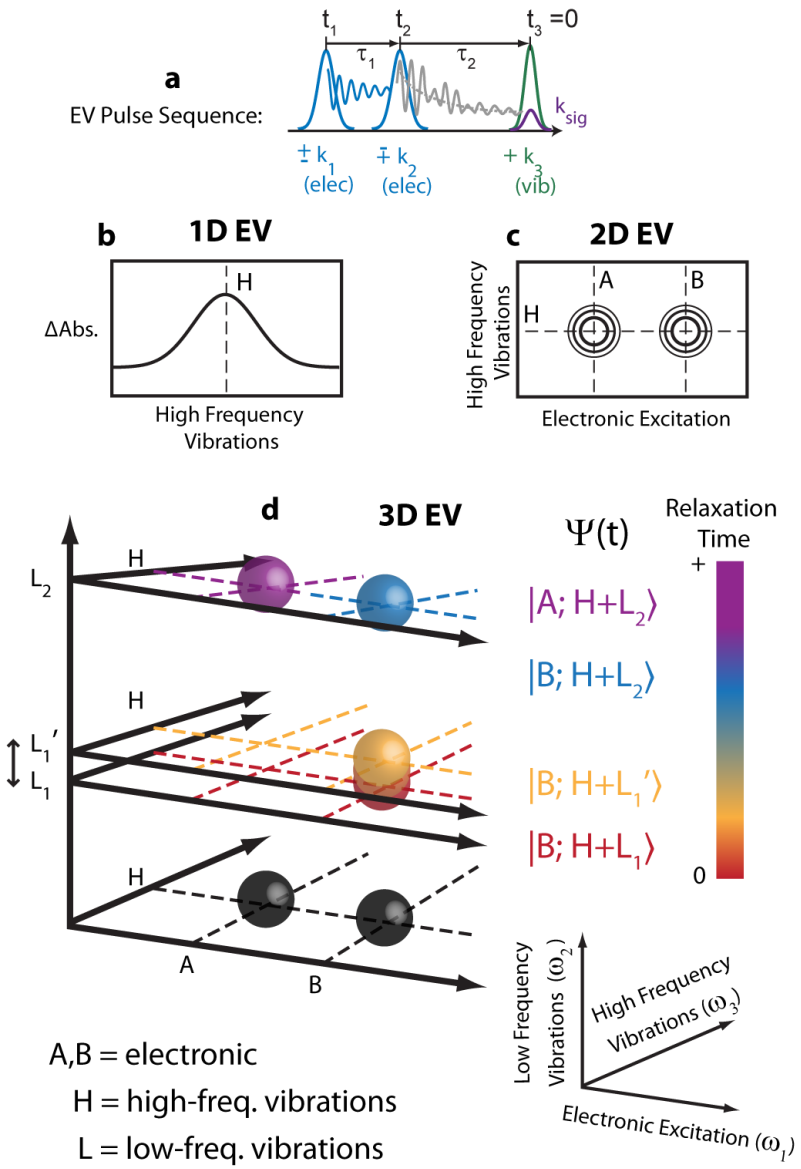


Figure 8.1. Multidimensional Electronic-Vibrational (EV) Spectroscopy. In each technique, the pulse sequence (a) induces an electronic excitation (pumps: $\mathbf{k}_1$, $\mathbf{k}_2$) and measures a high frequency vibrational response (probe: $\mathbf{k}_3$) in a sample. Consider a system where one high frequency vibration (H) vibronically couples to two electronic excited states (A, B) and to two low frequency vibrations ($L_1$, $L_2$) in A and/or B. (b) The pump-probe experiment (1D EV) measures the H vibrational spectrum ($\omega_3$) and kinetics during its relaxation times ($\tau_2$). At a given $\tau_2$ delay, (c) the 2D EV experiment resolves the electronic excitation spectrum ($\omega_1$) for H, defining the excited vibronic eigenstates ($\psi(t)$) by the couplings between H, the ground electronic state and either A or B. Collecting 2D EV spectra over a $\tau_2$ range measures population relaxation and coherent superpositions of eigenstates. The latter manifest as peak amplitude modulations; a FT over $\tau_2$ yields a (d) 3D EV spectrum where coherences (rainbow-colored spheres) separate in $\omega_2$ from population decays (black spheres) according to their beat frequency. The $\omega_2$ frequencies can indicate low frequency vibrations ($L_1$, $L_2$) coupled with vibronic eigenstates. Time-dependent 3D EV features, such as frequency shifts of low frequency modes as generally indicated by $L_1$ moving to $L_1$' in the $\omega_2$ frequency space, report on the temporal evolution and non-equilibrium relaxation of the vibronic eigenstates during photoexcited processes (depicted by the sphere coloration gradient).

can follow IC from the perspective of specific molecular coordinates that may be directly involved. Vibronic coherences can also be identified through out-of-phase oscillatory dynamics between different 3D EV features. In this way, the 3D FT experiment can unveil additional dark coordinates actively coupling the two motions measured in the 2D experiment, as well as coherences between molecular states facilitating energy transfer. While 3D FT studies have yielded exciting insight related to vibrations driving singlet fission,[25] quantum coherence in photosynthesis,[26] and tracking excited state photoisomerization,[27] no reported study previous to the work presented in this chapter[24] had fully exploited the potential of 3D FT spectroscopy to most completely describe molecular eigenstates in terms of three energetically disparate molecular coordinates.

## 8.3 Materials and Methods

### 8.3.1 *Sample Preparation*

The aqueous $N3^{4-}$ sample was prepared, characterized, and used in the same way as detailed in chapter 7.

### 8.3.2 *Experimental Details*

The same experimental configuration used for the polarization-selective 2D EV experiments in chapter 7 was used here, except the relative pump and probe polarizations were set to magic angle (54.7°) polarization to measure the isotropic response directly. At the sample, the pump beam was measured to be 240 nJ/pulse focused to a 220 μm diameter; the probe was measured to be 480 nJ/pulse focused to a 195 μm diameter. The instrument response subsided by $\tau_2$ = 200 fs, as measured by solvent response and a non-resonant Si tIR signal (see

Figure 8.9). A complete description of the data acquisition and processing is given in sections 8.12.2-8.12.4.

## 8.4 THE MLCT STATES AND THE HIGH FREQUENCY VIBRATIONAL REPORTER

As discussed in chapter 7, aqueous $N3^{4-}$ has two $^1$MLCT electronic absorption bands centered at 20,000 $cm^{-1}$ (500 nm) and 26,880 $cm^{-1}$ (372 nm). The $^1$MLCT absorption consisting of a dense manifold of MLCT excited states results in electron density with mixed Ru-$(NCS)_2$ character shifting to a dcbpy $\pi^*$ orbital.[8,28] The $^3$MLCT excited state manifold is also dense, which contributes to ultrafast ISC on a timescale comparable to one or two vibrational periods of the ligand high frequency vibrational modes.[6,8,13,15] The excited state intramolecular charge donor-acceptor dynamics are followed vibrationally here. The principal high frequency vibrational signatures of the excited electronic states for both the charge donor and acceptor in the $N3^{4-}$ transient-IR (tIR), or 1D EV, spectra (see section 8.12.5, Figure 8.13, and Table 8.3) were identified in chapter 7.[29] A closer look at the tIR spectra (Figure 8.13, section 8.12.5) shows that the vibrational linewidth of the symmetric stretching carboxylate mode ($\nu_{COO}$, $\omega_3$ = 1,328 $cm^{-1}$) narrows on a similar timescale to the growth of the ESA, within the first few picoseconds, while the other principal charge donor vibrational modes maintain constant vibrational linewidths. This is characteristic of a vibration undergoing non-equilibrium relaxation and experiencing a time-dependent distribution of varied environments. Thus, the $\nu_{COO}$ mode is expected to be most sensitive to the relaxation dynamics occurring during the initial 2 ps of non-equilibrium relaxation in the excited state. The $\nu_{COO}$ will be the high frequency vibrational reporter of interest, through which the initial ultrafast excited state relaxation dynamics will be viewed.

In the previous chapter, we discovered that two excited electronic states with $^1$MLCT character ($^1$MLCT$_A$ and $^1$MLCT$_B$) are vibronically coupled to charge donor and acceptor vibrations within the excited triplet manifold, likely facilitating ultrafast photoexcited charge transfer.[29] Now, 3D EV spectroscopy is used to measure the time-dependent modulation of the vibronic couplings between $\nu_{COO}$ and both MLCT$_A$ and MLCT$_B$ due to low frequency vibrational modes throughout the initial 1500 fs of the photochemical reaction. Here we omit the spin label to reflect that MLCT$_A$ and MLCT$_B$ are strongly spin-mixed states, which is expected from computational work on similar complexes[8,10] and supported in our data by a consistent $\omega_1$ peak maxima of $\nu_{COO}$ (section 0 and Figure 8.18). The ground state bleach (GSB, positive signal) and excited state absorption (ESA, negative signal) of the carboxylate region are shown in the 2D EV spectra (Figure 8.2a) with the MLCT$_A$, MLCT$_B$, and $\nu_{COO}$ transitions highlighted.

## 8.5 Time-Dependent Amplitude Oscillations in 2D EV Spectra

Nontrivial 2D EV amplitude modulations are observed over the initial 1,500 fs of the $\tau_2$ delay. The oscillatory amplitude of the 2D EV peak for $\nu_{COO}$ vibronically coupled with MLCT$_B$ is highlighted in Figure 8.2a. To observe the amplitude modulations more clearly, the exponential population kinetics are subtracted to obtain the residual amplitude of the integrated 2D area ($\omega_1$, $\omega_3$) for the greatest ~10-15% signal of the 2D EV peaks measuring the $\nu_{COO}$ vibronic coupling with MLCT$_A$ and MLCT$_B$ (gray in Figure 8.2b and e, respectively; see Table 8.2). In accord with previously reported wavepacket formation in N3,[12] two different $\tau_2$ ranges of the residuals are temporally selected (red and blue; Figure 8.2b and e) and Fourier transformed to identify the principal low frequency components modulating the 2D EV signal

within those $\tau_2$ ranges (Figure 8.2b-g). The details of the Fourier transform analysis are given in sections 8.12.3-8.12.4. Careful consideration of instrument noise is required as the oscillations are weak compared to the population decay. Hence, I only consider the $\omega_2$ features most prominently above experimental noise (i.e., $\nu_{Ru-N}$ and $\nu_{Ru-bpy}$) in Figure 8.2c-d and Figure 8.2f-g. The noise floor is set by performing the identical FT analysis on the 2D EV spectral region where the signal level is ≤ 5% of the maximum 2D EV signal (Figure 8.12). I have excluded features at $\omega_2 \geq 790$ cm$^{-1}$ given the 833 cm$^{-1}$ Nyquist sampling limit and the features approaching 0 cm$^{-1}$ (DC limit) due to imperfect population kinetics subtraction. During early relaxation times ($0<\tau_2<600$ fs, Figure 8.2c and f) a peak at $\omega_2 = 340$ cm$^{-1}$ is measured only for the $\nu_{COO}$ vibration of $MLCT_B$ character. The electronically-localized nature of this excited vibrational wavepacket reveals a stricter electronic characterization of this previously reported wavepacket.[12] At later relaxation times ($400<\tau_2<1{,}500$ fs) a low frequency vibrational mode at $\omega_2 \cong 742$ cm$^{-1}$ is clearly coupled to the $\nu_{COO}$ vibration of both $MLCT_A$ and $MLCT_B$ character. These spectra show a markedly different vibrational and electronic character of the measured coherences between the early and later relaxation periods.

Previous calculations[29] of the lowest energy triplet state vibrational spectrum of $N3^{4-}$ (section 8.12.11 and Figure 8.19) and resonance Raman experiments[30,31] aid the assignment of the 340 cm$^{-1}$ mode and the 742 cm$^{-1}$ mode as involving the stretching coordinate between the Ru and the dcbpy nitrogens (respectively called $\nu_{Ru-N}$ and $\nu_{Ru-bpy}$ here), with the $\nu_{Ru-bpy}$ primarily localized to the dcbpy ring. A recent surface-hopping trajectory calculation on $[Ru(bpy)_3]^{2+}$, a molecule similar to N3,[8] included on-the-fly, spin-orbit coupling and found low frequency vibrations analogous to $\nu_{Ru-N}$ and $\nu_{Ru-bpy}$ promoting ultrafast ISC due to excited state mixing.

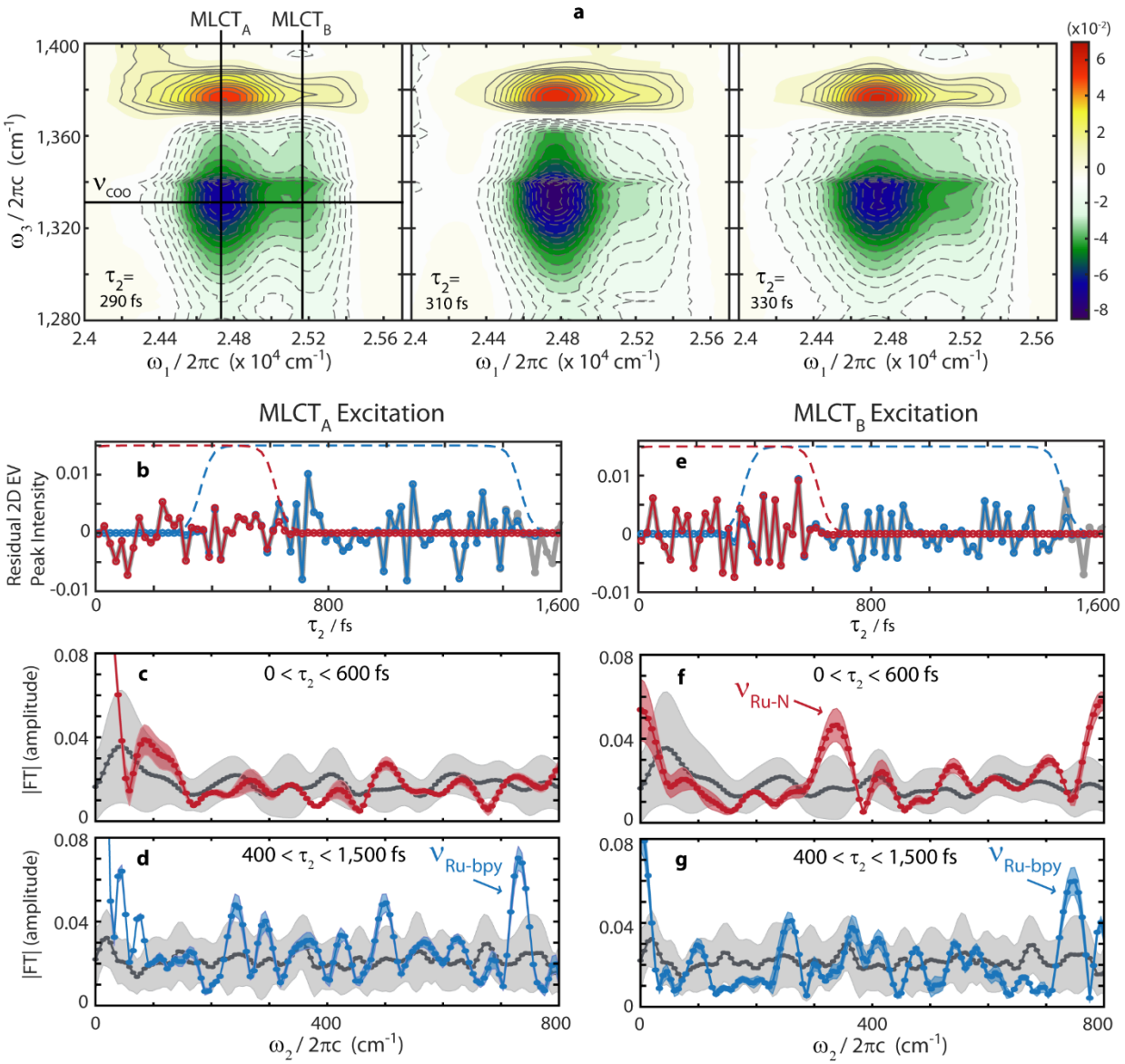


Figure 8.2. Low frequency amplitude modulations in two-dimensional electronic-vibrational (2D EV) spectra. (a) $\tau_2$-dependent 2D EV spectra show oscillatory amplitude; notably, the $\nu_{COO}$ ($\omega_3$ = 1,328 cm$^{-1}$) excited state vibration characterized by MLCT$_B$ ($\omega_1 \cong$ 25,200 cm$^{-1}$) excitation. Contour lines: solid (dashed) = positive (negative) signal, 5% intervals beginning at ±10%. Residual intensity of the integrated ($\omega_1$, $\omega_3$) 2D peak area for the $\nu_{COO}$ coupled to the (b) MLCT$_A$ ($\omega_1 \cong$ 24,700 cm$^{-1}$) and (e) MLCT$_B$ electronic excited states (gray, circles). Temporal filtering (dashed) isolates early relaxation times ($0 < \tau_2 < 600$ fs, red) or later relaxation times ($400 < \tau_2 < 1{,}500$ fs, blue) to identify transient, low frequency amplitude modulations in either time range. Fourier transformed (FT) spectra of the temporally-filtered [(c) early = red; (d) later = blue] 2D residuals of MLCT$_A$ excitation show principal low frequency components (i.e., $\nu_{Ru-N}$ and/or $\nu_{Ru-bpy}$) responsible for the 2D EV peak amplitude modulation. Corresponding FT spectra for MLCT$_B$ excitation are shown in (f) and (g). In all FT spectra, the gray spectra are the background (no EV signal); the shaded regions represent ± 1 standard deviation from the average data (shown by circles). See sections 8.12.3-8.12.4 for discussion of data processing. Number of ($\omega_1$, $\omega_3$) points: MLCT$_A$ = 45; MLCT$_B$ = 24; Background (signal ≤ 5% max) = 3295.

To understand the ligand's role in realizing long-lived charge separation, the relevant electronic and vibrational coordinates and their couplings must be mapped out. From Figure 8.2 the vibronic eigenstate basis explored here for $N3^{4-}$ is established and consists of: the excited electronic states ($MLCT_A$/$MLCT_B$), the charge-accepting high frequency vibration ( $\nu_{COO}$), and the low frequency vibrations ($\nu_{Ru-N}$ , $\nu_{Ru-bpy}$). An effective Hamiltonian for a

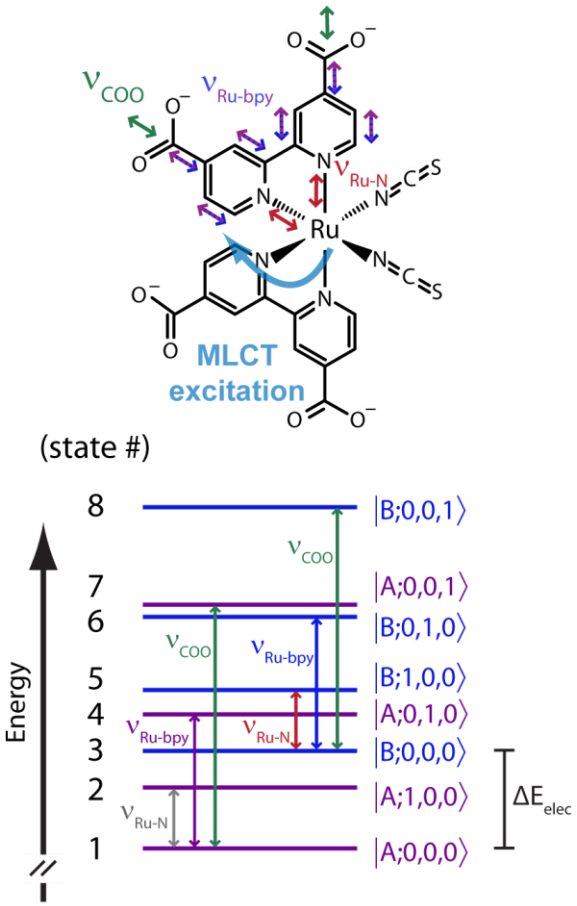


Figure 8.3. Vibronic eigenstate basis and energy level diagram. The measured eigenstate basis of $N3^{4-}$ is cast in terms of $\left|elec;\nu_{Ru-N},\nu_{Ru-bpy},\nu_{COO}\right\rangle$ where elec = A ($MLCT_A$, purple ) or B ($MLCT_B$, blue) and the three following quantum numbers relate the quanta in each of the vibrational modes listed in increasing transition energy. The relative energies are derived from the multidimensional EV measurements: $\Delta E_{elec} \cong 500$ cm$^{-1}$ from $\omega_1$; $\nu_{Ru-N}$ = 340 cm$^{-1}$ and $\nu_{Ru-bpy}$ = 742 cm$^{-1}$ from $\omega_2$; and $\nu_{COO}$ = 1,328 cm$^{-1}$ from $\omega_3$. The eigenstates are numbered in increasing energy for reference throughout the discussion. The $N3^{4-}$ structure (top) schematically depicts the electronic excitation (light blue) and the vibrational motions involved with photoexcited charge transfer. The vibrational mode arrow colors correspond to the respective transitions given in the energy level diagram below.

complicated, multi-coordinate system is distilled down to these measured vibronic eigenstates. For simplicity, I introduce the eigenstates and a density matrix element notation for use in the remaining discussion: $\rho_{ab}(\tau_2) = \left|a(\tau_2)\right\rangle\left\langle b(\tau_2)\right|$ specifies a density matrix element and $a,b \in \{1-8\}$ are the numbered vibronic eigenstates given in Figure 8.3 (e.g., the $\nu_{Ru-N}$ coherence is represented: $\left|B;0,0,0\right\rangle\left\langle B;1,0,0\right| = \rho_{35}$).

## 8.6 Early Time Dynamics: Electronically-Localized Excited State Vibrational Wavepacket

The 3D EV experiment provides a more complete description of the vibronic states involved in the coherent superposition composing the $MLCT_B$ excited state vibrational wavepacket measured at $\omega_2$ = 340 $cm^{-1}$. The red $\omega_2$ spectrum in Figure 8.2f demonstrates that the 2D EV peak intensity oscillations at early times arise from the $\rho_{35}$ density matrix element. The time-dependence of the frequencies in the vibrational wavepacket can be characterized by the spectral phase, $\phi(\omega_2) = \tan^{-1}\left(\frac{\mathrm{Im}[\mathrm{FT}(S(\tau_2))]}{\mathrm{Re}[\mathrm{FT}(S(\tau_2))]}\right)$, where $S(\tau_2)$ is the 2D EV residual signal during $0 < \tau_2 < 600$ fs for $MLCT_B$ shown in Figure 8.2e (red). The group delay is obtained from the spectral phase and is defined as, $\tau_d(\omega_2) = -d\phi(\omega_2)/d\omega_2$. Plotting $\tau_d(\omega_2)$ with the $\omega_2$ spectra, as shown in Figure 8.4, nicely illustrates how the $\omega_2$ frequencies of this initially excited wavepacket change during the initial 600 fs of non-equilibrium relaxation.

The spectral phase contains time versus frequency information of a wavepacket; for example, a quadratic variation in $\phi(\omega)$ corresponds to a linear group delay because the

frequencies of the wavepacket are changing linearly in time (see section 8.12.6 and Figure 8.14(a) and (b)).

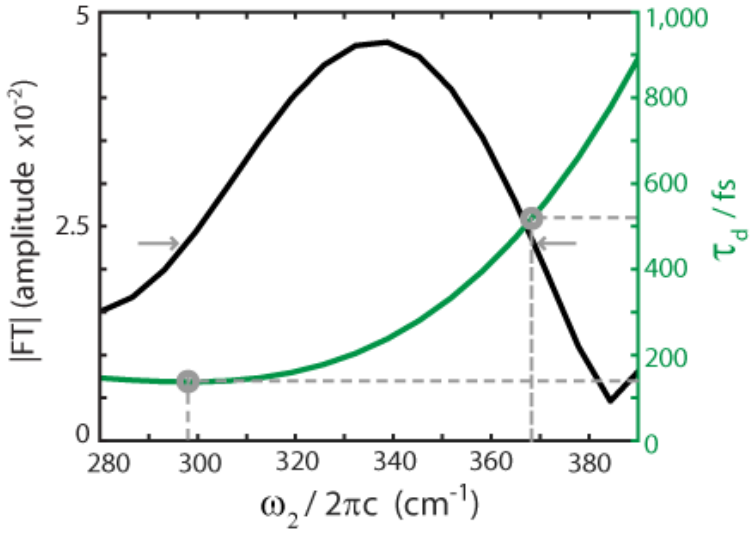


Figure 8.4. Early MLCT relaxation dynamics: electronically-localized excited state vibrational wavepacket. The $\omega_2$ spectral amplitude (black; FWHM = gray arrows) of the $MLCT_B$ excited state vibrational wavepacket arises due to coherence between the $\nu_{COO}$ and one quantum of a Ru-N stretching mode ($\nu_{Ru-N}$ = 340 cm$^{-1}$) within the excited state manifold. The $\tau_d$-dependence of the $\omega_2$ frequencies composing the wavepacket (green) indicate blue-shifting as the wavepacket propagates. Although the analytical form of $\tau_d(\omega_2)$ depends heavily on the polynomial function used to fit $\phi(\omega_2)$, the blue-shifting behavior of the wavepacket is consistent across many functions. See section 8.12.6, Figure 8.14 and Table 8.4 for spectral phase fits.

Notably, the extracted group delay (Figure 8.4, green) resulting from the best fit of the spectral phase is positive and predominantly quadratic within the $\omega_2$ region defined by the spectral FWHM (gray arrows). Interestingly, this form of the group delay describes the wavepacket shifting to higher frequencies (300 cm$^{-1}$ → 370 cm$^{-1}$ over 140 fs → 520 fs in $\tau_d$) in time. The blue-shift of the vibrational frequencies as a function of $\tau_2$ is also revealed through a sliding window short time Fourier transform analysis (Figure 8.15). We attribute the change in vibrational frequencies to the non-equilibrium relaxation of the excited wavepacket with respect to the $\nu_{Ru-N}$ coordinate measured experimentally during $0 < \tau_2 < 600$ fs. This dynamic

blue-shift is suggestive of a rapid vibrational relaxation of the highly excited $\nu_{Ru-N}$ coordinate on $MLCT_B$ down the multidimensional anharmonic potential of the $\nu_{Ru-N}$. Similar observations of blue-shifting of vibrational modes on photoexcited multidimensional surfaces have been made in organic complexes[32] and in reports of bridging cyanide ligand vibrational relaxation in mixed-valence complexes during photoexcited charge transfer.[33] Consistent with earlier studies,[12] the initial wavepacket has largely disappeared by 600 fs as shown by the absence of an $\omega_2$ = 340 $cm^{-1}$ peak in Figure 8.2d and g and it reflects the diminishing of the $\rho_{35}$ density matrix element, triggering subsequent electronic delocalization.

## 8.7 Later Time Dynamics: Vibronic Coherence Aids Nonadiabatic Internal Conversion

The later time ($400<\tau_2<1{,}500$ fs) dynamics utilize different low frequency vibrational mode couplings with the vibronic states. The $\omega_2 \cong 742$ $cm^{-1}$ features in Figure 8.2d and g demonstrate that $\nu_{Ru-bpy}$ has a time-dependent coupling with $\nu_{COO}$ and participates in the $\rho_{14}$ and $\rho_{36}$ coherences. The $\nu_{Ru-bpy}$ mode also changes the Ru-N (of dcbpy) distance, emphasizing the importance of this coordinate for ultrafast relaxation in $N3^{4-}$. Since the $\omega_2$ spectra (Figure 8.2) lack dynamical information occurring on shorter timescales within the $400<\tau_2<1{,}500$ fs period, a careful time-frequency analysis[34] (Figure 8.5a,b) is used to resolve oscillatory electronic character of the coherences involving $\nu_{Ru-bpy}$. Proper selection of the temporal filter used in our analysis is required to extract the transient $\nu_{Ru-bpy}$ dynamics and reasonably interpret the result (section 8.12.7). Importantly, the $\omega_2$ spectra during the later time period ($400<\tau_2<1{,}500$ fs, Figure 8.2d and g) show that the data sufficiently resolve only one low frequency mode

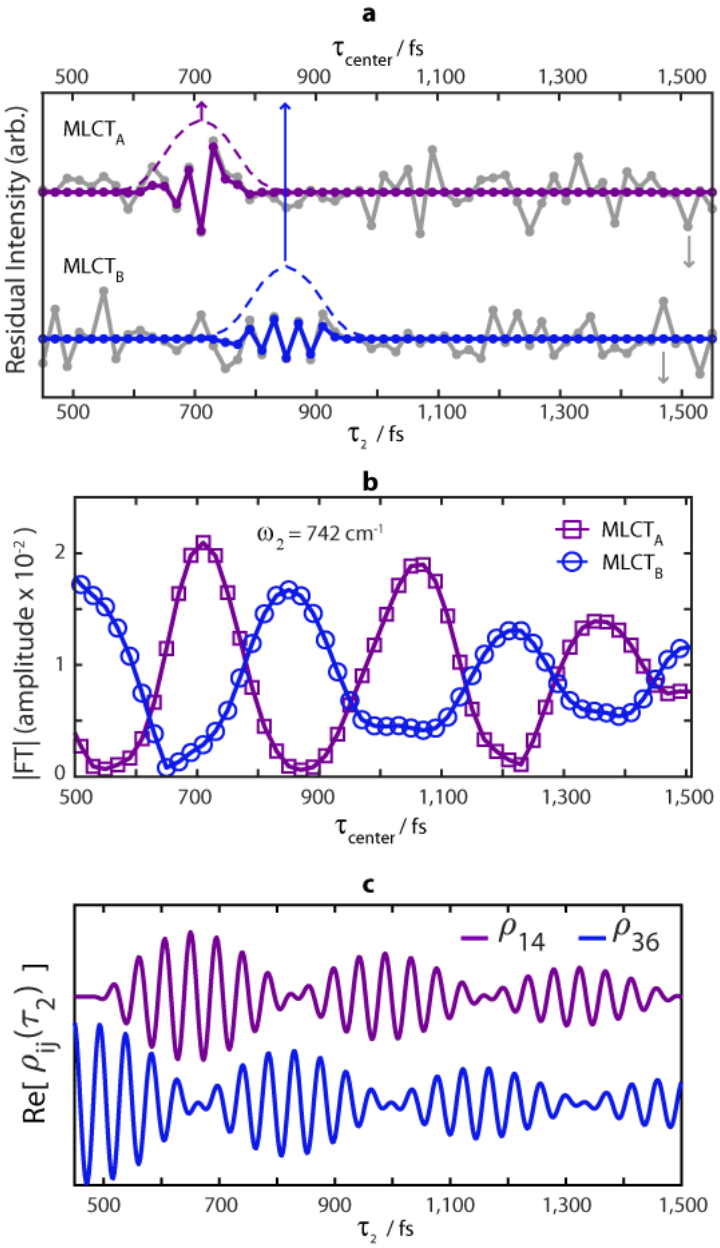


Figure 8.5. Later MLCT relaxation dynamics: nonadiabatic internal conversion through vibronic coherence. (a) Residual intensity (gray) of the integrated ($\omega_1$, $\omega_3$) 2D peak areas for the $\nu_{COO}$ vibration with $MLCT_A$ (top) and $MLCT_B$ (bottom) character; data is offset for plotting. Examples of the temporal filters (purple/blue, dashed) used in short time FT analysis (FWHM = 120 fs, centered at $\tau_{center}$ (top axis)) of the $\tau_2$-dependent residual intensity. The purple window ($\tau_{center}$ = 710 fs) highlights the $\nu_{Ru\text{-}bpy}$ (742 $cm^{-1}$) coherent beating with $\nu_{COO}$ having exclusively $MLCT_A$ character while at a later delay ($\tau_{center}$ = 850 fs) the blue window shows the $\nu_{Ru\text{-}bpy}$ coherence having exclusively $MLCT_B$ character. (b) Short time FT results reveal the oscillatory electronic character of the $\nu_{Ru\text{-}bpy}$ coherence signature between $MLCT_A$ and $MLCT_B$ with 340 ± 40 fs periodicity. (c) Simulation of the coherence block in the Redfield relaxation tensor for $\rho_{14}$ (purple) and $\rho_{36}$ (blue) during $\tau_2$ with an 800 fs coherence decay time where $\omega_{14} = \omega_{36}$ = 742 $cm^{-1}$ and a 50 $cm^{-1}$ nonadiabatic coupling reproduces electronic oscillatory behavior for the vibronic coherence involving $\nu_{Ru\text{-}bpy}$ with $MLCT_A$ and $MLCT_B$ (data offset). See section 8.12.9 for discussion of Redfield relaxation dynamics and section 8.12.8 for simulation details.

coupling: the $\nu_{Ru-bpy}$ mode at 742 $cm^{-1}$ which has a vibrational period of 45 fs. This is a case where a reliable time-frequency analysis is obtainable with a sliding window short time Fourier transform (STFT) method.[35] A temporal window that targets the presence of 45 fs oscillations in the $\tau_2$–dependent data is used to understand the dynamical behavior of the $\nu_{Ru-bpy}$ mode (see section 8.12.7 and Figure 8.16 - Figure 8.17 for extensive discussion of temporal windowing). This STFT analysis provides a stand-alone interpretation of the data because only one low frequency mode is relevant in the later time data as identified in Figure 8.2d and g, which is independent of the time-frequency analysis used in Figure 8.5. It is worthwhile to note here that the STFT method becomes less suitable as multiple frequency components contribute to a time-dependent signal of interest. This is because no single temporal window can be optimal for resolving many different frequency components in a time-frequency analysis, especially if they vary significantly in frequency and transient behavior. For those complicated cases, more advanced time-frequency transforms are required for reliable interpretation.[35] From our STFT analysis, a vibronic coherence is uncovered persisting throughout this later ~1 ps of relaxation which facilitates nonadiabatic IC.

The $\rho_{36}$ coherence appears (Figure 8.5b, blue) as the initially excited wavepacket diminishes. Thereafter, the $\rho_{36}$ coherence transfers to $\rho_{14}$ - changing in electronic character from $MLCT_B$ to $MLCT_A$ by $\tau_2 \cong$ 650-700 fs. This oscillatory dynamic continues for ~1 ps, as the amplitude of the $\rho_{36}$ and $\rho_{14}$ coherences oscillate out-of-phase with periodicity of 340 ± 40 fs. To quantify this dynamic, the time-dependent behavior of $\rho_{36}$ and $\rho_{14}$ is simulated as an isolated two-level system where a 50 $cm^{-1}$ nonadiabatic coupling reproduces the 340 ± 40 fs Rabi-like oscillation seen in the experimental data (Figure 8.5c; section 8.12.8). Here the

observed Rabi-like oscillations result from the vibronic coherence transfer between $\rho_{36}$ and $\rho_{14}$.[36]

## 8.8 Spectral Deconvolution with 3D EV Spectroscopy

One advantage to fully resolving the third order vibronic response function is that spectral features which are spectrally convolved in 1D and 2D spectra may be separated if they behave differently during $\tau_2$. This can be viewed directly by considering slices of the 3D EV spectrum at particular $\omega_2$ frequencies, as shown in Figure 8.6 below. Although the high frequency vibrational reporter of central interest in this 3D EV analysis has been the $\nu_{COO}$ centered at $\omega_3$ = 1328 cm$^{-1}$, this carboxylate symmetric stretch is only one of four similar modes involving the carboxylates in N3$^{4-}$. The TDDFT calculations in chapter 7 show that all four modes are nearly degenerate in the ground electronic state, composing the FTIR feature at 1375 cm$^{-1}$. These modes split in the excited triplet state, resulting in one mode significantly red-shifted to 1328 cm$^{-1}$ and the other three more or less overlapped with the ground state modes. Experimental evidence to support the calculation is present in both the tIR data and the 3D EV data. The tIR time trace for the GSB at $\omega_3$ = 1375 cm$^{-1}$ in Figure 8.13 shows a decay in signal on the same timescale as the 2.7 ps growth of the $\nu_{COO}$ ESA at 1328 cm$^{-1}$ which strongly suggests there are, in fact, other ESA features of the same character underlying this GSB. The 3D EV spectrum in Figure 8.6 below, particularly the $\omega_2$ slices at the $\nu_{Ru-N}$ and $\nu_{Ru-bpy}$ frequencies, shows spectral features that span more than just the $\nu_{COO}$ in $\omega_3$. The amplitude of the contours shown in the $\omega_2$ slices is also lower in the region where the positive GSB features appear in the 2D spectra (~1370-1380 cm$^{-1}$) but stronger on the wings, emphasizing that these signals are from electronically excited state vibrations. This strongly suggests that all of the

carboxylate vibrational modes are sensitive to the same dynamics reported here for only the $\nu_{COO}$, but this mode is simply a more distinct signature to analyze.

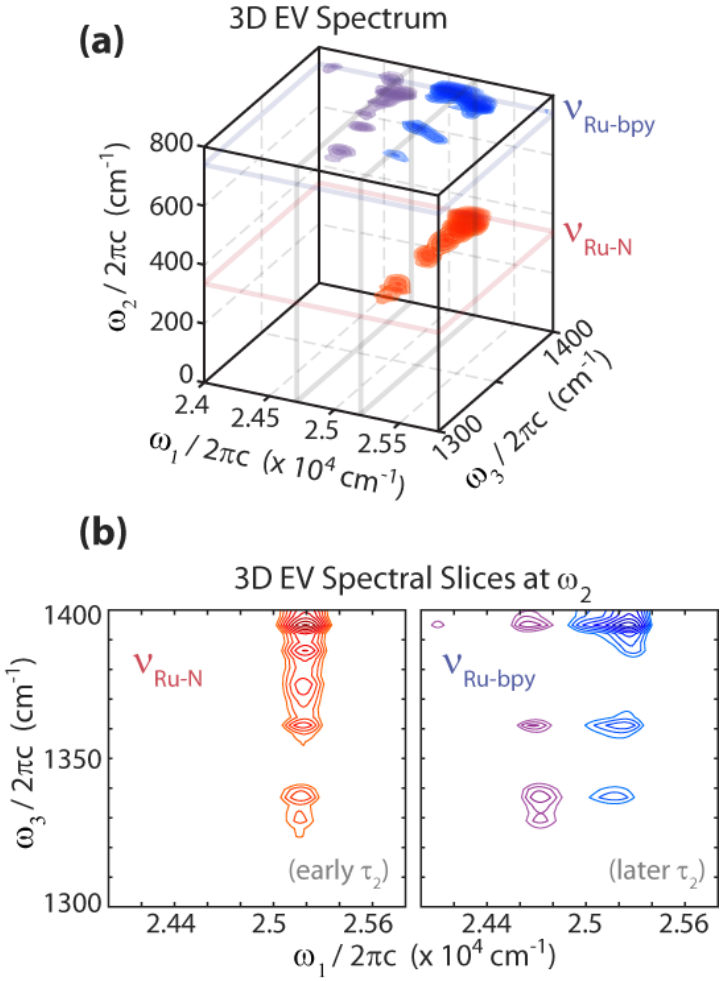


Figure 8.6. Full 3D EV Spectrum of Aqueous $N3^{4-}$. (a) The complete third order vibronic molecular response is plotted in its three frequency dimensions. (b) Slices at the $\nu_{Ru\text{-}N}$ (red) and $\nu_{Ru\text{-}bpy}$ (blue and purple) of the 3D EV spectrum. The time-dependent 3D frequency correlation between $MLCT_A$, $MLCT_B$, $\nu_{COO}$, $\nu_{Ru\text{-}N}$, and $\nu_{Ru\text{-}bpy}$ are described by the peaks at $\omega_3$ ~1328 $cm^{-1}$. Evidence for the other carboxylate modes is present in the 1350 $cm^{-1} < \omega_3 < 1400$ $cm^{-1}$ range. The coloration depicts the time dependence, as schematically illustrated in Figure 8.1. On this scale, 0 < red < blue < purple in $\tau_2$ according to the timescales discussed in the chapter. Note: the dimensionality of this plot does not allow for representing the nonadiabatic internal conversion between $MLCT_A$ and $MLCT_B$ during the later $\tau_2$ period, which is shown in Figure 8.5.

## 8.9 NONSECULAR RELAXATION IN THE 3D EV SIGNALS: COHERENCE-TO-POPULATION TRANSFER

The discussed dynamics occur during $\tau_2$ while many vibronic eigenstates are involved with the ultrafast intersystem crossing and relaxation within the triplet manifold. The center frequency and bandwidth of the pump pulse (see Table 8.1) in these experiments is sufficient to excite the following elements of the density matrix $\rho_{ab}$ where $a,b \in \{1,2,3,4,5\}$ as defined in Figure 8.3. The coherences observed during $\tau_2$ result from excitation of density matrix elements in which $a \neq b$. However, the density matrix elements that correspond to the $\nu_{COO}$ vibrations measured in $\omega_3$ are $\rho_{38}$ and $\rho_{17}$. The vibrational probe center frequency and bandwidth require that the system be in a population ($\rho_{33}$ or $\rho_{11}$), rather than a coherence, in order for the $\nu_{COO}$ to be detected at $\omega_3$ = 1328 cm$^{-1}$ throughout the duration of the experiments. In other words, the probe bandwidth requires the transitions induced by the third light-matter interaction (+$\mathbf{k}_3$) to be $\rho_{11} \xrightarrow{+\mathbf{k}_3} \rho_{17}$ or $\rho_{33} \xrightarrow{+\mathbf{k}_3} \rho_{38}$ because it is insufficient to both collapse the initially excited coherence *and* induce the first vibrational excitation of the $\nu_{COO}$, (e.g., $\rho_{35} \xrightarrow{+\mathbf{k}_3} \rho_{38}$). Thus, I suggest that a coherence-to-population transfer must occur during $\tau_2$ to account for the observed signals. This is a nonsecular relaxation pathway, $R_{35,33}$, where $\omega_{35} - \omega_{33} = \nu_{Ru-N}$ (340 cm$^{-1}$) that drives the early time excited state vibrational wavepacket dynamics ($0 \leq \tau_2 \leq 600$ fs); a representative double-sided Feynman Diagram for this pathway is given in Figure 8.7(a).

Whereas for the later time relaxation dynamics the excitation pulse center frequency and bandwidth is less important for determining the observed coherence during $\tau_2$, the probe pulse

center frequency and bandwidth still restrict the observable transitions in the same way as at early times. In these instances too, coherence-to-population transitions $\rho_{14} \xrightarrow{\tau_2} \rho_{11}$ and $\rho_{36} \xrightarrow{\tau_2} \rho_{33}$ during $\tau_2$ would still be required to observe the signals during $400 \leq \tau_2 \leq 1500$ fs, as shown in Figure 8.7(b). It is noted that the coherence-to-coherence transitions responsible for the observed oscillatory electronic character during nonadiabatic IC fall within the secular approximation because the $\nu_{Ru-bpy}$ vibrational mode is part of the $\tau_2$ coherence detected with both $MLCT_A$ and $MLCT_B$ character during the later relaxation time period which results in $\omega_{14} = \omega_{36}$. Based upon these arguments, nonsecular relaxation dynamics are suggested to contribute to the 3D EV signals discussed in this chapter. Further investigation of this mechanism may be possible if a probe pulse was used which was spectrally broad enough to collapse the $\tau_2$ coherence and excite one quantum of the $\nu_{COO}$.

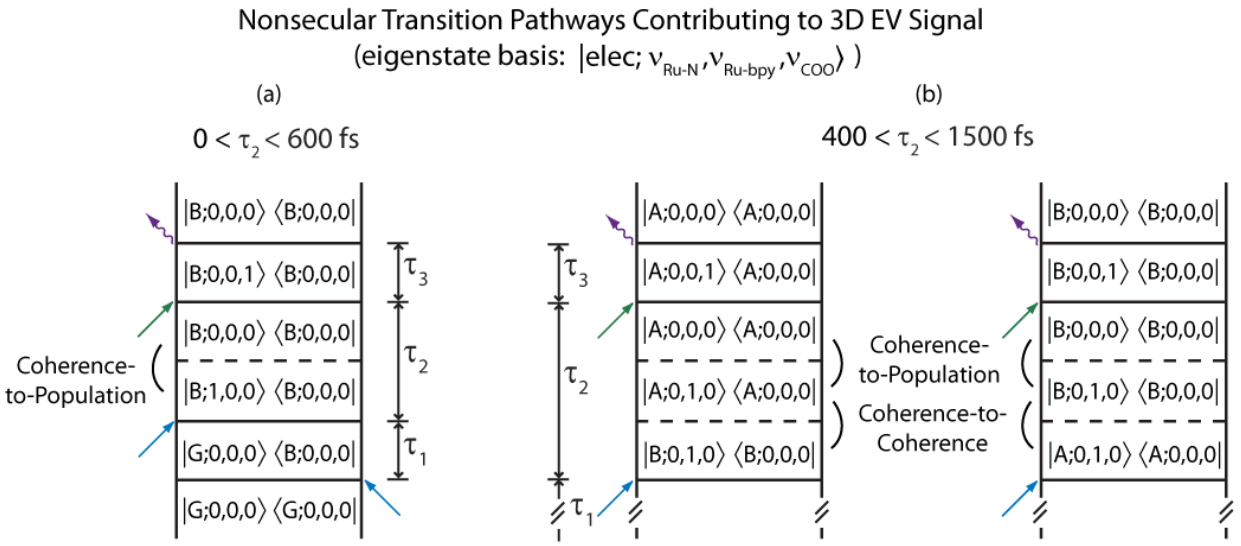


Figure 8.7. Exemplary Nonsecular 3D EV Relaxation Pathways in $N3^{4-}$. (a) A representative Feynman Diagram of the excited state vibrational wavepacket present during early time relaxation dynamics which requires a coherence-to-population transition for detection. (b) Two representative Feynman Diagrams depicting the later time relaxation dynamics resulting in the oscillatory electronic character discussed in the manuscript, which still requires a coherence-to-population pathway for detection. The dashed lines connecting different states in the Feynman Diagrams represent transitions undergone without external perturbation from a laser pulse.

For example, the observation of a peak at the difference frequency between $|B;1,0,0\rangle$ and $|B;0,0,1\rangle$ (~988 $cm^{-1}$) with a probe pulse containing this frequency as well as the mid-IR frequencies of this work could provide evidence that the $\tau_2$ coherence-to-population transfer is not absolutely required to view the signals reported in this chapter. Albeit, this would not rule out coherence-to-population transfer but only prove that it is not the only mechanism giving rise to the measured signals.

## 8.10 DISCUSSION

There is a great need for experimental methods that provide unambiguous measurement of vibronic coherences and couplings in order to uncover their role in ultrafast charge and energy transfer.[5,37,38] The results presented above clearly demonstrate the capability of multidimensional EV spectroscopy to directly monitor the temporal evolution of vibronic coherences and couplings during multi-coordinate photochemical processes. The progression of the photoexcited charge transfer process in $N3^{4-}$ measured in this study is summarized in Figure 8.8.

The early time $\rho_{35}$ coherence reveals an impressive degree of intramolecular couplings that propagate for the initial ~600 fs. This wavepacket is confined to $MLCT_B$ electronic character indicating that the Ru-N distance of the $\nu_{Ru-N}$ stretching coordinate specifically modulates the vibronic coupling between $\nu_{COO}$ and the $MLCT_B$ during the initial relaxation of photoexcited $N3^{4-}$ (Figure 8.8b, red well). The early time vibrational wavepacket measurement clearly differentiates the nature of the vibronic coupling between either $MLCT_A$ or $MLCT_B$

and the $\nu_{COO}$, which is a distinction that could not be made from a single 2D EV, tIR, or transient absorption (TA) experiment.

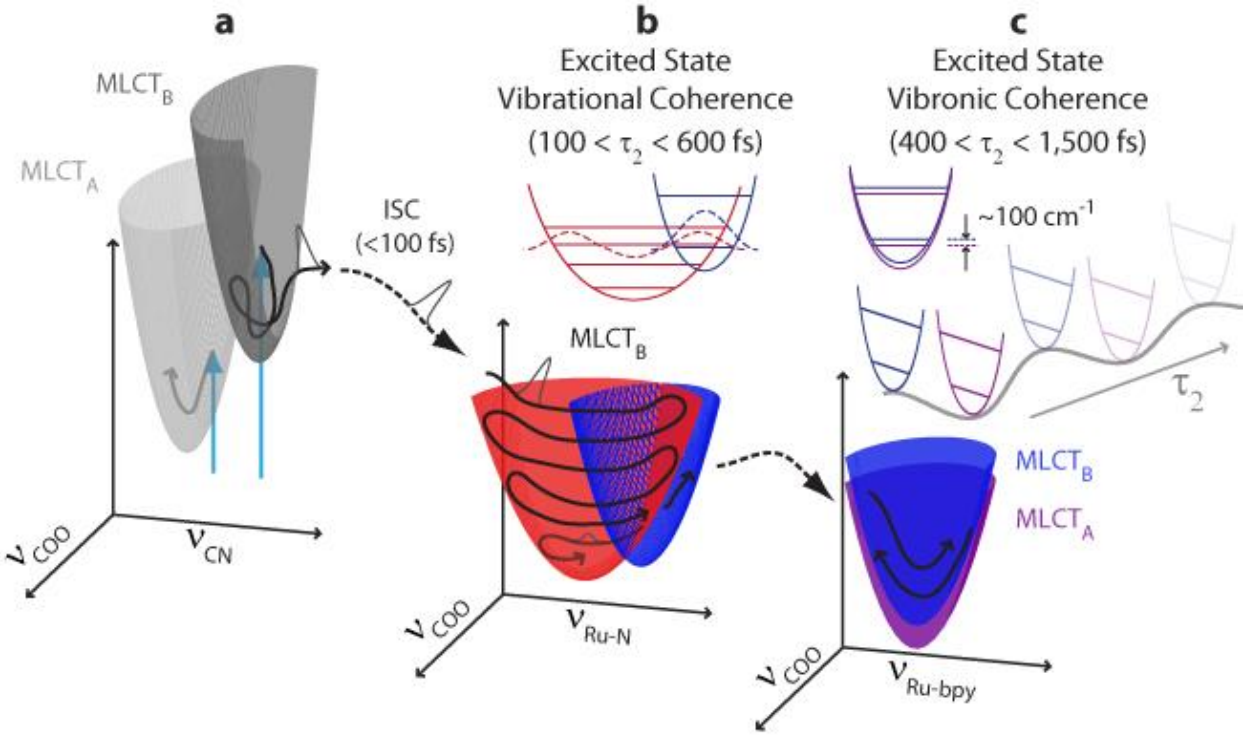


Figure 8.8. Coherence evolution during the relaxation of photoexcited $N3^{4-}$. A schematic representation of the first two picoseconds of photoexcited relaxation progresses from left to right (a-c). Initial MLCT electronic excitation (a) with MLCT states coupling the donor-acceptor vibrations shown ($MLCT_A$ = light gray well; $MLCT_B$ = dark gray well) and the initial wavepacket passing through ultrafast ISC. The ~600 fs propagation of the initial excited state vibrational coherence $\rho_{35}$ (b) involving $\nu_{Ru-N}$ of $MLCT_B$ (red wells); a coherence transfer to $\nu_{Ru-bpy}$ of $MLCT_B$ (blue wells) is merely suggested with sufficient wavefunction overlap involving the $\nu_{Ru-bpy}$ lowest energy vibration. The ~1 ps propagation of the excited state vibronic coherences $\rho_{36}$ and $\rho_{14}$ involving $\nu_{Ru-bpy}$ (c) depicts the nonadiabatic internal conversion between $MLCT_A$ (purple) and $MLCT_B$ (blue) through the 50 $cm^{-1}$ nonadiabatic coupling strength.

The nature of the initial excited state wavepacket, first reported by Kallioinen[12] using TA, can now be confidently assigned as an excited state vibrational coherence between $\nu_{COO}$ and $\nu_{Ru-N}$ due to the electronically-localized 3D EV signal. Confirmation of the triplet character of this excited state vibrational wavepacket is clear because the signal is detected through the

coherence with the triplet state $\nu_{COO}$, which answers this outstanding question in the field of N3 photophysics. I note that the known ISC time (≤ 100 fs) leaves the existence of the singlet vibrational wavepacket ambiguous because the $\nu_{Ru-N}$ vibrational period is on the same order as ISC, if not longer.

A transition occurs between the early and later relaxation periods as the wavepacket arising from the $\rho_{35}$ coherence diminishes and the later time wavepacket formed by the $\rho_{36}$ coherence emerges (Figure 8.8b, red to blue well). The fact that this transfer occurs between states of the same electronic character suggests that excited state vibrational coherence transfer bridges the early and later time dynamics; however, many other coordinates could also affect the $\rho_{35}$ coherence. Indeed, only a small window of the $^1$MLCT absorption is excited in these experiments, despite our efforts to implement a broadband excitation source; the observed dynamics will depend on the electronic structure of the initially excited states and the solvation environment.[39,40] Since the pump center frequency and bandwidth cannot directly excite $\rho_{36}$, this coherence must be accessed through intramolecular energy transfer. Conversely, the $\rho_{14}$ is directly excitable yet its signature is negligible until after the $\rho_{36}$ coherence has formed (Figure 8.5b). Importantly, the probe center frequency and bandwidth is insufficient to collapse the coherences observed during $\tau_2$ and excite the v=0→1 $\nu_{COO}$ vibrational transition required for detecting the ESA at $\omega_3$ = 1,328 cm$^{-1}$ (Table 8.1). Accounting for the quantum pathways capable of producing the measured oscillatory residuals implies that coherence-to-population transfer[41] plays an important role in the ultrafast photophysics of N3$^{4-}$ (see Figure 8.7). Together, these dynamics suggest that the vibronic couplings of MLCT$_B$ function as a gateway

for the initially excited vibrational coherence to transition into nonadiabatic IC and continue equilibrating within the excited triplet manifold.

Discovering the out-of-phase oscillations between the $\rho_{36}$ and $\rho_{14}$ coherences is key to characterizing the wavepacket evolving during the later relaxation period as an excited state vibronic coherence (Figure 8.8c). By comparison, a purely vibrational coherence, such as $\rho_{35}$, would be confined within a single electronic state. A purely electronic coherence would be expected to appear at the earliest delay times, to dephase within 10s-100s of fs, and to yield $\omega_2$ features at the difference frequency between the two electronic states independently of any vibrational coordinate. As we report here for $400<\tau_2<1{,}500$ fs, the amplitude of the vibrational coherence oscillates with the electronic character, it appears after 600 fs of relaxation, and it proceeds for ~1 ps. This prolonged coherence is characteristically vibronic, as the expected decoherence time slows when a more complete specification of the system eigenstates occurs;[42] we directly observe this quantum coherence with multidimensional EV spectroscopy. The 50 $cm^{-1}$ nonadiabatic coupling extracted from our simulations is consistent with the 340 ± 40 fs vibronic coherence transfer rate between $\rho_{36}$ and $\rho_{14}$, and the near-complete transfer observed in Figure 8.5b suggests the system is within the strong coupling regime. The combination of the 2D EV experiment to map out vibronic couplings between $\nu_{COO}$ and either $MLCT_A$ or $MLCT_B$,[29] and the 3D EV experiment to resolve additional excited state coherences involving $\nu_{Ru-N}$ and $\nu_{Ru-bpy}$ allow the evolution of photoexcited vibronic coherence to be unambiguously measured.

## 8.11 CONCLUSIONS

Progress towards tackling the long-standing challenge of characterizing non-equilibrated charge transfer mechanisms in photoexcited donor-acceptor complexes is achieved in this study. Our 3D EV measurements provide an account of how intramolecular charge transfer occurs in an archetypal photosensitizer, detailing the complex interplay between valence electron density and molecular structural dynamics on the fs timescale. I have shown that the cascading relaxation through the non-equilibrated MLCT manifold of $N3^{4-}$ is heavily influenced by Ru-N (of dcbpy) vibrations which effectively bridge the charge-donating $Ru(NCS)_2$ and charge-accepting dcbpy moieties through excited state vibronic couplings. From this I conclude that at least one excited state trajectory in aqueous $N3^{4-}$ that facilitates intramolecular charge transfer is initiated through an excited state vibrational coherence lasting for ~600 fs before transferring to a secondary coherence that is vibronic in nature and promotes nonadiabatic IC proceeding for another ~1 ps of relaxation. These results illuminate a mechanism for how solvated $N3^{4-}$ utilizes excited state, time-dependent vibronic couplings to achieve long-lived charge separation. In addition to a high density of states and strong spin-orbit coupling, we contribute evidence that structural relaxation involving metal-ligand bonding nitrogen atoms strongly influences excited state mixing and efficient formation of long-lived $^3$MLCT states.[6,8] This mechanistic insight may be particularly useful for designing more efficient and earth-abundant light harvesting complexes,[43] and for harnessing the typically untapped potential of unthermalized photoexcited states to control photochemical efficacy.[44] Following photochemical reactivity from the perspective of specific vibrational coordinates is a unique advantage of multidimensional EV spectroscopy which can be exploited to identify critical intramolecular coordinates governing non-equilibrium

photoexcited processes. Multidimensional EV spectroscopy will be an incisive tool for understanding photoexcited energy and charge transfer mechanisms during complex, multi-coordinate photochemical processes in molecular and material systems.

Translating the presented information of this chapter in terms of the football analogy of chapter 1: We have learned that there are other players involved in the play resulting in Liverpool's game-winning goal besides the major player identified in chapter 7. To extend this analogy, let's assume that one "state" of the ball's motion is defined by it being played on the right side of the pitch (analogous to the electronic state $MLCT_B$) and another "state" is defined by the ball being played down the left side (analogous to the electronic state $MLCT_A$). Indeed, from the perspective of this major player (let's say player B was that major player identified in the previous chapter; he is analogous to the $\nu_{COO}$ vibration), there is an additional player (player C; analogous to $\nu_{Ru-N}$) who is crucial to the first part of the play being executed correctly. Furthermore, during the early part of the play in which players B and C are coupled with the ball's motion, we have revealed that the ball was localized to the right side of the field. Then, we see that this first part of the play transitions into a completely different segment of the overall time period in which the goal was scored. This later period still involves player B but player C's contribution to the goal has largely finished. Now, player B is playing the ball very quickly with yet another player (player D; analogous to $\nu_{Ru-bpy}$) *and* the motion of these two players is resulting in the movement of the ball from the right side, to the left side, back to the right side, etc. It is as if the dynamic play from the combination of players B and D – and likely other players whose motion is not directly observable – has connected both sides of the field in a way that does not usually occur (this is analogous to the nonadiabatic IC).

Clearly, the Manchester United defense has become mesmerized by such dynamic play from the Liverpool team. Soon, the ball stops moving from side to side because, of course, it has found equilibrium - in the back of Manchester United's goal net. Liverpool 1 – 0 United (final score).

## 8.12 APPENDICES

### 8.12.1 *Instrumental Details*

The pulse spectra for the pump and probe beams are shown below. The temporal characterization of the instrument response is given by comparing a solvent only signal collected in the exact configuration as all of the tIR and 2D EV data is collected. The solvent response is also consistent with a non-resonant tIR trace collected in a 250 μm silicon wafer. The onset of the $N3^{4-}$ tIR signal outside of pulse overlap at $\tau_2$ = 180-200 fs is clear from the red trace below. Table 8.1 below also provides the spectral characteristics of the pump and probe beams, which are useful when considering the bandwidth requirements for measuring signals from particular quantum transition pathways. Solvent only 2D EV spectra present in Figure 8.10 indicate negligible contributions. All data presented here are linearly dependent on pump pulse energy.

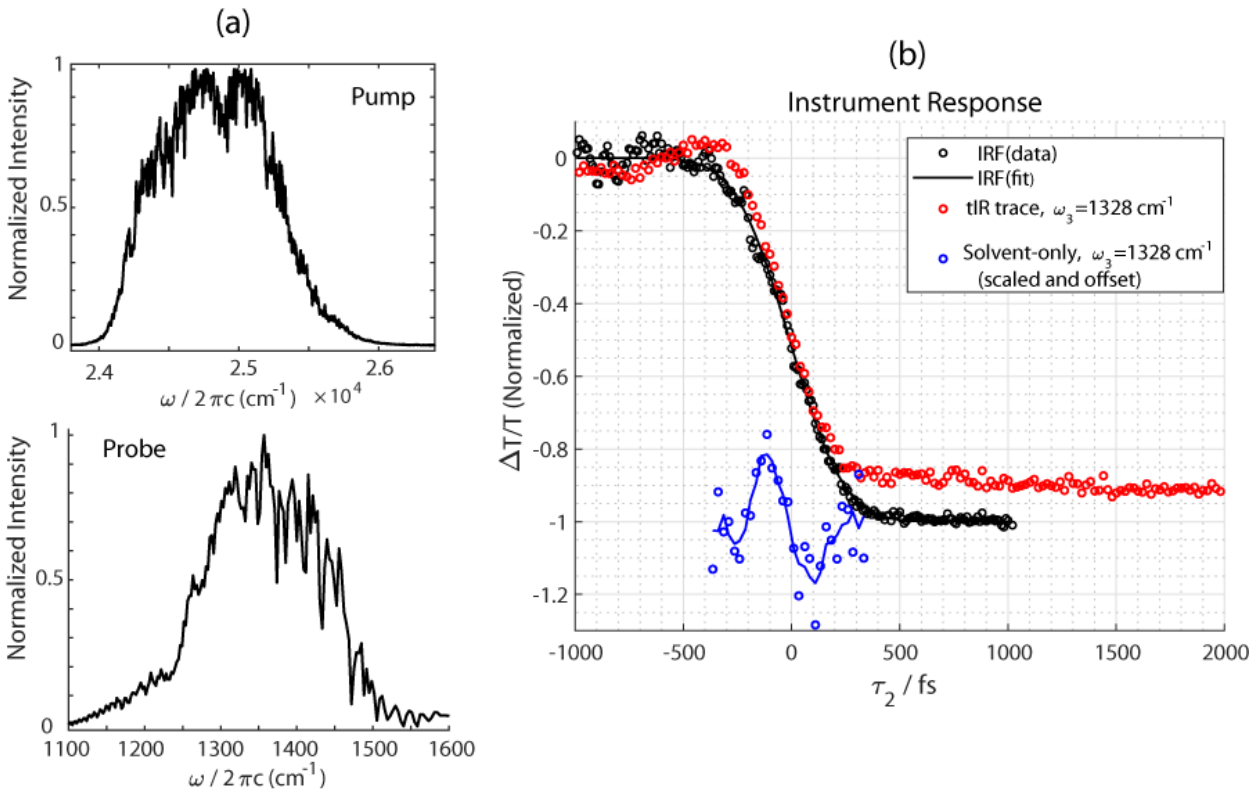


Figure 8.9. Instrument Characterization. (a) Broadband UV pump pulse spectrum and mid-IR probe pulse spectrum. (b) The instrument response function is assessed using the non-resonant tIR signal of a 250 μm Si wafer (black). The $N3^{4-}$ molecular response is observed outside of pulse overlap for $\tau_2 >$ 200 fs from the transient-IR trace for the $\nu_{COO}$ excited state absorption ($\omega_3$=1328 $cm^{-1}$, red ). The signals are normalized by the absolute value of the greatest magnitude signal and overlaid for comparison. The non-resonant solvent-only tIR signal (blue; circles are data and line is three-point moving average) is scaled and offset such that zero signal is $\Delta T/T = -1$ for comparison; the solvent response diminishes for $\tau_2 >$ 200 fs, consistent with the decay of the Si signal and the onset of the $N3^{4-}$ molecular signal.

Table 8.1. Pump and Probe Beam Center Frequencies and Bandwidths

| **Beam** | **Center Frequency $\omega_0 / 2\pi c$ ($cm^{-1}$)** | **Full Width 50% Max Intensity ($cm^{-1}$)** | **Full Width 20% Max Intensity ($cm^{-1}$)** |
|---|---|---|---|
| Broadband UV Pump | 24805 | 1090 | 1400 |
| Mid-Infrared Probe | 1361 | 198 | 245 |

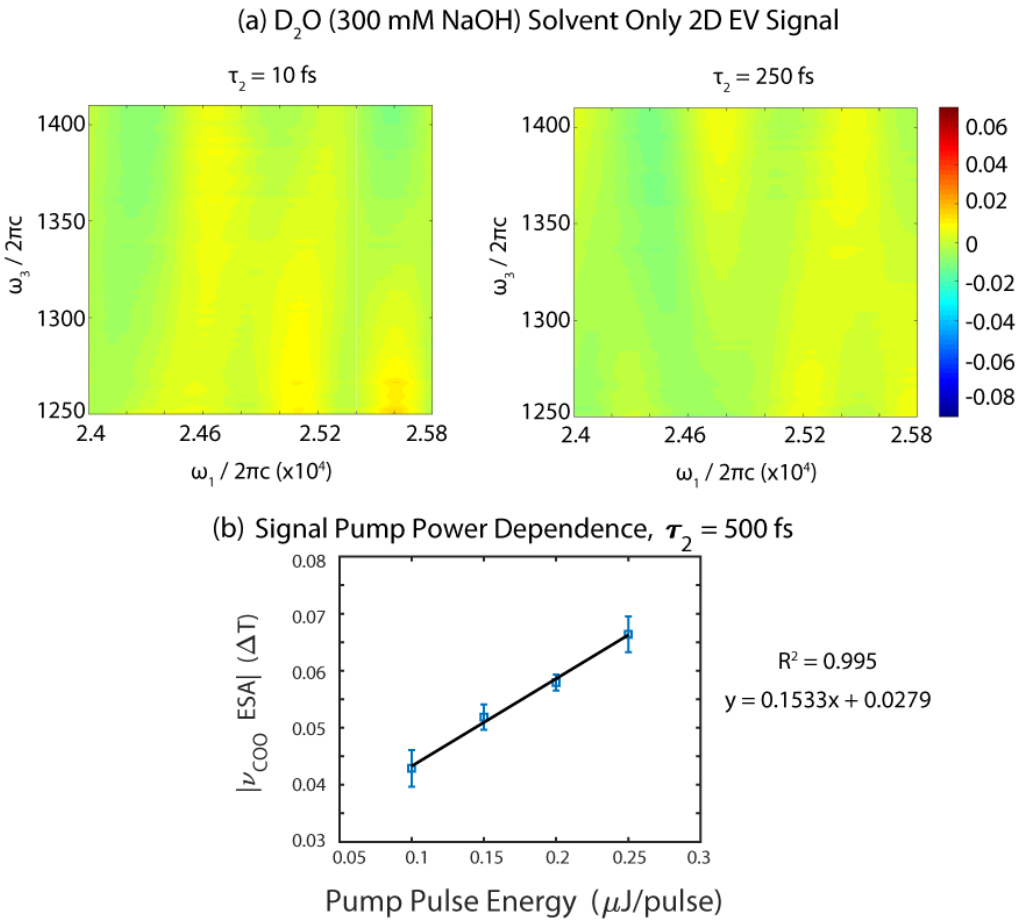


Figure 8.10. Solvent Background and Signal Pump Power Dependence. (a) 2D EV spectra of the solvent ($D_2O$ in 300 mM NaOH) collected in the same sample configuration as the $N3^{4-}$; no significant solvent contributions are present. (b) The magnitude of the $\nu_{COO}$ ESA ($\omega_3$=1328 $cm^{-1}$) plotted at different pump pulse energies shows the data measured are linearly dependent on pump energy. Blue squares are average of five difference spectra with the error bars reflecting +/- 1 standard deviation from the mean; the black line is a linear fit with the fit parameters shown on the right.

### 8.12.2 *Data Acquisition*

A well-averaged tIR data set used for 2D EV normalization is obtained by averaging 500 laser shots per difference spectrum while scanning over the range $-1 \leq \tau_2 \leq 200$ picoseconds consecutively in the forward direction; 20 completed $\tau_2$ scans are then averaged together for the final tIR data set. The entire tIR data set was collected in ~1.5 hours during the same laser run as the 2D EV data with the same experimental configuration to maintain consistency in as many systematic experimental parameters as possible. The tIR data set is divided by a well-

averaged (5000 laser shots) sample spectrum collected with the BBUV pump blocked to obtain $\Delta T/T$.

A single 2D EV spectrum at a given $\tau_2$ delay time is collected by scanning $\tau_1$ over the range [0:150] fs in 1.15 fs steps to expedite data acquisition using a partially rotated frame. The integrated field autocorrelation of the pump pulses scanned over $\tau_1$ is collected and Fourier transformed to ensure that the shape of the excitation spectrum is not compromised due to under sampling. At each fixed $\tau_1$ delay time and $\tau_2$ delay time, 500 laser shots are averaged to obtain the differential absorption spectrum. The total range of pump-probe delay times collected in these 2D EV experiments are $10 \leq \tau_2 \leq 2010$ fs at 20 fs intervals. Six 2D EV scans were averaged for each $\tau_2$ delay yielding a single averaged 2D EV data set. To minimize artifacts due to laser drift throughout the experiment, the entire $\tau_2$ range studied was collected in two parts: first by scanning $250 \leq \tau_2 \leq 2010$ fs and then scanning $10 \leq \tau_2 \leq 250$ fs. Acquisition of the first range ($250 \leq \tau_2 \leq 2010$ fs) was further divided into two separate experimental scans with 40 fs intervals: one for $250 \leq \tau_2 \leq 2010$ fs and the other for $270 \leq \tau_2 \leq 1990$ fs. Each of these subranges scanned with 40 fs intervals were scanned three times in the forward direction and three times in the reverse direction to further reduce artifacts from laser drift during the ~4.5 hour collection time of the 2D EV scan over the $\tau_2$ range. Acquisition of the second range ($10 \leq \tau_2 \leq 250$ fs) was collected in 20 fs intervals using the same approach, each scan taking ~1.5 hours of experimental collection time. Solvent-only 2D EV spectra were collected over $10 \leq \tau_2 \leq 450$ fs in 20 fs intervals to ensure no significant solvent features were present in the sample data (see Figure 8.10(a) below). The pump power dependence of the 2D EV signal was measured to be linear with respect to pump power, ensuring that no multiphoton absorption signals were present in the tIR or 2D EV data (see Figure 8.10(b)).

### 8.12.3 *2D EV Data Processing: Instrumental Noise Correction*

The same 2D FT data processing techniques as described in chapter 3 are used here to generate each 2D EV spectrum. Additional data processing steps are required to isolate the weak oscillatory 2D EV peak amplitudes discussed in this chapter. The purpose of the FT analysis over the $\tau_2$ delay time is to identify the frequencies of coherent oscillations that modulate the amplitude of the 2D EV peaks. These signatures reveal further information about the degrees of freedom coupling the vibronic states involved with the excited state charge transfer dynamics in $N3^{4-}$. Since these oscillations are very weak in our experiments, careful corrections for signal intensity fluctuations due to instrumental noise are required to isolate the coherent oscillations in 2D EV signal amplitude. As can be seen by comparing the blue and red time traces in Figure 8.11(bottom), instrumental noise can significantly overwhelm weaker oscillatory signals. We correct for this noise to isolate the $\tau_2$ oscillations of interest by normalizing the raw 2D EV data for each $\tau_2$ delay to a separate, well-averaged tIR data set which was collected within the same laser run using an identical experimental configuration. The six 2D EV scans at a given $\tau_2$ delay are first averaged in the time domain ($\tau_1$). Then the differential absorption spectrum from the 2D EV data set for $\tau_1 = 0$ is normalized to the well-averaged tIR spectrum for the same $\tau_2$ delay. Since these two data sets reflect an exactly identical experiment, the only difference between them is the experimental noise due to fewer scans averaged in the 2D EV experiment than in the tIR experiment. To ensure accurate comparison of spectra, the tIR spectrum is cubic spline interpolated to have finer time steps for the normalization procedure. The 2D EV ($\tau_1 = 0$) spectrum is fitted to the tIR spectrum with the following Equation:

$$S_{norm}^{2DEV}(\tau_1 = 0, \tau_2, \omega_3) = \alpha\left(S^{2DEV}(\tau_1 = 0, \tau_2, \omega_3)\right) + \beta \tag{8.1}$$

where a constant spectral intensity scalar ($\alpha$) and a constant offset ($\beta$) are applied to the averaged 2D EV spectrum ($S^{2DEV}(\tau_1 = 0, \tau_2, \omega_3)$) and optimized in a nonlinear least squares fitting routine to obtain the tIR-normalized 2D EV spectrum ($S^{2DEV}_{norm}(\tau_1 = 0, \tau_2, \omega_3)$).

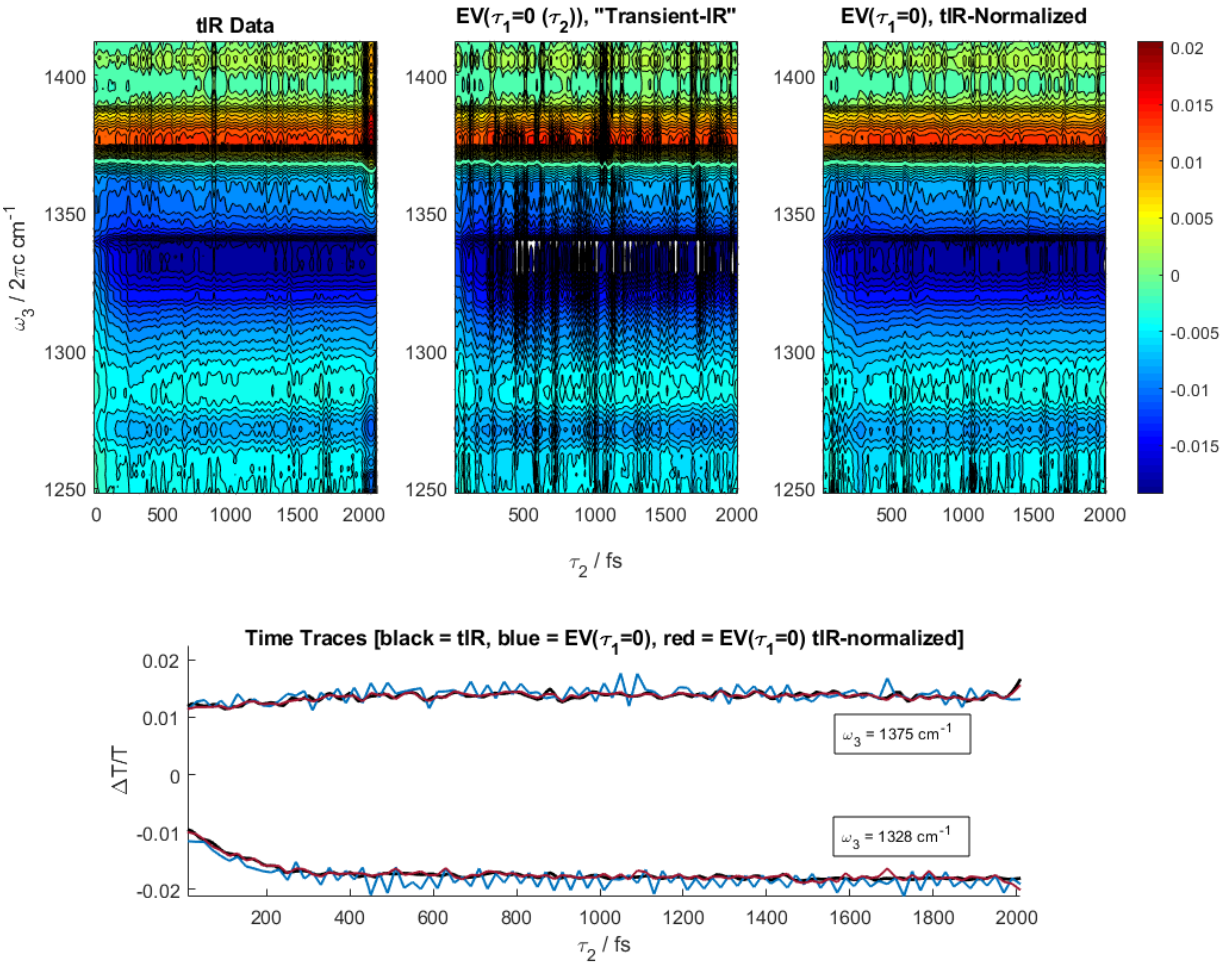


Figure 8.11. Pre-FT Data Processing of $\tau_2$-dependent 2D EV Data. (top, left) The cubic spline interpolated tIR spectrum collected independently, (top, center) the raw 2D EV spectra with $\tau_1$ = 0 for all $\tau_2$ delays, and (top, right) the 2D EV ($\tau_1$ = 0) data corrected for instrumental noise by normalization to the tIR data set. (bottom) The time traces of the carboxylate GSB and ESA for the data sets show the improvement in signal quality after removing further instrumental noise due to fewer 2D EV scans averaged than in the tIR data set. The blue traces = 2D EV ($\tau_1$=0) data set without normalization, red traces = with normalization, and black traces = interpolated tIR data (see discussion for details).

Initial values are set to $\alpha$ =1 and $\beta$ =0 in the fitting routine; we find $\bar{\alpha}$ = 0.97 (±0.06) and $\bar{\beta}$ =0.00015 (±0.00048) (where the bar denotes the average over the optimized parameters for all $\tau_2$ spectra). While the optimized parameters indicate that minimal adjustment to the original 2D EV spectrum is needed (i.e., on average, the intensities of the difference signals are scaled by less than 5% and offset by less than 2% of the signal magnitude for the $\nu_{COO}$ mode), this procedure effectively corrects for instrumental noise present in the 2D EV data as shown in Figure 8.11. The optimized scalar and offset for each $\tau_2$ spectrum are then applied to the raw 2D EV spectra over the complete range of $\tau_1$ composing the 2D EV data set using equation (8.1). Then the tIR-normalized 2D EV data undergoes the usual FT processing over $\tau_1$.

### 8.12.4 *2D EV Data Processing: Isolating Coherent Oscillatory Features in $\tau_2$-Dependent Data*

The 2D spectral regions of interest are the ($\omega_1$, $\omega_3$) areas of the greatest 10-15% signal for the two MLCT features vibronically coupled with the $\nu_{COO}$; these regions of interest are used throughout the remaining analysis (highlighted by red boxes in Figure 8.12, the ($\omega_1$, $\omega_3$) ranges are given in Table 8.2). I note that using slightly different bounds for the 2D EV regions of interest in the 10-15% signal range does not alter the conclusions from the analysis. I have assumed that measured population kinetics within the first 10 ps of the excited state triplet relaxation do not vary considerably between $MLCT_A$ and $MLCT_B$ because the fits to the tIR time traces described in section 8.12.5 only require a single exponential decay ($\tau_{short}$ in Table 8.3) in this $\tau_2$ period to fit the data well. To remove the population kinetics from the 2D EV regions of interest, the ($\omega_1$, $\omega_3$) data points within the region of interest at each $\tau_2$ delay are averaged to obtain what is effectively a tIR time trace for each excited MLCT state that is resolved by the 2D EV experiment. The population kinetics of the averaged 2D regions of

interest are then fitted using a Gaussian function convolved with two decaying exponentials (see chapter 7 for tIR fitting equation) while fixing the time constants ($\tau_{short}$ and $\tau_{long}$) to the values obtained from the tIR measurements (given in Table 8.3). The fitted population kinetics are then subtracted from the 2D data points in each region of interest to isolate coherent oscillatory dynamics that are modulating the 2D EV signal corresponding to the vibronically coupled $\nu_{COO}$ and either $MLCT_A$ or $MLCT_B$.

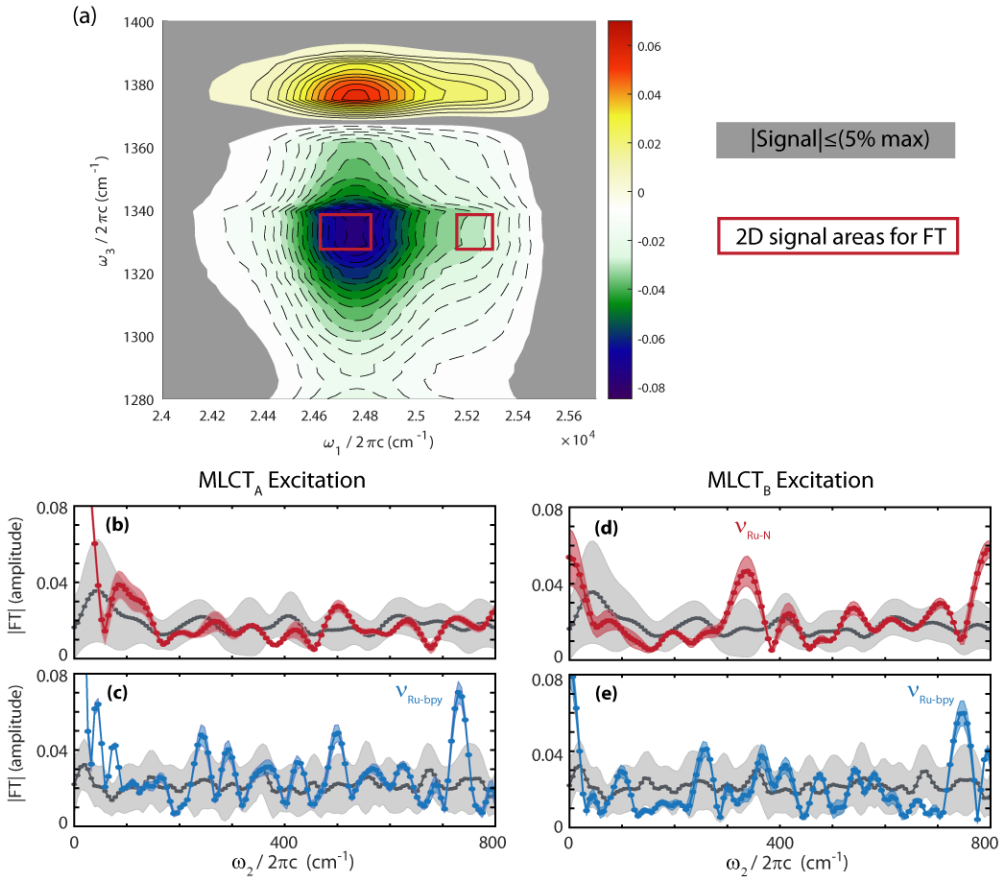


Figure 8.12. Assessing Signal-to-Noise in $\omega_2$ Spectra. (a) Averaged 2D EV spectrum over all $\tau_2$ surfaces; gray shows background signal and red boxes highlight 2D EV regions of interest for vibronic couplings between $\nu_{COO}$ and both $MLCT_A$ and $MLCT_B$. Spectra from FT analysis on $0 \leq \tau_2 \leq 600$ fs data (b, red) and on $400 \leq \tau_2 \leq 1500$ fs data (c, blue) for $MLCT_A$ excitation. Spectra from FT analysis on $0 \leq \tau_2 \leq 600$ fs data (d, red) and on $400 \leq \tau_2 \leq 1500$ fs data (e, blue) for $MLCT_B$ excitation. Gray spectra in (b-e) are from FT analysis of the background signal shown in (a). The circles represent the average $\omega_2$ spectrum and the shaded areas represent ± 1 standard deviation from the mean. Number of ($\omega_1$, $\omega_3$) points: $MLCT_A$ = 45; $MLCT_B$ = 24; Background (signal ≤ 5% max) = 3295.

Once population kinetics are removed, consequent FT analysis over the $\tau_2$ delay of the 2D EV regions of interest provides a low frequency spectrum, $\omega_2$, of the $\tau_2$-dependent 2D EV signal oscillations. As discussed in the manuscript, dynamics in the early time ($0 \leq \tau_2 \leq 600$ fs) and the later time ($400 \leq \tau_2 \leq 1500$ fs) periods involve different low frequency modes. A double-sided tanh time domain filter is used with the form:

$$F(\tau_2) = \begin{cases} \frac{1}{2} \cdot \tanh\left( \frac{\tau_2 - (\tau_c - \delta_{HW})}{B} \right) + \frac{1}{2}, & 0 \leq \tau_2 \leq \tau_c \\ -\frac{1}{2} \cdot \tanh\left( \frac{\tau_2 - (\tau_c + \delta_{HW})}{B} \right) + \frac{1}{2}, & \tau_c < \tau_2 \end{cases} \quad (8.2)$$

to select the signals in either the earlier or later $\tau_2$ periods. In equation (8.2), $\tau_c$ is the center of the tanh rise, $\delta_{HW}$ is the half-width of the double-sided tanh filter, and B is the rise time of the tanh function. The early time data is selected with $\tau_c = 270$ fs, $\delta_{HW} = 350$ fs, and B = 40 fs; the later time data is selected with $\tau_c = 910$ fs, $\delta_{HW} = 550$ fs, and B = 40 fs. The filtered data in each $\tau_2$ period are zero-padded to 256 points prior to FT. The FT then resolves the $\omega_2$ low frequency spectrum and the absolute value spectra are analyzed (Figure 8.12(b-e) and Figure 8.2(c-d, f-g)).

The signal-to-noise of the $\omega_2$ spectra is assessed by doing the same FT analysis on the respective $\tau_2$ periods for 2D EV spectral regions that are effectively the background – i.e., where there is no 2D EV signal. Since there are regions of the 2D EV spectra with dynamic intensities during $\tau_2$, I first averaged all of the 2D EV spectra over all $\tau_2$ delays (resulting averaged 2D EV spectrum is shown in Figure 8.12) and then I selected all ($\omega_1$, $\omega_3$) coordinates which have signal less than or equal to 5% of the 2D EV maximum signal in this averaged spectrum (0.0043). The solid gray contour shown in Figure 8.12(a) highlights this background

2D EV region. The early time ($0 \leq \tau_2 \leq 600$ fs) $\omega_2$ spectra are shown in Figure 8.12(b, d) and the later time ($400 \leq \tau_2 \leq 1500$ fs) $\omega_2$ spectra are shown in Figure 8.12(c,e). The gray spectra show the average $\omega_2$ spectrum and standard deviation of the background. The average $\omega_2$ spectrum and standard deviation of the early time 2D EV signal for $\nu_{COO}$ coupled to both $MLCT_A$ and $MLCT_B$ are shown in red and the later time 2D EV signals are shown in blue. As discussed in this chapter, these spectra provide clear evidence for the $\nu_{Ru\text{-}N}$ ($\omega_2 = 340$ cm$^{-1}$) and the $\nu_{Ru\text{-}bpy}$ ($\omega_2 = 742$ cm$^{-1}$) low frequency modes coupling with the vibronic eigenstates at different time periods within the first two picoseconds of the excited state triplet charge transfer and relaxation process. Other $\omega_2$ regions in the spectra above the background noise approach the DC frequency ($\omega_2$=0 cm$^{-1}$), which are likely due to imperfect population kinetics subtraction, and as the Nyquist sampling limit is approached ($\omega_2$=833 cm$^{-1}$). As a result, signals above $\omega_2 \cong 790$ cm$^{-1}$ are not considered further.

Table 8.2. Regions of Interest for $\omega_2$ Spectral Analysis.

| | **$\omega_1$ Range (cm$^{-1}$) [min:max]** | **$\omega_1$ Resolution (cm$^{-1}$)** | **# $\omega_1$ "pixels"** | **$\omega_3$ Range (cm$^{-1}$) [min:max]** | **$\omega_3$ Resolution (cm$^{-1}$)** | **# $\omega_3$ "pixels"** |
|---|---|---|---|---|---|---|
| **$MLCT_A$** | [24600:24800] | 14.1 | 15 | [1330:1337] | 2.6 | 3 |
| **$MLCT_B$** | [25200:25300] | 14.1 | 8 | [1330:1337] | 2.6 | 3 |

### 8.12.5 *A Closer Look at Transient-IR Spectra of $N3^{4-}$*

The timescales of the excited state vibrational features measured by parallel polarized tIR (see Figure 8.13 and Table 8.3) show that the triplet state CN stretches are formed within the instrument response and consequently static for the duration of the experiment (200 picoseconds). The constant intensity and center frequency of the CN excited state vibrational features indicate negligible intramolecular structural reorganization of the charge donor for at

least 200 picoseconds (ps) following photoexcitation and ultrafast intersystem crossing (ISC). This is consistent with other tIR studies on N3 which typically focused only on the CN stretching region, and with the fact that its $^{3}$MLCT manifold has a lifetime on the order of nanoseconds.

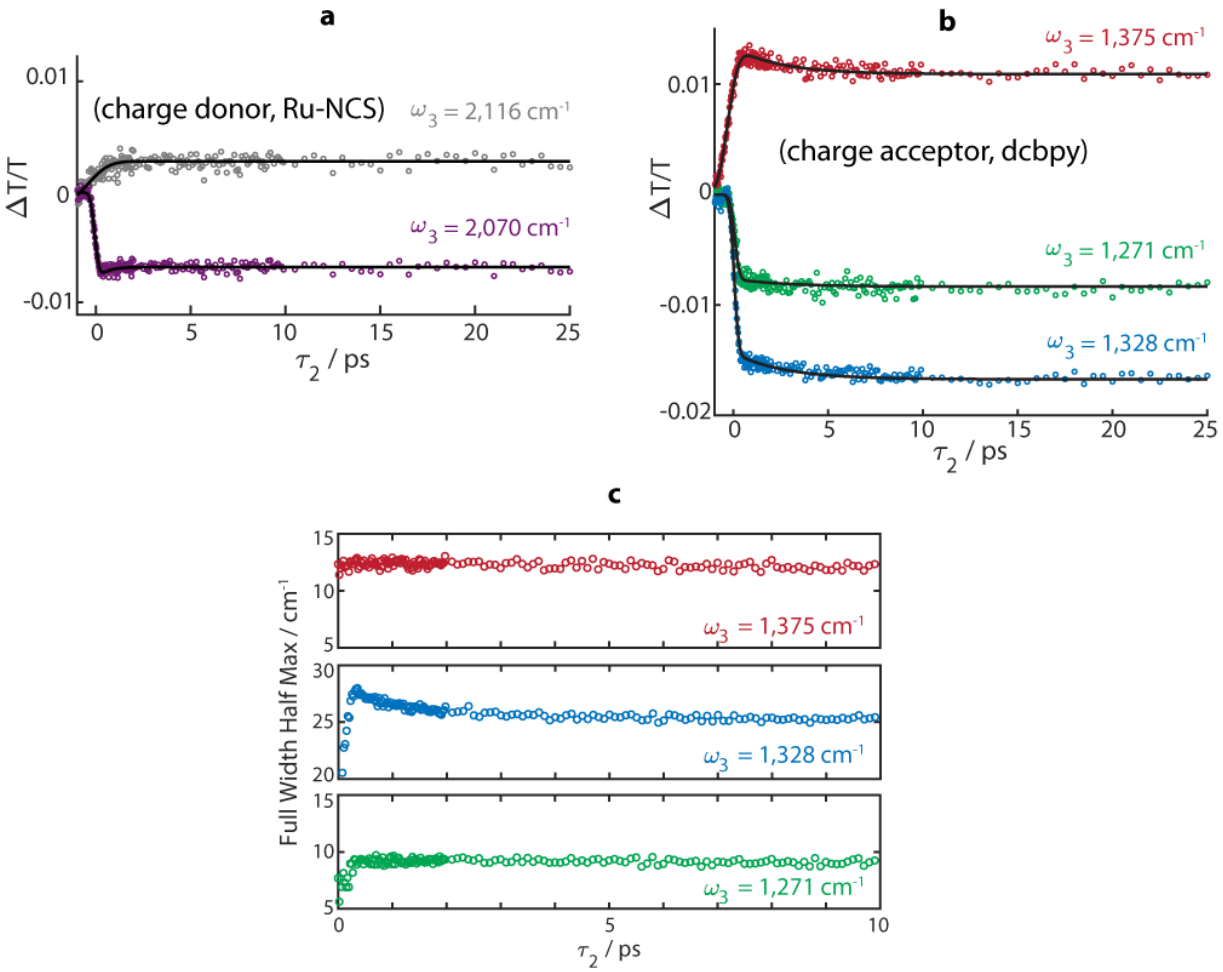


Figure 8.13. Transient-IR Spectroscopy of $N3^{4-}$. (a) tIR time traces of the CN stretch region reports on the Ru-$(NCS)_2$ charge donor dynamics; ground state bleach (GSB) = 2116 cm$^{-1}$ (gray circles), excited state absorption (ESA) = 2070 cm$^{-1}$ (purple circles), time trace fits shown by solid black lines. (b) tIR time traces of the dcbpy ligand stretching region reports on the charge acceptor dynamics; carboxylate symmetric stretch GSB = 1375 cm$^{-1}$ (red circles) and ESA = 1328 cm$^{-1}$ (blue circles), bipyridine stretching mode ESA = 1271 cm$^{-1}$ (green circles). (c) tIR line shapes identify which charge acceptor vibrations are sensitive to excited state relaxation, as shown by the $\tau_2$-dependent full-width-at-half-max for all three peaks; the carboxylate symmetric stretch ESA is most sensitive to excited state charge transfer dynamics in the first few picoseconds of relaxation.

The $\nu_{COO}$ ESA also forms significant amplitude within the instrument response but then continues to grow on a 2.7 ± 0.8 ps timescale. Additionally, the carboxylate symmetric stretching GSB at 1375 $cm^{-1}$ rises to its maximum intensity during the instrument response before decaying in amplitude on a 2.5 ± 0.8 ps timescale – effectively the same timescale as the $\nu_{COO}$ ESA growth. This is readily explained by the ESA dynamics of the overlapping carboxylate symmetric stretches noted in chapter 7. Although much weaker, other bpy ESA features also grow in over the first several picoseconds of delay time.

While many charge acceptor vibrations display ESA signal growth during the triplet manifold relaxation, they are not all equally sensitive to the intramolecular structural dynamics involved with this relaxation process. The time-dependent tIR vibrational peak widths of the $\nu_{COO}$ and the $\nu_{BPY}$ features demonstrate that the $\nu_{COO}$ vibration is the most sensitive coordinate to triplet relaxation processes probed in our experiments as its full-width-at-half-maximum (FWHM) broadens to 28 $cm^{-1}$ and narrows to 25 $cm^{-1}$ within the first three ps of relaxation; whereas, the $\nu_{BPY}$ rises to 9 $cm^{-1}$ within the instrument response and is unchanged thereafter. Together, the measured tIR timescales, line shapes, and negligible frequency shifts for both charge donor and acceptor ligand vibrations establish the photophysical picture of ultrafast triplet formation of $N3^{4-}$ and charge donation by the Ru-$(NCS)_2$ while the dcbpy ligand vibrations relax in a dense triplet manifold over the first several picoseconds post-excitation. The time traces of the tIR signals shown in Figure 8.13 above were fit to the same function as used in chapter 7, a Gaussian convolved with two exponential decays. The Table below gives the fitting parameters for all of the traces shown in Figure 8.13 above.

Table 8.3. Transient-IR Fitting Parameters.
[a] $A_{short}$ and $\tau_{short}$ have been set to zero in a separate fit of the excited state CN stretch at 2070 $cm^{-1}$ to show the lack of any significant decay component at early times, reflecting the instantaneous formation of the excited state charge donor.
[b] Ground state vibrational excitation at negative τ2 times affect the accuracy of fits for early time components in ground state bleach features.

| $\omega_3$ / $cm^{-1}$ | $A_{short}$ (ΔT/T) | $\tau_{short}$ /ps | $A_{long}$ (ΔT/T) | $\tau_{long}$ /ps | B / ps | $t_0$ / ps | $R^2$ (adj) |
|---|---|---|---|---|---|---|---|
| 2116[b] | 0.004 | 0.049 | 0.419 | 0.049 | 2.07 | -0.435 ±0.761 | 0.6815 |
| 2070 | -0.001 ±0.001 | 0.49 ±0.06 | -0.0067 ±0.0002 | 1.6E4 ±1.0E5 | 0.44 ±0.06 | -0.058 ±0.028 | 0.9723 |
| 2070[a] | 0 | 0 | -0.0069 | 16000 | 0.41 | -0.087 | 0.9705 |
| 1375[b] | 0.0026 ±0.0004 | 2.5 ±0.8 | 0.0109 ±0.00016 | 1.6E4 ±1.0E5 | 1.03 ±0.06 | -0.284 ±0.021 | 0.9746 |
| 1328 | 0.0024 ±0.0003 | 2.7 ±0.8 | -0.0168 ±0.0002 | 1.6E4 ±6.8E4 | 0.45 ±0.03 | 0.037 ±0.009 | 0.9936 |
| 1271 | 0.0007 ±0.0003 | 2.8 ±3.1 | -0.0083 ±0.0003 | 16E4 ±1.6E5 | 0.47 ±0.07 | 0.070 ±0.022 | 0.9689 |

### 8.12.6 *Characterizing the Initially Excited Vibrational Wavepacket*

The initially excited state vibrational wavepacket composed of a coherence with the $\nu_{Ru\text{-}N}$ mode is characterized by extracting the spectral phase of the $\omega_2$ spectrum, $\phi(\omega_2)$, fitting the phase to an n[th] order polynomial, and then obtaining the group delay, $\tau_d(\omega_2)$. Generally, a spectrum with arbitrary spectral phase variation can be written as $A(\omega-\omega_0)=\left|A(\omega-\omega_0)\right|e^{i\phi(\omega)}$. Here, the $\left|A(\omega-\omega_0)\right|$ factor is obtained by the absolute value of the Fourier transformed $\tau_2$-

dependent peak intensities over $0 \leq \tau_2 \leq 600$ fs (i.e., $\left|\mathrm{FT}(\tau_2)\right|$). The spectral phase and group delay are then obtained by [45]

$$\phi(\omega_2) = \tan^{-1}\left(\frac{\mathrm{Im}[\mathrm{FT}(\tau_2)]}{\mathrm{Re}[\mathrm{FT}(\tau_2)}\right) \tag{8.3}$$

$$\tau_d(\omega_2) = -\frac{d\phi(\omega_2)}{d\omega_2} \tag{8.4}$$

The group delay describes the time-dependence of the frequency components in a wavepacket, which in this case reflects the propagation of the wavepacket during $\tau_2$ in the excited MLCT manifold during the early time period, $0 \leq \tau_2 \leq 600$ fs. I have fit $\phi(\omega_2)$ over the spectral range of the $\omega_2$ feature obtained in the FT analysis ($\omega_2$ = 250-400 cm$^{-1}$) to polynomial functions of increasing order n, the coefficients ($P_{(n)}$) for each fit are given in Table 8.4. A meaningful description of the wavepacket propagation is obtained by observing the consistencies in $\tau_d(\omega_2)$, obtained by numerical differentiation of the polynomial function used in the fitting for different polynomial orders. The quartic polynomial (n=4) fit shown in Figure 8.14e is used to obtain the group delay curve presented in Figure 8.4, which is identical to the red curve shown in Figure 8.14f. As discussed in section Characterizing the Initially Excited Vibrational Wavepacket and shown in Figure 8.14, all fits demonstrate consistent evidence for a blue shifting of the initially excited vibrational wavepacket during the first 600 fs of excited state relaxation. Less emphasis is placed on any interpretation based on the values of the coefficients for a particular fit given their dependence on the polynomial order, and instead the general trends observed across all fits are considered.

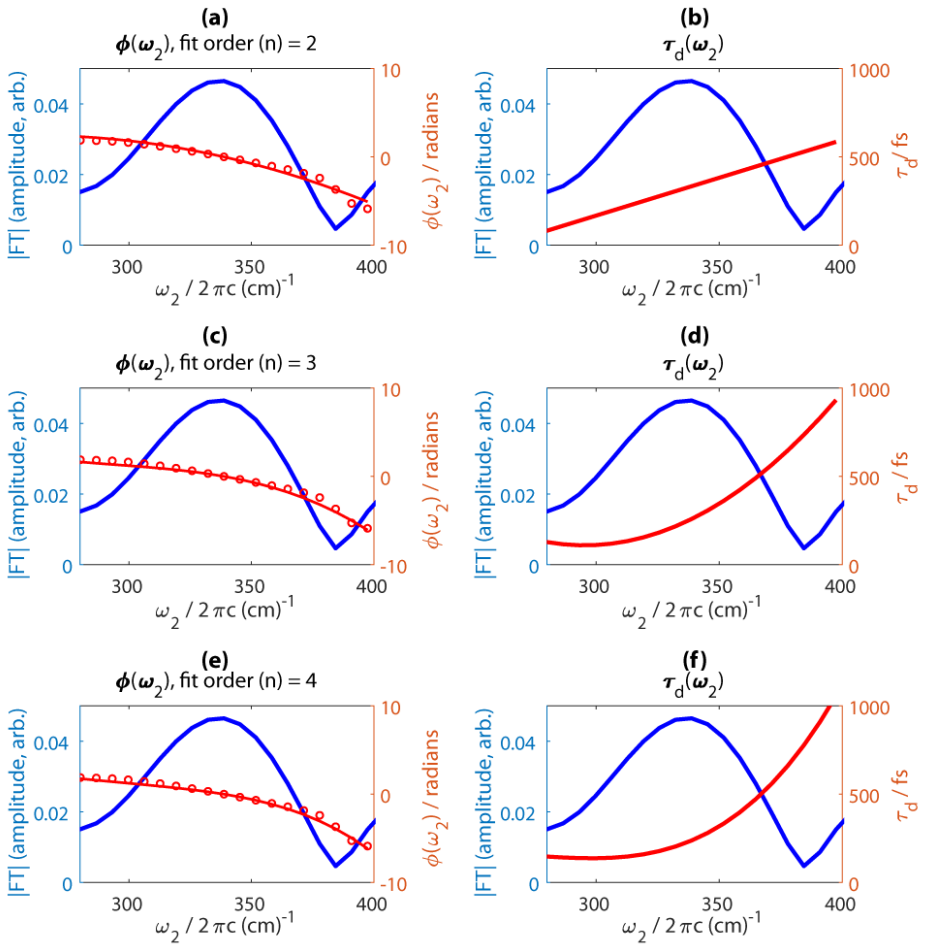


Figure 8.14. Characterizing the Initially Excited Vibrational Wavepacket. The blue lines in all figures are the same $\omega_2$ spectra for the $\nu_{Ru\text{-}N}$ wavepacket ($\omega_2$ = 340 cm$^{-1}$) present during $0 \leq \tau_2 \leq 600$ fs. The figures in the left column (a,c,e) plot the spectral phase, $\phi(\omega_2)$, in red; experimental data is shown by the open circles and the solid lines are fits. The figures in the right column (b,d,f) plot the group delay, $\tau_d(\omega_2)$, in red, obtained by numerical differentiation of $\phi(\omega_2)$ as explained in equation 5. The different rows denote a different order of polynomial used to fit $\phi(\omega_2)$ during the analysis.

Table 8.4. Spectral Phase ($\varphi(\omega_2)$) Fitting with n$^{th}$-order Polynomials

| Fit Order (n) | $P_{(0)}$ (rad) | $P_{(1)}$ (rad · s) | $P_{(2)}$ (rad · s$^2$) | $P_{(3)}$ (rad · s$^3$) | $P_{(4)}$ (rad · s$^4$) | Goodness of Fit ($R^2$) |
|---|---|---|---|---|---|---|
| 2 | -46.68 | 1.12 x10$^3$ | -1.14 x10$^4$ | - | - | 0.9705 |
| 3 | 113.73 | -7.00 x10$^3$ | 1.24 x10$^4$ | -7.42 x10$^5$ | - | 0.9923 |
| 4 | -153.04 | 1.10 x10$^4$ | -3.29 x10$^5$ | 4.27 x10$^6$ | -2.06 x10$^7$ | 0.9932 |

The same blue-shifting behavior is also observed through a short time Fourier transform (STFT) analysis of the earlier time data, as shown in Figure 8.15 below. We give preference to the group delay analysis shown in the manuscript over the STFT because the blue-shifting is occurring during the course of only a few cycles of the $\nu_{Ru\text{-}N}$ vibration, which is also comparable to the ~ 600 fs lifetime of the wavepacket. Thus, an appropriate choice of windowing function becomes more difficult. Nevertheless, the consistency between the group delay analysis and the STFT confirms the blue-shifting of the $\nu_{Ru\text{-}N}$ wavepacket during early times.

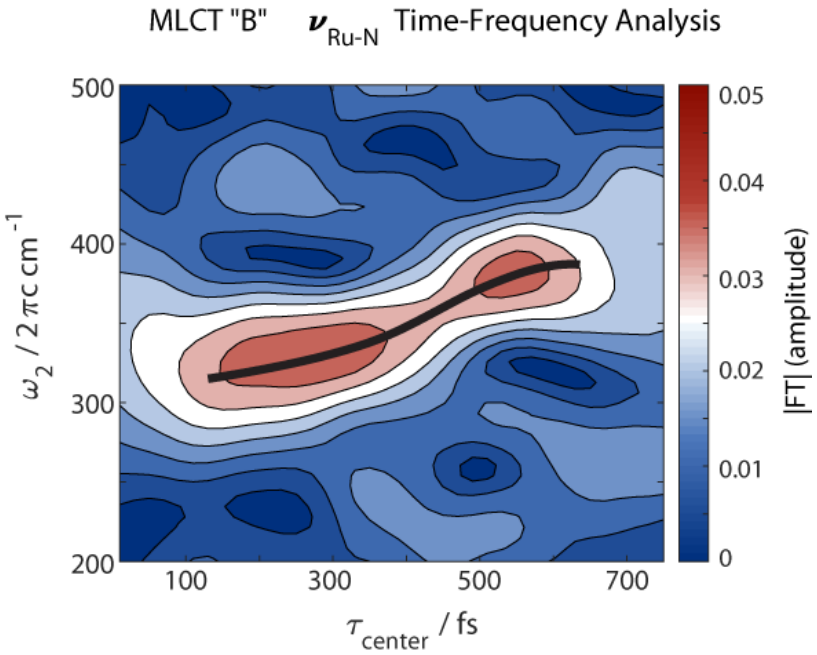


Figure 8.15. Short Time Fourier Transform Analysis of Initial Wavepacket. Analysis performed using the same windowing function used in the later time STFT analysis (double-sided tanh) discussed in more detail in section 8.12.7, but with a window FWHM of 500 fs that has $\tau_{center}$ delays varied through the corresponding earlier delay times $0 \leq \tau_2 \leq 600$ fs. The thick solid black line is a guide to the eye to highlight the blue-shifting of the $\nu_{Ru\text{-}N}$ center frequency. Measured in this way, the $\omega_2$ vibrational frequencies blue-shift by ~60 cm$^{-1}$ over the interval $250 \leq \tau_{center} \leq 570$ fs, consistent with the blue-shift measured by the spectral phase / group delay analysis in Figure 8.14.

### 8.12.7 *Time-Frequency Methods Used in Later Time Data Analysis*

The $\nu_{Ru\text{-}bpy}$ mode is the only prominently coupled low frequency mode apparent in our measurements during the later time relaxation dynamics, as shown in Figure 8.2(d,g), and it is clearly coupled to the $\nu_{COO}$ in both the $MLCT_A$ and $MLCT_B$. As Collini and co-workers have discussed,[35] the sliding window short time Fourier transform (STFT) is a useful time-frequency analytical method but it suffers when numerous frequency components with varying lifetimes contribute to a time-domain signal. This is due principally to an inherent uncertainty between temporal and frequency resolution in FT-based signal processing. The STFT uses a temporal window of a fixed width and a given temporal center to filter time-domain experimental data prior to Fourier transformation. In this way, a frequency spectrum for a temporally-localized portion of the time-domain data is obtained. This is repeated for many different temporal filter center positions to produce a two-dimensional time-frequency plot where the FT spectrum is plotted for every temporal filter center position. In the present analyses, $\omega_2$=742 $cm^{-1}$ is selected from the $\omega_2$ dimension of the time-frequency plot for consideration as it corresponds to the vibrational mode of interest, $\nu_{Ru\text{-}bpy}$, as identified by the $\omega_2$ spectra shown in manuscript Figure 8.2d and g obtained by considering all of the $\tau_2$-dependent data in the later time period. As described below, we can reliably use a temporal filter to isolate the $\nu_{Ru\text{-}bpy}$ dynamics because this is the only sufficiently resolved mode in the $\omega_2$ spectra for both $MLCT_A$ and $MLCT_B$ during later times. For time-domain signals containing multiple frequency components of interest that have significantly different periods of oscillation, the choice of a single temporal filter may favor a particular frequency component in the analysis over the others. Fortunately, that is not the case in our data.

In this analysis, only the $\nu_{Ru\text{-}bpy}$ is of primary interest as it is the strongest signal observed in $\omega_2$ when all of the later time relaxation data is Fourier transformed (see Figure 8.2). Without a time-frequency analysis, the electronic oscillatory behavior of the $\nu_{Ru\text{-}bpy}$ coherence discussed in the main text would be missed. The ~45 fs period of the $\nu_{Ru\text{-}bpy}$ appears in 2-3 cycle bursts beginning in $MLCT_B$ and then oscillating between $MLCT_A$ and $MLCT_B$. Fortunately, this dynamic provides a straightforward choice of filtering window to be used in the analysis: a temporal filter with ~120 fs width sufficiently isolates each 2-3 cycle oscillation of the $\nu_{Ru\text{-}bpy}$ to clearly extract the oscillations in electronic population shown in Figure 8.5. The single coherence of interest with a well-defined duration in $MLCT_A$ and $MLCT_B$ render the STFT analysis a suitable method in our case. In Figure 8.16 a comparison of time-frequency analyses using three different temporal windowing functions (double-sided hyperbolic tangent, Hanning, Gaussian) demonstrates that the choice of window function does not change the analysis or conclusions in any way. For all three functions, the full-width-at-half-max was set wide enough to span a single 2-3 cycle oscillation of $\nu_{Ru\text{-}bpy}$ when the window is centered over the coherence (examples shown for each MLCT state in Figure 8.16). There is negligible difference in the FT time traces (see Figure 8.16(b,d,f)) among analyses using different windowing functions of consistent temporal width. Conversely, the temporal width of the filter can have a large impact on the obtained results using a STFT in the time-frequency analysis. Figure 8.17 demonstrates the importance of an initial consideration about the nature of the time-domain signals that are of interest in a data set prior to conducting a time-frequency analysis. For a time-domain signal such as ours which contains transient and periodic coherences, a temporal filter that is too wide may result in a large offset in FT signal in addition to a phase relationship between oscillations that is shifted from the true phase relationship (e.g.,

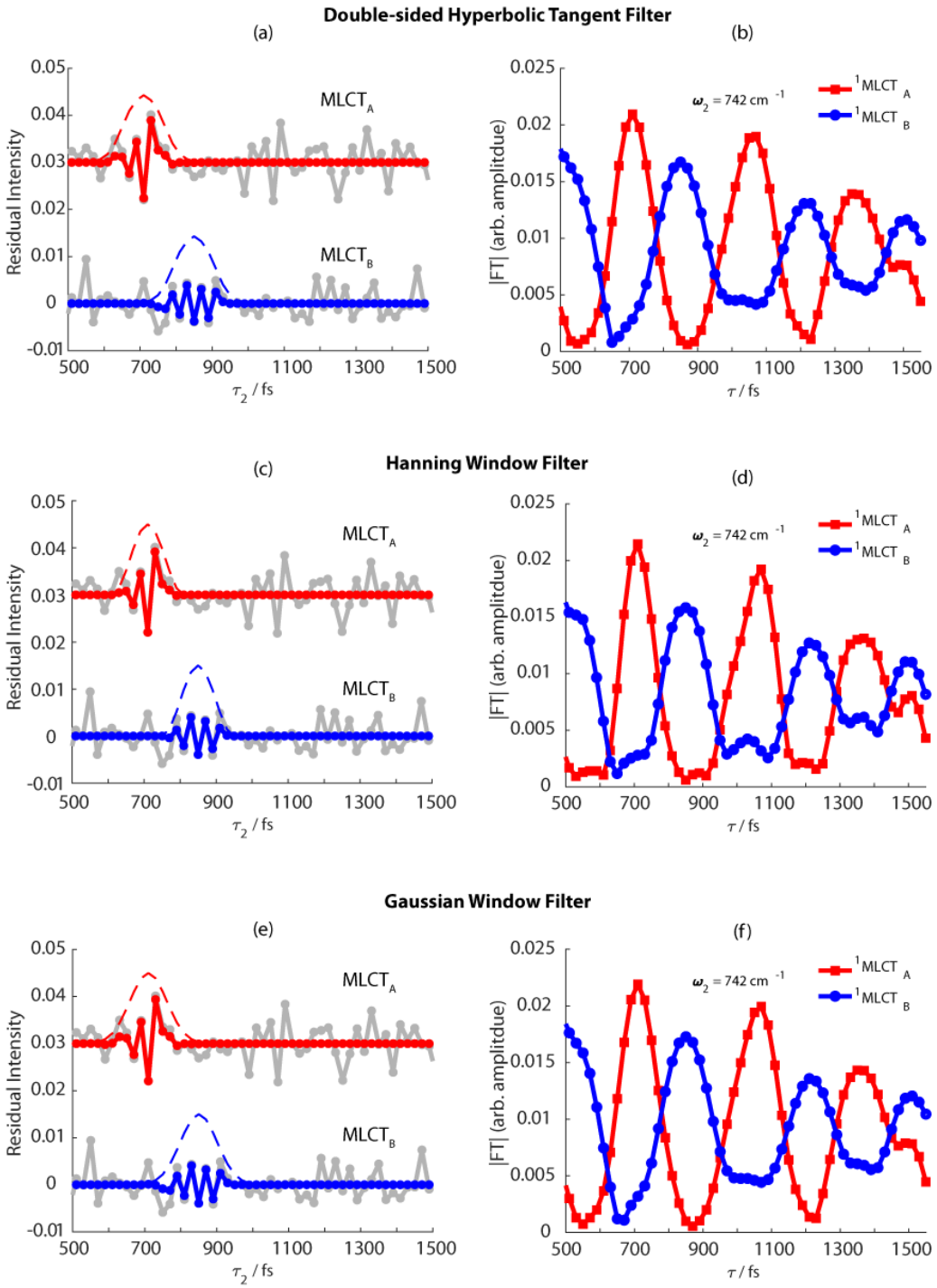


Figure 8.16. Temporal Windowing Function Effects on Time-Frequency Analysis. The left column (a, c, e) show the 2D EV residual data (gray) for the signal regions of the $\nu_{COO}$ vibronically coupled with the $MLCT_A$ (red) and $MLCT_B$ (blue); the dashed lines show the temporal windowing functions used in the three time-frequency analyses for comparison. The right column (b, d, f) are the time-frequency analyses results from a short time Fourier transform (details in the section 8.12.7 discussion) for $MLCT_A$ (red) and $MLCT_B$ (blue) at $\omega_3$ = 742 $cm^{-1}$. A double-sided hyperbolic tangent window (a,b), Hanning window (c,d), and a Gaussian window (e,f) are compared.

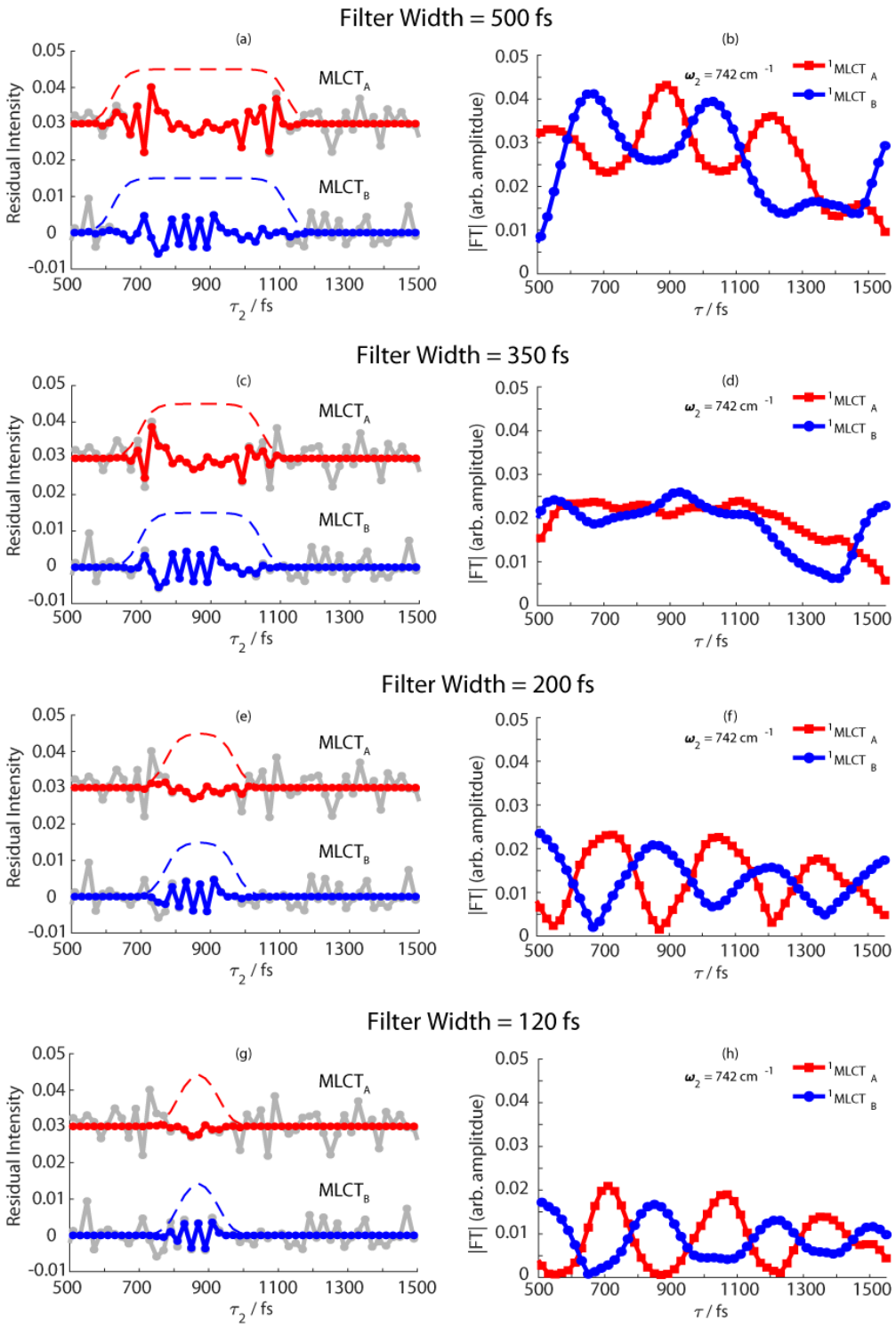


Figure 8.17. Effect of Temporal Filter Width on Time-Frequency Analysis. The time-frequency analyses for varying filter widths (FWHM) are shown for the double-sided tanh window: (a,b) 500 fs, (c,d) 350 fs, (e,f) 200 fs, (g,h) 120 fs. The 2D EV residual time-domain data and temporal filtering is shown in the left column and the short time Fourier transformed data is plotted in the right column. The same coloration as Figure 8.16 is used in this figure.

see Figure 8.17(a,b)). As the filtering window shrinks, the FT signal passes through a range in which only the offset is observed because the oscillatory information is not isolated well enough by the filter (e.g., see Figure 8.17(c,d)). When the filter width approaches the duration of the transient coherences of interest, then the time-frequency analysis via the STFT produces a reliable result (e.g., see Figure 8.17(e-h)). The time-frequency analysis in this paper uses the double-sided hyperbolic tangent window with a 120 fs FWHM temporal width, as shown in Figure 8.17 (g,h).

### 8.12.8 *Nonadiabatic Internal Conversion Simulations: A Two-Level System*

The time-dependent relaxation of the $\rho_{36}(\tau_2)$ and $\rho_{14}(\tau_2)$ coherences are simulated as shown in Figure 8.5c of the main text by solving the following system of differential equations:

$$\begin{pmatrix} \dot{\rho}_{36}(\tau_2) \\ \dot{\rho}_{14}(\tau_2) \end{pmatrix} = \begin{pmatrix} -i\omega_{36} - \Gamma_{36,36} & V_{NA}(\tau_2) \\ -V_{NA}(\tau_2) & -i\omega_{14} - \Gamma_{14,14} \end{pmatrix} \begin{pmatrix} \rho_{36}(\tau_2) \\ \rho_{14}(\tau_2) \end{pmatrix} \tag{8.5}$$

where $\omega_{36} = \omega_{14}$ = 742 cm$^{-1}$ is the frequency of the $\nu_{\text{Ru-bpy}}$ coherence measured from the 3D EV experiments, $\Gamma_{36,36} = \Gamma_{14,14}$ = 1/800 fs are the lifetimes of $\rho_{36}$ and $\rho_{14}$, and $V_{NA}$ = 50 cm$^{-1}$ is the time-independent nonadiabatic coupling strength found to reproduce the observed 340 ± 40 fs periodicity of the oscillations between electronic character of the vibrational coherence amplitude between $\rho_{36}$ and $\rho_{14}$. This observation is similar to the work of Dawlaty and co-workers[36] who found Rabi-like oscillations in the amplitudes of vibrational coherences in a hydrogen-bonded charge-transfer system, quinhydrone. The vibronic eigenstates that compose an effective Hamiltonian for the aqueous $N3^{4-}$ studied here are defined in terms of both

electronic and vibrational coupled degrees of freedom, providing a more complete view of an effective Hamiltonian capturing the dynamics of interest.

### 8.12.9 *Redfield Theory and Non-Secular Contributions to Relaxation Dynamics*

Redfield theory is often useful for describing the time evolution of molecular systems.[41,46,47] The Redfield equation for the reduced density matrix, $\rho_{ab}(t)$ (where subscripts a and b denote system eigenstates), is expressed

$$\frac{\partial \rho_{ab}(t)}{\partial t} = -i\omega_{ab}\rho_{ab}(t) + \sum_{c,d} R_{ab,cd}\rho_{cd}(t) \tag{8.6}$$

where $\omega_{ab} = {E_a - E_b}/{\hbar}$ and $R_{ab,cd}$ is the Redfield tensor describing the relaxation dynamics between different system eigenstates. The first term on the right side of equation (8.6) describes the system's evolution in isolation and the second term involving the Redfield tensor describes the system's interaction with a dissipative environment. The Redfield tensor can be expressed as

$$R_{ab,cd} = \Gamma^{+}_{db,ca} + \Gamma^{-}_{db,ca} - \delta_{bd}\sum_{\kappa}\Gamma^{+}_{a\kappa,\kappa c} - \delta_{ac}\sum_{\kappa}\Gamma^{-}_{d\kappa,\kappa b} \tag{8.7}$$

where

$$\begin{aligned}
\Gamma^{+}_{db,ca} &= \frac{1}{\hbar^2}\int_0^\infty dt \left\langle \left\langle d\left|H_{SB}(t)\right|b\right\rangle \left\langle c\left|H_{SB}\right|a\right\rangle \right\rangle_B e^{-i\omega_{ca}t}, \\
\Gamma^{-}_{db,ca} &= \frac{1}{\hbar^2}\int_0^\infty dt \left\langle \left\langle d\left|H_{SB}\right|b\right\rangle \left\langle c\left|H_{SB}(t)\right|a\right\rangle \right\rangle_B e^{-i\omega_{db}t}.
\end{aligned} \tag{8.8}$$

and the $\kappa$ index goes over system eigenstates. The system-bath Hamiltonian, $H_{SB}$, connects the system and the environment and is defined as $H_{SB}(t) = e^{(i/\hbar)H_B t} H_{SB} e^{-(i/\hbar)H_B t}$ where $H_B$ is the bath Hamiltonian. In equation (8.8), the thermal average over the bath is denoted $\langle \ldots \rangle_B$. The

Secular Approximation can be understood by recasting the Redfield equation within the interaction picture

$$\frac{\partial \rho_{ab}^{I}(t)}{\partial t} = \sum_{c,d} R_{ab,cd} \rho_{cd}^{I}(t) e^{i(\omega_{ab}-\omega_{cd})t} \tag{8.9}$$

and noticing that the integral averages to zero when both sides of equation (8.9) are integrated over a time interval $\Delta t >> (\omega_{ab} - \omega_{cd})^{-1}$ due to destructive interference. The Secular Approximation is made when only the terms satisfying $\omega_{ab} = \omega_{cd}$ are kept. However, nonsecular elements of $R_{ab,cd}$, those in which $\omega_{ab} \neq \omega_{cd}$, may become important when $\omega_{ab} - \omega_{cd}$ is very small which occurs in systems with strong system-bath coupling and/or when relaxation dynamics involve several eigenstates with molecular couplings represented by these nonsecular terms.

### 8.12.10 *Negligible Frequency Shifting of MLCT Peaks in* $\omega_1$

The peak maxima of the carboxylate vibrations, both the ground state bleach and the excited state absorption ($\nu_{COO}$) do not show any significant peak shifting after the pulse overlap

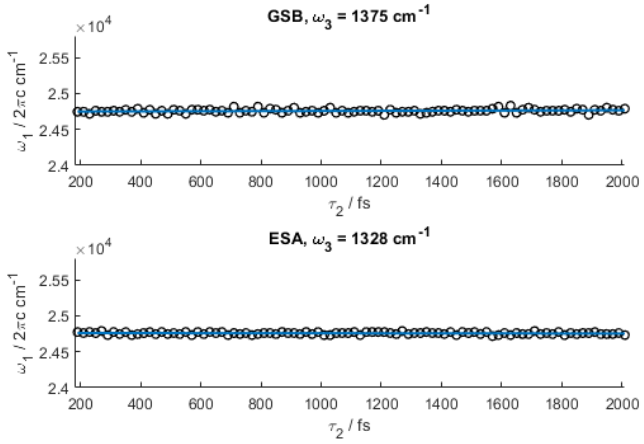


Figure 8.18. Carboxylate $\omega_1$ Peak Positions During $\tau_2$. The ground state bleach (top) and excited state absorption (below, $\nu_{COO}$) peak positions in $\omega_1$ show negligible peak shifting over the range $190 < \tau_2 < 2010$ fs.

and throughout the $\tau_2$ range probed in the 3D EV experiments. This provides evidence that the excited MLCT states are strongly spin mixed as no electronic features arise to suggest that transitions into different spin states is resolved in the data.

### 8.12.11 *Calculated Low Frequency Vibrational Modes*

The calculated IR spectrum of the $N3^{4-}$ lowest energy triplet, $T_0$, is reproduced from *Gaynor et al.*[29] to display the full spectrum, including the low frequency region (see zoom-in of the inset in Figure 8.19a below).

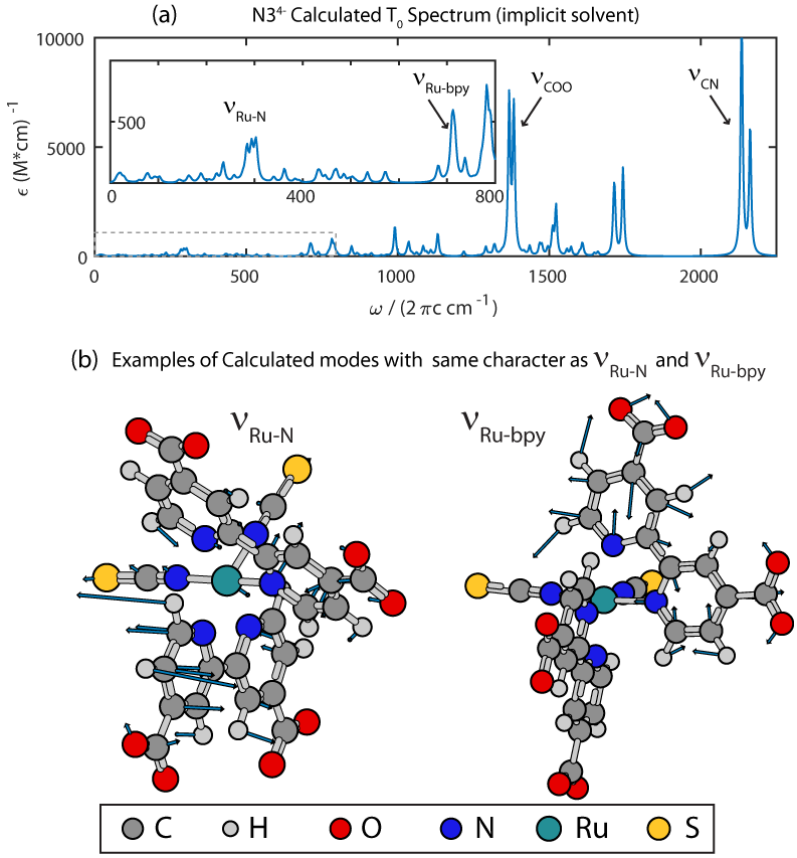


Figure 8.19. (a) Calculated IR spectrum of the lowest energy triplet of $N3^{4-}$ with implicit solvent; inset shows a zoom-in of dashed gray spectral region. (b) Example normal modes from calculations displaying vibrational character of the $\nu_{Ru\text{-}N}$ and $\nu_{Ru\text{-}bpy}$ modes. Mode 39 (303 $cm^{-1}$) shown for $\nu_{Ru\text{-}N}$ and mode 67 (710 $cm^{-1}$) shown for $\nu_{Ru\text{-}bpy}$.

The normal mode vibrations with vector displacements provide examples of the several calculated modes in the $\nu_{Ru\text{-}N}$ (260-430 $cm^{-1}$) region and the $\nu_{Ru\text{-}bpy}$ (710-755 $cm^{-1}$) region with the respective vibrational character of the low frequency vibrations discussed in the main manuscript. Computational details for these spectra can be found in *Gaynor et al.*[29] and its Supporting Information.

## 8.13 REFERENCES


(1) Mirkovic, T.; Ostroumov, E. E.; Anna, J. M.; Van Grondelle, R.; Govindjee; Scholes, G. D. Light Absorption and Energy Transfer in the Antenna Complexes of Photosynthetic Organisms; *Chem. Rev.* **2017**, *117*, 249-293.

(2) Hagfeldt, A.; Gratzel, M. Molecular photovoltaics; *Acc. Chem. Res.* **2000**, *33*, 269-277.

(3) Reece, S. Y.; Hamel, J. A.; Sung, K.; Jarvi, T. D.; Esswein, A. J.; Pijpers, J. J. H.; Nocera, D. G. Wireless Solar Water Splitting Using Silicon-Based Semiconductors and Earth-Abundant Catalysts; *Science* **2011**, *334*, 645-648.

(4) O'regan, B.; Gratzel, M. A Low-Cost, High-Efficiency Solar-Cell Based on Dye-Sensitized Colloidal $TiO_2$ Films; *Nature* **1991**, *353*, 737-740.

(5) Mccusker, J. K. Electronic structure in the transition metal block and its implications for light harvesting; *Science* **2019**, *363*, 484-488.

(6) Chergui, M. Ultrafast Photophysics of Transition Metal Complexes; *Acc. Chem. Res.* **2015**, *48*, 801-808.

(7) Mccusker, J. K. Femtosecond Absorption Spectroscopy of Transition Metal Charge-Transfer Complexes; *Acc. Chem. Res.* **2003**, *36*, 876-887.

(8) Atkins, A. J.; González, L. Trajectory Surface-Hopping Dynamics Including Intersystem Crossing in $[Ru(bpy)_3]^{2+}$; *J. Phys. Chem. Lett.* **2017**, *8*, 3840-3845.

(9) Mai, S.; Plasser, F.; Dorn, J.; Fumanal, M.; Daniel, C.; González, L. Quantitative wave function analysis for excited states of transition metal complexes; *Coord. Chem. Rev.* **2018**, *361*, 74-97.

(10) Penfold, T. J.; Gindensperger, E.; Daniel, C.; Marian, C. M. Spin-Vibronic Mechanism for Intersystem Crossing; *Chem. Rev.* **2018**, *118*, 6975-7025.

(11) Capano, G.; Penfold, T. J.; Chergui, M.; Tavernelli, I. Photophysics of a copper phenanthroline elucidated by trajectory and wavepacket-based quantum dynamics: a synergetic approach; *Phys. Chem. Chem. Phys.* **2017**, *19*, 19590-19600.

(12) Kallioinen, J.; Benko, G.; Myllyperkio, P.; Khriachtchev, L.; Skarman, B.; Wallenberg, R.; Tuomikoski, M.; Korppi-Tommola, J.; Sundstrom, V.; Yartsev, A. P. Photoinduced ultrafast dynamics of $Ru(dcbpy)_2(NCS)_2$-sensitized nanocrystalline $TiO_2$ films: The influence of sample preparation and experimental conditions; *J. Phys. Chem. B* **2004**, *108*, 6365-6373.

(13) Kallioinen, J.; Benko, G.; Sundstrom, V.; Korppi-Tommola, J. E. I.; Yartsev, A. P. Electron transfer from the singlet and triplet excited states of $Ru(dcbpy)_2(NCS)_2$ into nanocrystalline $TiO_2$ thin films; *J. Phys. Chem. B* **2002**, *106*, 4396-4404.

(14) Pettersson Rimgard, B.; Föhlinger, J.; Petersson, J.; Lundberg, M.; Zietz, B.; Woys, A. M.; Miller, S. A.; Wasielewski, M. R.; Hammarström, L. Ultrafast interligand electron transfer in *cis*-$[Ru(4,4'\text{-dicarboxylate-}2,2'\text{-bipyridine})_2(NCS)_2]^{4-}$ and implications for electron injection limitations in dye sensitized solar cells; *Chem. Sci.* **2018**, *9*, 7958-7967.

(15) Bram, O.; Messina, F.; El-Zohry, A. M.; Cannizzo, A.; Chergui, M. Polychromatic femtosecond fluorescence studies of metal-polypyridine complexes in solution; *Chem. Phys.* **2012**, *393*, 51-57.

(16) Zhang, X.; Smolentsev, G.; Guo, J.; Attenkofer, K.; Kurtz, C.; Jennings, G.; Lockard, J. V.; Stickrath, A. B.; Chen, L. X. Visualizing Interfacial Charge Transfer in Ru-Dye-Sensitized $TiO_2$ Nanoparticles Using X-ray Transient Absorption Spectroscopy; *J. Phys. Chem. Lett.* **2011**, *2*, 628-632.

(17) Van Kuiken, B. E.; Huse, N.; Cho, H.; Strader, M. L.; Lynch, M. S.; Schoenlein, R. W.; Khalil, M. Probing the Electronic Structure of a Photoexcited Solar Cell Dye with Transient X-ray Absorption Spectroscopy; *J. Phys. Chem. Lett.* **2012**, *3*, 1695-1700.

(18) Asbury, J. B.; Hao, E.; Wang, Y. Q.; Ghosh, H. N.; Lian, T. Q. Ultrafast electron transfer dynamics from molecular adsorbates to semiconductor nanocrystalline thin films; *J. Phys. Chem. B* **2001**, *105*, 4545-4557.

(19) Wernet, P. Chemical interactions and dynamics with femtosecond X-ray spectroscopy and the role of X-ray free-electron lasers; *Philos. Trans. R. Soc., A* **2019**, *377*.

(20) Lemke, H. T.; Kjaer, K. S.; Hartsock, R.; Van Driel, T. B.; Chollet, M.; Glownia, J. M.; Song, S.; Zhu, D. L.; Pace, E.; Matar, S. F.; Nielsen, M. M.; Benfatto, M.; Gaffney, K. J.; Collet, E.; Cammarata, M. Coherent structural trapping through wave packet dispersion during photoinduced spin state switching; *Nat. Commun.* **2017**, *8*.

(21) Auböck, G.; Chergui, M. Sub-50-fs photoinduced spin crossover in $[Fe(bpy)_3]^{2+}$; *Nat. Chem.* **2015**, *7*, 629.

(22) Kraus, P. M.; Zürch, M.; Cushing, S. K.; Neumark, D. M.; Leone, S. R. The ultrafast X-ray spectroscopic revolution in chemical dynamics; *Nat. Rev. Chem.* **2018**, *2*, 82-94.

(23) Chen, L. X.; Jäger, W. J. H.; Jennings, G.; Gosztola, D. J.; Munkholm, A.; Hessler, J. P. Capturing a Photoexcited Molecular Structure Through Time-Domain X-ray Absorption Fine Structure; *Science* **2001**, *292*, 262-264.

(24) Gaynor, J. D.; Sandwisch, J.; Khalil, M. Vibronic Coherence Evolution in Multidimensional Ultrafast Photochemical Processes; *Nat. Commun.* **2019**, *10*, 5621.

(25) Bakulin, A. A.; Morgan, S. E.; Kehoe, T. B.; Wilson, M. W. B.; Chin, A. W.; Zigmantas, D.; Egorova, D.; Rao, A. Real-time observation of multiexcitonic states in ultrafast singlet fission using coherent 2D electronic spectroscopy; *Nat. Chem.* **2016**, *8*, 16-23.

(26) Romero, E.; Augulis, R.; Novoderezhkin, V. I.; Ferretti, M.; Thieme, J.; Zigmantas, D.; Van Grondelle, R. Quantum coherence in photosynthesis for efficient solar-energy conversion; *Nat. Phys.* **2014**, *10*, 676.

(27) Ruetzel, S.; Diekmann, M.; Nuernberger, P.; Walter, C.; Engels, B.; Brixner, T. Multidimensional spectroscopy of photoreactivity; *Proc. Natl. Acad. Sci., USA* **2014**, *111*, 4764-4769.

(28) Tavernelli, I.; Curchod, B. F. E.; Rothlisberger, U. Nonadiabatic molecular dynamics with solvent effects: A LR-TDDFT QM/MM study of ruthenium (II) tris (bipyridine) in water; *Chem. Phys.* **2011**, *391*, 101-109.

(29) Gaynor, J. D.; Petrone, A.; Li, X.; Khalil, M. Mapping Vibronic Couplings in a Solar Cell Dye with Polarization-Selective Two-Dimensional Electronic–Vibrational Spectroscopy; *J. Phys. Chem. Lett.* **2018**, *9*, 6289-6295.

(30) Shoute, L. C. T.; Loppnow, G. R. Excited-state metal-to-ligand charge transfer dynamics of a ruthenium(II) dye in solution and adsorbed on $TiO_2$ nanoparticles from resonance Raman spectroscopy; *J. Am. Chem. Soc.* **2003**, *125*, 15636-15646.

(31) Greijer, H.; Lindgren, J.; Hagfeldt, A. Resonance Raman scattering of a dye-sensitized solar cell: Mechanism of thiocyanato ligand exchange; *J. Phys. Chem. B* **2001**, *105*, 6314-6320.

(32) Ishii, K.; Takeuchi, S.; Tahara, T. A 40-fs time-resolved absorption study on *cis*-stilbene in solution: observation of wavepacket motion on the reactive excited state; *Chem. Phys. Lett.* **2004**, *398*, 400-406.

(33) Lynch, M. S.; Slenkamp, K. M.; Khalil, M. Communication: Probing non-equilibrium vibrational relaxation pathways of highly excited CN stretching modes following ultrafast back-electron transfer; *J. Chem. Phys.* **2012**, *136*, 241101.

(34) Meneghin, E.; Volpato, A.; Cupellini, L.; Bolzonello, L.; Jurinovich, S.; Mascoli, V.; Carbonera, D.; Mennucci, B.; Collini, E. Coherence in carotenoid-to-chlorophyll energy transfer; *Nat. Commun.* **2018**, *9*, 3160.

(35) Volpato, A.; Collini, E. Time-frequency methods for coherent spectroscopy; *Opt. Express* **2015**, *23*, 20040-20050.

(36) Rury, A. S.; Dawlaty, J. M. Rabi-like vibrational coherence transfer in a hydrogen-bonded charge transfer material; *Phys. Rev. B* **2017**, *95*.

(37) Scholes, G. D.; Fleming, G. R.; Chen, L. X.; Aspuru-Guzik, A.; Buchleitner, A.; Coker, D. F.; Engel, G. S.; Van Grondelle, R.; Ishizaki, A.; Jonas, D. M.; Lundeen, J. S.; Mccusker, J. K.; Mukamel, S.; Ogilvie, J. P.; Olaya-Castro, A.*et al.* Using coherence to enhance function in chemical and biophysical systems; *Nature* **2017**, *543*, 647-656.

(38) Rafiq, S.; Scholes, G. D. From Fundamental Theories to Quantum Coherences in Electron Transfer; *J. Am. Chem. Soc.* **2018**, *141*, 708-722.

(39) Durrant, J. R.; Tachibana, Y.; Mercer, I.; Moser, J. E.; Gratzel, M.; Klug, D. R. The excitation wavelength and solvent dependance of the kinetics of electron injection in $Ru(dcbpy)_2(NCS)_2$ sensitized nanocrystalline $TiO_2$ films; *Z. Phys. Chem.* **1999**, *212*, 93-98.

(40) Benko, G.; Kallioinen, J.; Korppi-Tommola, J. E. I.; Yartsev, A. P.; Sundstrom, V. Photoinduced ultrafast dye-to-semiconductor electron injection from nonthermalized and thermalized donor states; *J. Am. Chem. Soc.* **2002**, *124*, 489-493.

(41) May, V.; Kuhn, O. *Charge and Energy Transfer Dynamics in Molecular Systems*; 2nd ed.; Wiley: Weinheim, 2004.

(42) Jonas, D. M. Vibrational and Nonadiabatic Coherence in 2D Electronic Spectroscopy, the Jahn–Teller Effect, and Energy Transfer; *Ann. Rev. Phys. Chem.* **2018**, *69*, 327-352.

(43) Chábera, P.; Liu, Y.; Prakash, O.; Thyrhaug, E.; Nahhas, A. E.; Honarfar, A.; Essén, S.; Fredin, L. A.; Harlang, T. C. B.; Kjær, K. S.; Handrup, K.; Ericson, F.; Tatsuno, H.; Morgan, K.; Schnadt, J.*et al.* A low-spin $Fe^{(III)}$ complex with 100-ps ligand-to-metal charge transfer photoluminescence; *Nature* **2017**, *543*, 695.

(44) Grumstrup, E. M.; Johnson, J. C.; Damrauer, N. H. Enhanced Triplet Formation in Polycrystalline Tetracene Films by Femtosecond Optical-Pulse Shaping; *Phys. Rev. Lett.* **2010**, *105*, 257403.

(45) Weiner, A. M. *Ultrafast Optics*; Wiley: Hoboken, New Jersey, 2009.

(46) Egorova, D.; Kuhl, A.; Domcke, W. Modeling of ultrafast electron-transfer dynamics: multi-level Redfield theory and validity of approximations; *Chem. Phys.* **2001**, *268*, 105-120.

(47) Redfield, A. G. In *Advances in Magnetic and Optical Resonance*; Waugh, J. S., Ed.; Academic Press: 1965; Vol. 1, p 1-32.

# Chapter 9. ELECTRONIC-VIBRATIONAL ANISOTROPY IN EXCITED STATE INTRAMOLECULAR PROTON TRANSFER

*The work presented in this chapter is being prepared for publication*

## 9.1 INTRODUCTION

The previous chapters have focused on understanding metal-to-ligand charge transfer behavior in a molecule that is particularly good at efficiently shuttling electron density across its molecular structure. In those studies, multidimensional EV spectroscopy was showcased as a great method for unveiling the nature of electronic excited states participating in this efficient charge transfer through vibronically coupled molecular motions and for determining how low frequency vibrations contribute to the charge transfer reactions. A key advantage of multidimensional EV spectroscopy was center stage in those experiments: the ability to follow ultrafast, multi-coordinate photochemical reactions through the lens of specific molecular structural coordinates. The focus of the present chapter is on understanding the excited state intramolecular proton transfer (ESIPT) mechanism that has been characterized in small organic molecules. At first glance, this chapter may appear to deviate substantially from the previous chapters because the molecular dynamics of interest do not involve transition-metal centered complexes or charge transfer between metals and coordinated ligands. In fact, the ESIPT mechanism is also characterized by the well-orchestrated movement of electronic and nuclear motions to very efficiently transfer energy intramolecularly in the excited electronic state. Whereas the previous MLCT dynamics studied in $N3^{4-}$ really captured a mechanistic description of this molecule's ability to move electron density, the current chapter focuses on

the mechanisms by which 10-hdyroxybenzo-[*h*]-quinoline (HBQ, Figure 9.1) moves protons efficiently within its molecular frame. Naturally, these dynamics will involve much more significant structural reorganization of the nuclei during what is effectively a enol- to keto-tautomerization reaction triggered by electronic excitation. Indeed, ultrafast transfer of electrons and protons represent two of the fastest chemical reactions occurring in nature.

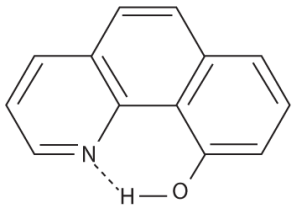


Figure 9.1. Molecular structure of 10-Hydroxybenzo-[*h*]-quinoline (HBQ).

Proton transfer is a widely studied and broadly important reaction in chemistry and biology.[1-3] The time scales for proton transfer reactions can make them some of nature's fastest reactions, occurring within the time span of single molecular vibrational periods (~10 fs). The transfer of a proton in an excited state was first observed by Weller in 1955 when an unusually large Stokes-shifted fluorescence spectrum was measured for methyl salicylate which then became the expected mirrored image emission upon methylation of the acidic proton.[4] Over the many decades since, ESIPT has been studied rigorously with the goal of determining the kinetics of the proton transfer and the mechanistic details of the reaction.[5-10] Two benchmark ESIPT systems have been particularly well studied in the last two decades: the 2-(2'-hydroxyphenyl)benzothiazole (HBT) molecule and HBQ. These two structures differ mainly by how geometrically constrained the proton is that participates in the transfer. Experimental and theoretical comparisons between these two systems have proven fruitful for determining general characteristics of the ESIPT reaction,[11-19] which is discussed further below for HBQ and schematically depicted in Figure 9.1.

In this chapter, the ESIPT mechanism of HBQ and its deuterated analogue, DBQ, in non-polar tetrachloroethylene (TCE) solvent is investigated using polarization-selective transient-IR (tIR) and 2D EV spectroscopies. The outstanding questions for the photophysics of HBQ include: How active is the proton is during its transfer in the excited state? What is the nature of the electronically excited potential energy surface on which this ESIPT process occurs? An analysis of the isotopic effects present in the electronic absorption spectrum and ground state vibrational spectrum suggest that strong coupling between the electronic and vibrational degrees of freedom exists in HBQ. The anisotropic measurements presented from the polarization-selective tIR experiments provide further support for this claim and the excitation-dependent anisotropy measured using 2D EV spectroscopy provides confirmation of the adiabatic electronic state, $S_1$, on which ESIPT proceeds.

## 9.2 Background: Excited State Intramolecular Proton Transfer in HBQ

The intramolecularly hydrogen bonded complex 10-hydroxybenzo-[*h*]-quinoline (HBQ) is a benchmark system for studying ESIPT dynamics. The rigid carbon backbone from its fused ring structure makes HBQ a convenient model system for investigating ESIPT. A distinctive photophysical feature of ESIPT molecules is a significantly Stokes shifted emission spectrum (>10,000 $cm^{-1}$ for HBQ) which is indicative of significant structural reorganization and relaxation in the excited state. In the ground state, HBQ is stable in its enol form (E). Immediately following electronic excitation ($S_0 \rightarrow S_1$, $\pi\pi^*$) the excited state enol form (E*) describes the Franck-Condon region of the $S_1$ potential energy surface. Nearly immediately thereafter, ESIPT occurs as the ultrafast transfer of the phenolic proton to the quinolic nitrogen, forming the excited state keto isomer (K*) of HBQ. Many investigations using femtosecond

transient electronic absorption (TA) and time-resolved fluorescence (TRF) have outlined the general kinetics of the ESIPT reaction in HBQ.[15,20-25] These dynamics are schematically illustrated in Figure 9.2.

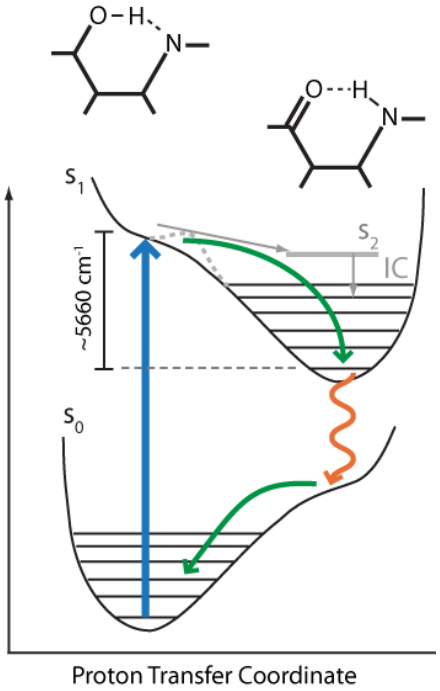


Figure 9.2. Schematic photophysical picture of ESIPT in HBQ. The colored arrows represent the excitation of the ground state enol to the excited state enol (blue), the ultrafast proton transfer and consequent relaxation in the excited state (green, curved on $S_1$), the fluorescence of the equilibrated keto form in the excited state (orange, wavy), and the relaxation of the hot ground state keto form as it reverts back to the enol form (green, curved on $S_0$). The gray dashed and solid lines, as well as the $S_2$ excited state (~1860 $cm^{-1}$ lower than the Franck-Condon excitation point) indicate photophysical dynamics that are debated in the literature.

These studies widely agree upon a ~260-300 ps lifetime of the K* product following ESIPT; this timescale describes the reported fluorescence decay times from K* and exponential decays of TA signals observed primarily from the excited state stimulated emission (ESE) of the K*.[20,22,23] It is important to note that excitation energy dependent TA studies by Schriever *et al.*[23] show the same K* lifetime when the Franck-Condon region of the $S_2$ state is nearly exclusively excited using 325 nm pump pulses.[23] This result provides evidence that $S_2 \rightarrow S_1$ ultrafast internal conversion does occur in HBQ when $S_2$ is directly excited and it suggests that

the predominant electronic state relevant to the excited state relaxation dynamics is the $S_1$ state. Most of these studies have also found a second timescale in the ~10 ps range that can be attributed to the vibrational cooling of the excited state keto isomer.[20,22] An exception to this is reported by Schriever *et al.*[23] who attribute the 10.5 ps exponential decay to a solvated electron in the cyclohexane solvent due to multiphoton ionization, arguing that a consistent spectral shape of their TA signal runs contrary to the suggested vibrational relaxation mechanism. Consistent with their excitation energy independent K* lifetime, these authors also report this 10.5 ps decay time is observed irrespective of exclusively exciting $S_1$ or $S_2$. However, Takeuchi and Tahara show convincingly that the thermal diffusivity of the cyclohexane solvent used in their studies (and in the work by Schriever *et al.*[23]) corresponds to a cooling rate that is consistent with the 8.3 ps decay component in their measurement. These authors also show that while the ESA decreases in intensity and maintains a constant band shape, the ESE undergoes a spectral blue shift characteristic of emission from an initially vibrationally "hot" K* isomer shifting toward emission from a thermally equilibrated K* species.[22] Altogether, a clear picture of the picosecond dynamics from these TA studies emerges wherein the $S_1$ state is the primary electronic potential surface describing the ESIPT relaxation dynamics.

A ~350 fs decay component has also been consistently measured at the earliest resolvable experimental delay times;[20,22,23] the physical mechanism underlying this dynamic is still the subject of debate. An early report of this faster decay lifetime was made by Chou *et al.*[20] for HBQ dissolved in cyclohexane using TRF with sum frequency detection where the excitation pulses were in the 385-400 nm range to predominantly excite $S_1$. They explained this observation as an ultrafast internal conversion ($S_2 \rightarrow S_1$) where the initial proton transfer must

populate the $S_2$ state on the same ultrafast timescale as the proton transfer, despite their excitation pulse spectrum being overlapped with the red-edge of the $S_0 \rightarrow S_1$ absorption. Based upon the structural similarities of HBQ to phenanthrene, two low-lying excited electronic states of $\pi\pi^*$ character that were first characterized by Platt[26] as "$L_a$" and "$L_b$" states were invoked by the authors as the two excited electronic states involved in the $S_2 \rightarrow S_1$ internal conversion (this mechanism is illustrated in Figure 9.2, gray). These states differ in their electronic nodal structure where the $L_a$ state has nodes between carbon atoms and $L_b$ has nodes at the carbon positions. Importantly, these electronic structures result in electronic dipole moments that are orthogonal to one another, with one in the longitudinal direction of the molecular axis and the other perpendicular. A change in the electronic transition dipole moments was the basis for suggesting internal conversion as the mechanism giving rise to the 330 fs dynamic. While vibronic relaxation, solvent reorientation, and internal (intramolecular) vibrational relaxation were mentioned as possible explanations of early time dynamics, the study suggests that these mechanisms would all be much longer than the 330 fs decay measured. Takeuchi and Tahara also observed a 350 fs dynamic of the transient absorption around 430 nm (likely corresponding to a highly vibrationally excited K*).[22] However, these authors report impulsively excited low frequency vibrational coherences that persist for several picoseconds on the excited state. Moreover, using a sliding window FT analysis (similar to that used in chapter 8 for $N3^{4-}$), Takeuchi and Tahara identify one coherently excited vibration at 242 $cm^{-1}$ that has a dephasing time of $0.5 \pm 0.1$ ps by comparison to three other identified low frequency vibrations which dephase in a few ps with the observed wavepacket amplitude. From this result, they make two convincing arguments: 1) that the coherently excited nuclear wavepacket proceeds in an adiabatic fashion on $S_1$ because it is retained in the K* product (i.e., it would

not survive the internal conversion suggested by Chou *et al.*[20]), and 2) that the faster dephasing time of the 242 $cm^{-1}$ mode reflects its coupling with the proton transfer reaction coordinate. For these reasons, intramolecular vibrational redistribution is used to explain the 350 fs decay.

Of course, one of the greatest dynamics of interest is the proton transfer event itself. However, sufficient time resolution to measure the proton transfer event has proven experimentally challenging. The stimulated emission signal reported by Takeuchi and Tahara[22] suggests the proton transfer time is $25\pm15$ fs while Schriever *et al.*[23] report proton transfer times of ~35 fs from their combined experimental and theoretical work. An interesting description of the ESIPT process in HBQ is given by Schriever *et al.*[23]: ultrafast proton transfer takes place on the 30-40 fs timescale originating from the Franck-Condon region of $S_1$ by means of low frequency vibrational modes that deform the carbon backbone to shorten the O-N distance allowing proton transfer to occur essentially barrierlessly. This study compared HBQ dynamics to those of HBT and found that these low frequency skeletal motions trigger the proton migration but the OH stretch plays a more active role in HBQ than it does in HBT where the proton is completely passive during the proton transfer. For both molecules, the ESIPT mechanism is suggested to occur without a barrier and, thus, no need for quantum mechanical tunneling. This mechanistic description of ESIPT is very similar to other descriptions arrived at experimentally and/or computationally involving coherently excited low frequency vibrational modes, which has supported this explanation as the general mechanism by which ESIPT proceeds.[6,11,13,14,18,19,24,27-36] More recently, an important study was published on the ESIPT of HBQ and HBT in methanol solution that provided the first evidence of an isotope effect in HBQ.[15] In this study, Lee *et al.* show from femtosecond TRF measurements of the E* isomer that HBQ undergoes proton transfer in $12 \pm 6$ fs and DBQ (the

deuterated analogue) transfers the deuterium in 25 ± 5 fs, providing an isotope effect consistent with the expected $\sqrt{(2)}$ rate dependence within experimental uncertainty. Impressively, the same experiments were performed on HBT which displayed no isotope effect similar to many other reports on HBT;[12,27,34] the HBT (DBT) proton (deuterium) transfer time scales were measured at 62 fs (63 fs).[15] This result has challenged the conventional wisdom of the general ESIPT mechanism being generalizable to include a barrierless transfer of the proton, and it has also raised the question of exactly how active of a role the proton plays during ESIPT. Finally, Lee *et al.*[15] also observed ~300-400 fs decay times of the TRF signals of the K* for both HBQ and DBQ. In a later publication, the same group conducted the TRF experiment in a spectrally resolved manner where the time-dependent fluorescence anisotropy of the K* emission at 580 nm showed a 310 fs decay.[25] By comparing a 360 fs red shift of the emission spectral density to the 310 fs decay of the fluorescence anisotropy at 580 nm (center of the K* emission spectrum), the authors made two principal conclusions: 1) that the K* emission spectrum at early times is composed of emission from $S_2 \rightarrow S_0$ and $S_1 \rightarrow S_0$, and 2) the presence of these excited states suggests that internal conversion ($S_2 \rightarrow S_1$) accounts for the 310 fs decay in anisotropy where these two states are the $L_a$ and $L_b$ states initially proposed by Chou *et al.*[20]

From this brief excursion into the ESIPT literature of HBQ, it is clear that ambiguity still shrouds the immediate non-equilibrated aftermath of the proton transfer event over the first several hundred femtoseconds. Yet, this intermediate dynamic has important implications for our understanding of ESIPT photophysics and the two operative explanations for it are quite different. The time-dependent anisotropy of the reported TRF signal makes a compelling argument for a change in electronic state, such as would occur during internal conversion. However, Lee *et al.*[25] assert that the dipole moment of the K* emission cannot be influenced

by relaxation along the nuclear coordinates in a TRF measurement which would arise from solvation effects, IVR, and vibronic relaxation. These phenomena have been the other main explanations for the several hundred femtosecond decay dynamic. In the following, a consistent notion is suggested that the electronic and vibrational degrees of freedom in the HBQ excited state governing the ESIPT mechanism are much more strongly coupled than has been assumed. This leads to the conclusion that the immediate aftermath of the proton transfer can be characterized by IVR and vibronic relaxation of vibrationally hot K* molecules on an electronically adiabatic potential, probably on $S_1$.

## 9.3 Isotope Effects in the Electronic and Vibrational Linear Absorption Spectra of HBQ

An initial observation of the electronic motion being coupled with the vibrational degrees of freedom in a molecule is possible when a clear vibronic progression in the electronic absorption spectrum is present. In this case, an electronic transition can be largely represented by a collective molecular coordinate that has a displaced equilibrium geometry in the excited state by comparison to the ground state, giving rise to a progression of peaks separated by the excited state vibrational spacing of the displaced molecular coordinate.[37] The electronic absorption spectrum of HBQ in cyclohexane (absorptions to $S_1$ and $S_2$) was fit by Schriever *et al.*[23] to the sum of five Gaussian peaks, but no in-depth discussion of this fitting was discussed beyond quantifying the spectral overlap of the $S_1$ and $S_2$ bands. In Figure 9.3, I have shown that the electronic absorption spectrum of HBQ in tetrachloroethylene (TCE), as well as DBQ, can be fit assuming one anharmonic vibrational mode is responsible for each vibronic progression (different Franck-Condon active modes for $S_1$ and $S_2$) where each vibronic peak

is fit with Gaussian broadening. For all fits of the electronic absorption spectra, only the absorption of the ground state enol absorption was considered, which leaves a small residual

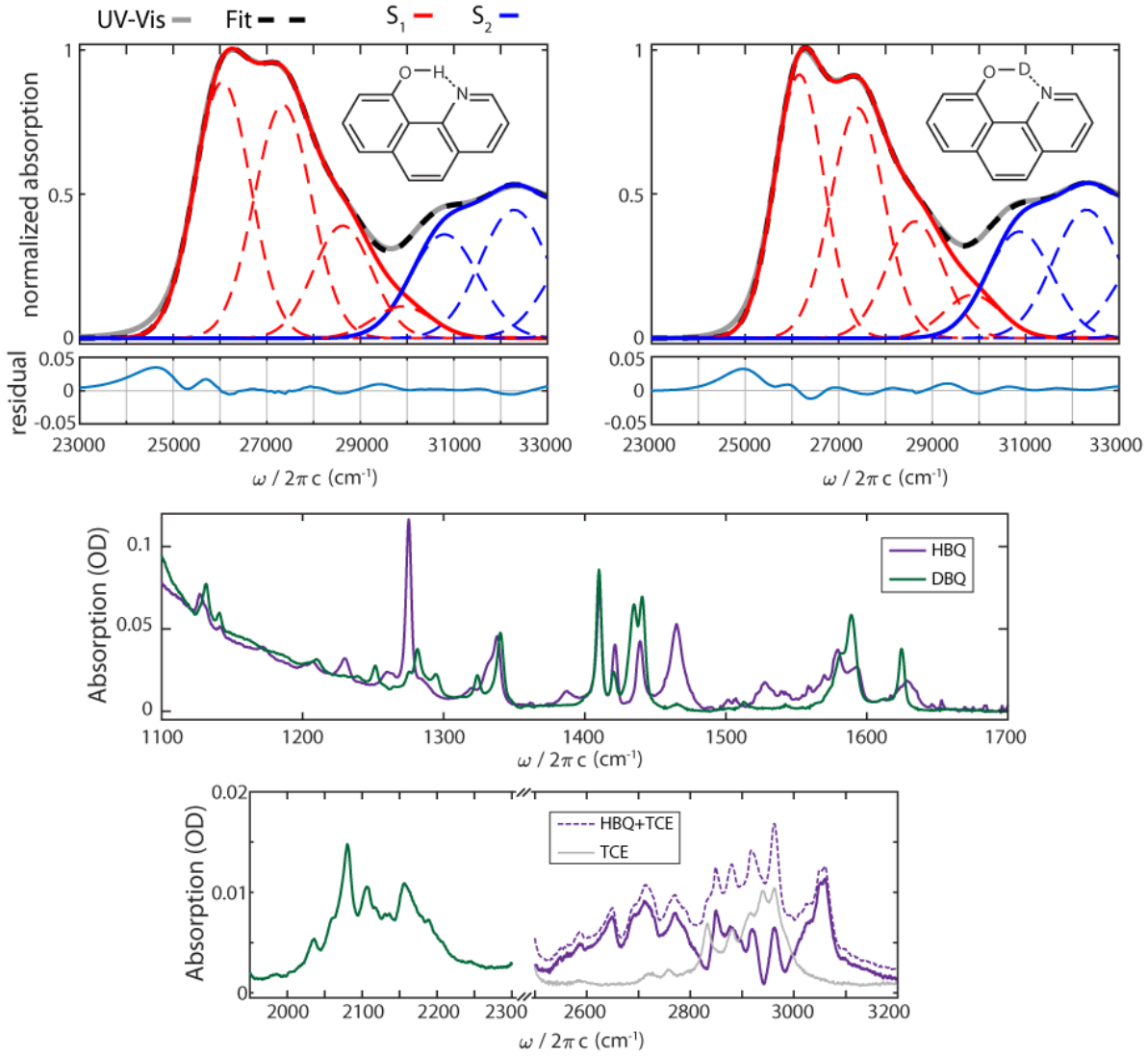


Figure 9.3. Electronic and Vibrational Linear Absorption Spectra of HBQ and DBQ. (top row) The electronic absorption of HBQ (left) and DBQ (right) is shown (gray) and the vibronic progression is fit for the $S_1$ (red) and $S_2$ (blue) absorptions to a displaced, anharmonic vibrational mode model (vibronic fits = dashed, sum = solid). The sum of the fits to both absorptions is shown in dashed black, and the residual (gray – dashed black) are in teal below the absorption spectra. (bottom) The solvent subtracted vibrational spectra of the ground electronic state HBQ (purple, solid) and DBQ (green, solid) are shown the fingerprint region and the OH and OD stretching region in the middle and bottom rows. Due to significant spectral overlap in the OH stretch region, the spectrum without solvent subtraction (purple dashed) and the solvent-only spectrum (gray solid) are also shown.

on the very red edge of the absorption spectra assumed to be due to a very small fraction (≲ 1-2% of total molecules) of ground state keto isomers. This Franck-Condon active anharmonic vibration model accounts for >99% of the ground state enol absorption, as shown by the residuals. The peak positions in the vibronic progression of each $S_0 \rightarrow S_n$ absorption were fit independently using a Franck-Condon active anharmonic vibration model. In this model, the 0-0' transition frequency, $\omega_{eg}$, defines the low energy onset of the absorption (i.e., between the lowest energy vibrational state in the ground electronic state, v=0, and in the $S_n$ excited electronic state, v'=0'), and the vibronic transition frequencies, $\omega_{vibronic}(\mathrm{v}')$, into "hot" vibrations are defined as a function of excited state vibrational quanta ( $\mathrm{v}' \in \{1-3\}$ ):

$$\omega_{vibronic}(\mathrm{v}') = \omega_{eg} + \sum_{\mathrm{v}'=1}^{3} (\mathrm{v}')\omega_{e,1'} - (\mathrm{v}'-1)\Delta_{2'1'} \tag{9.1}$$

where $\omega_{e,1'} = |e,1'\rangle - |e,0'\rangle$ and $\Delta_{2'1'} = \omega_{e,1'} - \omega_{e,2'}$ as defined in chapter 2. Each vibronic transition is given its own bandwidth, $\delta\omega_{0\mathrm{v}'}$, and amplitude, $A_{0\mathrm{v}'}$, in the fitting routine to fit to the sum of gaussians: $\sum_{\mathrm{v}'=0'}^{3} A_{0\mathrm{v}'} \exp\left[ -(\omega - \omega_{vibronic}(\mathrm{v}'))^2 \Big/ 2\sigma^2 \right]$ where $\sigma = \delta\omega_{0\mathrm{v}'} \Big/ 2\sqrt{(2ln(2))}$. The fit is optimized by minimizing the residuals to ≤1% using the adjustable parameters $\omega_{eg}$, $\omega_{e,1'}$, $\Delta_{2'1'}$, $\delta\omega_{0\mathrm{v}'}$ and $A_{0\mathrm{v}'}$. The optimized values for the fits shown in Figure 9.3 are presented in Table 1 below.

The electronic absorption profiles of HBQ and DBQ both clearly show vibronic progressions of a Franck-Condon active anharmonic mode in the $S_0 \rightarrow S_1$ electronic transition. The fitted excited state anharmonic vibration for HBQ (DBQ) is 1290 $cm^{-1}$ (1245 $cm^{-1}$) with 10 $cm^{-1}$ (15 $cm^{-1}$) anharmonicity. A comparison of the $S_1$ vibronic transition bandwidths for HBQ and DBQ suggest that the Franck-Condon active anharmonic mode involves the phenolic

proton involved in ESIPT because the 0-0’ and 0-1’ transition linewidths display isotopic dependence; for example, the DBQ 0-0’ bandwidth narrows to ~89% of the HBQ 0-0’ transition bandwidth. Although strong anharmonic mixing even in the $S_1$ Franck-Condon

Table 9.1. Vibronic Progression Fitting Parameters for Electronic Absorption Spectra of HBQ and DBQ. The gray shaded values of $S_2$ reflect less-certain values given the experimental electronic absorption spectra does not extend beyond 300 nm. Accordingly, very little confidence is placed in the fitted anharmonicity for $S_2$, but the fits to the first two vibronic peaks in $S_2$ are reliable.

| | | ***S1*** ($\omega_{e,1'}$ =1290 cm$^{-1}$; $\Delta_{2'1'}$ =10 cm$^{-1}$) | | | | ***S2*** ($\omega_{e,1'}$ = 1490 cm$^{-1}$; $\Delta_{2'1'}$ =40 cm$^{-1}$) | | | |
|---|---|---|---|---|---|---|---|---|---|
| | | **0-0’** | **0-1’** | **0-2’** | **0-3’** | **0-0’** | **0-1’** | **0-2’** | **0-3’** |
| **HBQ** | **A** | 0.89 | 0.81 | 0.39 | 0.11 | 0.36 | 0.445 | 0.28 | 0.05 |
| | **ω (cm$^{-1}$)** | 26055 | 27345 | 28625 | 29905 | 30800 | 32290 | 33740 | 35190 |
| | **δω (cm$^{-1}$)** | 1400 | 1435 | 1465 | 1470 | 1690 | 1710 | 1720 | 1750 |

| | | ***S1*** ($\omega_{e,1'}$ =1245 cm$^{-1}$; $\Delta_{2'1'}$ = 15 cm$^{-1}$) | | | | ***S2*** ($\omega_{e,1'}$ =1430 cm$^{-1}$; $\Delta_{2'1'}$ =40 cm$^{-1}$) | | | |
|---|---|---|---|---|---|---|---|---|---|
| | | **0-0’** | **0-1’** | **0-2’** | **0-3’** | **0-0’** | **0-1’** | **0-2’** | **0-3’** |
| **DBQ** | **A** | 0.9150 | 0.8 | 0.405 | 0.15 | 0.37 | 0.445 | 0.28 | 0.05 |
| | **ω (cm$^{-1}$)** | 26160 | 27405 | 28635 | 29865 | 30870 | 32300 | 33690 | 35080 |
| | **δω (cm$^{-1}$)** | 1240 | 1350 | 1430 | 1430 | 1620 | 1670 | 1700 | 1750 |

minimum should be expected from previous reports of an effectively barrierless potential in the proton transfer coordinate, the 0-0’ transitions should have the least amount of anharmonic mixing and represent the most “localized” vibrational mode character of this Franck-Condon active vibrational mode (note that the observed vibronic progression is not necessarily exclusively representative of the proton transfer reaction coordinate). The vibronic progression fitting is consistent with this notion as the bandwidths increase for vibronic excitation into higher lying vibrational states in both molecules. Moreover, the isotopic dependence also follows this description as the bandwidth ratios ($\delta\omega_{0v'}^{HBQ} / \delta\omega_{0v'}^{DBQ}$, see Figure 9.4) for increasing v’ go from 1.13 for the 0-0’ transition to 1.02 for the 0-2’ transition. It is noted that the best fits

will result from the first two vibronic transitions because spectral overlap of the $S_2$ features is absent for these transitions and overlapped for 0-2' and 0-3'. Nevertheless, the minimization of the residual intensity in the fitting process required the bandwidths to result in this ratio starting greater than 1 and trending towards 1 for greater v'. Examining the trends in the vibronic peak bandwidth for increasing v' separately for HBQ and then for DBQ, specifically the change in bandwidth between two vibronic peaks (e.g., the difference between the 0-0' and 0-1' bandwidths, etc.), shows that the DBQ 0-0' transition is significantly narrower (90 $cm^{-1}$) than its 0-1' transition, which is 80 $cm^{-1}$ narrower than the 0-2' transition. In comparison to HBQ, the DBQ bandwidths increase by a factor of ~2.5 times more than HBQ as the vibronic progression increases from v'=0'→1' and then again from v'=1'→2'. Thus, the trend in the isotopic bandwidth ratios are a result of the DBQ's bandwidth being much narrower for the first two vibronic transitions relative to HBQ. Accordingly, the anharmonicity of the DBQ Franck-Condon active mode is observed to be greater (~50%) than that of HBQ. This suggests that the Franck-Condon region for the $S_0 \rightarrow S_1$ excitation includes an anharmonic vibrational coordinate that strongly depends on the phenolic proton that transfers during ESIPT. With this in mind, it is reasonable to expect an isotopic effect to be observable in ESIPT dynamics of HBQ, as shown by Lee *et al.*[15] if the relevant electronic state(s) are influenced by vibrational coordinates that are of the same, or similar, character to the Franck-Condon active anharmonic vibrational coordinates identified by the vibronic progression of the electronic absorption. It is emphasized again that the Franck-Condon region may very likely be defined by *more* than just this Franck-Condon active anharmonic vibration. As Tahara[22] and Schriever[23,34] have described, low frequency skeletal vibrations coupling with the proton transfer are integral to ESIPT.

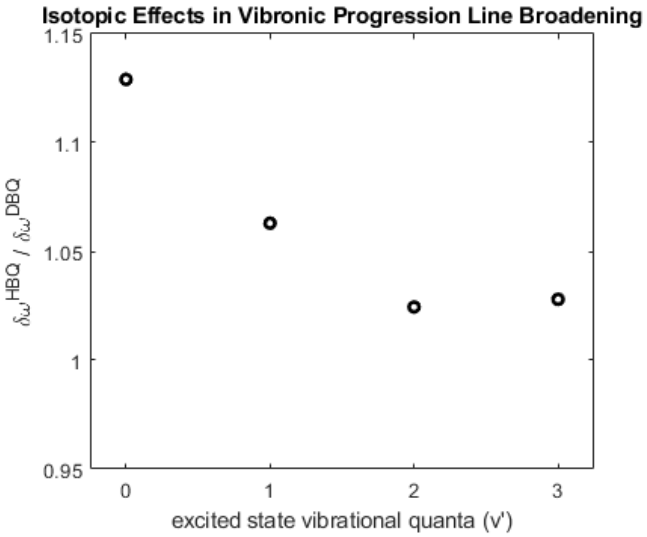


Figure 9.4. Line Broadening Comparison Between HBQ and DBQ. The ratio of the bandwidths were obtained from the vibronic progression fitted parameters in Table 1.

Although fitting the vibronic peaks of HBQ and DBQ have required Gaussian broadening which reflect inhomogeneous vibronic dephasing dynamics, a brief discussion of the vibronic line broadening mechanisms as derived in the homogeneous dephasing limit in chapter 2 for the electronic excitation dimension of the 2D EV line shapes may be instructive. The $\tau_1$' components of the 2D EV analytical dephasing functions reflect that vibronic excitation into "hot" vibrational states should broaden with respect to the 0-0' vibronic excitation if there is electronic-state-dependent vibrational dephasing ($\lambda$>1) due to contributions directly from the vibronic energy gap cross-correlation function, $\left\langle \delta\omega_{g1,g0}(t)\delta\omega_{e0',g0}(0)\right\rangle$, and the vibrational energy gap autocorrelation function, $\left\langle \delta\omega_{g1,g0}(t)\delta\omega_{g1,g0}(t)\right\rangle$. If the definition $\lambda = \delta\omega_{e1',e0'}(t)/\delta\omega_{g1,g0}(t)$ is used to rewrite these correlation functions directly in terms of the excited state vibrations, then the vibronic cross-correlation function becomes $\left\langle \delta\omega_{e0',g0}(t)\delta\omega_{e1',e0'}(0)\right\rangle$ and the relevant excited state vibrational correlation function becomes $\left\langle \delta\omega_{e1',e0'}(t)\delta\omega_{e1',e0'}(0)\right\rangle$. These two correlation functions represent excited state vibronic and

vibrational contributions to line broadening, respectively. Using the dephasing functions given in chapter 2 to describe the $\delta\omega_{0v'}^{HBQ}$ / $\delta\omega_{0v'}^{DBQ}$, the 0-0' line broadening would be represented as

$$\frac{\Gamma_{eg,eg}^{HBQ}}{\Gamma_{eg,eg}^{DBQ}} \propto \frac{\left\langle \delta\omega_{e0',g0}(t)\delta\omega_{e0',g0}(0)\right\rangle_{HBQ}}{\left\langle \delta\omega_{e0',g0}(t)\delta\omega_{e0',g0}(0)\right\rangle_{DBQ}} \tag{9.2}$$

where a value greater than 1 arises due to the electronic energy gap correlation function for HBQ fluctuating more than DBQ. In other words, this would reflect that the zero-point energy fluctuations must be larger in HBQ than in DBQ. This should be the case because the zero-point energy for DBQ will be smaller due to the lower effective mass from deuterium reducing the vibrational frequency. This would be the result if the DBQ zero-point energy sits lower in a very slight potential well minimum on $S_1$ such that its vibrational character is comparably more localized (or less anharmonically mixed) than HBQ even for a small difference in zero-point energy. The excited state vibrational frequencies obtained from fitting the electronic absorption suggest the zero-point energy difference would be ~23 $cm^{-1}$.

As the vibronic excitation energy increases and more vibrational quanta are excited, the line broadening contributions begin to include more than just fluctuations in zero-point energy. Considering the bandwidth ratio as it would be expressed in terms of the dephasing functions for the 0-1' transitions in HBQ and DBQ:

$$\frac{\Gamma_{eg,eg}^{HBQ}+(2\lambda)\Gamma_{eg,v}^{HBQ}+(\lambda^2)\Gamma_{v,v}^{HBQ}}{\Gamma_{eg,eg}^{DBQ}+(2\lambda)\Gamma_{eg,v}^{DBQ}+(\lambda^2)\Gamma_{v,v}^{DBQ}} \propto \frac{\left\langle \delta\omega_{e0',g0}(t)\delta\omega_{e0',g0}(0)\right\rangle_{HBQ}+2\left\langle \delta\omega_{e0',g0}(t)\delta\omega_{e1',e0'}(0)\right\rangle_{HBQ}+\left\langle \delta\omega_{e1',e0'}(t)\delta\omega_{e1',e0'}(0)\right\rangle_{HBQ}^{2}}{\left\langle \delta\omega_{e0',g0}(t)\delta\omega_{e0',g0}(0)\right\rangle_{DBQ}+2\left\langle \delta\omega_{e0',g0}(t)\delta\omega_{e1',e0'}(0)\right\rangle_{DBQ}+\left\langle \delta\omega_{e1',e0'}(t)\delta\omega_{e1',e0'}(0)\right\rangle_{DBQ}^{2}} \tag{9.3}$$

one can see that the excited state vibronic and vibrational contributions to the DBQ line broadening would have to be stronger than in HBQ in order for the bandwidth ratio

$\delta\omega_{0v'}^{HBQ} / \delta\omega_{0v'}^{DBQ}$ to approach a value of 1; this effect is clearly observed in Figure 9.4. While the physical dephasing mechanisms that are described by the analytical forms of the energy gap correlation functions may typically include solute-solvent interactions, the fused ring structure of HBQ makes this phenolic proton and the ESIPT mechanism fairly robust against solvent influence, as well as the fact that all of HBQ and DBQ experiments discussed in this chapter have been done in the nonpolar solvent TCE. Thus, the description of the bath in the case of these HBQ and DBQ spectra may be more accurate if it is considered to be a bath of intramolecular degrees of freedom which are not directly part of the ESIPT reaction coordinates; those which are particularly obvious candidates are the coherently excited low frequency vibrational modes that have been widely reported in experiments and theoretical calculations mentioned earlier. Finally, consideration of the amplitudes from the $S_1$ vibronic progressions of HBQ and DBQ suggests that the displacement of the Franck-Condon active anharmonic modes may be slightly different between the two molecules. Although it is difficult to separate effects from the narrower 0-0' and 0-1' vibronic bandwidths and the slightly varied peak amplitudes between the first two vibronic transitions within the error of the vibronic progression fitting. Altogether, the analysis of the linear electronic absorption spectrum of HBQ and DBQ suggest that the vibronic character of the $S_1$ potential energy surface will increase with increased excitation energy and that the DBQ peak broadening and anharmonicity suggests that the zero-point energy of DBQ may actually be low enough in energy to be considered a more localized vibration in the v=0' state than HBQ; such a scenario would be mildly consistent with the reported isotope effect in its ESIPT mechanism.[15]

Considering the ground state vibrational (FTIR) spectra of HBQ and DBQ shown in the lower portion of Figure 9.3, there are clear isotopic effects as to be expected. The $\omega_{OH} / \omega_{OD}$

yields an approximate value of 1.27 (i.e., 2700 $cm^{-1}$/2125 $cm^{-1}$) which approaches the expected $\sqrt{(2)}$ dependence for a vibrational coordinate solely involving an isotopically substituted proton. Given the definition of an oscillator's frequency, $\omega = \sqrt{\frac{k}{\mu}}$ where k is the force constant and μ is the reduced mass, deviations from the $\sqrt{(2)}$ isotopic ratio may be due to one of two reasons: 1) the vibrational coordinates are not solely defined by the motion of the proton (deuterium) in the OH (OD) stretching motions but involve other atoms which contribute to the reduced mass of the oscillator, or 2) that the force constant for the two vibrations is not exactly the same.[37,38] The latter of these two options could arise when the potential function describing the normal modes composing the very broad, and structured, OH and OD stretching features is not completely described by the pure electronic part of the Hamiltonian in the Schrödinger equation but that it requires nuclear dependence.[38] In this case, the Born-Oppenheimer separation of the electronic and nuclear coordinates is not an entirely accurate description of the electronic potentials with respect to these particular vibrational coordinates.

Similar explanations are valid for the vibrational modes found in the fingerprint region for HBQ and DBQ. For example, a clear isotopic dependence is observed for the peak shift of the HBQ vibration at 1465 $cm^{-1}$ which appears to red-shift to 1435 $cm^{-1}$ yielding a smaller isotopic effect of 1.02 for the isotopic ratio of vibrational frequency as well as narrowing in bandwidth. This is not terribly surprising due to the nature of the fingerprint vibrational modes involving many more nuclei than just the isotopically substituted proton; this suggests the displacement amplitude of the phenolic proton in this mode is not the most dominant motion. Notably, there are also changes in vibrational peak intensities due to isotopic substitution with much smaller peak shifts (e.g., the two vibrations at 1421 $cm^{-1}$ and 1411 $cm^{-1}$ in HBQ versus at 1420 $cm^{-1}$

and 1410 $cm^{-1}$ in DBQ). The vibrational peak intensities are directly reflective of the magnitude of the vibrational transition dipole moment[39] which is fairly approximated by the expectation value

$$\mu^{a,b} = \left\langle \psi^a(r,Q) \,|\, \psi^b(r,Q) \right\rangle \left\langle \chi_a(Q) \,|\, \mathbf{M}_{vib} \,|\, \chi_b(Q) \right\rangle \tag{9.4}$$

where the initial and final vibronic states, a and b, respectively, are defined as $\left|a(r,Q)\right\rangle = \left|\psi^a(r,Q)\right\rangle \left|\chi^a(Q)\right\rangle$ and $\left|b(r,Q)\right\rangle = \left|\psi^b(r,Q)\right\rangle \left|\chi^b(Q)\right\rangle$ which implies the Born-Oppenheimer separation by separating the electronic wavefunction $\left|\psi^n(r,Q)\right\rangle$ from the pure vibrational wavefunction $\left|\chi^n(Q)\right\rangle$ for the $n^{th}$ state with electronic coordinates, r, and nuclear coordinates, Q (where Q parametrizes the electronic wavefunction). When this separation approximates the molecular physics well, the overlap integral in equation (9.4) goes to unity and the pure vibrational transition dipole moment gives the intensity of the transition subject to the IR-active vibrational selection rules. With this in mind, the isotopic dependence appearing most dramatically through a change in intensity reveals that the following physical aspects may be present in the system: 1) that the isotopic substitution affects the electronic coordinates enough to reduce the electronic overlap integral from unity, or 2) that the isotopic substitution affects magnitude of the expectation value by changing the symmetry of the vibrational mode or the orientation of the vibrational dipole moment. The vibrational peaks in the fingerprint region of the FTIR spectrum show that many of these high frequency vibrations display isotopic dependence, even if it is very subtle. This reflects the fact that the phenolic proton, which undergoes the excited state proton transfer, is likely coupled to many different intramolecular vibrational coordinates simultaneously even in the ground state, where the enol form is stable and no proton transfer is occurring.

## 9.4 Breaking Down Born-Oppenheimer with Transient-IR Anisotropy

The analysis of the ground state vibrational spectrum in the previous section demonstrated that the phenolic proton is likely coupled with many vibrational degrees of freedom even in the ground electronic state where no ESIPT dynamics are occurring. The electronic absorption spectral analysis also demonstrated that the HBQ and DBQ vibronic progressions show distinct isotopic effects, principally in the vibronic linewidths, and that the character of the 0-0' transition in DBQ may be fairly different from HBQ effectively resulting from a lower zero-point energy and stronger anharmonicity. These analyses resulted in discussions including caveats which became relevant when the Born-Oppenheimer approximation is not entirely accurate for the motions under investigation. To induce the ESIPT dynamics and view the excited state vibrational spectrum in HBQ and DBQ, the physical aspects of the electronic absorption spectrum and the ground state vibrational spectrum discussed above will now be convolved, necessarily, in the tIR and 2D EV experiments that follow.

Figure 9.5 shows tIR spectra of the fingerprint region for HBQ and DBQ at $\tau_2$ = 250 fs in the parallel polarized experiment. The strongest feature in both spectra have nearly identical spectral shapes centered at 1446 $cm^{-1}$; note both spectra have been normalized to compare

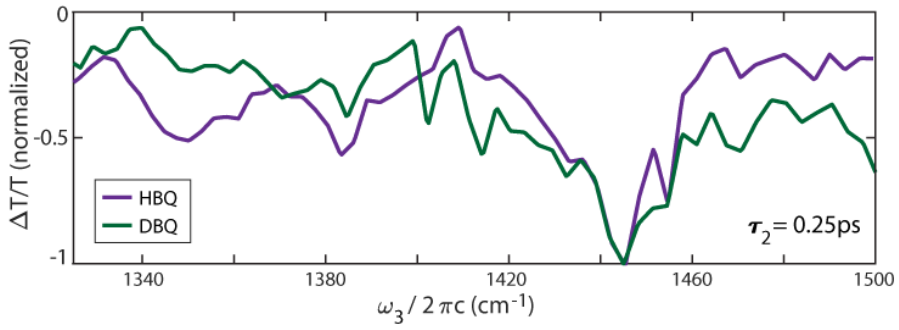


Figure 9.5. Transient-IR Spectra of HBQ and DBQ in the Fingerprint Region. The difference spectra are normalized to the greatest magnitude signal found at 1446 $cm^{-1}$.

spectral shape and DBQ has a weaker signal which accounts for some of the difference spectrum observed as an offset outside of the main feature.

The signal is principally negative indicating much stronger excited state absorptions from the vibrations of the K* than the ground state bleaches from E. A tentative assignment of this most prominent feature can be made from TDDFT calculations in which the $S_1$ keto geometry has been optimized for HBQ in the gas phase. A mode calculated to be at 1457 $cm^{-1}$ is suggested to represent the feature observed in the tIR spectra[40] (Figure 9.6). The atomic displacements indicate this vibration can be described as N-H wagging motion of the transferred proton in the K* isomer which also has other C-H wagging character from the hydrocarbon fused ring backbone and slight carbon-carbon ring distortions.

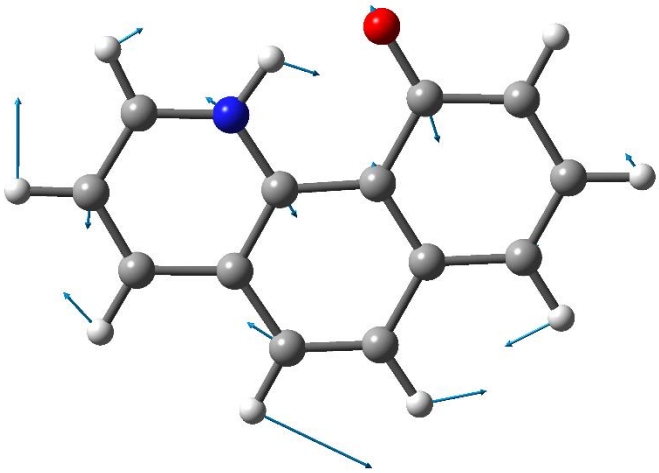

Figure 9.6. Gas Phase TDDFT Calculation of HBQ in the $S_1$ Keto (K*) State. The vibrational mode was calculated to be at 1457 $cm^{-1}$ and appears to involve the proton participating in ESIPT as an N-H wagging motion with other hydrocarbon backbone motions. (dark gray = carbon, light gray = hydrogen, blue = nitrogen, red = oxygen)

The motion of the proton that is transferred during ESIPT has a displacement vector with a principal component along the O-N direction whereas the magnitudes of the O and N displacements appear much lesser by comparison to the transferred proton's motion. This type of motion appears qualitatively consistent with the most recent report of the proton playing an

active role in ESIPT.[15] The first 10 ps of the polarization-dependent tIR spectra for both HBQ and DBQ are shown in Figure 9.7. The spectra have all been normalized locally for easy comparison of spectral shapes during this earlier time window in $\tau_2$. Notably, there is a strong polarization-dependent response for both HBQ and DBQ.

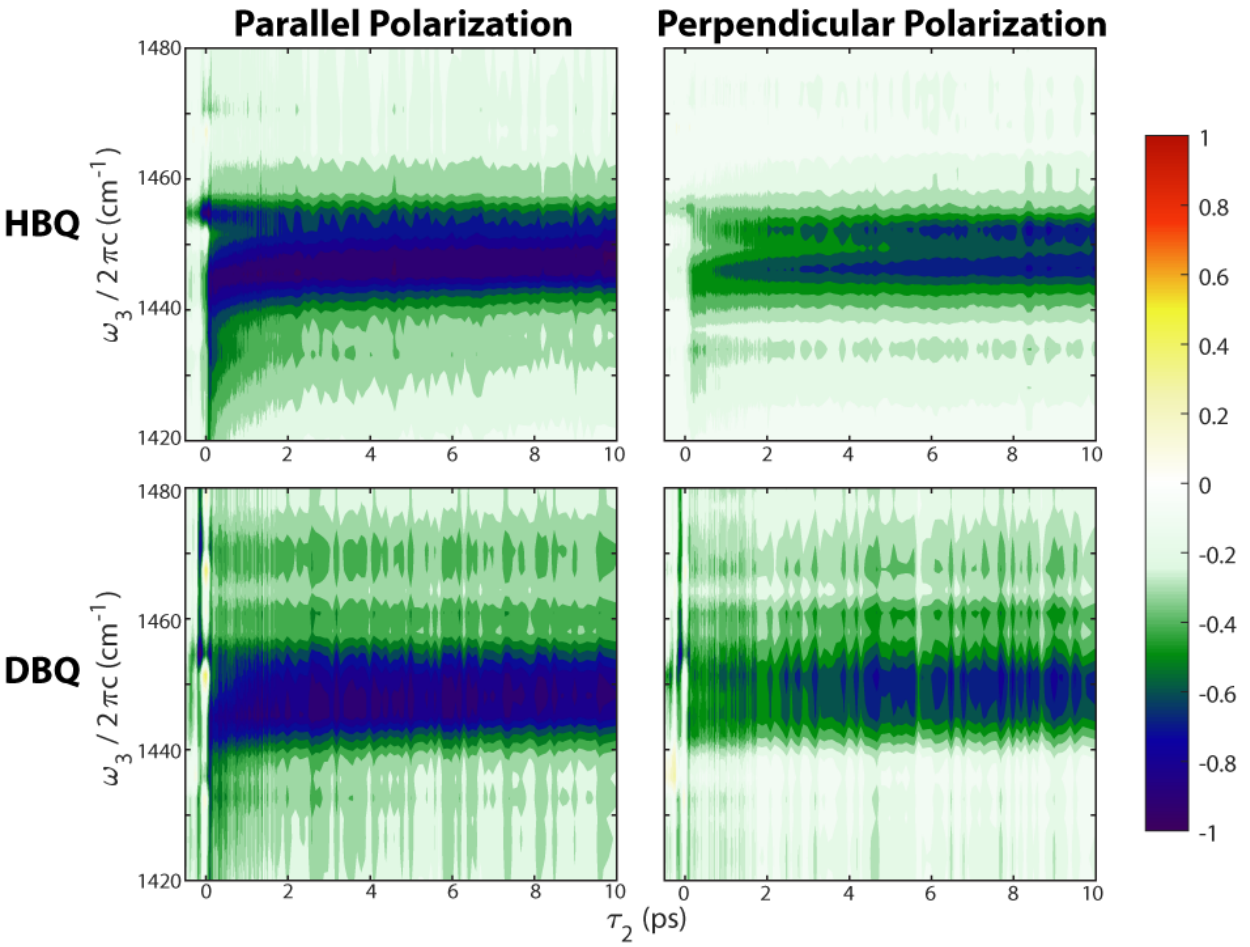


Figure 9.7. Polarization-Selective Transient-IR Spectra for HBQ and DBQ. Spectra are locally normalized for comparison of spectral shapes.

At very early times ($\tau_2 < 1$ ps), the parallel polarized spectra show much broader line widths spanning the 1430 – 1460 cm$^{-1}$ range by comparison to the perpendicularly polarized spectra. Furthermore, the decay profiles at early time is much more rapid for the parallel polarization experiments. The spectral features in both molecules and both polarizations appear to have a

double peak structure which merge together on ~10 ps timescale and continue to blue-shift to have a spectral centroid of ~1450 $cm^{-1}$ on the 300 ps timescale characteristic of the K* lifetime. This blue-shifting is consistent with the vibrational cooling reported by many other studies, and the ~300 ps K* lifetime is also observed in the tIR experiments discussed here.

Given the polarization-dependent responses in the HBQ and DBQ tIR spectra, the time-dependent anisotropy can be determined and compared to the time-dependent fluorescence anisotropy measurements reported by Lee *et al.*[25] An important distinction between these two anisotropies will prove insightful. Namely, a benefit of TRF anisotropy over a TA anisotropy measurement, where all transition dipole moments that interact are (nearly) degenerate and of principally electronic origin, is that TRF avoids spectrally overlapping signals of the ESA and ESE pathways which often are convolved in TA experiments. In addition, the TRF measurement is sensitive directly to excited state emission so the signals are specific to excited state dynamics. However, in a tIR experiment, the pump and probe pulses are sufficiently separated in energy that one can also isolate signals from the excited electronic state specifically as no stimulated emission is possible between electronic states within the mid-IR probe pulse's bandwidth (provided the 0-0' vibronic transition is excited). More importantly, the distinction between TRF and tIR anisotropies resides in the difference of the probed transition dipole moment. In TRF, it is an excited state emission of principally electronic character while in tIR it is a vibrational transition dipole moment that can provide spatially localized structural information, such as how the nuclear structure dynamics are coupled to a non-equilibrated electronic state.

The first 50 ps of the tIR time traces ($\omega$ = 1450 $cm^{-1}$) are shown for both polarizations and for both molecules in Figure 9.8 (top) where the polarization-dependence of the signals is very

clear. To ensure that the long-time dynamics of each polarized experiment matched as they should for pump-probe signal after reorientational diffusion has occurred (reorientation relaxation is expected on a ~35 ps timescale in HBQ[25]), a single scalar was used to scale the parallel data to match the perpendicular data at long delays ($\tau_2$ > 50 ps). This corrects for inconsistencies in signal level between experiments that are not reflective of the molecular dynamics.[41,42]

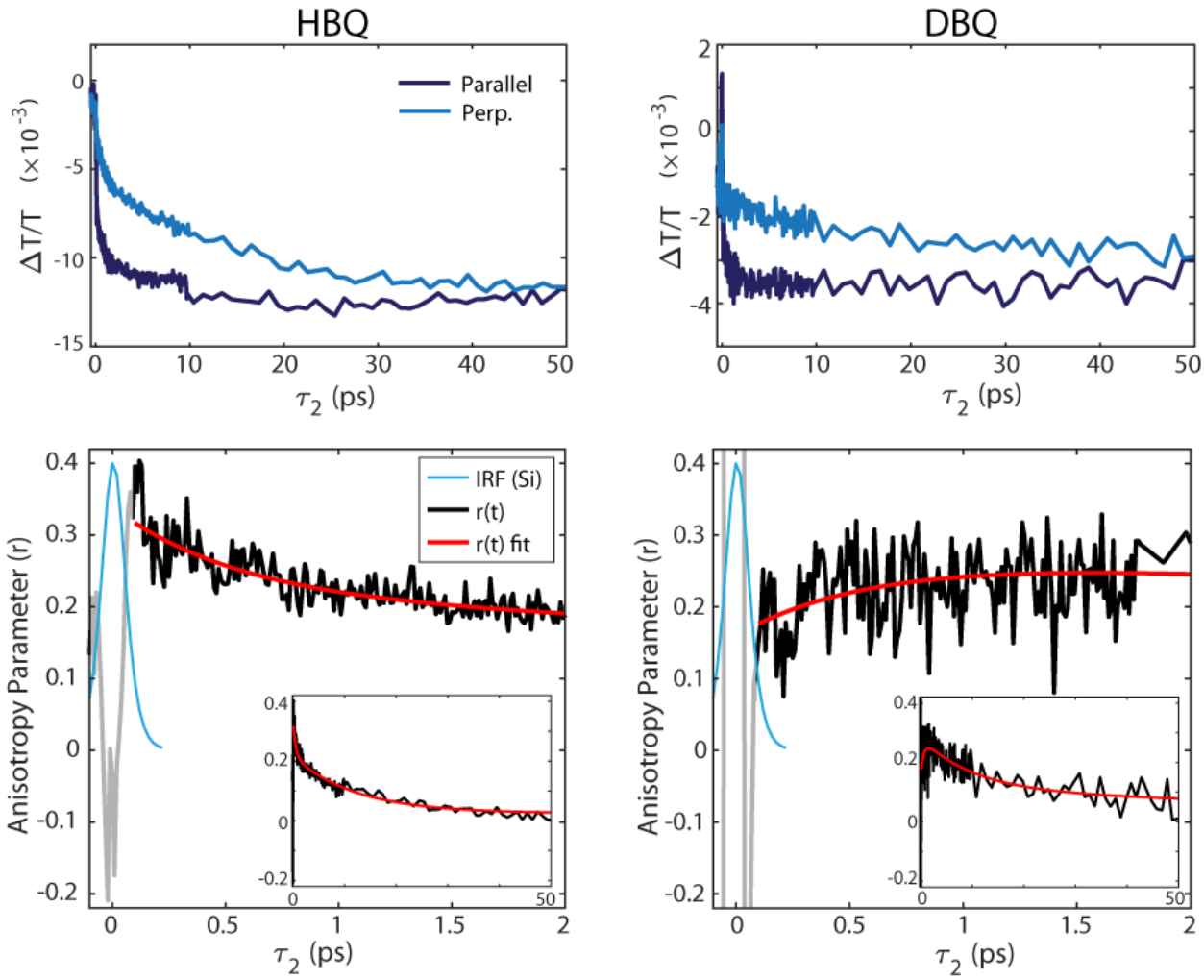


Figure 9.8. Transient-IR Anisotropy of HBQ and DBQ. (top) the parallel (dark blue) and perpendicular (light blue) time traces for HBQ (left) and DBQ (right) are shown for the first 50 ps of $\tau_2$ and vibrational frequency of 1450 $cm^{-1}$. (bottom) The tIR anisotropy, r(t), is calculated (black) and fits to the anisotropy (red) are shown for both molecules of the first 2 ps on data collected outside of the instrument response function (IRF, teal). The insets shows the 50 ps anisotropy.

The anisotropy is calculated by dividing the difference between the two polarized experiments by the isotropic signal, which is calculated by the sum of the parallel and two times the perpendicular experiments.[43,44]

From the fits to the anisotropy of HBQ at $\tau_2$ = 100 fs, the dipole angle between the electronic excitation and the 1450 $cm^{-1}$ vibrational motion is ~22° whereas the DBQ anisotropy fit yields ~38°. There is a strong resemblance between the HBQ anisotropy shown in Figure 9.8 and the TRF anisotropy of HBQ reported by Lee *et al.*[25] The tIR anisotropy fitting parameters are given in Table 9.2. The resemblance between these measurements is particularly interesting because of how different they are in principle due to the different transition dipole moments probed. While the maximum magnitude of the tIR anisotropy fit (100 fs) is not quite as large (0.32) as the reported TRF anisotropy (0.4), the tIR anisotropy clearly decays on a several hundred femtosecond timescale similar to what was reported in TRF. In our measurement, the anisotropy decay is a little longer than the reported ~350 fs

Table 9.2. Transient-IR Anisotropy Fitting Parameters for HBQ and DBQ. The time-dependent anisotropies for data following the instrument response ($\tau_2$ = 100 fs) were fit to the sum of three exponential decays. The amplitudes and lifetimes are given.

| | $A_1$ | $\tau_1$ (ps) | $A_2$ | $\tau_2$ (ps) | $A_3$ | $\tau_3$ (ps) |
|---|---|---|---|---|---|---|
| **HBQ** | 0.1 | 0.54 | 0.04 | 10 | 0.15 | 12.93 |
| **DBQ** | -0.12 | 0.62 | 0.16 | 9.54 | 0.07 | 50 |

decay of the TRF anisotropy; however, the similarity of anisotropic magnitude and timescales for this early time anisotropy raises the question of why apparently different measurements give such similar results. It was argued that the fluorescence emission dipole moment would not be affected by intramolecular vibrational redistribution or vibronic relaxation in order to assign the 310 fs anisotropy decay timescale to internal conversion.[25] Undoubtedly, the tIR anisotropic measurements include excited state vibrational information by describing the time-

dependent orientation of the electronic transition dipole moment and the vibrational transition dipole moment throughout the ESIPT process. The additional information provided by the tIR anisotropy of DBQ is also very interesting, as its anisotropy *grows in* rather than decays on a several hundred femtosecond timescale. It is notable that the calculated kinetic isotope effect from the decay times of the anisotropies yields 1.14, which does fit within the error estimate reported for the isotopic dependence of the TRF signal by Lee et al.[15] Of course, this several hundred femtosecond timescale is much too slow to reflect the actual proton transfer kinetic isotope effect as reported, but it suggests that other relaxation mechanisms that are isotopically sensitive are occurring on the sub-picosecond timescale in HBQ and DBQ. This strongly suggests that vibrational and vibronic relaxation mechanisms can account for this early, several hundred femtosecond lifetime without invoking the internal conversion from $L_a$ to $L_b$ mechanism used to explain the TRF anisotropy. Moreover, it may be reasonable to expect a greater change (in TRF anisotropy during the reported 310 fs anisotropy decay time if ultrafast internal conversion was occurring between two electronic states with dipole moments of significantly different orientation (e.g., $L_a$ and $L_b$ are orthogonal in phenanthrene).[26] Thus, the observed tIR anisotropies of HBQ and DBQ in this work can be attributed to intramolecular vibrational redistribution and vibronic relaxation as Schriever[23] and Tahara[22] conclude.

## 9.5 Excitation-Dependent Anisotropy Measured by 2D EV: Internal Conversion or Non-equilibrium Vibronic Relaxation?

The above discussion surrounding how to explain the several hundred femtosecond anisotropy decay times may be resolved through conducting a polarization-selective 2D EV experiment. In the same way that the tIR anisotropy can be obtained, the 2D EV experiment can further resolve the electronic excitation dependence of the anisotropy. If the 2D EV

experiment is conducted at a $\tau_2$ time when two different electronic states are relevant to the excited state dynamics, then the excitation dependent anisotropy may resolve these two electronic states. Figure 9.9 presents the polarization-selective 2D EV spectra of HBQ at $\tau_2$ = 150 fs for the same vibrational mode discussed in the tIR experiments. Importantly, only one peak in $\omega_1$ is measured in both polarized experiments. The 2D EV peaks both look to have very symmetric intensity profiles. These two spectral characteristics suggest that negligible difference in anisotropy will be viewed across $\omega_1$. To confirm this, the excitation dependent anisotropy is calculated for the $\omega_3$ peak maximum, which is shown in Figure 9.10.

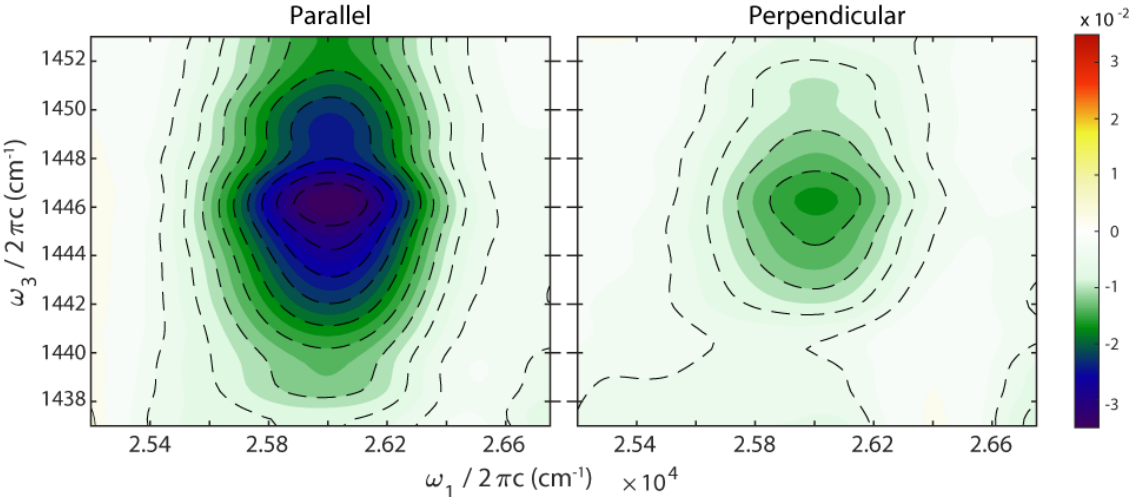


Figure 9.9. Polarization-Selective 2D EV Spectra of HBQ at $\tau_2$ = 150 fs. The spectra are globally normalized to show the relative signal amplitudes between the two polarized experiments. Dashed contours are negative and spaced at 10% intervals of the maximum 2D EV signal.

The constant anisotropy value of ~0.31 over the bandwidth of the electronic excitation in the 2D EV experiments provide strong evidence that the ESIPT dynamics at 150 fs in the K* relaxation can be described by only one electronic state. Given that the 150 fs delay in relaxation time is in the middle of the discussed ~350 fs anisotropy decay time, an $\omega_1$-dependent anisotropy should be observable if internal conversion between the $L_a$ and $L_b$ states was occurring. The excitation dependent anisotropy measured in the 2D EV spectra provide

confirmation that the internal conversion mechanism invoked to explain the 350 fs anisotropy decay may be ruled out and that this dynamic can instead be attributed to intramolecular vibrational redistribution and vibronic relaxation of the K* isomer on the $S_1$ potential energy surface.

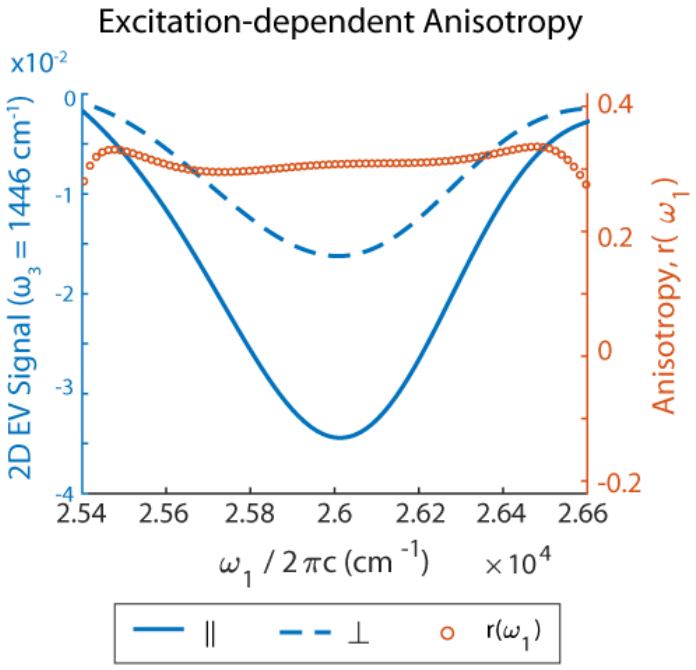


Figure 9.10. Electronic Excitation Dependent Anisotropy From Polarization-Selective 2D EV of HBQ. The parallel (perpendicular) traces of $\omega_1$ chosen for the 2D EV peak maximum at $\omega_3$=1446 $cm^{-1}$ is shown in solid (dashed) blue, the anisotropy is shown as red open circles.

## 9.6 CONCLUSIONS

In conclusion, the first 2D EV experiments of the ESIPT mechanism have been reported in this chapter. The ESIPT mechanism in HBQ and DBQ was investigated by fitting the electronic absorption spectra to a vibronic progression of a Franck-Condon active anharmonic vibrational mode and analyzing the ground state FTIR spectra to identify isotopic dependence. The tIR anisotropy of HBQ is shown to be surprisingly similar to reported TRF anisotropies of HBQ

and an isotopic dependence of the tIR anisotropy strongly suggests that this effect is governed by intramolecular vibrational redistribution on the several hundred femtosecond timescale following proton transfer. Finally, electronic-excitation dependent anisotropy measured from polarization-selective 2D EV on HBQ confirms that the ESIPT mechanism can be described as effectively adiabatic on $S_1$ without needing to invoke an ultrafast internal conversion dynamic between close-lying $L_a$ and $L_b$ as has been proposed previously.

More broadly, the results from this chapter demonstrate the potential for polarization-selective EV experiments to be insightful tools for understanding the orchestrated motions of electrons and nuclei during excited state proton transfer and proton-coupled electron transfer reactions. One can envision these methods being applied to more precisely define the nature of electronically excited chemical reaction coordinates that involve significant structural rearrangement of both the electronic and nuclear configurations. The intramolecular proton transfer studied in HBQ and DBQ with nonpolar solvent has made a convenient model system in which the proton transfer is mostly independent of solvent motion and so the bath degrees of freedom can be considered as the other intramolecular coordinates not directly involved with the proton transfer. This framework provides a somewhat internally consistent intramolecular parameter set in which the ESIPT mechanism can be described for HBQ. These experiments should soon be expanded to studying less constrained molecular systems displaying different flavors of excited state proton transfer, both intra- and intermolecularly. In these cases, more information may be obtainable through dynamic 2D EV line shape changes. Implementing the BBIR probe source to fully span the OH stretches that are most direct vibrational reporters of proton transfer dynamics in the typical $-O-H\cdots X$ molecular scheme will prove particularly informative. Pushing beyond a 2D EV experiment and

performing a 3D EV experiment with sufficiently short experimental time resolution to study an excited state proton transfer or proton-coupled electron transfer event as it occurs in real-time is a particularly exciting prospect – and one that may not be too far out of reach!

## 9.7 REFERENCES


(1) Mayer, J. M. Proton-coupled electron transfer: A reaction chemist's view; *Ann. Rev. Phys. Chem.* **2004**, *55*, 363-390.

(2) Gensch, T.; Heberle, J.; Viappiani, C. Proton transfer in biological systems; *Photochem. Photobiol. Sci.* **2006**, *5*, 529-530.

(3) Chou, P. T.; Solntsev, K. M. Photoinduced Proton Transfer in Chemistry and Biology; *J. Phys. Chem. B* **2015**, *119*, 2089-2089.

(4) Weller, A. Uber Die Fluoreszenz Der Salizylsaure Und Verwandter Verbindungen; *Naturwissenschaften* **1955**, *42*, 175-176.

(5) Barbara, P. F.; Brus, L. E.; Rentzepis, P. M. Intramolecular Proton-Transfer and Excited-State Relaxation in 2-(2-Hydroxyphenyl)Benzothiazole; *J. Am. Chem. Soc.* **1980**, *102*, 5631-5635.

(6) Ding, K.; Courtney, S. J.; Strandjord, A. J.; Flom, S.; Friedrich, D.; Barbara, P. F. Excited-State Intramolecular Proton-Transfer and Vibrational-Relaxation in 2-(2-Hydroxyphenyl)Benzothiazole; *J. Phys. Chem.* **1983**, *87*, 1184-1188.

(7) Elsaesser, T.; Schmetzer, B.; Lipp, M.; Bauerle, R. J. Excited-State Proton-Transfer in 2-(2'-Hydroxyphenyl)Benzothiazole - Transient Electronic Absorption Measured on the Picosecond Time Scale; *Chem. Phys. Lett.* **1988**, *148*, 112-118.

(8) Elsaesser, T.; Kaiser, W. Picosecond Spectroscopy of Intramolecular Proton-Transfer in Aromatic-Molecules; *Kvantovaya. Elektron.* **1988**, *15*, 1168-1172.

(9) Arnaut, L. G.; Formosinho, S. J. Excited-State Proton-Transfer Reactions .1. Fundamentals and Intermolecular Reactions; *J. Photoch. Photobio. A* **1993**, *75*, 1-20.

(10) Formosinho, S. J.; Arnaut, L. G. Excited-State Proton-Transfer Reactions .2. Intramolecular Reactions; *J. Photoch. Photobio. A* **1993**, *75*, 21-48.

(11) Laermer, F.; Elsaesser, T.; Kaiser, W. Femtosecond Spectroscopy of Excited-State Proton-Transfer in 2-(2'-Hydroxyphenyl)Benzothiazole; *Chem. Phys. Lett.* **1988**, *148*, 119-124.

(12) Frey, W.; Laermer, F.; Elsaesser, T. Femtosecond Studies of Excited-State Proton and Deuterium Transfer in Benzothiazole Compounds; *J. Phys. Chem.* **1991**, *95*, 10391-10395.

(13) Barbatti, M.; Aquino, A. J. A.; Lischka, H.; Schriever, C.; Lochbrunner, S.; Riedle, E. Ultrafast internal conversion pathway and mechanism in 2-(2 '-hydroxyphenyl) benzothiazole: a case study for excited-state intramolecular proton transfer systems; *Phys. Chem. Chem. Phys.* **2009**, *11*, 1406-1415.

(14) Lochbrunner, S.; Wurzer, A. J.; Riedle, E. Microscopic mechanism of ultrafast excited-state intramolecular proton transfer: A 30-fs study of 2-(2 '-hydroxyphenyl)benzothiazole; *J. Phys. Chem. A* **2003**, *107*, 10580-10590.

(15) Lee, J.; Kim, C. H.; Joo, T. Active Role of Proton in Excited State Intramolecular Proton Transfer Reaction; *J. Phys. Chem. A* **2013**, *117*, 1400-1405.

(16) Kim, C. H.; Joo, T. Coherent excited state intramolecular proton transfer probed by time-resolved fluorescence; *Phys. Chem. Chem. Phys.* **2009**, *11*, 10266-10269.

(17) Petrone, A.; Lingerfelt, D. B.; Williams-Young, D. B.; Li, X. S. Ab lnitio Transient Vibrational Spectral Analysis; *J. Phys. Chem. Lett.* **2016**, *7*, 4501-4508.

(18) Higashi, M.; Saito, S. Direct Simulation of Excited-State Intramolecular Proton Transfer and Vibrational Coherence of 10-Hydroxybenzo[h]quinoline in Solution; *J. Phys. Chem. Lett.* **2011**, *2*, 2366-2371.

(19) Luber, S.; Adamczyk, K.; Nibbering, E. T. J.; Batista, V. S. Photoinduced Proton Coupled Electron Transfer in 2-(2'-Hydroxyphenyl)-Benzothiazole; *J. Phys. Chem. A* **2013**, *117*, 5269-5279.

(20) Chou, P. T.; Chen, Y. C.; Yu, W. S.; Chou, Y. H.; Wei, C. Y.; Cheng, Y. M. Excited-state intramolecular proton transfer in 10-hydroxybenzo[h]quinoline; *J. Phys. Chem. A* **2001**, *105*, 1731-1740.

(21) Chou, P. T.; Wei, C. Y. Photophysics of 10-hydroxybenzo[h]quinoline in aqueous solution; *J. Phys. Chem.* **1996**, *100*, 17059-17066.

(22) Takeuchi, S.; Tahara, T. Coherent Nuclear Wavepacket Motions in Ultrafast Excited-State Intramolecular Proton Transfer: Sub-30-fs Resolved Pump−Probe Absorption Spectroscopy of 10-Hydroxybenzo[h]quinoline in Solution; *J. Phys. Chem. A* **2005**, *109*, 10199-10207.

(23) Schriever, C.; Barbatti, M.; Stock, K.; Aquino, A. J. A.; Tunega, D.; Lochbrunner, S.; Riedle, E.; De Vivie-Riedle, R.; Lischka, H. The interplay of skeletal deformations and ultrafast excited-state intramolecular proton transfer: Experimental and theoretical investigation of 10-hydroxybenzo[h]quinoline; *Chem. Phys.* **2008**, *347*, 446-461.

(24) Schriever, C. *Kohärenz auf reaktiven Potentialflächen: Beobachtung und Analyse molekularer Dynamik* Ph.D. Dissertation, Ludwig Maximilian University, 2008.

(25) Lee, J.; Joo, T. Photophysical Model of 10-Hydroxybenzo[h]quinoline: Internal Conversion and Excited State Intramolecular Proton Transfer; *B. Korean Chem. Soc.* **2014**, *35*, 881-885.

(26) Platt, J. R. Classification of Spectra of Cata-Condensed Hydrocarbons; *J. Chem. Phys.* **1949**, *17*, 484-495.

(27) Lochbrunner, S.; Schultz, T.; Schmitt, M.; Shaffer, J. P.; Zgierski, M. Z.; Stolow, A. Dynamics of excited-state proton transfer systems via time-resolved photoelectron spectroscopy; *J. Chem. Phys.* **2001**, *114*, 2519-2522.

(28) Lochbrunner, S.; Wurzer, A. J.; Riedle, E. Ultrafast excited-state proton transfer and subsequent coherent skeletal motion of 2-(2 '-hydroxyphenyl)benzothiazole; *J. Chem. Phys.* **2000**, *112*, 10699-10702.

(29) Stock, K.; Schriever, C.; Lochbrunner, S.; Riedle, E. Reaction path dependent coherent wavepacket dynamics in excited state intramolecular double proton transfer; *Chem. Phys.* **2008**, *349*, 197-203.

(30) Douhal, A.; Lahmani, F.; Zewail, A. H. Proton-transfer reaction dynamics; *Chem. Phys.* **1996**, *207*, 477-498.

(31) Herek, J. L.; Pedersen, S.; Banares, L.; Zewail, A. H. Femtosecond Real-Time Probing of Reactions .9. Hydrogen-Atom Transfer; *J. Chem. Phys.* **1992**, *97*, 9046-9061.

(32) Arthenengeland, T.; Bultmann, T.; Ernsting, N. P.; Rodriguez, M. A.; Thiel, W. Singlet Excited-State Intramolecular Proton-Transfer in 2-(2'-Hydroxyphenyl)Benzoxazole - Spectroscopy at Low-Temperatures, Femtosecond Transient Absorption, and Mndo Calculations; *Chem. Phys.* **1992**, *163*, 43-53.

(33) Chudoba, C.; Riedle, E.; Pfeiffer, M.; Elsaesser, T. Vibrational coherence in ultrafast excited state proton transfer; *Chem. Phys. Lett.* **1996**, *263*, 622-628.

(34) Schriever, C.; Lochbrunner, S.; Ofial, A. R.; Riedle, E. The origin of ultrafast proton transfer: Multidimensional wave packet motion vs. tunneling; *Chem. Phys. Lett.* **2011**, *503*, 61-65.

(35) Rini, M.; Kummrow, A.; Dreyer, J.; Nibbering, E. T. J.; Elsaesser, T. Femtosecond mid-infrared spectroscopy of condensed phase hydrogen-bonded systems as a probe of structural dynamics; *Faraday Discuss.* **2003**, *122*, 27-40.

(36) Mohammed, O. F.; Luber, S.; Batista, V. S.; Nibbering, E. T. J. Ultrafast Branching of Reaction Pathways in 2-(2 '-Hydroxyphenyl)benzothiazole in Polar Acetonitrile Solution; *J. Phys. Chem. A* **2011**, *115*, 7550-7558.

(37) Harris, D. C.; Bertolucci, M. D. *Symmetry and Spectroscopy: An Introduction to Vibrational and Electronic Spectroscopy*; Dover: New York, 1989.

(38) Wilson, E. B.; Decius, J. C.; Cross, P. C. *Molecular Vibrations*; Dover Publications: New York, 1980.

(39) Herzberg, G. *Infrared and Raman Spectra of Polyatomic Molecules*; D. Van Nostrand Co.: New York, NY., 1945; Vol. II.

(40) Petrone, A. (unpublished data).

(41) Stark, C. W.; Schreier, W. J.; Lucon, J.; Edwards, E.; Douglas, T.; Kohler, B. Interligand Electron Transfer in Heteroleptic Ruthenium(II) Complexes Occurs on Multiple Time Scales; *J. Phys. Chem. A* **2015**, *119*, 4813-4824.

(42) Pettersson Rimgard, B.; Föhlinger, J.; Petersson, J.; Lundberg, M.; Zietz, B.; Woys, A. M.; Miller, S. A.; Wasielewski, M. R.; Hammarström, L. Ultrafast interligand electron transfer in *cis*-[Ru(4,4′-dicarboxylate-2,2′-bipyridine)$_2$(NCS)$_2$]$^{4-}$ and implications for electron injection limitations in dye sensitized solar cells; *Chem. Sci.* **2018**, *9*, 7958-7967.

(43) Golonzka, O.; Tokmakoff, A. Polarization-selective third-order spectroscopy of coupled vibronic states; *J. Chem. Phys.* **2001**, *115*, 297-309.

(44) Wynne, K.; Hochstrasser, R. M. Coherence Effects in the Anisotropy of Optical Experiments; *Chem. Phys.* **1993**, *171*, 179-188.

# Chapter 10. EPILOGUE

## 10.1 Concluding This Journey

This journey began with the statement that extending our understanding of chemical reactivity to include a full description of how the complex choreography of different molecular coordinates contribute to a photochemical reaction is a demanding, but necessary, endeavor. Among many molecular coordinates, the interplay between the electronic and vibrational degrees of freedom are particularly important in condensed phase photochemistry; thus, the aim of the work in this dissertation was to construct a molecular-level description of the correlations between electronic and vibrational degrees of freedom. In many senses, this aim has been achieved. It would be naïve to suggest that a truly *complete* molecular-level description of the vibronic dynamics of interest in this work has been presented here. Ideally, the experimentalist is able to perform an experiment which fully resolves the *entire* molecular coordinate space – an "N-dimensional" experiment – and the relationships that connect each of these dimensions. Such an experiment would represent a significant leap toward completely satisfying the aim of this dissertation. However, in the same way that the theoretician must inevitably make simplifying assumptions to progress a line of inquiry, the experimentalist must "assume" away many dimensions of the molecule's true coordinate space because they may not be resolvable in practice – at least, not in *one* experiment. Of course, performing many different experiments that inform one another can be a tractable strategy for mapping the N-dimensional molecular coordinate space; although, the connections between these dimensions become less well defined in the absence of a direct observable in one experiment that describes the interrelation between two different molecular coordinates. In this way, I have achieved the aim by expanding the observable molecular coordinate space of a few selected photochemical

examples into two- and three-dimensions representing different molecular coordinates and quantified the couplings between these coordinates. These observables then allowed for constructing a more subtle description of multi-coordinate photochemical reactions, such as metal-to-ligand charge transfer (MLCT) and excited state intramolecular proton transfer (ESIPT). This contribution, while satisfying, is tempered with the realism that the true N-dimensional coordinate space is invariably much larger than two or three in most photochemical reactions.

Experimentally, this dissertation has contributed developments of the 2D EV spectroscopic technique to monitor photochemistry occurring on a broader range of excited states accessed in the UV region through the lens of many high frequency vibrational coordinates. Specifically, these experiments lend insight into the nature of the couplings between these degrees of freedom and how they may be involved with photochemical reactions. Instrumental developments such as these are important for continuing to expand the multidimensional spectroscopic toolbox at the disposal of scientists working on various photophysical problems.

Equally important to building the experiment is building the theoretical infrastructure for understanding the experimental signals once measured. These theoretical developments include an interpretation of the signatures from molecular vibronic phenomena in 2D EV and 2D VE spectra for a simplified molecular system consisting of two electronic states and one anharmonic vibration that experiences excited state equilibrium displacement and frequency-shifting. A set of vibronic selection rules resulted from this, which show that these spectroscopies are directly sensitive to (i) vibronic couplings (displacement and frequency shifting), (ii) to any nuclear dependence of the electronic transition dipole moment (non-Condon effects resulting from the breakdown of the Franck-Condon approximation), and (iii)

to vibrational dephasing dynamics which are electronic-state-dependent. This simplified case was then extended for 2D EV spectroscopy to include two vibrational modes with excited state vibronic couplings, which featured the sensitivity to Duschinsky mixing (excited state vibrational mixing). A treatment of the nonlinear orientational response showed that polarization-selective 2D EV spectroscopy can reveal both orientational and scalar non-Condon effects due to the vectoral nature of the electronic transition dipole moments. Altogether, this theoretical treatment emphasizes the potential benefits of conducting both 2D EV and 2D VE spectroscopies in tandem to obtain a more complete and self-consistent description of molecular vibronic couplings in solution. Complementary to important theoretical contributions describing intermolecular electronic delocalization over many molecules and harmonic vibrations,[1-3] the theoretical contributions of this dissertation are important for understanding complicated 2D EV spectra involving principally intramolecular dynamics of anharmonic high frequency vibrational motions with explicitly described vibronic couplings during photochemical processes. This theoretical infrastructure, understanding the role of high frequency vibrational motions in intramolecular charge transfer may be possible.

In the examples of molecular systems discussed in the previous chapters, particularly in the case of $N3^{4-}$, multidimensional EV spectroscopy has been showcased as a useful tool for unraveling complicated excited state multi-coordinate molecular processes in the condensed phase. In general, the studies on chemical systems show that excited state charge transfers and electronic delocalization about the intramolecular framework can be more fully understood using 2D and 3D EV spectroscopy. Additionally, photochemical processes in which significant structural reorganization occurs can be productively examined using multidimensional EV spectroscopy, such as a proton transfer event or a photoinduced isomerization. Finally, the use

of polarization-selectivity in multidimensional EV spectroscopy allows the experimentalist to gain valuable insight within the molecular frame to help distinguish between different electronic states and potentially observe time-dependent structural reorganization occurring on non-equilibrated excited state potential surfaces.

## 10.2 Future Directions and Uses for 2D EV Spectroscopy

### 10.2.1 *Coupled Electron-Proton Transfers in the Condensed Phase*

The study of ESIPT using 2D EV spectroscopy is only just beginning. While the first 2D EV experiments on HBQ have been discussed in this dissertation and yielded potentially valuable insight into the nature of the excited electronic state on which ESIPT proceeds in HBQ, these represent the initial results. A more complete and systematic study on this benchmark ESIPT system will include 2D EV spectra on the deuterated analogue, DBQ, which synthetically perturbs the nuclear degrees of freedom that should be most relevant during the proton (deuterium) transfer. The initial tIR results comparing HBQ and DBQ strongly suggest that the electronic and nuclear motions cannot be decoupled from one another as the Born-Oppenheimer approximation assumes. Rather, it is possible that one could consider the excited electronic state relevant for ESIPT as a system composed of an adiabatic enol state and a displaced adiabatic keto state which are mixed through a non-adiabatic mixing parameter. In this picture, the magnitude of the mixing parameter would provide the state on which ESIPT proceeds through the linear combination of the two adiabatic states and the physical interpretation of the mixing parameter may likely include some nuclear dependence. A very exciting future study on ESIPT would use a synthetic perturbation to the electronic degrees of freedom, such as by adding electron withdrawing groups to the aromatic backbone,[4] to measure a systematic change in the excited state nuclear dynamics as a function of the electronic

structure. In this way, a more detailed understanding of the nature of excited electronic states that promote ultrafast molecular structural changes, such as proton transfer, will be derived.

The ESIPT mechanism of HBQ represents a convenient way to constrain the molecular parameter space that could influence the structural dynamics of interest during *intra*molecular proton transfer. It is also a well-studied model system for the ESIPT dynamic which makes it a great starting point for a foray into studying proton-coupled electron transfer (PCET) dynamics with 2D EV spectroscopy. The study of *inter*molecular proton transfer[5-7] could prove even more exciting after a firm basis for studying excited state proton transfers with 2D EV has been established. In the intermolecular scenario, one could imagine a more rich molecular dynamics including solvent motion being required to fully describe the types of PCET dynamics which are currently garnering substantial research interest.[8-10] The 2D EV experiment could potentially be illuminating in these instances through measuring dynamic changes in the 2D EV peak positions, line shapes, and amplitudes.

### 10.2.2 *Multimode Vibronic Couplings in Multiple Excited Electronic States*

The theoretical description of the 2D EV and 2D VE spectroscopies in this dissertation has been simplified to include only two electronic states: the ground state and one excited state. This was useful for explicitly including vibronic couplings and anharmonicity into the excited electronic manifold, but it is a dramatic simplification by comparison to most photochemical reactions in which more than one electronic excited state is involved or where non-adiabatic electronic dynamics play a role. The extension of the one- and two-mode theoretical treatments discussed in this dissertation to include two excited electronic states which can be mixed through off-diagonal matrix elements in the Hamiltonian describing the excited electronic state manifold will be an exciting development. In particular, a treatment similar to more recent

work by the Jonas Group[11-13] but including the vibronically-coupled, anharmonic vibrations discussed here should be possible.

One could imagine two principal applications of this theoretical extension being directly pursued: 1) casting the two anharmonic vibrational modes developed here as the "tuning" and "coupling" coordinates that are relevant for the passage through a conical intersection,[14,15] and 2) the treatment of a (pseudo) Jahn-Teller system using 2D EV spectroscopy. In working through a specific example of the passage through a conical intersection, it would be particularly useful to highlight distinct spectral characteristics of 2D EV spectra that can identify specific vibrational modes as either tuning or coupling modes, or characterize them as spectator modes which play no direct role in the passing through the conical intersection. While some initial experiments[16] and theoretical work[17] has been done along these lines, a complete treatment has yet to be formally described. Explorations of polarization-selective 2D electronic spectroscopy signals at conical intersections[18] suggest that the treatment of the nonlinear orientational response in this dissertation could be useful for describing 2D EV anisotropic signatures at a conical intersection. The (pseudo) Jahn-Teller effect is a classic example of when vibronic couplings strongly influence molecular behavior.[19,20] It seems reasonable that a treatment of just one vibrational mode which is responsible for breaking the symmetry between two (near) degenerate electronic states is a feasible extension of the single anharmonic vibrational mode treatment discussed in this work for both 2D EV and 2D VE spectroscopy.

### 10.2.3 *Connecting IR-Active and Raman-Active Excited State Vibrational Spectroscopies*

There is great interest in following excited state molecular dynamics using a structurally sensitive probe such as molecular vibrations. One direct way of doing this is by using Raman-active spectroscopies. These techniques are experimentally convenient because the vibrational

information is obtained without needing light pulses of different frequencies from those used in an electronic transient absorption set-up. The popularity of femtosecond stimulated Raman spectroscopy (FSRS) for studying excited state structural dynamics on femtosecond timescales emphasizes the level of interest in this type of an investigation.[21-24] In principle, 2D EV spectroscopy provides similar information to FSRS because it is capable of following excited state dynamics on femtosecond timescales through monitoring structural motion of vibrations. However, these two techniques are distinguished by the types of vibrational motions that can be monitored. 2D EV spectroscopy specifically looks at IR-active vibrational motions through *resonantly driving* a vibrational motion, requiring a change in the molecular transition dipole moment as per IR-active vibrational selection rules; FSRS is specifically sensitive to Raman-active vibrations that are accessed *non-resonantly* through Raman scattering processes, requiring a change in the molecular polarizability to be detected according to vibrational selection rules.[25] In some ways, 2D EV spectroscopy has the potential to more directly probe structural modulations in excited electronic states because the vibrational motions are resonantly driven and 2D EV spectroscopy does not suffer from the same level of transient-absorption background signals that are intrinsic to FSRS for obtaining a vibrational spectrum. There are challenges associated with 2D EV spectroscopy which FSRS naturally avoids, such as the dramatic difference in molar absorptivity for an electronic transition versus a vibrational transition which can pose issues for sample selection and preparation in 2D EV spectroscopy. Considering symmetry arguments in the electronic selection rules within the Franck-Condon limit naturally suggests that following a Raman-active vibration may be more favorable because Raman activity requires the typically more symmetric changes of the polarizability tensor.[26] However, numerous examples of transient-IR and 2D EV experiments show that

many IR-active vibrations still contain symmetry components that do not render a zero-valued electronic transition moment integral. It seems reasonable that the differences between the IR and Raman vibrational selection rules could be exploited productively to understand greater detail about the nature and symmetry of excited electronic state dynamics by comparing FSRS and 2D EV experimental results on the same molecule. Furthermore, the 3D EV experiment has the potential to lend incredible insight into IR-Raman vibrational couplings and, at the very least, to identify excited state vibrational motions that are both IR and Raman active. This should arise because Raman-active vibrations can still be excited from the electronic transitions during the 2D EV pulse sequence, their detection just relies upon some physical interaction with the IR-active vibrational motions that are resonantly probed in the 2D EV experiment. As a result of such an interaction, it is possible that the excited state vibrations detected in the 2D EV experiment could be modulated by these Raman-active modes which would appear as an intensity modulation of the 2D EV features during $\tau_2$. Such an experiment could yield similar information to early attempts to measure IR-Raman vibrational couplings.[27]

### 10.2.4 *Using 2D EV and 2D VE Spectroscopies in Tandem*

Although the 2D EV and 2D VE spectroscopies are still relatively new and not yet used by more than a small handful of research groups worldwide, the opportunity to use both techniques on the same molecular system may prove advantageous. While each technique is directly sensitive to the same set of vibronic phenomena, each technique is more sensitive to one subset of vibronic characteristics to which the other is less sensitive. Thus, it is apparent that using both techniques in tandem could provide a more self-consistent framework for extracting and quantifying the role of vibronic phenomena in a photochemical reaction. The obvious differences between them include the fact that 2D VE spectroscopy does not directly

resolve any electronically excited state vibrational motions whereas 2D EV spectroscopy measures vibrations in both the ground and excited electronic states. However, 2D VE spectroscopy is intrinsically more sensitive to the equilibrium displacement of the excited state vibrations; obtaining the same sensitivity to excited state displacement in the 2D EV experiment may be more system-dependent and more experimentally challenging. Therefore, excited state molecular structural parameters, such as vibrational frequency shifts, anharmonicities, vibrational dephasing times, etc. are best probed with 2D EV whereas excited state displacements of vibrational coordinates are more easily revealed with 2D VE spectroscopy. For photochemical processes in which significant structural reorganization occurs in both the excited state and on a vibrationally hot ground state (e.g., continued ground state structural equilibration following internal conversion from an excited state), the 2D EV and 2D VE spectroscopies should prove most beneficial; together, they provide insights into the excited state and ground state potential energy surfaces from the perspective of specific vibrational coordinates involved in the complete photophysical cycle under investigation.

### 10.2.5 *Quantifying Intramolecular Electronic Localization and Delocalization*

The substantial interest in describing the extent of electronic localization and delocalization during photoinduced chemical dynamics is a research area to which 2D EV spectroscopy is naturally-suited. Within the specific framework of *intra*molecular electronic dynamics, the polarization-selective multimode theoretical treatment of 2D EV signals in this dissertation presents a number of different quantifiers for electronic localization/delocalization. The fact that Duschinsky mixing may be tractably investigated and interpreted through a single parameter in the vibronic Hamiltonian suggests that this parameter could also be interpreted as an extent of excited state electronic localization/delocalization depending on the orientation of

the vibrations that are mixed in the excited state. In the extreme case, two vibrational coordinates principally involving motions on opposing ends of a molecular structure become mixed upon electronic excitation implying that the excited electronic state has a delocalized effect about the entire molecule versus being localized to one side of the molecule. A time-dependent Duschinsky mixing parameter may also reveal the timescales for electronic localization and delocalization. These types of investigations would complement time-resolved X-ray based spectroscopies which exploit elementally-specific signals as reporters on electronic localization and delocalization. The analysis accomplished using 2D EV spectroscopy would provide a nice description of valence level electronic localization dynamics which are of central importance during the making and breaking of chemical bonds.

## 10.3 REFERENCES


(1) Lewis, N. H. C.; Dong, H.; Oliver, T. a. A.; Fleming, G. R. A method for the direct measurement of electronic site populations in a molecular aggregate using two-dimensional electronic-vibrational spectroscopy; *J. Chem. Phys.* **2015**, *143*, 124203.

(2) Dong, H.; Lewis, N. H. C.; Oliver, T. a. A.; Fleming, G. R. Determining the static electronic and vibrational energy correlations via two-dimensional electronic-vibrational spectroscopy; *J. Chem. Phys.* **2015**, *142*, 174201.

(3) Lewis, N. H. C.; Dong, H.; Oliver, T. a. A.; Fleming, G. R. Measuring correlated electronic and vibrational spectral dynamics using line shapes in two-dimensional electronic-vibrational spectroscopy; *J. Chem. Phys.* **2015**, *142*.

(4) Marciniak, H.; Hristova, S.; Deneva, V.; Kamounah, F. S.; Hansen, P. E.; Lochbrunner, S.; Antonov, L. Dynamics of excited state proton transfer in nitro substituted 10-hydroxybenzo[h]quinolines; *Phys. Chem. Chem. Phys.* **2017**, *19*, 26621-26629.

(5) Westlake, B. C.; Brennaman, M. K.; Concepcion, J. J.; Paul, J. J.; Bettis, S. E.; Hampton, S. D.; Miller, S. A.; Lebedeva, N. V.; Forbes, M. D. E.; Moran, A. M.; Meyer, T. J.; Papanikolas, J. M. Concerted electron-proton transfer in the optical excitation of hydrogen-bonded dyes; *Proc. Natl. Acad. Sci. USA* **2011**, *108*, 8554-8558.

(6) Weinberg, D. R.; Gagliardi, C. J.; Hull, J. F.; Murphy, C. F.; Kent, C. A.; Westlake, B. C.; Paul, A.; Ess, D. H.; Mccafferty, D. G.; Meyer, T. J. Proton-Coupled Electron Transfer; *Chem. Rev.* **2012**, *112*, 4016-4093.

(7) Hammes-Schiffer, S. When electrons and protons get excited; *Proc. Natl. Acad. Sci. USA* **2011**, *108*, 8531-8532.

(8) Hammes-Schiffer, S. Proton-Coupled Electron Transfer: Moving Together and Charging Forward; *J. Am. Chem. Soc.* **2015**, *137*, 8860-8871.

(9) Lennox, J. C.; Kurtz, D. A.; Huang, T.; Dempsey, J. L. Excited-State Proton-Coupled Electron Transfer: Different Avenues for Promoting Proton/Electron Movement with Solar Photons; *ACS Energy Lett.* **2017**, *2*, 1246-1256.

(10) Parada, G. A.; Goldsmith, Z. K.; Kolmar, S.; Pettersson Rimgard, B.; Mercado, B. Q.; Hammarström, L.; Hammes-Schiffer, S.; Mayer, J. M. Concerted proton-electron transfer reactions in the Marcus inverted region; *Science* **2019**, *364*, 471-475.

(11) Tiwari, V.; Peters, W. K.; Jonas, D. M. Electronic energy transfer through non-adiabatic vibrational-electronic resonance. I. Theory for a dimer; *J. Chem. Phys.* **2017**, *147*, 154308.

(12) Tiwari, V.; Jonas, D. M. Electronic energy transfer through non-adiabatic vibrational-electronic resonance. II. 1D spectra for a dimer; *J. Chem. Phys.* **2018**, *148*, 084308.

(13) Peters, W. K.; Tiwari, V.; Jonas, D. M. Nodeless vibrational amplitudes and quantum nonadiabatic dynamics in the nested funnel for a pseudo Jahn-Teller molecule or homodimer; *J. Chem. Phys.* **2017**, *147*, 194306.

(14) Domcke, W.; Yarkony, D. R. Role of Conical Intersections in Molecular Spectroscopy and Photoinduced Chemical Dynamics; *Annu. Rev. Phys. Chem.* **2012**, *63*, 325-352.

(15) Domcke, W.; Yarkony, D. R.; Koppel, H. *Conical Intersections: Electronic Structure, Dynamics & Spectroscopy*; World Scientific: Singapore, 2004; Vol. 15.

(16) Oliver, T. a. A.; Fleming, G. R. Following Coupled Electronic-Nuclear Motion through Conical Intersections in the Ultrafast Relaxation of beta-Apo-8 '-carotenal; *J. Phys. Chem. B* **2015**, *119*, 11428-11441.

(17) Lewis, N. H. C. *Two-Dimensional Electronic-Vibrational Spectroscopy* Ph.D. Dissertation, 2016.

(18) Farrow, D. A.; Qian, W.; Smith, E. R.; Ferro, A. A.; Jonas, D. M. Polarized pump-probe measurements of electronic motion via a conical intersection; *J. Chem. Phys.* **2008**, *128*, 144510.

(19) Bersuker, I. B. Modern Aspects of the Jahn−Teller Effect Theory and Applications To Molecular Problems; *Chem. Rev.* **2001**, *101*, 1067-1114.

(20) Fulton, R. L.; Gouterman, M. Vibronic Coupling .1. Mathematical Treatment for 2 Electronic States; *J. Chem. Phys.* **1961**, *35*, 1059-&.

(21) Kukura, P.; Mccamant, D. W.; Mathies, R. A. Femtosecond stimulated Raman spectroscopy; *Annu. Rev. Phys. Chem.* **2007**, *58*, 461-488.

(22) Hoffman, D. P.; Ellis, S. R.; Mathies, R. A. Characterization of a Conical Intersection in a Charge-Transfer Dimer with Two-Dimensional Time-Resolved Stimulated Raman Spectroscopy; *J. Phys. Chem. A* **2014**, *118*, 4955-4965.

(23) Hoffman, D. P.; Mathies, R. A. Femtosecond Stimulated Raman Exposes the Role of Vibrational Coherence in Condensed-Phase Photoreactivity; *Acc. Chem. Res.* **2016**, *49*, 616-625.

(24) Fang, C.; Frontiera, R. R.; Tran, R.; Mathies, R. A. Mapping GFP structure evolution during proton transfer with femtosecond Raman spectroscopy; *Nature* **2009**, *462*, 200-U274.

(25) Herzberg, G. *Infrared and Raman Spectra of Polyatomic Molecules*; D. Van Nostrand Co.: New York, NY., 1945; Vol. II.

(26) Harris, D. C.; Bertolucci, M. D. *Symmetry and Spectroscopy: An Introduction to Vibrational and Electronic Spectroscopy*; Dover: New York, 1989.

(27) Courtney, T. L.; Fox, Z. W.; Slenkamp, K. M.; Lynch, M. S.; Khalil, M. In *19th International Conference on Ultrafast Phenomena*; Optical Society of America: Okinawa, 2014, p 09.Wed.A.03.

# VITA

James Gaynor was born in Renton, WA. in 1991 and grew up in Vancouver, WA. He graduated from Columbia River High School in 2009 and was an intensely competitive soccer player throughout his childhood. James attended Concordia University (Portland) from 2009-2012 to play on the men's soccer team and study chemistry. In 2012, he transferred to the University of Portland to complete his chemistry degree with a focus on physical chemistry and optics. He graduated from the University of Portland with honors and high distinction in 2014, earning a Bachelor of Science degree in Chemistry (minors in Physics and Math). In Autumn 2014, James entered the Ph.D. program in Chemistry at the University of Washington and joined the research group of Professor Munira Khalil. In graduate school, James met his wife, Katie, who was also a chemistry graduate student. In December 2019, James completed his Doctor of Philosophy degree in Chemistry. He will begin as a postdoctoral scholar at U.C. Berkeley / Lawrence Berkeley National Lab working in the group of Professor Stephen Leone.

James is a Liverpool supporter, a cyclist, he enjoys dancing tango, and is a proud husband.

*Selected Honors and Awards*

| | |
|---|---|
| 2019 | Schmidt Science Fellowship Nominee |
| 2014-2019 | National Science Foundation Graduate Research Fellow |
| 2018 | Emil Wolf Outstanding Paper, OSA Frontiers in Optics |
| 2017 | Time Resolved Vibrational Spectroscopy Meeting Poster Prize |
| 2017 | Norman and Lillian Gregory Fellowship, University of Washington |
| 2016 | Siegman International School on Lasers Poster Prize |
| 2014-2016 | Clean Energy Institute Fellow, University of Washington |
| 2014-2015 | Outstanding Teaching Assistant Award, University of Washington |
| 2013 | Barry M. Goldwater Scholar |